Open Lake Disposal (Sediment and Water Quality Evaluation)

APPENDIX B4
INTEGRATED ANALYSIS OF UNCONFINED SEDIMENT ON NEAR SHORE SENSITIVE AREAS

Report No. 1
Data Analysis of the 1996 Arms Field Experiments in the Western Basin of Lake Erie

Report No.2
Climatological Analysis of Lake Erie Circulation and Transport for Sensitive Site Impacts

Report No. 3
A Multi-Size, Multi-Source Formulation for Determining Impacts of Sediments on Near-Shore Sensitive Areas

U.S. Army Engineer District, Buffalo • 1776 Niagara Street • Buffalo New York 14207

Integrated Analysis of the Impact of Unconfined Placement Activities on Nearshore Sensitive Areas

REPORT NO. 1

DATA ANALYSIS OF THE 1996 ARMS FIELD EXPERIMENTS IN THE WESTERN BASIN OF LAKE ERIE

by

Shiu-Chung Fan and Keith W. Bedford
Department of Civil and Environmental Engineering and Geodetic Science
The Ohio State University
Columbus, Ohio

Contract DACW39-95-K-0018
US Army Corps of Engineers
Waterways Experiment Station
Vicksburg, MS

January 22, 1998

TABLE OF CONTENTS

LIST OF TABLES

LIST OF FIGURES

APPENDIX LIST OF FIGURES

PROJECT OVERVIEW

There have been concerns expressed for some time that unconfined placement of material from dredging activities would cause potential adverse impacts on sensitive nearshore areas. Typical nearshore sensitive areas are beaches, water intakes (private or municipal), and wetlands and all are typically located some distance away from the placement site. Two issues require elaboration before answers can be obtained about the potential impact. The first question becomes, is the material from the site actually transported to the sensitive area?; while the second questions is what are the intensities of the water quality constituents associated with particles once (of if) they arrive at the nearshore zone from the placement site? Simple measurements at the nearshore site are the integrated sum of the sediments being carried to the site from not only the disposal site, but from other natural sources such as river tributary input or wind-driven circulation. Therefore, separating out the impacts specifically due to the disposal site is not achieved and the more basic question of whether placement site particles even get to the area is not addressed.

To perform the correct analysis, one must know not only the magnitude of the sediments entrained at the site, but the frequency, duration, and magnitude of the resulting particle transport to the sensitive areas. Therefore, it is necessary to describe the conditions required to cause the nearshore impact and, if necessary, this must be a probabilistic description. The presumption of this project is that the most robust assessment of the impacts must include data necessary to address both questions outlined above but that to date the first question has been ignored in most impact assessments. This proposed research program is therefore designed to respond robustly to the first question by pursuit of three objectives.

a. Determine by field measurements and model elaboration the entrainment and sediment flux climatology of the placement site;

b. Determine and quantify the conditions that most probably will result in placed material being transported to the sensitive area and the duration and intensities of the resulting particle loads; and

c. Compare the relative intensities of the sensitive site particle load from the placement site to those sensitive site loads originating from other sources (such as tributary input or local resuspension), during those times when placed particles are delivered to the nearshore site.

This project emphasizes and quantifies the physical conditions which are the basis for the impacts and leaves the associated water quality issues to other projects.

This report, Volume 1, by S. Fan and K. Bedford, is the first of a series of reports documenting the progress towards and results from pursuing these objectives. Volume 1 summarizes data from the field experiments performed at the site in 1996. The conclusions of the report are: First, barotropic motions due to seiches and storms are the

dominant source of low frequency currents at the site; second, wind waves arise quickly at the site and rapidly evolve into shallow water waves which erode material from the bottom; and third, water level and water column velocities from the Great Lakes Forecasting System were sufficient to track the wind and seiche effects.

The project WEB pages at http://superior.eng.ohio-state.edu/~sean/field.html and http://superior.eng.ohio-state.edu/~jklee/cooldata.html contains significant amounts of field data and site characteristics and these pages must be included and reviewed as a portion of the report.

CHAPTER 1. INTRODUCTION : BACKGROUND, OBJECTIVES, AND SCOPE

Due to the shallowness of the western basin of Lake Erie, regular dredging is necessary to maintain waterway traffic. The subsequent disposal of the dredged material, however, raises environmental concerns. After disposal at an offshore site, the dredged spoil may be released back to the water column via sediment entrainment or resuspension. The spoil material may be spatially transported and cause the degradation of water quality, for example, at a water supply intake. Therefore, the determination and selection of a suitable sediment-dumping site needs to be thoroughly investigated.

In order to fulfill the above-mentioned purposes, the US Army Corps of Engineers considered the possibility of reopening a previously used sediment dredge spoil dumping site in the western basin of Lake Erie. However, the previous knowledge about this sediment-dumping site was based on the irregular and sparse on-site sampling. Therefore, in the summer of 1996, five field data deployments were performed by The Ohio State University with the Acoustic Resuspension Measurement System (ARMS), which provided high quality data of the wind wave, current velocity and the suspended sediment climates at the spoil dumping site.

The objective of this report is to analyze information obtained from the sediment dredge spoil dumping site in the western basin of Lake Erie. The analysis is based upon the results from a field data collection project (ARMS) and a set of data obtained from the numerical model output (Great Lakes Forecasting System, GLFS, developed by the Ohio State University). By comparing the ARMS field data with the data output from the GLFS model, we can evaluate the model performance. The comparison of data and model output results is also a good indication for future studies such as selecting a proper sediment transport model or calibrating the parameters in the model calculations.

There are five main sections in the following report. Chapter 2 contains a description of the data used in this study from ARMS and GLFS, and includes an introduction to the setup of the '96 ARMS experiment. Chapter 3 summarizes the data comparison results between ARMS and GLFS. Chapter 4 illustrates the sediment

resuspension response to the important forcing functions, wave and current, at the site of interest. Chapter 5 includes a simplified seiche analysis which tries to quantify long wave effects on the bottom current. Chapter 6 contains a discussion and makes conclusions.

CHAPTER 2. DATA DERIVATION

2.1 Field Data from ARMS Experiment

Please refer to the project WEB pages listed in the project overview for additional information concerning the field data and deployment.

2.1.1 Deployment Site and Experiment Time Periods

The deployment site was located in the western basin of Lake Erie at (41°48'36" N, 83°17'00" W) (Figure 1). A total of five data sets, each from a 4-day continuous deployment, were collected near the bottom of the water column at the deployment site. During each deployment, ARMS collected more than 110 MB of data and stored the data in an on-board laptop computer. The deployment time periods are listed in Table 1.

Table 1. ARMS Deployment Time Periods for the 1996 Lake Erie Experiment

Data Number	Deployment Beginning Time			Deployment Ending Time		
Data Set #1	07/23	04:20 pm	EST	07/27	04:20 pm	EST
Data Set #2	08/02	01:39 pm	EST	08/06	01:39 pm	EST
Data Set #3	08/14	02:16 pm	EST	08/18	02:16 pm	EST
Data Set #4	08/22	12:55 pm	EST	08/26	12:55 pm	EST
Data Set #5	09/11	12:48 pm	EST	09/15	12:48 pm	EST

2.1.2 Measurement Variables, Locations, and Sampling Rates

ARMS collects four kinds of data. First, four vertically aligned 4 Hz Benthic Acoustic Stress Sensors (BASS) measure the three dimensional velocity field at heights of 125 cm (BASS I), 90 cm (BASS II), 55 cm (BASS III), 20 cm (BASS IV) above the bottom (AB). Second, an Acoustic Concentration Profiler (ACP), with a 1 Hz sampling rate, resolves the sediment concentration profile by 107 bins from the bottom to 124 cm AB. Third, two 4 Hz pressure transducers at 533 cm and 195 cm AB record the water pressure variation. Finally, a thermister records the water temperature every 3.2 minutes at 180 cm AB.

2.1.3 Available ARMS Data

Collections of pressure and sediment concentration data were unsuccessful in data sets #1 and #2 due to sensor malfunction. Temperature data were also lost during the second deployment. Except for the data mentioned above, all the other data items are available. Table 2 is a list of available data items from these five data sets.

Table 2. Available Data from ARMS Deployments

	Pressure	Velocity	Conductivity	Temperature
Data Set #1	No	Yes	No	Yes
Data Set #2	No	Yes	No	No
Data Set #3	Yes	Yes	Yes	Yes
Data Set #4	Yes	Yes	Yes	Yes
Data Set #5	Yes	Yes	Yes	Yes

2.2 ARMS Data Preprocessing

2.2.1 Time Scales

Physical processes, which take place in the water column, can be categorized by their differing time scales. Low frequency events, such as astronomical tides or seiches, usually have periods of more than 12 hours or several hours. Periods of long gravity waves range from about 5 minutes to several hours while periods of short gravity waves range from 1 to 30 seconds. Other higher frequency processes (turbulence) often have periods of less than 1 second. When dealing with specific phenomena, it is natural that one will try to separate the effects from those belonging to other different categories: This can be done by applying the averaging technique. Therefore, before data are subject to further analysis, the determination of proper time scales for the averaging process is an essential step and requires careful consideration.

2.2.2 Block Averaging

Reynolds averaging in time (τ) is the most common averaging scheme which can be expressed as follows:

$$\overline{\alpha} = \frac{1}{T}\int_{t}^{t+T} \alpha(\tau)\,d\tau \qquad (1)$$

where $\overline{\alpha}$ is the arithmetic averaged value of data time series, $\alpha(\tau)$;

T is the temporal averaging period, or the averaging window size;

t is the beginning time of the time series data $\alpha(\tau)$.

Through the averaging procedure, one can filter out high frequency fluctuations in the data. However, a proper choice of the averaging window size is very important. Another thing which needs to be considered during the selection of window size is the data stationarity. Bedford et al. (1990) indicated that in order to adhere to the requirement of stationarity, the typical averaging window size should be ten to fifteen minutes.

As a result, a data length of 10 minutes was selected to be the averaging window size when analyzing wave parameters. For longer period activities like current and seiche, a larger window size of 20 minutes was first selected to filter out the high fluctuation activities. In this way we can avoid the unnecessary confusion caused by the activities with periods less than 20 minutes.

An 84-hour time series data length was selected for the analysis of the ARMS parameters. The same 84-hour time period was also selected when we made data comparison between GLFS and ARMS. The reason for not selecting the total length of the data record is to avoid field effects introduced from the beginning setup activities (caused by the diver). The first 5 to 6 hours is considered as an adjustment time for ARMS.

2.2.3 Power Spectrum Analysis

Power spectrum analysis is widely used to examine the periodic features in time series data. It is a standard procedure and the details will not be stated here. Basically it is accomplished by performing a Fast Fourier Transform (FFT) to transform data from the time domain into the frequency domain. Before the data are subject to the FFT, however, they need to be filtered and detrended to reduce noise, as well as filtered with a Hanning window to reduce data leakage (for details, see Stull, 1988).

The software package applied to perform the power spectral analysis in this report was MATLAB (version 4.2c.1). From the results of the power spectral analysis, one can easily determine distinct spikes in the frequency domain, and then find the corresponding

time periods of different events (tides, seiches, long waves, group waves, short waves, etc.) contained in the time series data.

It should be noted that the Nyquist frequency, which represents the highest frequency that can be resolved by the power spectrum, is equal to $1/(2\Delta t)$ if the sampling time interval is Δt. Therefore, for an 84-hour data length, a data interval of 20 minutes is sufficient enough to resolve the long period activities like a seiche or current.

2.2.4 Calculations of ARMS Parameters

The equations and the procedures for the derivations of ARMS data are briefly described in this section.

2.2.4.1 Water Elevation (Water Surface Fluctuation)

Based on the hydrostatic assumption, time series of water elevation records can be derived from the pressure data through the following equations:

$$\eta = \frac{p + \rho g z}{\rho g K_p} \tag{2}$$

where η is the elevation of water surface relative to the still water level (SWL); p is pressure; ρ is the water density; g is the gravitational acceleration; z is the depth below the SWL of the pressure transducer; K_p is the pressure response factor expressed as:

$$K_p(z) = \frac{\cosh k(d+z)}{\cosh kd} \tag{3}$$

where k is the wave number and d is the water depth.

2.2.4.2 Wave Parameters

The wave parameters include the significant wave height, the significant wave period, the mean wave direction, the wave orbital velocity, and the bottom excursion amplitude. Calculation of these parameters is described as follows:

(1) Significant Wave Height and Wave Period

Significant wave height and wave period are determined by performing a zero up-crossing technique on the water elevation data. For each selected block (10 minutes), one can calculate the averaged water elevation as the SWL, then count the zero up-crossing events and record both the individual wave heights and wave periods in that block. The averaged value of the highest one third individual wave heights will be the significant wave height, and the corresponding averaged wave period will be the significant wave period.

(2) Wave Height Correction

Due to dynamic effects in the flow field, there usually exists a discrepancy during the process of pressure-water elevation transformation. It is necessary to correct this error for the wave height calculation and equation (2) will be rewritten as:

$$\eta=\frac{N(p+\rho gz)}{\rho g K_p} \tag{4}$$

where N is a correction factor which accounts for the dynamic effects in the transformation process, and all the other variables remain the same as in the equation (2).

Values of N depend on wave period, water depth, wave steepness, relative depth between the SWL and the pressure transducer, etc. Usually $N < 1$ for short-period waves and $N > 1$ for long-period waves (SPM, 1984). However, information about how these factors influence N is still not complete due to the complexity of the influencing factors. The nonlinearity induced by K_p also causes some degree of difficulty during wave height calculations. For the reasons mentioned above, Kuo and Chiu (1994) proposed a transfer function technique to combine the dynamic effects of N and K_p in the wave height calculations.

Based on the laboratory experiments performed by Kuo and Chiu (1994), the transfer function only depends on the location of the pressure transducer, z; the wave angular frequency, ω; and the gravitational acceleration, g. During the procedures of wave height correction, the transfer function has its major advantage of reducing the complexity and uncertainty from the determinations of N and K_p. The relationship between the transfer function and the wave heights is expressed as:

$$TF = \frac{\overline{P}}{H} \tag{5}$$

where TF is the transfer function; $\overline{P}$ is the wave height based on equation (2); and H is the wave height after the correction. The transfer function is calculated by:

$$TF = \exp(-0.905\frac{\omega^2 z}{g} - 0.027), \text{ with } 0.1 \le \frac{\omega^2 z}{g} \le 5.0 \text{ and } \frac{d}{L} \ge 0.07 \tag{6}$$

where d is the water depth and L is the wave length.

(3) Mean Wave Direction

By estimating the directional spreading function, one can calculate the mean wave direction from the spectral representation of wave properties (i.e., cospectra and covariances of p and u, or p and v). Buchan (1984) illustrated these procedures and performed the calculations in both the frequency domain and the time domain. The results of these two approaches show good agreement (Buchan, 1984). The equation for the calculation of mean wave directions $\overline{\theta}_{wav}$ in the time domain is as follows:

$$\overline{\theta}_{wav} = \arctan\{\frac{C_{pv}}{C_{pu}}\} \tag{7}$$

where C_{pv} is the covariance of pressure and v-velocity; C_{pu} is the covariance of pressure and u-velocity. The covariance is calculated by:

$$C_{\beta\gamma} = \frac{1}{N}\sum_{i=1}^{N}(\beta_i - \overline{\beta})(\gamma_i - \overline{\gamma}) \tag{8}$$

where N is the total data number in one block; β and γ represent p and u, or p and v, respectively; $\bar{\beta}$ and $\bar{\gamma}$ are the averaged values of β and γ in that block, respectively. The mean wave direction $\bar{\theta}_{wav}$ is then converted to the compass direction (69 degree offset, see Figure 1).

(4) Wave Orbital Velocity and Amplitude at Bottom (U_b and A_b)

According to linear wave theory, the wave orbital velocity at the bottom U_b is calculated by:

$$U_b = \frac{HgT}{2L}\cosh kd \tag{9}$$

where L is the wave length and T is the wave period. L can be derived through wave number k by solving the dispersion equation (Dean and Dalrymple, 1991). The bottom excursion amplitude A_b is calculated by:

$$A_b = \frac{HgT^2}{4\pi L}\frac{1}{\cosh kd} \tag{10}$$

2.2.4.3 Horizontal Bottom Current

Horizontal bottom current velocity can be calculated from the u and v velocity components collected by the BASS. Data collected by BASS IV (20 cm AB) are selected to compare with GLFS data for the reason that near bottom areas are of most concern for sediment transport. After block averaging, the magnitude of horizontal bottom current velocity is calculated by:

$$U = \sqrt{\bar{u}^2 + \bar{v}^2} \tag{11}$$

where $\bar{u}$ and $\bar{v}$ are the block averaged values of the u and v velocity components, respectively. The bottom current direction θ_{cur} can be calculated by:

$$\theta_{cur} = \arctan(\frac{\bar{v}}{\bar{u}}) \tag{12}$$

Same as the calculation procedures of mean wave direction ($\overline{\theta}_{wav}$), θ_{cur} is then converted to the compass reading.

2.2.4.4 Temperature

Temperature data are retrieved and compared directly with the data from the numerical model output. However, the recording time periods for temperature are a little different from those of other ARMS sensors. The four successful recording time periods for temperature are listed in Table 3. The time series temperature data are first converted from EST to UTC time and then the proper 84-hour periods are selected for comparison.

Table 3. Temperature Recording Time Periods (EST Time)

	Data Set #1	Data Set #2	Data Set #3	Data Set #4
Beginning Time	07/23 12:00:01	08/14 12:19:24	08/22 11:36:47	09/11 12:20:01
Ending Time	07/27 11:56:49	08/18 12:16:12	08/26 11:33:35	09/15 12:16:49

2.2.4.5 Sediment Concentration and Grain Size Distribution Analysis

Two one-liter grab samples were taken from each of the last four ARMS deployments at two positions (top: about 1.0 m AB; bottom: about 10 to 15 cm AB) at the experiment site. Grab samples were then brought back to laboratory to analyze. The measurements of the total suspended solid were based on Standard Methods for the Examination of Water and Wastewater, 16th ed., 1985. The measurements were carried out at Dr. Hal Walker's Water Chemistry Laboratory, 130 Agriculture Engineering, The Ohio State University. Each grab sample was partitioned into three parts to enable repeated measurements. The results of total suspended solid (sediment concentration) for each sample are shown in Table 4.

The grain-size distribution was measured by the Automatic Particle Size Analyzer, Hiac Model-320, at Dr. Keith Bedford's Coastal Engineering Laboratory, 018 Civil Engineering, The Ohio State University. Again, each grab sample was partitioned into two or three parts to enable repeated measurements. The analysis results were plotted by MATLAB to calculate the values of d_{50} for each sub-sample. Table 5 lists the analysis results of d_{50}.

The ACP records 140 bins (bin #1 is on top) of acoustic signals. With the help of total suspended solid analysis, the acoustic signals are converted to concentration values (mg/l). The concentration data, which corresponds to the same 84-hour time periods (UTC) of the other variables, are then extracted from Data Sets #3, #4, and #5 for future analysis.

Table 4. Total Suspended Solid Analysis

Sample Date (UTC)	Sample No.	Filter Disk Mass (g)	Filter Disk + SS Mass (g)	Sample Vol. (ml)	TSS Conc. (mg/l)	Mean TSS Conc. (mg/l)	STD Conc. (mg/l)
8/2 Bottom	1-1	0.1974	0.2007	208	15.87		
	1-2	0.1963	0.1997	188	18.09	16.58	1.31
	1-3	0.1983	0.2010	171	15.79		
8/2 Top	2-1	0.2037	0.2040	203	1.48		
	2-2	0.2020	0.2023	211	1.42	1.45	0.04
	2-3	0.1935	0.1936	205	(0.49)*	(1.13)*	(1.12)*
8/14 Bottom	3-1	0.2004	0.2046	211	19.91		
	3-2	0.1985	0.2034	220	22.27	21.89	1.82
	3-3	0.1967	0.2022	234	23.50		
8/22 Bottom	4-1	0.1915	0.2025	213	51.64		
	4-2	0.1918	0.2036	224	52.68	52.90	1.39
	4-3	0.2000	0.2124	228	54.39		
8/22 Top	5-1	0.1919	0.1924	220	2.27		
	5-2	0.1912	0.1917	238	2.10	2.06	0.24
	5-3	0.1976	0.1980	222	1.80		
9/11 Bottom	6-1	0.1927	0.2028	232	45.53		
	6-2	0.1861	0.1984	236	52.12	49.15	3.71
	6-3	0.1794	0.1910	224	51.79		
9/11 Top	7-1	0.1831	0.1855	230	10.43		
	7-2	0.1931	0.1957	229	11.35	10.25	1.20
	7-3	0.1993	0.2014	234	8.97		

* Numbers in parentheses represent outliers or statistics including outliers.

The distance between two adjacent bins is about 1.16 cm. After observing the time series concentration data at bins #107, #108, and #109 (Figure 2, 3, and 4), we define bin #108 as the bottom for all three data sets (#3, #4, and #5). The location of bin #1 is then defined at 124 cm AB.

Table 5. Values of d_{50}

Sample Date	Sample Number	d_{50} (mm) for Each Subsample	Mean d_{50} (mm) for Each Sample	Standard Deviation (mm)
8/2 Bottom	1-1	51.29	45.55	8.12
	1-2	39.81		
8/2 Top	2-1	39.11	36.11	4.24
	2-2	33.11		
8/14 Bottom	3-1	43.35		
	3-2	41.69	42.90	1.06
		43.65		
8/22 Bottom	4-1	45.60		
	4-2	43.15	43.97	1.41
	4-3	43.15		
8/22 Top	5-1	43.65		
	5-2	41.69	41.12	2.86
	5-3	38.02		
9/11 Bottom	6-1	45.37		
	6-2	42.66	42.16	3.48
	6-3	38.46		
9/11 Top	7-1	43.15	39.73	4.84
	7-2	36.31		

2.3 GLFS Data

Based on the Princeton Ocean Model (POM) and GLERL-Donelan wave model, the Great Lakes Forecasting System (Bedford & Schwab, 1994) provides estimated data for comparison with the field data collected by ARMS at the '96 experiment site. The corresponding hourly data from GLFS includes water elevations, wave parameters (height, period, and direction), analytical wind field information (velocity and direction), current information, and water temperature.

The grid resolution currently used by GLFS in Lake Erie is 2 km. The experiment site is surrounded by four grid points (Figure 1) and estimates from these four points are extracted from the model first. After examining the model output, we found only small differences among these four points. Thus, instead of a linear interpolation, data from the nearest point is selected for comparison with field data. The distance between the selected model grid point and the deployment site is about 0.9 km.

GLFS is based on the sigma coordinate system for model calculation. For the Lake Erie application, eleven layers of grid points are used in the vertical direction (1st layer: water surface; 11th layer: bottom). The depth at the selected grid point is about 6.1 m. As a result, data from the 10th layer (about 61 cm AB) is extracted for data comparison. However, the averaged local depth is about 7.7 m around the ARMS deployment site. This gives an error of about 1.6 m in the water depth.

GLFS operates according to the UTC, which is 5 hours ahead of the EST. It should be noticed that the time difference must be converted before performing the data comparisons. The time conversion between UTC and EST is UTC = EST + 5 hrs.

CHAPTER 3. DATA COMPARISONS BETWEEN ARMS AND GLFS

3.1 Time Periods for Data Comparisons

For the reasons mentioned in section 2.1.3, the data comparison will concentrate on Data Sets #3, #4 and #5. Time period for data comparison begins right after the ARMS adjusting time period (the first 5 to 6 hours in each data set). A total of 84-hour time period is selected from each of these three data sets (#3, #4, and #5) as the comparison time period.

3.2 Water Surface Fluctuations (η)

The water surface fluctuations from GLFS show good agreement in trend with the field data (Figures 5, 6, and 7), except there is a phase lag in Data Set #4. The averaged root-mean-square (rms) errors for η between GLFS and ARMS are listed in Table 6.

Table 6. Averaged RMS Errors Between ARMS and GLFS:
Water Surface Fluctuations and Wave Parameters

	η(cm)	H_{m0}(cm)	T_p(sec)	Wave Dir. (deg)	Wind & Wave Dir (deg)
Data Set #3	3.73	9.74	0.57	±10.96	±14.71
Data Set #4	4.65	6.71	0.59	±16.67	±23.07
Data Set #5	7.92	16.77	0.48	±12.40	±12.19

*Calculations for the averaged rms errors are under high wave conditions only.

3.3 Wave Parameters and Wind

The maximum wave heights from ARMS are 57.24, 50.48, and 106.35 cm for Data Sets #3, #4, and #5, respectively. Table 4 also lists the values of the averaged rms errors for all wave parameters. The predicted wave heights from GLFS basically follow the trends of ARMS data (Figures 8, 9, and 10). Time series ratios of wave heights (GLFS/ARMS) are plotted in Figure 11.

Wave periods show a larger discrepancy for the low-wave periods. Time series ratios of wave periods (GLFS/ARMS) are plotted in Figure 12. Wave directions are close to each other during the high-wave periods. That is, in Data Set #3, 08/15/06:00 to 08/16/06:00 (UTC); Data Set #4, 08/24/03:00 to 15:00 (UTC) ; and Data Set #5,

09/14/00:00 to 09/15/12:00 (UTC). During these high-wave periods, ARMS wave directions also follow GLFS wind directions very well. As a result, except for the wave height parameter, the averaged rms errors for all the other wave parameters are calculated only for these high-wave periods.

Time series ratios of water depth to wave length (d/L) are given in Figure 13. All of the waves in Data Set #3 and #4 belong to the category of deep water waves ($d/L > 0.5$). Most of the time, waves in Data Set #5 are deep water waves. However, from 09/14/13:00 to 09/15/04:00 (UTC) waves belong to the category of transitional waves ($0.05 < d/L < 0.5$).

It is obvious that wave height relates to wind velocity strongly. Wind is always the main forcing function to increase the wave height. However, an exceptional case is found in Data Set #4 during the time period 08/24/00:00 to 08/24/12:00. In this time period we find a significant increase of wave heights corresponding to an insignificant variation of local wind velocity. The reason why this happens can be found after we examine the corresponding plots of the global wind field and the plots of wave heights for Lake Erie (Figures 14 and 15, products from GLFS). In Figure 14 (08/24/00:00, UTC), the wind field is calm around the deployment site. But in the northeast part of the western basin, there is a stronger wind from NEE to SWW. High waves in this region are heading toward the deployment site. In Figure 15 (6 hours later) we find that the waves caused by this stronger wind field have arrived at the deployment site. Thus, the increase of wave heights at our deployment site during this period of time can be explained as a result of the wave propagation from the northeast of the western basin.

3.4 Bottom Current and Wind

Maximum bottom current velocities from ARMS (BASS IV) are 6.38, 5.82, 7.37 cm/s for data #3, #4, and #5, respectively. The corresponding averaged rms errors of bottom current velocities between ARMS and GLFS are 2.02, 1.83, and 4.09 cm/s, respectively. Plots of time series horizontal bottom current velocity (BASS IV) and the GLFS surface wind direction are given in Figures 16, 17, and 18. Comparisons have also been made for bottom current directions between GLFS and ARMS as well as the direc-

tions between bottom current (ARMS) and incoming wind (GLFS) (Figures 16, 17, and 18). There were no special patterns between wind directions and bottom current directions, though a reversed current phenomenon was first expected at the beginning of the analysis.

It is interesting that in Data Set #5, even during the high-wave periods (large storm events), the bottom current exhibits small variations in magnitudes in the ARMS data. This implies that the bottom current velocity is not sensitive to the magnitude of surface wind velocity.

3.5 Bottom Temperature

Temperature data from GLFS follows the trends of the ARMS data closely (Figure 19). It shows a very good agreement in Data Set #3 (the temperature deviations between GLFS and ARMS are within 1 °C). In Data Sets #4 and #5, however, there is a deviation of about 2 to 3 °C. The averaged rms values of temperature for Data Sets #3, #4, and #5 are 0.75, 2.14, and 3.15 degrees, respectively.

CHAPTER 4. WAVE AND CURRENT EFFECTS ON THE BOTTOM

4.1 Wave Orbital Velocity and Bottom Excursion Amplitude

In the bottom boundary layer, waves are more efficient in causing sediment resuspension, while currents are more capable of transporting the suspended load horizontally. Accordingly, the sediment transport models are usually categorized into three directories: the pure wave model, the pure current model, and the combined wave-current model. As a result, except for information about wave height and wave period, the values of wave orbital velocity at the bottom U_b, and the bottom excursion amplitude A_b are also important indices for the selection of a proper model in the shallow or transitional water areas.

Values of U_b and A_b for Data Sets #3, #4, and #5 are shown in Figures 20, 21, and 22, respectively. Most of the time, both values of U_b and A_b are small. And both values are only significant under the high-wave conditions. The maximum magnitudes of U_b for Data Sets #3, #4 and #5 are 3.73, 3.89, and 12.02 cm/s, respectively. The maximum A_b are 1.72, 2.03, 7.10 cm, respectively. When U_b and A_b are small, current becomes the dominant forcing function for the sediment transport.

4.2 Sediment Concentration Response to Wave and Current at Bottom

Time series sediment concentration at 20 cm AB and the integrated sediment mass (from bottom to 124 cm AB, per 1 cm^2) for Data Sets #3, #4, and #5 are shown in Figures 23, 24, 25, respectively. For viewing convenience, time series of the ARMS wave height, horizontal bottom current velocity and direction (20 cm AB) are re-plotted with sediment concentration (20 cm AB) and shown in Figures 26, 27, and 28. Because of the different effects of wave action (to initiate sediment suspension) and current (to keep sediment suspended), we expect that conditions with higher sediment concentration would be associated with high-wave and larger current time periods.

Combined wave and current effects on the bottom sediment concentration can be observed in Data Sets #3, from 08/15/06:00 to 08/16/03:00. After 08/16/03:00, current keeps sediment suspended and lasts until 08/16/20:00. During the second period of sediment resuspension time (08/16/03:00 to 08/16/20:00), the magnitude of bottom velocity

is not very significant. However, after observing the bottom current directions, we first assume that sediment resuspension conditions are favorable when current directions point to north or range from southwest to south.

In Data Set #4, although the higher waves begin to form at 08/24/03:00, the current directions within this period of time are mostly heading toward the east. Without the help from current (current is not within the favorable directions), sediment concentration at 20 cm AB during this period of time is even less than that under a mild wave condition which is associated with a SSW current (08/25/18:00 to 08/26/00:00). A mild combined-wave and current condition can still be found during this time period. However, the peak concentration at 08/25/13:00 defies explanation at this moment. The first peak in the concentration at 08/23/13:00 may be caused by the current only (current directions point to near north or range from S to SSW).

Data Set #5 displays the most dramatic time series sediment concentration record. From 09/13/06:00 to 09/14/12:00 almost nothing happens on the bottom, despite the fact that wave heights and current magnitudes are both larger than those in the previous two data sets. High-wave conditions prevail during this deployment time period. Directional current effects on the sediment resuspension can only partially explain the small sediment concentration between 09/13/06:00 and 09/14/12:00 (current directions are not within the favorable ranges most of the time), because effects from wave heights should not be ignored (wave heights keep on increasing from 30 to 80 cm) during this period of time. However, after 09/14/12:00, the sediment concentration begins to increase and the combined-wave and current effects are clearly shown after this point. Waves would be the dominant forcing function during the time period 09/12/12:00 to 09/13/06:00, because current directions are not within the favorable ranges most of the time. With a little help from the current, the time series concentration shows a small peak at 09/12/21:00.

The directional current effects on the sediment concentration might be attributed to the characteristics of the local bottom topography. However, the resolution of current site-scan sonar maps (bathymetry data) in hand (maps with Journal of The Great Lakes Research, 1997, vol. 2) is not sufficient enough to describe detailed bottom features of the

experiment site. Bathymetry data with higher resolution at the deployment site would be very beneficial for any further analysis.

CHAPTER 5. SEICHE EFFECTS ON THE BOTTOM CURRENT

Seiches are standing waves. They can be found in enclosed basins like seas, lakes, and inlets, as well as in open basins like channels or bay areas. Wind, air pressure fluctuations, tide, earthquake, etc can generate seiches. However, one of the most common origins of seiche activity in a closed lake basin is caused by the wind-induced piling-up of water at one end of the basin, which leads to the fluctuating and periodic motion of water when the wind decreases.

People often overlook seiches because their effects usually do not last very long. Another reason is due to the low frequency of occurrence of extreme events. However, for sediment transport in the bottom boundary layer after a storm event, if there is no other significant external force to change the water dynamics, seiching could be an important factor.

5.1 Seiche Periods

A power spectrum analysis was performed on Data Sets #3, #4, and #5 for water elevation (Figures 29, 30, and 31) , u-velocity (Appendix), and v-velocity (Appendix), respectively. The distinct periods which correspond to the peak frequencies are found from the power spectrum diagrams for each data set and their values are listed in Tables 7, 8, and 9. The lowest six seiche periods for the Lake Erie basin, from Hamblin (1987), are listed in Table 10 for comparison.

Although the 14.56-hour period, which corresponds to the first mode seiche in Lake Erie, has been found in all three data sets, it is most frequently shown in Data Set #3. This should not be a surprise after examining the water elevation data, wind field data, and wave height information (in the plots of wave parameters). In Data Set #3 (Figures 5 and 8), a storm event is followed by a long period of mild wind condition, which is perfect for observing the seiche activity. Data Set #4 (Figures 6 and 9) is a little too calm to initiate a

Table 7. Spectral Analysis on Data Set #3 (20-Minute Averaging)

DATA TYPE									
Water Elevations		Velocity (BASS)				Velocity (BASS)			
P1	P2	I	II	III	IV	I	II	III	IV
Period, hr		Period, hr				Period, hr			
14.56	14.31	10.82					14.56	14.56	
5.38	5.48	7.12	5.38	4.29		5.38	5.38	5.48	5.48
3.93	3.86								
2.18	3.08	3.08	2.72	3.30	3.19	2.82	3.93	3.93	
1.73	1.79					1.94			

Table 8. Spectral Analysis on Data Set #4 (20-Minute Averaging)

DATA TYPE									
Water Elevations		Velocity (BASS)				Velocity (BASS)			
P1	P2	I	II	III	IV	I	II	III	IV
Period, hr		Period, hr				Period, hr			
14.56	14.56					14.45			
							8.63		
6.17	6.19	6.19	6.19	6.19	6.19		4.85		6.19
3.93	3.93	3.60	3.93			3.93	3.60	3.25	3.93
1.73	1.88		2.06	2.15			2.72		3.08
	1.40								

Table 9. Spectral Analysis on Data Set #5 (20-Minute Averaging)

DATA TYPE									
Water Elevations		Velocity (BASS)				Velocity (BASS)			
P1	P2	I	II	III	IV	I	II	III	IV
Period, hr		Period, hr				Period, hr			
			14.56						
		6.19	6.19	6.19	6.19				
3.93		3.93	3.93	3.93	3.93	3.93	3.93	3.93	3.93
	2.59	2.82	2.82	2.82	2.82				
1.87		2.05		2.05					
	1.49								

significant variation of water elevation, while Data Set #5 (Figures 7 and 10) is generally a series of storm periods. However, both Data Sets #4 and #5 show two distinct peaks of 6.19 and 3.93 hours, which are close to the third and the fifth mode seiche periods, respectively.

Table 10. Observed & Computed Periods of the Lowest Six Gravitational Seiches of Lake Erie (after Hamblin 1987)

Mode	Observed Period, hr Spectral Analysis*	Computed Period, hr 1-D Model**	Computed Period, hr Inviscid Model**	% Error in Inviscid Periods***	Computed Period, hr Viscid Model***
1	14.38	14.08	14.14	-1.6	14.40
2	9.14	8.92	8.95	-2.0	9.10
3	5.93	5.70	5.84	-1.5	5.91
4	4.15	4.11	4.20	1.2	4.18
5	—	3.69	3.72		3.80
6		3.32			—

*Platzman & Rao (1964a) **Platzman & Rao (1964b) ***Hamblin (1976)

It is worth mentioning that in Data Set #3 the first mode period (14.56 hours) is only shown in the elevation and v-velocity data. This can be explained by the fact that the v-direction is almost identical with the longitudinal direction of Lake Erie, and the u-direction is perpendicular to it (see Figure 1).

The basin length for possible transverse seiches passing the deployment site is about 30 km (Figure 1). Based on the Merian formula, if an averaged depth in the western basin of Lake Erie is 8 m (Saylor and Miller, 1987), the 30 km transverse length in the western basin will give a 1st-mode transverse seiche period of 1.88 hours. From the power spectrum diagram of water elevation data of Data Sets #3 and #4 (Figures 29 and 30), a distinct spike with period of 1.73 hours has been found and would be close to this 1st-mode transverse seiche. Another possible longitudinal seiche which could pass the deployment site is between the west end of the western basin and Pelee Island (Figure 1). The distance between these two point is about 93 km. When we apply the Merian formula with the average depth of 8 m, a 1st-mode seiche period of 5.83 hours for the western basin can be derived.

It should be noted that the Merian formula is only a rough estimation of the seiche period. This formula is based on the assumption of a rectangular basin with a uniform depth everywhere. It also neglects the effects due to the earth's rotation as well as friction at the water-air and water-bottom interfaces. As a result, one should be very careful when

applying this formula. For the seiche analysis, the Merian formula can only be used as a tool for testing calculations.

5.2 Theory and Equations for Seiche Calculations in Closed Basins

5.2.1 Equations for Standing Waves (Long Waves)

Seiches in Lake Erie can be considered standing waves in shallow water (long wave theory). The wave celerity C can be calculated by:

$$C = \sqrt{gd} \tag{13}$$

The simplest formula used to calculate the seiche period is the Merian formula:

$$T_{sch} = \frac{2l}{n\sqrt{gd}} \tag{14}$$

where T_{sch} is the seiche period corresponding to nth node; l is the basin length.

For a standing wave in a long rectangular basin, water elevation, η_s, is expressed as:

$$\eta_s = \frac{H}{2}\cos kx \cos \omega t \tag{15}$$

The horizontal water particle velocity, U_s, under a standing wave is:

$$U_s = \sqrt{\frac{g}{d}}\frac{H}{2}\sin kx \sin \omega t \tag{16}$$

According to the long wave theory, the vertical particle velocity is insignificant when compared with the horizontal particle velocity. Long waves can be considered as shallow water waves (the wave length is much greater than the depth of water body). Water particle motion under a wave follows a circular orbit. When water depth becomes shallow, the circular orbit will gradually change to an elliptical orbit. In the limit as the water depth becomes extremely shallow, the orbit will become a line (Figure 32). As a result, if the ratio of wave length to water depth becomes extremely large, the horizontal particle velocities will be nearly the same for one particular cross section (from water surface to the bottom). Further, for a standing wave, U_s is maximum under the nodal point and zero under the wave crest.

5.2.2 Standing Waves with Frictional Damping

The seiche phenomena is a kind of free oscillation in a water body. It usually dies out gradually due to disturbances from outside forcing. When the wind is mild and has little effect on water body, bottom friction plays an important role in seiche damping. The quadratic friction law can be applied to the long wave and is expressed as follows:

$$\tau_b = \frac{\rho f U|U|}{8} \tag{17}$$

where f is the Darcy-Weisbach friction factor and U is the fluid velocity. The absolute sign is introduced to show the periodic change of friction direction. $U = U_m \cos \omega t$ and U_m is the maximum magnitude of U. After Fourier expansion and an approximation for $U|U|$:

$$\tau_b = \frac{\rho f U_m^2}{3\pi} \cos \omega t = \frac{\rho f U_m U}{3\pi} \tag{18}$$

For uniform depth the vertically integrated equation of motion in the *x*-direction becomes:

$$\frac{\partial U}{\partial t} = -g\frac{\partial \eta}{\partial x} - \frac{\tau(-d)}{\rho d} = -g\frac{\partial \eta}{\partial x} - AU \tag{19}$$

where $A = fU_m/3\pi d$. After combining with the continuity equation, the wave equation can be derived as:

$$\frac{\partial^2 \eta}{\partial t^2} + A\frac{\partial \eta}{\partial t} = gd\frac{\partial^2 \eta}{\partial x^2} \tag{20}$$

Assuming the solution has the form

$$\eta = \frac{H_I}{2} F(\omega_I t) \cos k_I x \tag{21}$$

where the subscript I represents the undamping conditions, and substituting (21) into (20), the solution becomes:

$$\eta = \frac{H_I}{2} e^{-\omega_i t} \cos \omega_r t \cos kx \tag{22}$$

where $\omega_i = \frac{A}{2}$ and $\omega_r = \omega_I \sqrt{1 - \frac{1}{4}(\frac{A}{\omega_I})}$

The horizontal velocity can be derived through the continuity equation:

$$U_d = \frac{H_I}{2k_I d} \sqrt{\omega_r^2 + \omega_i^2} e^{-\omega_i t} \sin(\omega_r t + \varepsilon) \sin k_I x \tag{23}$$

where $\varepsilon = \arctan \frac{\omega_i}{\omega_r}$

A detailed derivation of the above equations may be found in Dean and Dalrymple (1991).

5.3 Water Elevations and Horizontal Velocities Under Seiche Effects

Because Data Set #3 is the most possible time period for the seiche activities, it is selected as the data set for seiche analysis. Only the first mode seiche will be considered here due to the fact that energy in the lowest mode is much larger than that in all the other modes. Energy of a distinct peak in a power spectrum diagram can be derived by summing up the area under that peak (see Figures 29 and 30 as examples).

The starting time of the seiche activity is assumed to happen when the water elevation difference between Toledo and Buffalo reaches its maximum after a storm period. By observing the water elevation data of Toledo and Buffalo (Figure 33), which is output from GLFS and corresponds to Data Set #3, this starting time is determined to be 08/16/04:00, and the water elevation difference is near 40 cm. From the wind velocity data (Figure 5), we find that the wind velocity decreases gradually after this point and the magnitude is less than 5 m/s after 08/16/12:00 and further decreases down to 2 or 3 m/s for the rest of the time. As a result, surface wind effects are assumed to be negligible after 08/16/12:00. Tidal effects are not considered to be significant in Lake Erie. Platzman and Rao (1964b) have shown that the increase of seiche period caused by the earth rotation

(Coriolis force) in Lake Erie is only about 1.3%. Therefore, effects from tidal and Coriolis force are both neglected here.

Lake Erie is considered to be a rectangular basin with an average depth of 18.6 m. The length of the lake is assumed to be 354 km (SPM, 1984). These assumptions will give a 1st mode seiche period with the value of 14.56 hours according to Merian formula. Calculating the difference between the maximum and minimum in the water elevation data before the time of 08/16/12 derives an initial wave height (about 30 cm). The location of the deployment site is about 10 km southeast of Monroe, Michigan. The values of the friction coefficient f range from 0.0025 (smooth) to 0.3 (rough) for long waves (Dietrich, 1980). For Lake Erie, most bottom areas in the western and central basin are quite flat. And the vertical scale is very small compared to the horizontal scale. As a result, Lake Erie is assumed to have a smooth bottom. Seiche activity will have a much smaller friction factor than the value of f illustrated by Dietrich et al. (1980).

The results from the calculations of η and U_d under frictional damping are given in Figure 33. The water surface fluctuation, η, closely simulates the field data. The maximum value of the horizontal particle velocity U_d (under a damping seiche) is about 2.5 cm/s in the longitudinal direction of Lake Erie. This value is about 25% of the maximum magnitude of bottom current velocity in Data Set #3.

CHAPTER 6. DISCUSSIONS AND CONCLUSIONS

Data from GLFS is compared with the field data collected by ARMS in the summer of 1996. The average depth at the deployment site is about 7.7 m. Data comparisons between GLFS and ARMS show that water surface fluctuations are close to each other. GLFS wave heights follow the trends of field data closely, but the wave periods deviate from the field data during low-wave time periods. The wave directions follow the field data during the high-wave periods. These results lead to the same conclusion, that is, only under a strong effect of external forcing function (wind) can the model clearly resolve the wave parameters. The random characteristics of the waves are the main reasons for difficulty in the model simulations.

The maximum bottom current velocity is usually under 8 cm/s. Even under strong wind forcing, the field data shows that there are no special patterns matched between wind directions and bottom current directions. The bottom current circulation in western basin of Lake Erie is not sensitive to the surface wind for the conditions observed here. However, circulation patterns of bottom current are hard to be resolved by only a one-point measurement. A muti-point spatially distrubuted measurements in the current field would be very useful for further analysis.

Temperature data from GLFS matches the trend of the field data, though there is a small offset (1 to 3 °C) between them. The reason for this discrepancy might be attributed to the difference between the real water depth and the digitized grid depth (about 1.6 m difference between them) because temperature calculated from the POM is very sensitive to the water depth.

The small values of U_b and A_b from field data imply that a current is more frequently the dominant forcing at the experiment site. Sediment resuspension events at the deployment site are sensitive to wave heights, horizontal bottom current velocities and directions. The favorable bottom current directions for sediment resuspension activities are found to be near north or when they range from south to south southwest. The directional current effects on the sediment concentration at the deployment site might be

caused by the local bottom topography characteristics. The current site-scan sonar maps with low resolutions are not accurate enough to support the analysis results. A detailed description of bathymetry data at the deployment site will be crucial in future analysis.

Power spectrum analyses have been perfomed on pressure, u-velocity, and v-velocity data from ARMS Data Set #3, #4, and #5. The results show a clear 14.56-hour seiche period (first mode), which is quite close to the observed value of 14.38 hours (Platzman and Rao, 1964a) and the theoretical value of 14.40 hours (Hamblin 1976). Seiche with damping effects has been studied based on a simple Merian formula. The calculated water surface fluctuations agree with field data very well. The horizontal water particle velocity caused by seiches has the same order of magnitude as the bottom current velocity. The maximum seiche-induced horizontal velocity in the longitudinal lake direction is about 25% of the magnitude of maximum bottom current velocity. According to Platzman and Rao (1964b), if a one foot amplitude is assigned to Buffalo and a free oscillation begins, a maximum current speed of about 0.1 ft/s will appear at the location nearby the deployment site. The simple calculations of seiche based on the Merian formula are encouraging. However, a more accurate model should be applied for further analysis.

REFERENCES

Bedford, K. W., and Schwab, D., 1994. The Great Lake Forecasting System, An Overview. Proceedings, National Conference on Hydraulic Engineering, Aug. 1-5, 1994, Buffalo, NY, pp.197-201.

Bedford, K. W., O. Wai, R. V. Evra III, P. Velissariou, J. Lee and C. Libicki, 1990. The Local Near-Bottom Response of a Dredged Material Placement Site to Wind and Tide Effects. *Report U.S. Army Corps of Engineers*, Coastal Engineering Research Center, Vicksburg, MS.

Buchan, S. J., Steedman, R. K., Stroud, S. A., and Provis, D. G., 1984. A Shallow Water Directional Wave Recorder. *Coastal Engineering-1984*, pp.287-303.

Dean, Robert G., and Dalrymple, Robert A., 1991. *Water Wave Mechanics for Engineers and Scientists.* , 2nd ed., World Scientific Publishing Co. Pte. Ltd.

Dietrich, G., Kalle, K., Krauss, W., Siedler, G., 1980. *General Oceanography.* 2nd ed., John Wiley & Sons, Inc.

Hamblin, P. F., 1987. Meteorological Forcing and Water Level Fluctuations on Lake Erie. *Journal of Great Lakes Research*, vol.13, no.4, pp.436-453.

Kuo, Y. Y, and Chiu, Y. F., 1994. Transfer Function Between Wave Height and Wave Pressure for Progressive Waves. *Coastal Engineering*, vol.23, pp.81-93.

Platzman, George W., and Rao, Desiraju B., 1964a. Spectra of Lake Erie Water Levels. *Journal of Geophysical Research.* vol. 60, pp.2525-2535.

Platzman, George W, and Rao, Desiraju B., 1964b. The Free Oscillations of Lake Erie. *Study on Oceanography* (Hidaka Vol.), K. Yashida, Ed., pp.359-382.

Saylor, James H., and Miller, Gerald S., 1987. Studies of Large-Scale Currents in Lake Erie, 1979-80. *Journal of Great Lakes Research*, vol. 13, no. 4, pp.487-514.

Coastal Engineering Research Center, Dept. of the Army Waterways Experiment Station, Corps of Engineers. *Shore Protection Manual, 1984.* 4th ed., Superintendent of Documents, U.S. Government Printing Office, Washington, D.C. 20402.

Stull, R. Roland, 1988. *An Introduction to Boundary Layer Meteorology.* Dordrecht, Boston, Kluwer Academic Publishers.

Figure 1. Lake Erie '96 Experiment Site

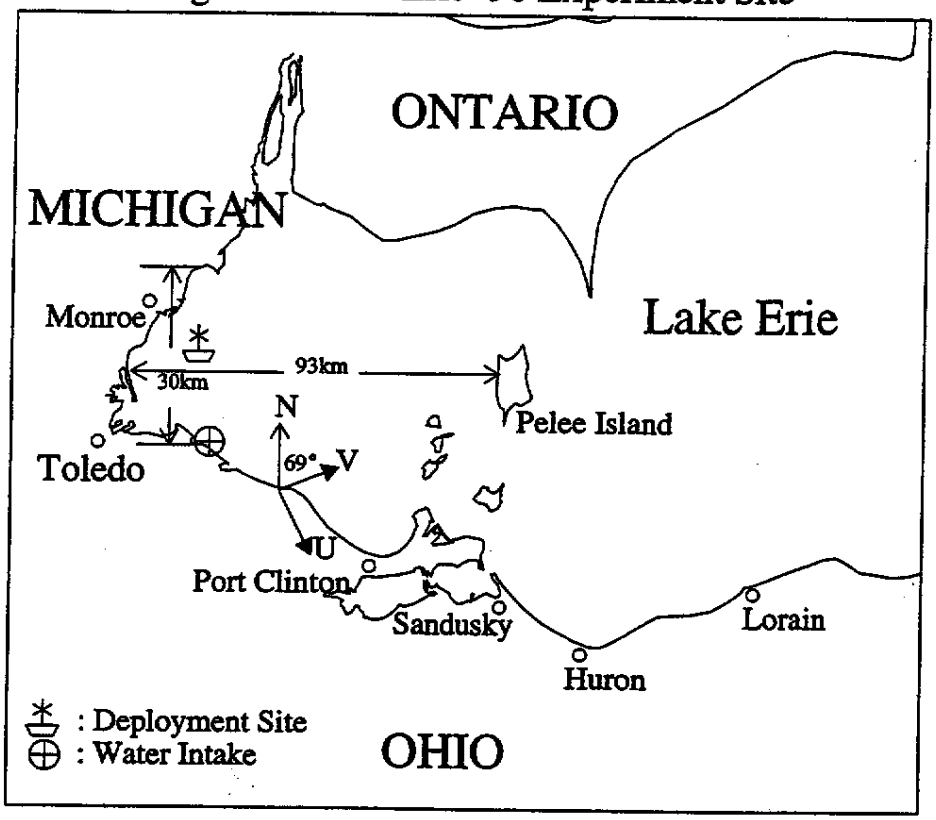

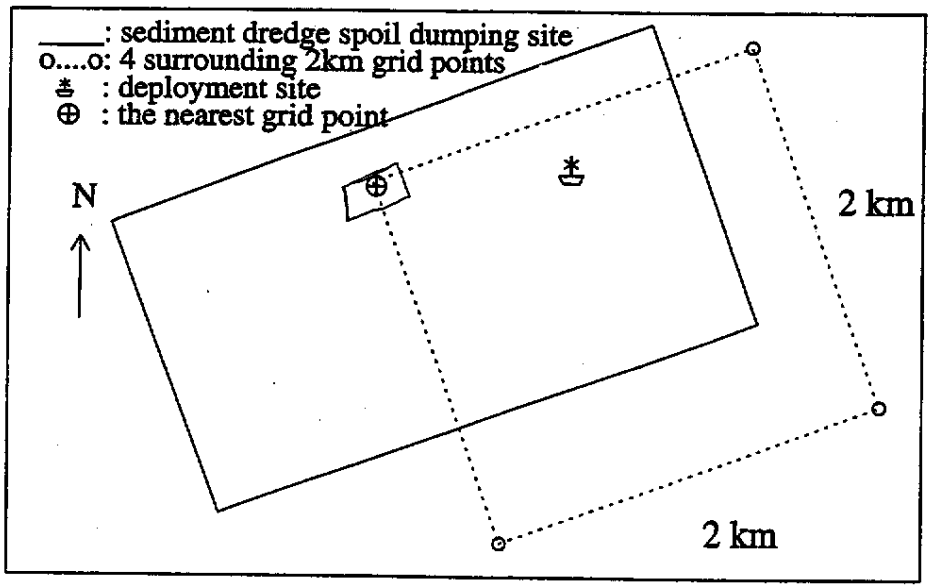

Figure 2. Time Series of Sediment Concentration at Bottom (Data Set #3)

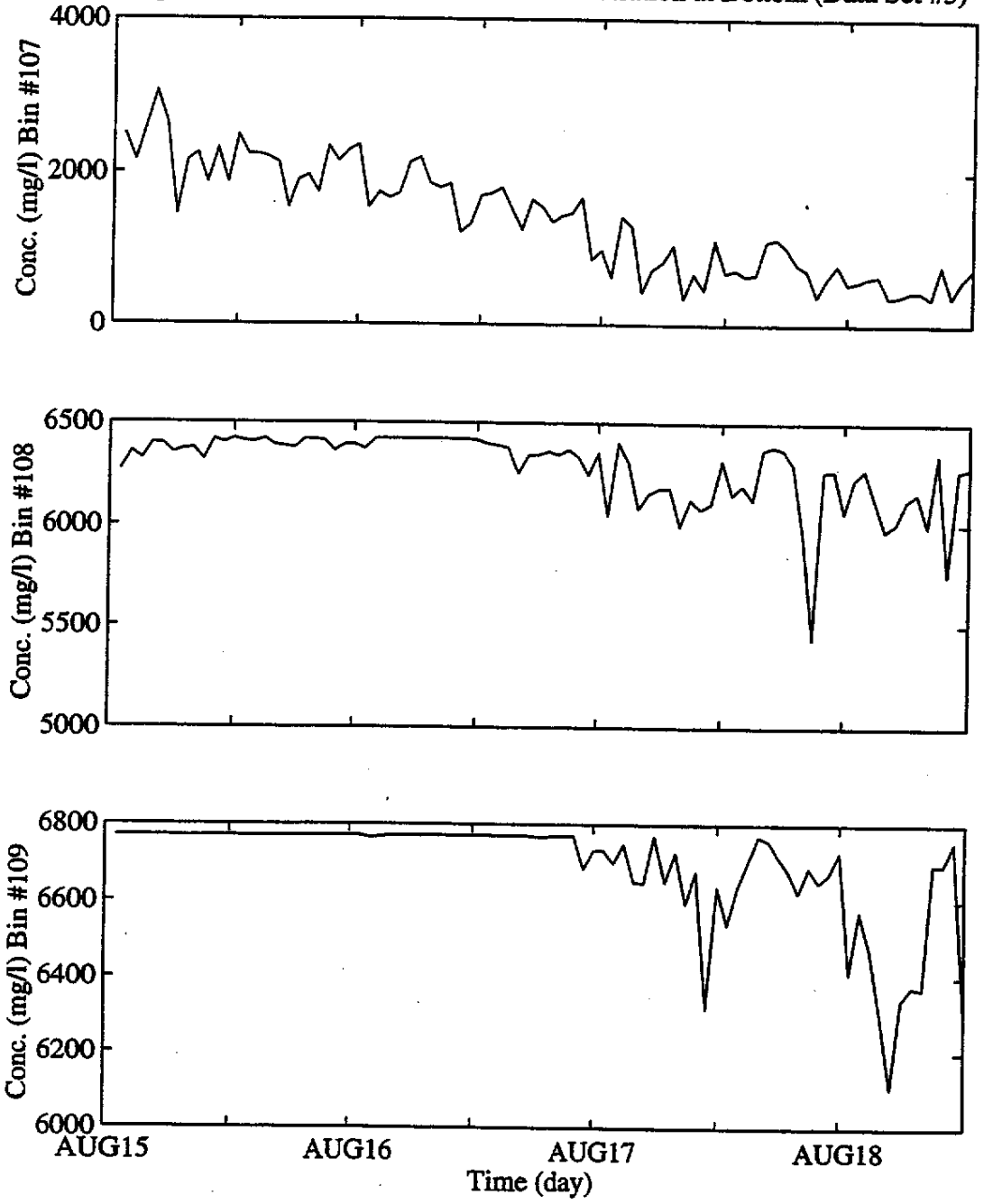

Figure 3. Time Series of Sediment Concentration at Bottom (Data Set #4)

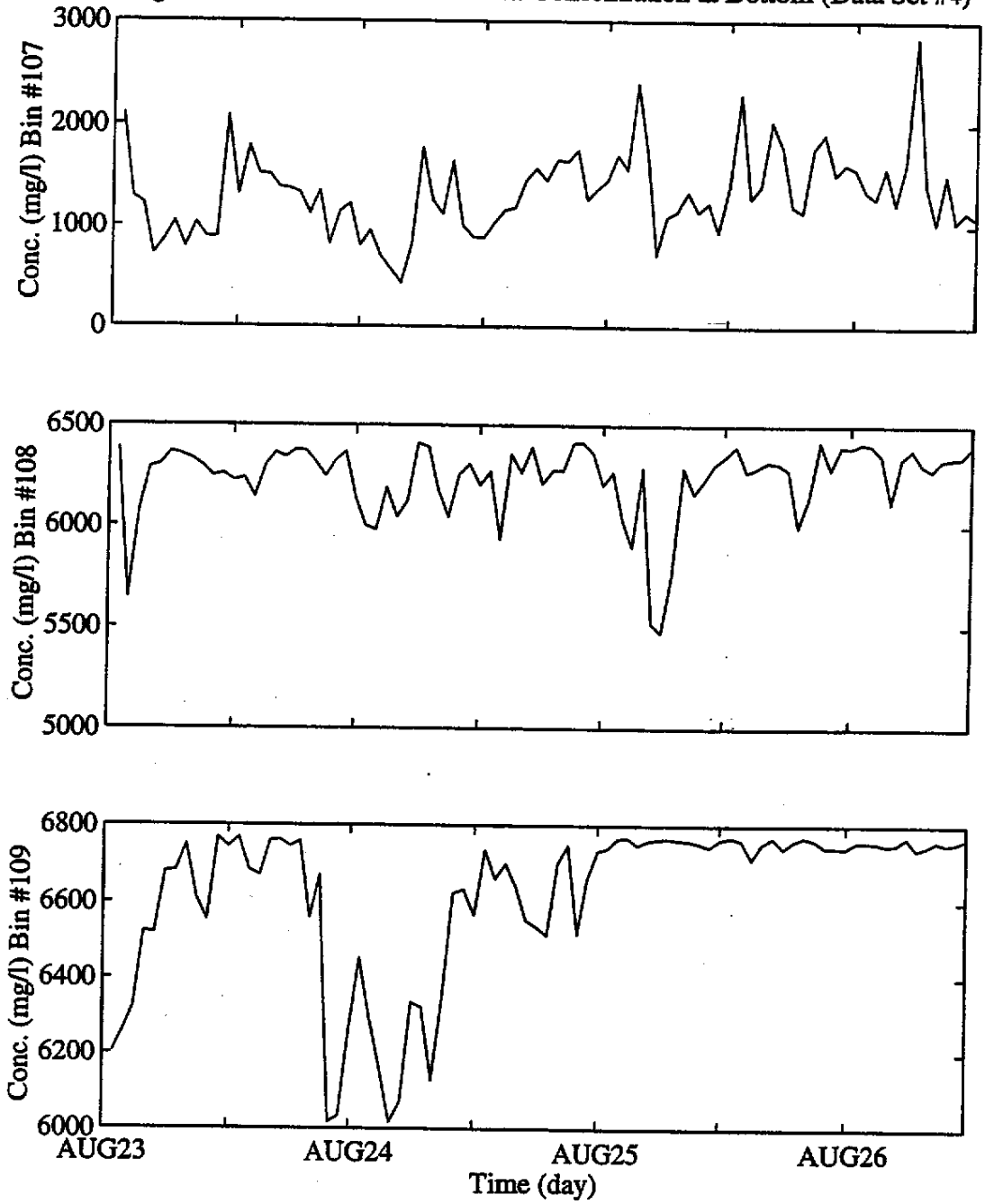

Figure 4. Time Series of Sediment Concentration at Bottom (Data Set #5)

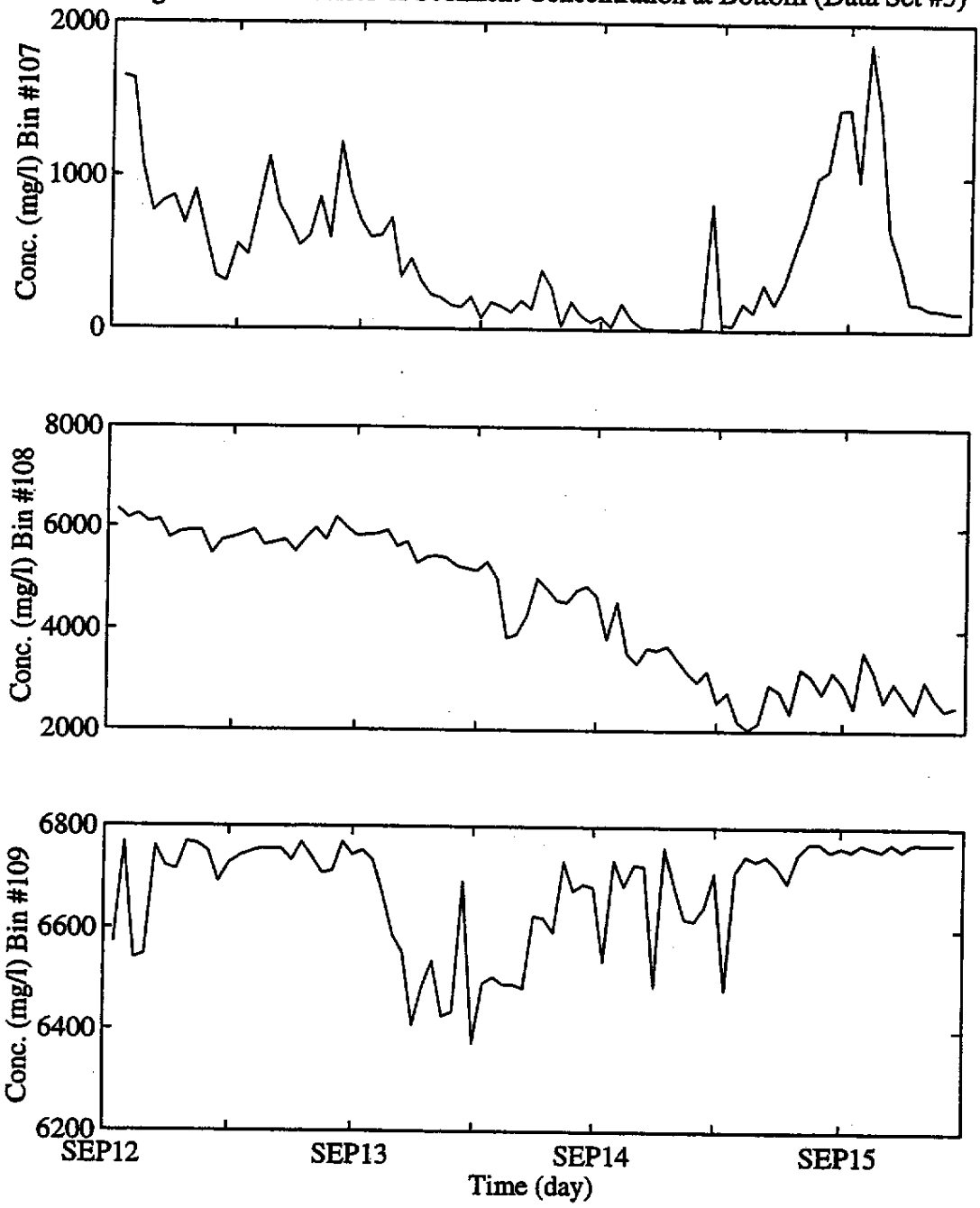

Figure 5. Wind & Water Surface Fluctuations (Data Set #3)

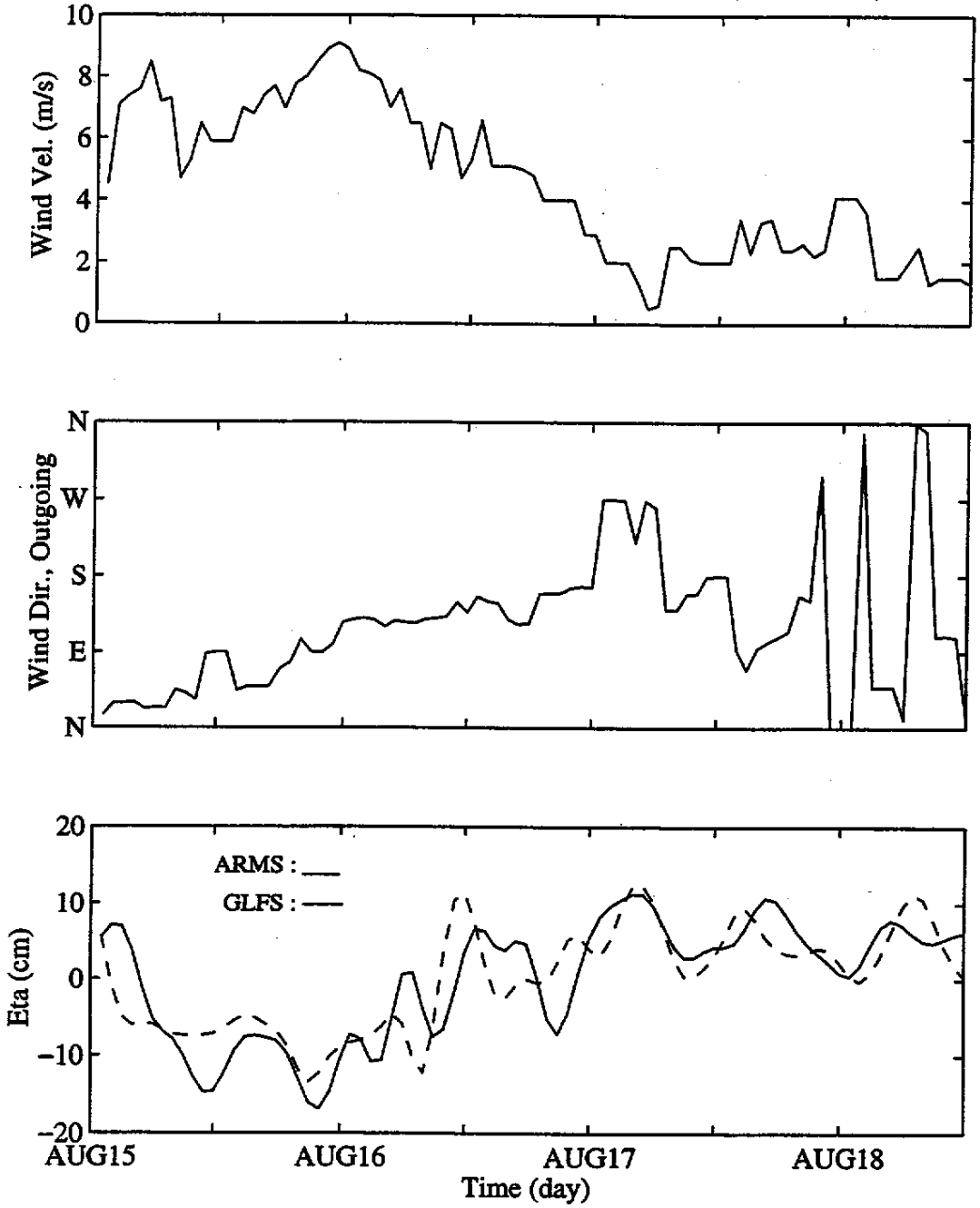

Figure 6. Wind & Water Surface Fluctuations (Data Set #4)

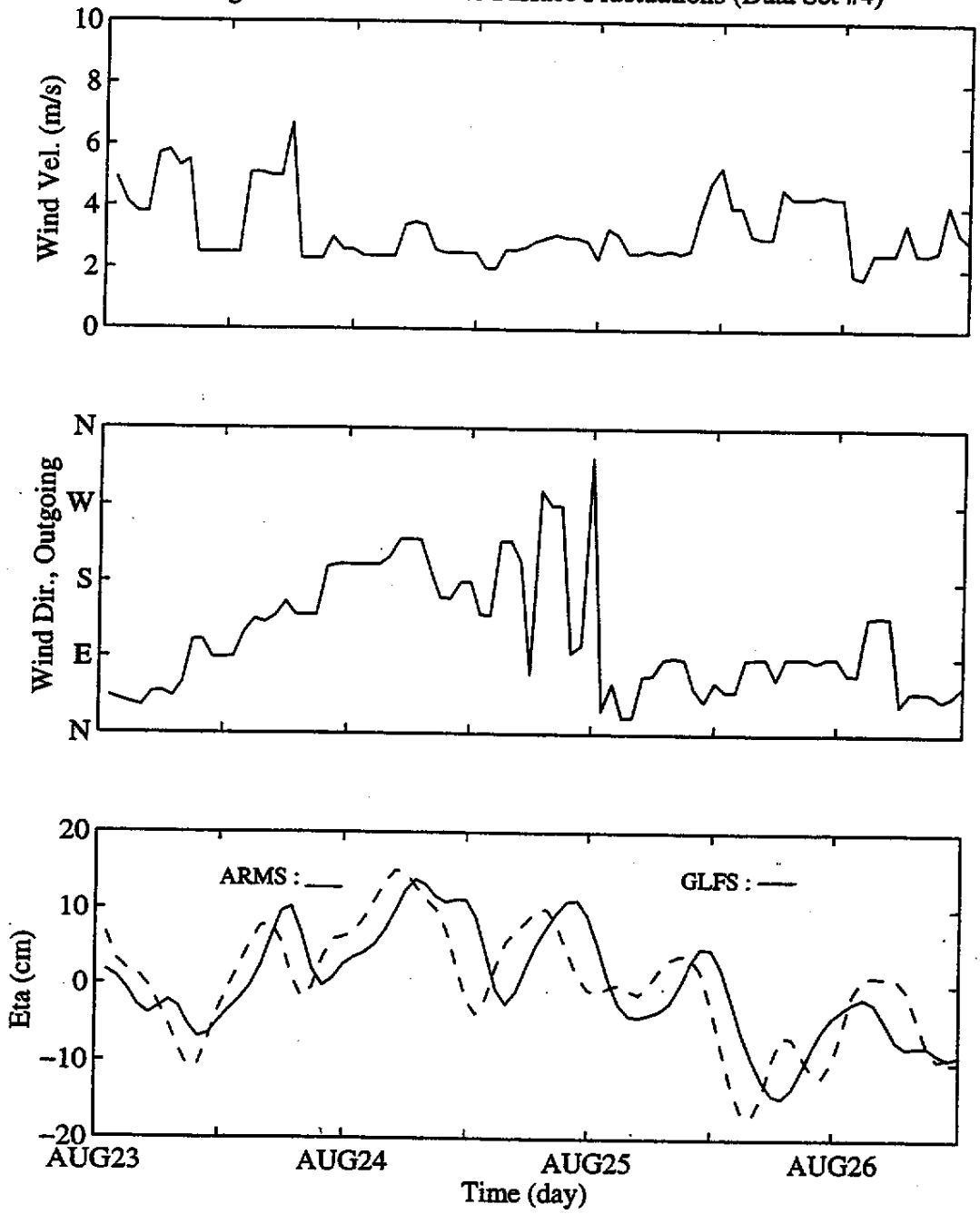

A.23. Power Spectral Density of V–Velocity (Data Set #5, BASS III)

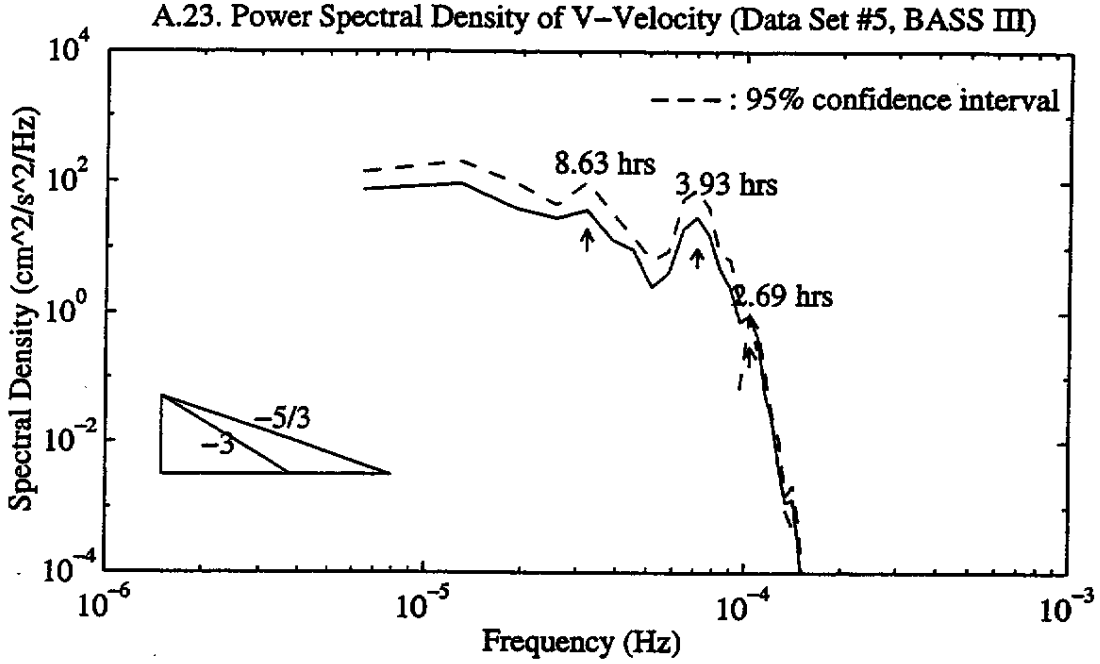

A.24. Power Spectral Density of V–Velocity (Data Set #5, BASS IV)

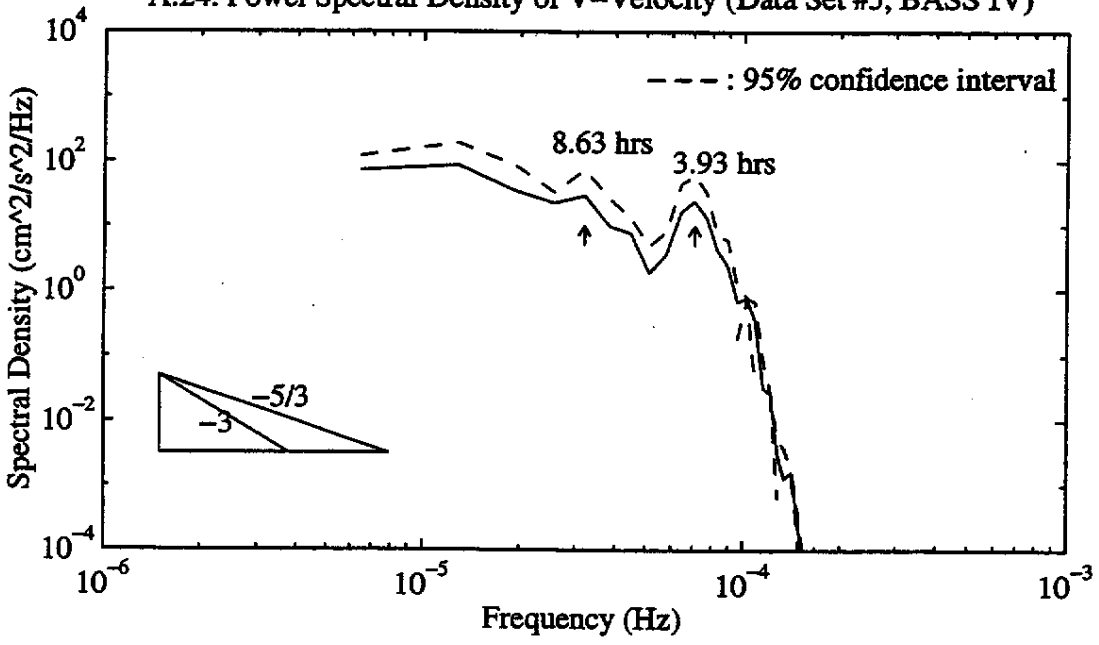

Figure 7. Wind & Water Surface Fluctuations (Data Set #5)

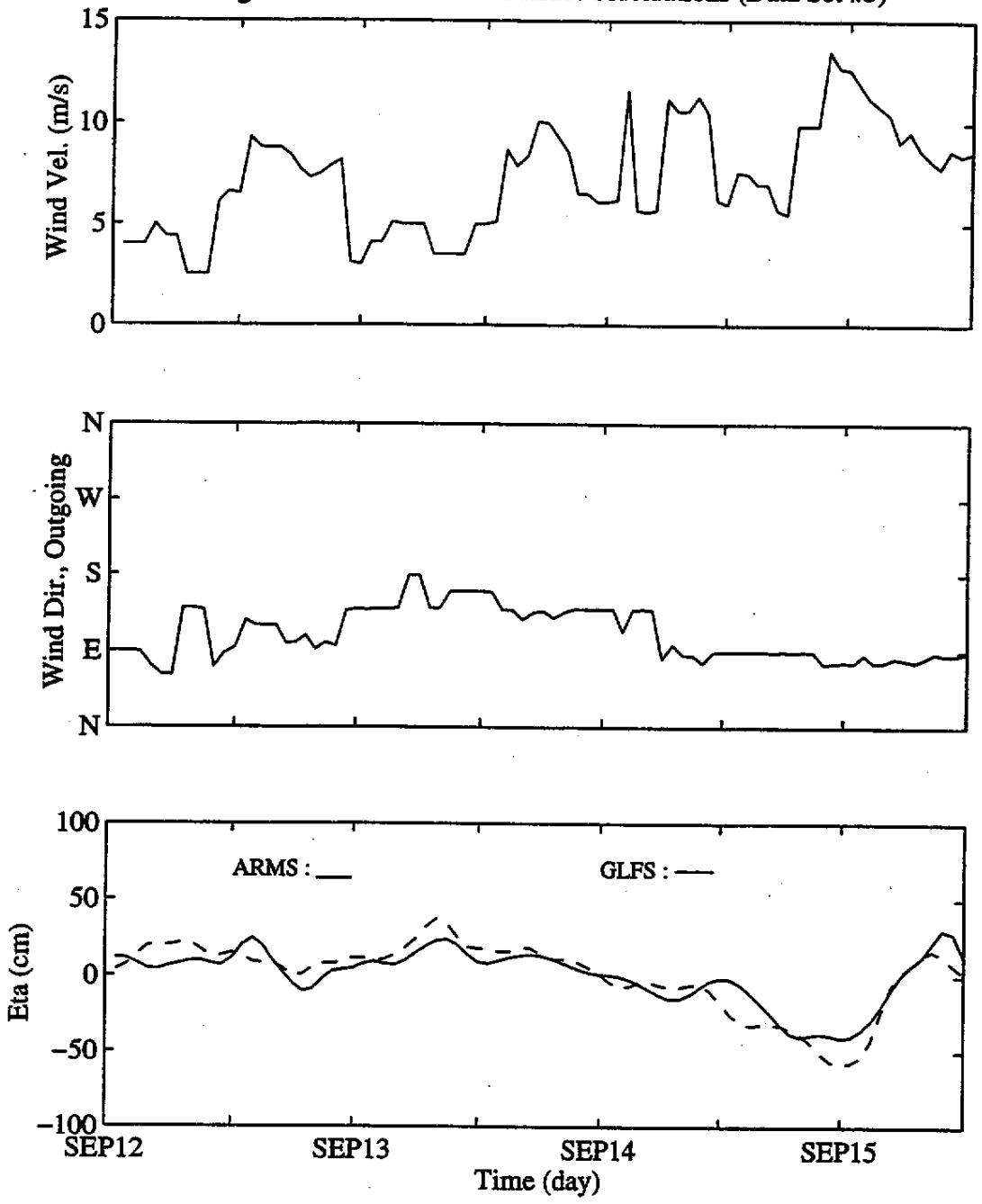

Figure 8. Wave Parameters (ARMS : ___ GLFS : ----) Data Set #3

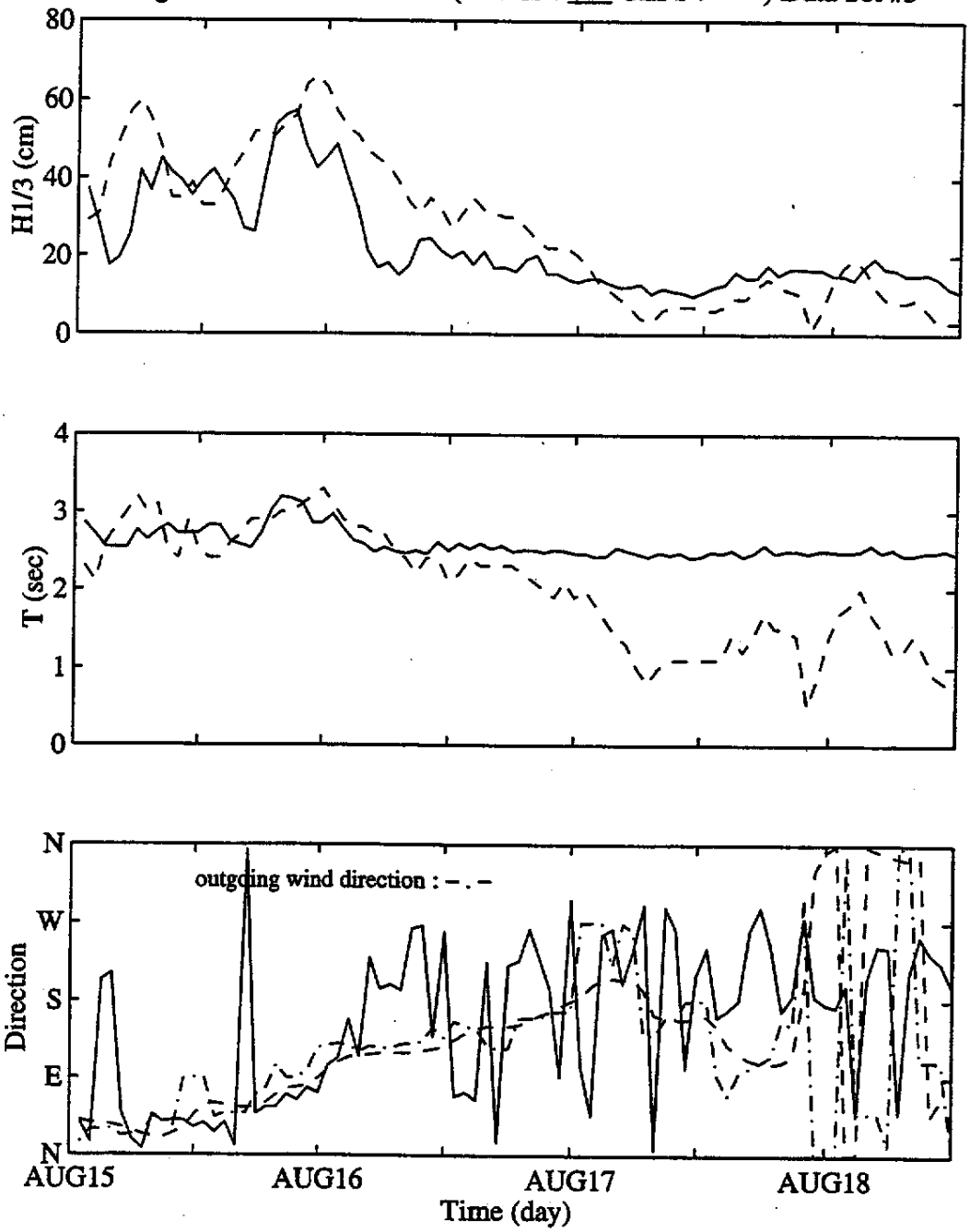

Figure 9. Wave Parameters (ARMS : ___ GLFS : ——) Data Set #4

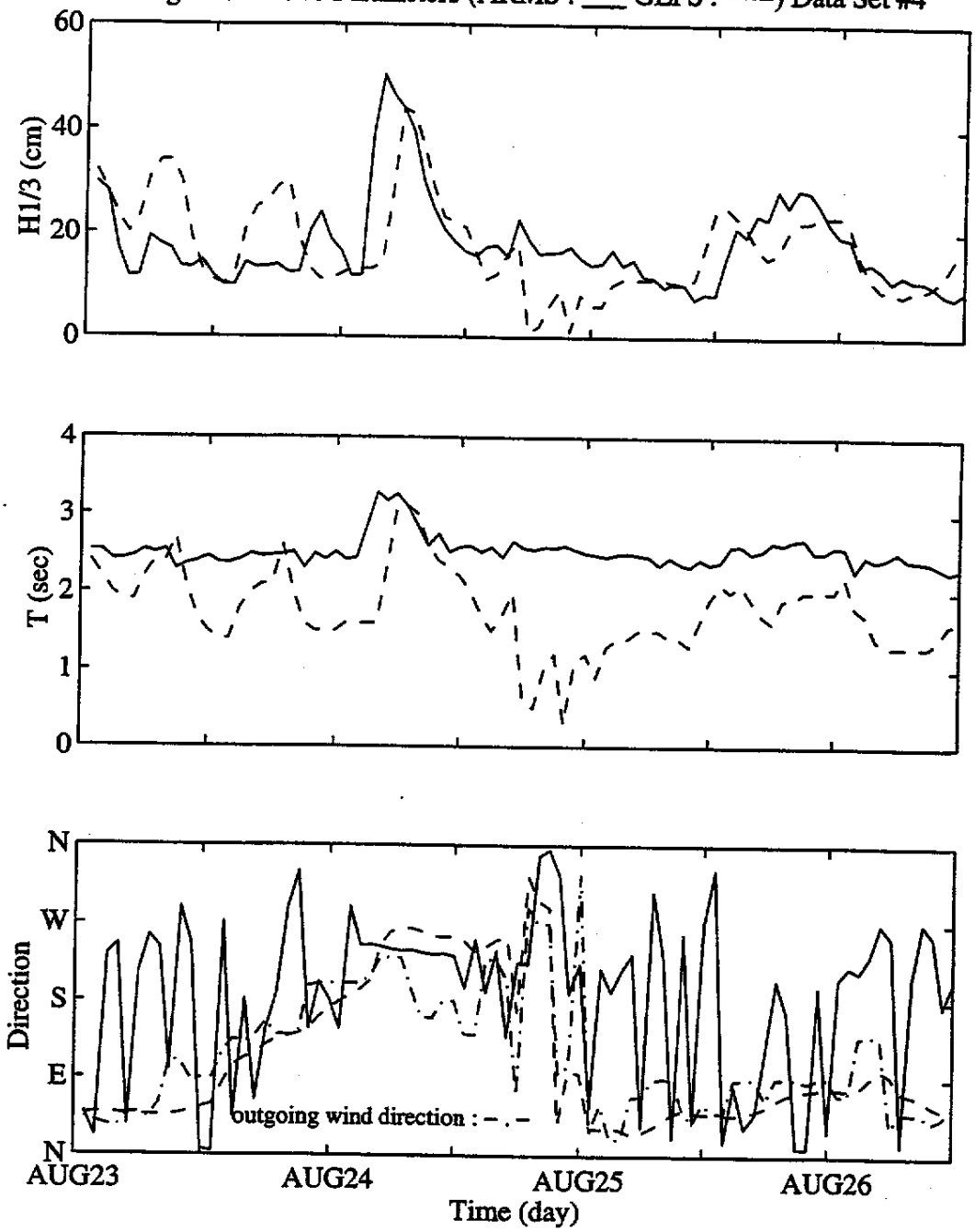

Figure 10. Wave Parameters (ARMS : ___ GLFS : ——) Data Set #5

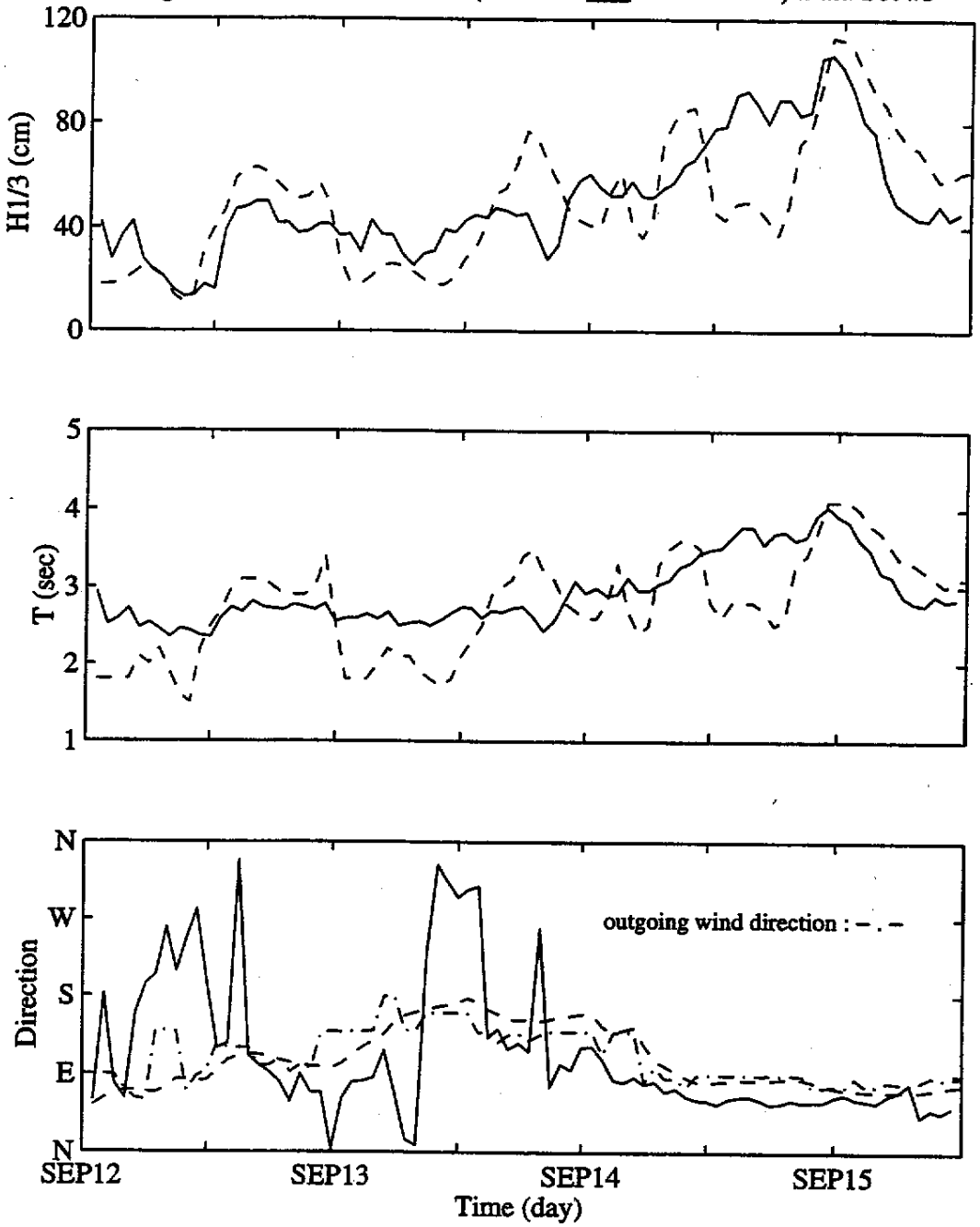

Figure 11. Ratios of Wave Heights

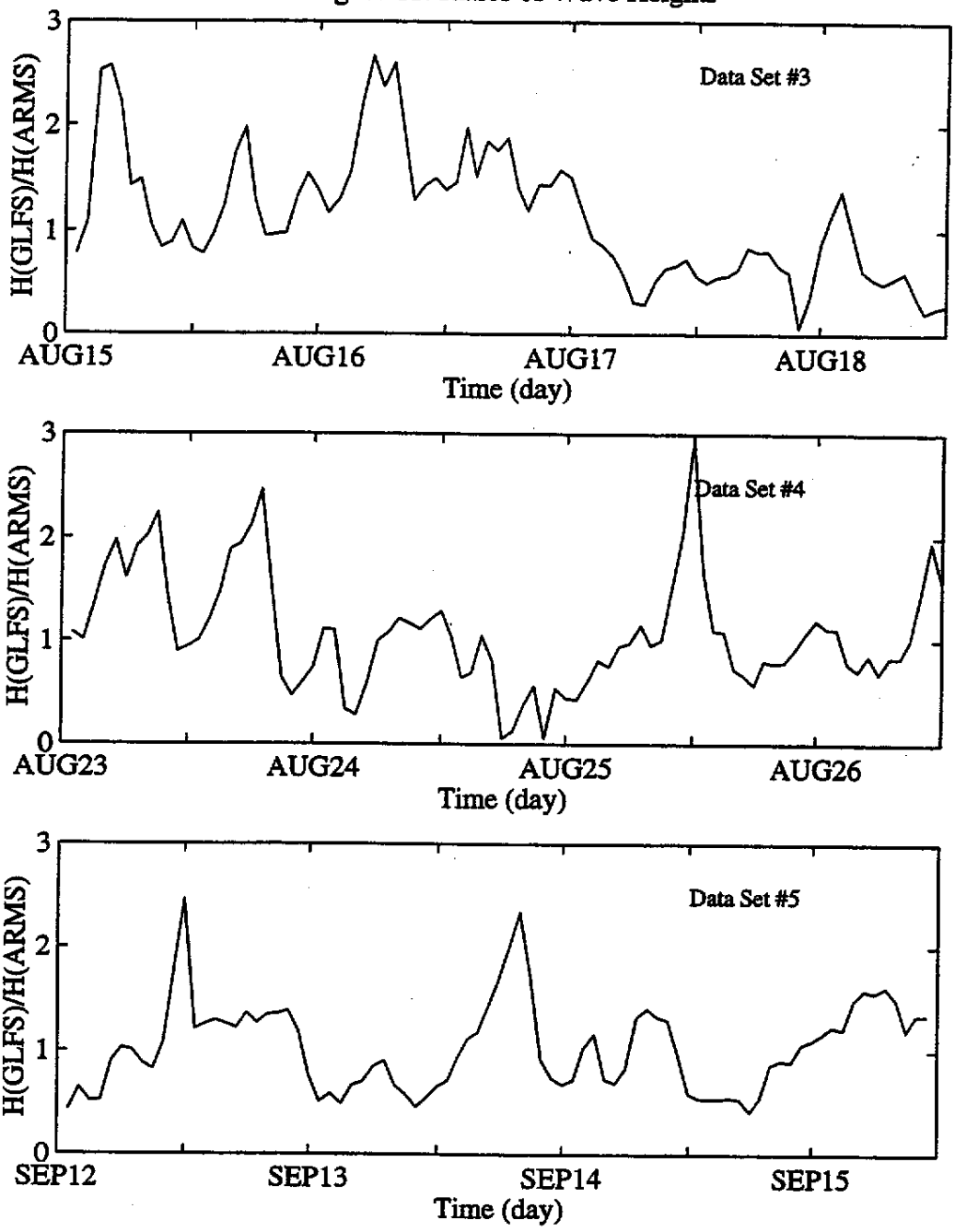

Figure 12. Ratios of Wave Periods

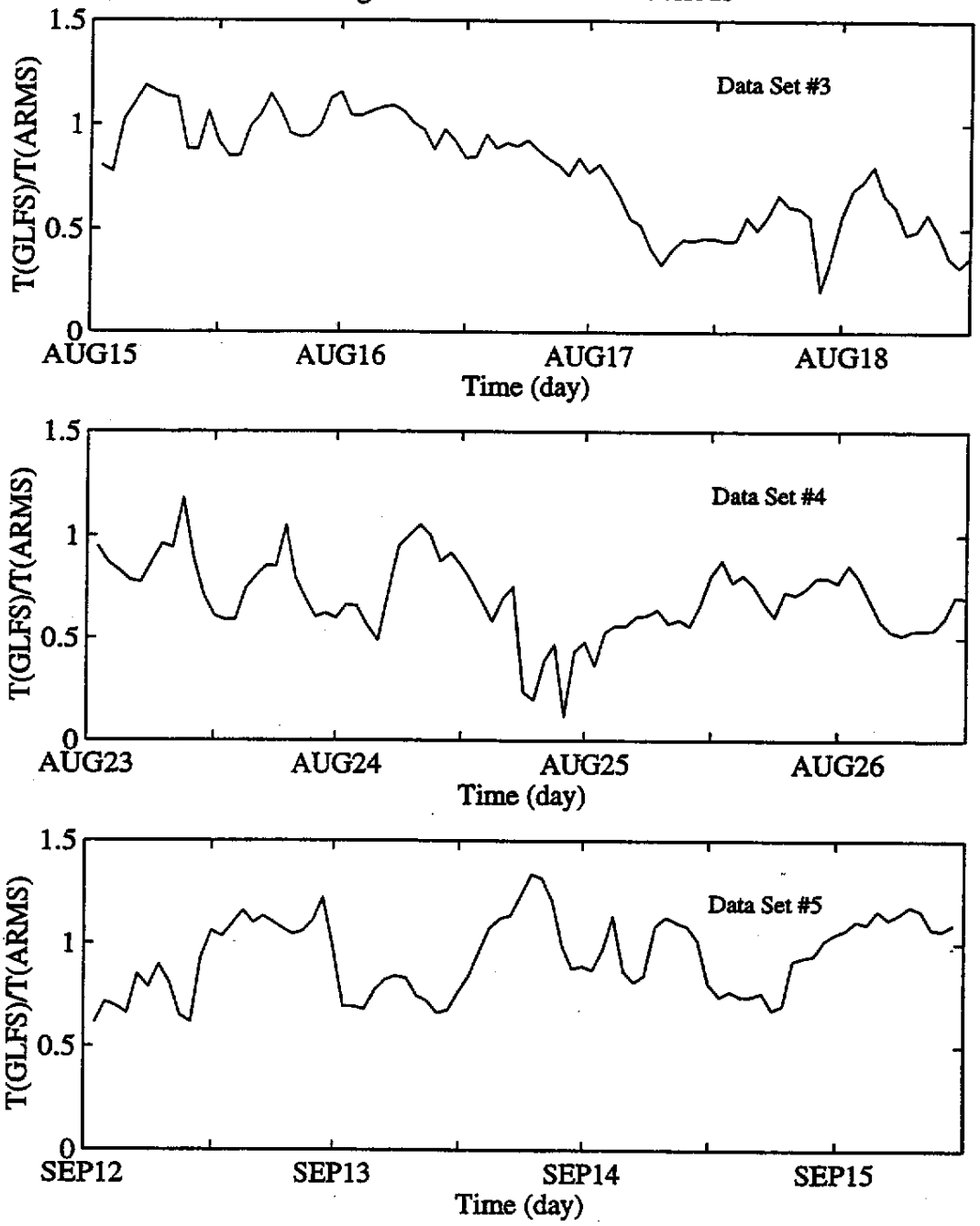

Figure 13. Values of d/L (Depth/Wave Length)

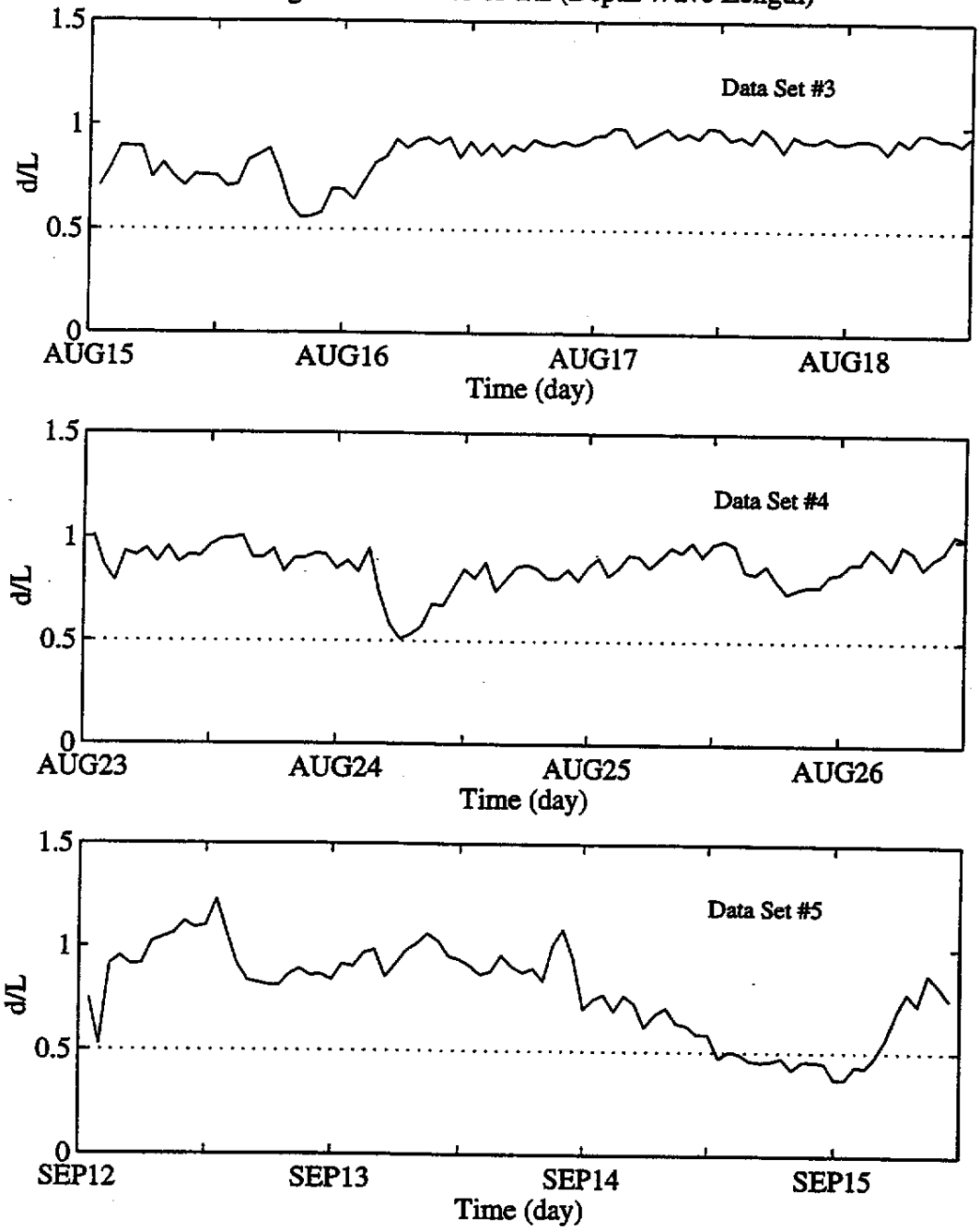

Figure 14. Wind Field and Wave Information From GLFS
(August 24, 1996 00:00 UTC)

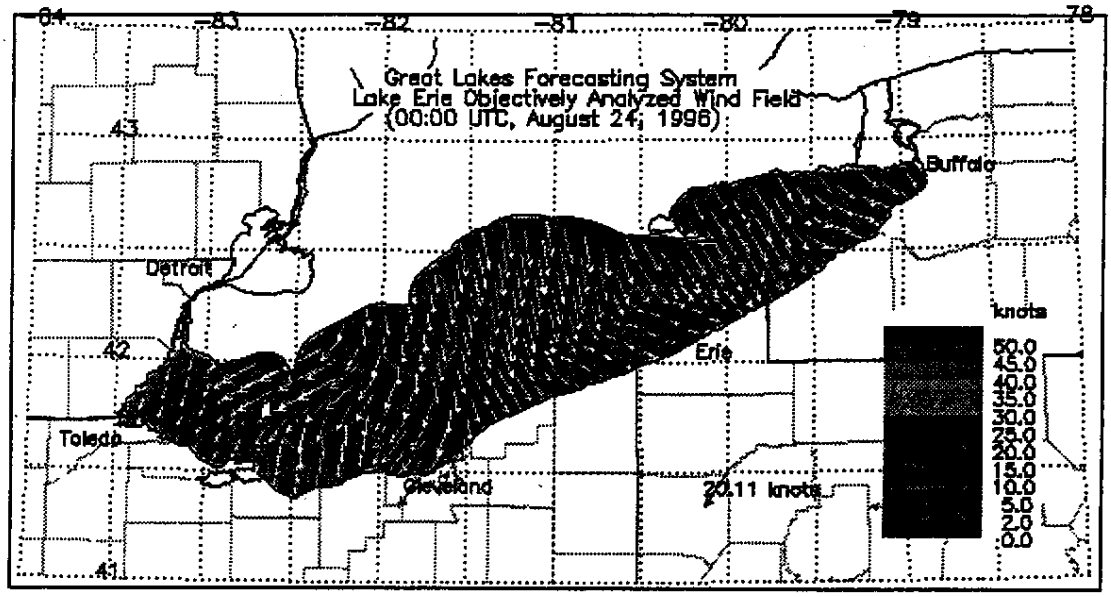

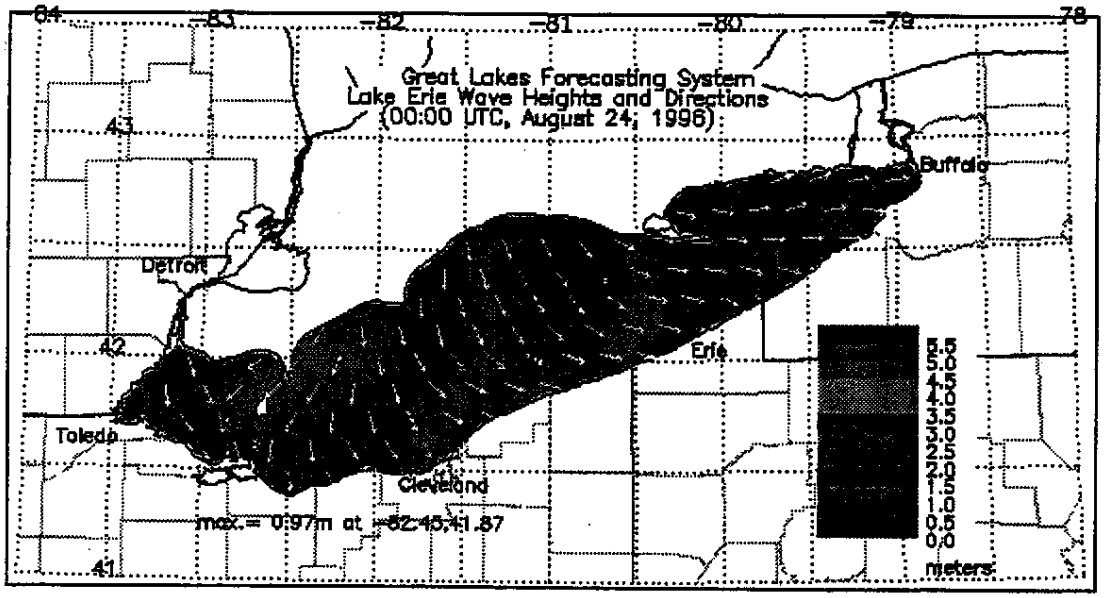

Figure 15. Wind Field and Wave Information From GLFS
(August 24, 1996 06:00 UTC)

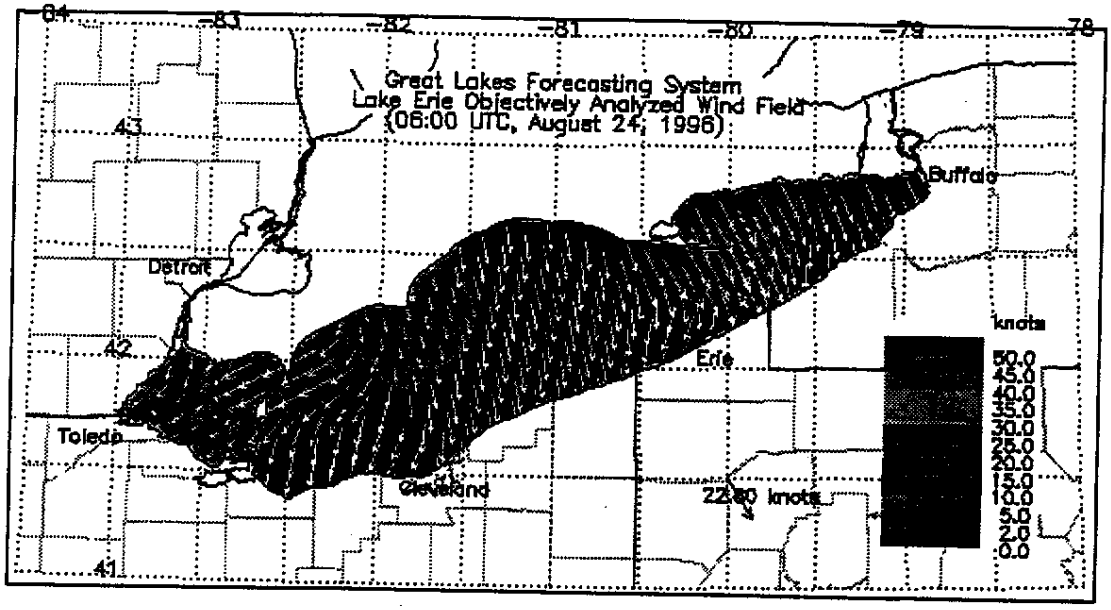

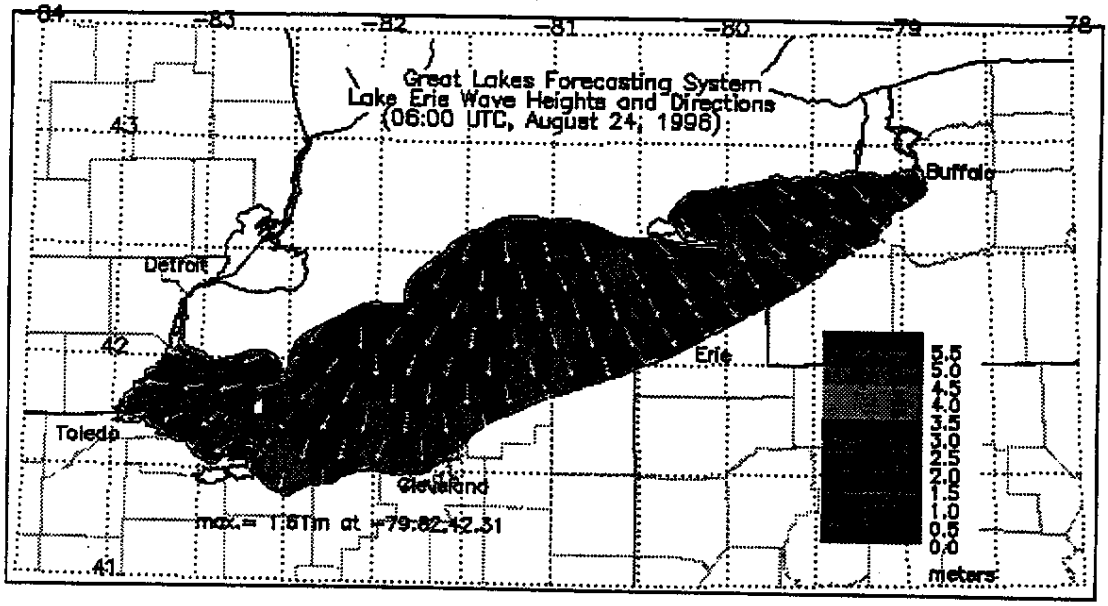

Figure 16. Wind & Bottom Currents (Data Set #3)

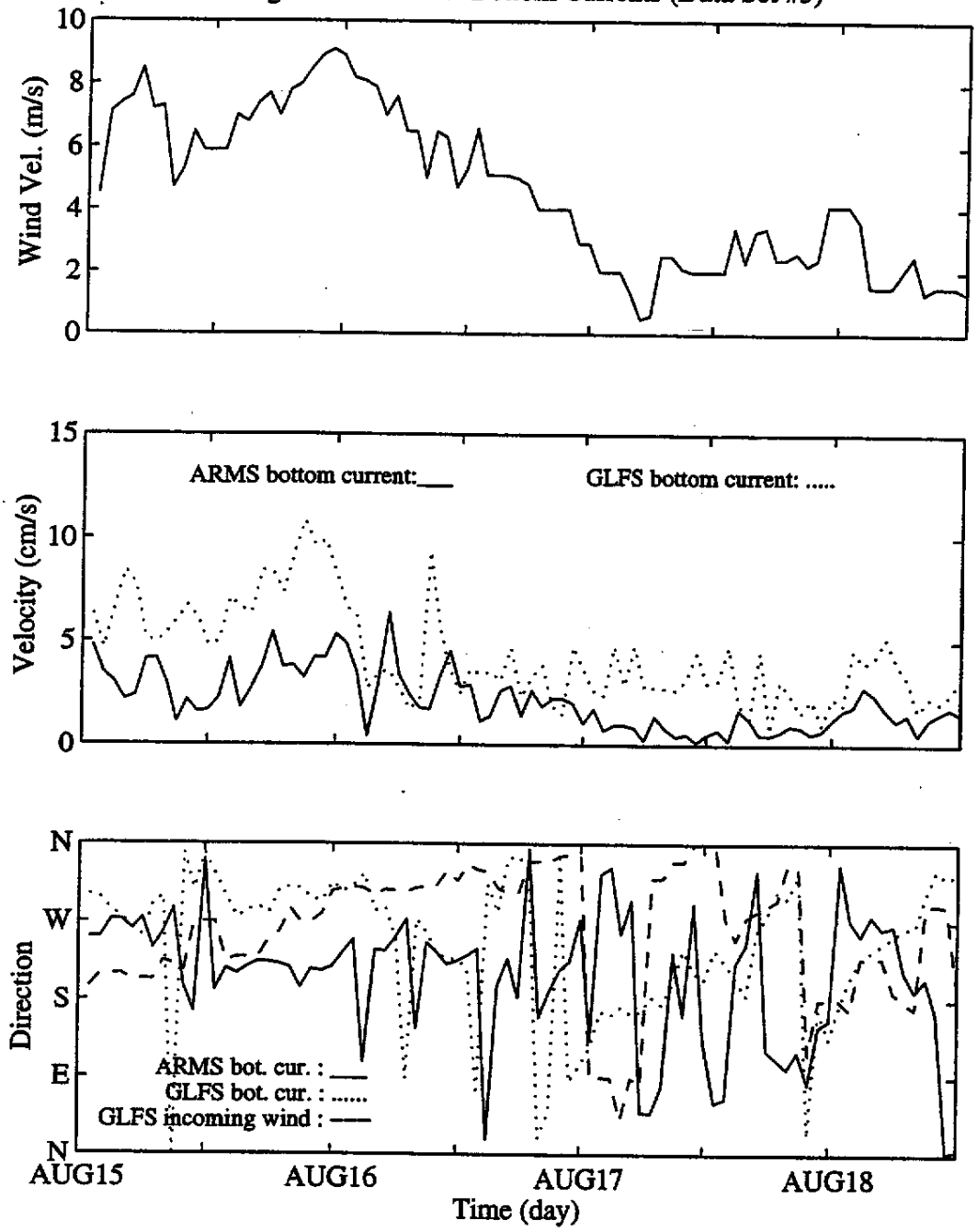

Figure 17. Wind & Bottom Currents (Data Set #4)

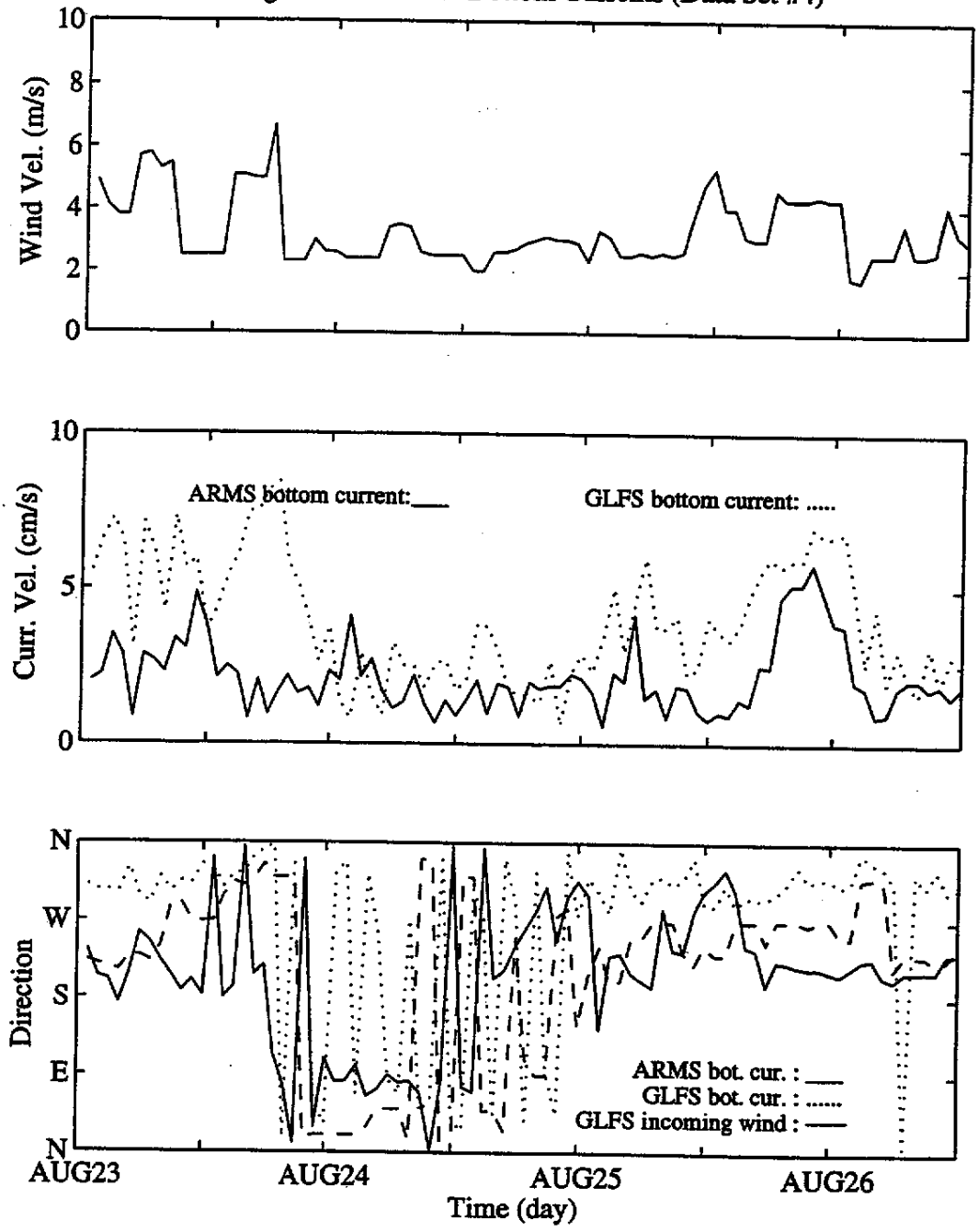

Figure 18. Wind & Bottom Currents (Data Set #5)

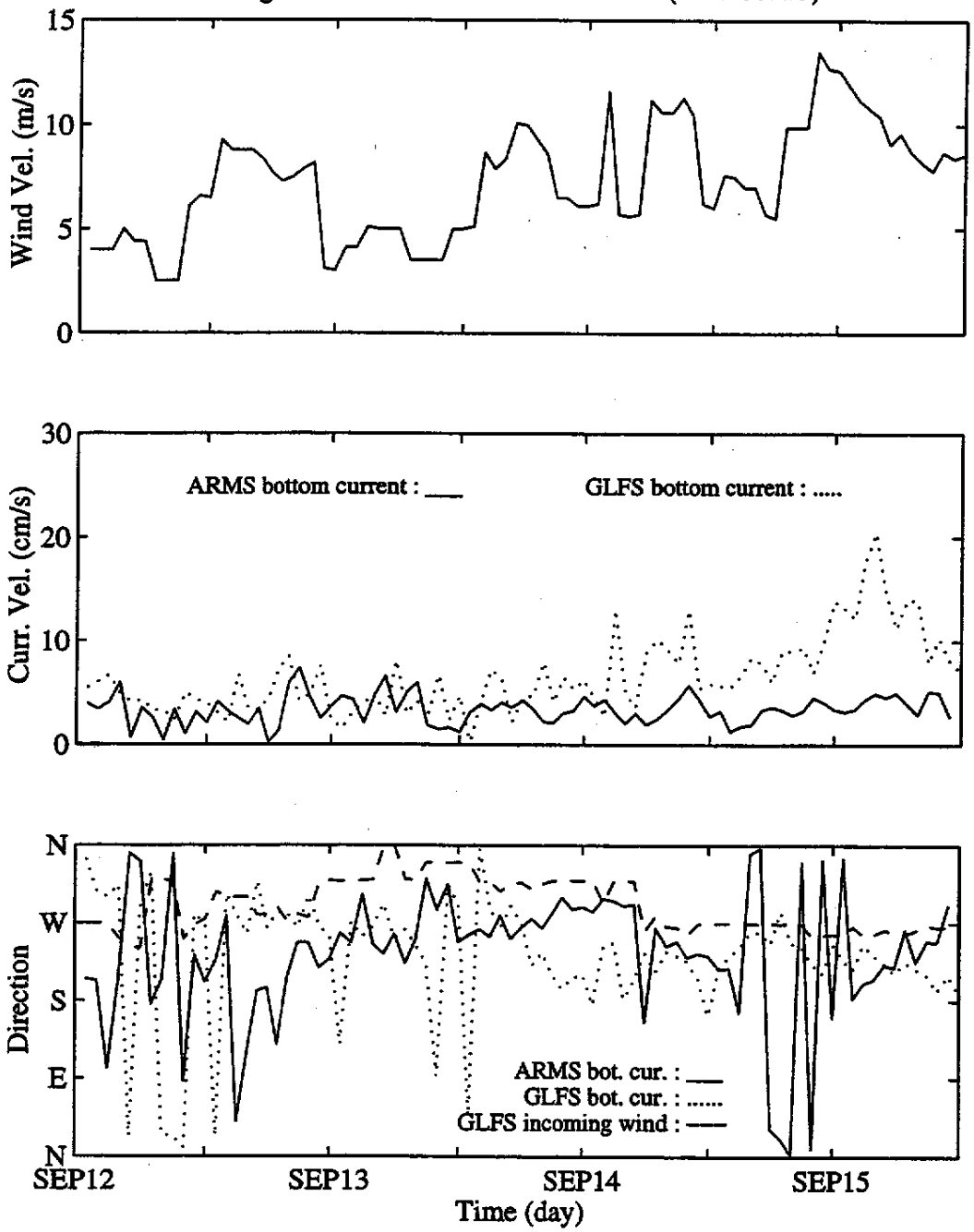

Figure 19. Bottom Temperature Comparisons (ARMS : ___ GLFS : ——)

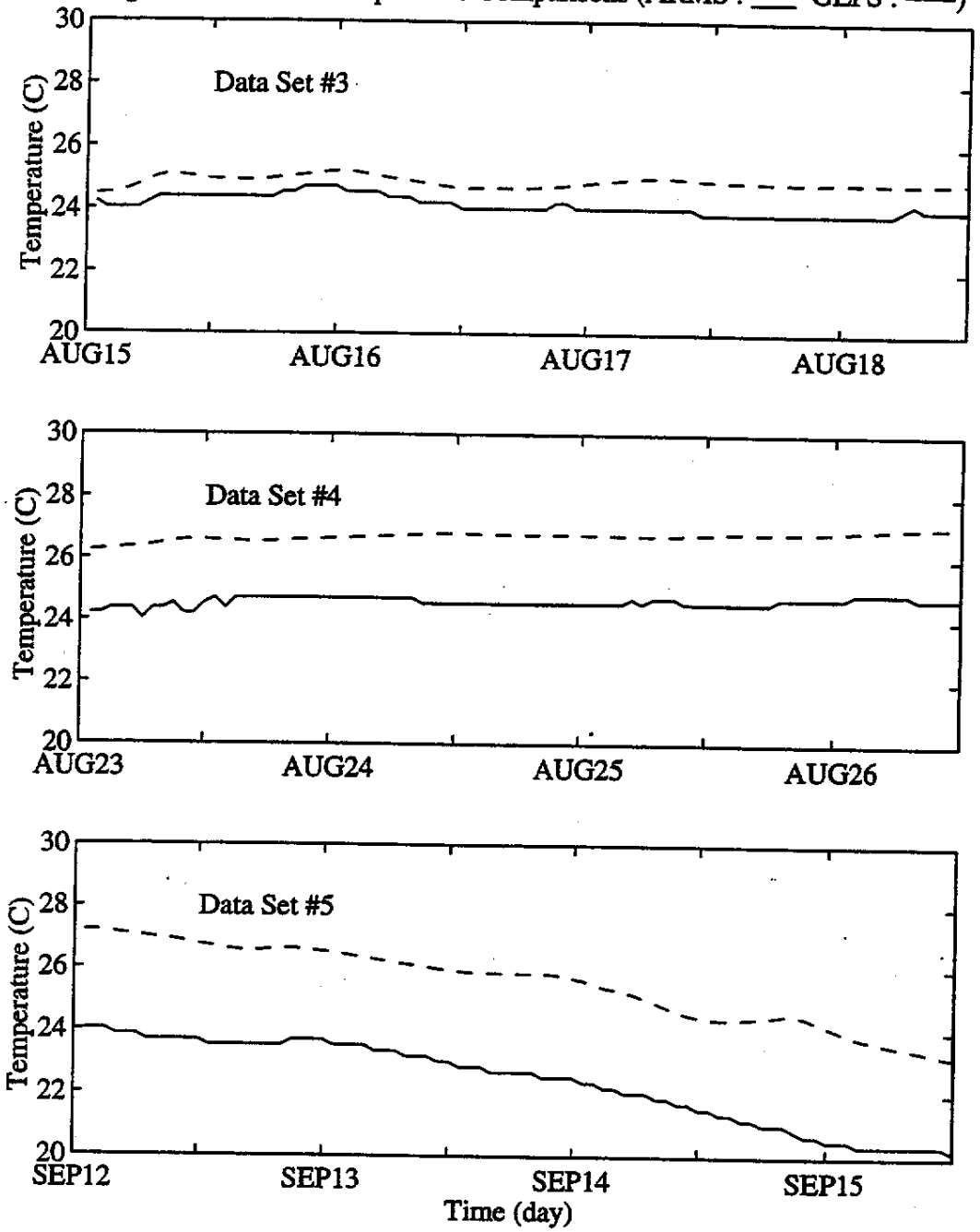

Figure 20. Wave Orbital Velocity and Amplitude at Bottom (Data Set #3)

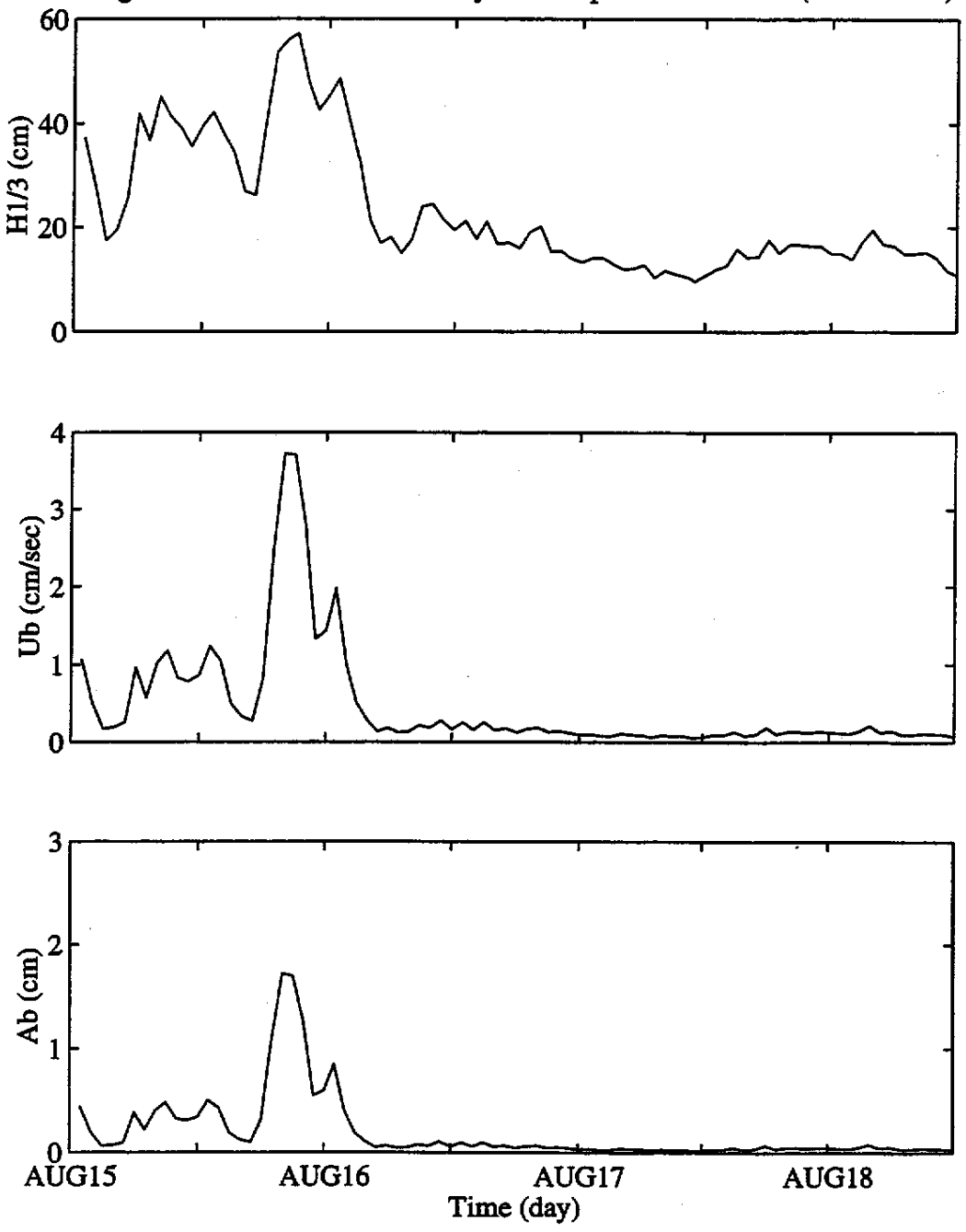

Figure 21. Wave Orbital Velocity and Amplitude at Bottom (Data Set #4)

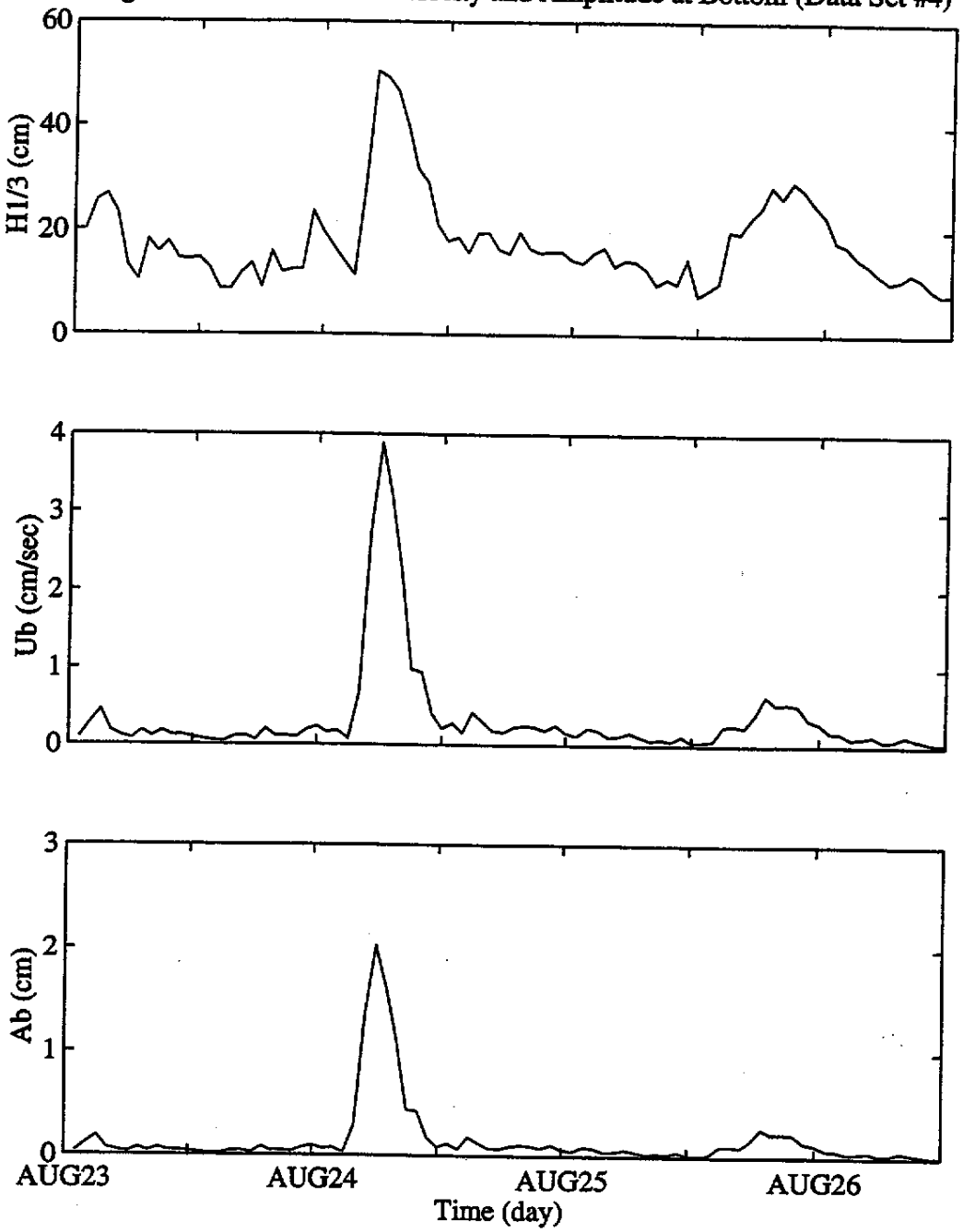

Figure 22. Wave Orbital Velocity and Amplitude at Bottom (Data Set #5)

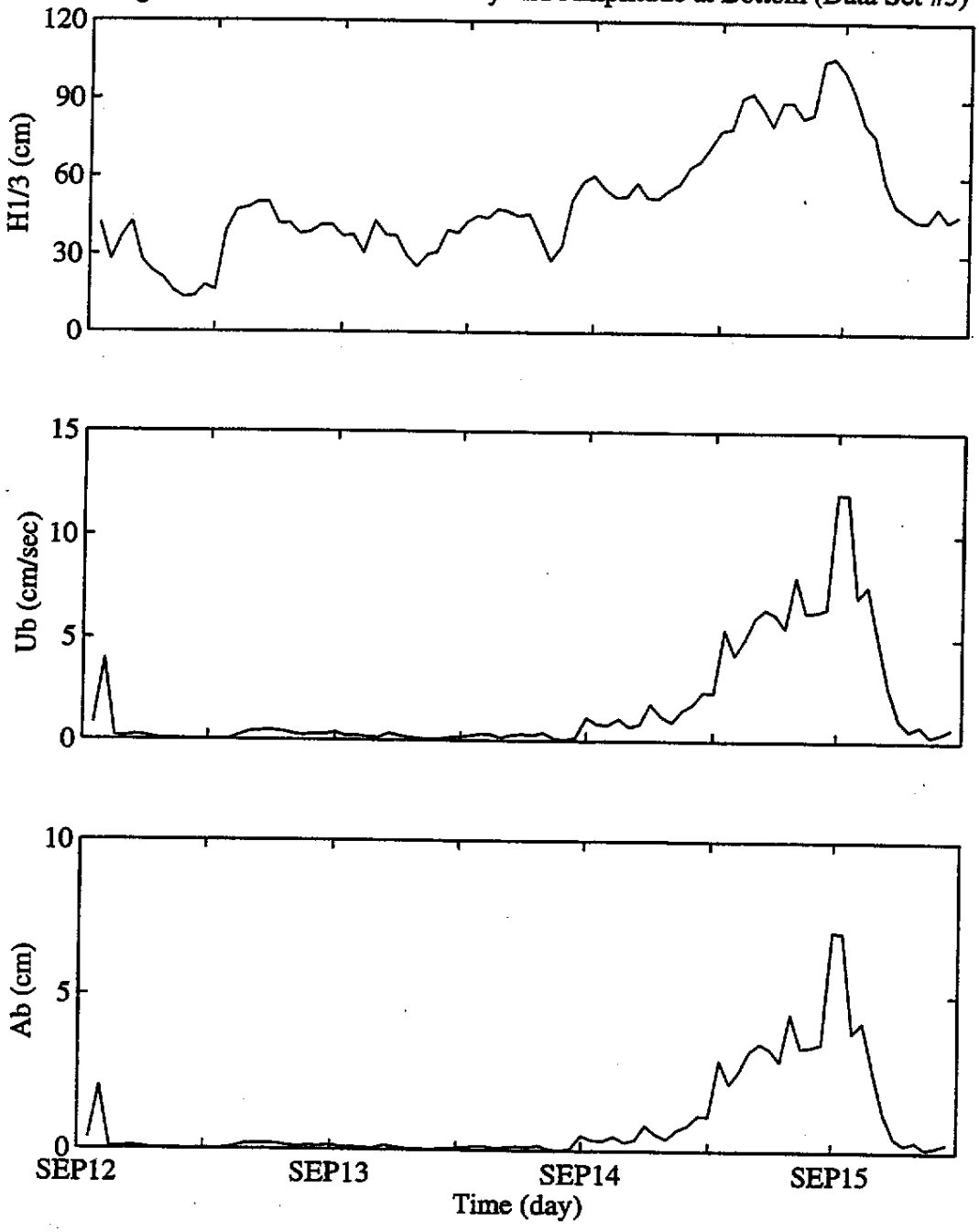

Figure 23a. Time Series of Sediment Concentration at 20cm AB (Data Set #3)

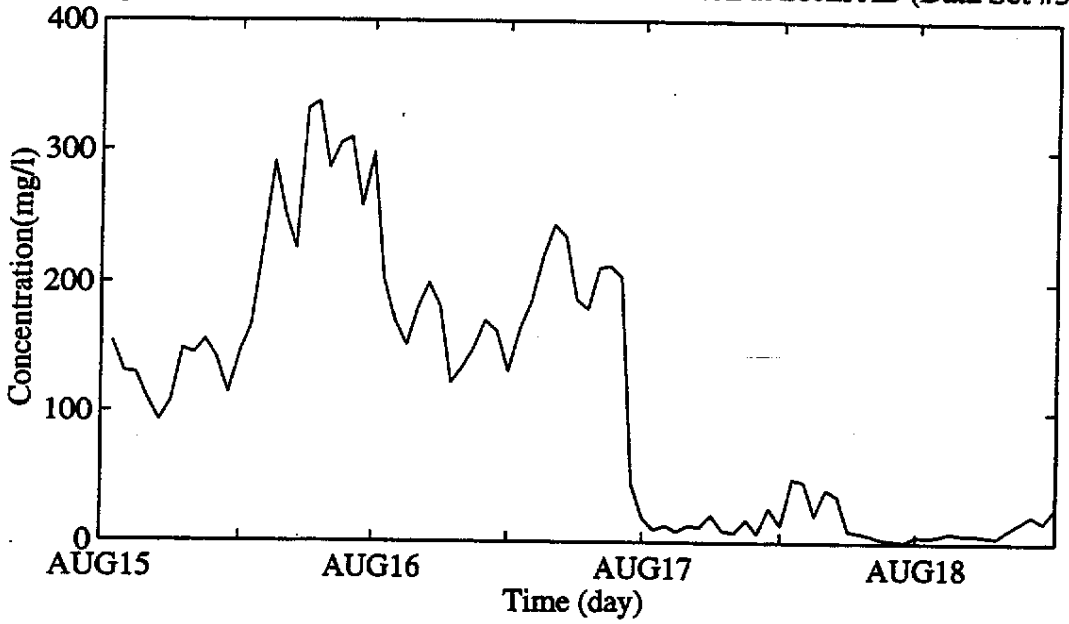

Figure 23b. Integrated Sediment Concentration (Data Set #3)

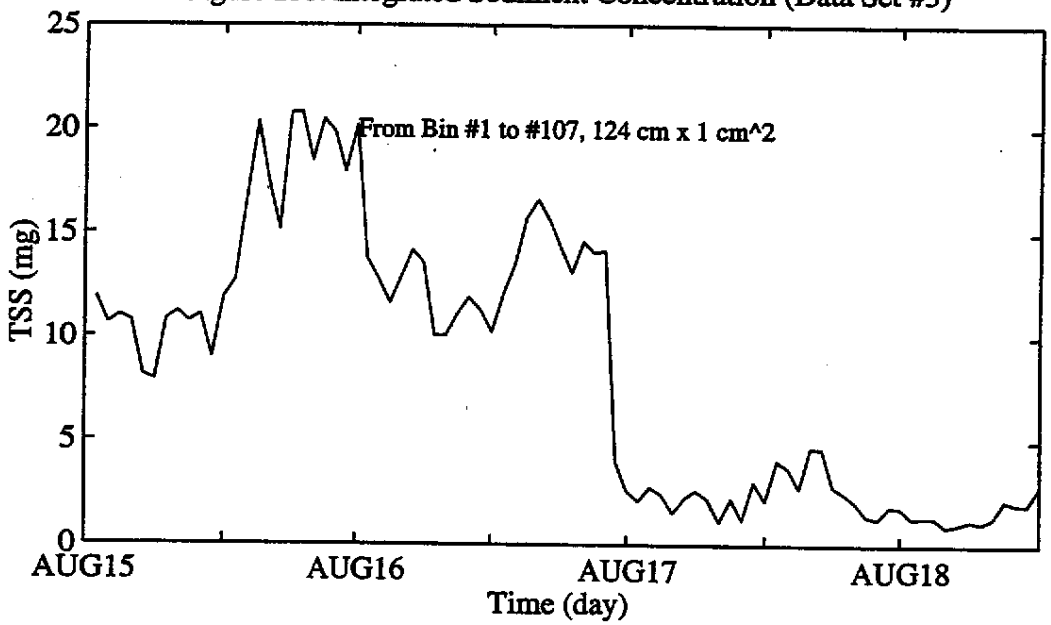

Figure 24a. Time Series of Sediment Concentration at 20cm AB (Data Set #4)

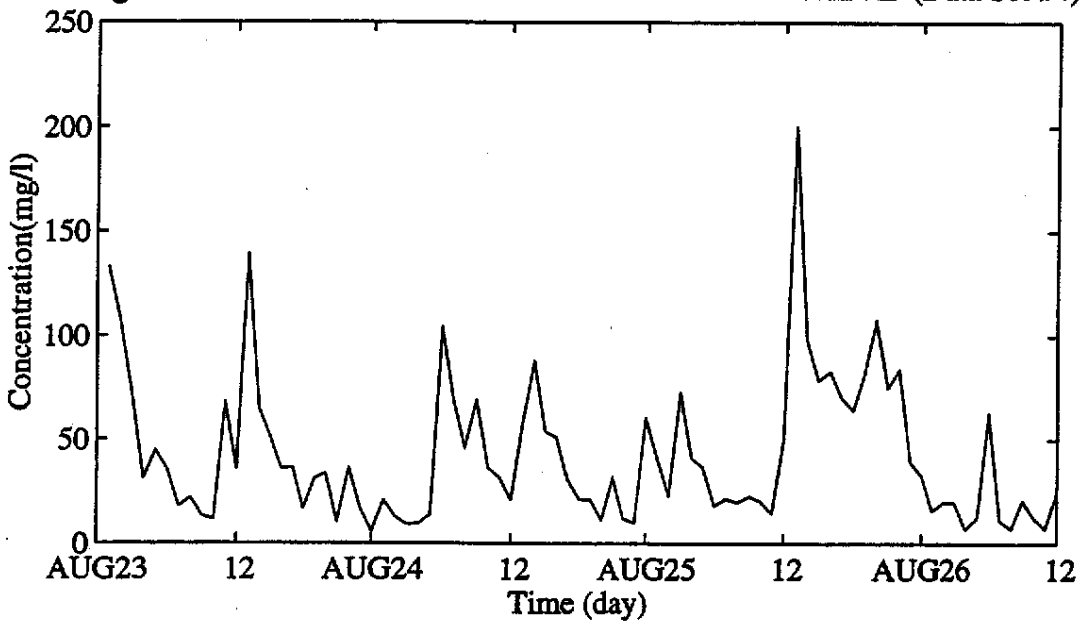

Figure 24b. Integrated Sediment Concentration (Data Set #4)

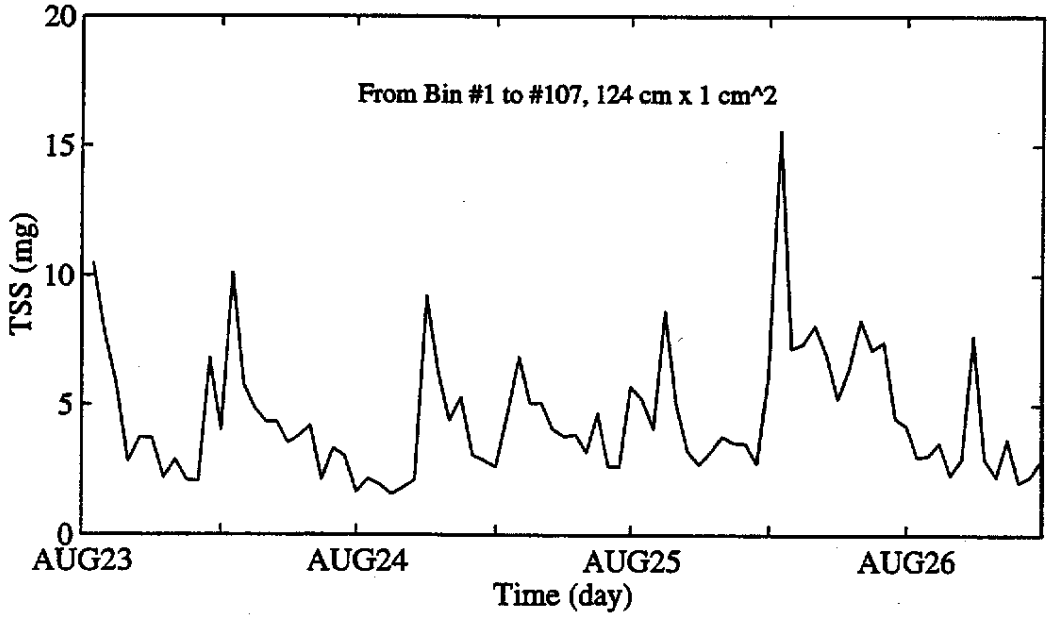

Figure 25a. Time Series of Sediment Concentration at 20cm AB (Data Set #5)

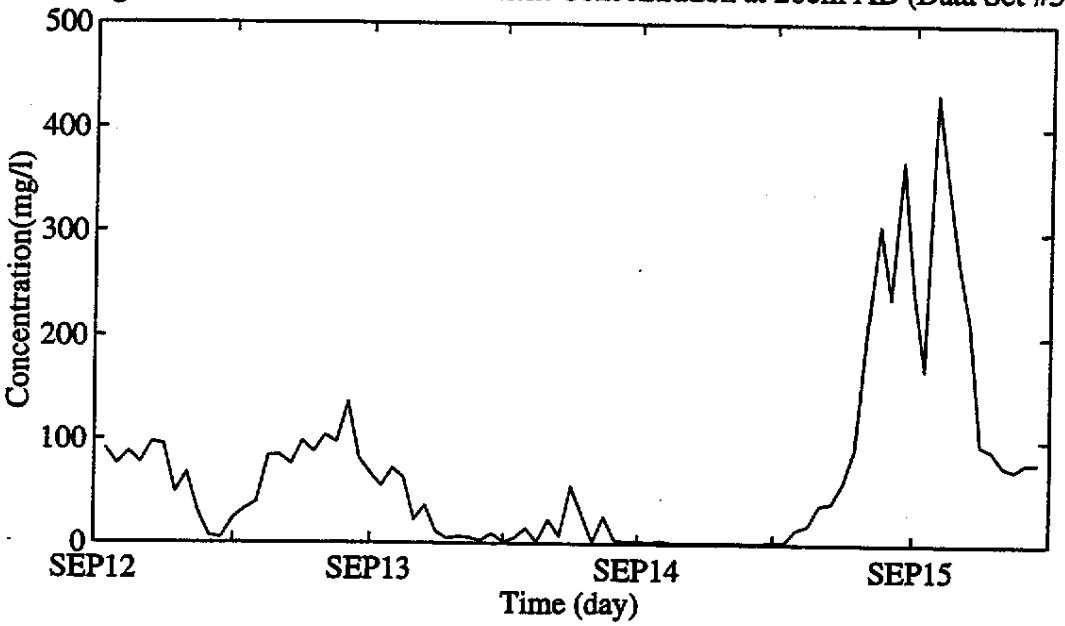

Figure 25b. Integrated Sediment Concentration (Data Set #5)

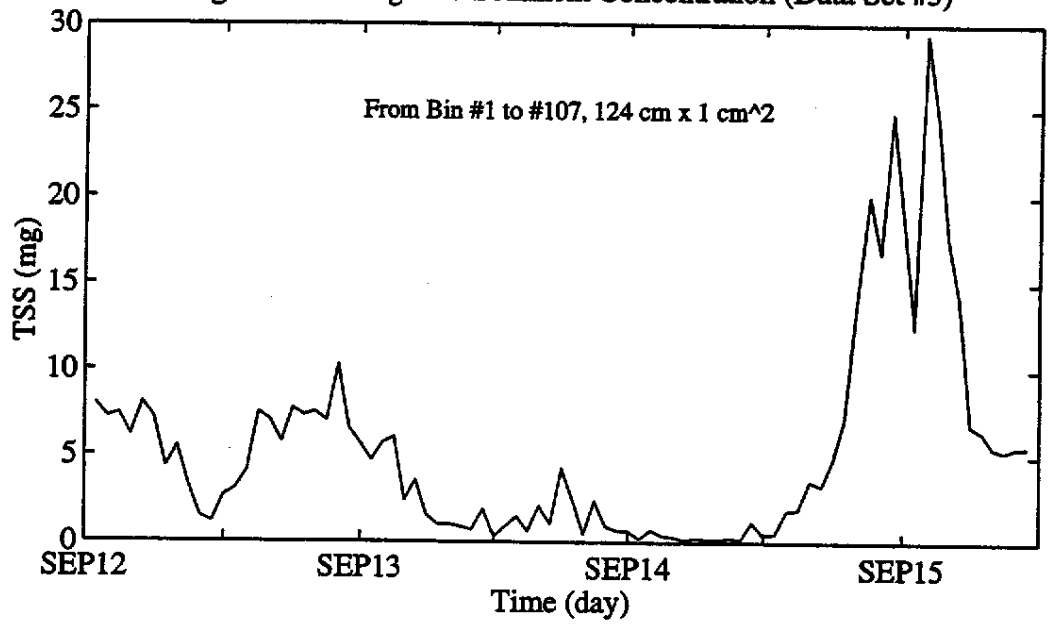

Figure 26. Conc., H1/3, Bottom Cur. Vel. and Dir. (ARMS Data Set #3)

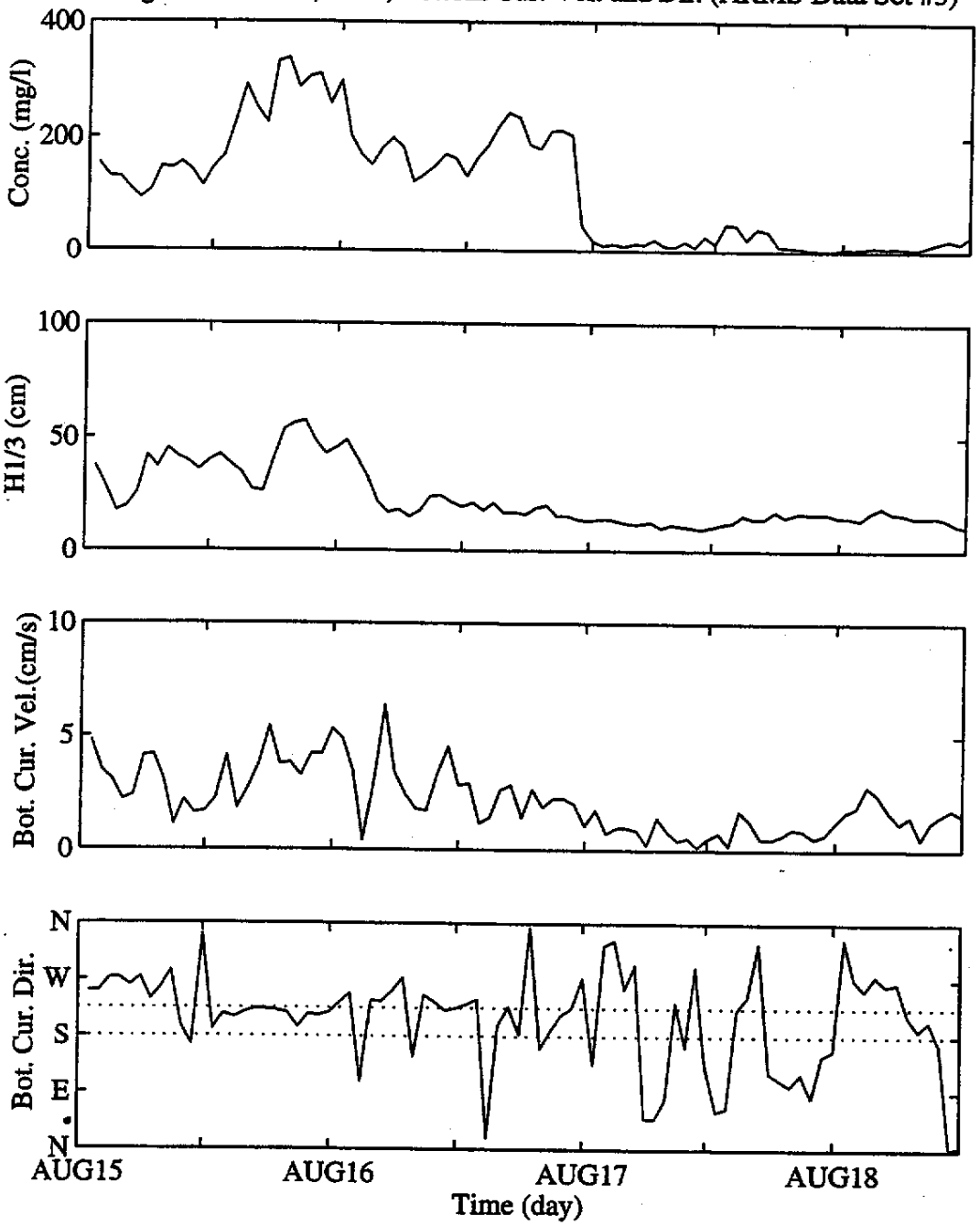

Figure 27. Conc., H1/3, Bottom Cur. Vel. and Dir. (ARMS Data Set #4)

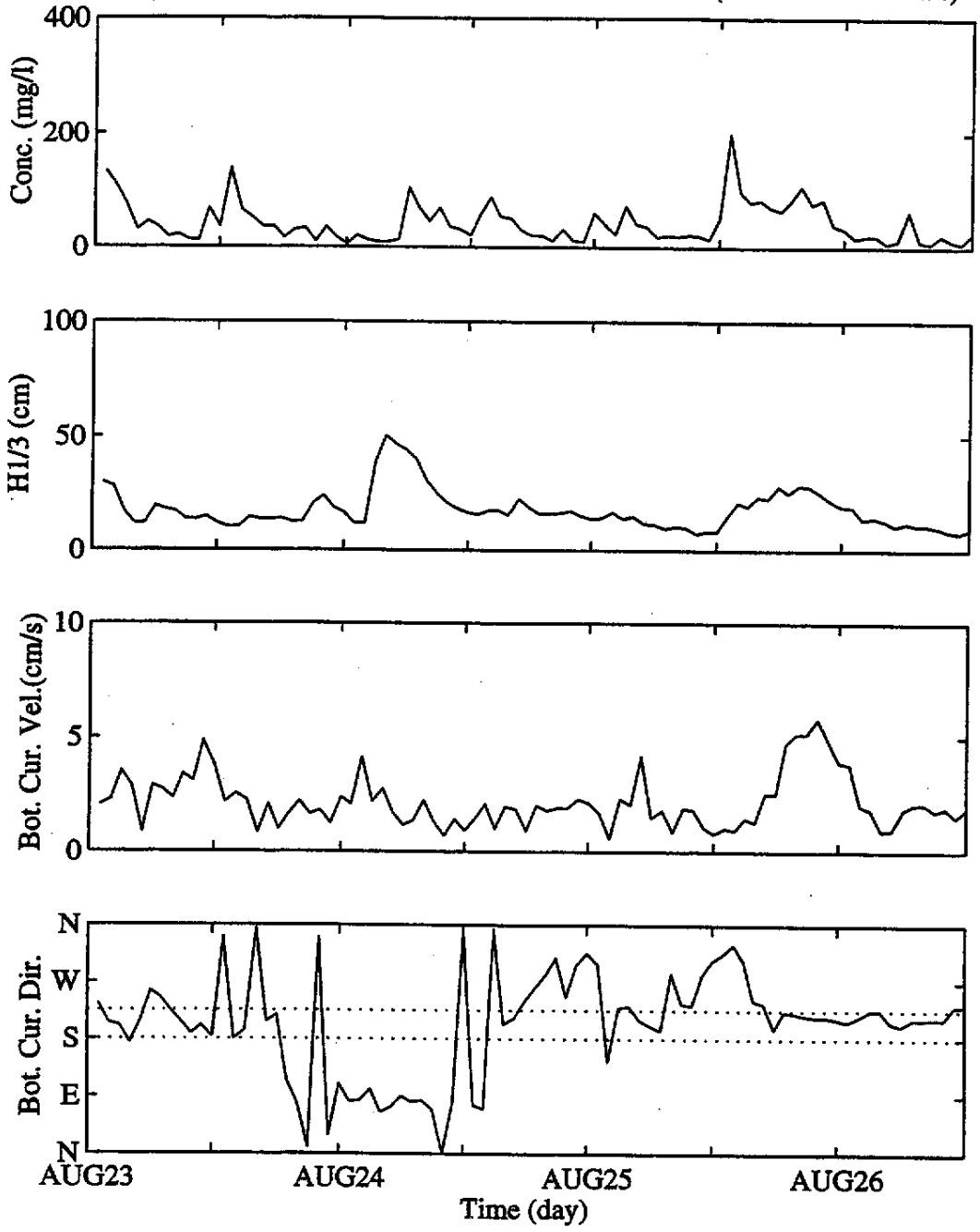

Figure 28. Conc., H1/3, Bottom Cur. Vel. and Dir. (ARMS Data Set #5)

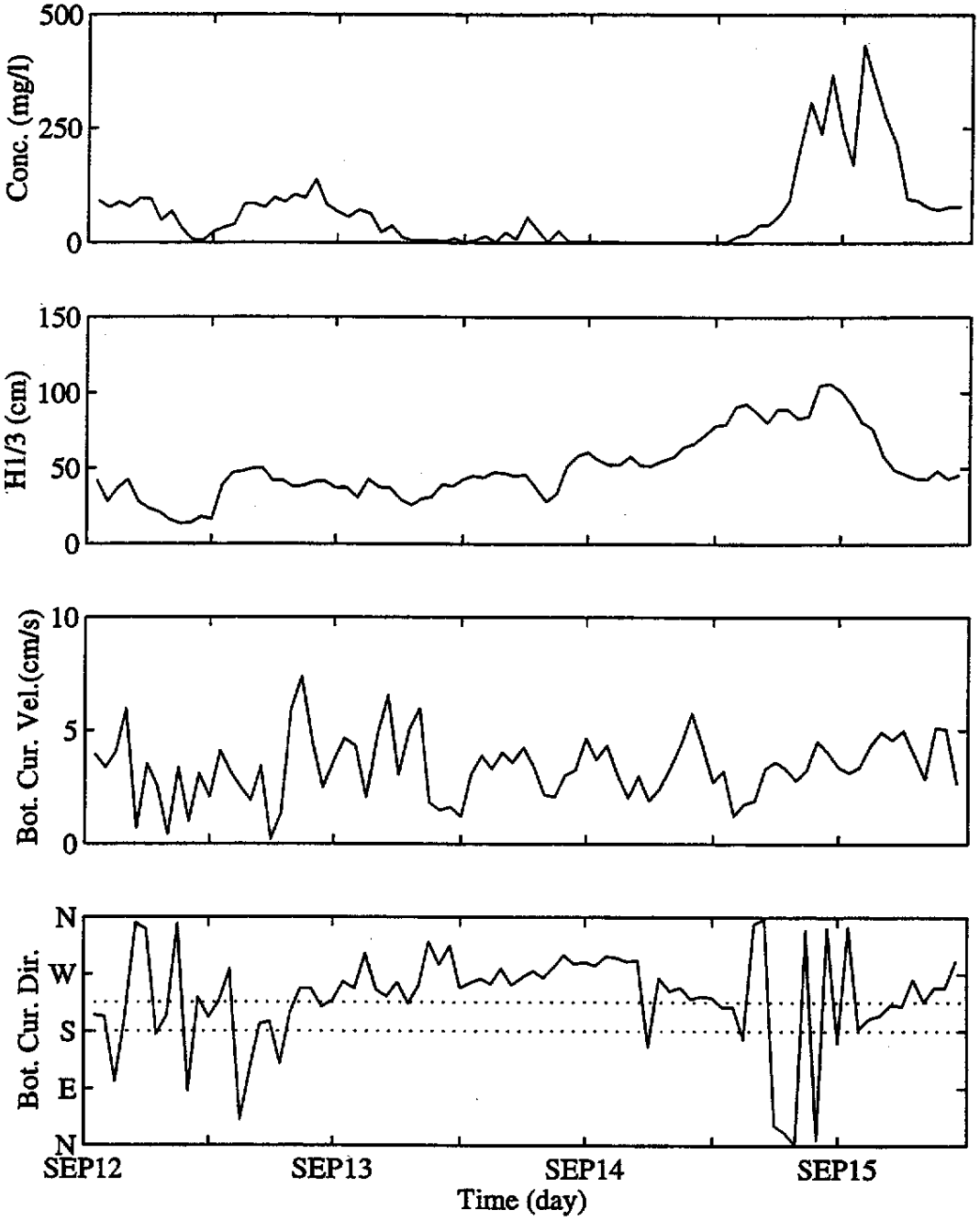

Figure 29a. Power Spectral Density of Water Elevation (Data Set #3, P1)

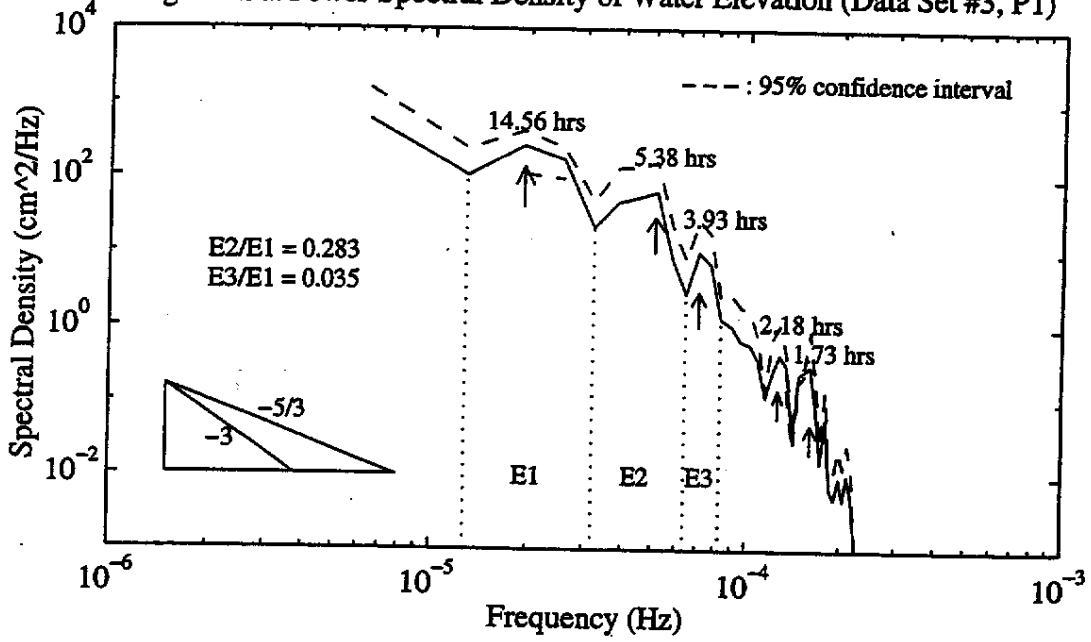

Figure 28b. Power Spectral Density of Water Elevation (Data Set #3, P2)

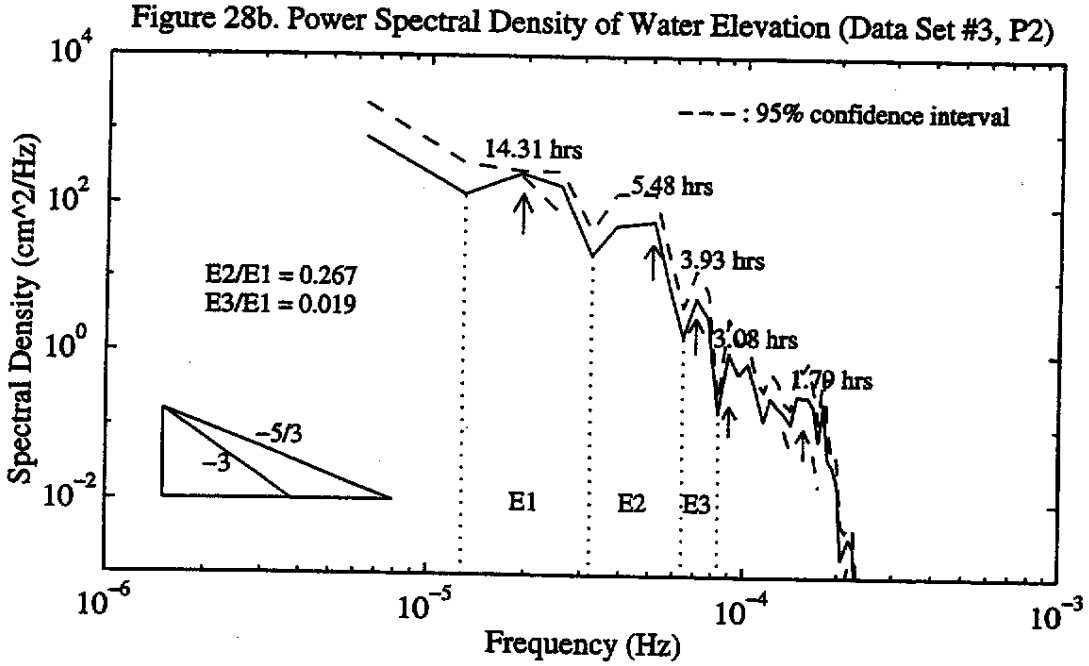

Figure 30a. Power Spectral Density of Water Elevation (Data Set #4, P1)

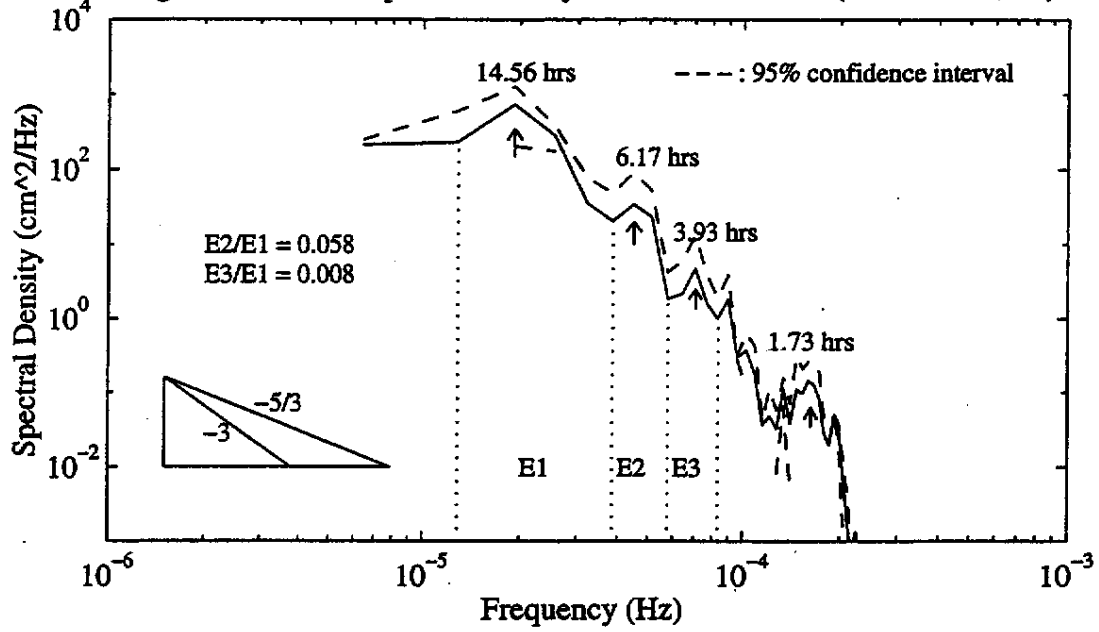

Figure 30b. Power Spectral Density of Water Elevation (Data Set #4, P2)

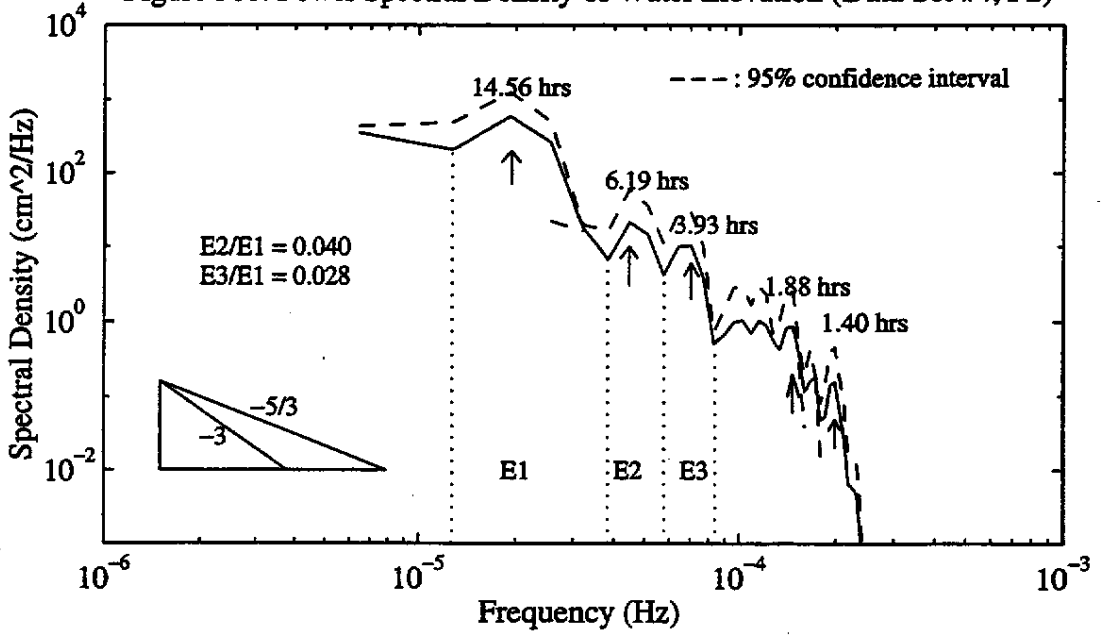

Figure 31a. Power Spectral Density of Water Elevation (Data Set #5, P1)

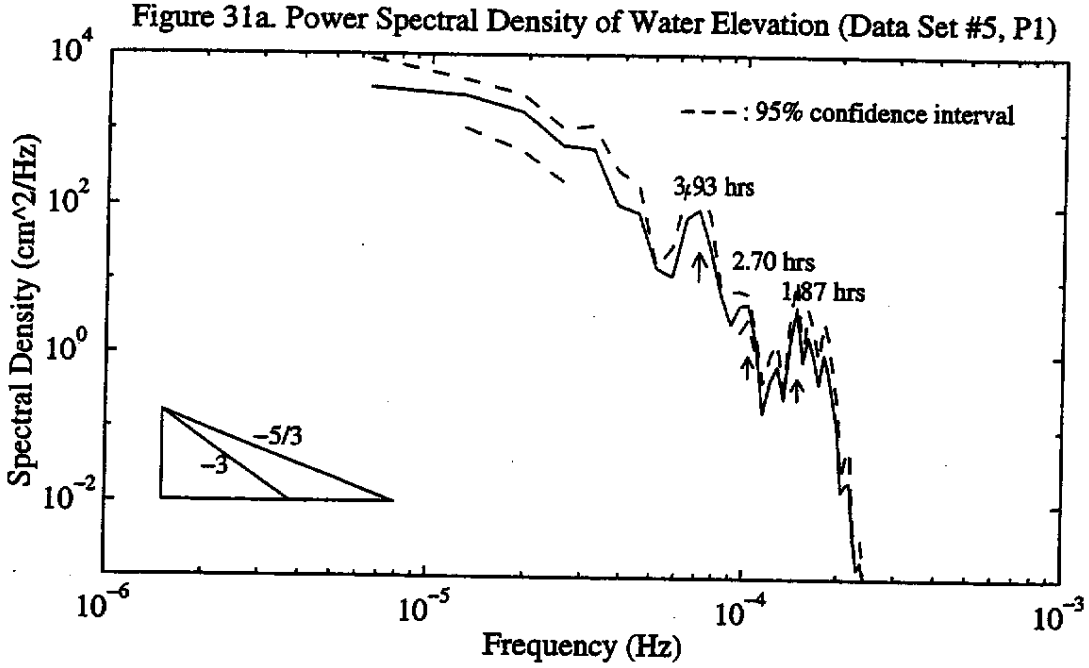

Figure 31b. Power Spectral Density of Water Elevation (Data Set #5, P2)

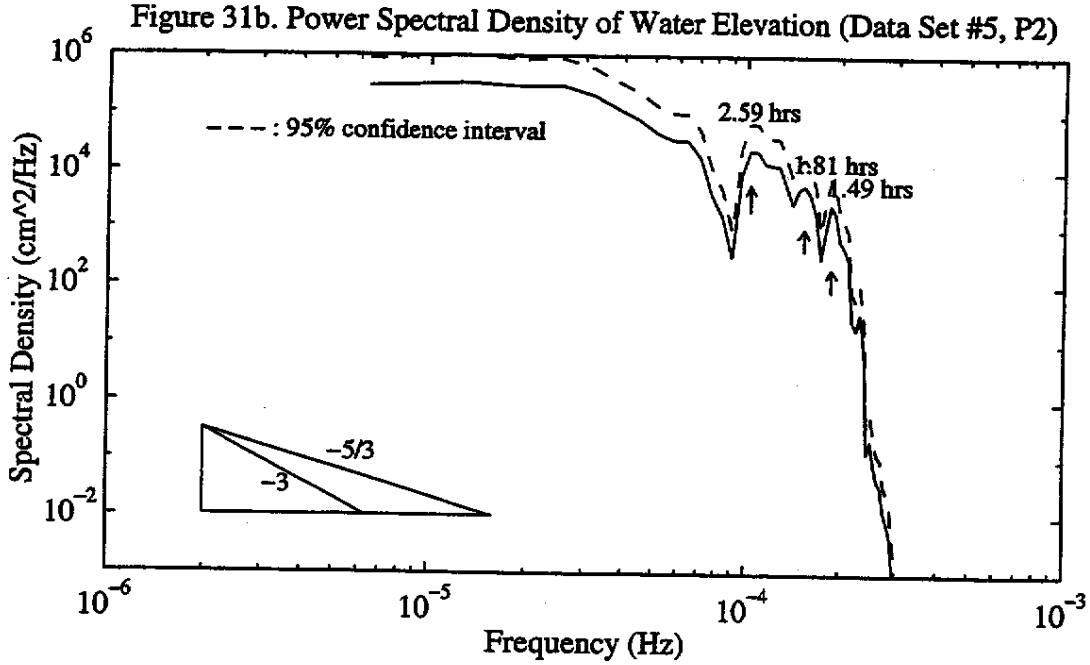

Figure 32. Water Particle Motion Under Shallow Water Wave
(Figure Source: Shore Protection Manual, 1984)

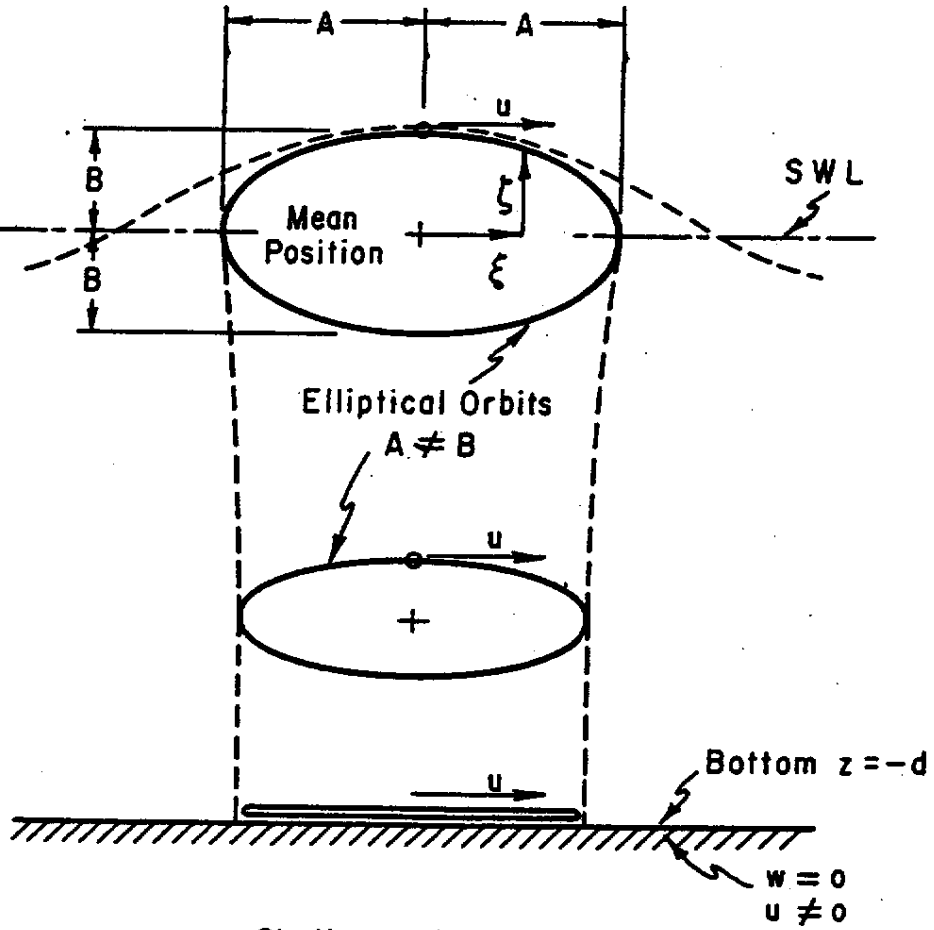

Shallow-water wave
or
Transitional-water wave

$\frac{d}{L} < \frac{1}{2}$

Figure 33. Water Surface Fluctuation and Velocity Caused by Seiche

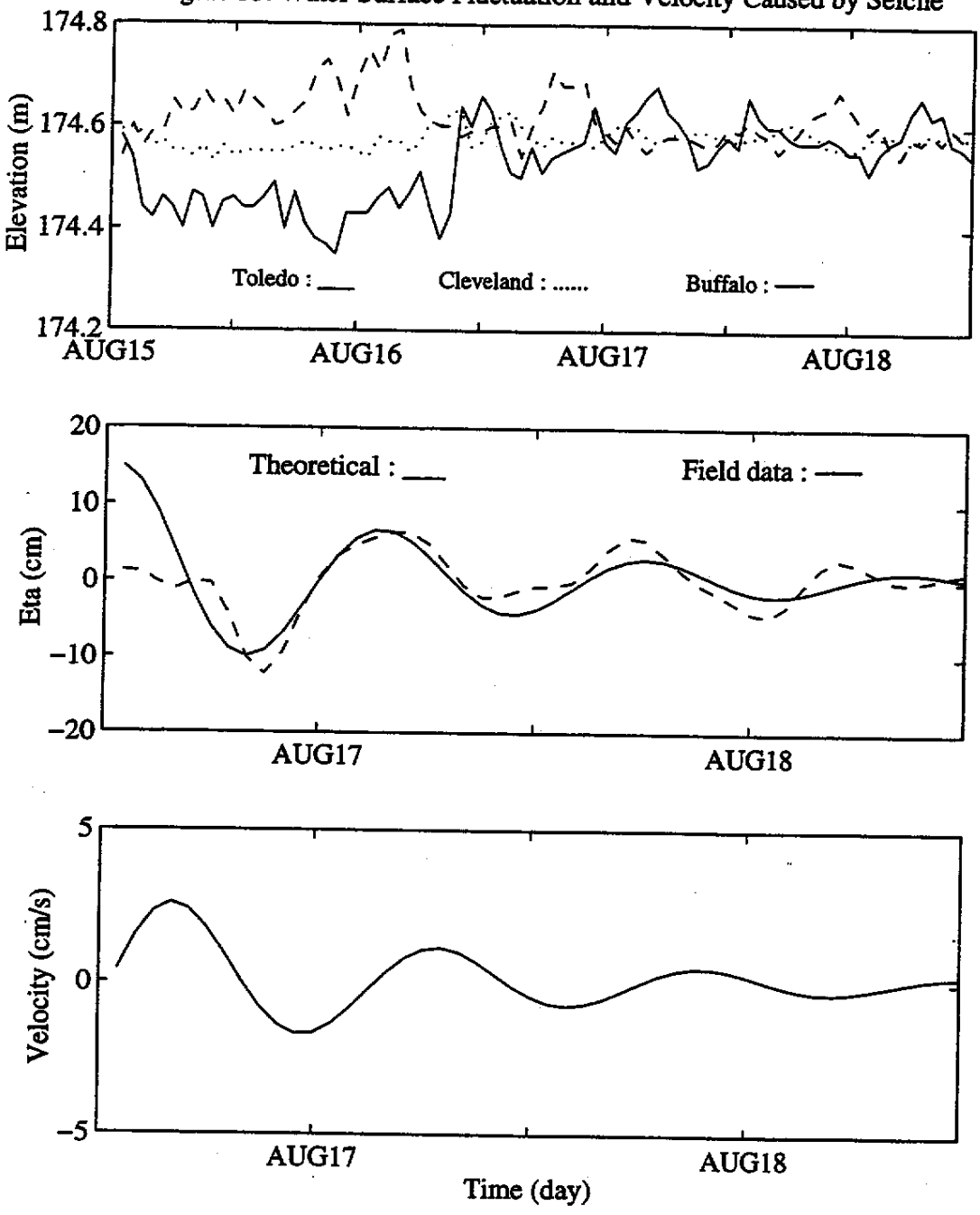

APPENDIX

Power Spectrum Diagrams for U And V Velocities

A.1. Power Spectral Density of U–Velocity (Data Set #3, BASS I)

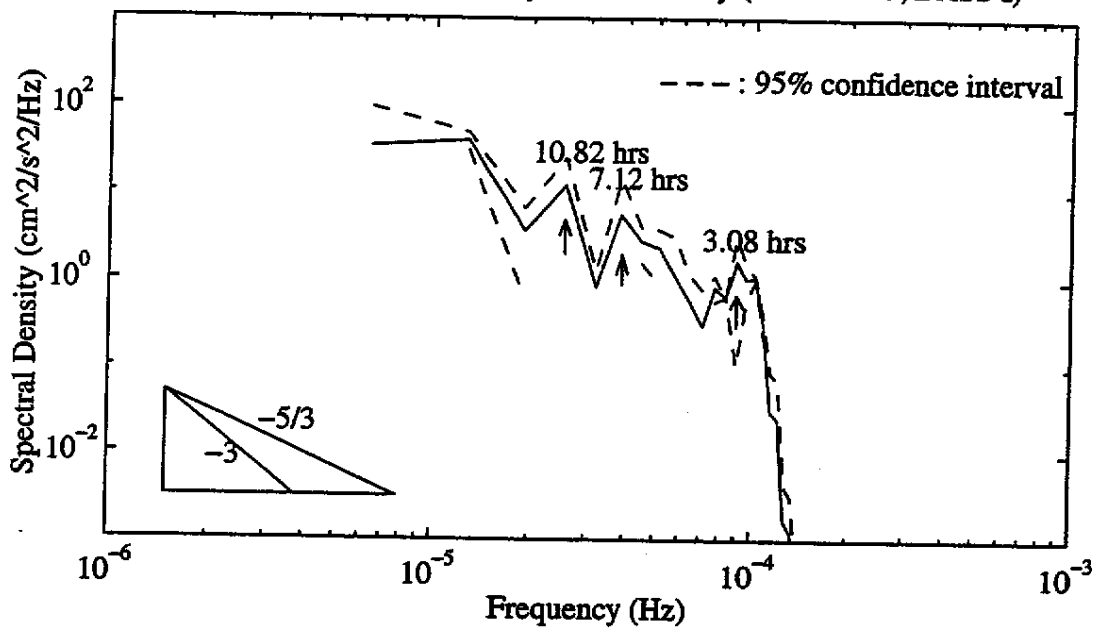

A.2. Power Spectral Density of U–Velocity (Data Set #3, BASS II)

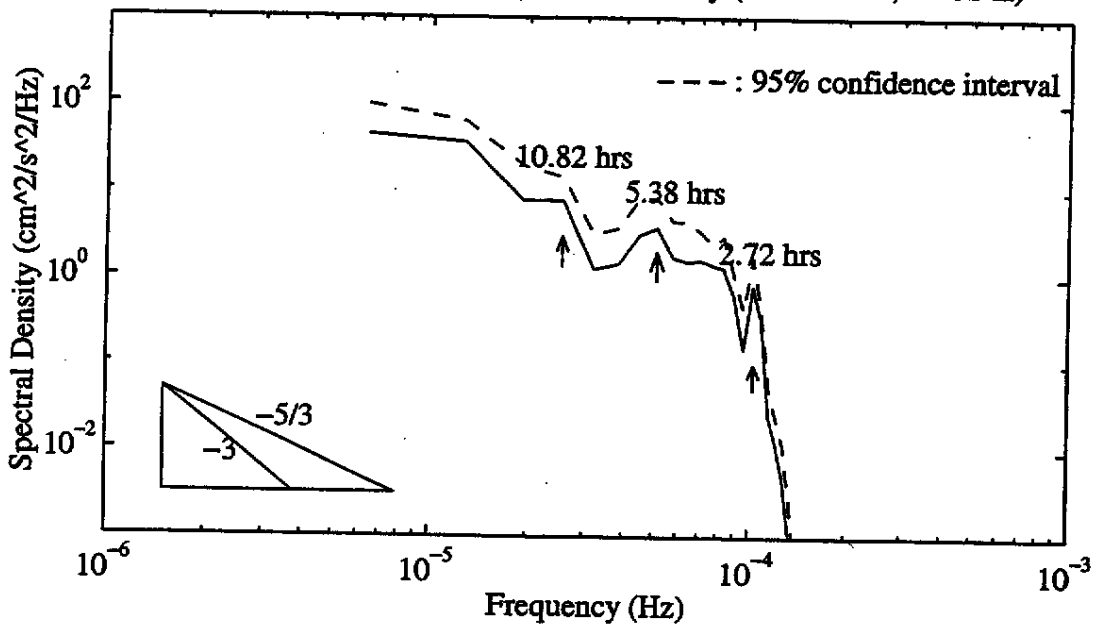

A.3. Power Spectral Density of U–Velocity (Data Set #3, BASS III)

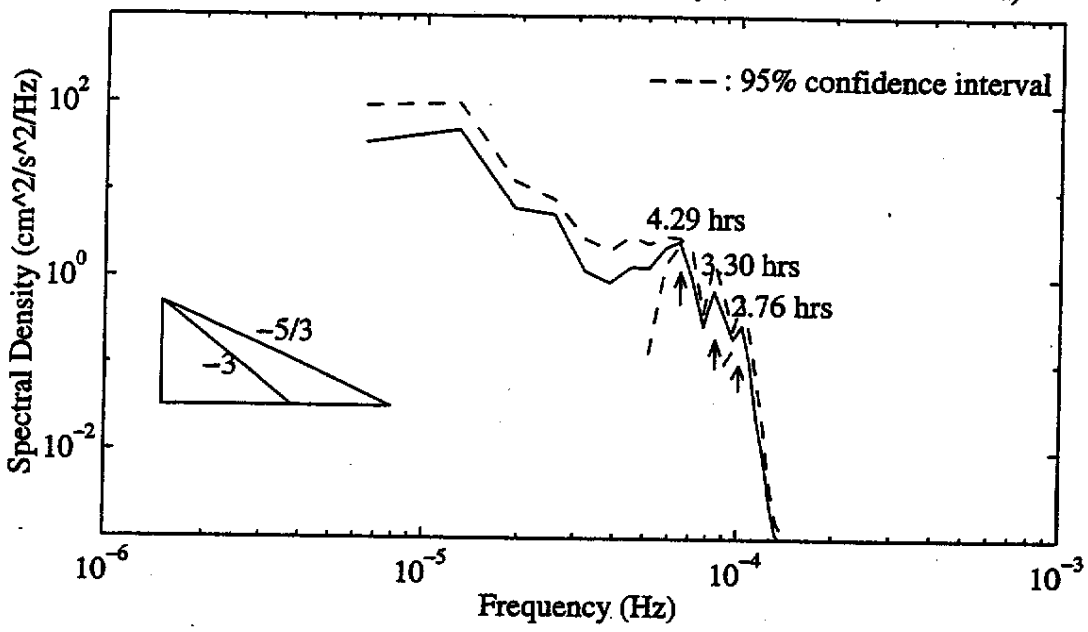

A.4. Power Spectral Density of U–Velocity (Data Set #3, BASS IV)

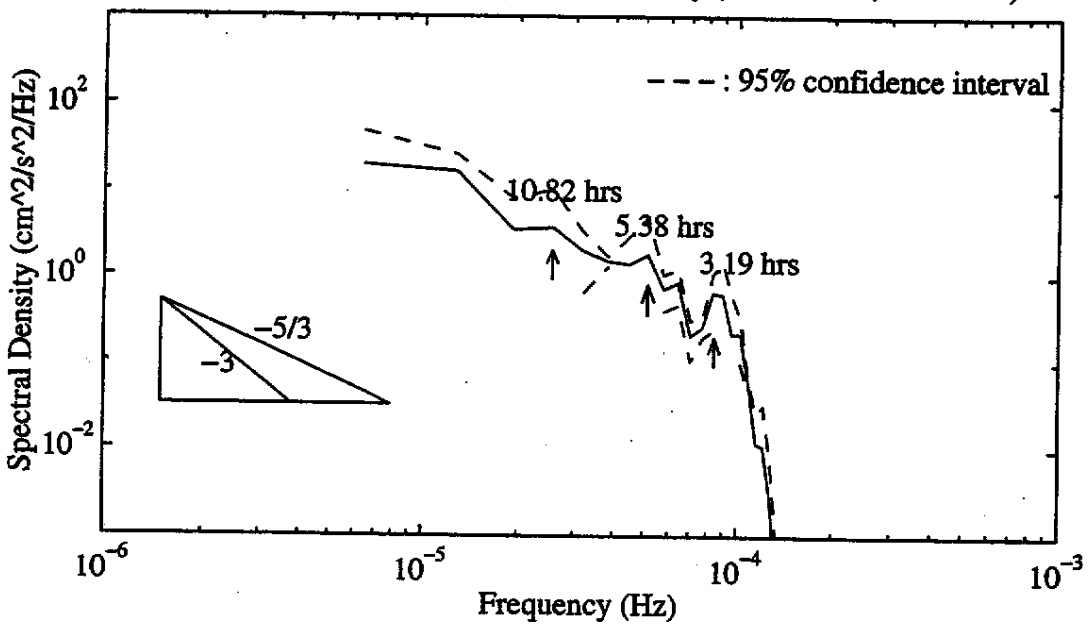

A.5. Power Spectral Density of V–Velocity (Data Set #3, BASS I)

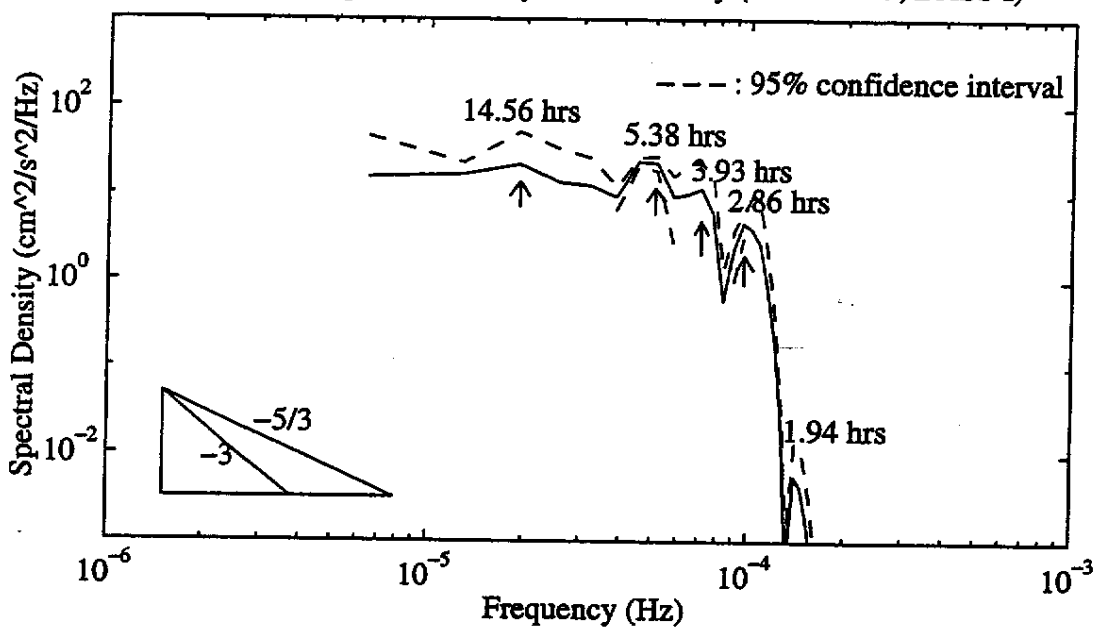

A.6. Power Spectral Density of V–Velocity (Data Set #3, BASS II)

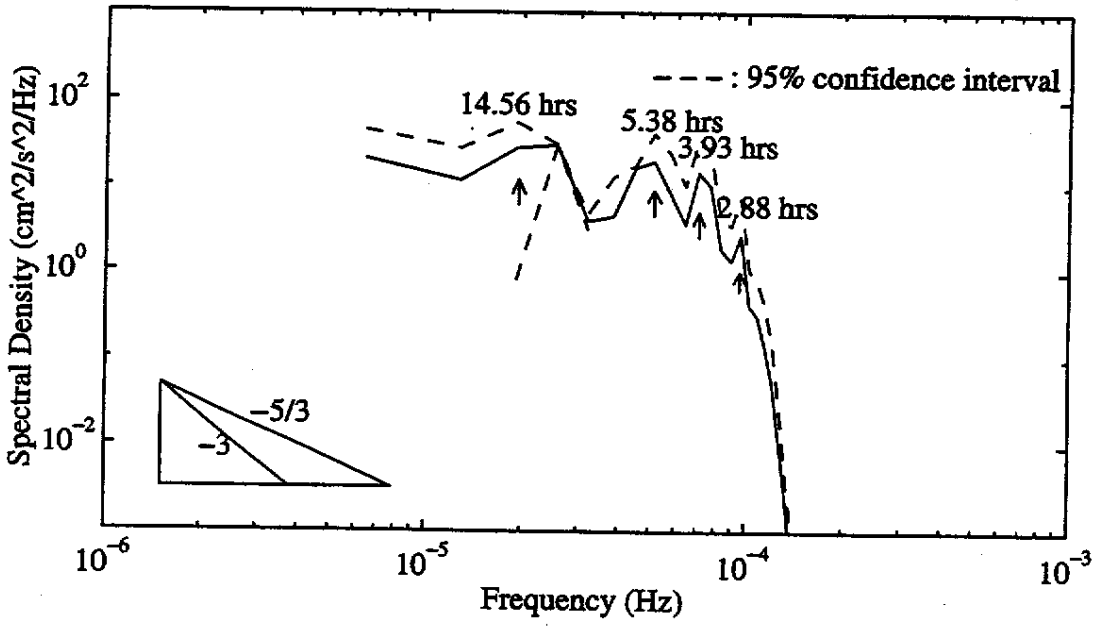

A.7. Power Spectral Density of V–Velocity (Data Set #3, BASS III)

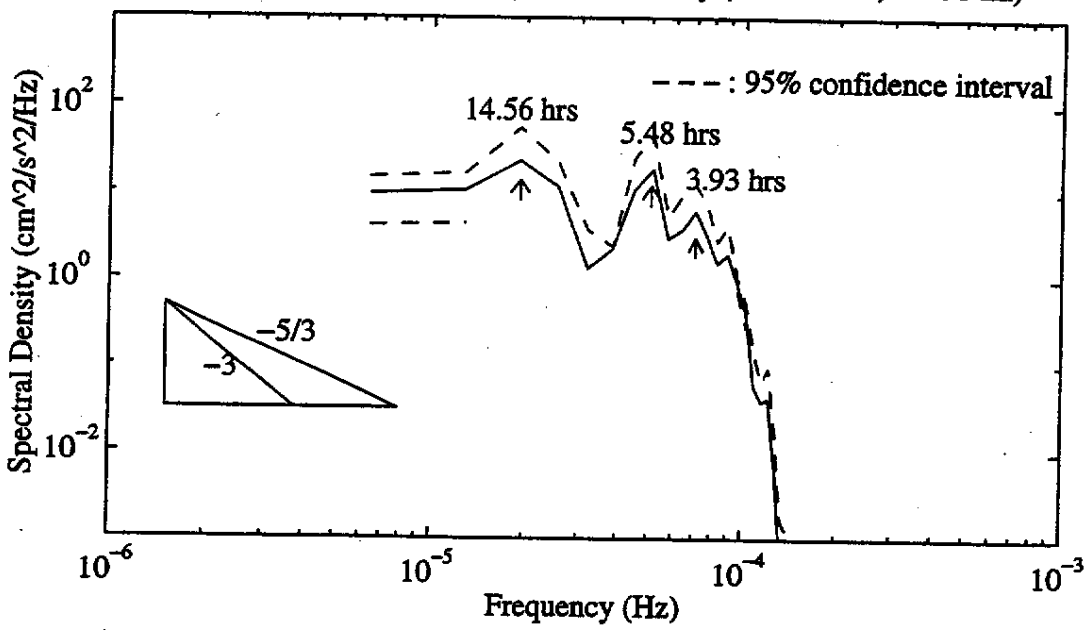

A.8. Power Spectral Density of V–Velocity (Data Set #3, BASS IV)

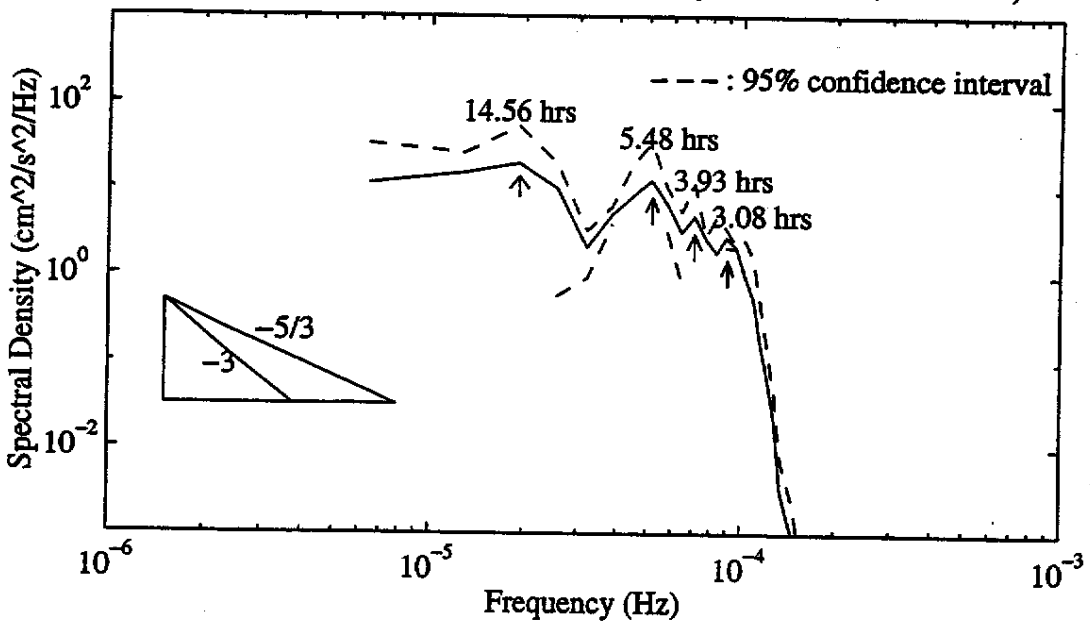

A.9. Power Spectral Density of U–Velocity (Data Set #4, BASS I)

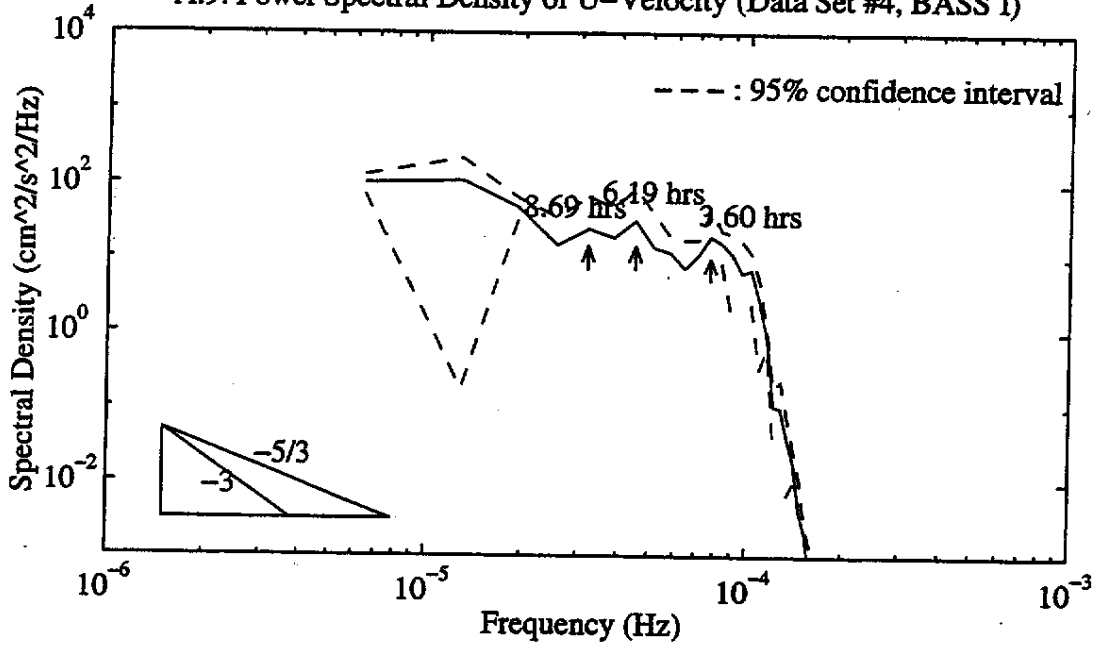

A.10. Power Spectral Density of U–Velocity (Data Set #4, BASS II)

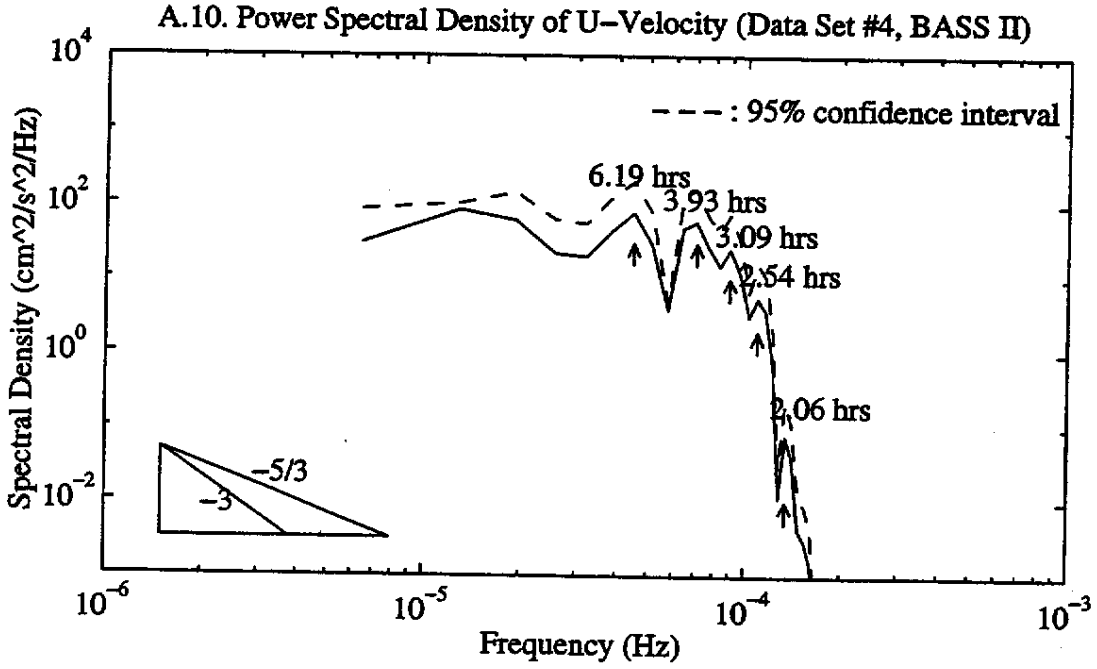

A.11. Power Spectral Density of U–Velocity (Data Set #4, BASS III)

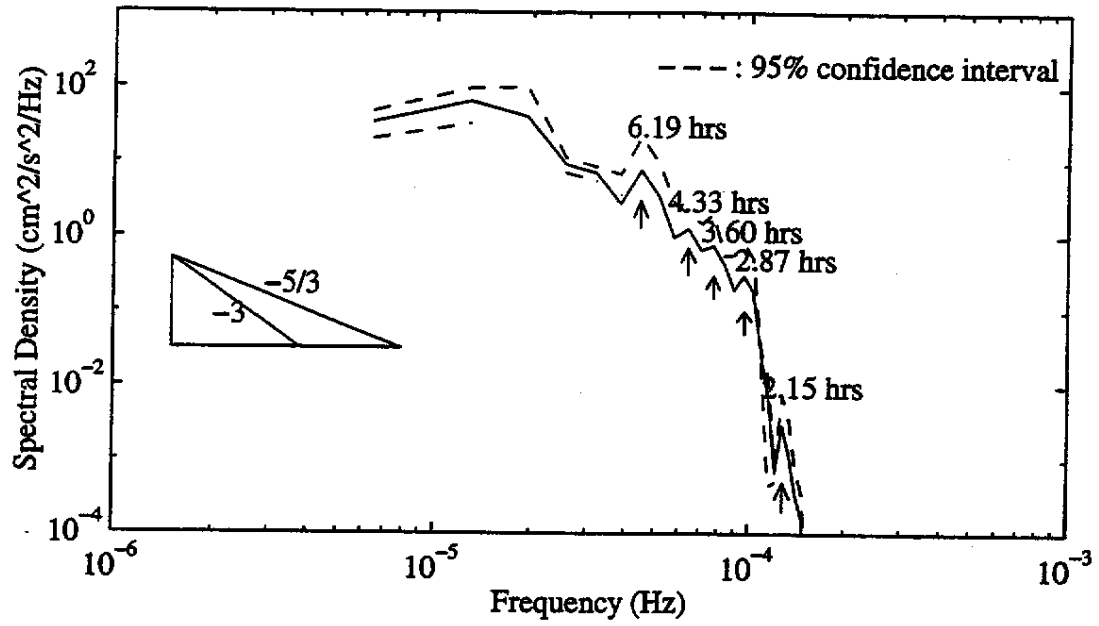

A.12. Power Spectral Density of U–Velocity (Data Set #4, BASS IV)

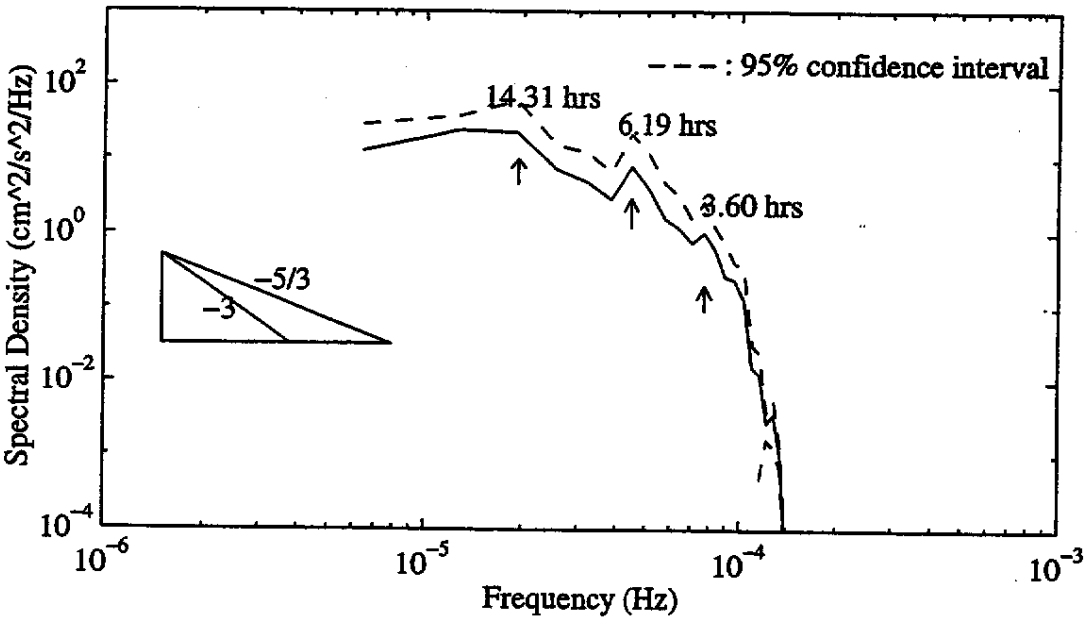

A.13. Power Spectral Density of V–Velocity (Data Set #4, BASS I)

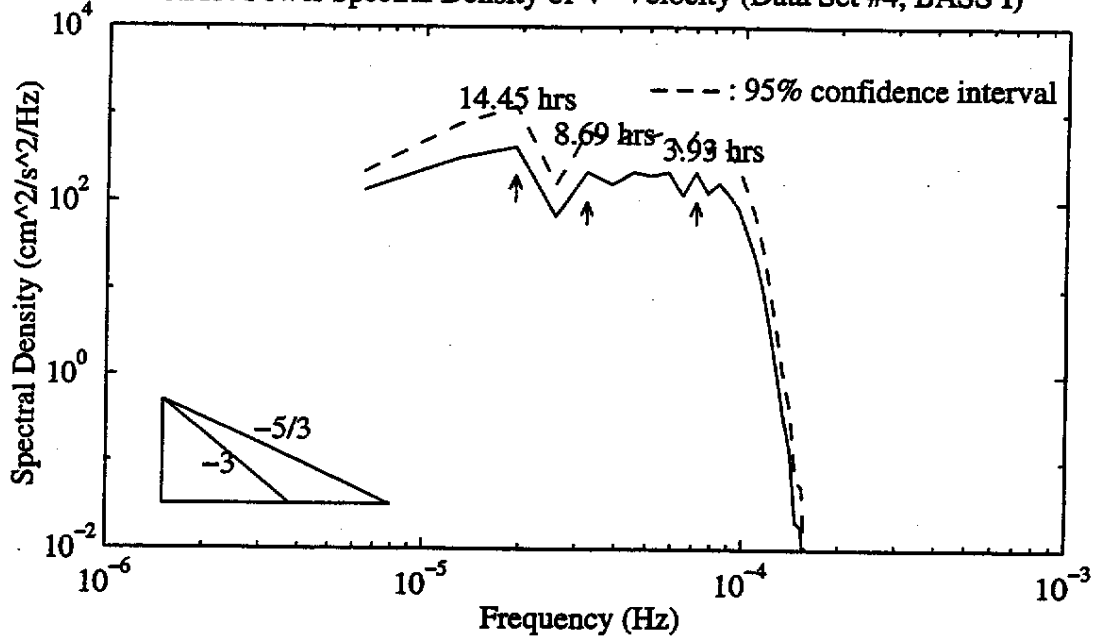

A.14. Power Spectral Density of V–Velocity (Data Set #4, BASS II)

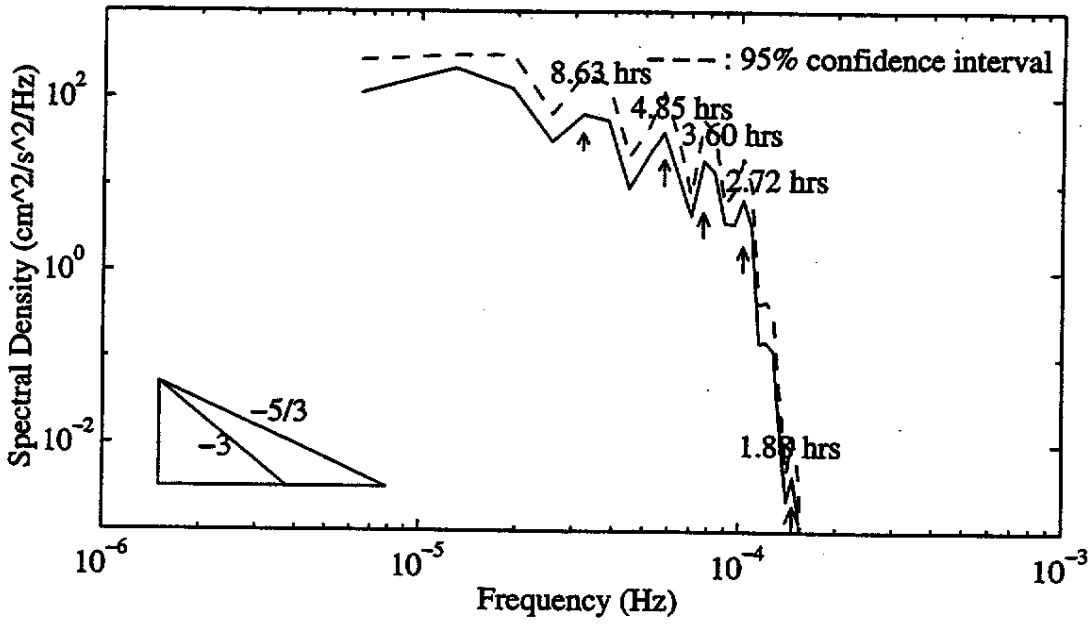

A.15. Power Spectral Density of V–Velocity (Data Set #4, BASS III)

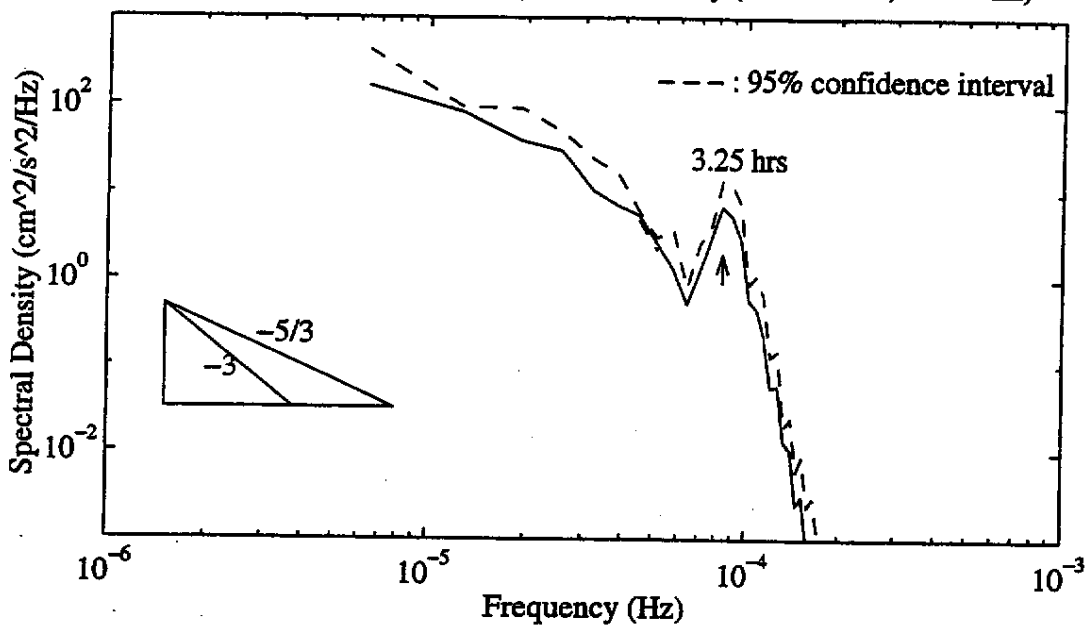

A.16. Power Spectral Density of V–Velocity (Data Set #4, BASS IV)

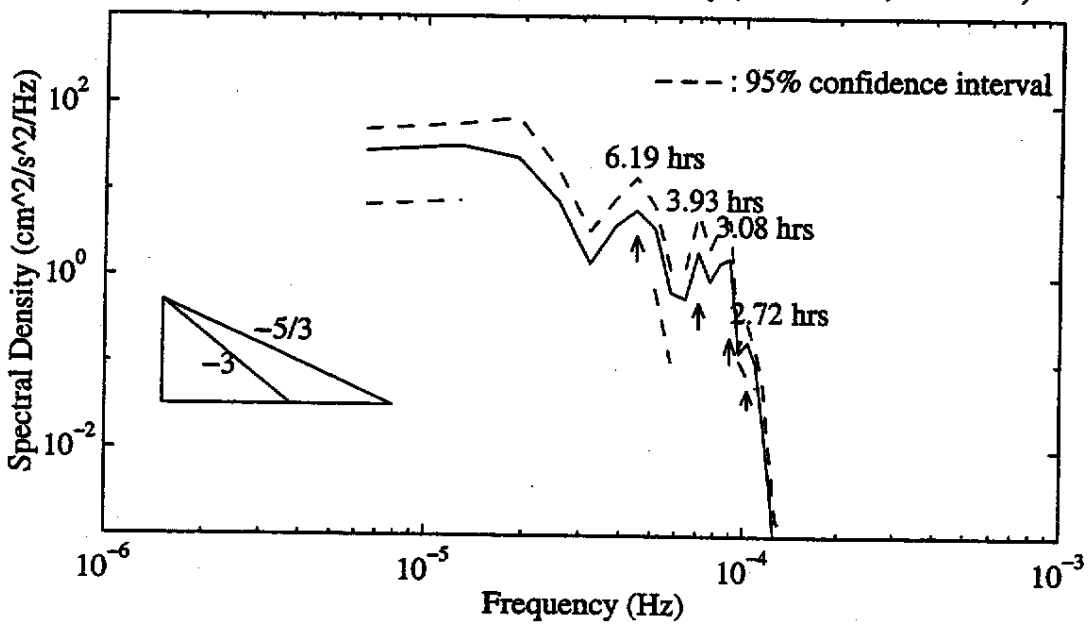

A.17. Power Spectral Density of U–Velocity (Data Set #5, BASS I)

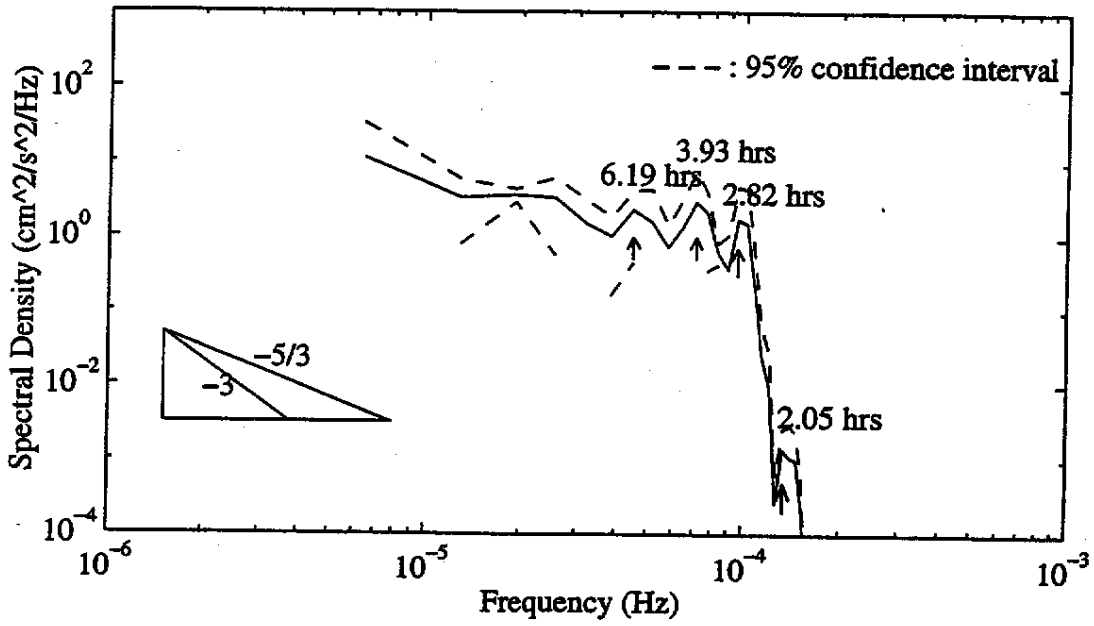

A.18. Power Spectral Density of U–Velocity (Data Set #5, BASS II)

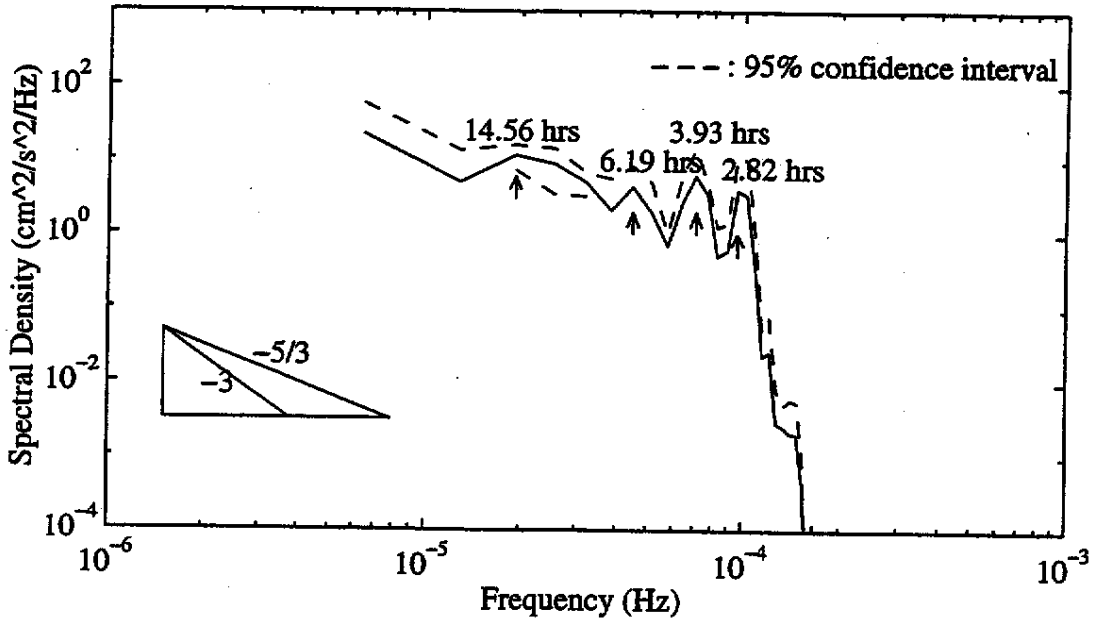

Integrated Analysis of the Impact of Unconfined Placement Activities on Nearshore Sensitive Areas

REPORT NO. 2

CLIMATOLOGICAL ANALYSIS OF LAKE ERIE CIRCULATION AND TRANSPORT FOR SENSITIVE SITE IMPACTS

by
Ahlem Ben Othman and Keith W. Bedford
Civil and Environmental Engineering and Geodetic Science
The Ohio State University
Columbus, Ohio

Contract DACW39-95-K-0018
US Army Corps of Engineers
Waterways Experiment Station
Vicksburg, MS

April 3, 1998

TABLE OF CONTENTS

LIST OF TABLES

LIST OF FIGURES

PROJECT OVERVIEW

There have been concerns expressed for some time that unconfined placement of material from dredging activities would cause potential adverse impacts on sensitive nearshore areas. Typical nearshore sensitive areas are beaches, water intakes (private or municipal), and wetlands and all are typically located some distance away from the placement site. Two issues require elaboration before answers can be obtained about the potential impact. The first question becomes, is the material from the site actually transported to the sensitive area?; while the second question is what are the intensities of the water quality constituents associated with particles once (or if) they arrive at the nearshore zone from the placement site? Simple measurements at the nearshore site are the integrated sum of the sediments being carried to the site from not only the disposal site, but from other natural sources such as river tributary input or wind-driven circulation. Therefore, separating out the impacts specifically due to the disposal site is not achieved and the more basic question of whether placement site particles even get to the area is not addressed.

To perform the correct analysis, one must know not only the magnitude of the sediments entrained at the site, but the frequency, duration, and magnitude of the resulting particle transport to the sensitive areas. Therefore, it is necessary to describe the conditions required to cause the nearshore impact and, if necessary, this must be a probabilistic description. The presumption of this project is that the most robust assessment of the impacts must include data necessary to address both questions outlined above but that to date the first question has been ignored in most impact assessments. This proposed research program is therefore designed to respond robustly to the first question by pursuit of three objectives.

a. Determine by field measurements and model elaboration the entrainment and sediment flux climatology of the placement site;
b. Determine and quantify the conditions that most probably will result in placed material being transported to the sensitive area and the duration and intensities of the resulting particle loads; and
c. Compare the relative intensities of the sensitive site particle load from the placement site to those sensitive site loads originating from other sources (such as tributary input or local resuspension), during those times when placed particles are delivered to the nearshore site.

This report is Number 2 of the series and is authored by A. Ben Othman and K. Bedford. The objective of this report is to document the use of an existing database of 25-year hourly circulation data for Lake Erie to determine the frequency and duration of storms and transport that result in materials from the placement site being directly transported to the nearshore sensitive site. The basis of this report is the 25-year historical database recreated by the Great Lakes Forecasting System. The models are briefly described as is the climatologic database. The frequency, duration, time of travel, and number of site "hits" are summarized. The results indicate that wind driven circulation and seiches are dominant and that in every year of the 20-year record, at least one event is of sufficient magnitude and duration to have surface currents reach the vicinity of the intake pipes.

The same cannot be said of the bottom currents for which no event is even of sufficient strength and duration to reach the intake pipes. These results suggest that clay particles, easily entrained from the placement site and mixed to the surface, could also be transported to the intake pipes by at least one event per year.

The project WEB pages at http://superior.eng.ohio-state.edu/~sean/field.html and http://superior.eng.ohio-state.edu/~jklee/cooldata.html contains significant field data and site characteristics and these pages must be included as a portion of the report.

CHAPTER 1: INTRODUCTION AND OBJECTIVES

1.1 The Management Problem

It has been a common practice to dredge the channels of the Maumee River and the bottom of Lake Erie and then dispose the material at a location in the lake, particularly the Western Basin. However, there have been growing concerns that this unconfined placement of dredged material could cause serious effects on sensitive shoreline regions due to material transport from the site. These sensitive sites are typically beaches and municipal and private water intakes. Based on the potential threat to these sensitive areas, some questions need to be answered. The first question is: "can the material from the disposal site actually reach the sensitive sites?" The second question is: "when and if these materials reach the sensitive sites, what are the intensities?" The latter question can be addressed by conducting basic field experiments. These experiments would consist of measuring the sediment concentration at the sensitive area. However, this simple method does not indicate whether the measured particles originated at the disposal site or not. Chances are they did not because there are many contributing sources of sediments (tributaries) that would cause materials to reach the shoreline and because winds could resuspend and carry particles anywhere in the lake. Therefore, it is worthwhile to conduct a study focusing on the effects of the dredged material placed at the sensitive sites. The study of the transport of placement site particles to the shoreline, necessitates the recognition that these particles are carried away by wind, gravity, wave and current-driven water column physics which derive from randomly occurring storms. Consequently, one must know not only the magnitude of the sediments entrained at the site, but the frequency, duration, and magnitude of the resulting particle transport to the sensitive areas. Furthermore one must describe the conditions probabilistically.

1.2 The Technical Problem and Proposed Solutions

In order to address the problem probabilistically, a robust data base needs to be accumulated and tools necessary to analyze that data must be developed. This study also requires field data that would ensure as much as possible the reliability of the results.

The system used to conduct this study is the Forecasting/Nowcasting system, called the Great Lakes Forecasting System (GLFS). It was designed to make regularly scheduled predictions of the physical status of each one of the Great Lakes. The GLFS products are the following variables: the full three dimensional temperature and velocity distributions, the water surface levels and fluctuations, along with the deepwater and nearshore wind wave distributions. GLFS uses the three-dimensional Princeton Ocean Model (POM), otherwise known as the Mellor Blumberg Model, which will be discussed further in Chapter 3. It also uses the US Army Corps SHALWAVE spectral based wave prediction code and the NOAA GLERL Donelan wave prediction code.

1.3 Objectives

Using GLFS, this study is going to provide a system for determining the susceptibility of a sensitive site to impact from an offshore activity site. A series of probabilities and histograms will be determined to display the magnitude and duration of the sensitive site exposure to the material transported from the unconfined disposal site. Velocity predictions made by GLFS will be the basis for predicting the transport conditions under which a particle at the placement site could possibly reach the sensitive sites. The analysis resulted in the creation of a statistical summary of the patterns that govern the transport of the activity site material towards the sensitive areas.

CHAPTER 2: THE SETTING

2.1 Lake Erie Weather and Flow Patterns

Among the Great Lakes, Lake Erie seems to attract considerable attention from both researchers and the public. The attraction results from several characteristics of this lake. Lake Erie is the shallowest of all the Great Lakes, its maximum depth is 64 meters in the central basin. It is the most sediment dominated, with shorelines subject to erosion through wind waves and storm surges and significant sediment input from the Detroit River, Lake Saint Clair, and the Maumee River watersheds. Because of its shallowness, Lake Erie is susceptible to meteorological activities. These come in the form of wind induced storm surges and seiches.

2.2 Western Basin Site Characteristics

The Western Basin of Lake Erie (Fig. 2.1) is the shallowest section of the lake. Its maximum depth is 10 meters. It is bounded by South Bass, Middle and North Bass Island on the East. The Maumee and Detroit Rivers enter the Western Basin and are the major sources of riverine sediment input to Lake Erie.

2.2.1 The Army Corps Placement Site

The dredged material placement site is located at 41°48.6' N and 83°17.0' W in water of 6.1 to 7.0 meters of depth relative to IGLD Low Water Datum. During the 1996 study season, the average water level was 1.07 m above datum, yielding a depth range of 7.17 to 8.07 meters.

2.2.2 Location of Water Intake Pipes

The sensitive site analyzed here is the Toledo water intake pipes located on shore 12,600 meters from the placement site. If a coordinate system is positioned at the placement site, such that North is 0°, East is 90°, South is 180°, and West is 270°, then the water intake pipes lay southwest of the placement site 12,600 meters distant at the sector angle 210-225°. Note this sector as our results probabilities are presented by dividing the 360° arc into 24 15° sectors. The water intake pipes are in the Sector 14 direction.

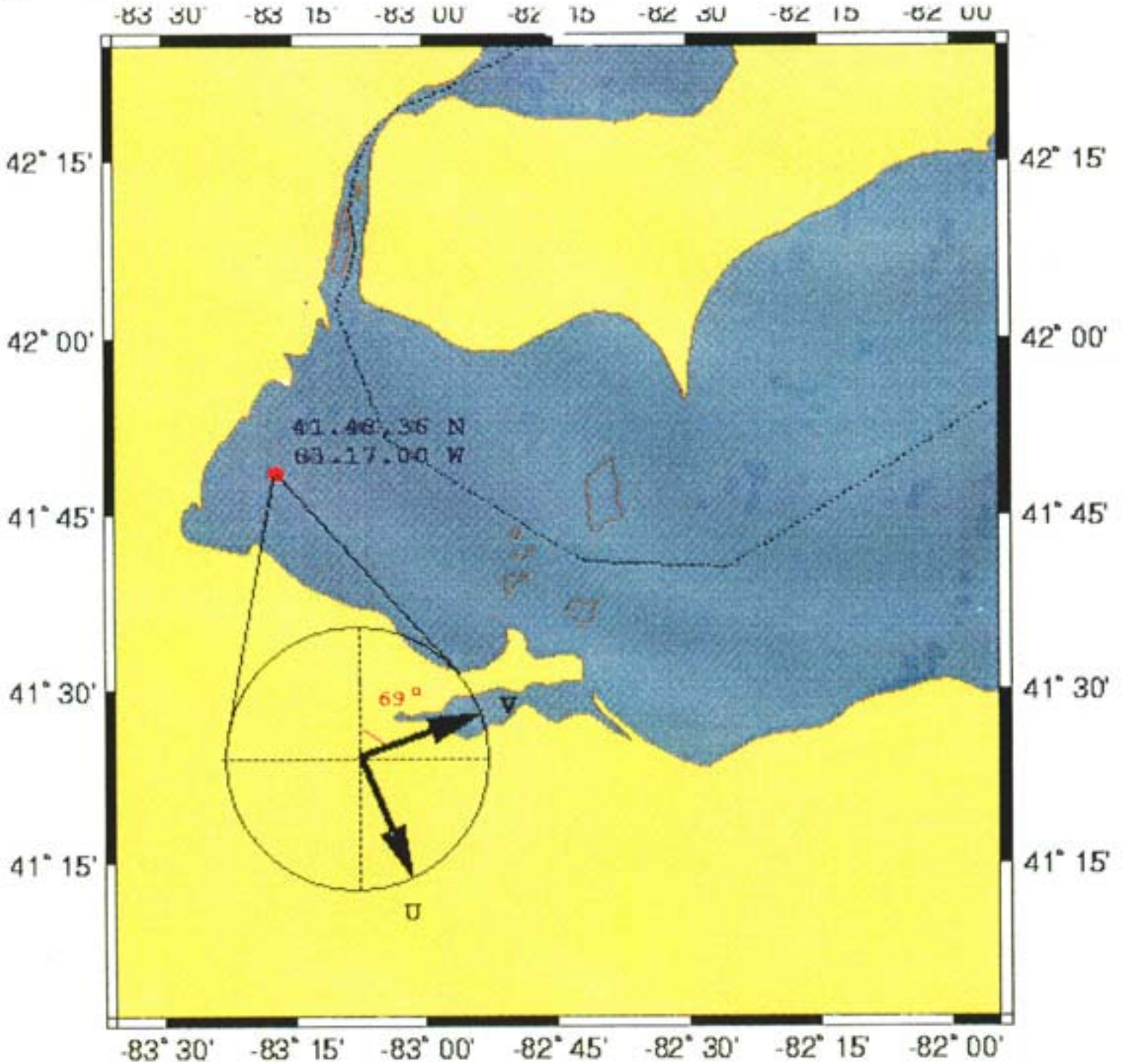
-83° 30'
-83° 15'
-83° 00'
-82° 45'
-82° 30'
-82° 15'
-82° 00'
42° 15'
42° 00'
41° 45'
41° 30'
41° 15'
41.46.36 N
63.17.00 W
69°
V
U

CHAPTER 3: THE LAKE ERIE DATABASE

3.1 The NEORSD CSO Project

The North East Ohio Regional Sewer District (NEORSD) found it necessary to search for a solution to the problem caused by the Combined Sewer Overflow (CSO) discharges from the Cleveland Ohio area. These discharges were adding up to 1.9 billion gallons of untreated water that goes directly into Lake Erie every year during storms (Podber, et al., 1994). The solution consisted of hiring a team of consultants who would prepare a phase 1 CSO facilities plan. There were several members in this team. The Ohio State University Great Lakes Forecasting System (GLFS) team of Ohio State was contracted to perform real-time forecasts of Lake Erie conditions. Their mission was to quantify the velocity and thermal state of Lake Erie waters over a 20-year period. A 20-year database of hourly velocity, temperature, and water level data resulted from this study. Historical meteorological data were used as the input forcing for the purpose of this task and GLFS was run in hindcast mode. The numerical model used for the calculation of Lake Erie currents, temperatures, and turbulence was the Princeton Ocean Circulation Model (POM) (Blumberg and Mellor 1987). The Podber et al. (1994) paper is included in the Appendix to this report for a more detailed review of the NEORSD project.

3.2 The GLFS Mellor Blumberg Model

The core numerical model used in the Great Lakes Forecasting System is a coastal ocean circulation model developed by the Geophysical Fluid Dynamics Program at Princeton University. The model, as depicted by Blumberg and Mellor (1987), is a quasi three-dimensional, nonlinear primitive equation coastal ocean circulation model with a second moment turbulence closure submodel embedded to provide a realistic parameterization of the vertical mixing processes. The prognostic variables are the three components of current velocity, free water surface elevation, water temperature, turbulent kinetic energy, and turbulent macroscale. Other main features of the model include: Boussinesq and hydrostatic approximations, a flux form of the equations, a variable Coriolis parameter, a bottom following vertical coordinate (sigma-coordinate), the

Smagorinsky horizontal diffusion subgrid formulation, a centered space and time leapfrog finite difference scheme, an implicit scheme for vertical mixing calculations, and an Arakawa-C staggered numerical grid arrangement.

In order to save computer time in three dimensional simulations, this model uses a mode splitting technique to solve the barotropic mode for the fast moving external gravity waves such as free surface elevations and the vertically averaged horizontal currents, and the baroclinic mode for the slow moving internal gravity waves and the full three dimensional current, temperature, and turbulence structures. This model has been widely used and it has been successful in modeling estuaries, bays, and coastal oceans (Kuan, 1996).

3.2.1 The Governing Equations

The dynamic and thermodynamic equations governing the circulation of the lake depict the velocity, free surface elevation, and temperature fields. These equations include the continuity equation

$$\nabla \cdot V + \frac{\partial u}{\partial z} = 0 \tag{3.1}$$

the momentum equations

$$\frac{\partial u}{\partial t} + V \cdot \nabla u + w\frac{\partial u}{\partial z} - fv = -\frac{1}{\rho_o}\frac{\partial p}{\partial x} + \frac{\partial}{\partial z}(K_M \frac{\partial u}{\partial z}) + F_u \tag{3.2}$$

and

$$\frac{\partial u}{\partial t} + V \cdot \nabla v + w\frac{\partial u}{\partial z} + fu = -\frac{1}{\rho_o}\frac{\partial p}{\partial y} + \frac{\partial}{\partial z}(K_M \frac{\partial u}{\partial z}) + F_v \tag{3.3}$$

$$\rho g = -\frac{\partial p}{\partial z} \tag{3.4}$$

the conservation equation for thermal energy

$$\frac{\partial \theta}{\partial t} + V \cdot \nabla \theta + w\frac{\partial \theta}{\partial z} = \frac{\partial}{\partial z}(K_H \frac{\partial \theta}{\partial z}) + F_\theta \tag{3.5}$$

The hydrostatic approximation yields

$$\frac{p}{\rho_o} = g(\eta - z) + g\int_z^\eta \frac{\rho - \rho_o}{\rho_o} dz' \tag{3.6}$$

In these equations, V is the horizontal velocity vector with components (u,v); w is the vertical velocity; and θ is the temperature. The free surface is located at $z = \eta(x,y,t)$ and the bottom is at $z = -H(x,y)$ where η is the free surface elevation and H defines the bottom topography. The quantity f is the Coriolis parameter; g is the gravitational acceleration; p is the pressure; ρ_o is the reference density; and ρ , is the in situ density and it is a function of temperature and time. The quantities K_M and K_H denote the vertical eddy viscosity and diffusivity of turbulent mixing for momentum and heat equations respectively. All of the motions that are not directly resolved by the model grid are parameterized in terms of horizontal mixing processes and most of these processes are dominated by the large scale motions. The terms F_u, F_v, and F_θ found in equations (3.2),-(3.3), and (3.5) represent these unresolved subgrid scale features. In contrast to the process of vertical diffusion which is controlled primarily by the small-scale motions, it is the large-scale motions that lead to horizontal mixing. In general, horizontal mixing is modeled in direct analogy to molecular diffusion. The horizontal Reynolds stresses and fluxes are assumed to be the gradient of a mean property multiplied by an empirical factor. F_u, F_v, and F_θ in the Princeton ocean model are given by

$$F_u = \frac{\partial}{\partial x}(2A_M\frac{\partial u}{\partial x}) + \frac{\partial}{\partial y}[A_M(\frac{\partial u}{\partial y}+\frac{\partial v}{\partial x})] \tag{3.7}$$

$$F_v = \frac{\partial}{\partial y}(2A_M\frac{\partial u}{\partial y}) + \frac{\partial}{\partial x}[A_M(\frac{\partial u}{\partial y}+\frac{\partial v}{\partial x})] \tag{3.8}$$

$$F_\theta = \frac{\partial}{\partial x}(A_H\frac{\partial \theta}{\partial x}) + \frac{\partial}{\partial y}(A_H\frac{\partial \theta}{\partial y}) \tag{3.9}$$

where A_M and A_H are the horizontal eddy viscosity and diffusivity coefficients, respectively. These coefficients can be expressed in terms of the mean flow quantities. By assuming that the horizontal eddy coefficients are related to the size of the largest eddies being resolved in a model and to the local deformation field, the Smagorinsky formulation for A_M is used

$$A_M = (C_H\Delta)^2 D \tag{3.10}$$

where C_H is a constant and Δ is the grid spacing. The deformation field, D, is defined as

$$D = [(\frac{\partial u}{\partial x})^2 + \frac{1}{2}(\frac{\partial v}{\partial x} + \frac{\partial u}{\partial y})^2 + \frac{\partial v}{\partial y})^2] \tag{3.11}$$

The coefficient C_H is usually determined by trial and error as it depends in part on the size of the eddies present. The Princeton ocean circulation model uses Smagorinsky's formulation to determine A_H which is directly related to A_M by

$$A_H = \frac{A_M}{\sigma_t} \tag{3.12}$$

where σ_t is the turbulent Prandtl or Schmidt number for which a constant value is assumed.

3.2.2 The Mellor--Yamada Turbulence Closure

One of the most important features in numerical hydrodynamic modeling for lakes and oceans is the parameterization of turbulence. Based on Rotta's (1951) energy redistribution hypothesis and Kolmogoroff's (1941) hypothesis of local, small-scale isotropy, Mellor and Yamada (1974) make a sequence of closure assumptions to form a set of equations for the Reynolds stress tensor $\overline{u_i u_j}(i,j = x,y,z)$, $\overline{u_i \theta}$, and $\overline{\theta^2}$. The vertical mixing coefficients K_M and K_H are calculated from

$$K_M = qlS_M, \quad K_H = qlS_H \tag{3.13}$$

where S_M and S_H are analytically derived stability functions, prescribed from the quasi-equilibrium modification by Galperin et al. (1988), of the level 2 1/2 model of the Mellor and Yamada second-moment closure hierarchy (Mellor and Yamada, 1982):

$$\begin{aligned} S_M = {} & A_1 \frac{1 - 3C_1 - (6A_1 / B_1)}{[1 - 3A_2 G_H (B_2 + 6A_1)](1 - 9A_1 A_2 G_H)} \\ & - A_1 \frac{3A_2 G_H \{(B_2 - 3A_2)\{1 - (6A_1 / B_1)\} - 3C_1 (B_2 + 6A_1)\}}{[1 - 3A_2 G_H (B_2 + 6A_1)](1 - 9A_1 A_2 G_H)} \end{aligned} \tag{3.14}$$

$$S_H = A_2 \frac{1-(6A_1/B_1)}{1-3A_2G_H(B_2+6A_1)} \tag{3.15}$$

where $$G_H = (\frac{l}{q})^2 \frac{g}{\rho_o}\frac{\partial \rho}{\partial z} \tag{3.16}$$

The turbulence velocity scale q is calculated by the turbulence energy equation

$$\frac{\partial q^2}{\partial y} + V\cdot\nabla q^2 + w\frac{\partial q^2}{\partial z} = \frac{\partial}{\partial z}(qlS_q\frac{\partial q^2}{\partial z}) + 2(P_s + P_b - \varepsilon) + F_q \tag{3.17}$$

and the master length scale, l, is given by the q^2 l equation (Mellor and Yamada, 1982)

$$\frac{\partial q^2 l}{\partial z} + V\cdot\nabla(q^2 l) + w\frac{\partial q^2 l}{\partial z} = \frac{\partial}{\partial z}(qlS_q\frac{\partial q^2 l}{\partial z}) + E_1 l(P_s + E_3P_b)$$

$$- l\varepsilon[1 + \frac{l}{\kappa L})^2] + F_l \tag{3.18}$$

where

$$\varepsilon = \frac{q^3}{B_1 l} \tag{3.19}$$

$$P_s = K_M[(\frac{\partial u}{\partial z})^2 + (\frac{\partial v}{\partial z})^2] \tag{3.20}$$

$$P_b = K_H\frac{g}{\rho_o}\frac{\partial \rho}{\partial z} \tag{3.21}$$

In equations (3.17)--(3.21) P_s represents the transfer of kinetic energy from the mean motion to the turbulent motion or the shear production; P_b represents the exchange between the turbulent kinetic energy and the potential energy of the flow system or the buoyant production; and ε is the viscous dissipation converting the kinetic energy into internal energy of the fluid. The length scale calculated by these equations is a characteristic length of the turbulent motion at any point in space or time. The terms F_q and F_l in equations (3.17) and (3.18) represent the horizontal mixing terms and are parameterized in direct analogy to that of θ except that q^2 and $q^2 l$ replace θ. L is a measure of the distance from a solid surface. For lake problems $L^{-1} = (\eta - z)^{-1} + (H + z)^{-1}$. Near a surface (where $z = -\eta$ or $z = H$) it may be shown that both l and L are

proportional to the distance from the surface and κ (=0.4) is the constant of the proportionality. Various length scales of turbulence are related to the master length scale following Mellor and Yamada (1982):

$$(A_1,A_2,B_1,B_2) = (0.92, 0.74, 16.6, 10.1) \tag{3.22}$$

and

$$(E_1,E_2) = (1.8,1.33) \tag{3.23}$$

Mellor(1975) shows that the remaining constant, C_1, is related to the others according to

$$C_1 = \frac{1}{3}(1-6A_1B_1^{-1}-A_1^{-1}B_1^{-1/3}) = 0.08 \tag{3.24}$$

3.3 Bottom Following, σ, Coordinate Transformation and Final Model Equations

It has been known that the use of the ordinary x, y, and z coordinate system in numerical modeling has certain computational disadvantages in the vicinity of bathymetric irregularities. Phillips (1957) therefore introduced a modified coordinate system which is obtained by transforming the vertical coordinate, z, in the x, y, z, and t-system to an independent variable sigma such that

$$x^* = x,\ y^* = y,\ \sigma = \frac{z-\eta}{H+\eta},\ t^* = t. \tag{3.25}$$

Using this definition, equations (3.1), (3.2), (3.3), (3.5), (3.17), and (3.18) are transformed to the following final model equations:

$$\frac{\partial\eta}{\partial t}+\frac{\partial uD}{\partial x}+\frac{\partial vD}{\partial y}+\frac{\partial w}{\partial\sigma} = 0 \tag{3.26}$$

$$\frac{\partial uD}{\partial t}+\frac{\partial u^2D}{\partial x}+\frac{\partial uvD}{\partial y}+\frac{\partial uw}{\partial\sigma}-fvD+gD\frac{\partial\eta}{\partial x}$$
$$= \frac{\partial}{\partial\sigma}(\frac{K_M}{D}\frac{\partial u}{\partial\sigma})-\frac{gD^2}{\rho_o}\int_\sigma^o(\frac{\partial\rho}{\partial x}-\frac{\sigma}{D}\frac{\partial D}{\partial x}\frac{\partial\sigma}{\partial\sigma})d\sigma'+F_x \tag{3.27}$$

$$\frac{\partial vD}{\partial t}+\frac{\partial uvD}{\partial x}+\frac{\partial u^2D}{\partial y}+\frac{\partial vw}{\partial \sigma}+fuD+gD\frac{\partial \eta}{\partial y}$$

$$=\frac{\partial}{\partial \sigma}(\frac{K_M}{D}\frac{\partial v}{\partial \sigma})-\frac{gD^2}{\rho_o}\int_\sigma^o(\frac{\partial \rho}{\partial y}-\frac{\sigma}{D}\frac{\partial D}{\partial y}\frac{\partial \sigma}{\partial \sigma})d\sigma'+F_y \qquad (3.28)$$

$$\frac{\partial \theta D}{\partial t}+\frac{\partial \theta uD}{\partial x}+\frac{\partial \theta vD}{\partial y}+\frac{\partial \theta w}{\partial \sigma}=\frac{\partial}{\partial \sigma}(\frac{K_M}{D}\frac{\partial \sigma}{\partial \sigma})+F_\Theta$$

$$=\frac{\partial q^2D}{\partial t}+\frac{\partial ug^2D}{\partial x}+\frac{\partial vq^2D}{\partial y}+\frac{\partial wq^2}{\partial \sigma}+\frac{\partial}{\partial \sigma}(\frac{K_q}{D}\frac{\partial q^2}{\partial \sigma}) \qquad (3.29)$$

$$+\frac{2K_M}{D}[(\frac{\partial u}{\partial \sigma})^2+(\frac{\partial v}{\partial \sigma})^2]+\frac{2g}{\rho_o}K_H\frac{\partial \rho}{\partial \sigma}-\frac{2Dq^3}{\Lambda_1}+F_Q \qquad (3.30)$$

$$\frac{\partial q^2lD}{\partial t}+\frac{\partial ug^2lD}{\partial x}+\frac{\partial vq^2D}{\partial y}+\frac{\partial wq^2l}{\partial \sigma}+\frac{\partial}{\partial \sigma}(\frac{K_q}{D}\frac{\partial q^2l}{\partial \sigma})$$

$$+E_1l\frac{K_M}{D}[(\frac{\partial u}{\partial \sigma})^2+(\frac{\partial v}{\partial \sigma})^2]+E_3\frac{g}{\rho_o}K_H\frac{\partial \rho}{\partial \sigma}-\frac{Dq^3}{B_1}\varpi+DF_L \qquad (3.31)$$

where $\varpi=(1+E_2/\kappa L)$

The horizontal viscosity and diffusion terms are defined as

$$F_x = \frac{\partial}{\partial x}(2DA_M\frac{\partial u}{\partial x})+\frac{\partial}{\partial y}[DA_M(\frac{\partial u}{\partial y}+\frac{\partial v}{\partial x})] \qquad (3.32)$$

$$F_y = \frac{\partial}{\partial x}[DA_M\frac{\partial u}{\partial y}+\frac{\partial v}{\partial x}]+\frac{\partial}{\partial y}(2DA_M\frac{\partial v}{\partial y}) \qquad (3.33)$$

$$F_\Theta = \frac{\partial}{\partial x}(DA_H\frac{\partial \theta}{\partial x})+\frac{\partial}{\partial y}[DA_H(\frac{\partial \theta}{\partial y}] \qquad (3.34)$$

$$F_Q = \frac{\partial}{\partial x}(DA_H\frac{\partial q^2}{\partial x})+\frac{\partial}{\partial y}[DA_H(\frac{\partial q^2}{\partial y}] \qquad (3.35)$$

$$F_L = \frac{\partial}{\partial x}(DA_H\frac{\partial q^2l}{\partial x})+\frac{\partial}{\partial y}[DA_H(\frac{\partial q^2l}{\partial y}] \qquad (3.36)$$

It should be noted that these horizontal diffusion terms are not what one would obtain by transforming the conventional forms to the sigma coordinate system. Justification for the present forms can be found in Mellor and Blumberg (1985).

3.4 The 20-Year Climatological Database

The Great Lakes Forecasting System was used at the Ohio State University to perform the 20-year hindcast of Lake Erie water properties, thus generating the 20-year database of conditions from 1972 to 1992. Even though GLFS was developed to make real-time forecasts of lake conditions, the system was easily modified to perform hindcasts by substituting historical data sets for the usual real-time data acquisition of the system (Podber, et al., 1994). The POM model was used by GLFS to produce this database. The model used a 5 km grid resolution which generated a horizontal grid of 81 by 24 grid cells. In the vertical direction 11 slices were used.

In 1990, the POM was run for twenty years, consecutively. For each year the historical data was used as input for boundary conditions. The result was the creation of a twenty-year database that contained the following information. The hourly three-dimensional velocity components: u, v, and w velocities; temperature; integrated velocity; heat fluxes; wind stress; water elevation; and depth. The values are stored in a permanent database and can be extracted by means of a FORTRAN program that will print out any variable by accessing the elements of its array. The velocity arrays are three-dimensional.

For this study, the full 20-year hourly database of the variables listed above were extracted for the placement site defined in Chapter 2 and subsequently analyzed for frequency, direction, duration, time of travel, and magnitude of the events at the placement site. Therefore, a complete climatology of the placement site can be obtained.

CHAPTER 4: DATA PREPARATION

Climatology data and subsequent probabilistic analyses are discussed in this chapter.

4.1 Selection of Data

The Lake Erie disposal site in the Western Basin falls in the following meridians: (41 degrees 48 minutes and 36 seconds North and 83 degrees 17 minutes and 0 seconds West) this corresponds to the grid node (5,20) in the 5 kilometer grid of the Princeton model. These data were extracted from magnetic tapes and were stored into the temporary directory of the Cray Y-MP8 supercomputer. The Cray supercomputer was used because of its ability to handle large jobs. The data in ASCII format were stored in separate files that contained u and v velocities of a water column in the chosen location. The data in the water column at the placement site had to be sliced in order to extract the surface velocity, and the bottom velocity. These values were sorted into surface velocity files, contained velocity values one cell below the surface, bottom velocity files, contained velocity values one cell above the bottom of the lake, and an integrated velocity. Several small UNIX shell scripts were written to slice the data in the desired manner and provide new files that contain the hourly u and v velocities for each year. This was the final step in preparing the data for analysis.

4.2 Computational Methods

There are several computational methods that can be used in order to draw some conclusions about the data. Since the main goal of this study is to determine if Lake Erie flow has a preferred direction from the disposal placement site location to the Toledo water intake pipes, the first step of the analysis is to determine whether or not the data possess a directional bias. Computationally, two methods were chosen: the Rayleigh Test of Uniformity and the Mean Value. The computations showed that there was a directional bias. A series of computational models were created for further study in order to reveal the bias and provide detailed information about the data.

4.2.1 The Statistics

The first statistic determined was the mean. Of course, this is the simplest method to use. As the data were plotted, initially the mean served as an aid to determine uniformity of the data. The second statistic is the p value, it represents the Rayleigh test of uniformity. This test calculates the probability of the null hypothesis that the data are distributed in a uniform manner. A probability less than the chosen significance level (.05 by default) indicates that the data are not distributed uniformly and consequently they show evidence of a preferred direction, (Kovach, 1994). As we will see in the analysis of the results, the mean proved to be not needed for the purpose of this study. The Rayleigh test of uniformity was also dismissed because of the strong bias the data has shown.

4.2.2 Computer Models for Statistical Analysis

The raw data generated by the POM model had to be sorted even further. The first analysis model computed the direction of the flow every hour. A FORTRAN program was written for that purpose. It successfully converted all the u and v velocities into two pieces of information: the first was the hourly change of direction of the flow and the second was the magnitude of that velocity. The first model read the values of the magnitudes of u and v velocities and computed the direction in degrees. Adjustments were made to ensure that 0° represents the North direction. Then a subroutine was called to sort the data. The subroutine used the computed directions as input and converted the 360° possible directions into 24 sectors. Sector 0 represents 0-15° North. Sector 6 represents 90-105° East. Sector 18 represents 270-285° South, etc.

The subroutine was designed to perform pattern recognition. This method was necessary in order to group all the velocities in their respective directions, thus being able to count the number of events going towards any direction. Frequency of occurrence was calculated and statistics were compiled for each one of the sectors separately.

There were 6960 hours worth of data per year, representing three seasons: Spring, Summer, and Autumn. Since the lake is frozen during winter there was no need to

generate any velocity values from the model for the icy season. Each one of those hours was inspected by the pattern recognition procedure and was saved under an array in the FORTRAN model. Most of the array variables that were created by this model were doubly subscripted integer arrays. They store the sector number, thus tracking the direction, and the hour during which the event has passed through that particular sector. The primary step was to sort all the events into direction specific events by comparing the sector number to the direction of the event. When all the events were finally sorted into their respective sectors, another subroutine was used in order to determine the duration of those events. The new subroutine used the same pattern recognition principle that is, it checked the direction of an "event hour" associated with it. If the following event was also tracked by the model into the same sector then the hour was checked again in order to determine a duration for that event. The duration of an event is determined by the number of consecutive hourly events that are tracked into the same sector. Several repetition and selection structures were necessary in producing the code for this particular task in the computer model.

The model also kept a count of the duration of each event. The model output consists from a set of integer values that give the sector number, the total events and the number of events for each duration starting with the one hour events and ending with the events that last more than 10 hours.

4.3 Output Presentation

Circular plots and rose diagrams were used in conjunction with linear histograms to present the results. An IDL computer graphics program was written to plot the statistical information generated by the computational models.

4.3.1 Rose Diagrams

Rose diagrams consist of different wedges emerging from the center of a circle. The center of the circle represents the study location and each sector represents the direction towards which the flow is moving. The radius of each one of the wedges represents the number of events, meaning the number of hours during the time period studied that the flow is following that direction. Different colors (or shades) represent the duration of each type of event. The shorter the radius, the longer the duration. Each rose diagram visually showed several pieces of information regarding the flow in a particular location. The project WEB page contains color versions of the IDL figures. Figures 4.1-4.2 contain the 1979 plots for surface and integrated velocities.

The IDL program for the rose diagrams reads the integer values generated by the computational models. These values are the following: Sector number, total events per sector, number of times the flow changed directions; and a flag, set to detect the longest duration event specific to the direction determined by the sector number. The trick was detected by the number of events being zero. If it is not zero, the flag is incremented by one, indicating a longer duration. If the event were zero, then the flag would default to its last value. This was systematically done by using an iteration based on the hours 1 to 11.

After the lengths of the radii were generated above, the wedges were drawn and colored. Several repetition structures were used to complete the coordinates of the polygon vertices in order to repeatedly draw and fill the polygons for each sector and each duration. The graphics procedures use several additional routines to draw and calibrate the rosette.

Number of Events per Direction: Surface Velocity surface_vel_79.stat

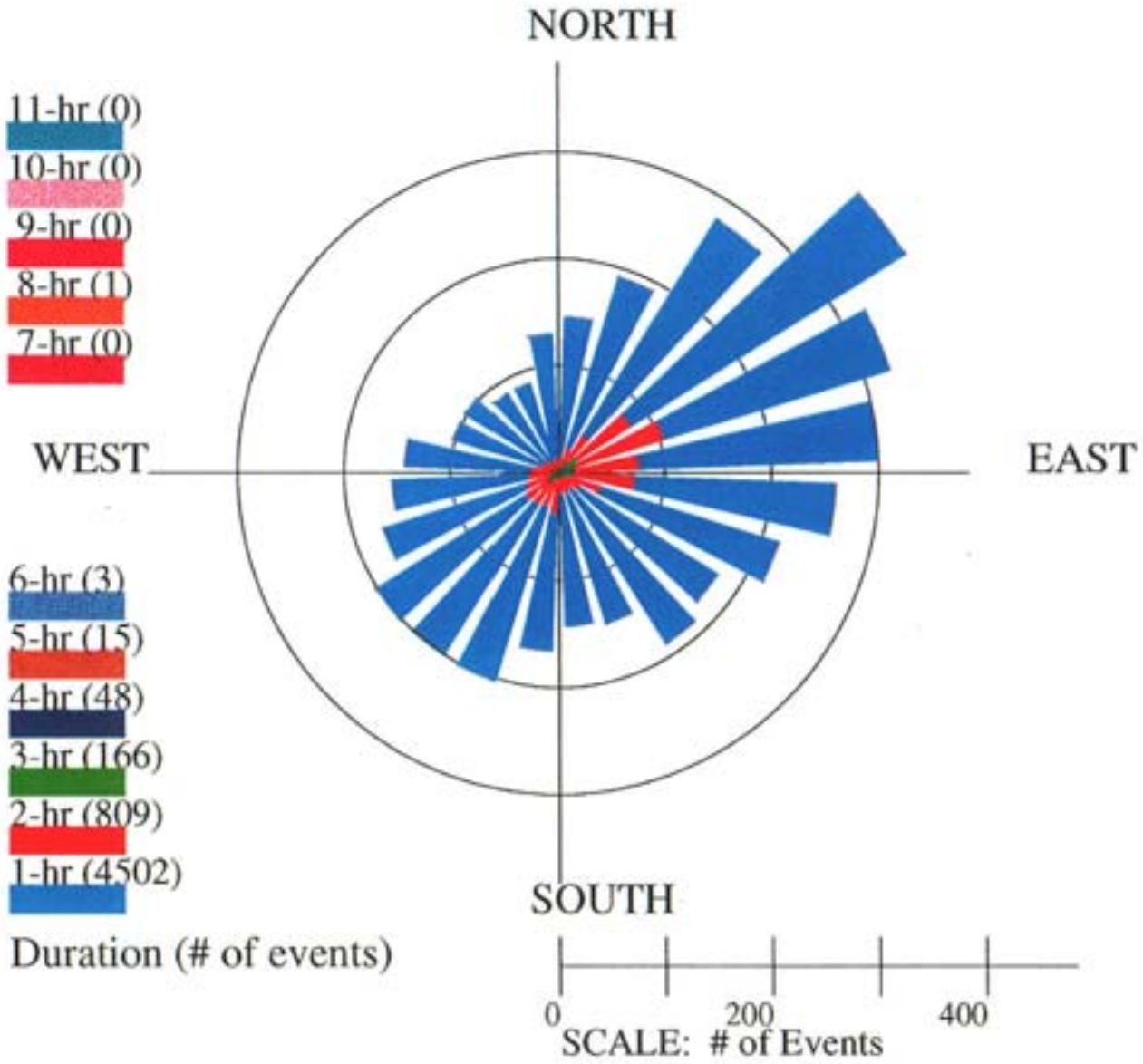

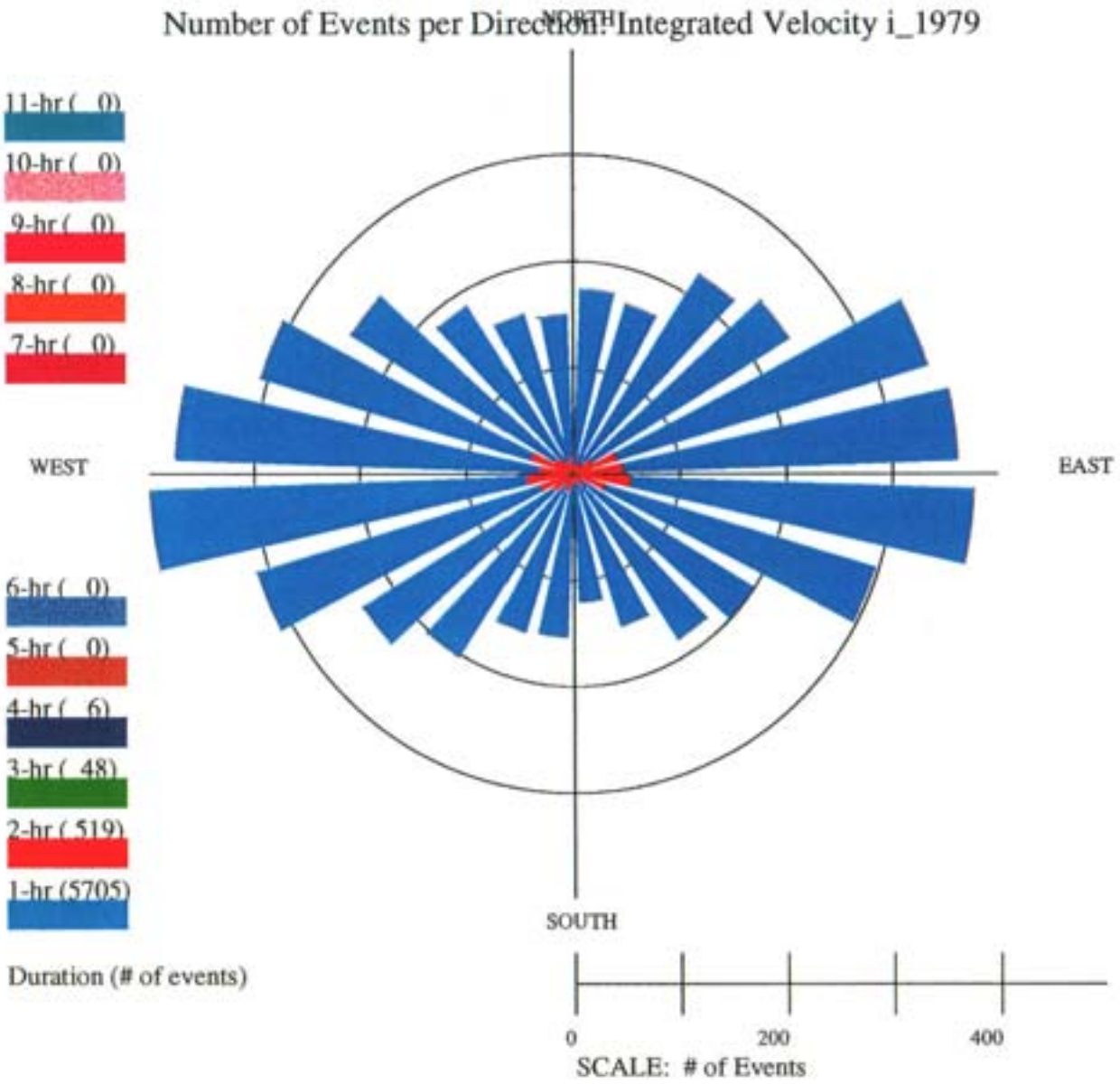
Number of Events per Direction: Integrated Velocity i_1979
NORTH
11-hr (0)
10-hr (0)
9-hr (0)
8-hr (0)
7-hr (0)
WEST
EAST
6-hr (0)
5-hr (0)
4-hr (6)
3-hr (48)
2-hr (519)
1-hr (5705)
Duration (# of events)
SOUTH
0
200
400
SCALE: # of Events

4.3.2 Linear Histograms

Linear histograms were generated to display the same information as the rosettes. These linear histograms emphasized less the direction of the flow and more the number of events and their duration for each direction. See Figure 4.3 for a 1979 surface velocity example.

As for the longest duration per sector, after plotting all the linear histograms, the longest durations were extracted for each direction and year. These longest durations served as a major tool in computing the worst case scenario for the directional analysis of the flow from the disposal site. These tasks were accomplished using the same techniques used in the linear histograms. The method was based upon extracting the longest duration for each one of the sectors. As it turns out, that value was already extracted by using a counter that increments every time the number of events in the sector is not zero. The longest duration is the number associated with the last non-zero value of events per sector. For an example, refer to Figure 4.4.

To graph the magnitudes associated with each direction for each one of the velocity values, the maximum value, the minimum value, and the average value of the magnitudes per direction for each one of the years studied were chosen. The graphs were created from the previous data files and an IDL program that used the same pattern recognition techniques described above. Maximum values were denoted by an asterisk, the minimum values were denoted by an x, and the average values by an o. The information relevant to sector 14 was again highlighted with a different color by the use of a conditional statement and a repeat structure. Figure 4.5 is an example of this plot for the 1979 bottom velocities.

Two additional graphs were generated: the first combined the results from the longest duration plots and the magnitude plots to generate a maximum distance plot, and the second put the aggregated distance traveled towards the sensitive site together

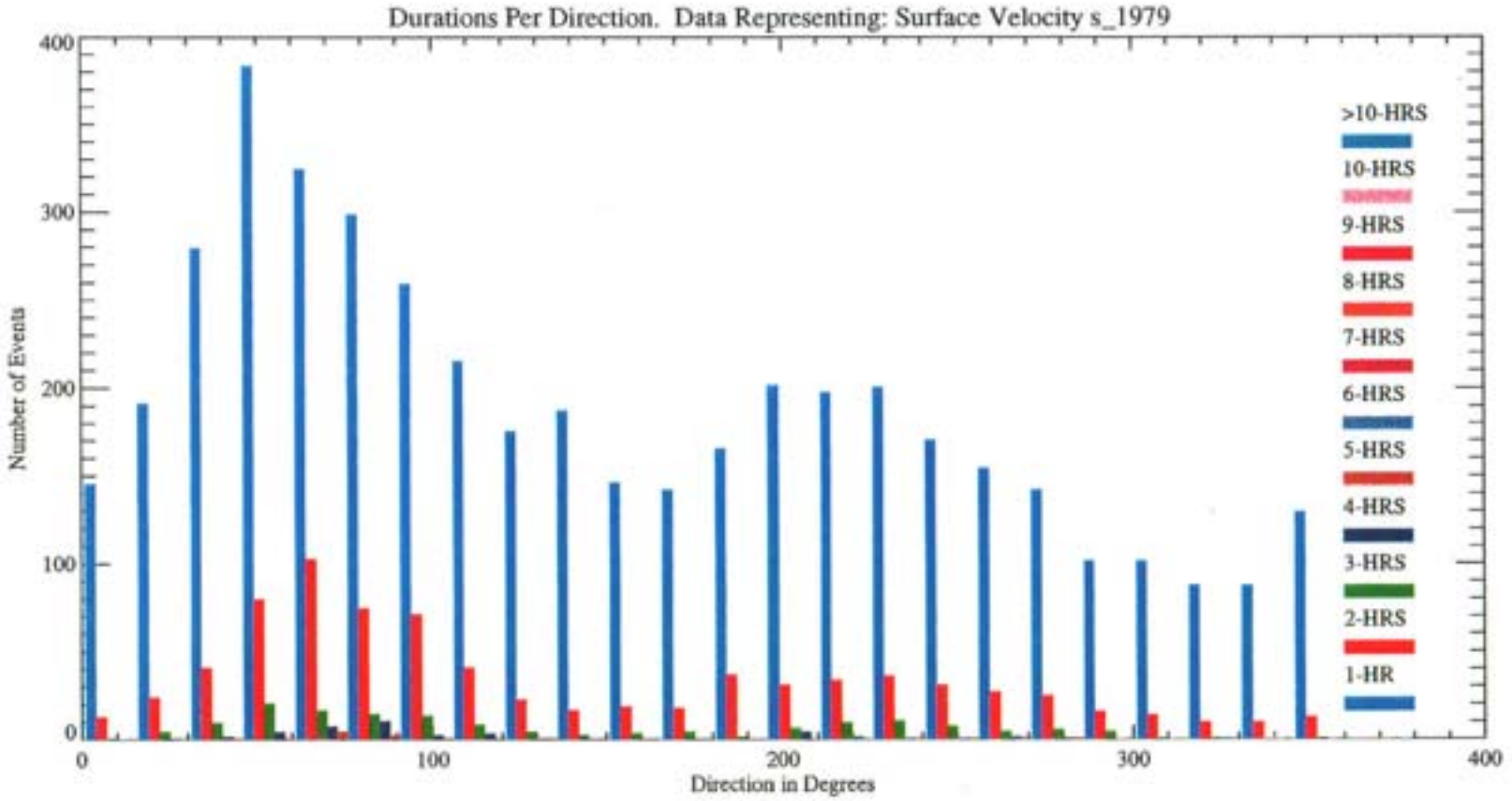
Durations Per Direction. Data Representing: Surface Velocity s_1979
Number of Events
Direction in Degrees
0
100
200
300
400
>10-HRS
10-HRS
9-HRS
8-HRS
7-HRS
6-HRS
5-HRS
4-HRS
3-HRS
2-HRS
1-HR

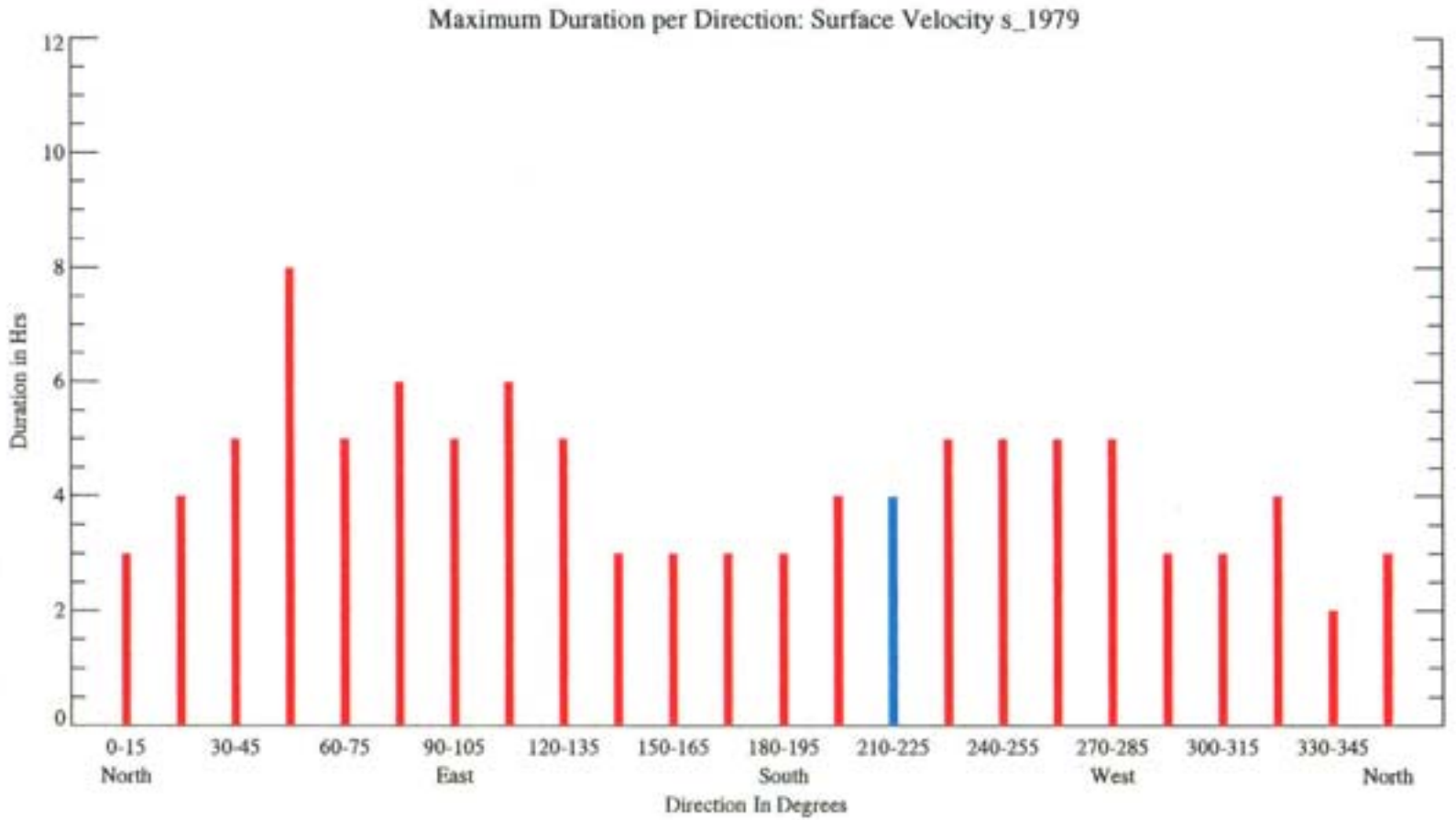
Maximum Duration per Direction: Surface Velocity s_1979
Duration in Hrs
0
2
4
6
8
10
12
0-15
North
30-45
60-75
90-105
East
120-135
150-165
180-195
South
210-225
240-255
270-285
West
300-315
330-345
North
Direction In Degrees

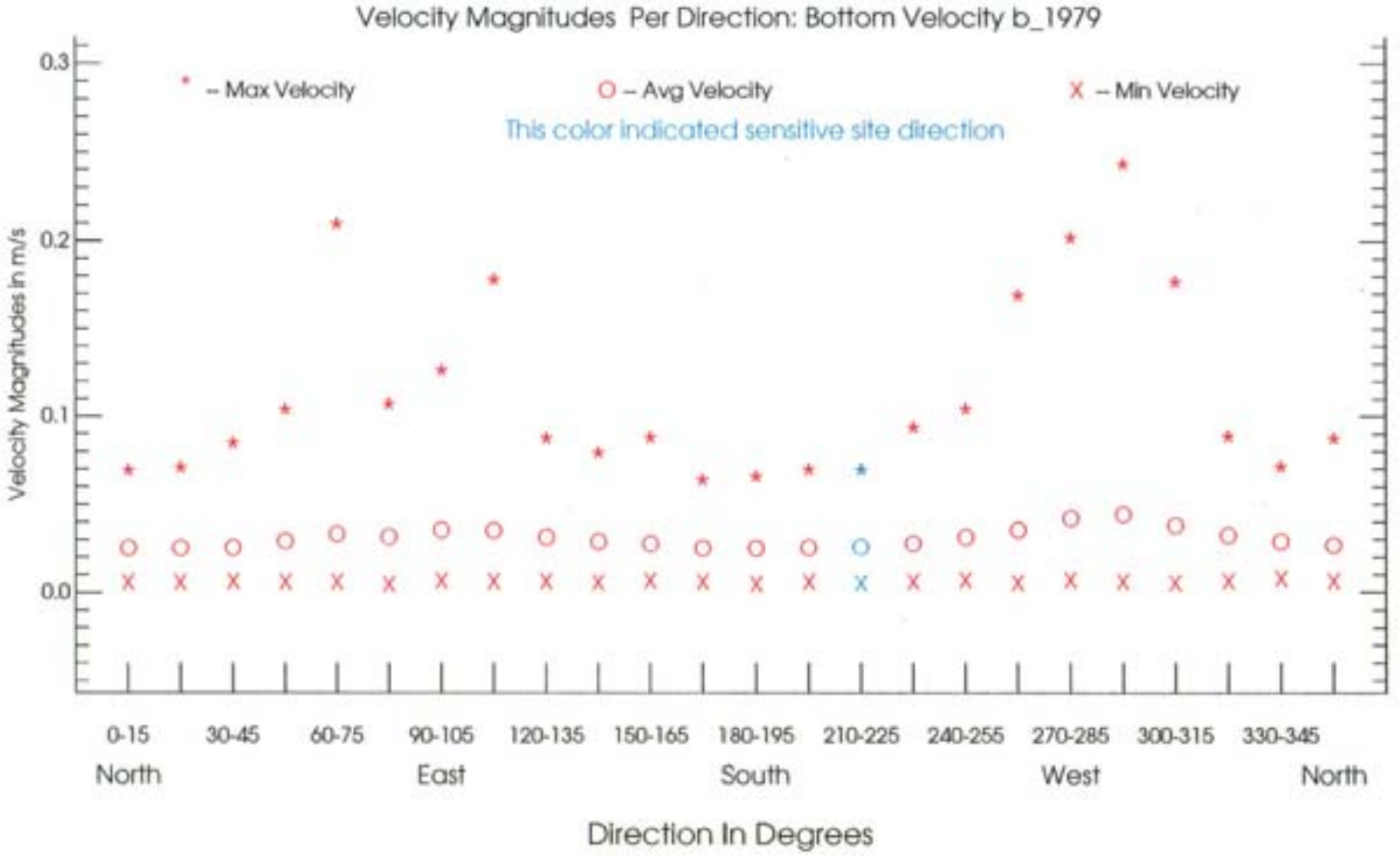
Velocity Magnitudes Per Direction: Bottom Velocity b_1979
* – Max Velocity
O – Avg Velocity
X – Min Velocity
This color indicated sensitive site direction
Velocity Magnitudes In m/s
0.3
0.2
0.1
0.0
0-15
30-45
60-75
90-105
120-135
150-165
180-195
210-225
240-255
270-285
300-315
330-345
North
East
South
West
North
Direction In Degrees

into one plot. Techniques used to generate the first type of plot were the same as the magnitude plots. The second and final type of plot, however, needed a few manipulations. In order to extract the maximum distance traveled towards the sensitive site for each year, the IDL program that constructed the distance plot had to be run repeatedly for each year; a new step that would open a file to be updated each time the program is run. The values stored in this file were the distances traveled towards the sensitive area, thus creating yet another input file for the final IDL plot. This last plot than displays the maximum distance traveled towards the site fore each year under study. Figure 4.6 is an example of this plot.

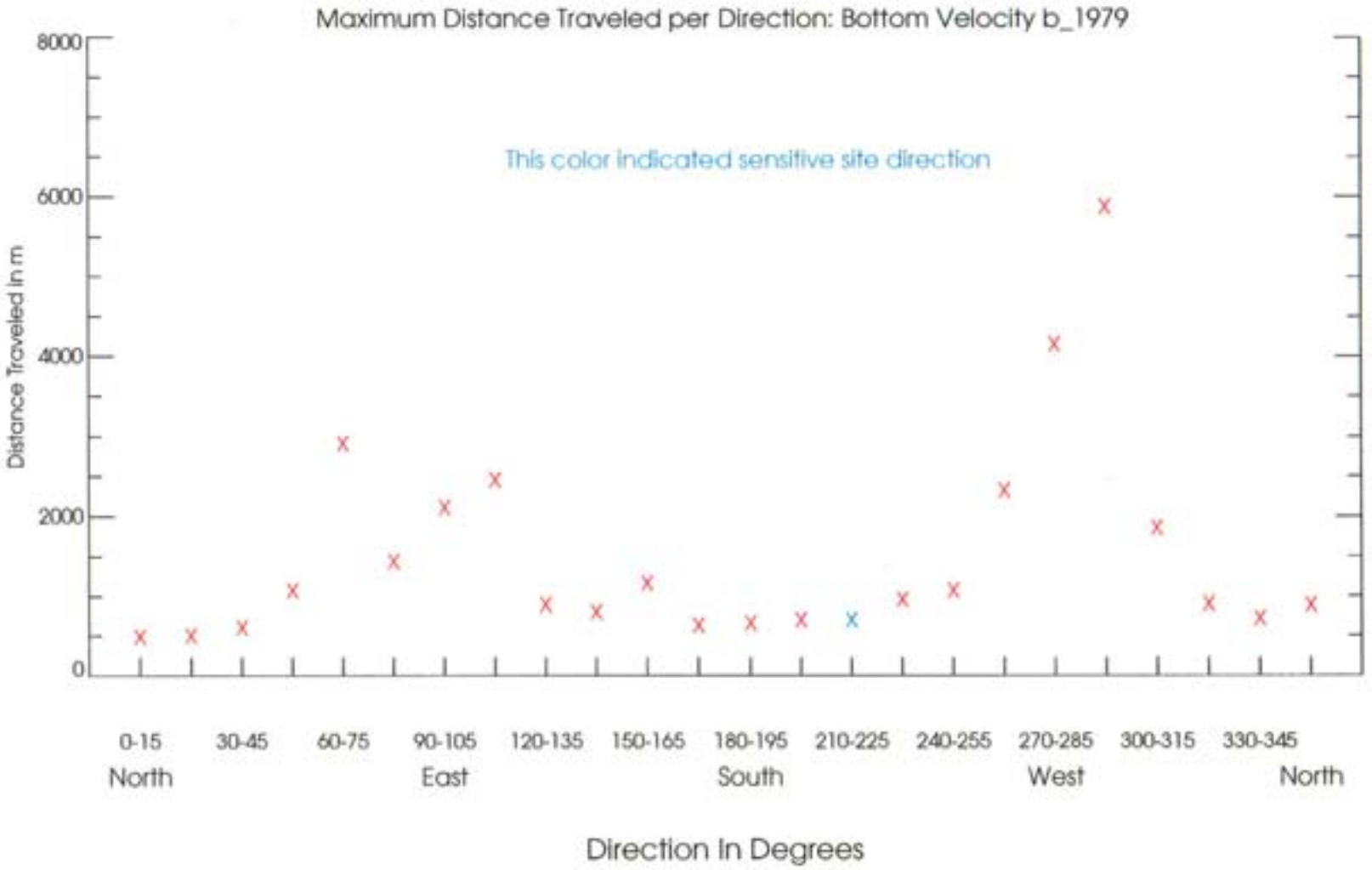
Maximum Distance Traveled per Direction: Bottom Velocity b_1979
This color indicated sensitive site direction
Distance Traveled in m
8000
6000
4000
2000
0
0-15
30-45
60-75
90-105
120-135
150-165
180-195
210-225
240-255
270-285
300-315
330-345
North
East
South
West
North
Direction In Degrees

CHAPTER 5: DISPOSAL SITE CLIMATOLOGY

The Rayleigh p test results showed a strong bias in the data. The values were not clustered around the mean and the p values were almost zero for most of the cases, which is a clear indication that the data had a preferred direction. The pattern analysis detected the number of events in each sector (Table 5.1). These events are the combination of the one hour events and the longer duration events as well. Please refer to appendix F for more statistics.

Table 5.1 Integrated Velocity Event Statistics

Sector Number	Number of Events
0	155
1	198
2	207
3	238
4	345
5	521
6	468
7	348
8	273
9	238
10	219
11	186
12	197
13	211
14	264
15	332
16	448
17	533
18	485
19	325
20	277
21	184
22	161
23	147

5.1 Annual Flow Patterns

There is an obvious pattern that governs all the annual data. Even though there are differences in total numbers from year to year, the data show that the preferred direction for the events is consistent from year to year. For the surface flow the preferred direction

is between 45 to 90° from North, with the majority showing an East to North East preference. When examining the linear histograms, we can almost predict the second set of 10 year preferred direction by projecting off of the first set of 10 year data. The dominant direction is noticed as well as a second dominant direction which is 180° away from the preferred direction. The differences occur when we examine the longest durations, especially when focusing on the direction towards the Toledo water intake pipes.

5.1.1 Surface Flow Patterns

After generating the flow rosettes, the directional patterns were gathered for the surface flow. All the yearly data showed very similar patterns. Each year showed a dominant direction of flow going to East North East (ENE) This direction is affected by the wind direction since it is a surface flow. The linear histograms show the same information but they emphasize the direction in degrees. Also the linear histograms show two peaks 180° apart. The first peak is very evident but the second one is not nearly as high in frequency of events.

5.1.2 Bottom Flow Patterns

The dominant flow direction in the bottom is 180° opposite from the dominant direction of the surface. This means that the flow at the bottom is going West South West (WSW). On some occasions we find the flow going West or West North West (WNW). This is due to the seiches in the western basin of lake Erie.

5.1.3 Integrated Flow Patterns

The integrated velocity patterns were very interesting. In fact if we would overlay a surface velocity histogram and a bottom velocity histogram for the same year, they would produce the integrated velocity histogram. The integrated velocity showed a bimodal pattern, in that there were two peak directions 180° apart. This is exactly what should happen with the integrated velocity since it is the barotropic response of the lake and therefore reflects the seiche motion of the lake particularly well.

5.2 Aggregated 20-Year Patterns

The statistical analysis of the entire data proved a definite directional bias of the data. Whether the data was representing surface, bottom or integrated flow, the results showed that the data did not cluster around the mean. This indicated that the directional distribution is not a normal distribution. The surface and bottom flows were unimodal but did contain subsidiary observable secondary peaks, while the integrated velocity was bimodal.

Even though there were distinct differences between all the patterns the cumulative data representation of the surface flow matched everywhere the data were picked. The circular histograms as well as the linear histograms continued to show that the preferred direction of the surface flow is the ENE direction. Of course, the values of events added up to a very large number because of the cumulative effect from all the years studied, while that of the bottom is WNW and the integrated velocity again has a bimodal character.

CHAPTER 6: SENSITIVE SITE RISK

In the previous chapter the results were discussed and flow patterns were compiled and categorized into surface patterns, bottom patterns and integrated patterns. At this point we need to determine the impact of these patterns on the concerns of this study. All along we have kept track of the magnitudes of the velocities traveling towards each direction. The pattern recognition models (computational or graphical) have identified the longest duration event for each one of the directions. Based on these results, the magnitudes and durations of the events and their directions were extracted for each year studied, and the worst case event was identified for each year. In this chapter, attention is shifted to the sensitive site and the impact of this directionally biased flow at this site. The water intake pipes lie southwest of the disposal site, which corresponds to sector number fourteen, which is between 210 and 215° from North.

6.1 Annual Event and Duration Climatology

Before proceeding to a cumulative summary, it is necessary to analyze the behavior of the annual data. The annual event histograms were reviewed previously. Here, each event is analyzed to determine the longest duration of flow in any one direction for each event. Using 1979 as an example, Figures 6.1-6.3 contain the histograms displaced according to sector. Please note Sector 14 is the direction of the water intake pipes. It is seen that rarely is there a surface flow event of more than 5 hours in duration and for Sector 14 whether the integrated, surface, or bottom velocity directions are greater than three hours. Figures 6.4-6.6 contain the maximum duration per sector per event for the year 1979, which further confirms the histogram analysis.

Velocities are associated with these events and Figures 6.7-6.9 contain the 1979 sector plots for maximum, average, and minimum velocities in each sector. The blue color denotes the intake sector and again the dominance of the bimodal seiche is apparent.

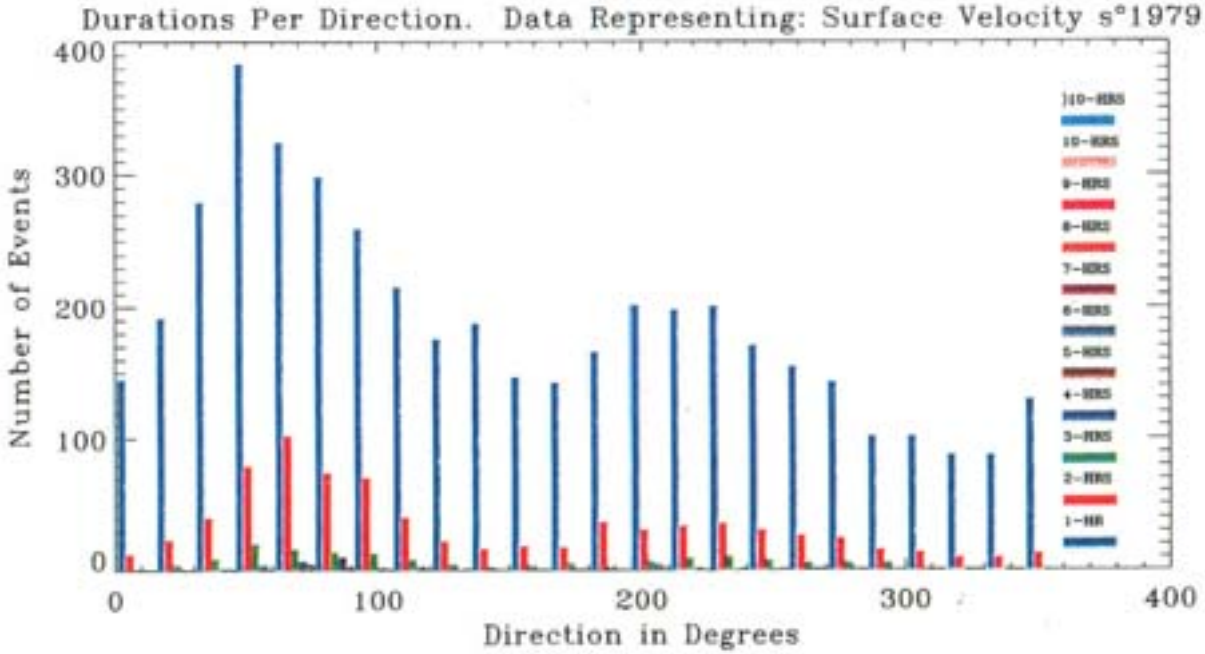
Durations Per Direction. Data Representing: Surface Velocity s°1979
Number of Events
Direction in Degrees
0
100
200
300
400
1-HR

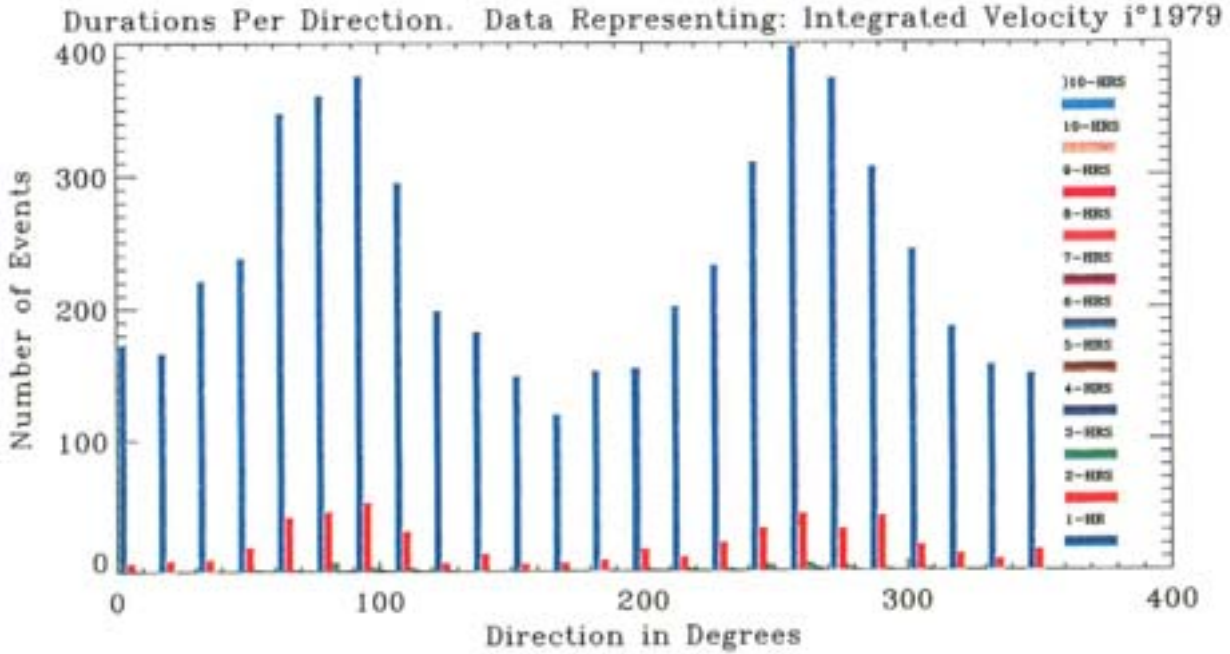
Durations Per Direction. Data Representing: Integrated Velocity i°1979
Number of Events
Direction in Degrees
0
100
200
300
400

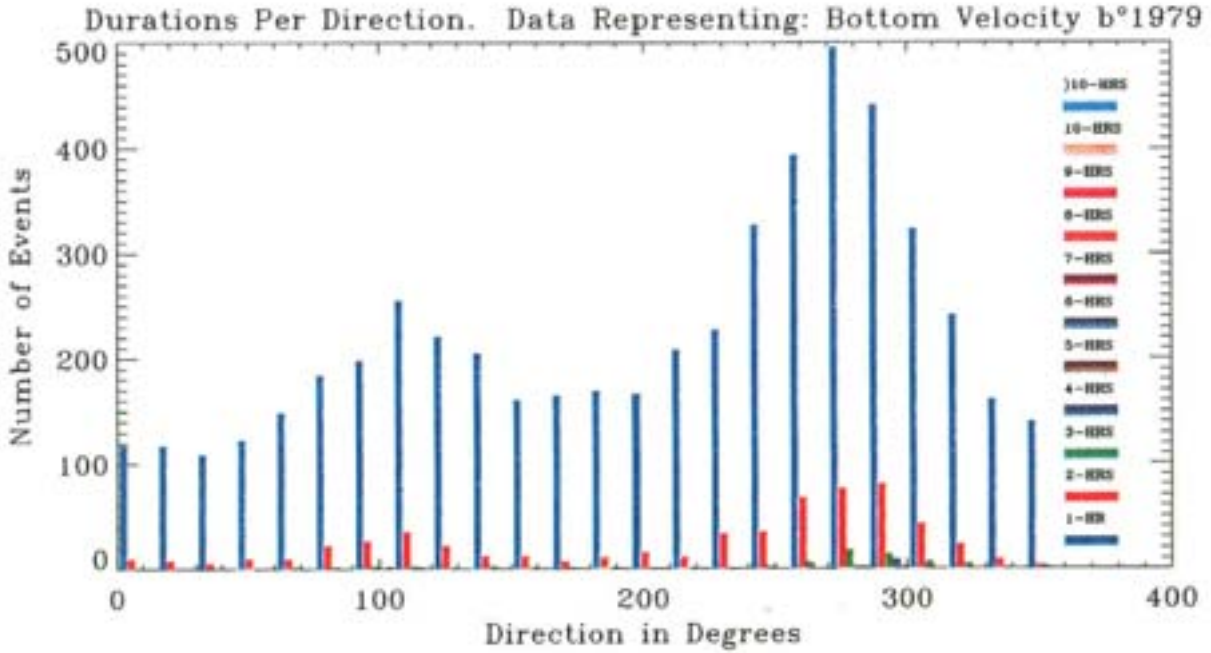
Durations Per Direction. Data Representing: Bottom Velocity b°1979
Number of Events
Direction in Degrees
0
100
200
300
400
500

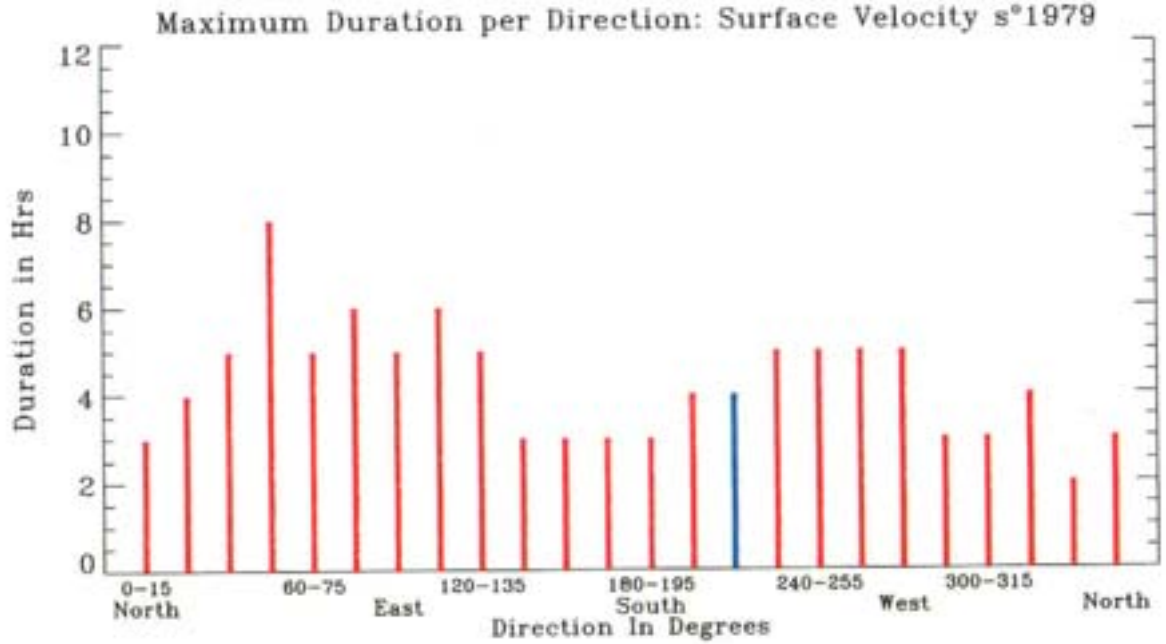
Maximum Duration per Direction: Surface Velocity s°1979
Duration in Hrs
0
2
4
6
8
10
12
0-15
North
60-75
East
120-135
South
180-195
West
240-255
300-315
North
Direction In Degrees

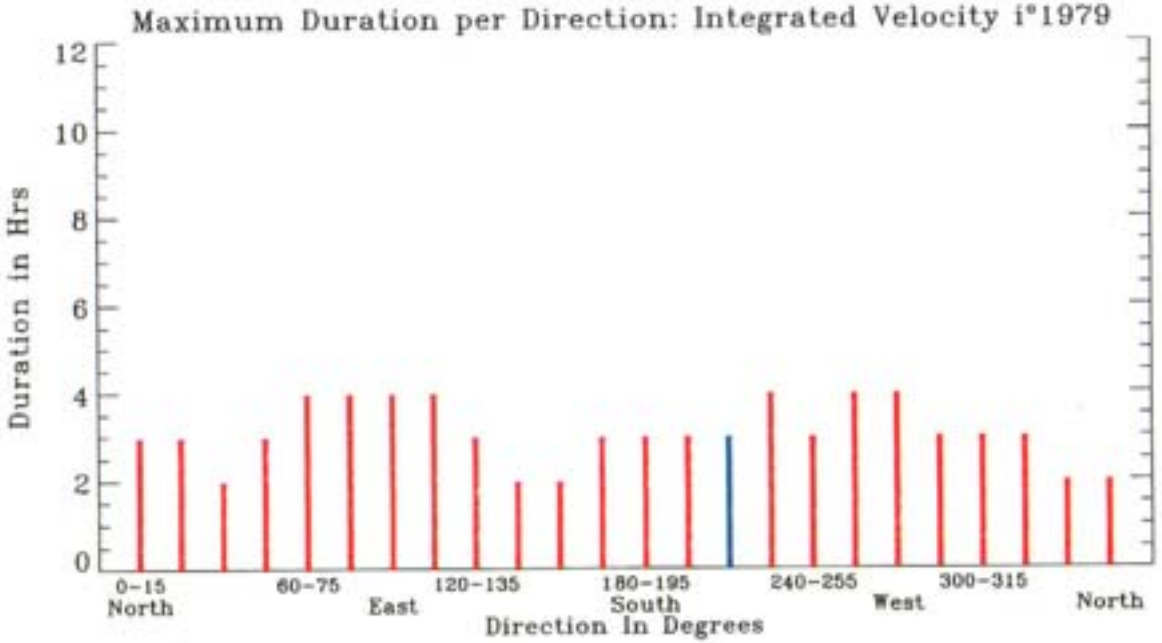
Maximum Duration per Direction: Integrated Velocity i°1979
Duration in Hrs
12
10
8
6
4
2
0
0-15
North
60-75
East
120-135
180-195
South
240-255
West
300-315
North
Direction In Degrees

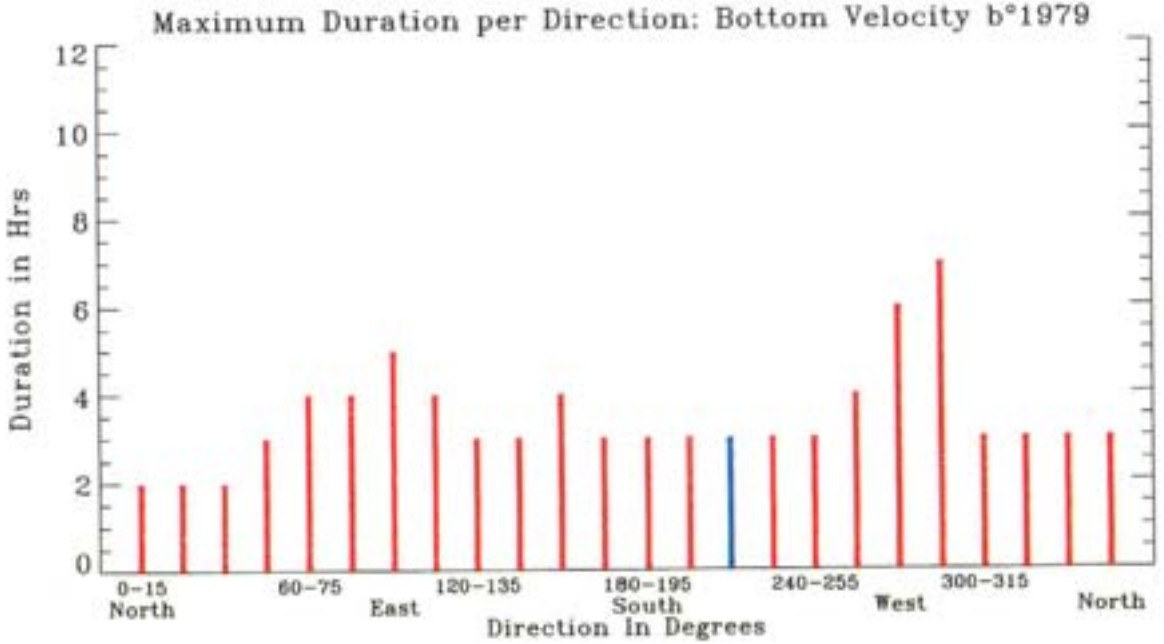
Maximum Duration per Direction: Bottom Velocity b°1979
Duration in Hrs
0
2
4
6
8
10
12
0-15
North
60-75
East
120-135
180-195
South
240-255
West
300-315
North
Direction In Degrees

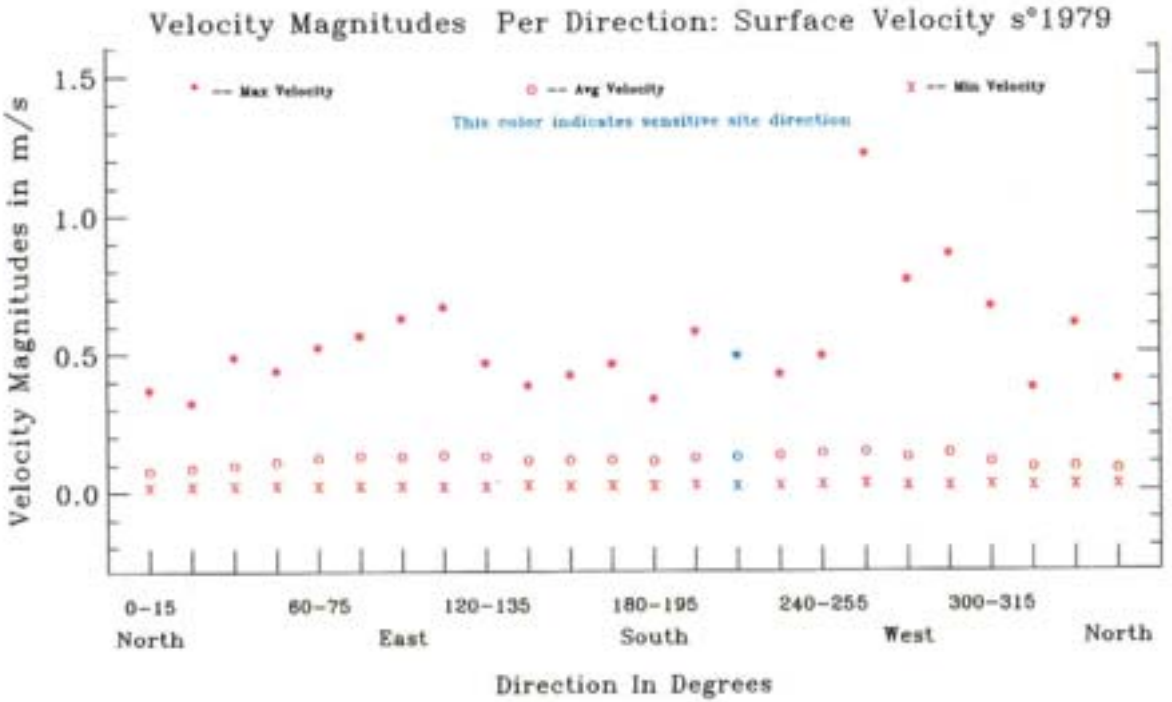
Velocity Magnitudes Per Direction: Surface Velocity s°1979
Velocity Magnitudes in m/s
1.5
1.0
0.5
0.0
* -- Max Velocity
o -- Avg Velocity
x -- Min Velocity
This color indicates sensitive site direction
0-15
North
60-75
East
120-135
180-195
South
240-255
West
300-315
North
Direction In Degrees

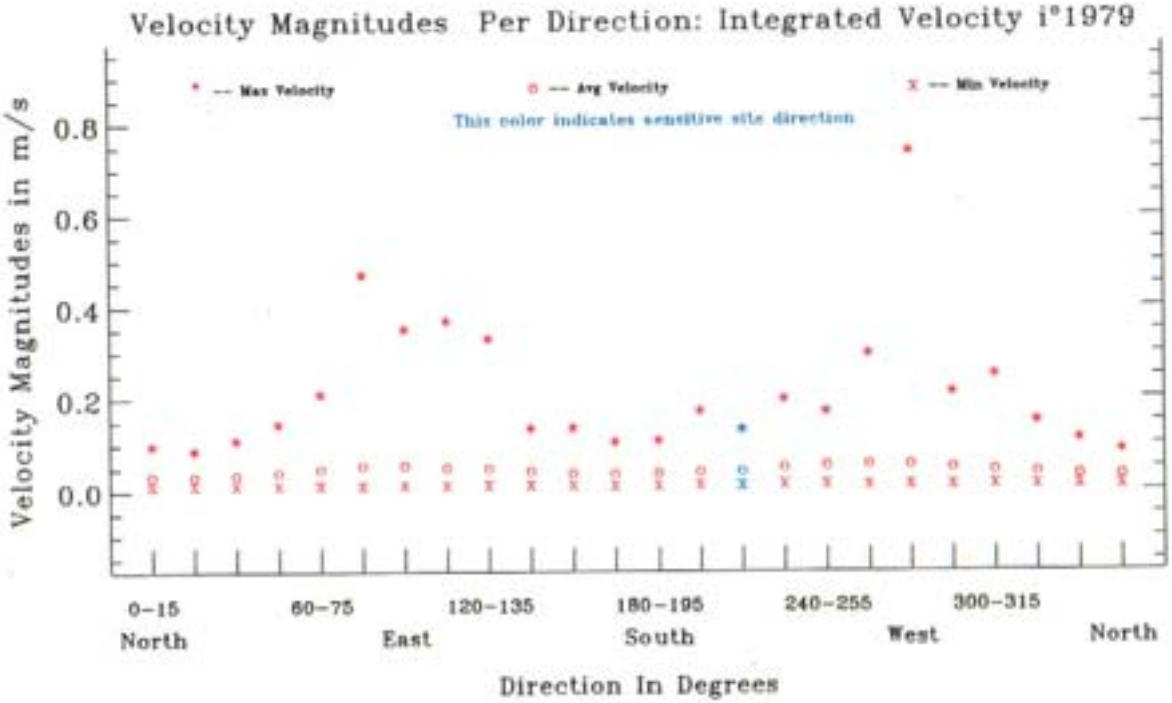
Velocity Magnitudes Per Direction: Integrated Velocity i°1979
* -- Max Velocity
o -- Avg Velocity
x -- Min Velocity
This color indicates sensitive site direction
Velocity Magnitudes in m/s
0.0
0.2
0.4
0.6
0.8
0-15
North
60-75
East
120-135
180-195
South
240-255
West
300-315
North
Direction In Degrees

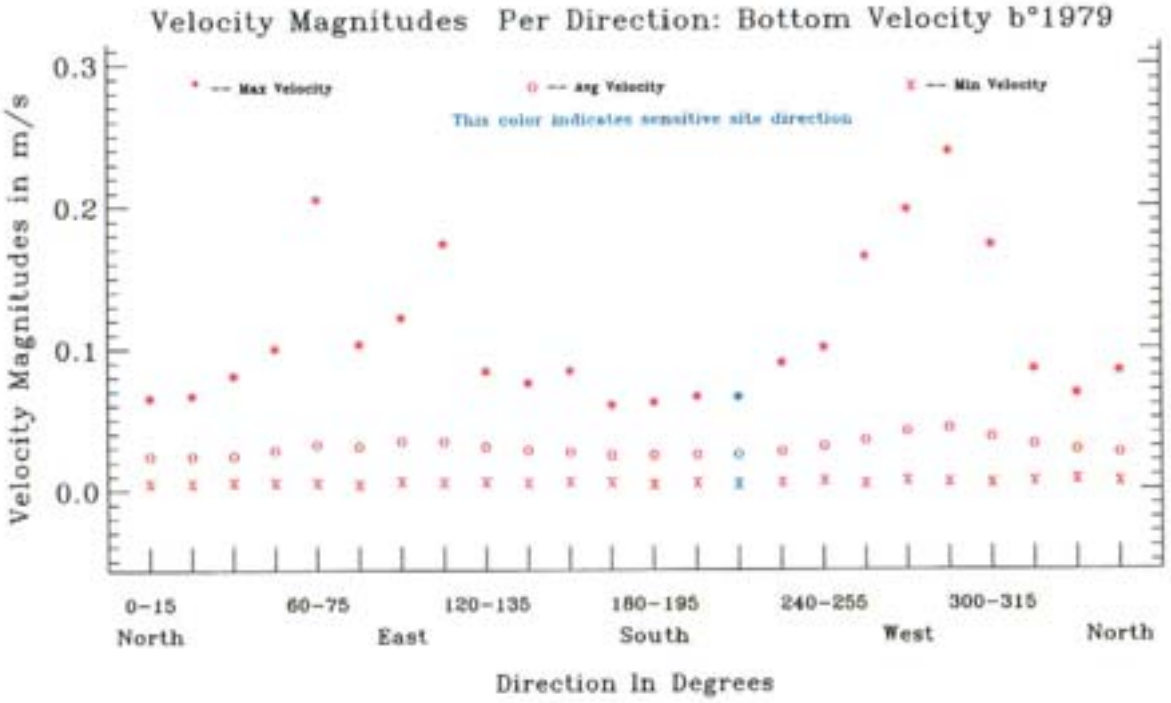
Velocity Magnitudes Per Direction: Bottom Velocity b°1979
* -- Max Velocity
o -- avg Velocity
x -- Min Velocity
This color indicates sensitive site direction
Velocity Magnitudes in m/s
0.3
0.2
0.1
0.0
0-15
North
60-75
East
120-135
South
180-195
240-255
West
300-315
North
Direction In Degrees

Finally, for each year the maximum velocity per sector is multiplied by the maximum duration per sector to obtain an estimate of the possible travel distance an inert particle would travel in one event. The 1979 data contained in Figures 6.10-6.12 reveal small possible excursion distances for the integrated and bottom event but, as may be seen in the surface velocity plot, considerable distances of travel are possible with the surface velocities.

6.2 Cumulative Sector 14 Impact

Figures 6.13-6.15 contain cumulative estimates of the maximum potential excursion distance due to any one continuous event. As is seen in the bottom and integrated velocity distance traveled plots, no one event transports material very far from the placement site. However, it is quite possible during a one surface velocity event clay or silt particles to be carried to the intakes.

In conclusion, Figure 6.16 contains the surface velocity distance traveled plot for the sector (#15) west of Sector 14 and it is readily seen that particles may travel a significant distance during certain events.

CHAPTER 7: CONCLUSIONS

While a considerable amount of visual information was generated in this study, the conclusions relative to the goals of the research program are relatively straight forward.

First, over the 20-year period of the study record the dominant circulation features are wind driven currents and the resulting storm derived seiches. The wind derived surface currents are predominantly to the northwest, away from the water intakes. A corresponding bottom return flow is directed 180° opposite to the surface. Bottom currents are always smaller than the surface currents. Integrated currents reflect the expected bi-directional seiche activity, in neither case, directly towards the intake pipes.

Second, in the 20-year record, no single flow event was of sufficient magnitude or direction to result in bottom currents carrying material entirely to the intake paper. The same result occurred for the integrated velocity field.

Third, in the 20-year period of record each year contained at least one single event with a surface velocity of magnitude and direction sufficient to carry material to within the intake pipe vicinity.

Fourth, with regard to conclusion two, it is implied that heavier sand sized particles at the placement site will remain near the bottom during transport and will not reach the intake pipe as the bottom currents are insufficient during any one single event.

Fifth, with regard to conclusion three, fine particles such as clays will easily resuspend into the near surface of the water column and could reach the sensitive site during any one annual event.

Sixth, the analysis here considers only single events and the possibility of even bottom sitting sand particles to reaching the intake pipes during a succession of transport events is high.

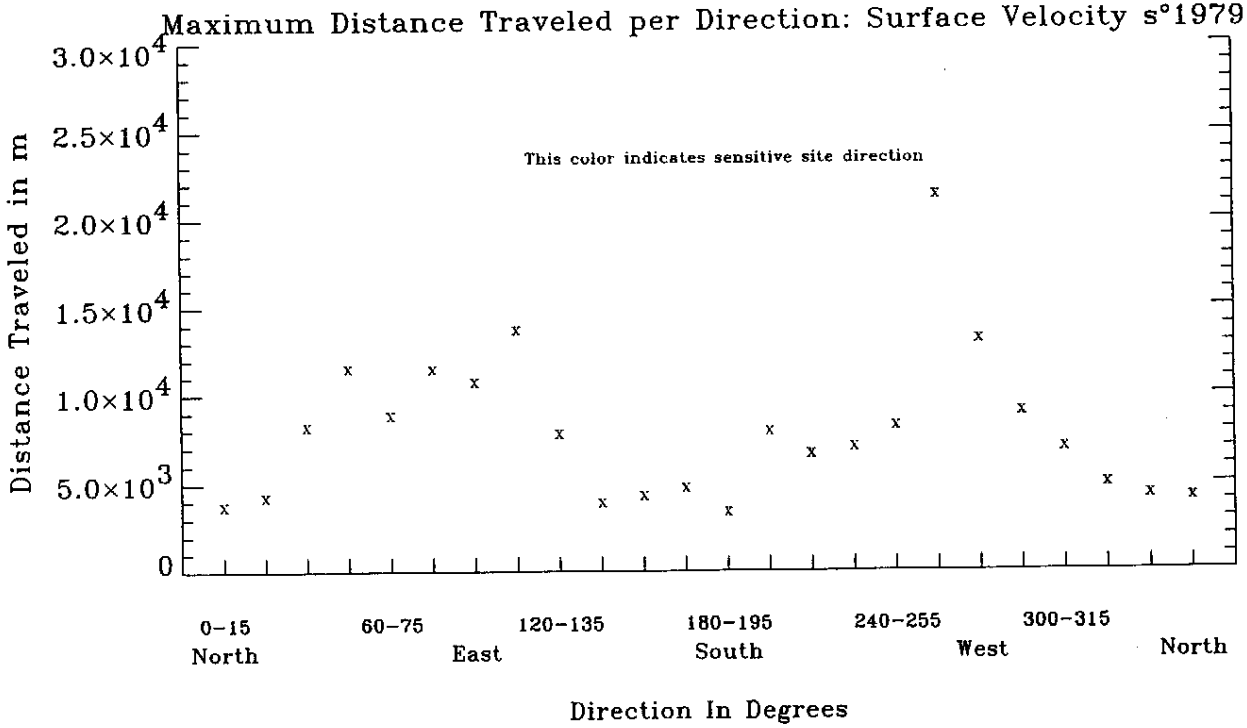
Maximum Distance Traveled per Direction: Surface Velocity s°1979
Distance Traveled in m
3.0×10^4
2.5×10^4
2.0×10^4
1.5×10^4
1.0×10^4
5.0×10^3
0
This color indicates sensitive site direction
0–15
North
60–75
East
120–135
180–195
South
240–255
West
300–315
North
Direction In Degrees

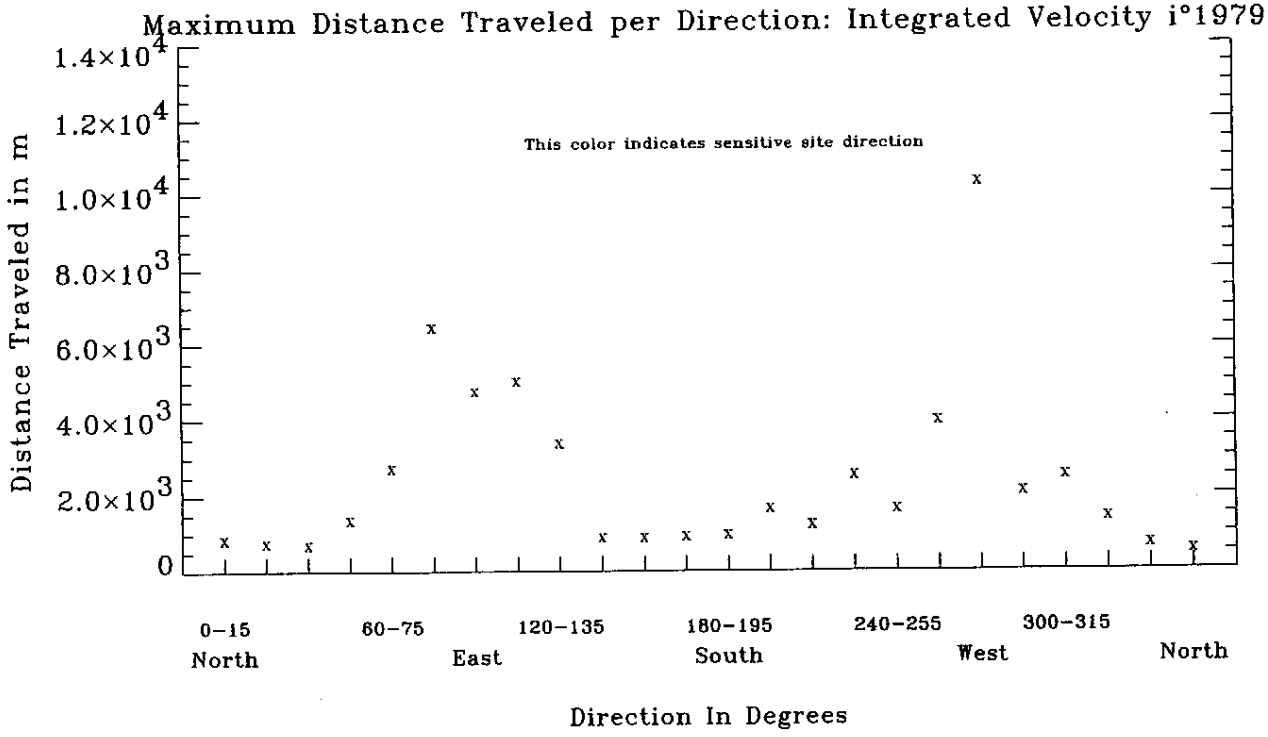
Maximum Distance Traveled per Direction: Integrated Velocity i°1979
Distance Traveled in m
1.4×10^4
1.2×10^4
1.0×10^4
8.0×10^3
6.0×10^3
4.0×10^3
2.0×10^3
0
This color indicates sensitive site direction
0–15
North
60–75
East
120–135
South
180–195
240–255
West
300–315
North
Direction In Degrees

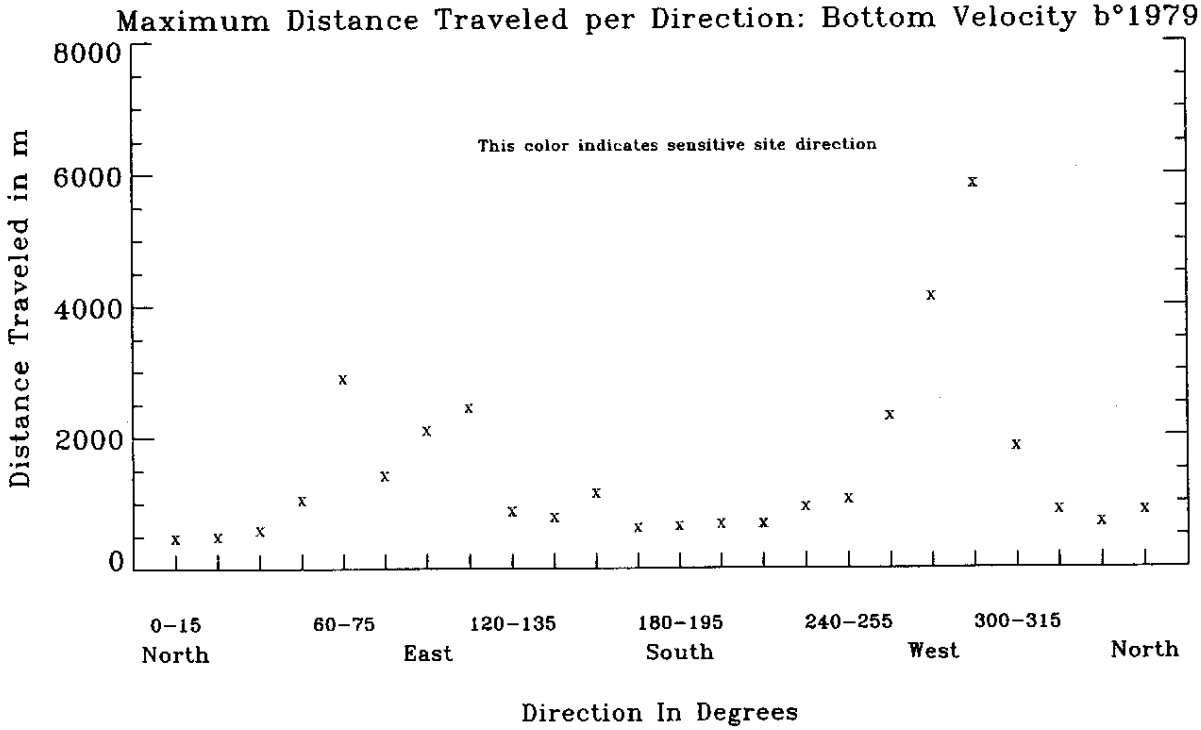
Maximum Distance Traveled per Direction: Bottom Velocity b°1979
Distance Traveled in m
8000
6000
4000
2000
0
This color indicates sensitive site direction
0–15
North
60–75
East
120–135
South
180–195
240–255
West
300–315
North
Direction In Degrees

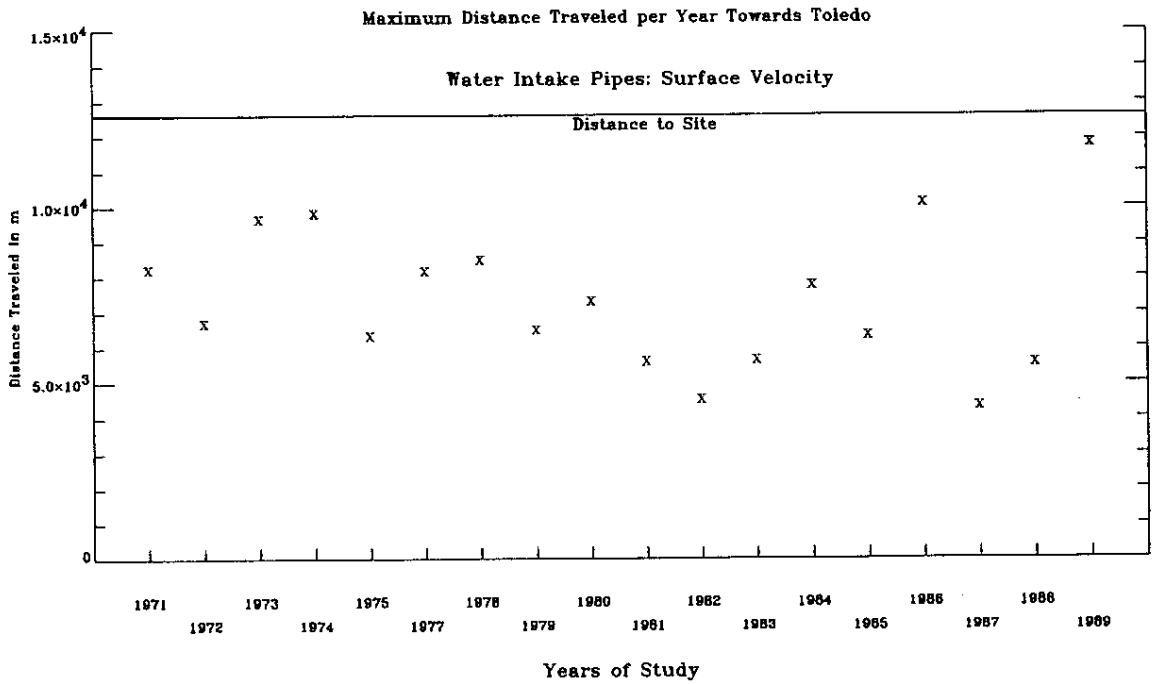
Maximum Distance Traveled per Year Towards Toledo
Water Intake Pipes: Surface Velocity
Distance to Site
1.5×10^4
1.0×10^4
5.0×10^3
0
Distance Traveled in m
1971
1972
1973
1974
1975
1977
1978
1979
1980
1981
1982
1983
1984
1985
1986
1987
1988
1989
Years of Study

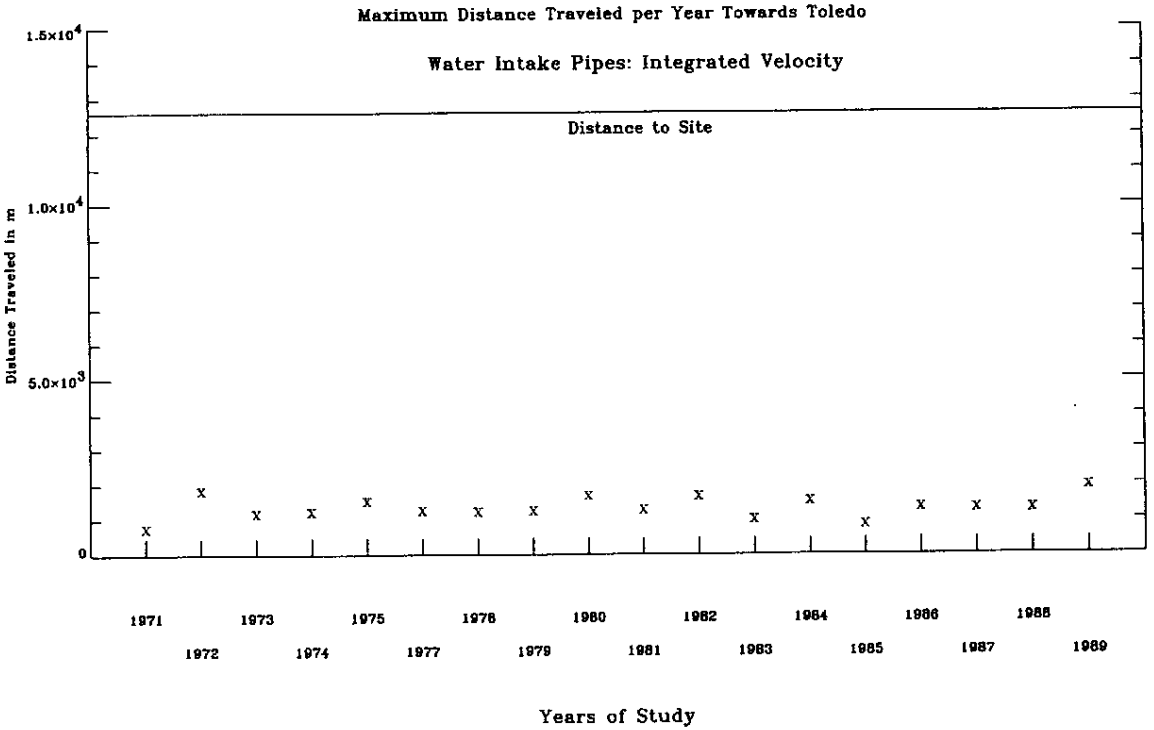
Maximum Distance Traveled per Year Towards Toledo
Water Intake Pipes: Integrated Velocity
Distance to Site
Distance Traveled in m
1.5x10^4
1.0x10^4
5.0x10^3
0
1971
1972
1973
1974
1975
1976
1977
1978
1979
1980
1981
1982
1983
1984
1985
1986
1987
1988
1989
Years of Study

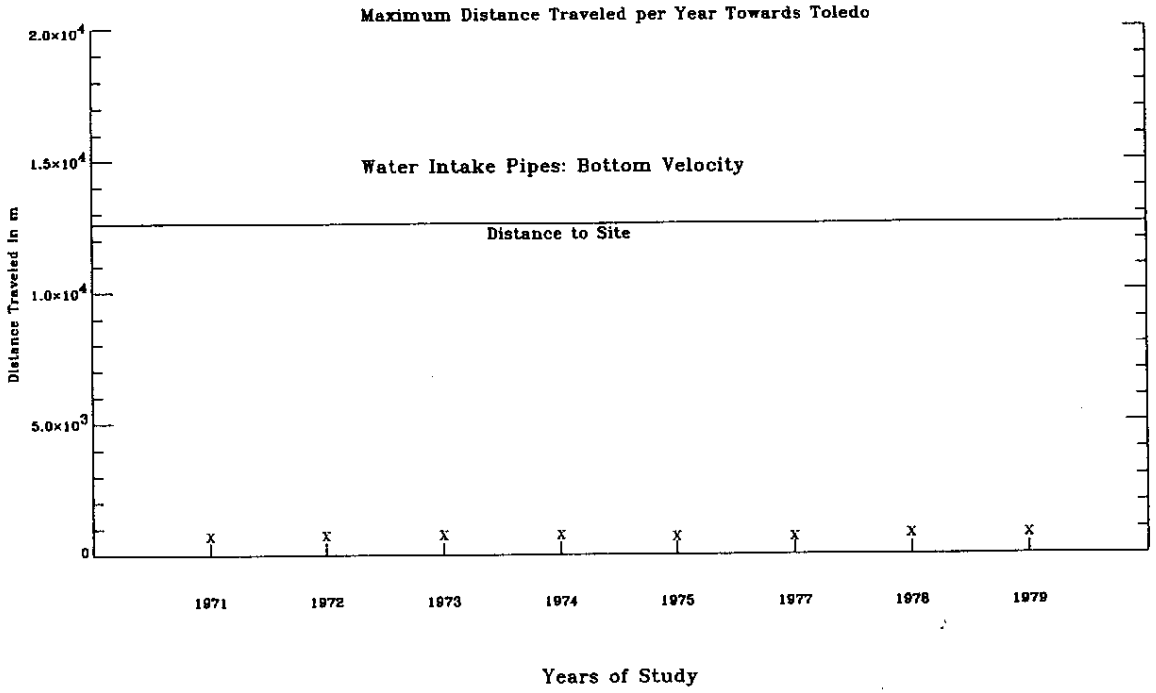
Maximum Distance Traveled per Year Towards Toledo
Water Intake Pipes: Bottom Velocity
Distance to Site
Distance Traveled in m
2.0×10^4
1.5×10^4
1.0×10^4
5.0×10^3
0
1971
1972
1973
1974
1975
1977
1978
1979
Years of Study

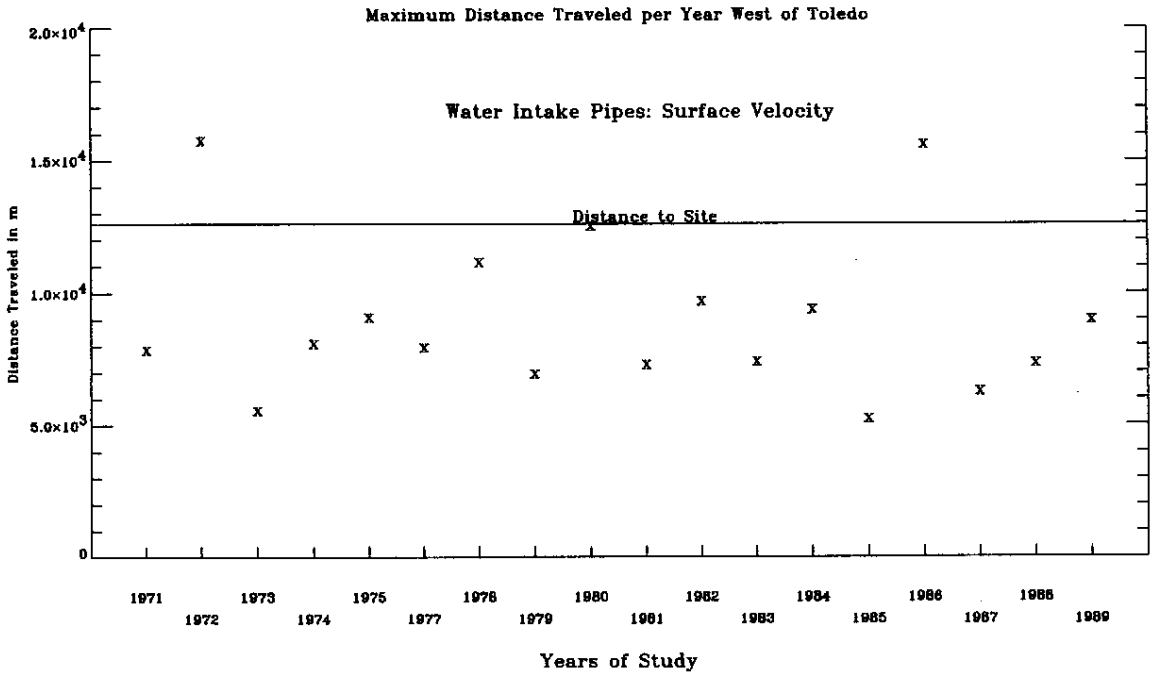
Maximum Distance Traveled per Year West of Toledo
Water Intake Pipes: Surface Velocity
Distance to Site
Distance Traveled in m
2.0×10^4
1.5×10^4
1.0×10^4
5.0×10^3
0
1971
1972
1973
1974
1975
1976
1977
1978
1979
1980
1981
1982
1983
1984
1985
1986
1987
1988
1989
Years of Study

BIBLIOGRAPHY

Allen F. Blumberg and George L. Mellor. A description of a three-dimensional coastal ocean circulation model. In Norman S. Heaps, editor, *Three-dimensional Coastal Ocean Models*, Coastal and Estuarine Sciences 4, pages 1-16. American Geophysical Union, 1987.

David P. Podber, Chieh-Cheng J. Yen, Lou Regenmorter, Keith W. Bedford, and Onyx W.H. Wai. A nearshore model for Cleveland CSO remediation design selection. In George V. Controneo and Ralph R. Rumer, editors, *Hydraulic Engineering '94, Proceedings of the Conference*, pages 222-226, Buffalo, NY, 1994, ASCE.

APPENDIX A
The Rose Diagrams

The following are the rosettes that represent the directional flow emanating from the location at the center point.

Figure Captions

A.1 Surface Velocity: Rose Diagram for the Cumulative Data
A.2 Surface Velocity: Rose Diagram for the Year 1970
A.3 Surface Velocity: Rose Diagram for the Year 1971
A.4 Surface Velocity: Rose Diagram for the Year 1972
A.5 Surface Velocity: Rose Diagram for the Year 1973
A.6 Surface Velocity: Rose Diagram for the Year 1974
A.7 Surface Velocity: Rose Diagram for the Year 1975
A.8 Surface Velocity: Rose Diagram for the Year 1977
A.9 Surface Velocity: Rose Diagram for the Year 1978
A.10 Surface Velocity: Rose Diagram for the Year 1980
A.11 Surface Velocity: Rose Diagram for the Year 1981
A.12 Surface Velocity: Rose Diagram for the Year 1982
A.13 Surface Velocity: Rose Diagram for the Year 1983
A.14 Surface Velocity: Rose Diagram for the Year 1984
A.15 Surface Velocity: Rose Diagram for the Year 1985
A.16 Surface Velocity: Rose Diagram for the Year 1986
A.17 Surface Velocity: Rose Diagram for the Year 1987
A.18 Surface Velocity: Rose Diagram for the Year 1988
A.19 Surface Velocity: Rose Diagram for the Year 1989
A.20 Integrated Velocity: Rose Diagram for the Year 1971
A.21 Integrated Velocity: Rose Diagram for the Year 1972
A.22 Integrated Velocity: Rose Diagram for the Year 1973
A.23 Integrated Velocity: Rose Diagram for the Year 1974
A.24 Integrated Velocity: Rose Diagram for the Year 1975
A.25 Integrated Velocity: Rose Diagram for the Year 1977
A.26 Integrated Velocity: Rose Diagram for the Year 1978
A.27 Integrated Velocity: Rose Diagram for the Year 1980
A.28 Integrated Velocity: Rose Diagram for the Year 1981
A.29 Integrated Velocity: Rose Diagram for the Year 1982
A.30 Integrated Velocity: Rose Diagram for the Year 1983
A.31 Integrated Velocity: Rose Diagram for the Year 1984
A.32 Integrated Velocity: Rose Diagram for the Year 1985
A.33 Integrated Velocity: Rose Diagram for the Year 1986
A.34 Integrated Velocity: Rose Diagram for the Year 1987

Number of Events per Direction: Surface Velocity s_cumulative

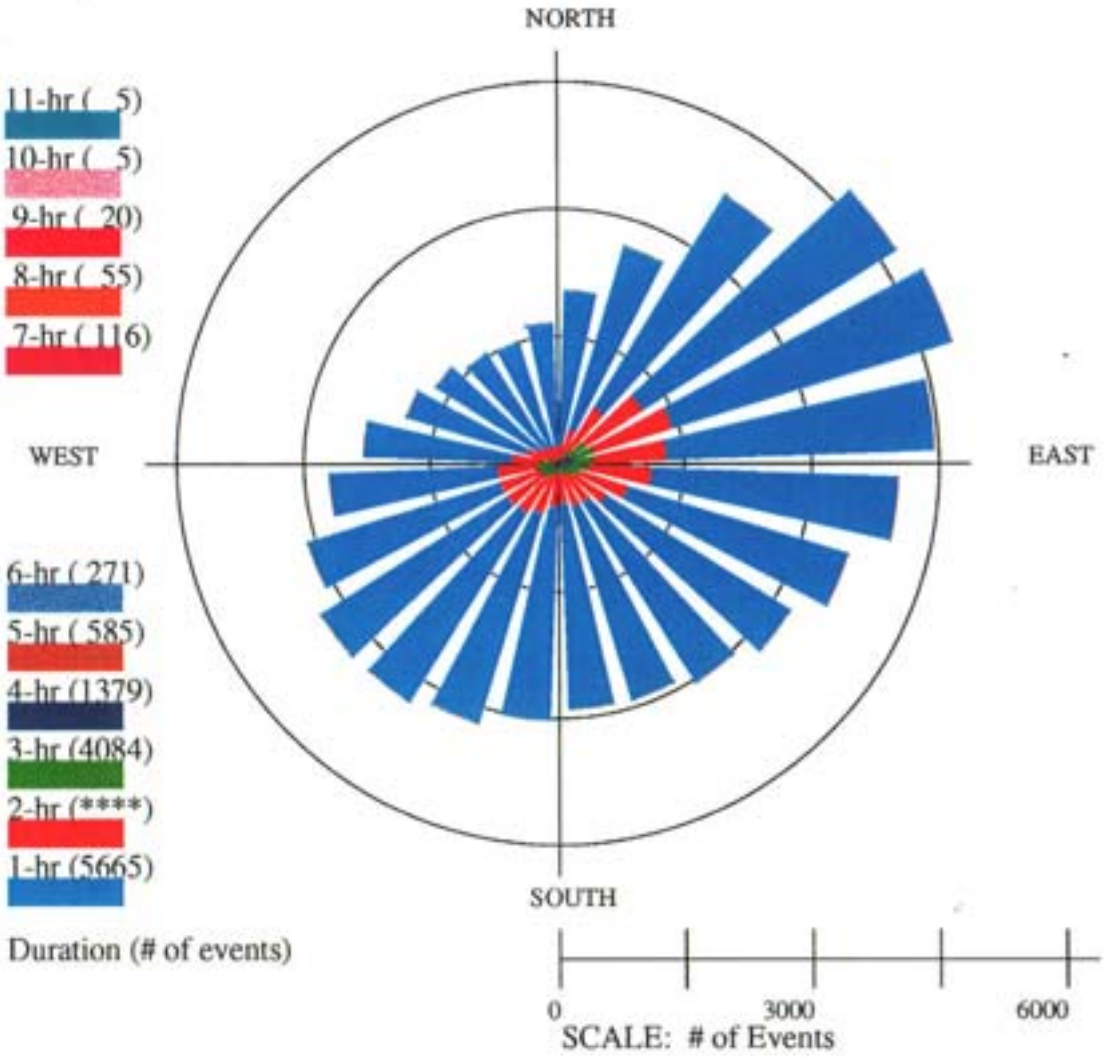

Number of Events per Direction: Surface Velocity surface_vel_70.stat

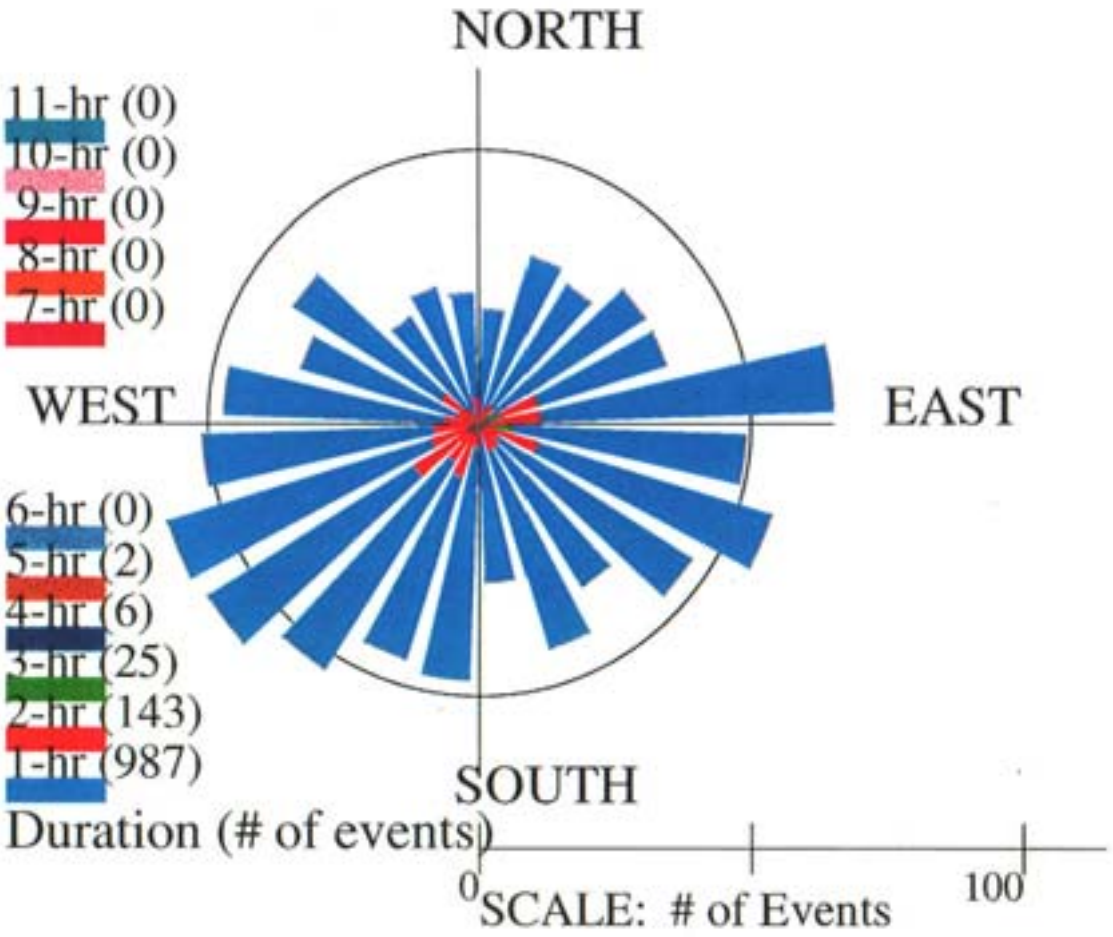

Number of Events per Direction: Surface Velocity surface_vel_71.stat

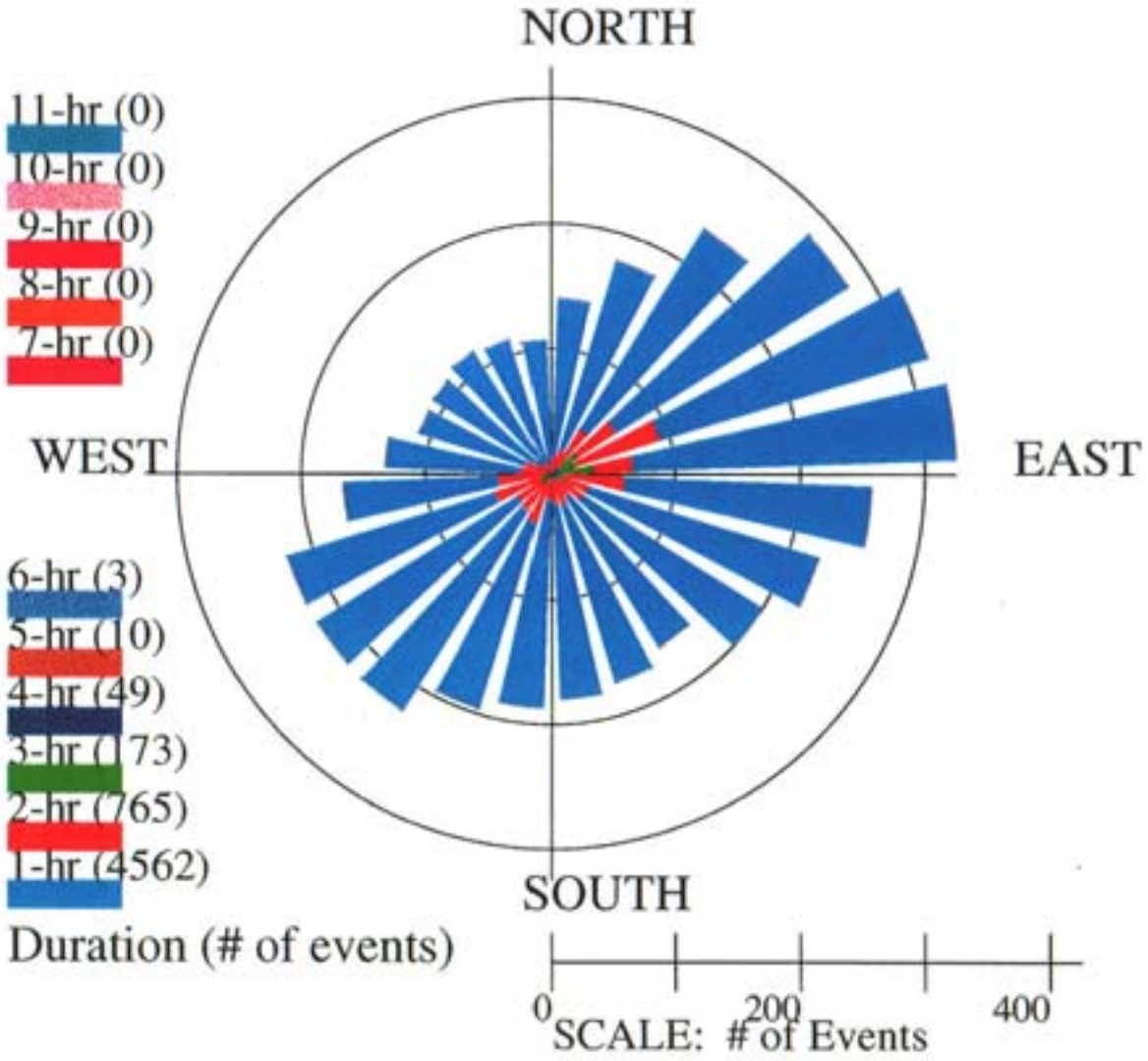

Number of Events per Direction: Surface Velocity surface_vel_72.stat

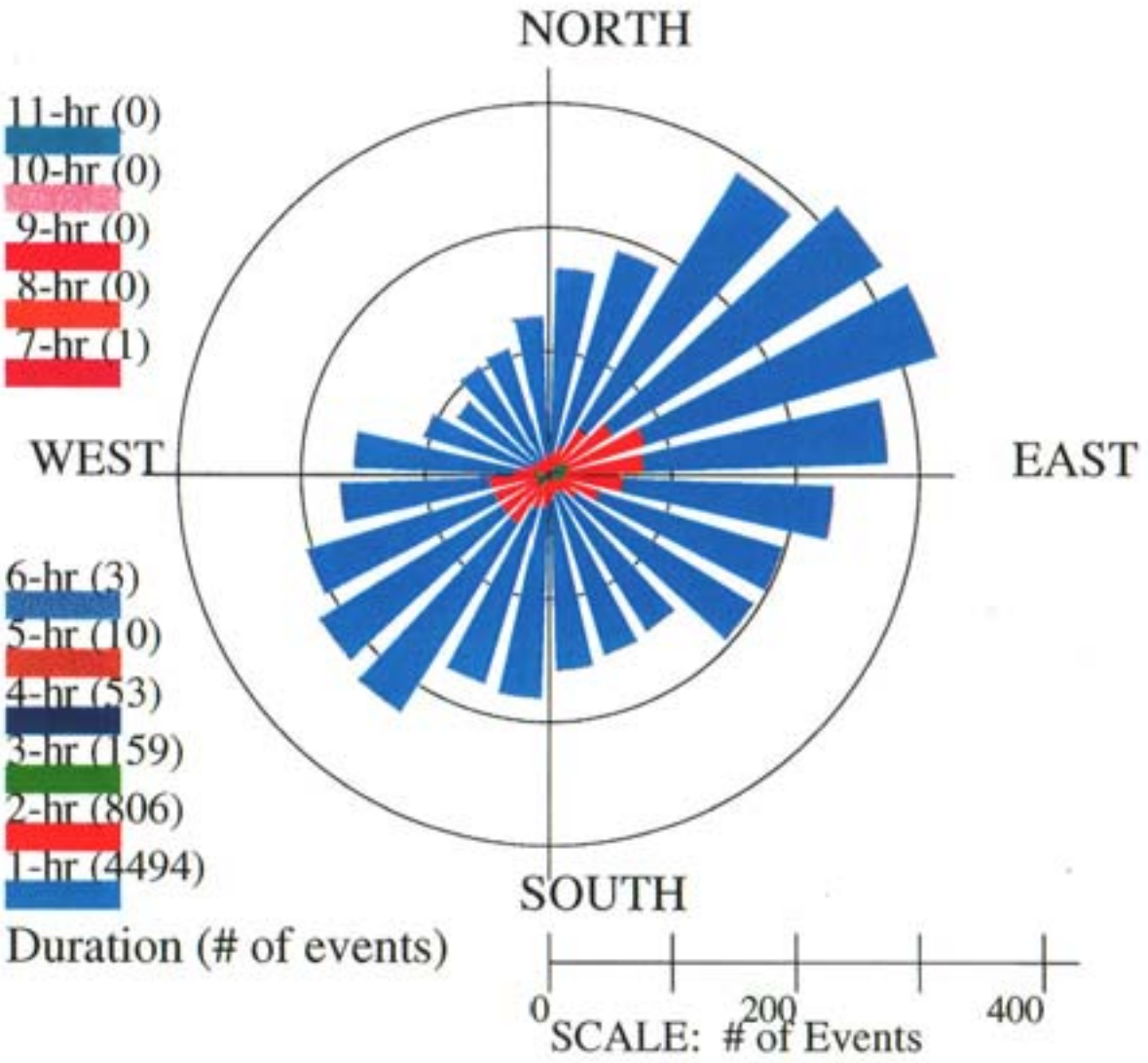

Number of Events per Direction: Surface Velocity surface_vel_73.stat

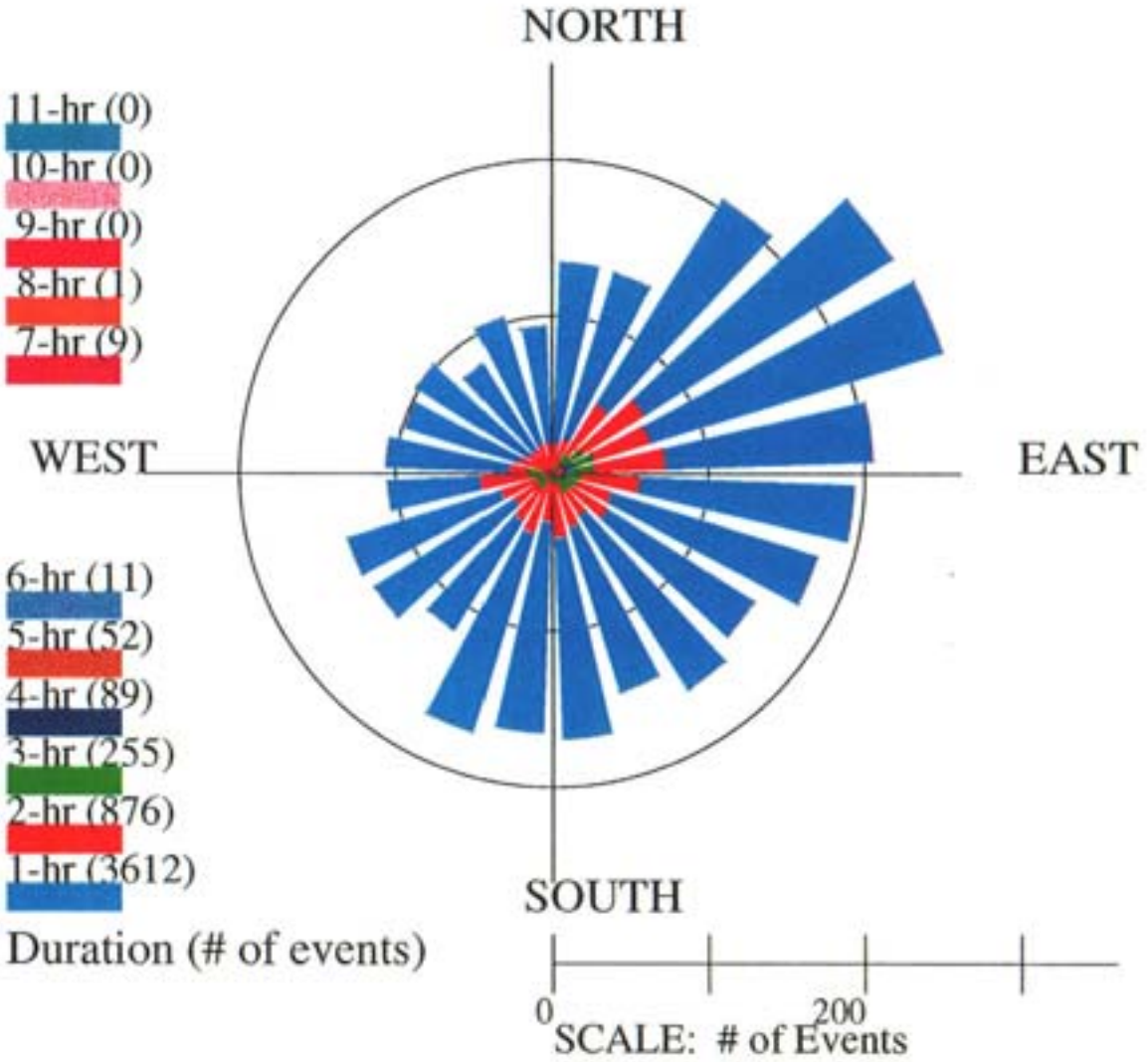

Number of Events per Direction: Surface Velocity surface_vel_74.stat

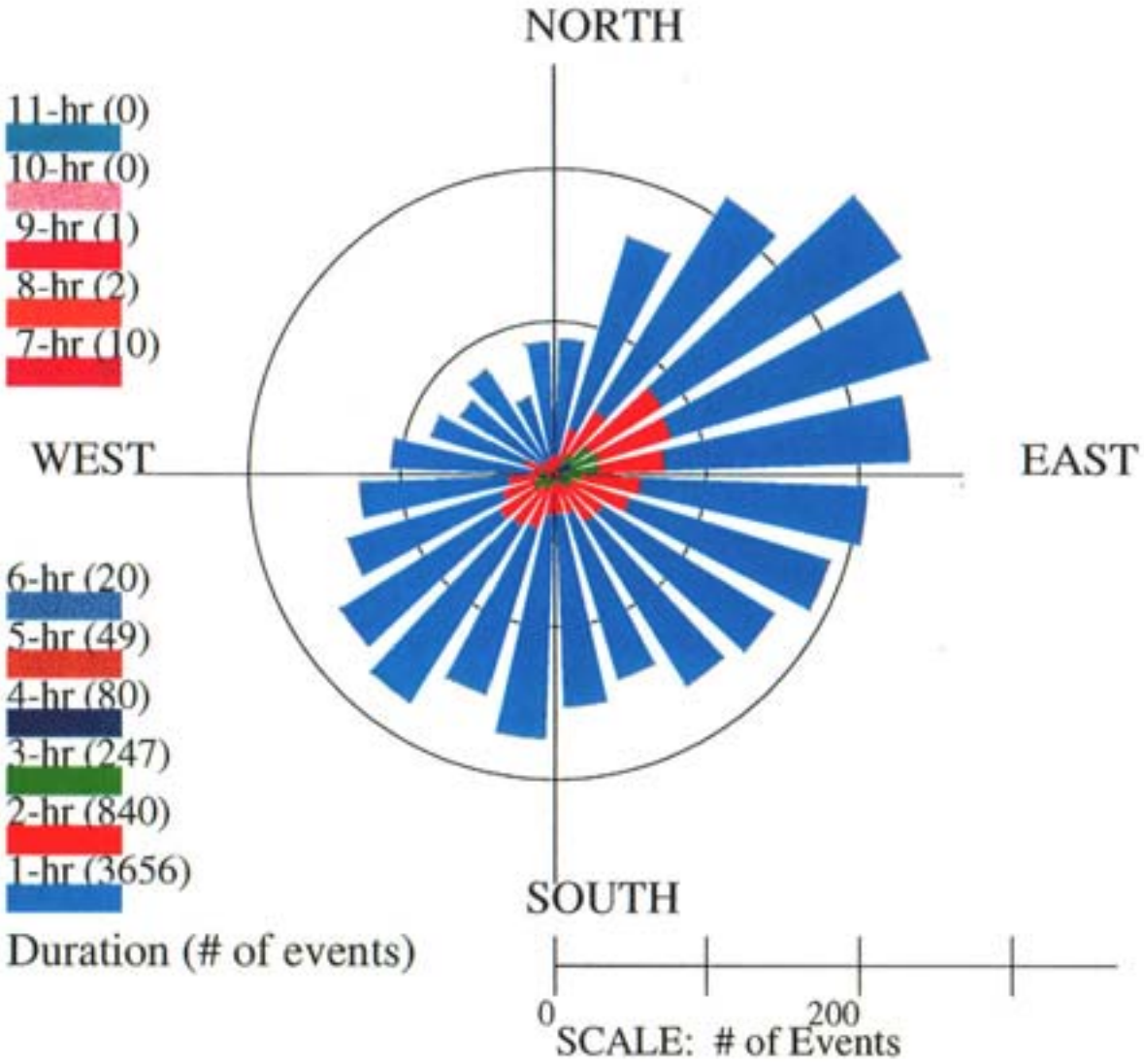

Number of Events per Direction: Surface Velocity surface_vel_75.stat

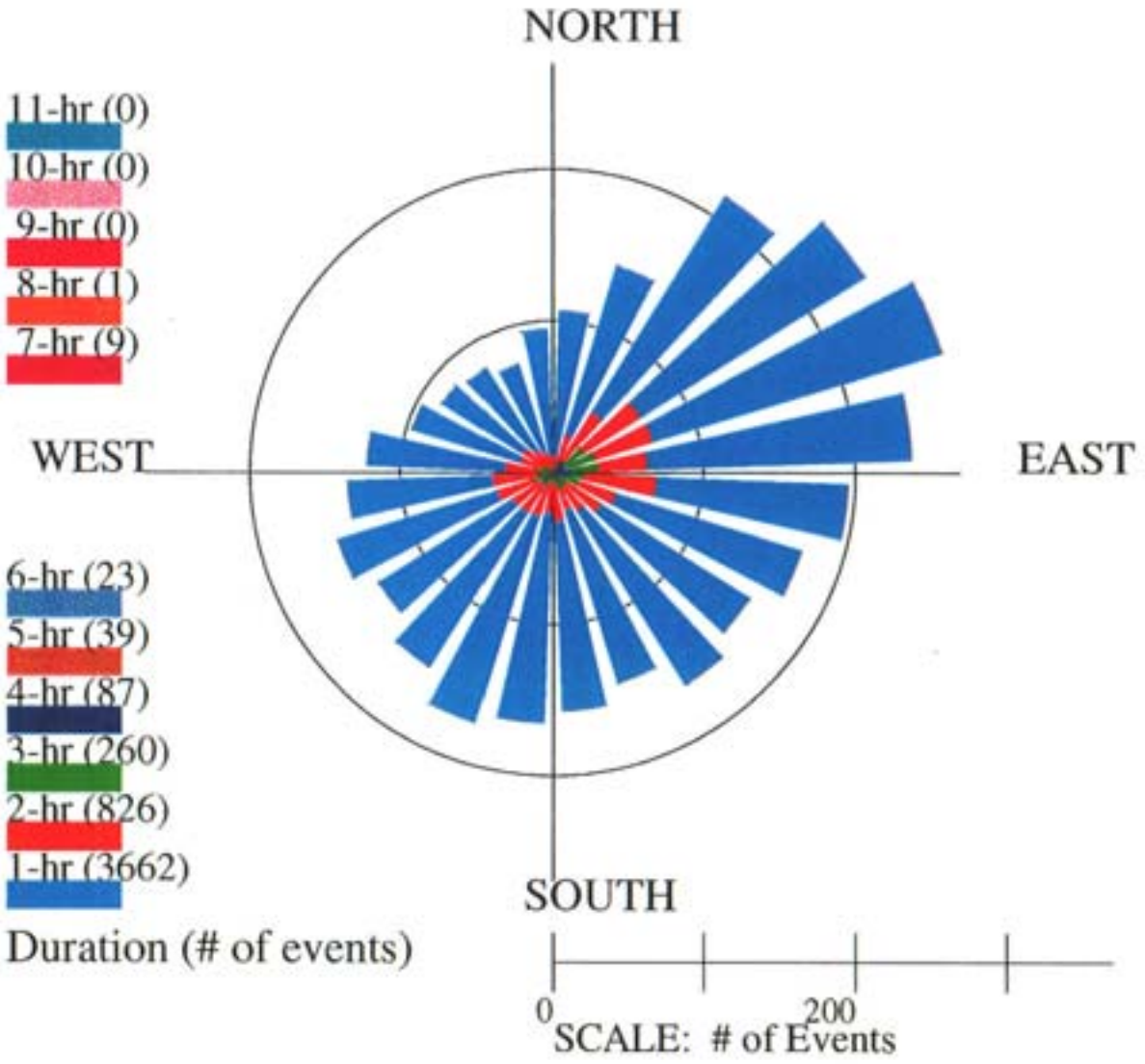

Number of Events per Direction: Surface Velocity surface_vel_77.stat

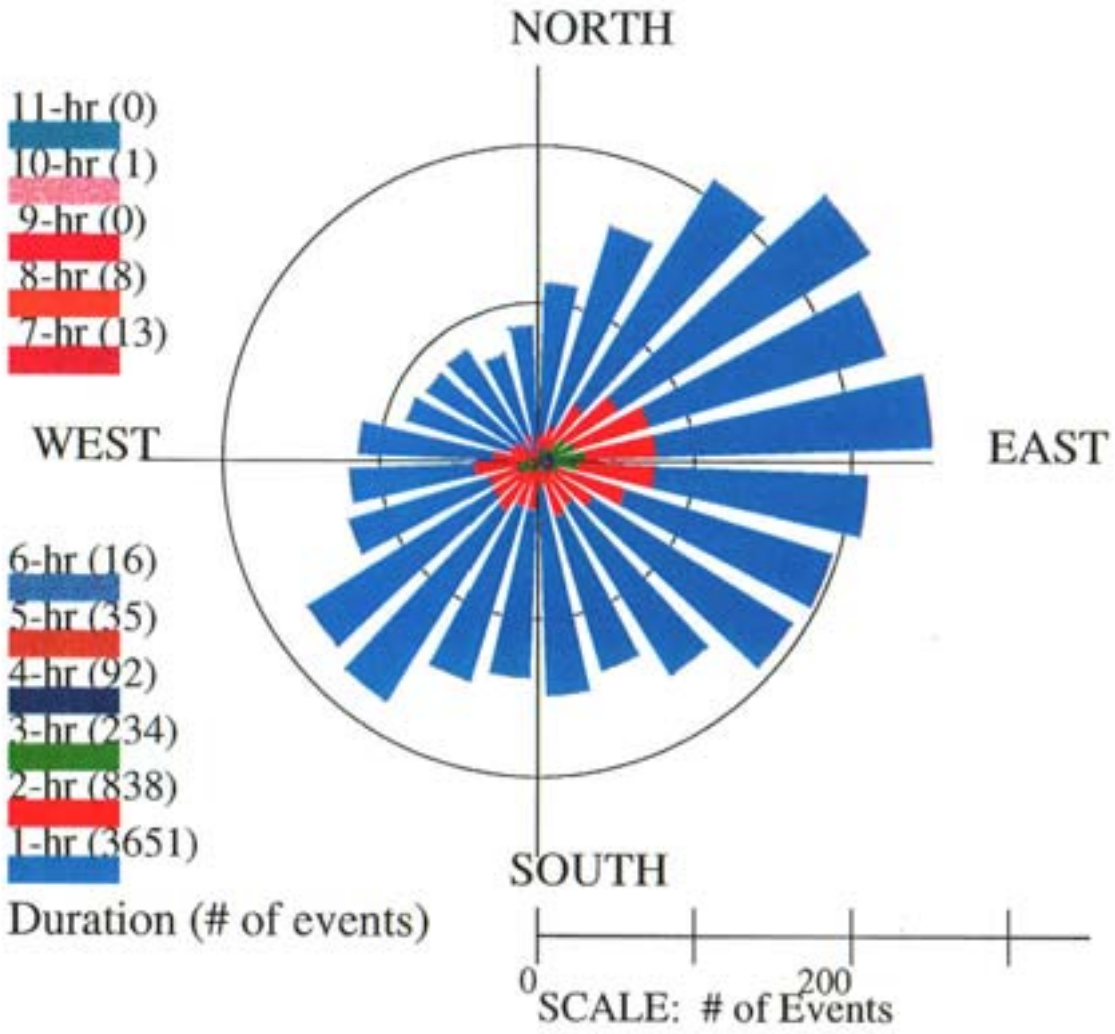

Number of Events per Direction: Surface Velocity surface_vel_78.stat

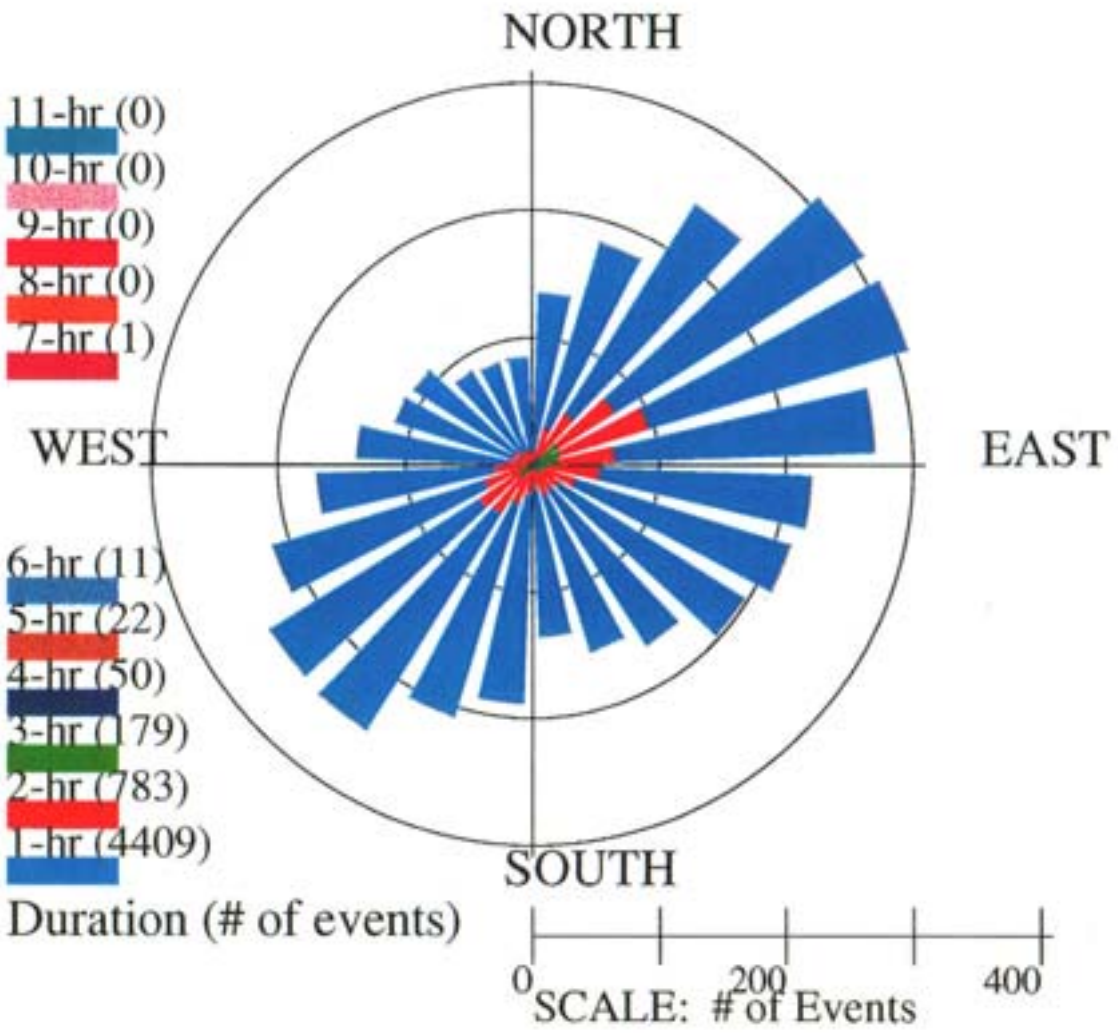

Number of Events per Direction: Surface Velocity surface_vel_80.stat

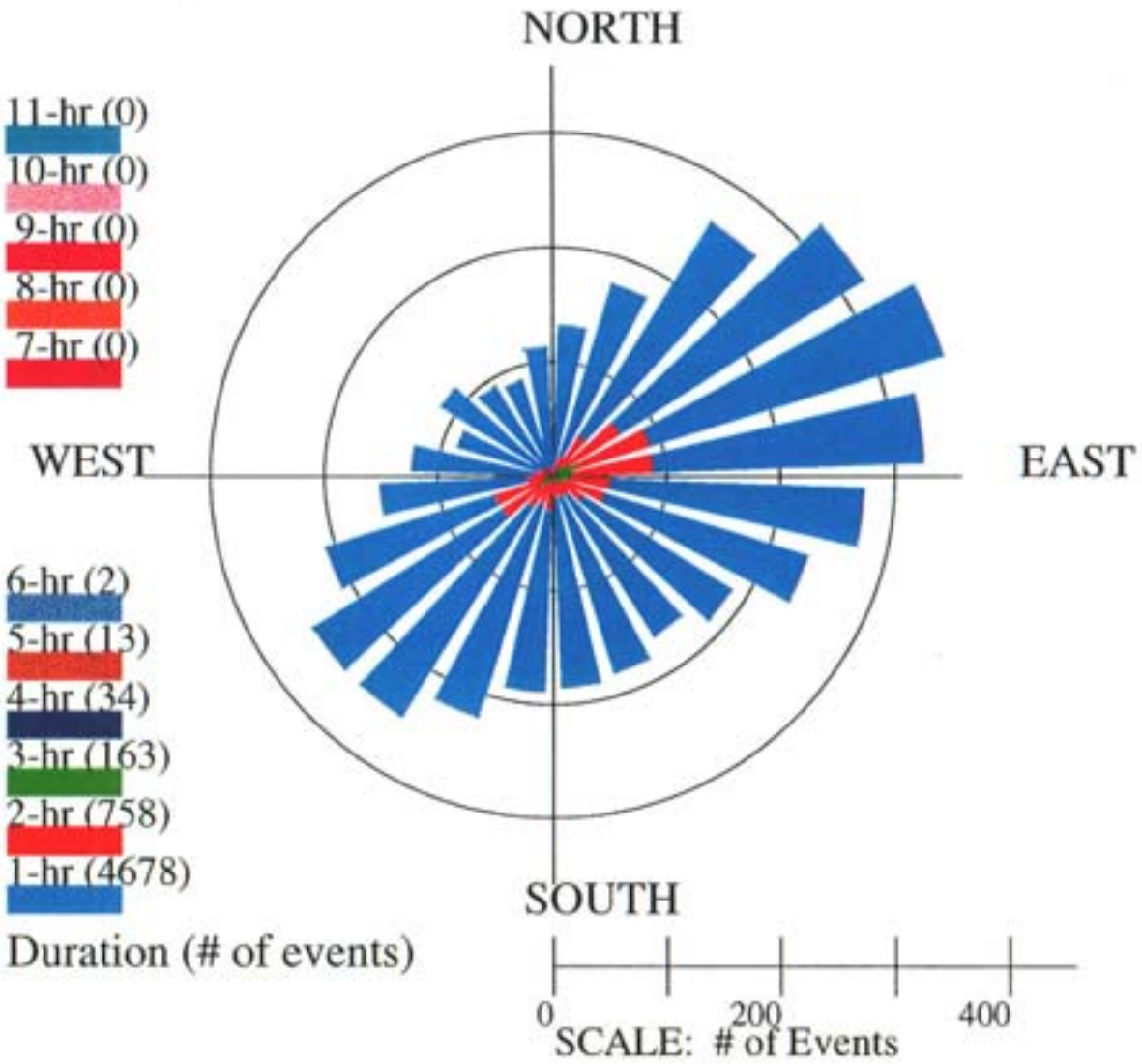

Number of Events per Direction: Surface Velocity surface_vel_81.stat

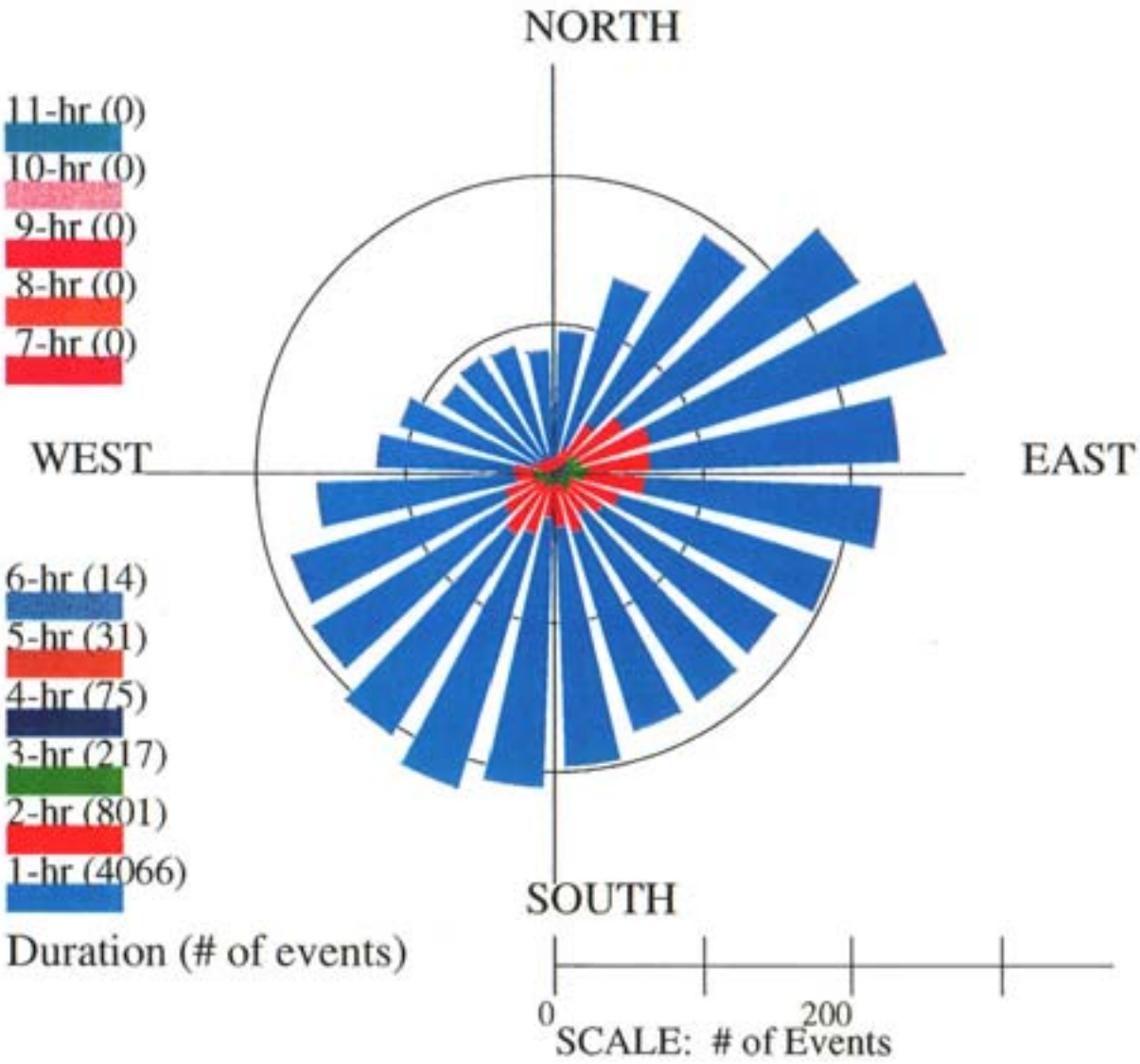

Number of Events per Direction: Surface Velocity surface_vel_82.stat

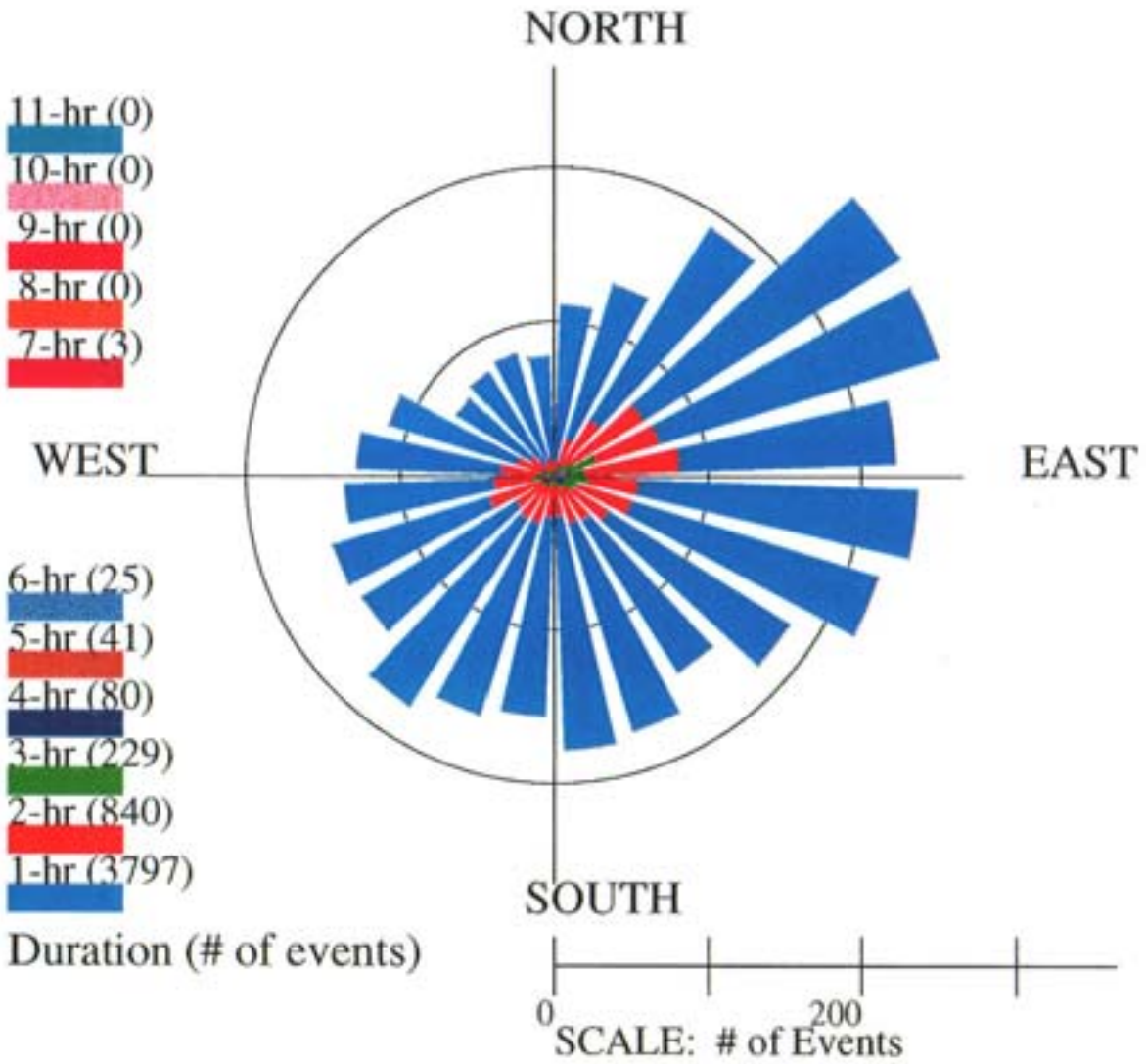

Number of Events per Direction: Surface Velocity surface_vel_83.stat

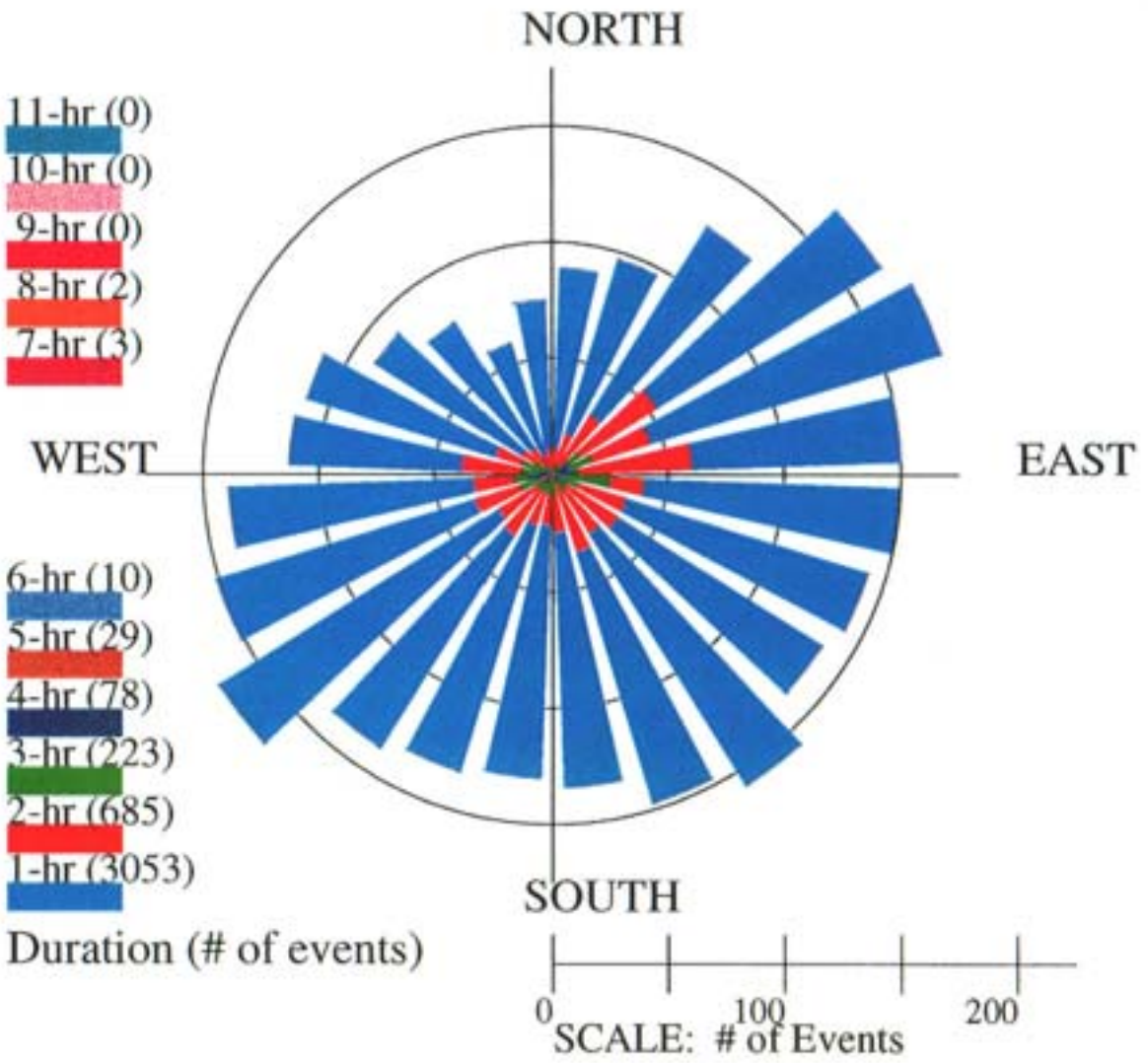

Number of Events per Direction: Surface Velocity surface_vel_84.stat

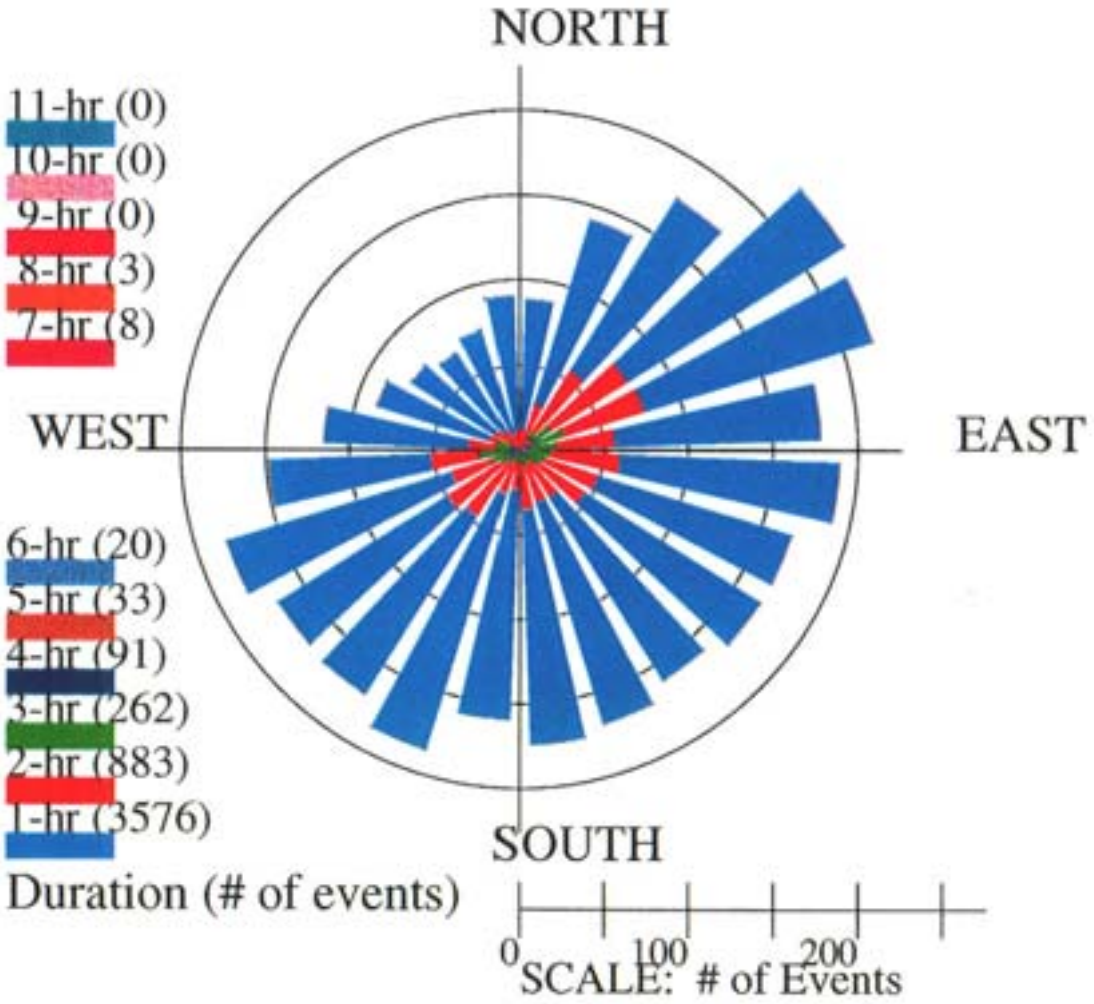

Number of Events per Direction: Surface Velocity surface_vel_85.stat

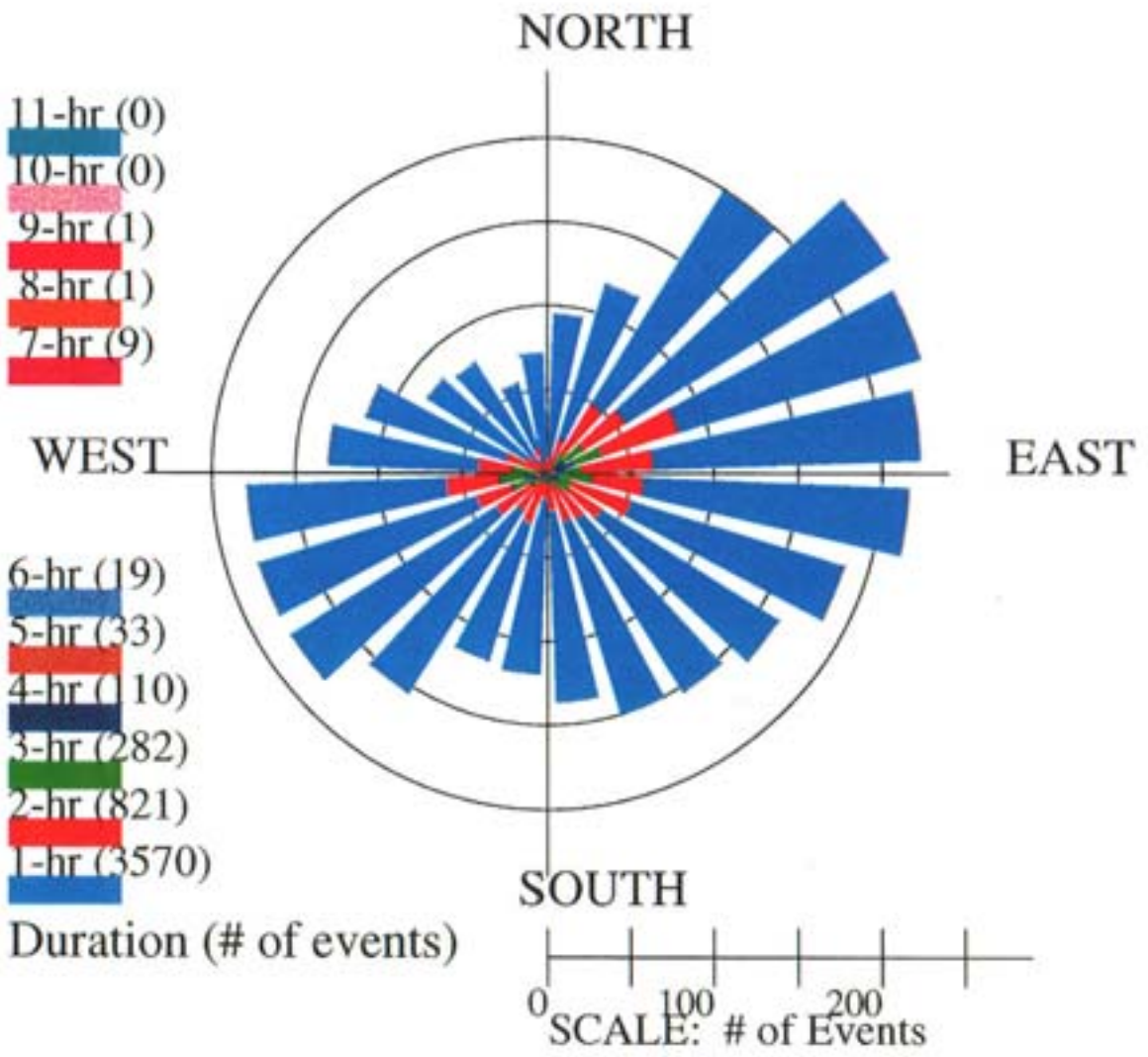

Number of Events per Direction: Surface Velocity surface_vel_86.stat

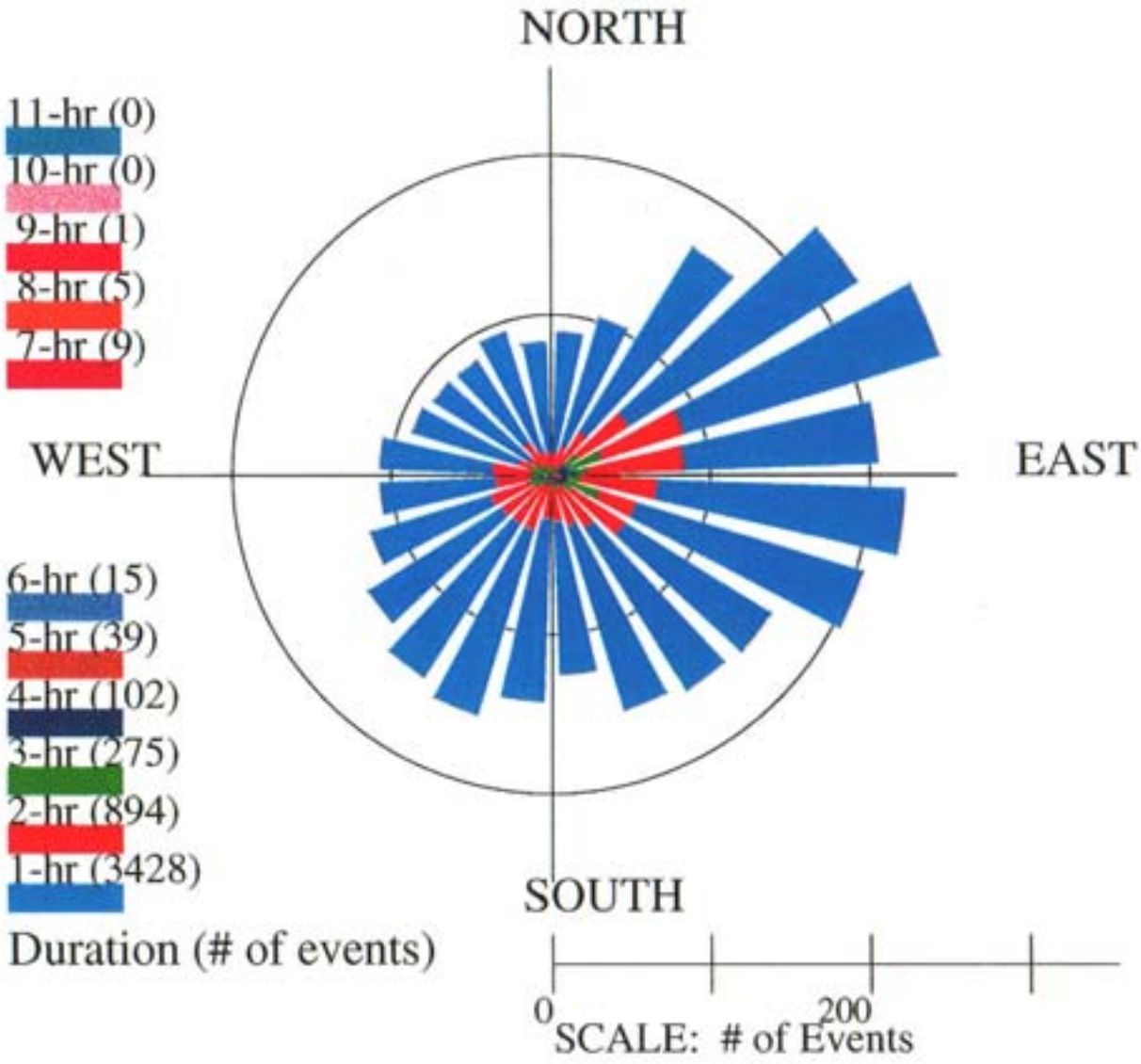

Number of Events per Direction: Surface Velocity surface_vel_87.stat

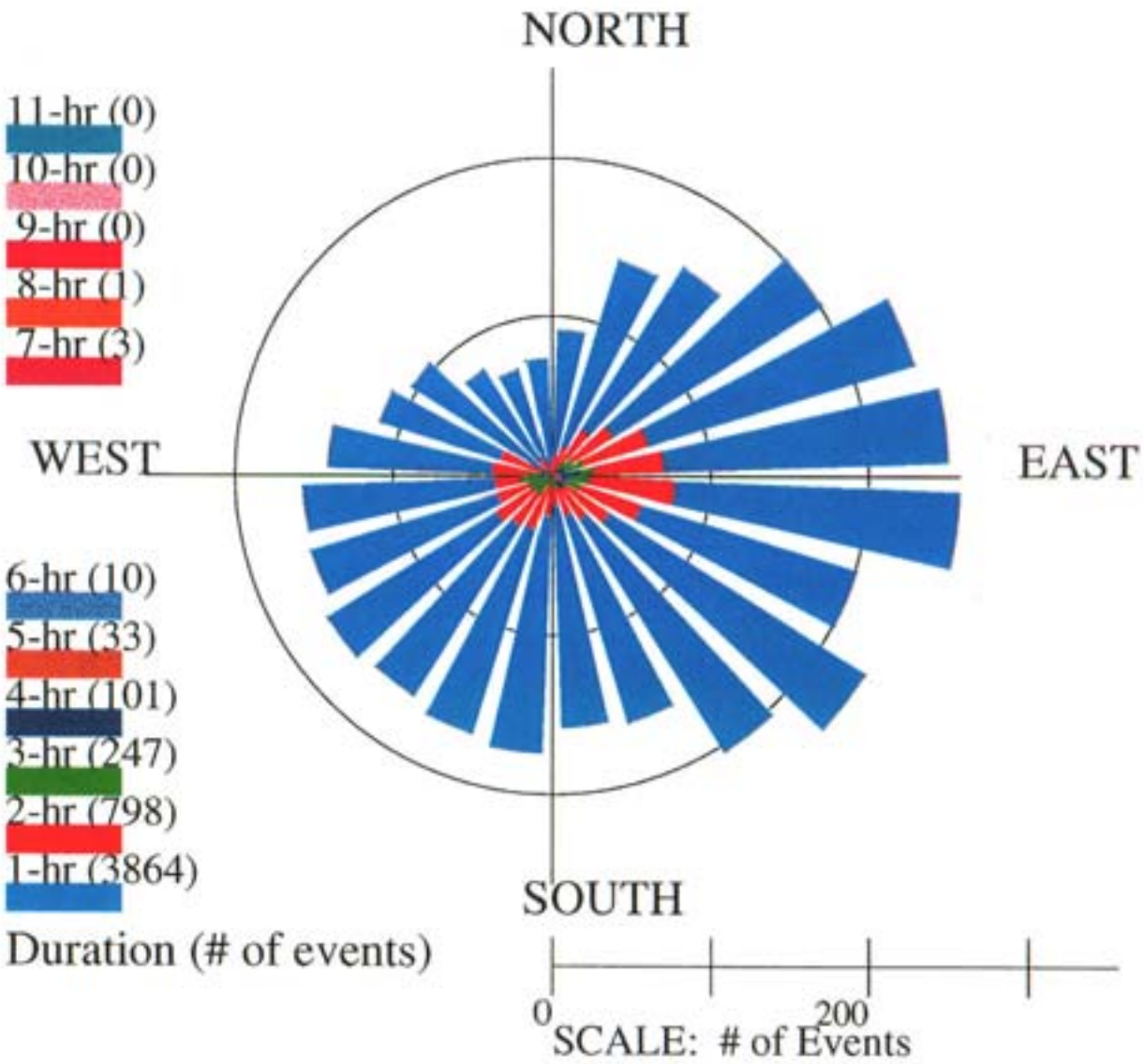

Number of Events per Direction: Surface Velocity surface_vel_88.stat

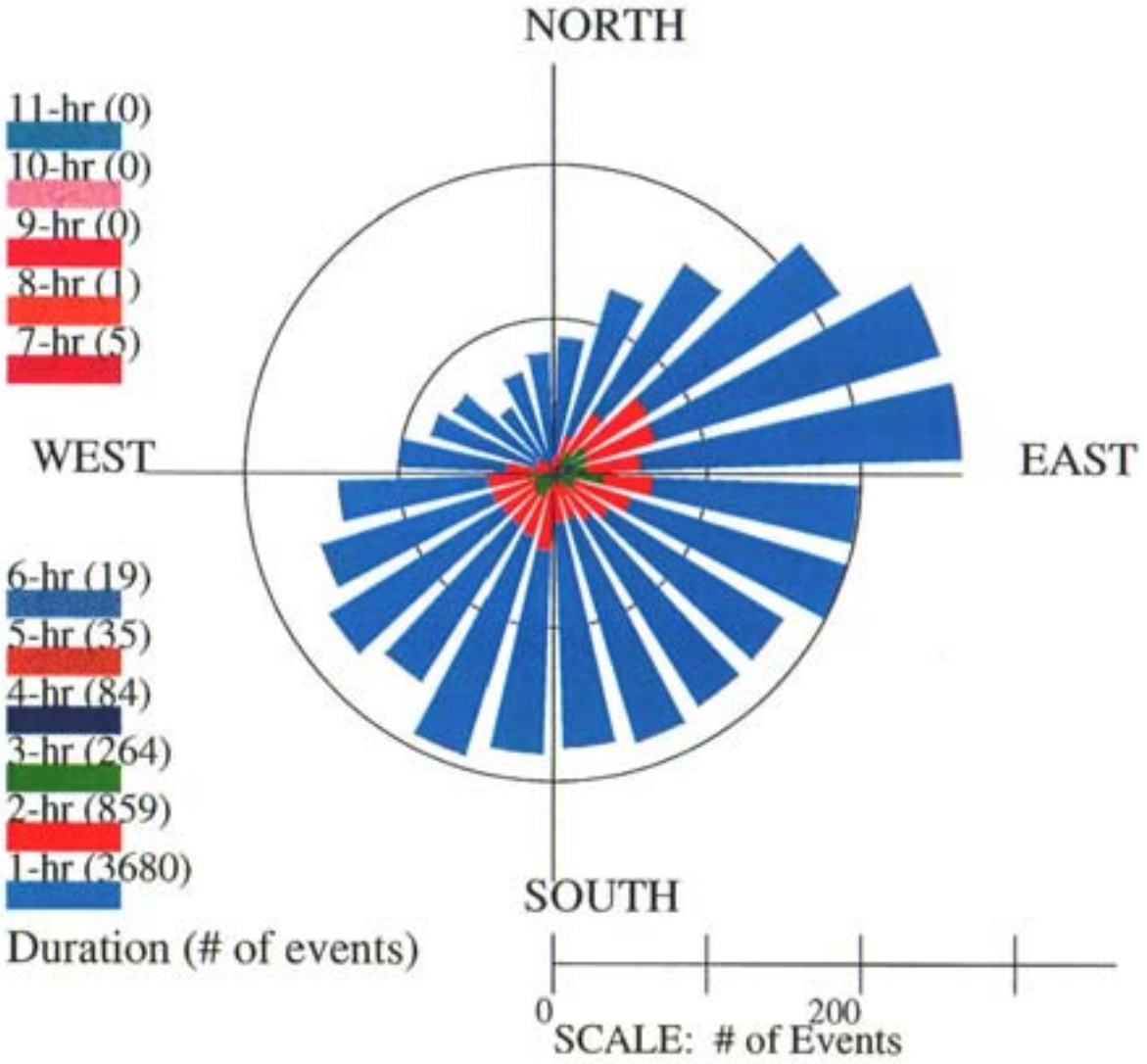

Number of Events per Direction: Surface Velocity surface_vel_89.stat

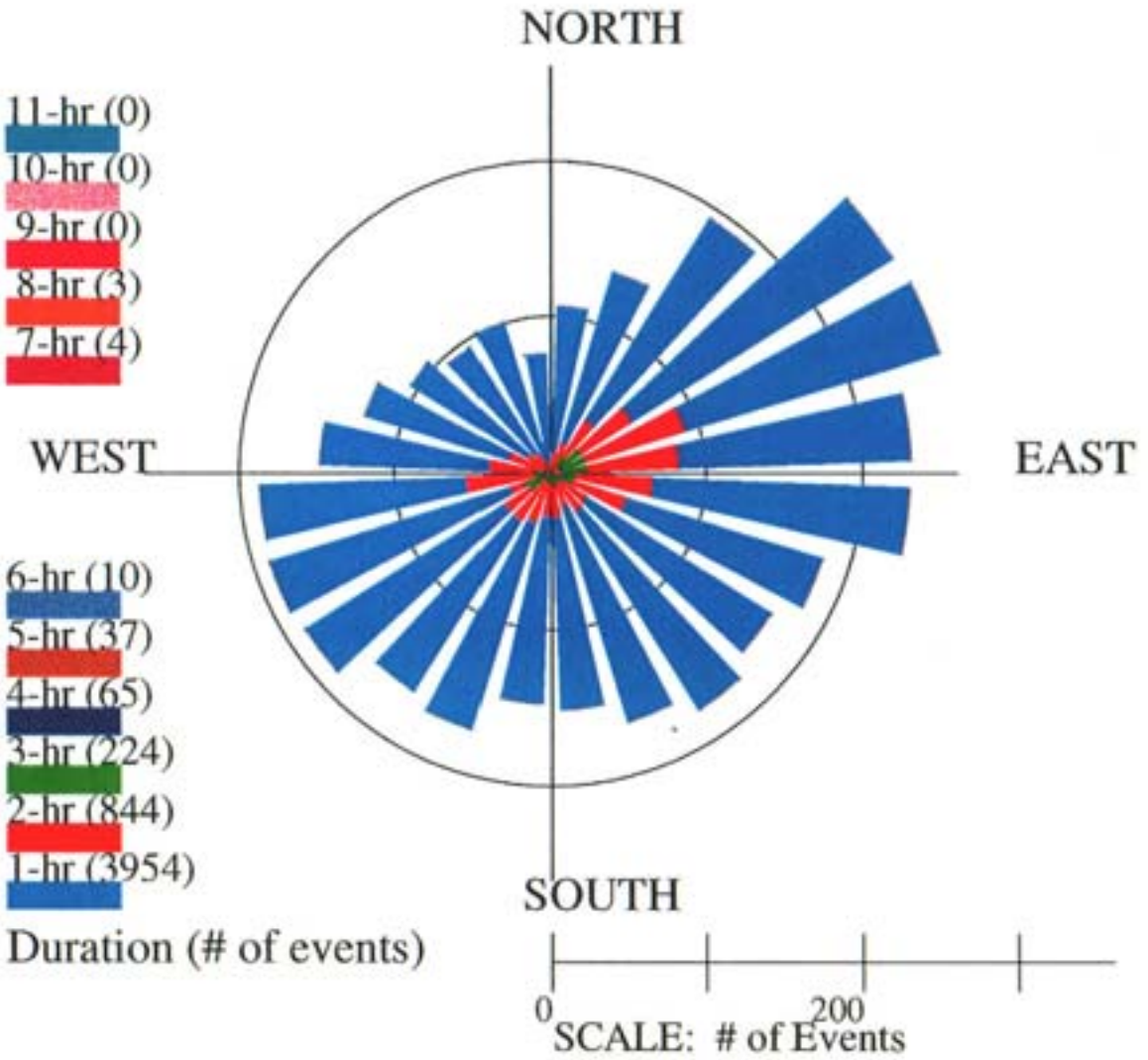

Number of Events per Direction: Integrated Velocity i_1971

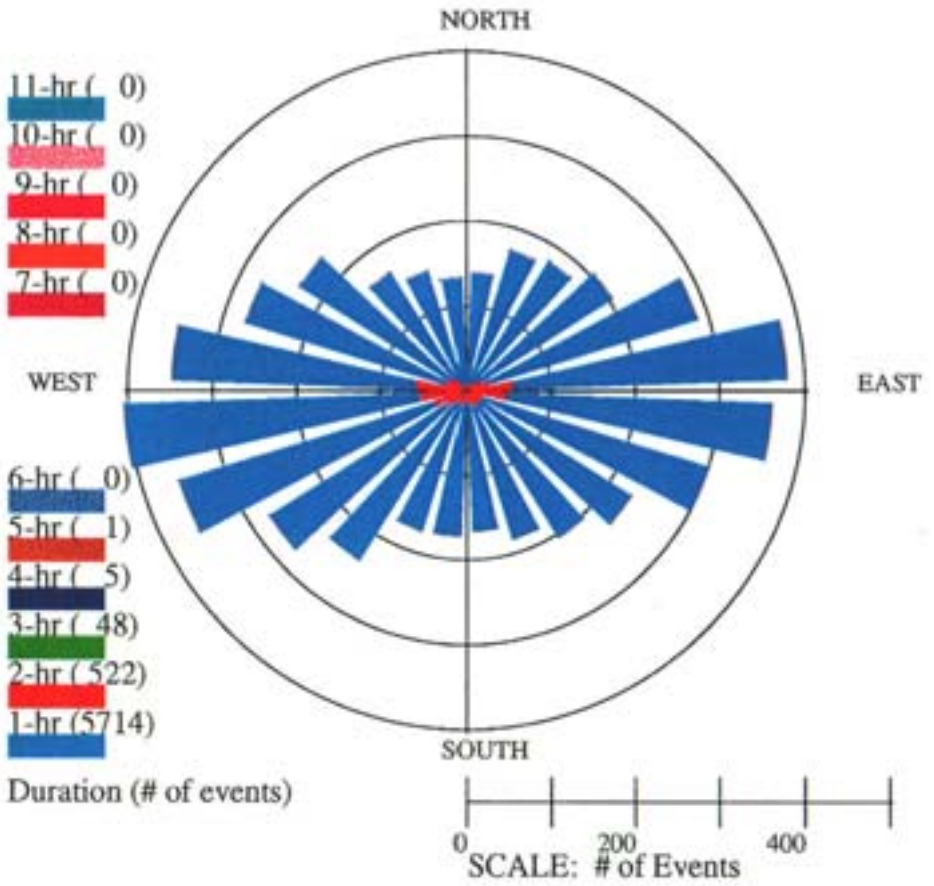

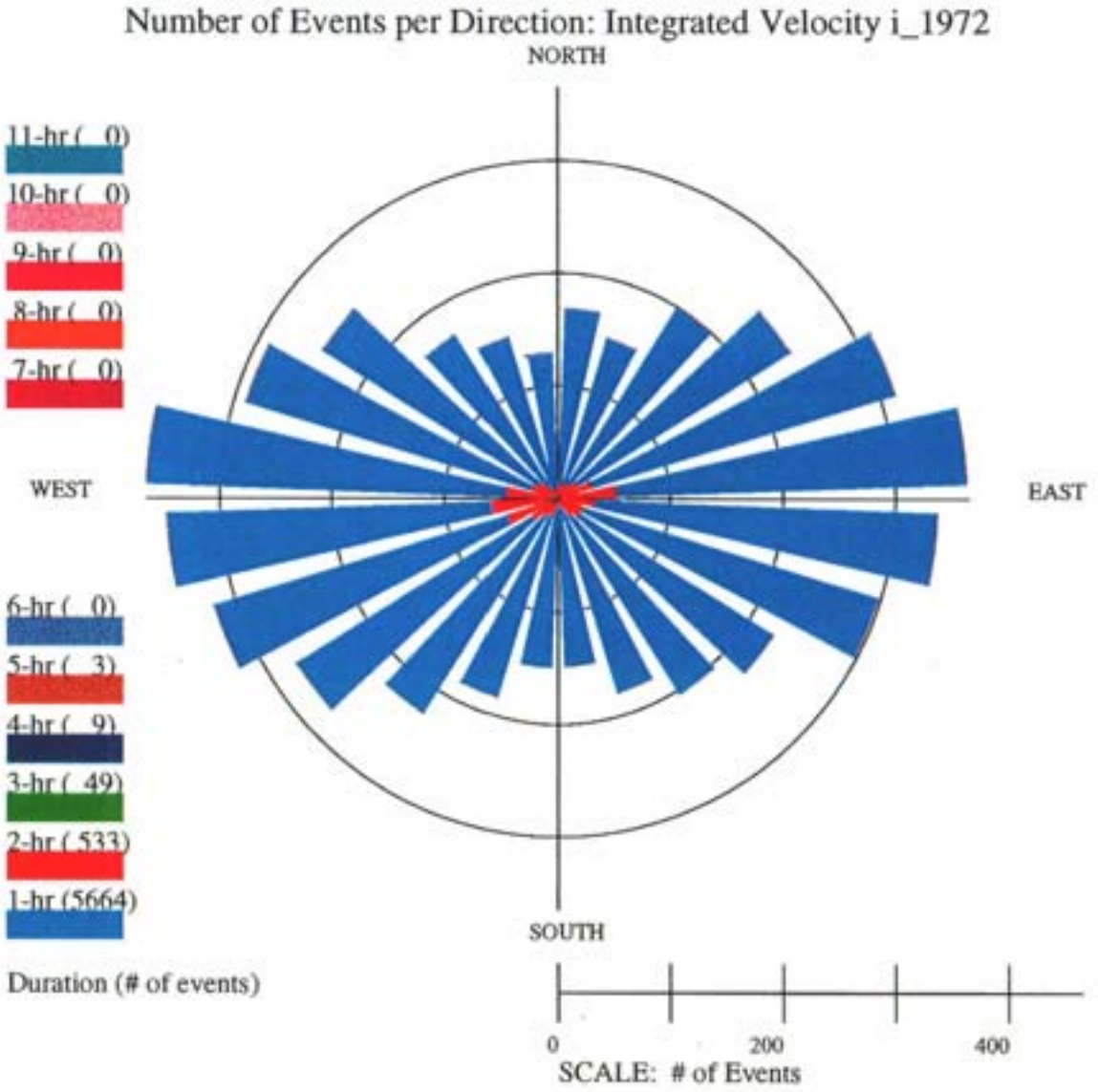
Number of Events per Direction: Integrated Velocity i_1972
NORTH
11-hr (0)
10-hr (0)
9-hr (0)
8-hr (0)
7-hr (0)
WEST
EAST
6-hr (0)
5-hr (3)
4-hr (9)
3-hr (49)
2-hr (533)
1-hr (5664)
SOUTH
Duration (# of events)
0
200
400
SCALE: # of Events

Number of Events per Direction: Integrated Velocity i_1973

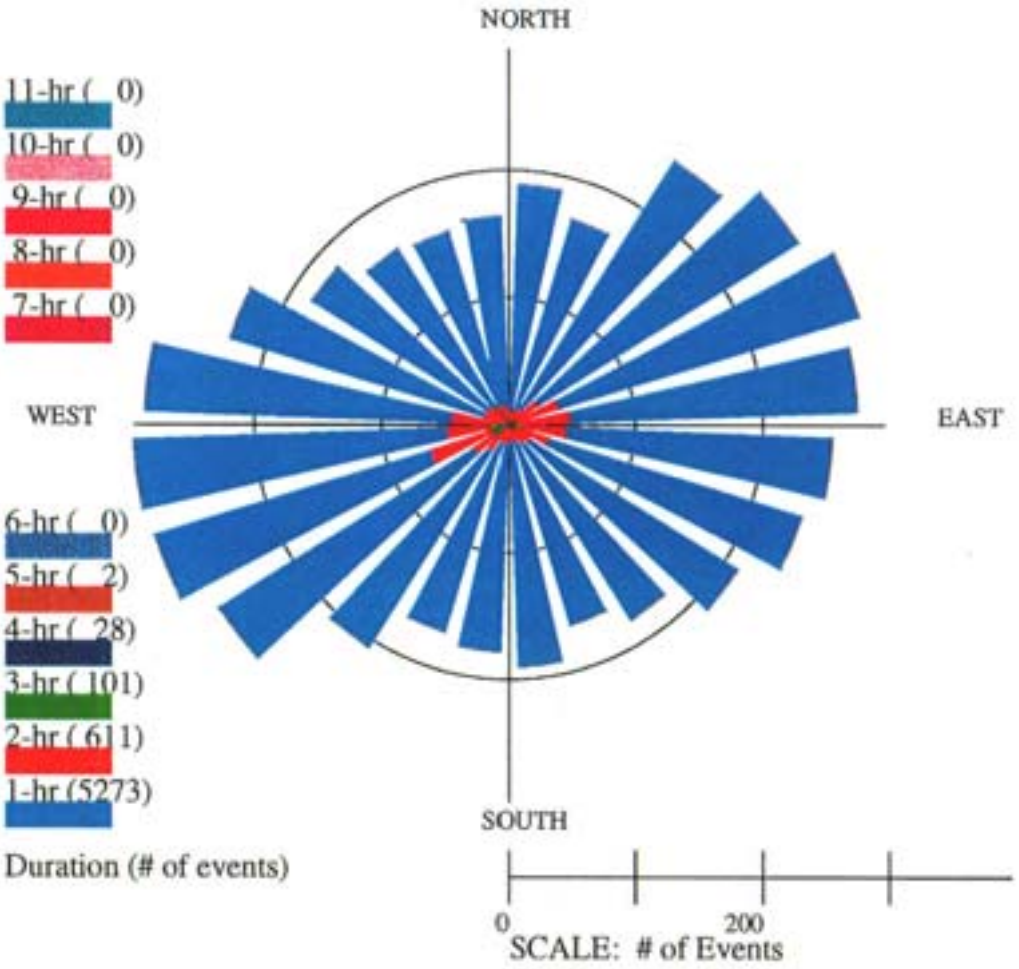

Number of Events per Direction: Integrated Velocity i_1974

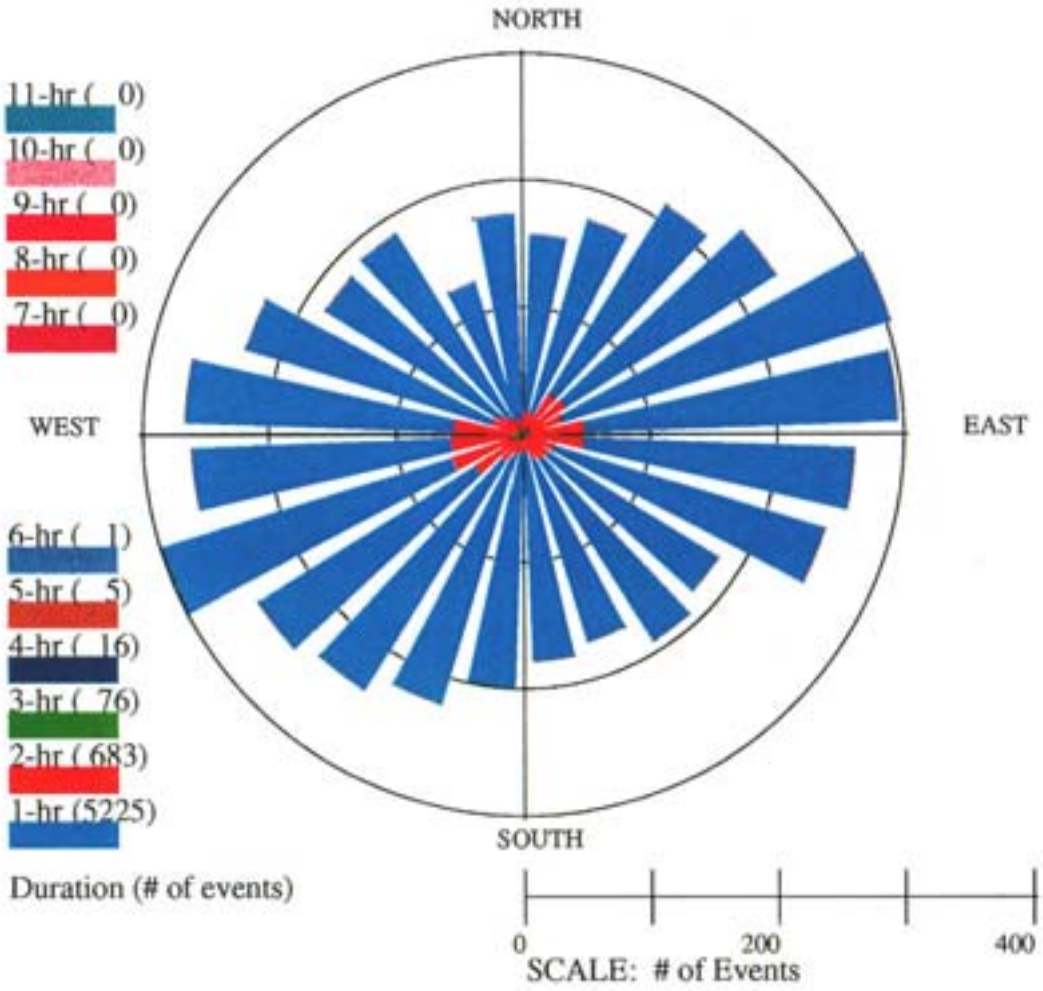

Number of Events per Direction: Integrated Velocity i_1975

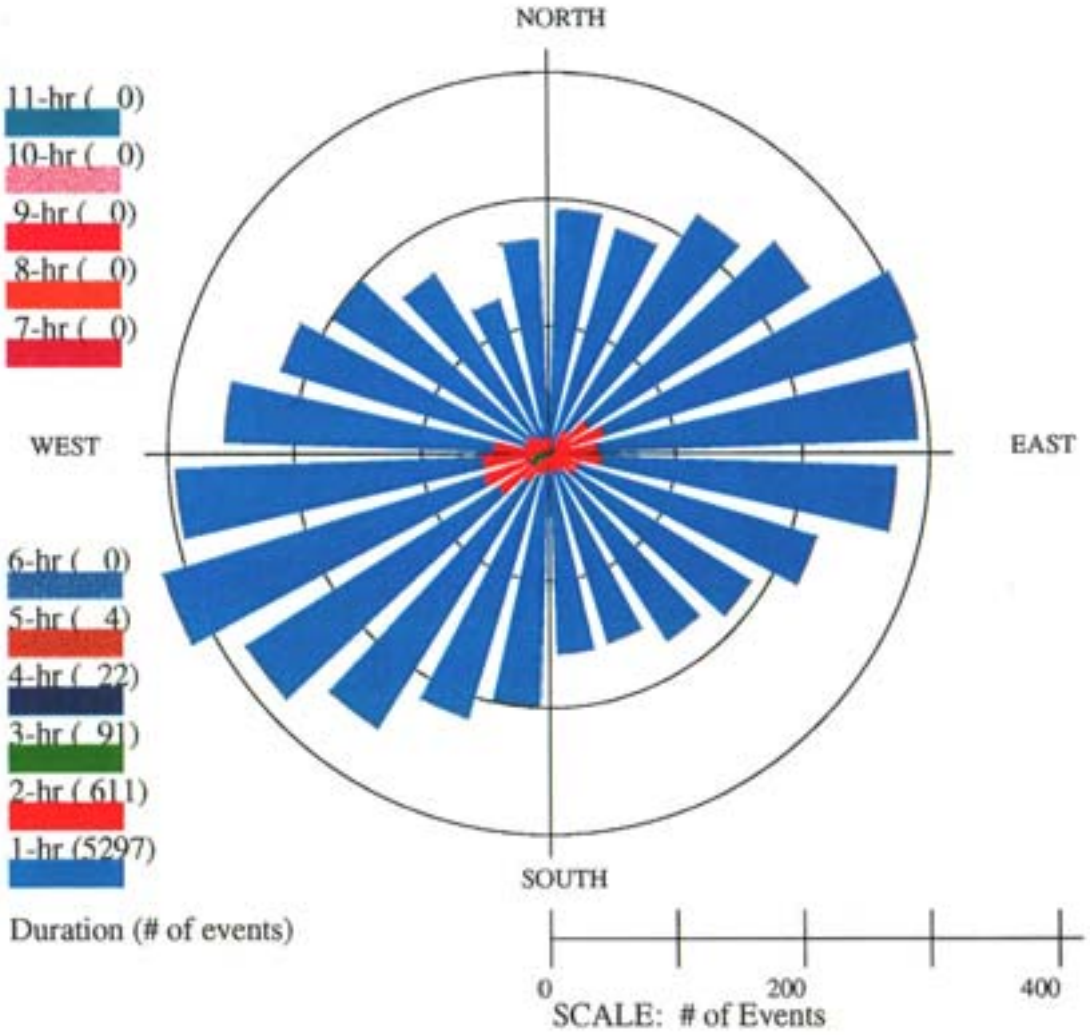

Number of Events per Direction: Integrated Velocity i_1977

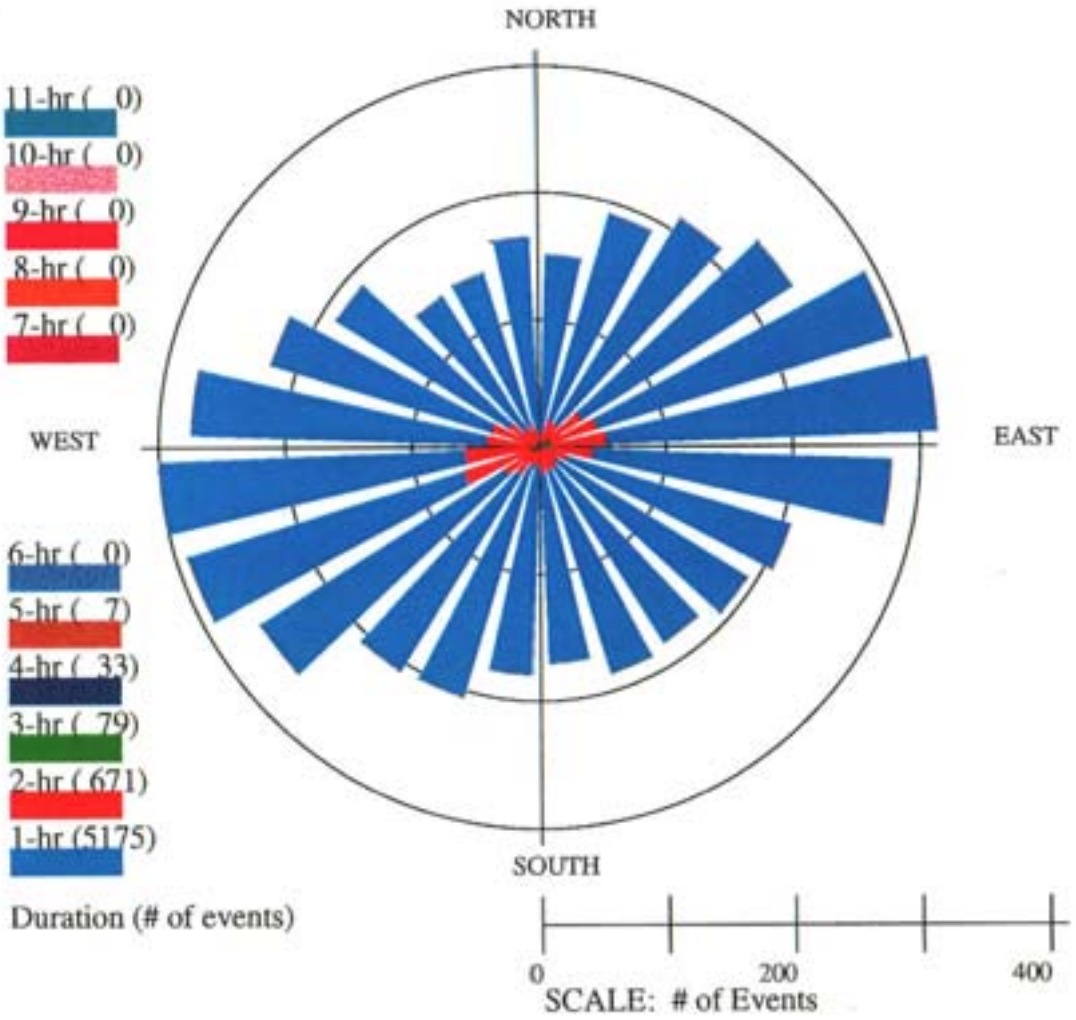

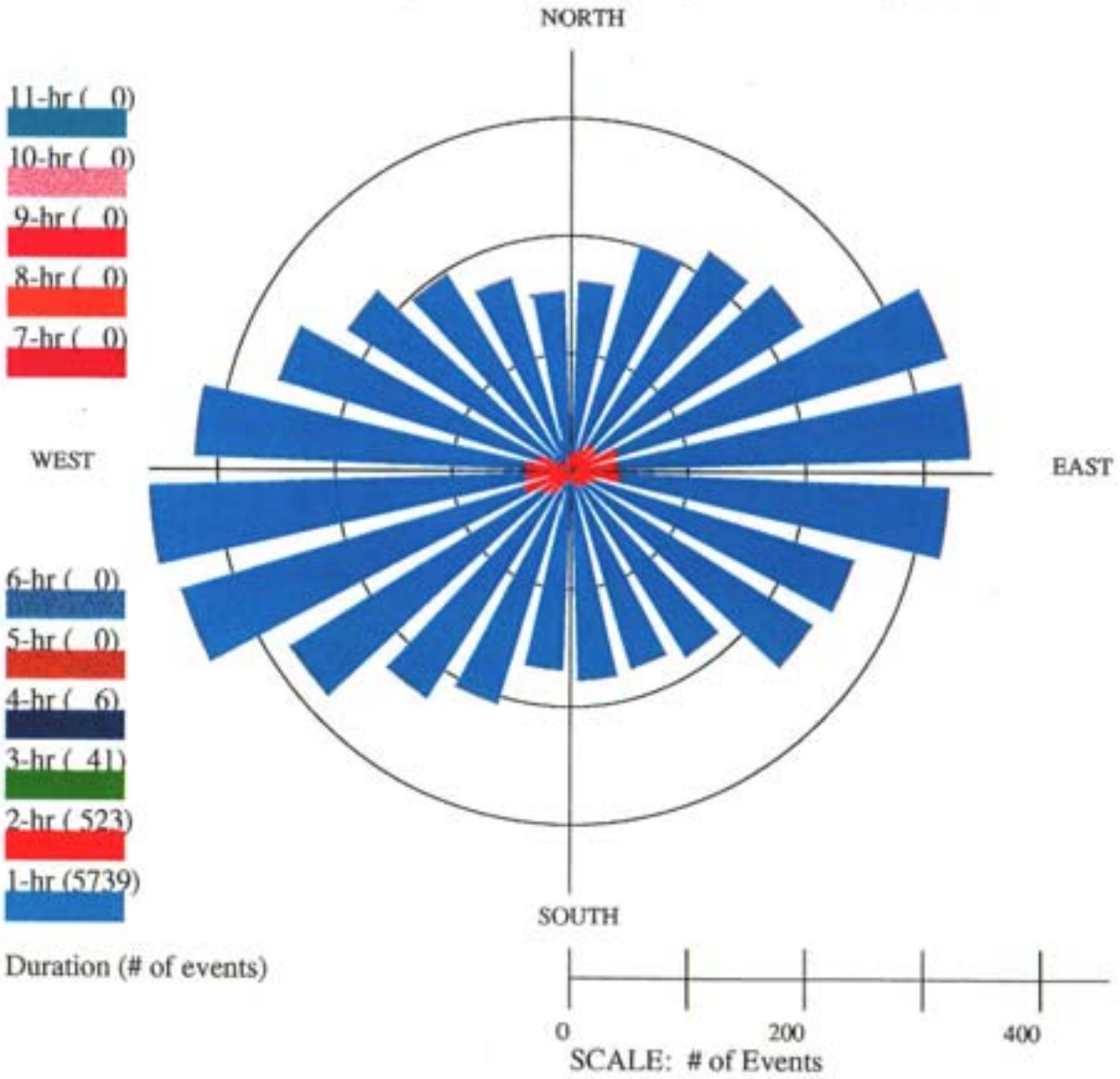
Number of Events per Direction: Integrated Velocity i_1978
NORTH
11-hr (0)
10-hr (0)
9-hr (0)
8-hr (0)
7-hr (0)
WEST
EAST
6-hr (0)
5-hr (0)
4-hr (6)
3-hr (41)
2-hr (523)
1-hr (5739)
Duration (# of events)
SOUTH
0
200
400
SCALE: # of Events

Number of Events per Direction: Integrated Velocity i_1980

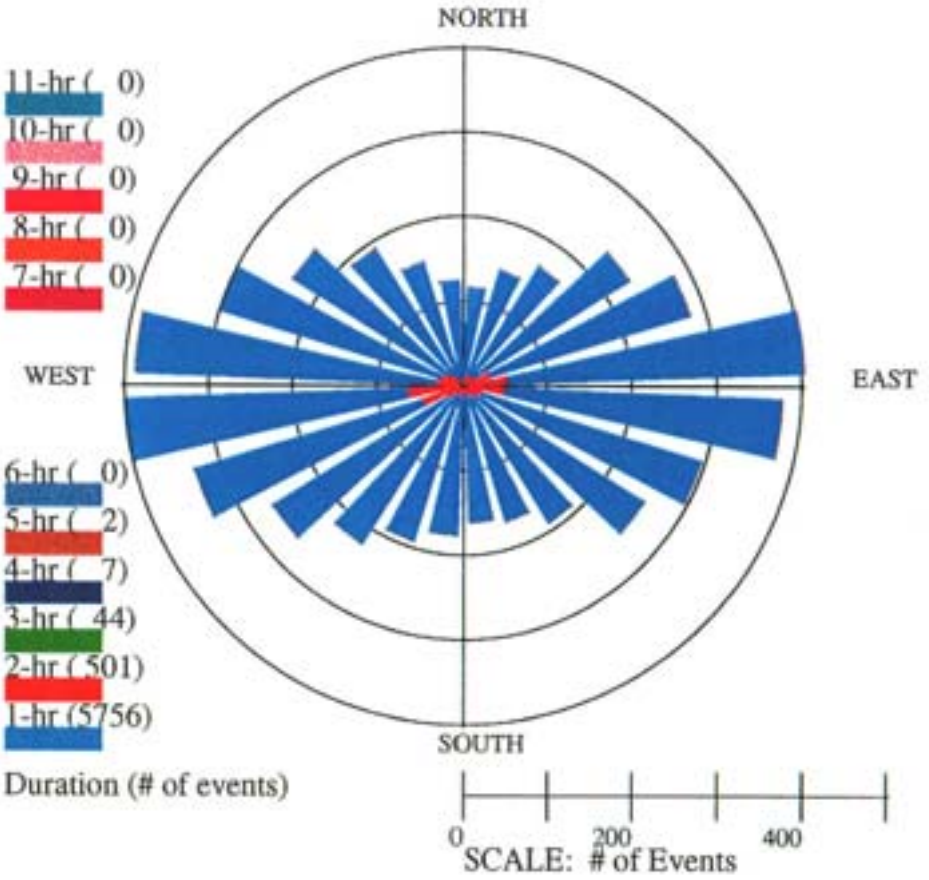

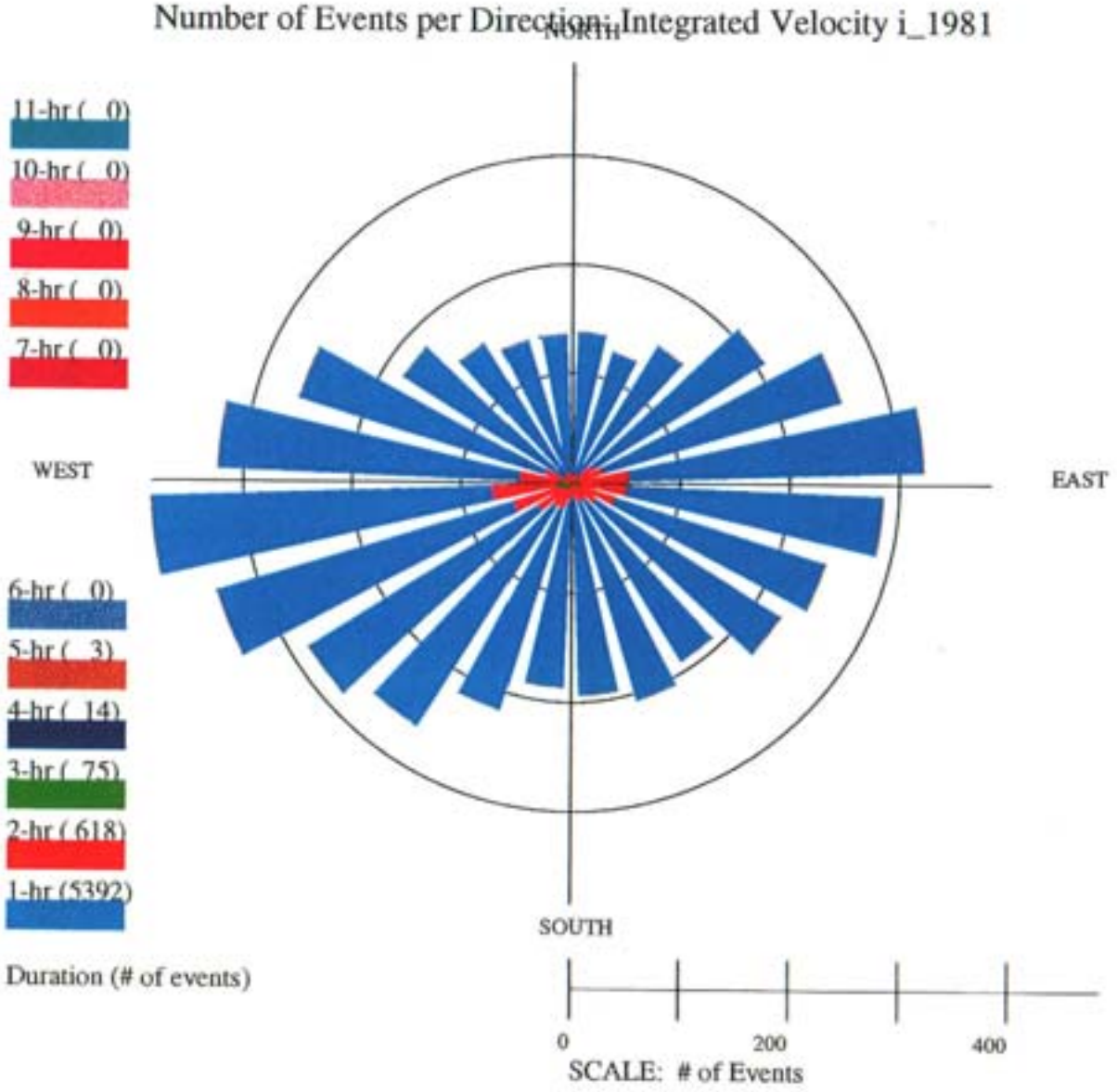
Number of Events per Direction; Integrated Velocity i_1981
NORTH
11-hr (0)
10-hr (0)
9-hr (0)
8-hr (0)
7-hr (0)
WEST
EAST
6-hr (0)
5-hr (3)
4-hr (14)
3-hr (75)
2-hr (618)
1-hr (5392)
SOUTH
Duration (# of events)
0
200
400
SCALE: # of Events

Number of Events per Direction: Integrated Velocity i_1982

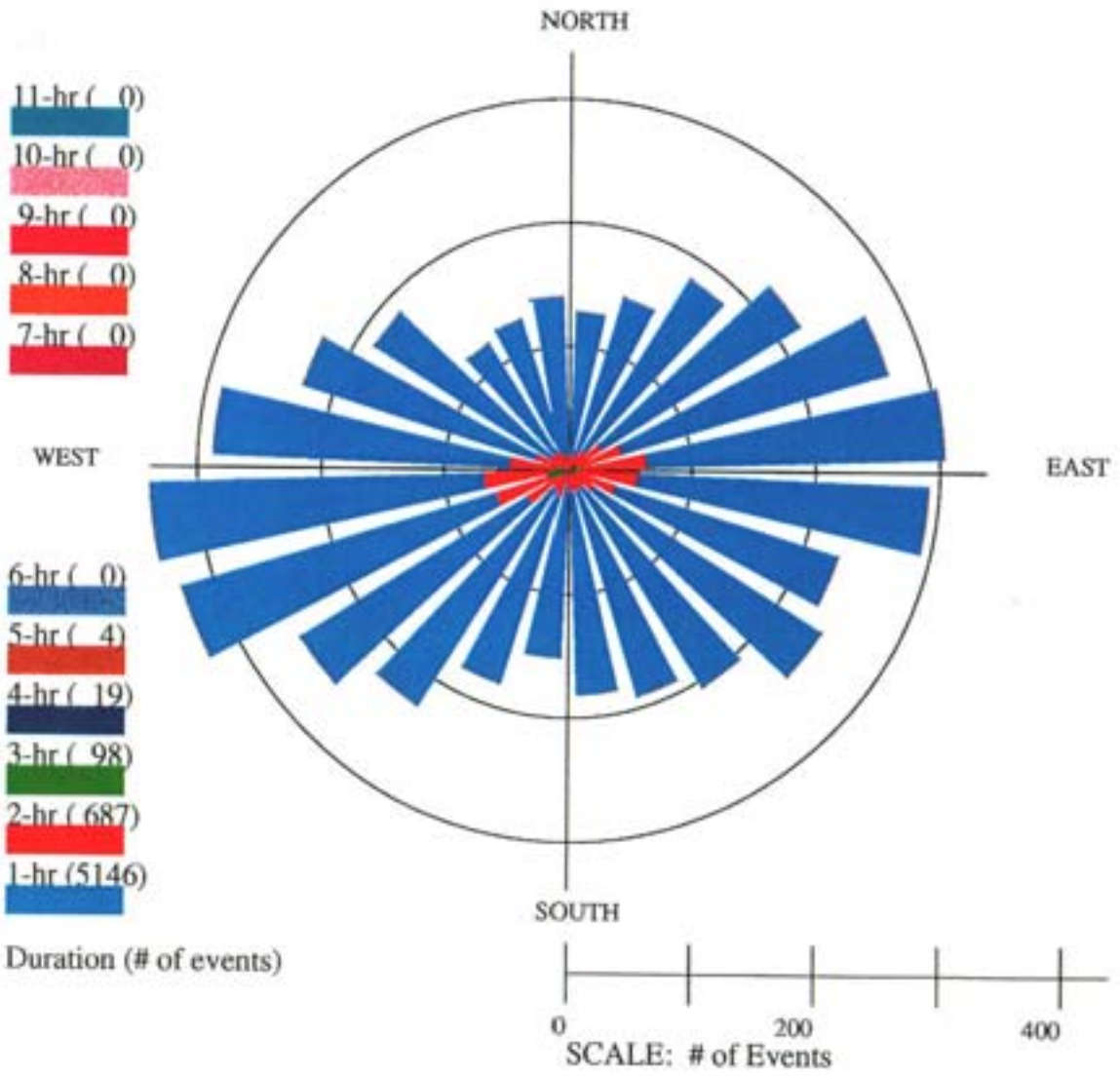

Number of Events per Direction: Integrated Velocity i_1983

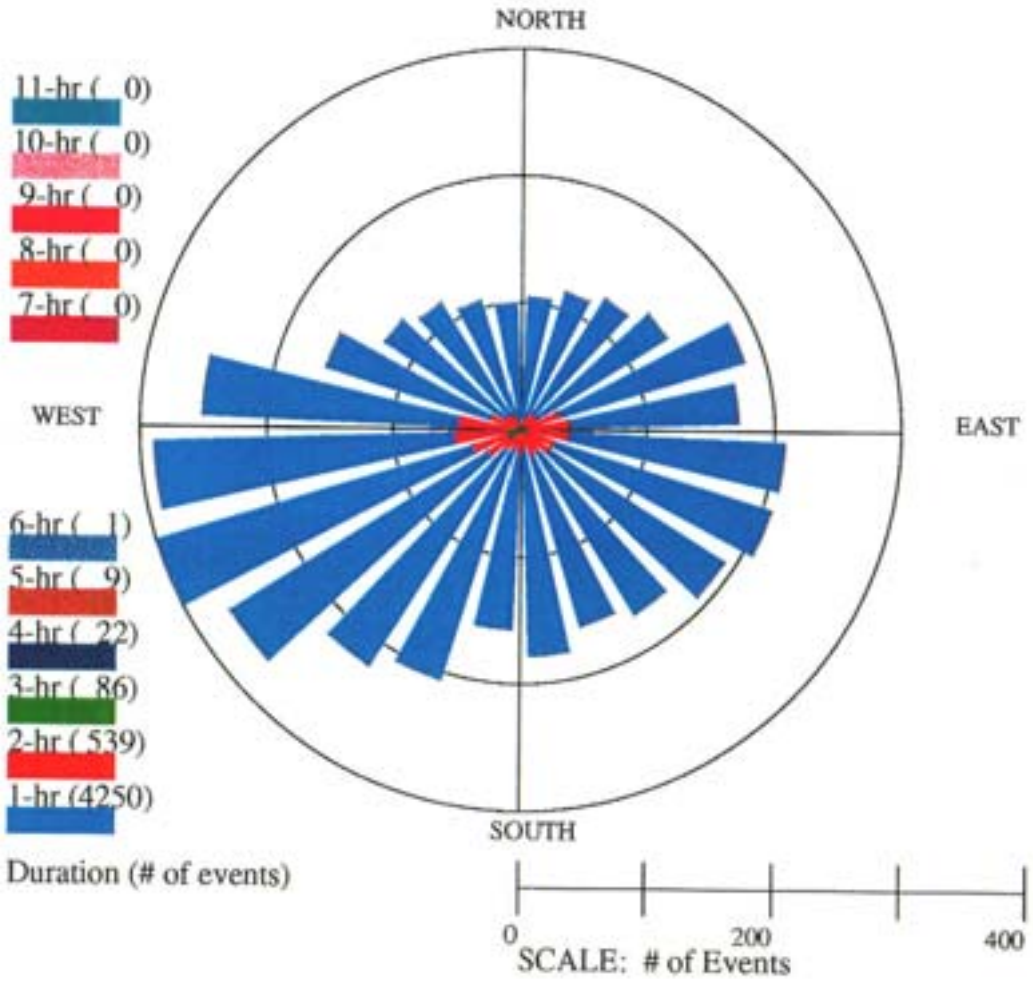

Number of Events per Direction: Integrated Velocity i_1984

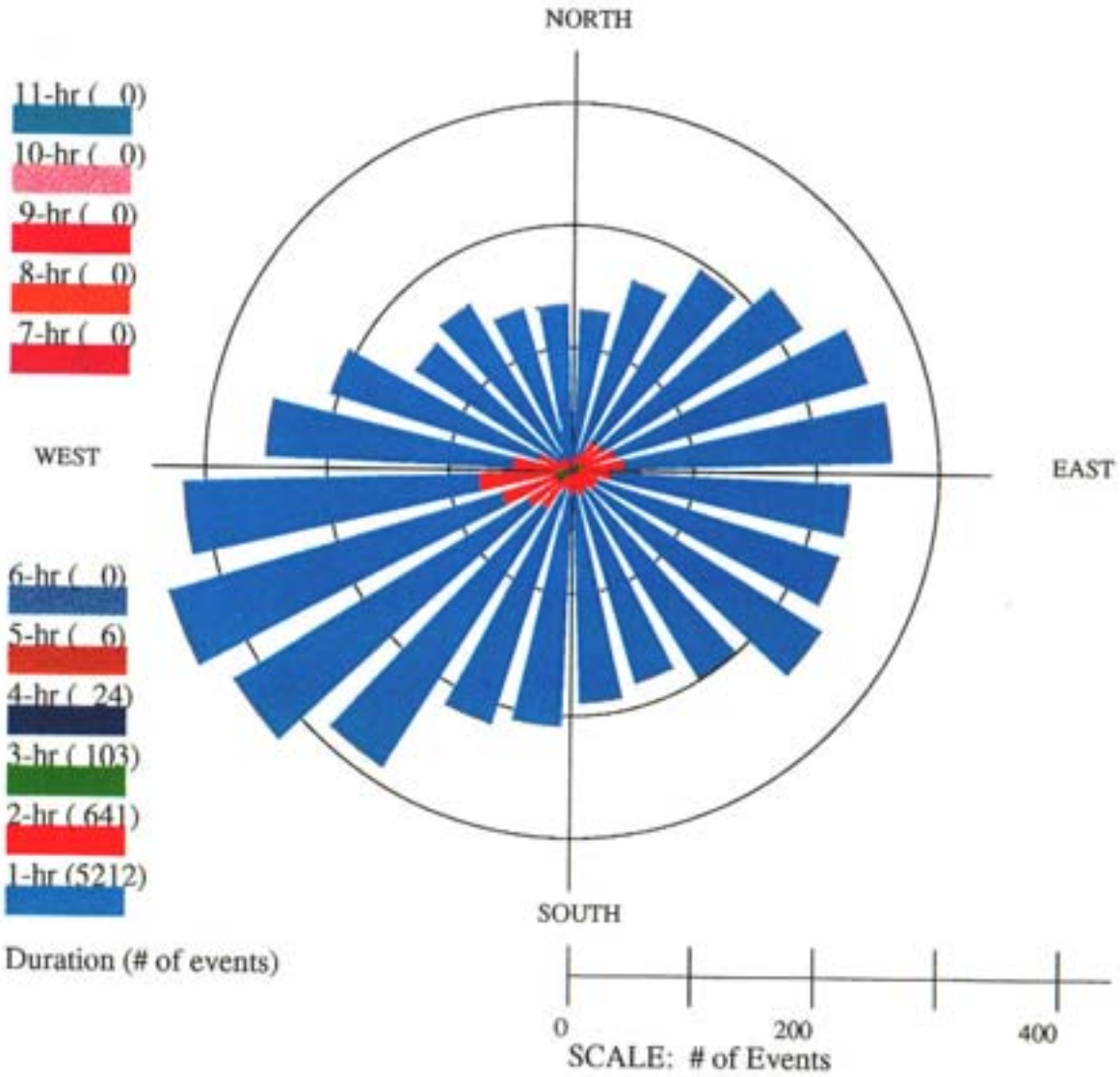

Number of Events per Direction: Integrated Velocity i_1985

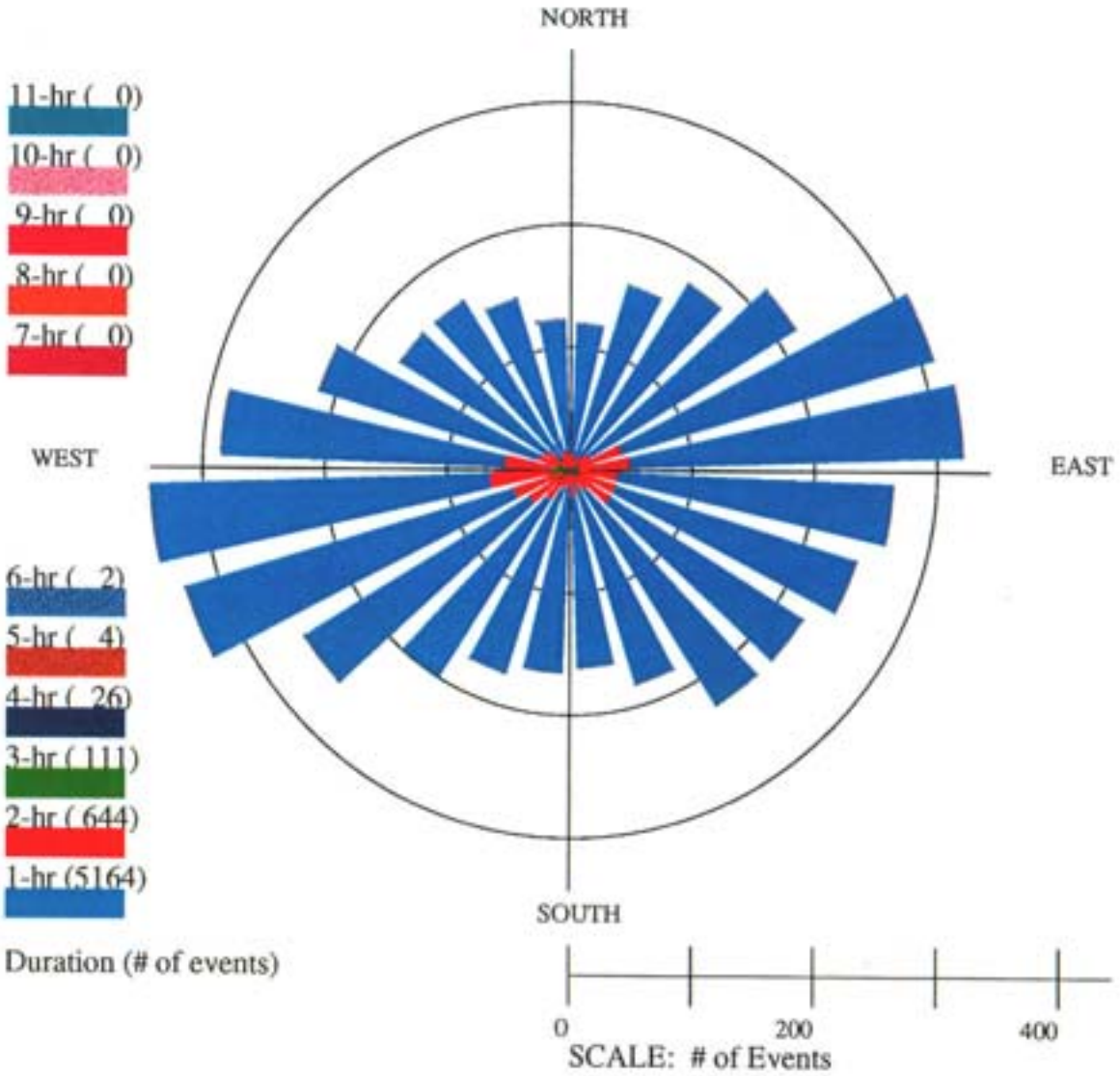

Number of Events per Direction: Integrated Velocity i_1986

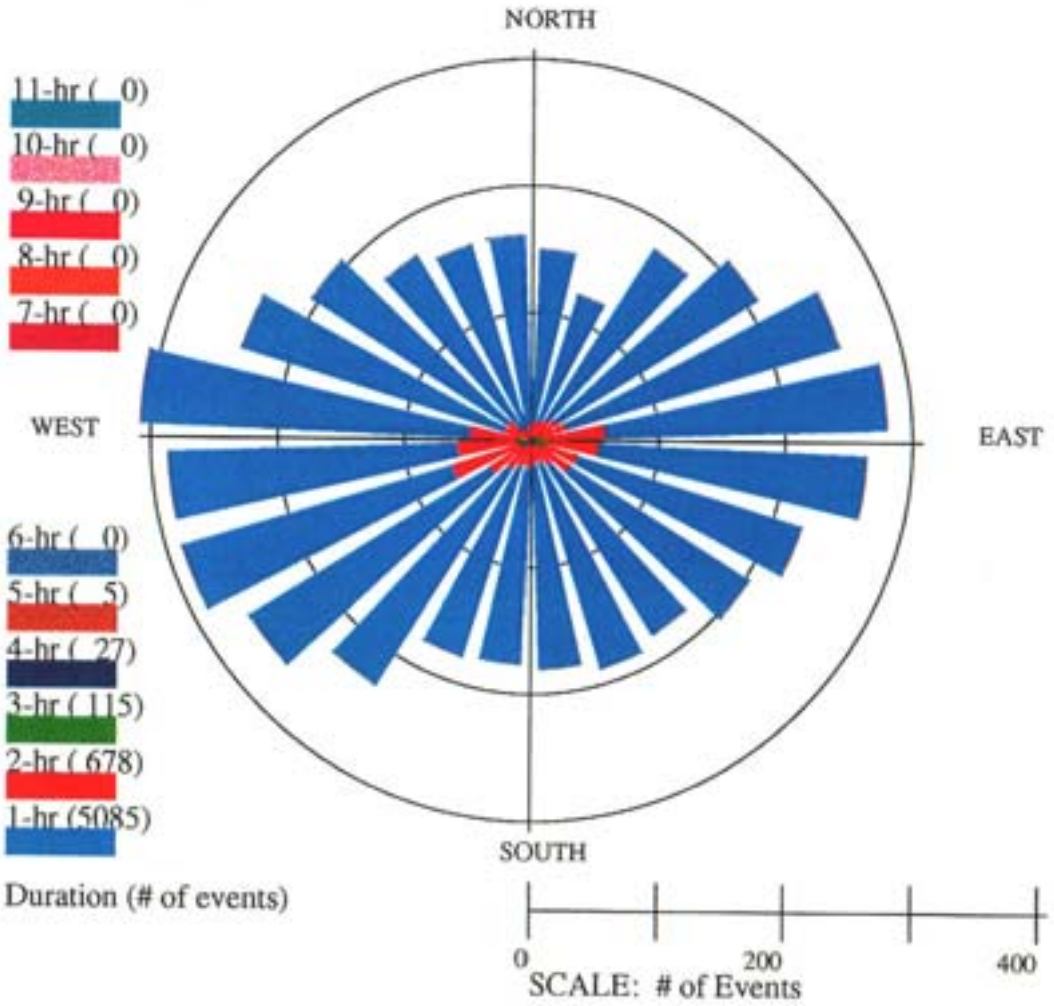

Number of Events per Direction: Integrated Velocity i_1987

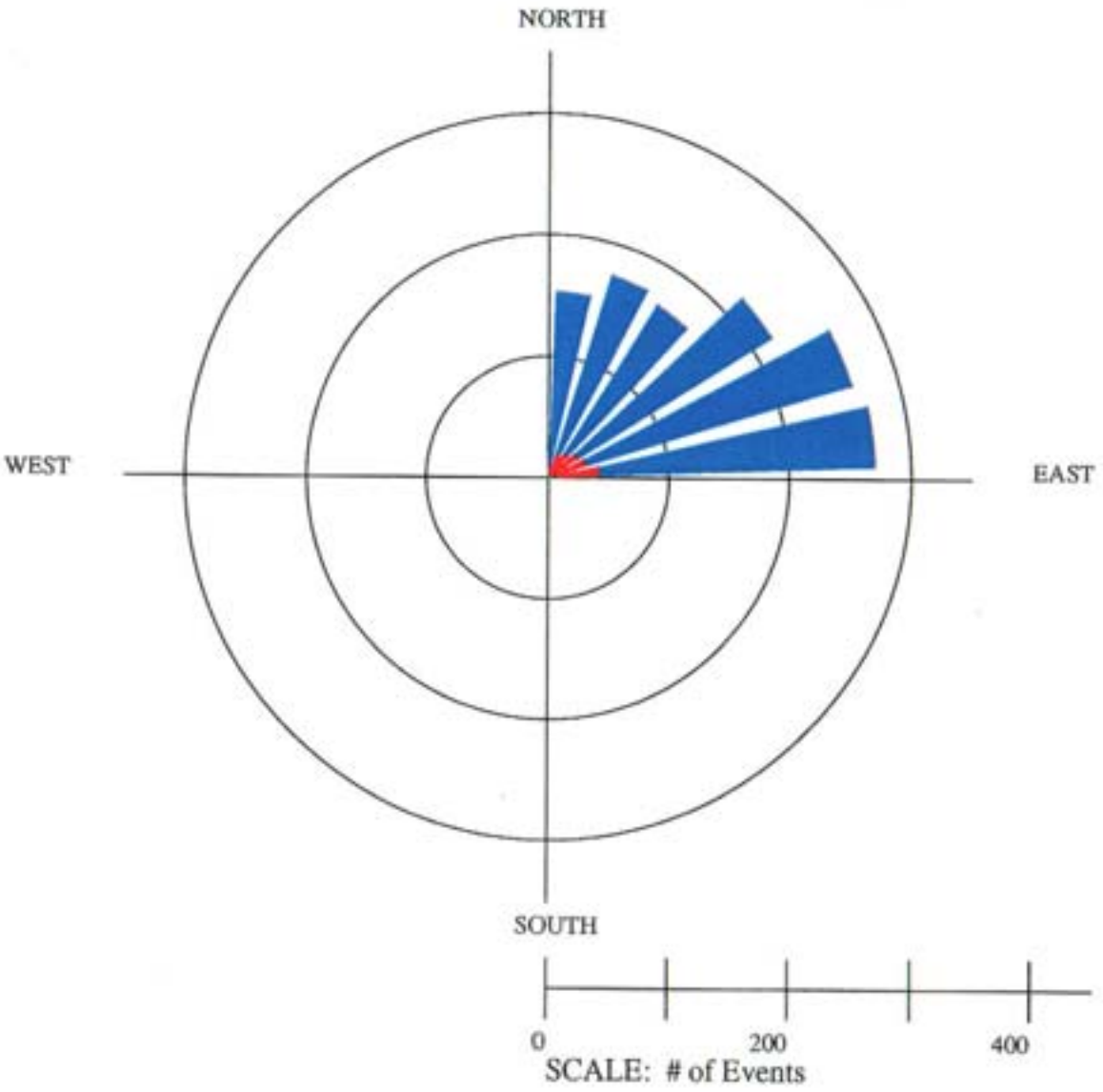

APPENDIX B
The Duration/Direction Plots

The following plots will show the longest durations that have been registered for each one of the years and the seasons. The cumulative data is also represented.

Figure Captions

B.1 Surface Velocity: Duration per Direction for the Year 1971
B.2 Surface Velocity: Duration per Direction for the Year 1972
B.3 Surface Velocity: Duration per Direction for the Year 1973
B.4 Surface Velocity: Duration per Direction for the Year 1974
B.5 Surface Velocity: Duration per Direction for the Year 1975
B.6 Surface Velocity: Duration per Direction for the Year 1977
B.7 Surface Velocity: Duration per Direction for the Year 1978
B.8 Surface Velocity: Duration per Direction for the Year 1980
B.9 Surface Velocity: Duration per Direction for the Year 1981
B.10 Surface Velocity: Duration per Direction for the Year 1982
B.11 Surface Velocity: Duration per Direction for the Year 1983
B.12 Surface Velocity: Duration per Direction for the Year 1984
B.13 Surface Velocity: Duration per Direction for the Year 1985
B.14 Surface Velocity: Duration per Direction for the Year 1986
B.15 Surface Velocity: Duration per Direction for the Year 1987
B.16 Surface Velocity: Duration per Direction for the Year 1988
B.17 Surface Velocity: Duration per Direction for the Year 1989
B.18 Surface Velocity: Duration per Direction for Cumulative Data
B.19 Integrated Velocity: Duration per Direction for the Year 1971
B.20 Integrated Velocity: Duration per Direction for the Year 1972
B.21 Integrated Velocity: Duration per Direction for the Year 1973
B.22 Integrated Velocity: Duration per Direction for the Year 1974
B.23 Integrated Velocity: Duration per Direction for the Year 1975
B.24 Integrated Velocity: Duration per Direction for the Year 1977
B.25 Integrated Velocity: Duration per Direction for the Year 1978
B.26 Integrated Velocity: Duration per Direction for the Year 1979
B.27 Integrated Velocity: Duration per Direction for the Year 1980
B.28 Integrated Velocity: Duration per Direction for the Year 1981
B.29 Integrated Velocity: Duration per Direction for the Year 1982
B.30 Integrated Velocity: Duration per Direction for the Year 1983
B.31 Integrated Velocity: Duration per Direction for the Year 1984
B.32 Integrated Velocity: Duration per Direction for the Year 1985
B.33 Integrated Velocity: Duration per Direction for the Year 1986
B.34 Integrated Velocity: Duration per Direction for the Year 1987
B.35 Integrated Velocity: Duration per Direction for the Year 1988
B.36 Integrated Velocity: Duration per Direction for the Year 1989
B.37 Integrated Velocity: Duration per Direction for Cumulative Data

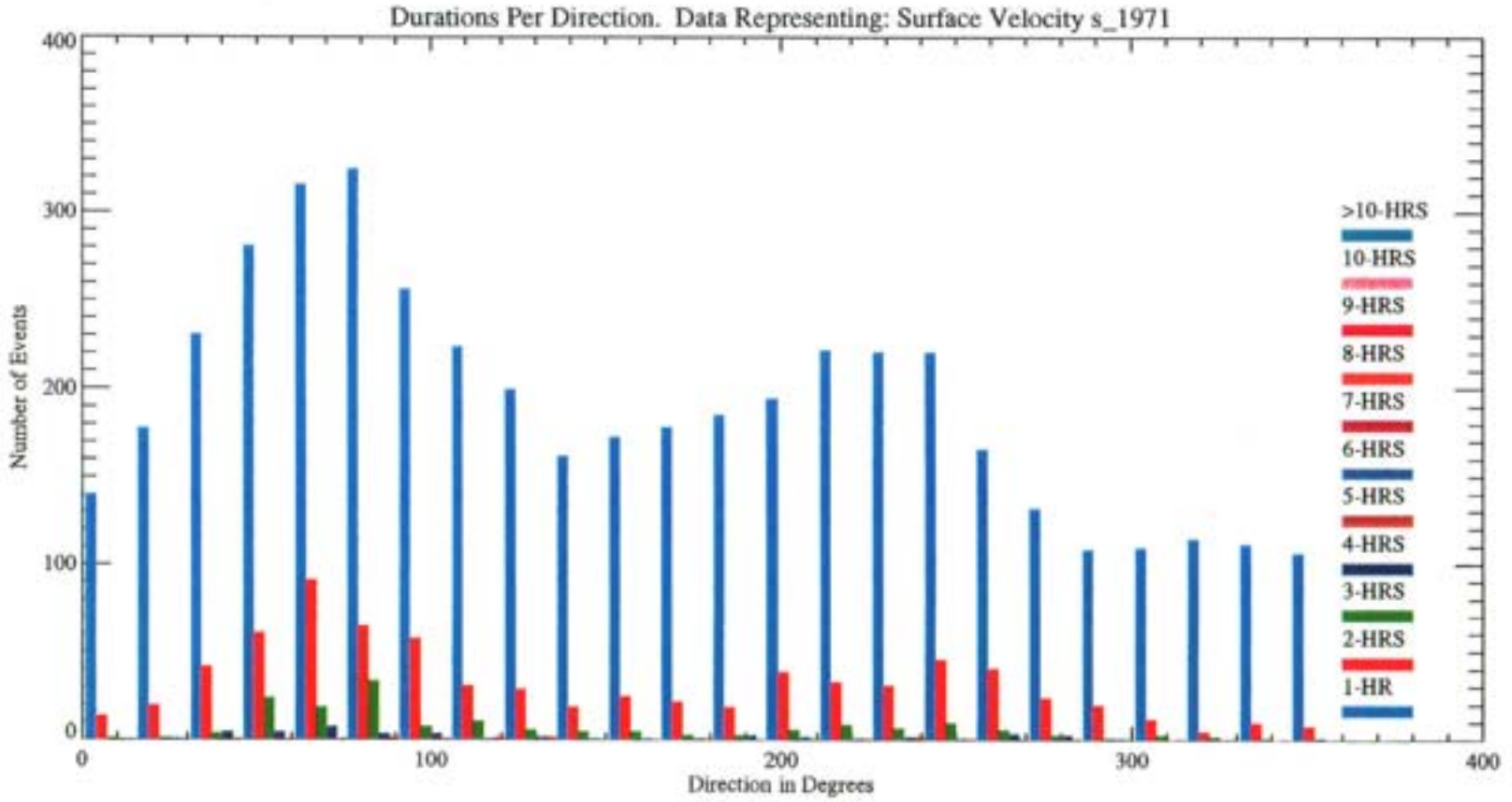
Durations Per Direction. Data Representing: Surface Velocity s_1971
Number of Events
Direction in Degrees
0
100
200
300
400
>10-HRS
10-HRS
9-HRS
8-HRS
7-HRS
6-HRS
5-HRS
4-HRS
3-HRS
2-HRS
1-HR

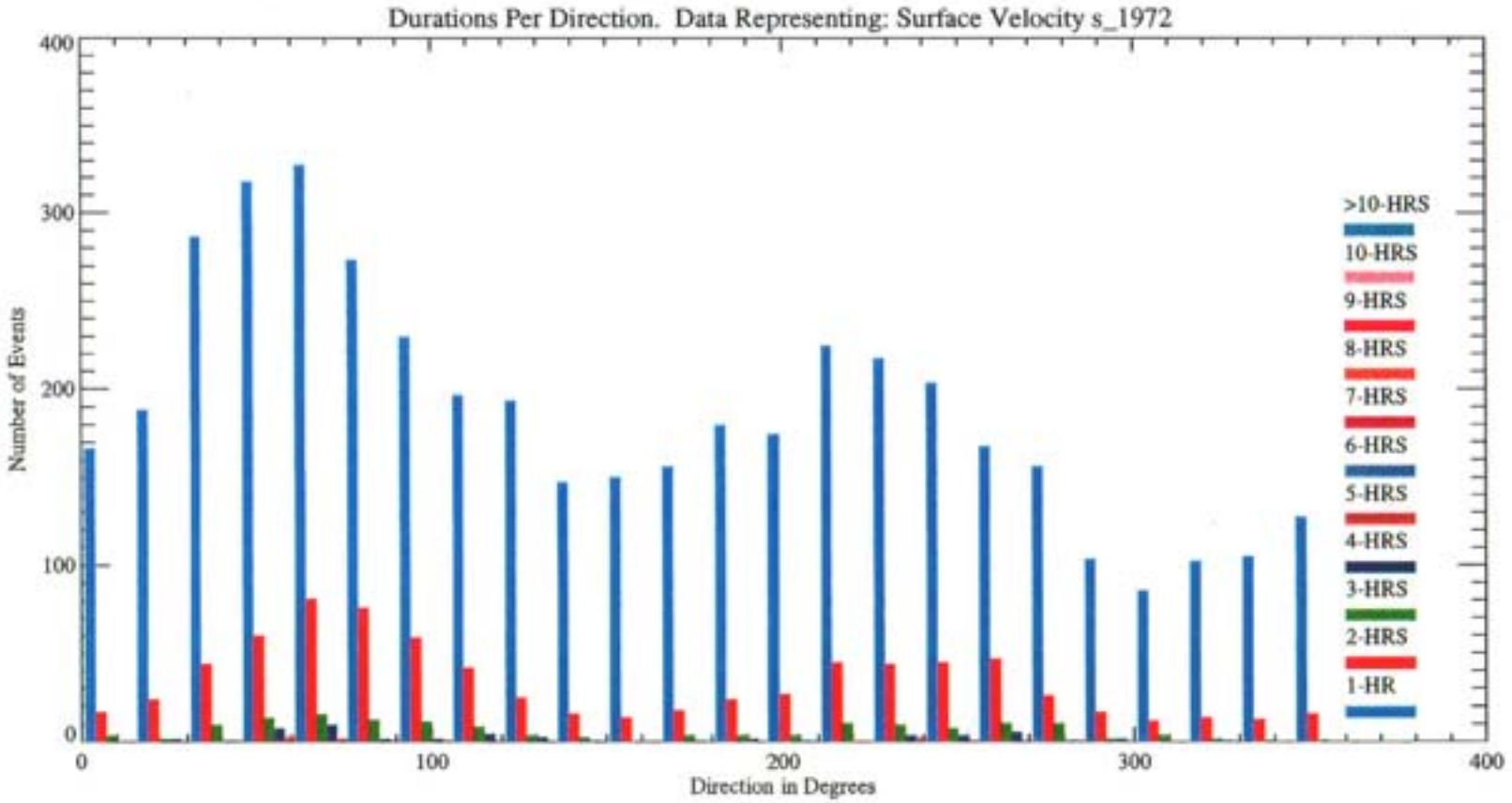
Durations Per Direction. Data Representing: Surface Velocity s_1972
Number of Events
Direction in Degrees
0
100
200
300
400
>10-HRS
10-HRS
9-HRS
8-HRS
7-HRS
6-HRS
5-HRS
4-HRS
3-HRS
2-HRS
1-HR

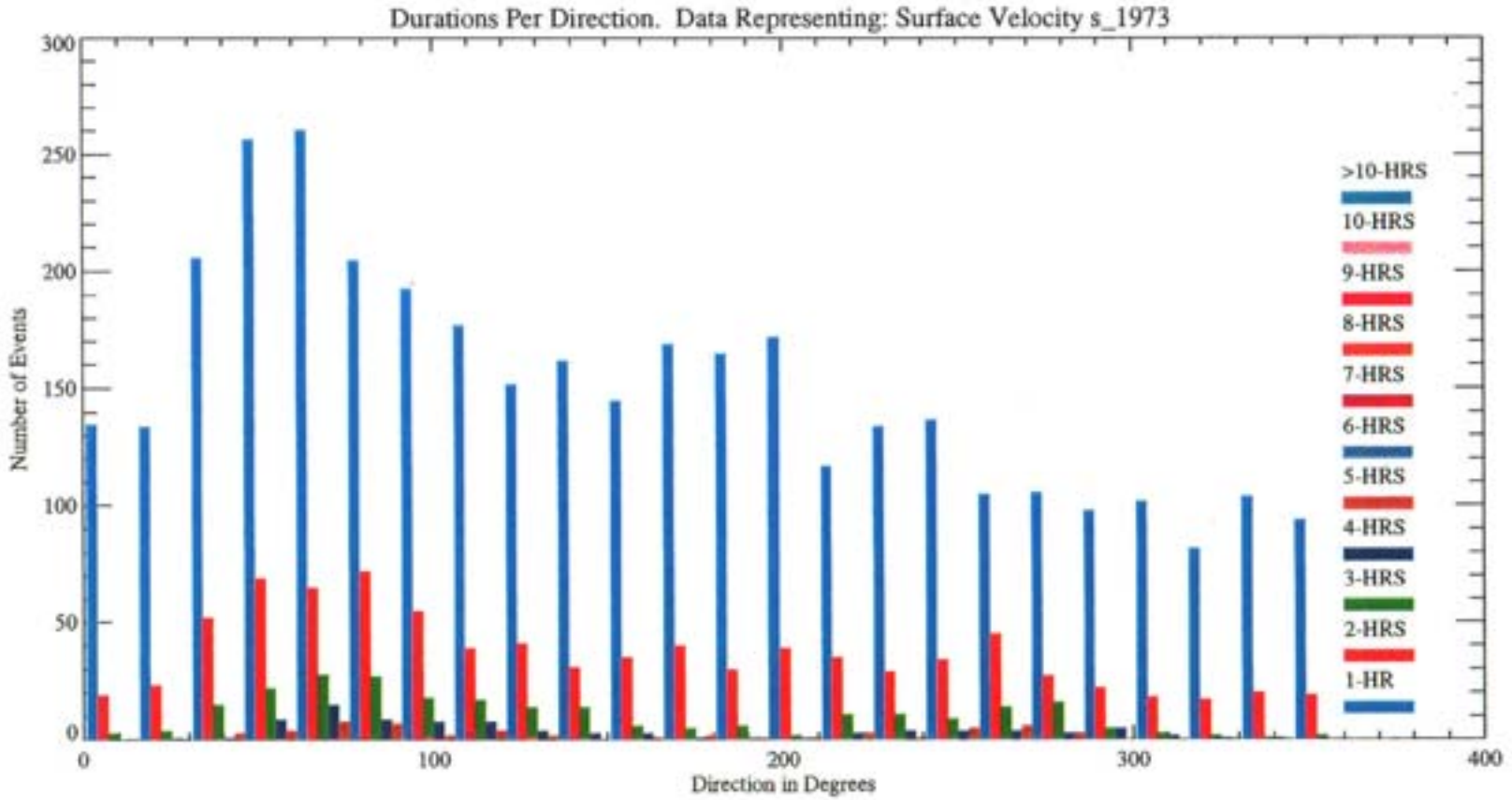
Durations Per Direction. Data Representing: Surface Velocity s_1973
Number of Events
Direction in Degrees
0
50
100
150
200
250
300
0
100
200
300
400
>10-HRS
10-HRS
9-HRS
8-HRS
7-HRS
6-HRS
5-HRS
4-HRS
3-HRS
2-HRS
1-HR

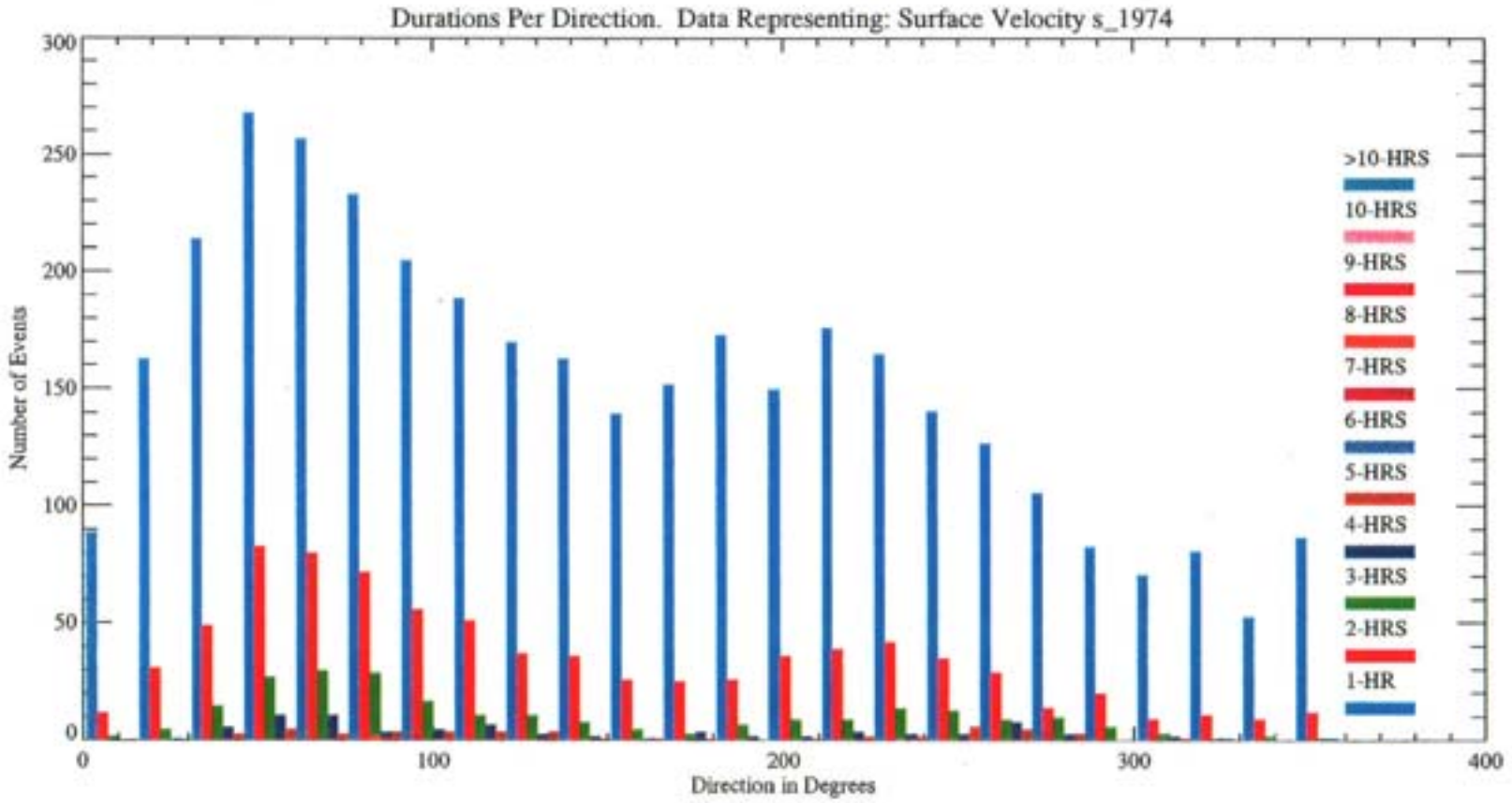
Durations Per Direction. Data Representing: Surface Velocity s_1974
Number of Events
Direction in Degrees
0
50
100
150
200
250
300
0
100
200
300
400
>10-HRS
10-HRS
9-HRS
8-HRS
7-HRS
6-HRS
5-HRS
4-HRS
3-HRS
2-HRS
1-HR

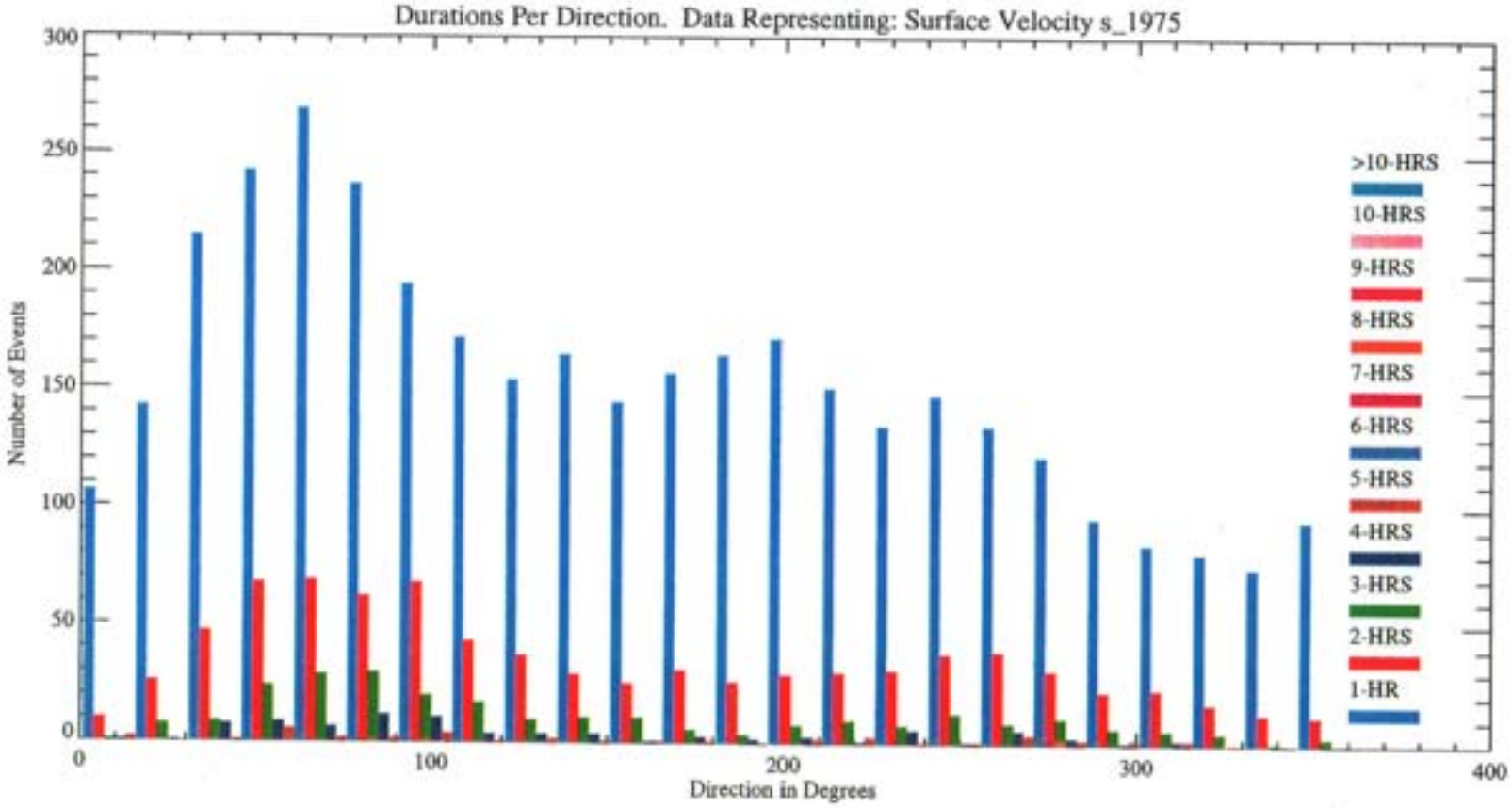
Durations Per Direction. Data Representing: Surface Velocity s_1975
Number of Events
Direction in Degrees
0
50
100
150
200
250
300
0
100
200
300
400
>10-HRS
10-HRS
9-HRS
8-HRS
7-HRS
6-HRS
5-HRS
4-HRS
3-HRS
2-HRS
1-HR

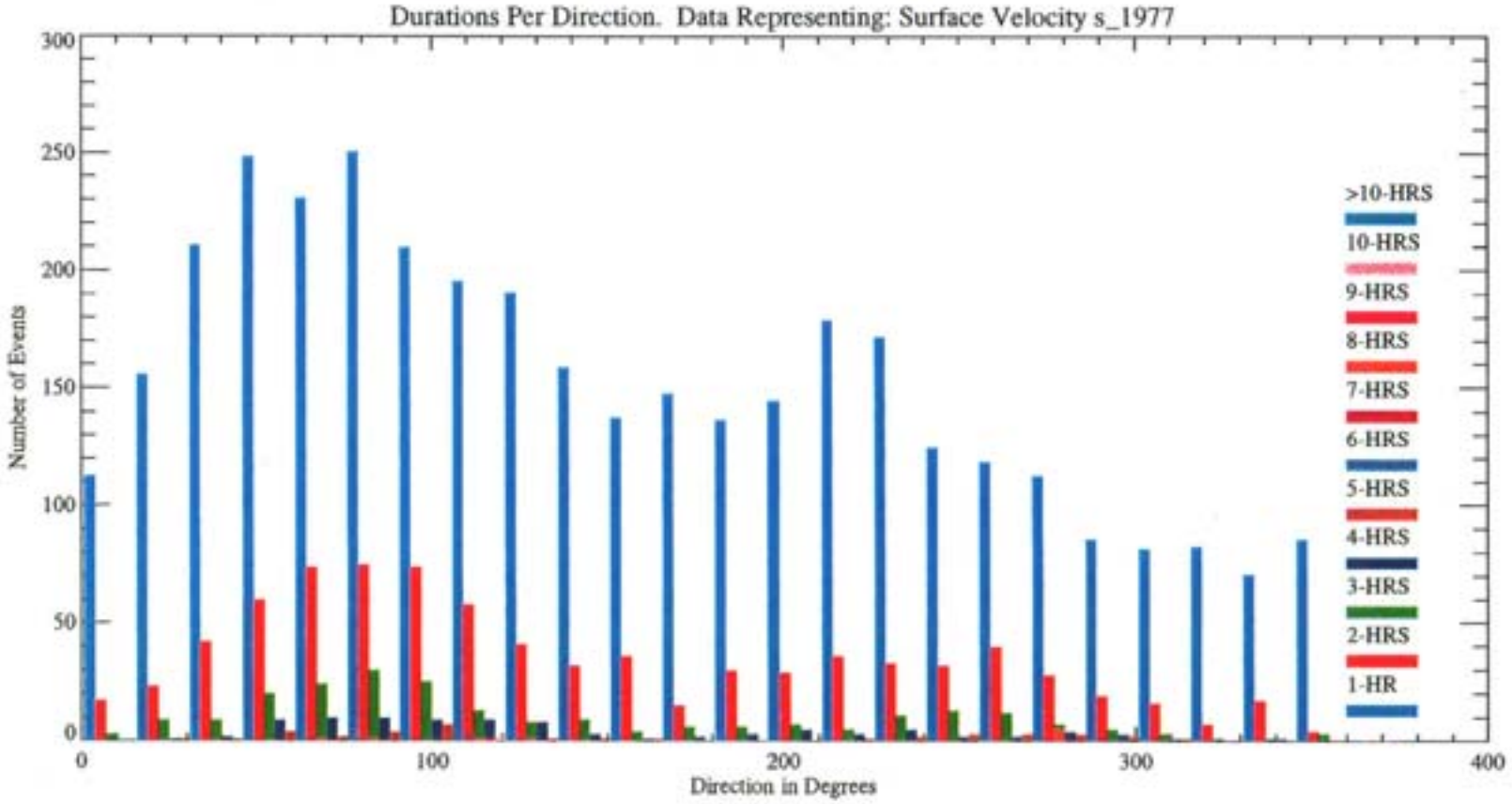
Durations Per Direction. Data Representing: Surface Velocity s_1977
Number of Events
Direction in Degrees
0
50
100
150
200
250
300
0
100
200
300
400
>10-HRS
10-HRS
9-HRS
8-HRS
7-HRS
6-HRS
5-HRS
4-HRS
3-HRS
2-HRS
1-HR

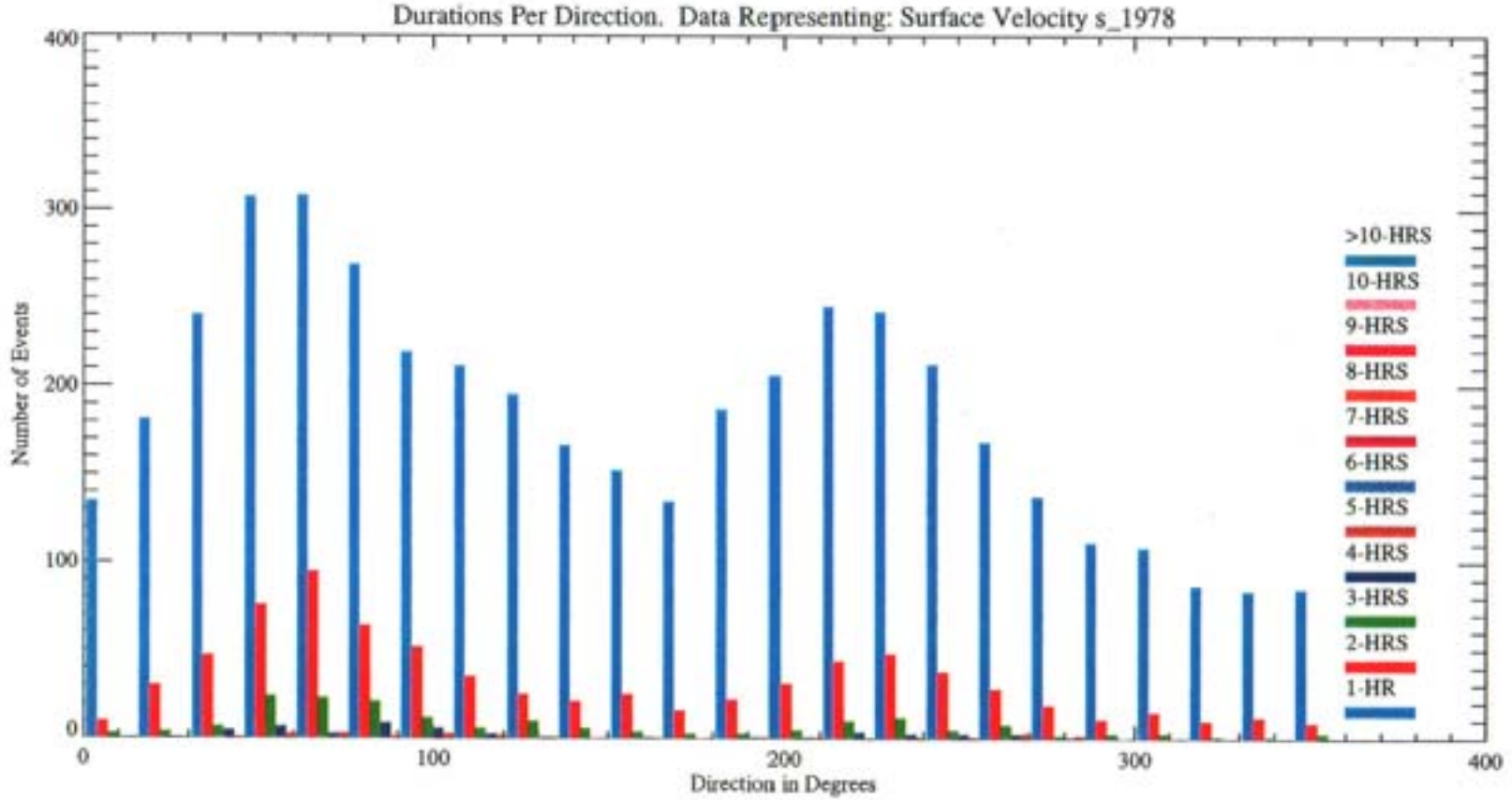
Durations Per Direction. Data Representing: Surface Velocity s_1978
Number of Events
Direction in Degrees
0
100
200
300
400
>10-HRS
10-HRS
9-HRS
8-HRS
7-HRS
6-HRS
5-HRS
4-HRS
3-HRS
2-HRS
1-HR

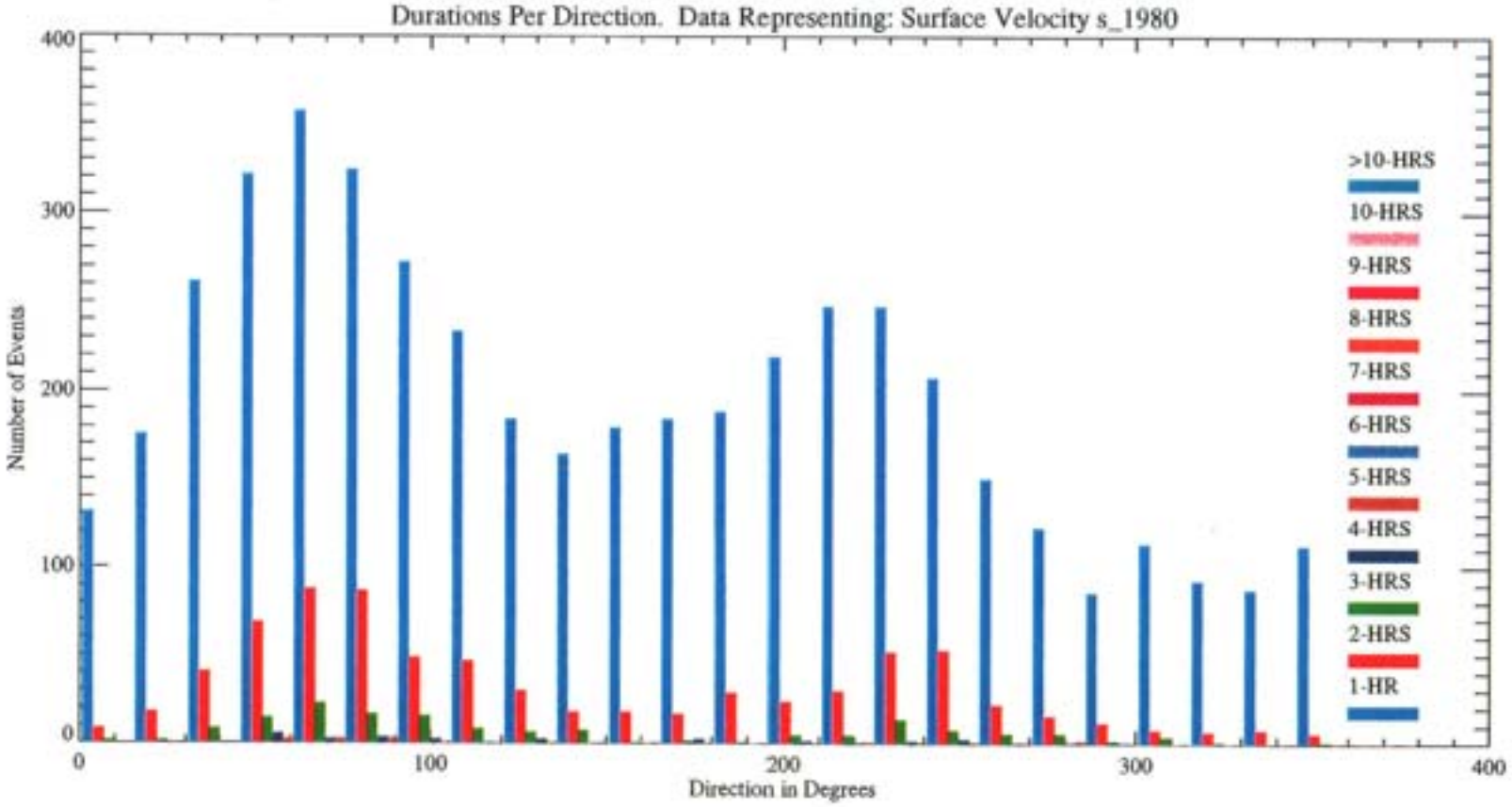
Durations Per Direction. Data Representing: Surface Velocity s_1980
Number of Events
Direction in Degrees
0
100
200
300
400
>10-HRS
10-HRS
9-HRS
8-HRS
7-HRS
6-HRS
5-HRS
4-HRS
3-HRS
2-HRS
1-HR

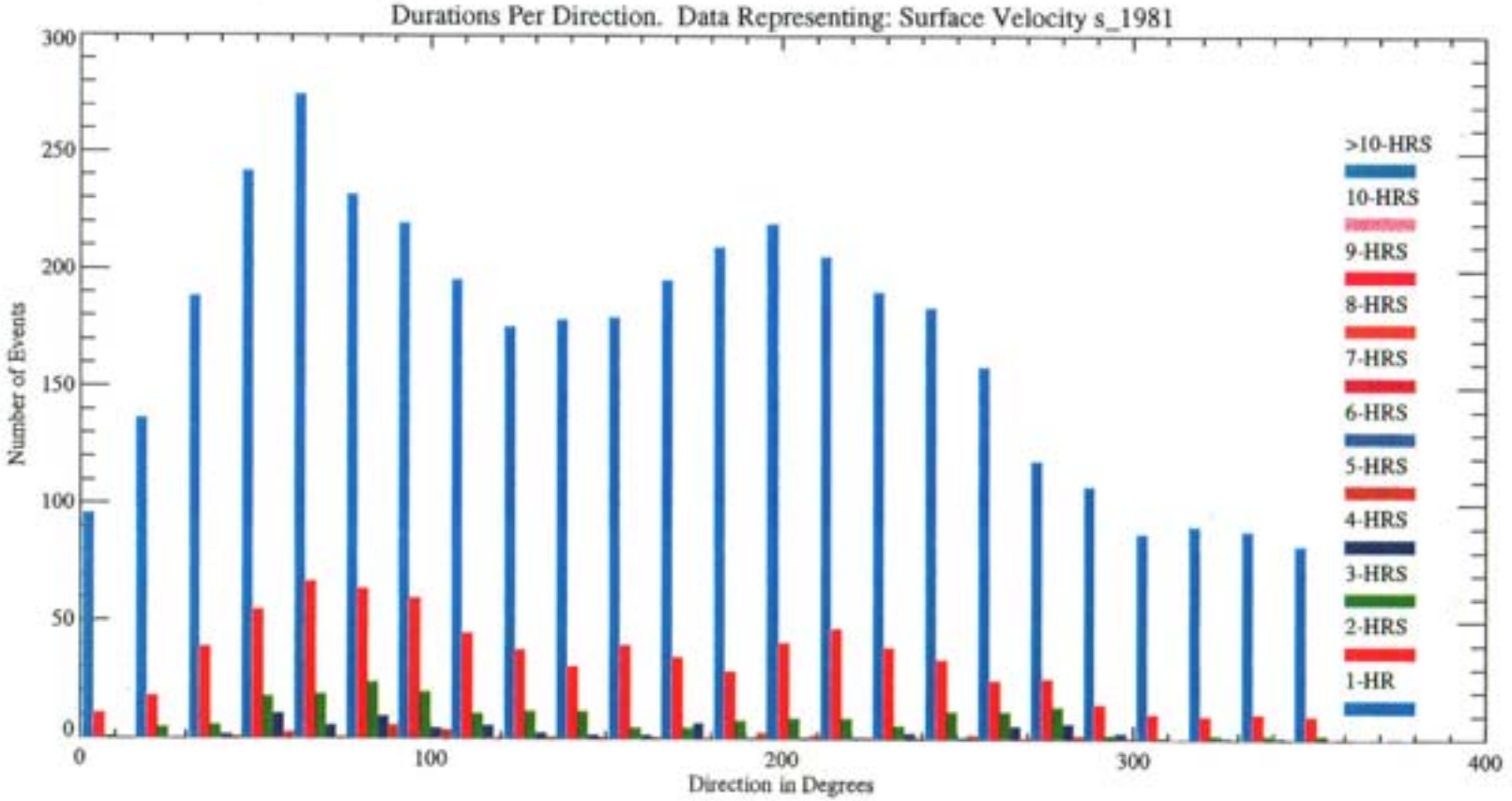
Durations Per Direction. Data Representing: Surface Velocity s_1981
Number of Events
Direction in Degrees
0
50
100
150
200
250
300
0
100
200
300
400
>10-HRS
10-HRS
9-HRS
8-HRS
7-HRS
6-HRS
5-HRS
4-HRS
3-HRS
2-HRS
1-HR

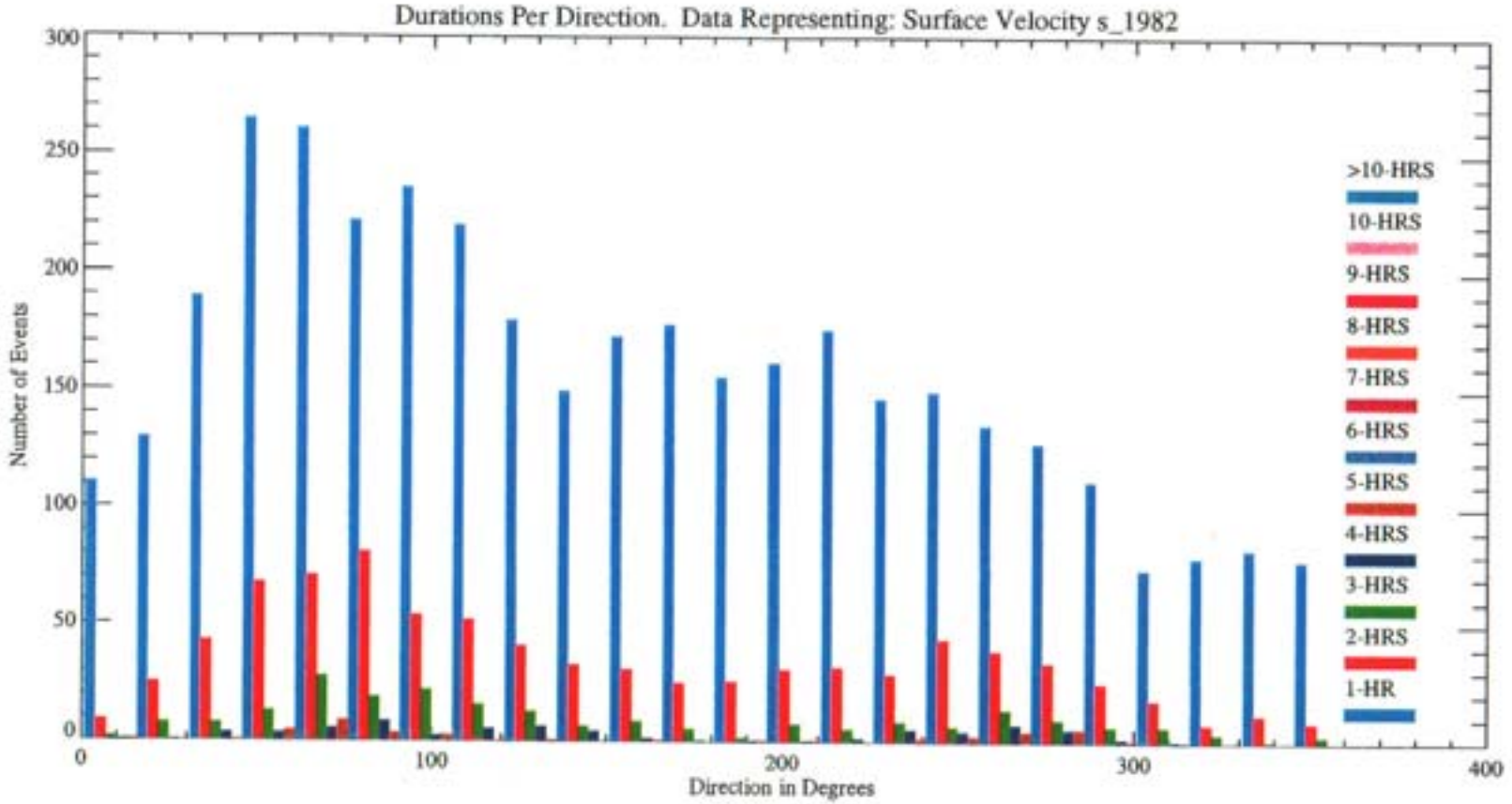
Durations Per Direction. Data Representing: Surface Velocity s_1982
Number of Events
Direction in Degrees
0
50
100
150
200
250
300
0
100
200
300
400
>10-HRS
10-HRS
9-HRS
8-HRS
7-HRS
6-HRS
5-HRS
4-HRS
3-HRS
2-HRS
1-HR

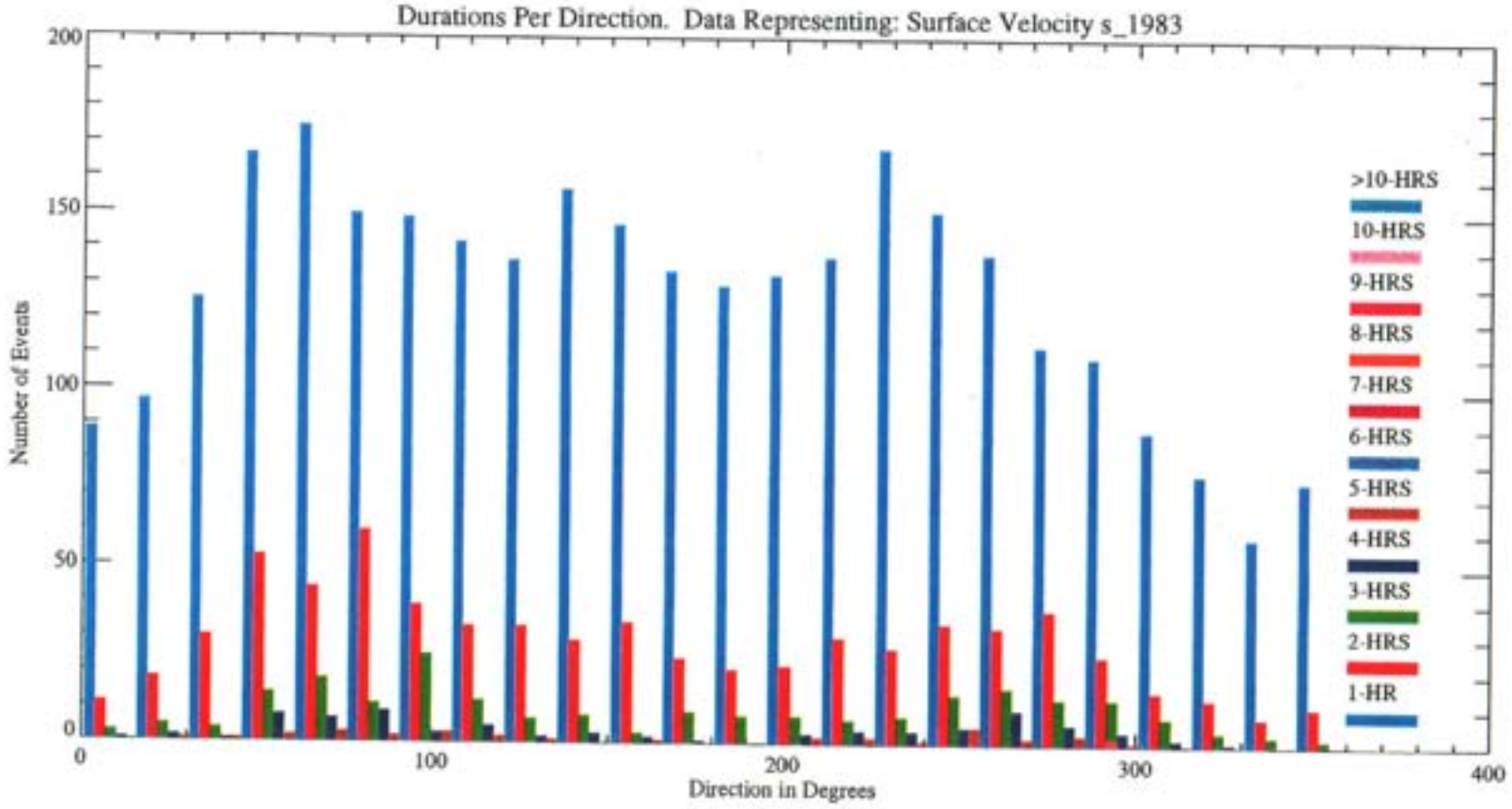
Durations Per Direction. Data Representing: Surface Velocity s_1983
Number of Events
Direction in Degrees
0
50
100
150
200
0
100
200
300
400
>10-HRS
10-HRS
9-HRS
8-HRS
7-HRS
6-HRS
5-HRS
4-HRS
3-HRS
2-HRS
1-HR

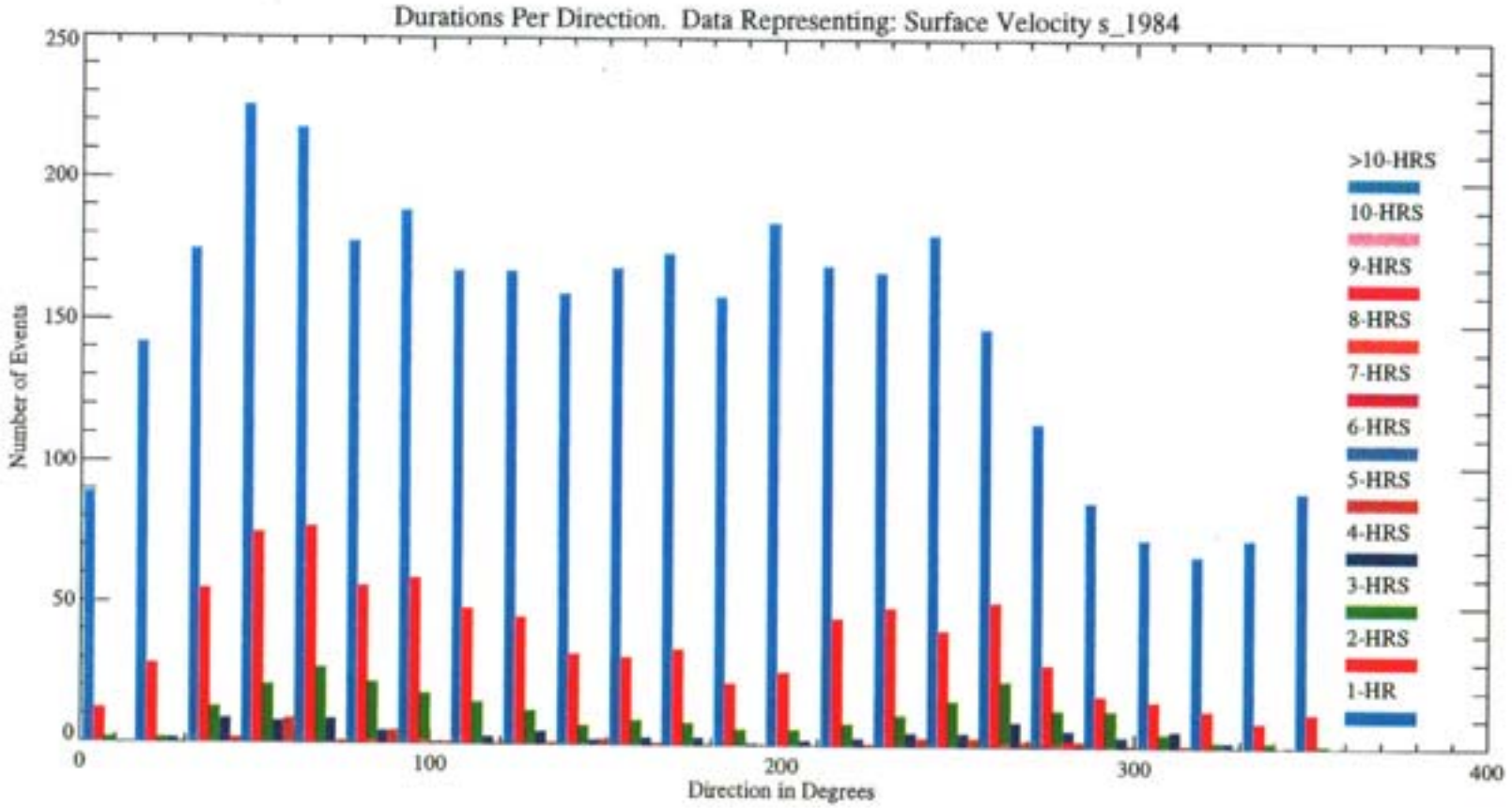
Durations Per Direction. Data Representing: Surface Velocity s_1984
Number of Events
Direction in Degrees
0
50
100
150
200
250
0
100
200
300
400
>10-HRS
10-HRS
9-HRS
8-HRS
7-HRS
6-HRS
5-HRS
4-HRS
3-HRS
2-HRS
1-HR

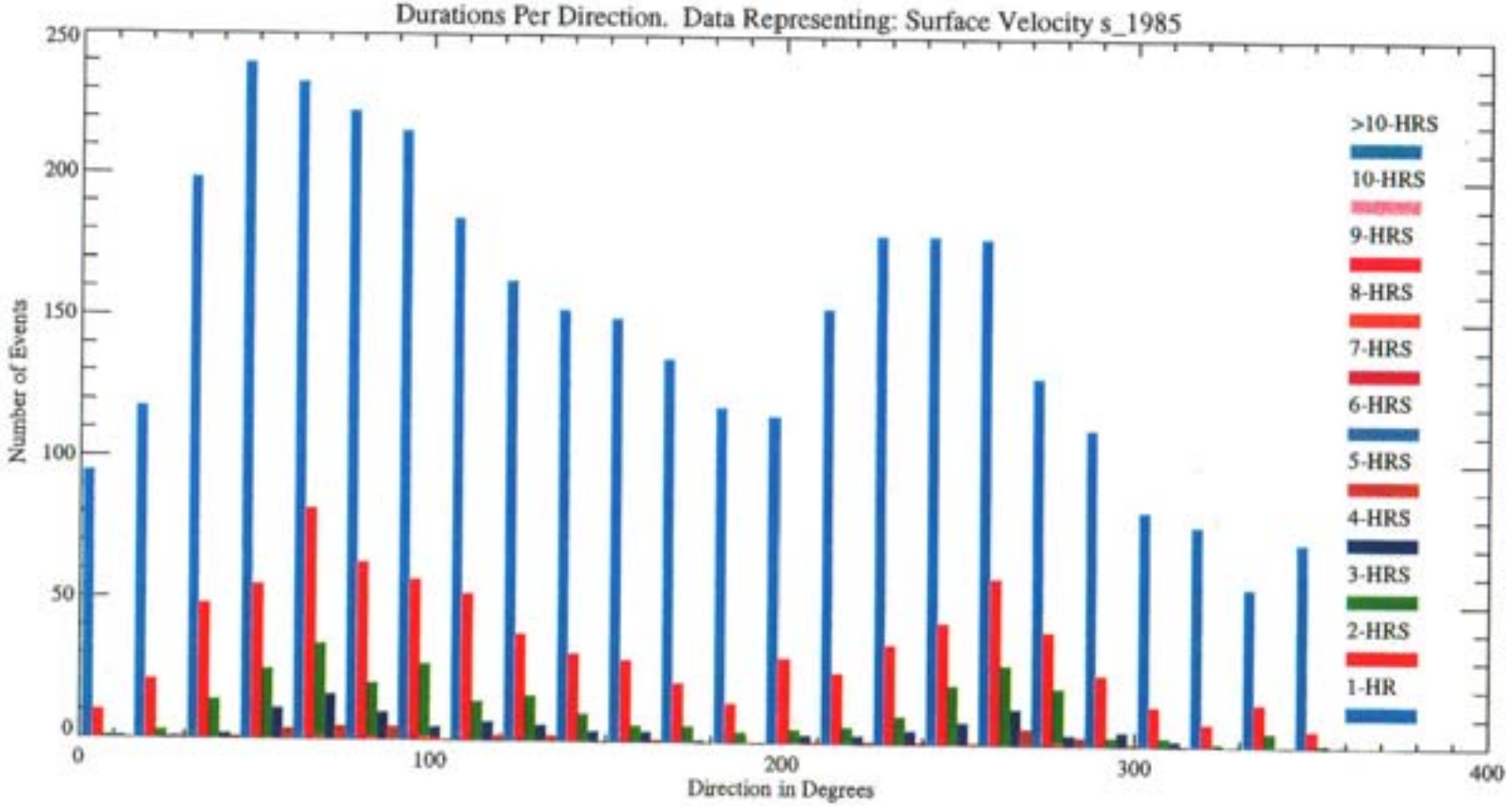
Durations Per Direction. Data Representing: Surface Velocity s_1985
Number of Events
Direction in Degrees
0
50
100
150
200
250
0
100
200
300
400
>10-HRS
10-HRS
9-HRS
8-HRS
7-HRS
6-HRS
5-HRS
4-HRS
3-HRS
2-HRS
1-HR

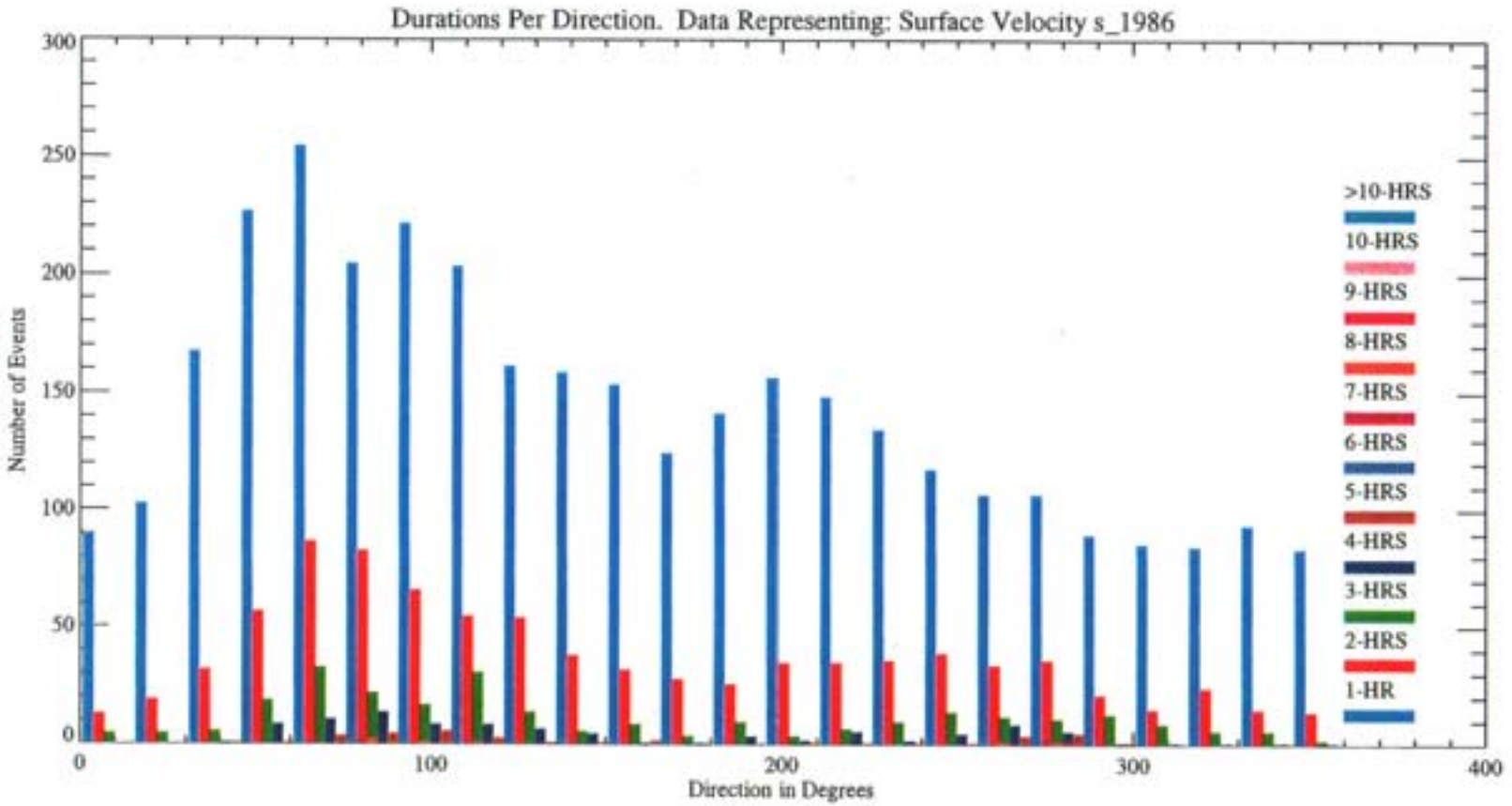
Durations Per Direction. Data Representing: Surface Velocity s_1986
Number of Events
Direction in Degrees
0
50
100
150
200
250
300
0
100
200
300
400
>10-HRS
10-HRS
9-HRS
8-HRS
7-HRS
6-HRS
5-HRS
4-HRS
3-HRS
2-HRS
1-HR

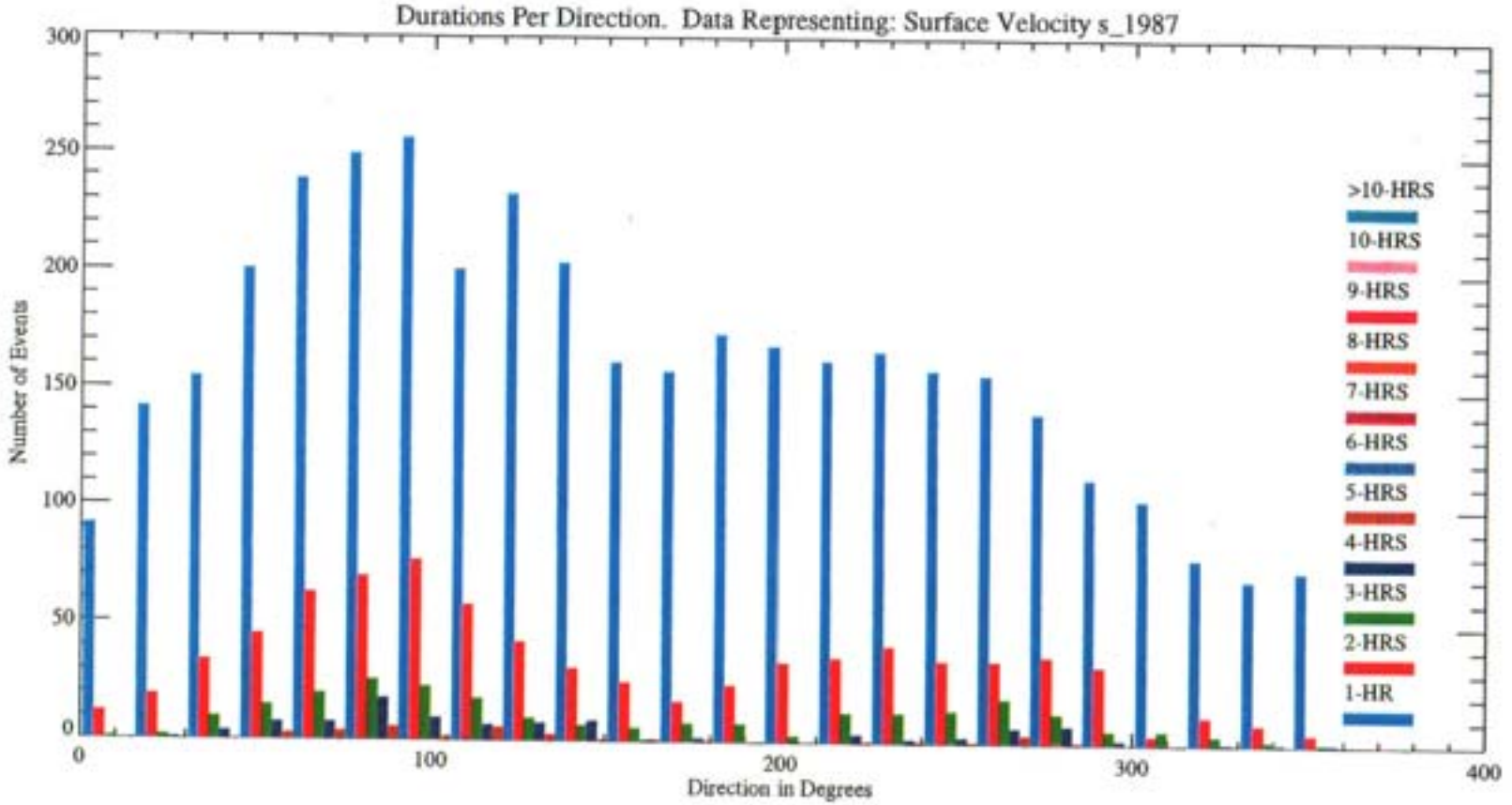
Durations Per Direction. Data Representing: Surface Velocity s_1987
Number of Events
Direction in Degrees
0
50
100
150
200
250
300
0
100
200
300
400
>10-HRS
10-HRS
9-HRS
8-HRS
7-HRS
6-HRS
5-HRS
4-HRS
3-HRS
2-HRS
1-HR

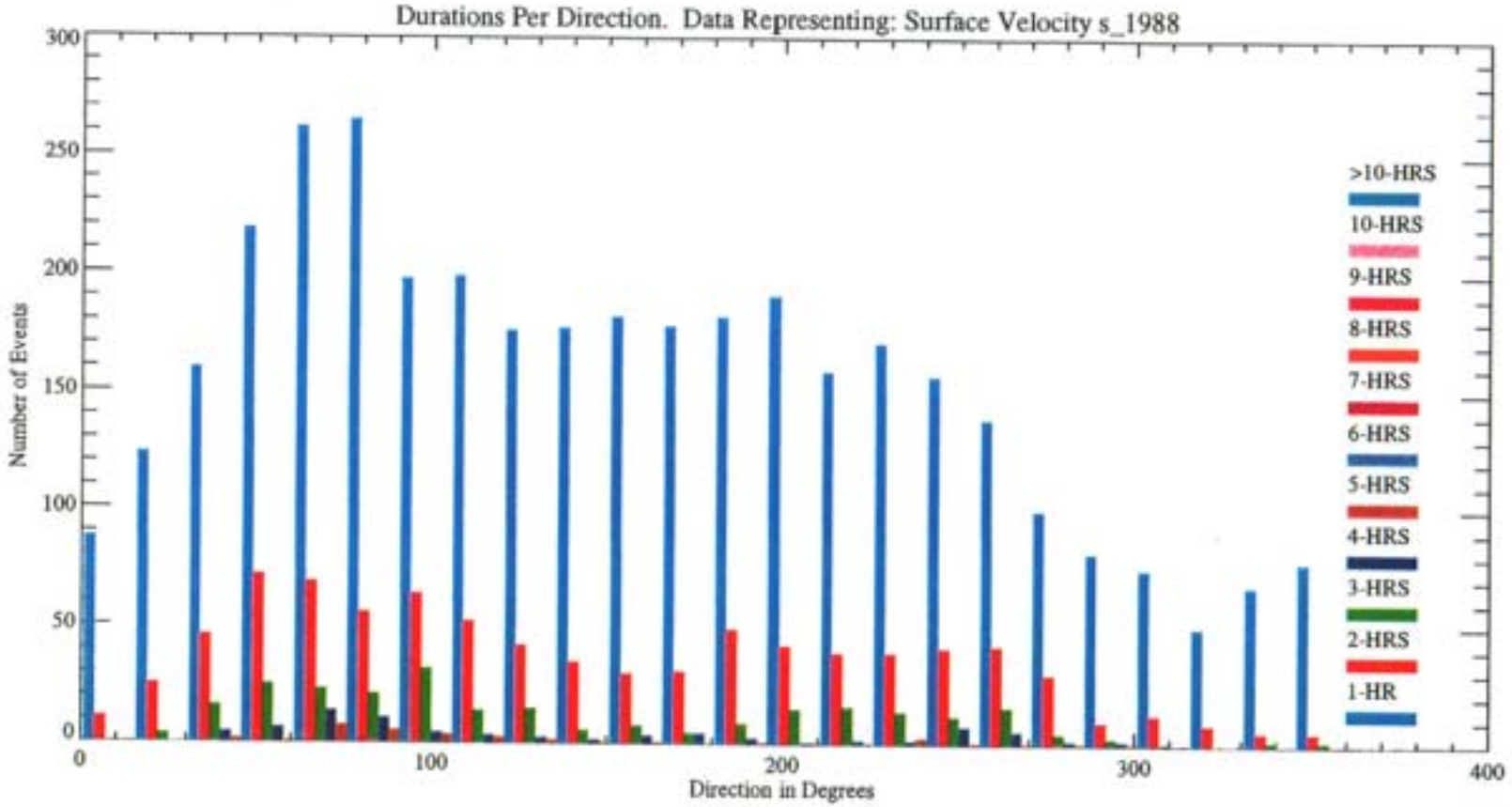
Durations Per Direction. Data Representing: Surface Velocity s_1988
Number of Events
Direction in Degrees
0
50
100
150
200
250
300
0
100
200
300
400
>10-HRS
10-HRS
9-HRS
8-HRS
7-HRS
6-HRS
5-HRS
4-HRS
3-HRS
2-HRS
1-HR

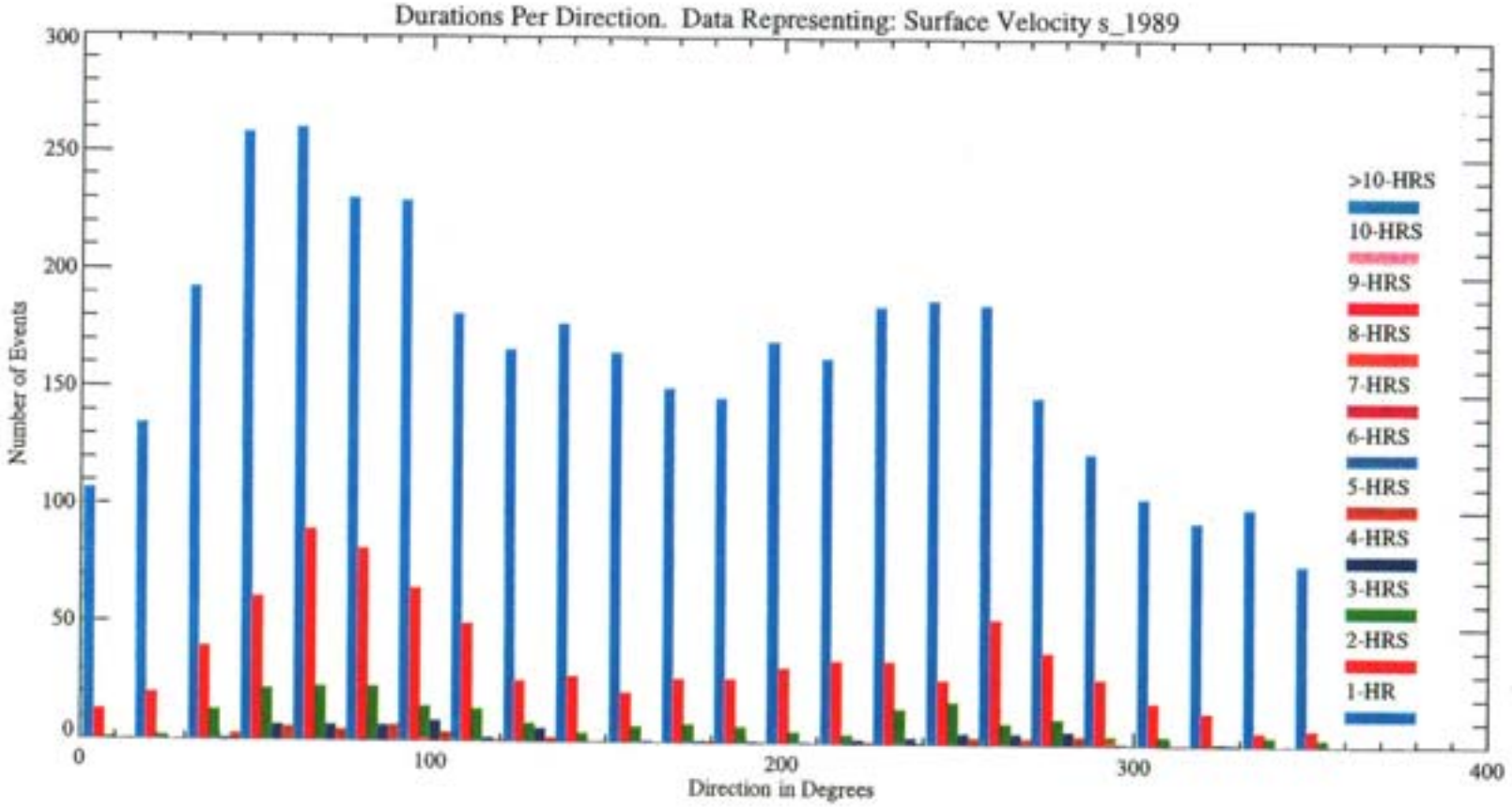
Durations Per Direction. Data Representing: Surface Velocity s_1989
Number of Events
Direction in Degrees
0
50
100
150
200
250
300
0
100
200
300
400
>10-HRS
10-HRS
9-HRS
8-HRS
7-HRS
6-HRS
5-HRS
4-HRS
3-HRS
2-HRS
1-HR

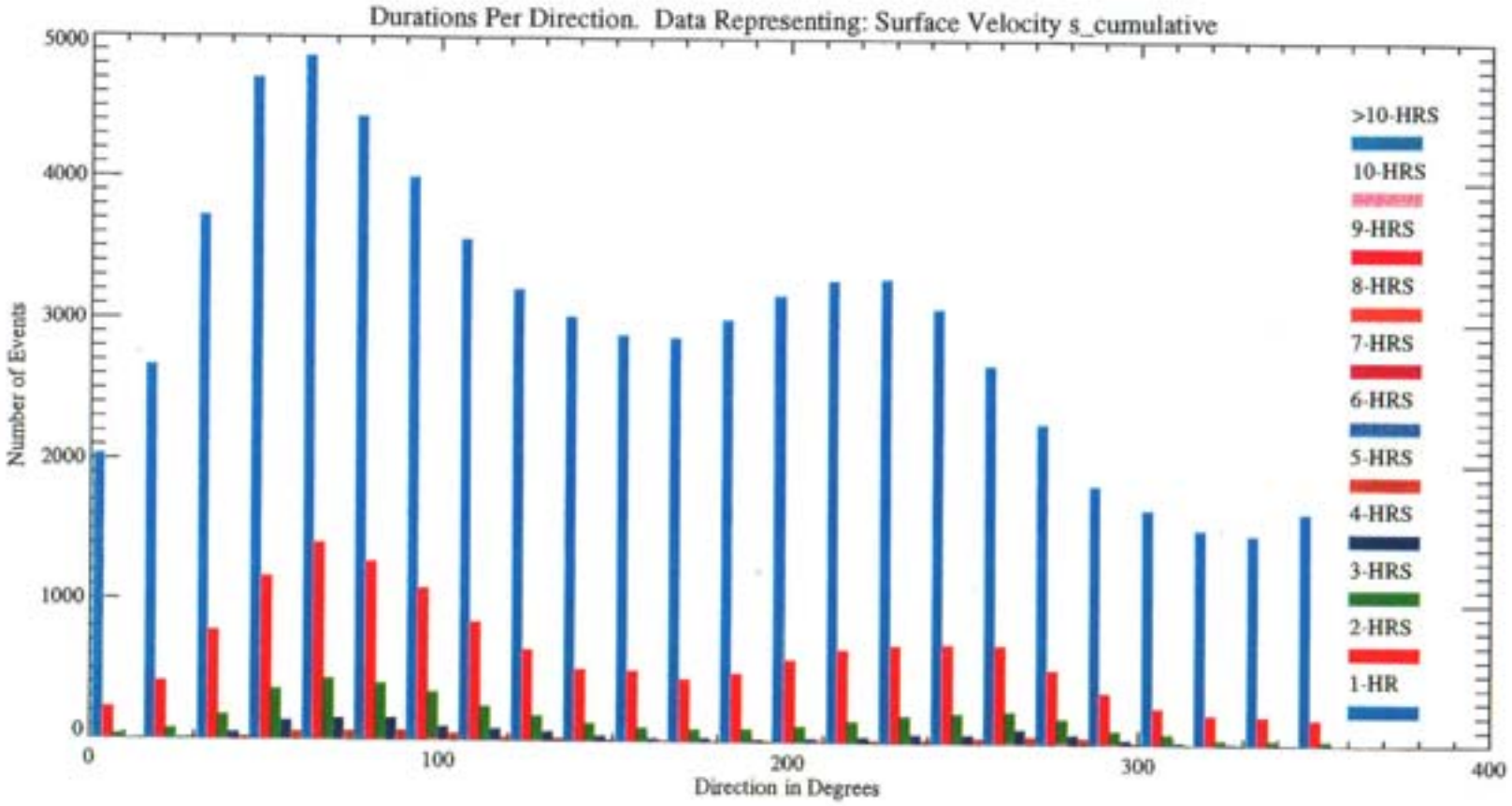
Durations Per Direction. Data Representing: Surface Velocity s_cumulative
Number of Events
Direction in Degrees
0
1000
2000
3000
4000
5000
0
100
200
300
400
>10-HRS
10-HRS
9-HRS
8-HRS
7-HRS
6-HRS
5-HRS
4-HRS
3-HRS
2-HRS
1-HR

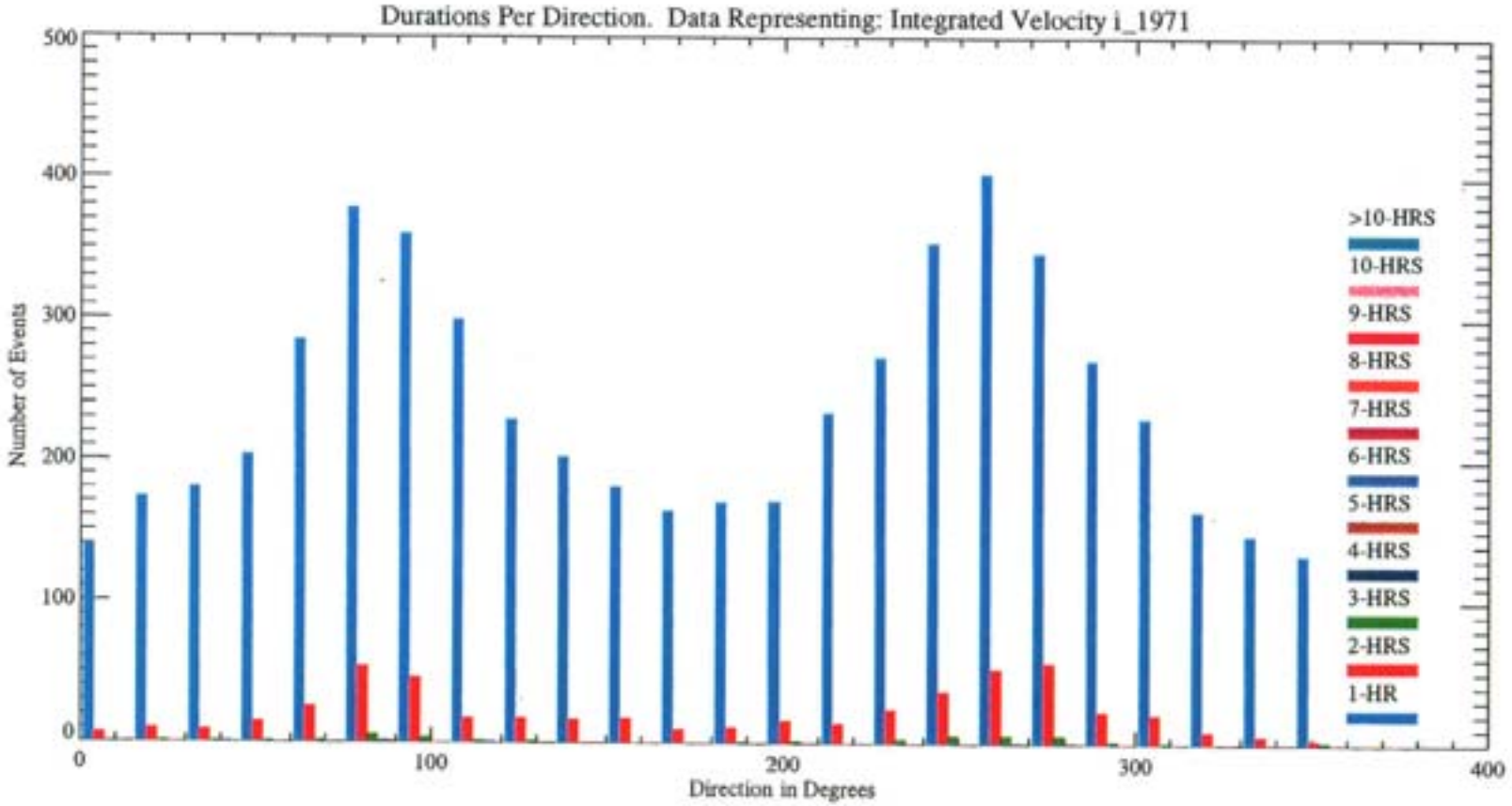
Durations Per Direction. Data Representing: Integrated Velocity i_1971
Number of Events
Direction in Degrees
0
100
200
300
400
500
>10-HRS
10-HRS
9-HRS
8-HRS
7-HRS
6-HRS
5-HRS
4-HRS
3-HRS
2-HRS
1-HR

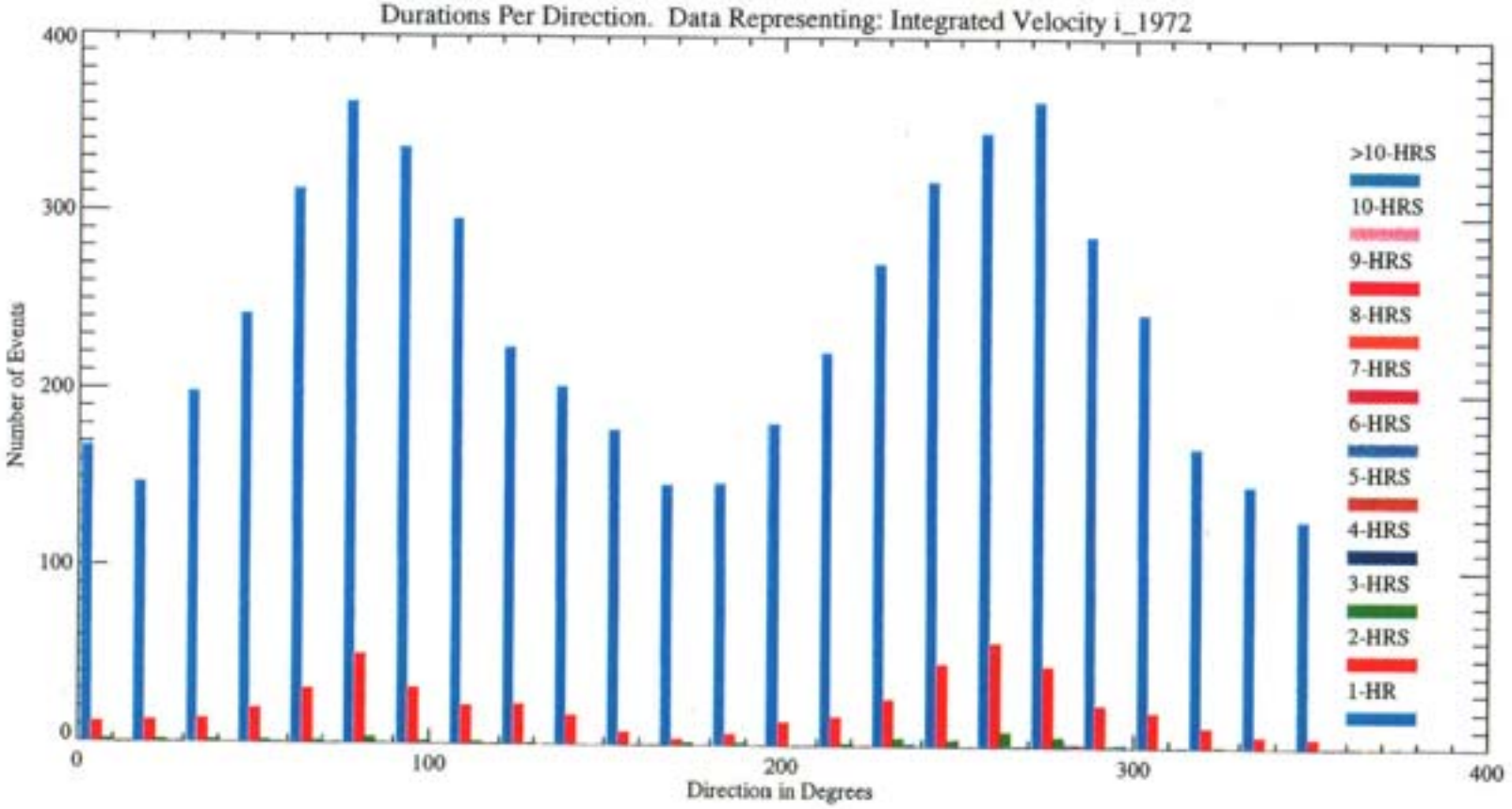
Durations Per Direction. Data Representing: Integrated Velocity i_1972
Number of Events
Direction in Degrees
0
100
200
300
400
>10-HRS
10-HRS
9-HRS
8-HRS
7-HRS
6-HRS
5-HRS
4-HRS
3-HRS
2-HRS
1-HR

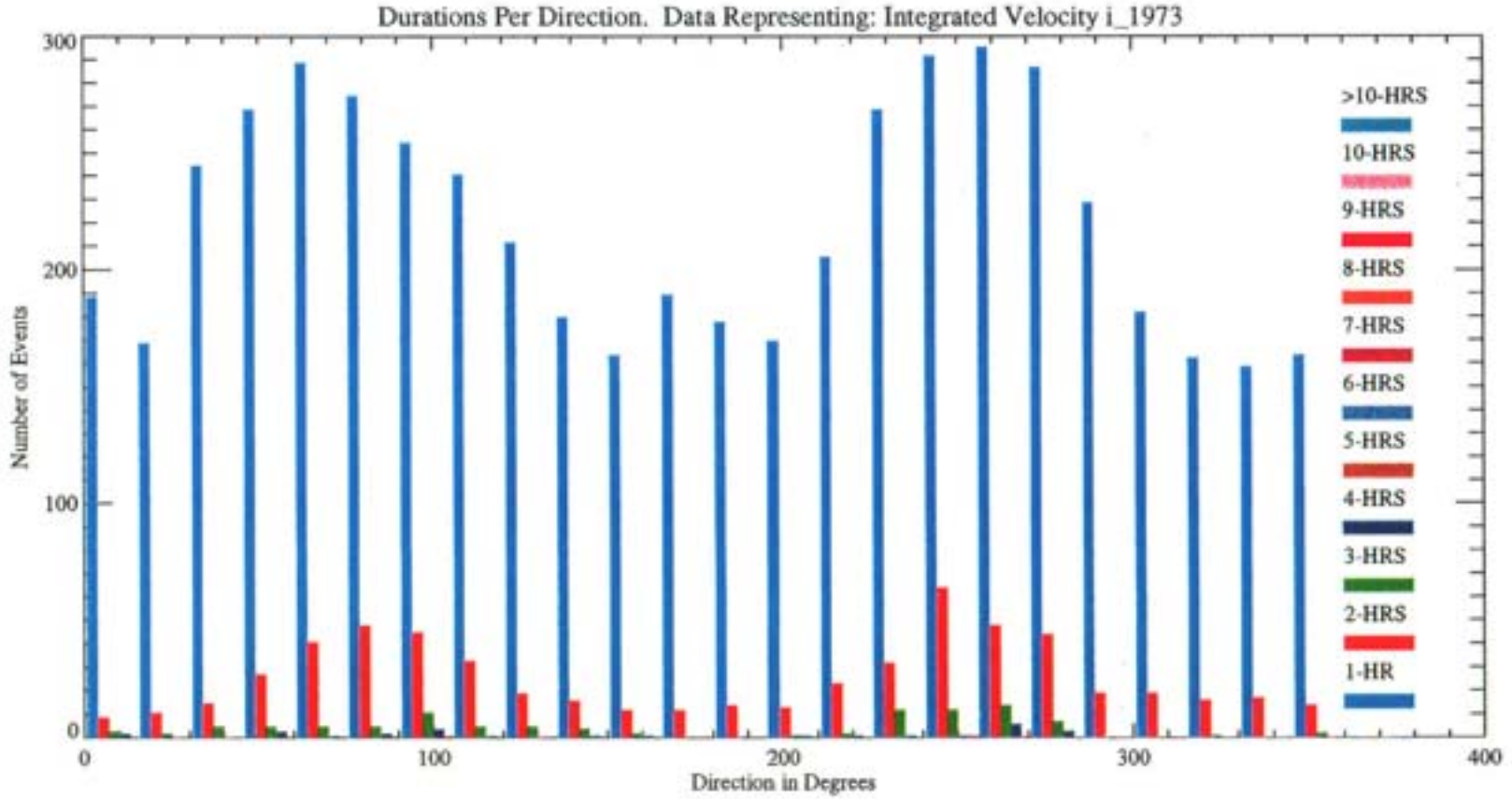
Durations Per Direction. Data Representing: Integrated Velocity i_1973
Number of Events
Direction in Degrees
0
100
200
300
400
>10-HRS
10-HRS
9-HRS
8-HRS
7-HRS
6-HRS
5-HRS
4-HRS
3-HRS
2-HRS
1-HR

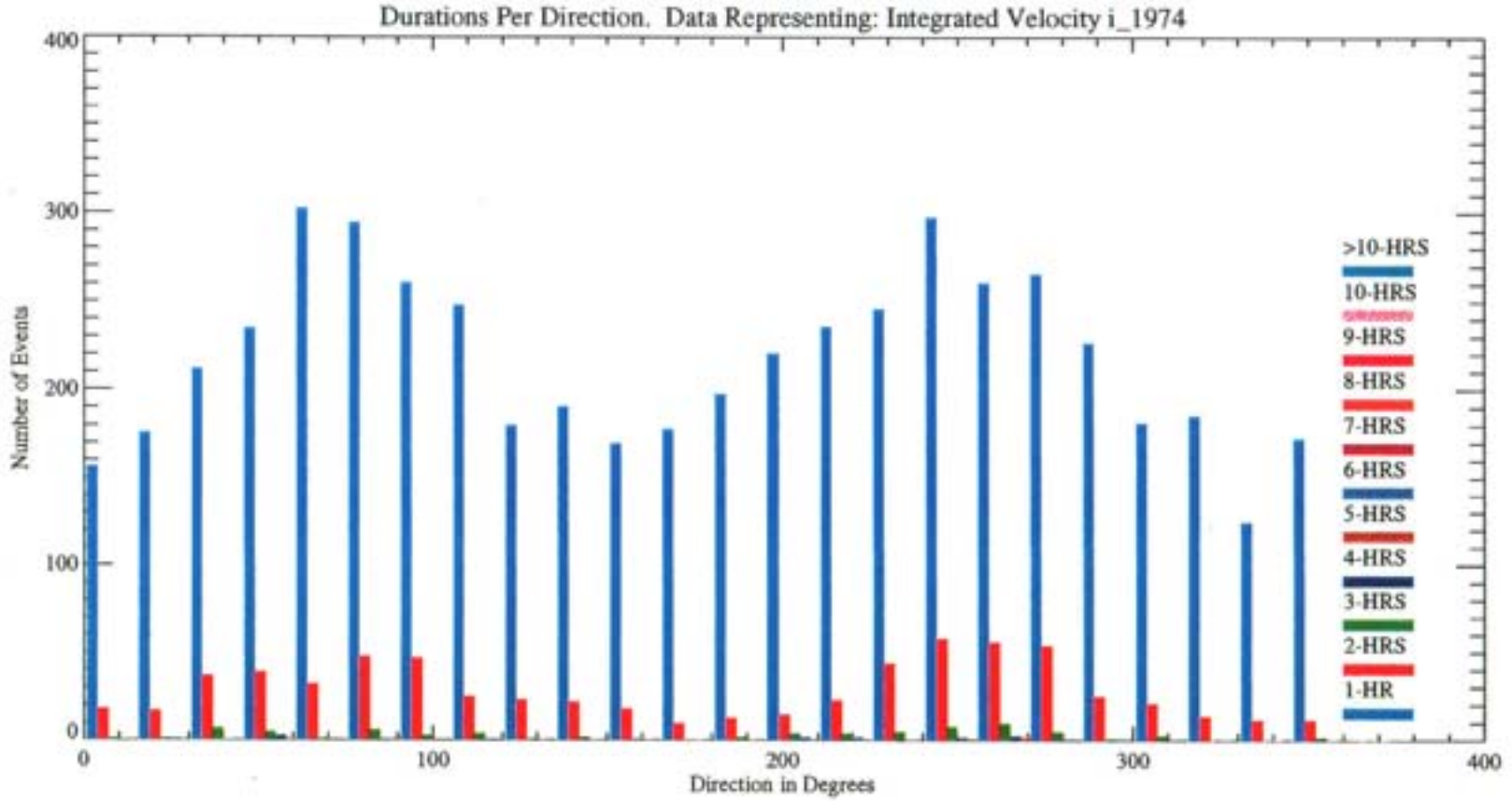
Durations Per Direction. Data Representing: Integrated Velocity i_1974
Number of Events
Direction in Degrees
0
100
200
300
400
>10-HRS
10-HRS
9-HRS
8-HRS
7-HRS
6-HRS
5-HRS
4-HRS
3-HRS
2-HRS
1-HR

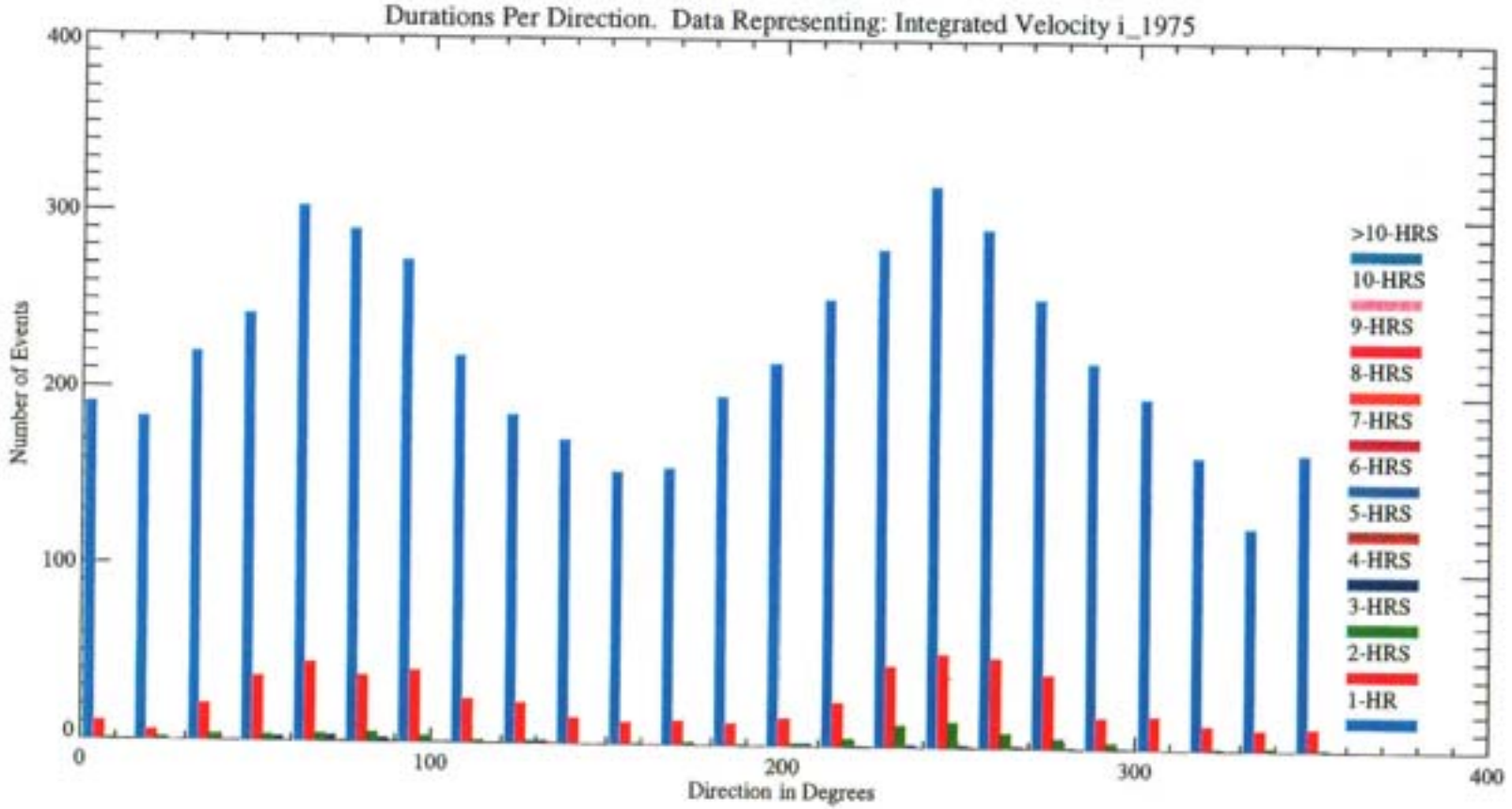
Durations Per Direction. Data Representing: Integrated Velocity i_1975
Number of Events
Direction in Degrees
0
100
200
300
400
>10-HRS
10-HRS
9-HRS
8-HRS
7-HRS
6-HRS
5-HRS
4-HRS
3-HRS
2-HRS
1-HR

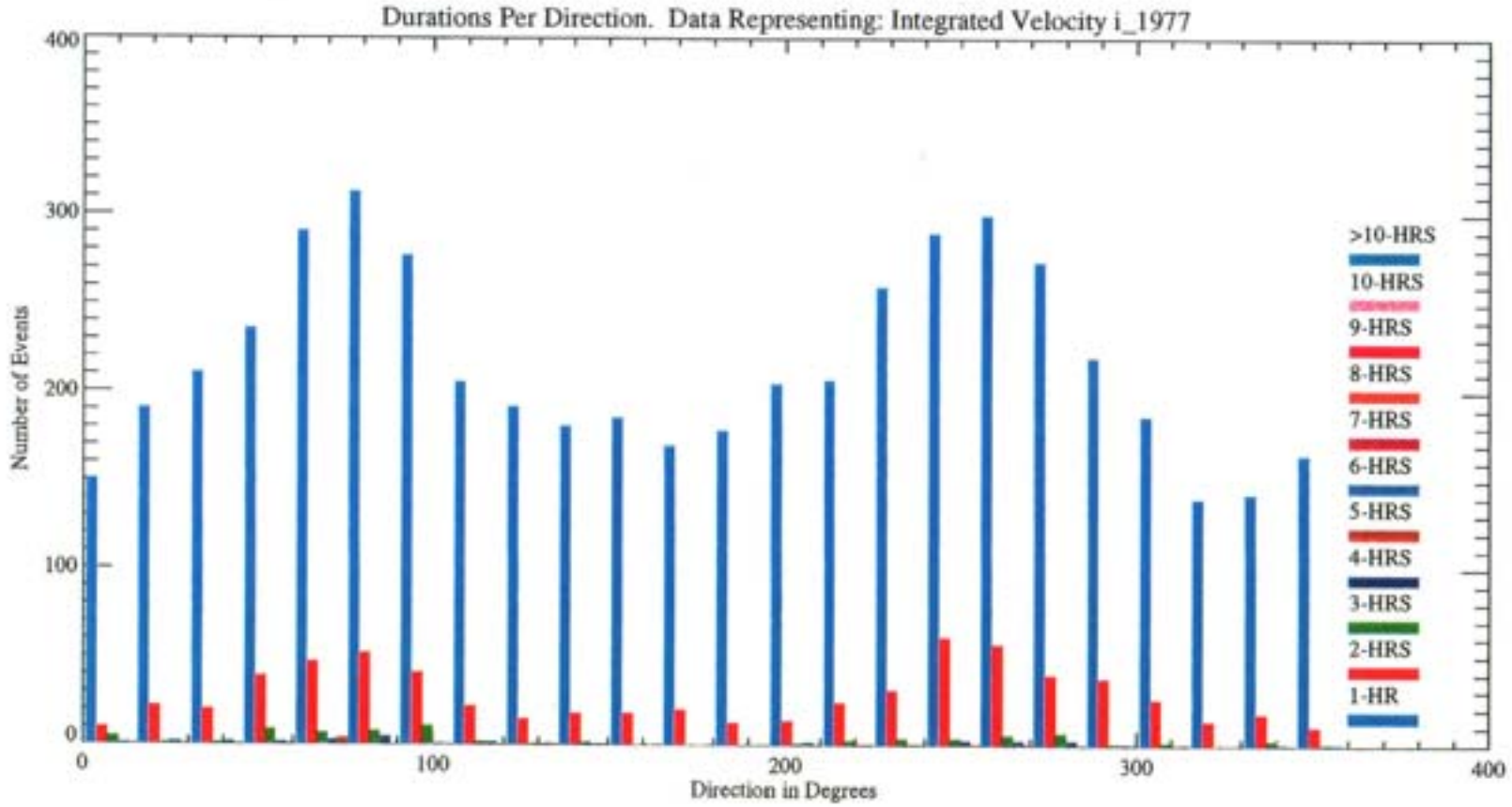
Durations Per Direction. Data Representing: Integrated Velocity i_1977
Number of Events
Direction in Degrees
0
100
200
300
400
>10-HRS
10-HRS
9-HRS
8-HRS
7-HRS
6-HRS
5-HRS
4-HRS
3-HRS
2-HRS
1-HR

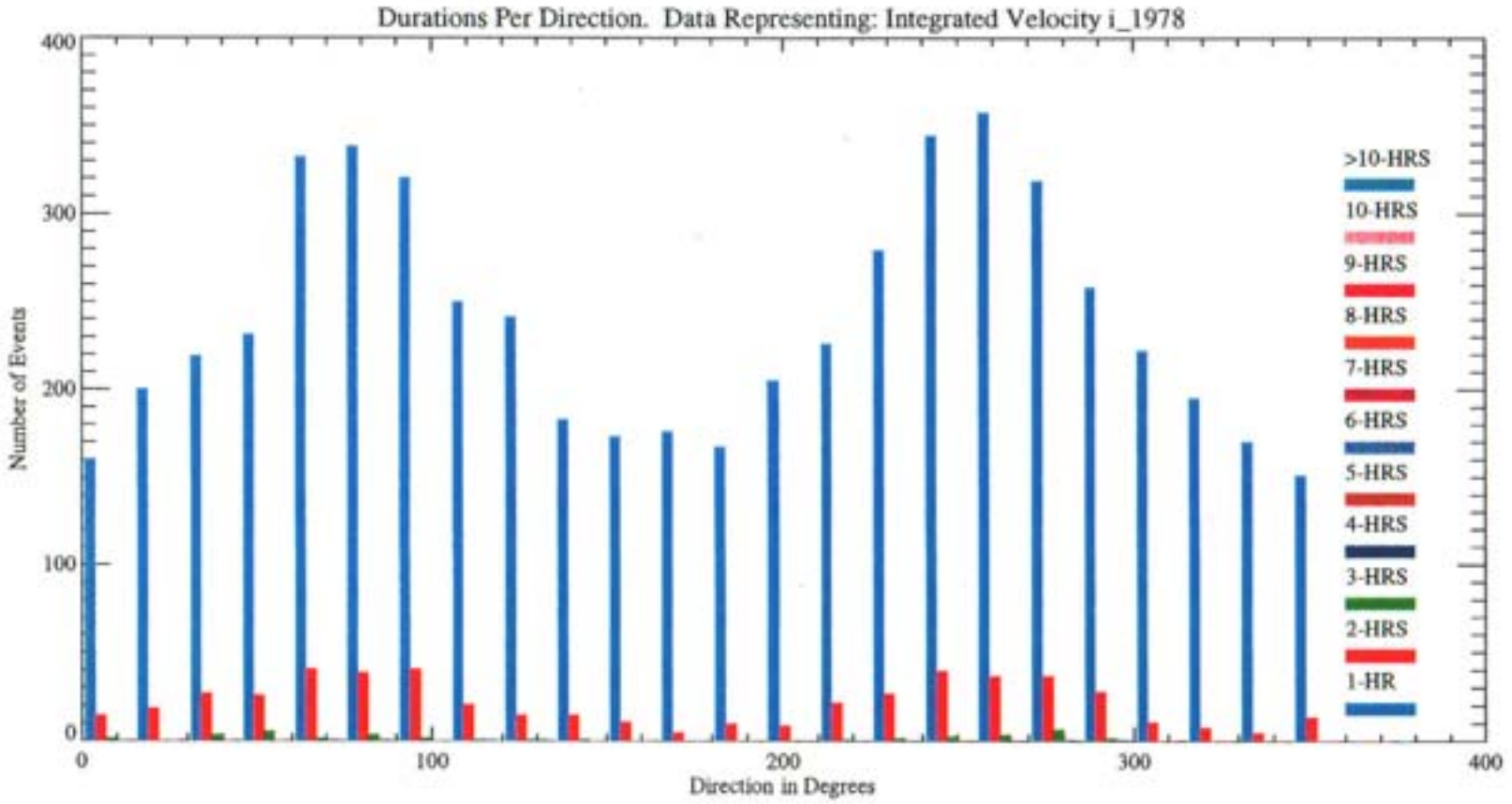
Durations Per Direction. Data Representing: Integrated Velocity i_1978
Number of Events
Direction in Degrees
0
100
200
300
400
>10-HRS
10-HRS
9-HRS
8-HRS
7-HRS
6-HRS
5-HRS
4-HRS
3-HRS
2-HRS
1-HR

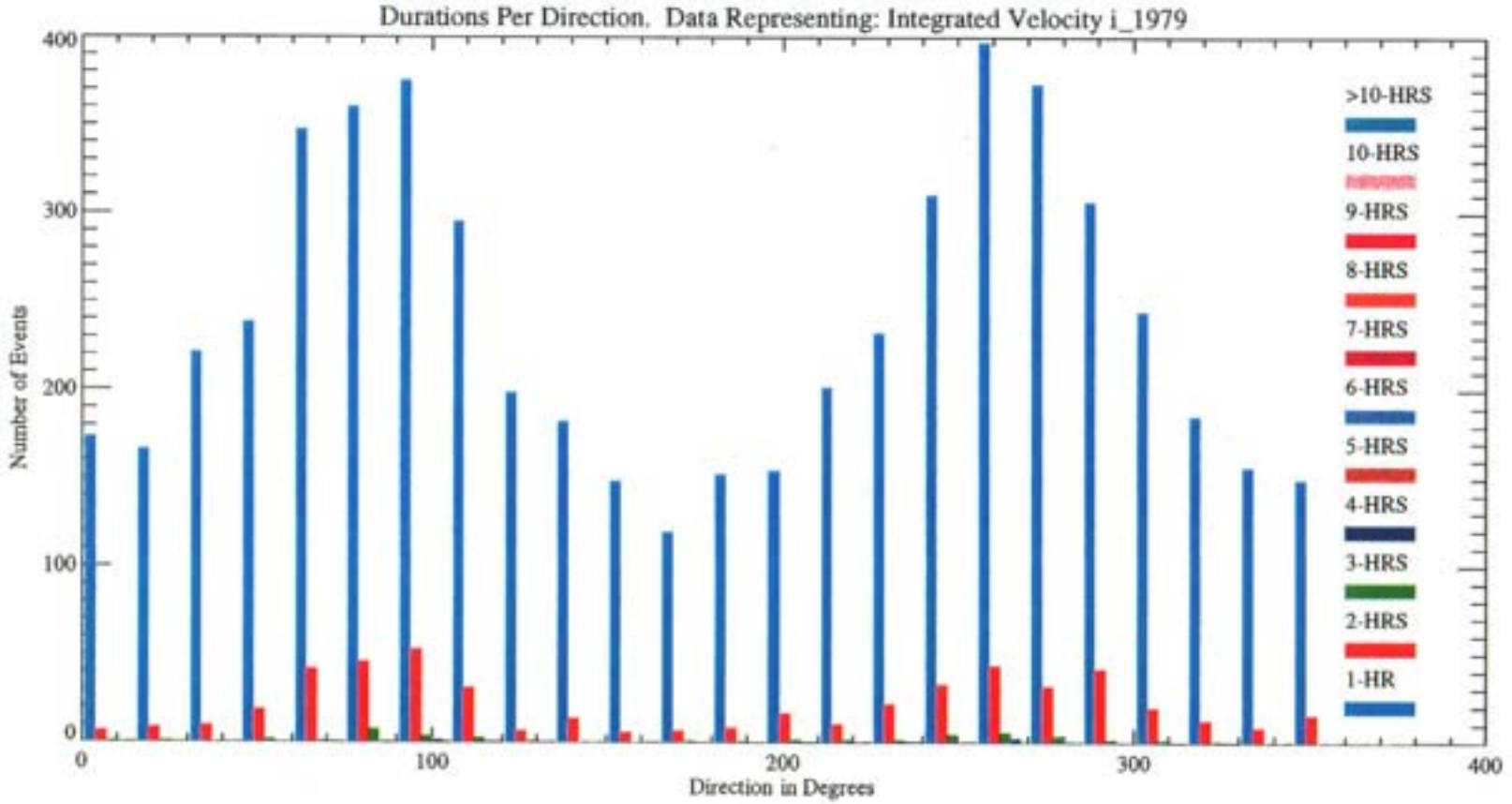
Durations Per Direction. Data Representing: Integrated Velocity i_1979
Number of Events
Direction in Degrees
0
100
200
300
400
>10-HRS
10-HRS
9-HRS
8-HRS
7-HRS
6-HRS
5-HRS
4-HRS
3-HRS
2-HRS
1-HR

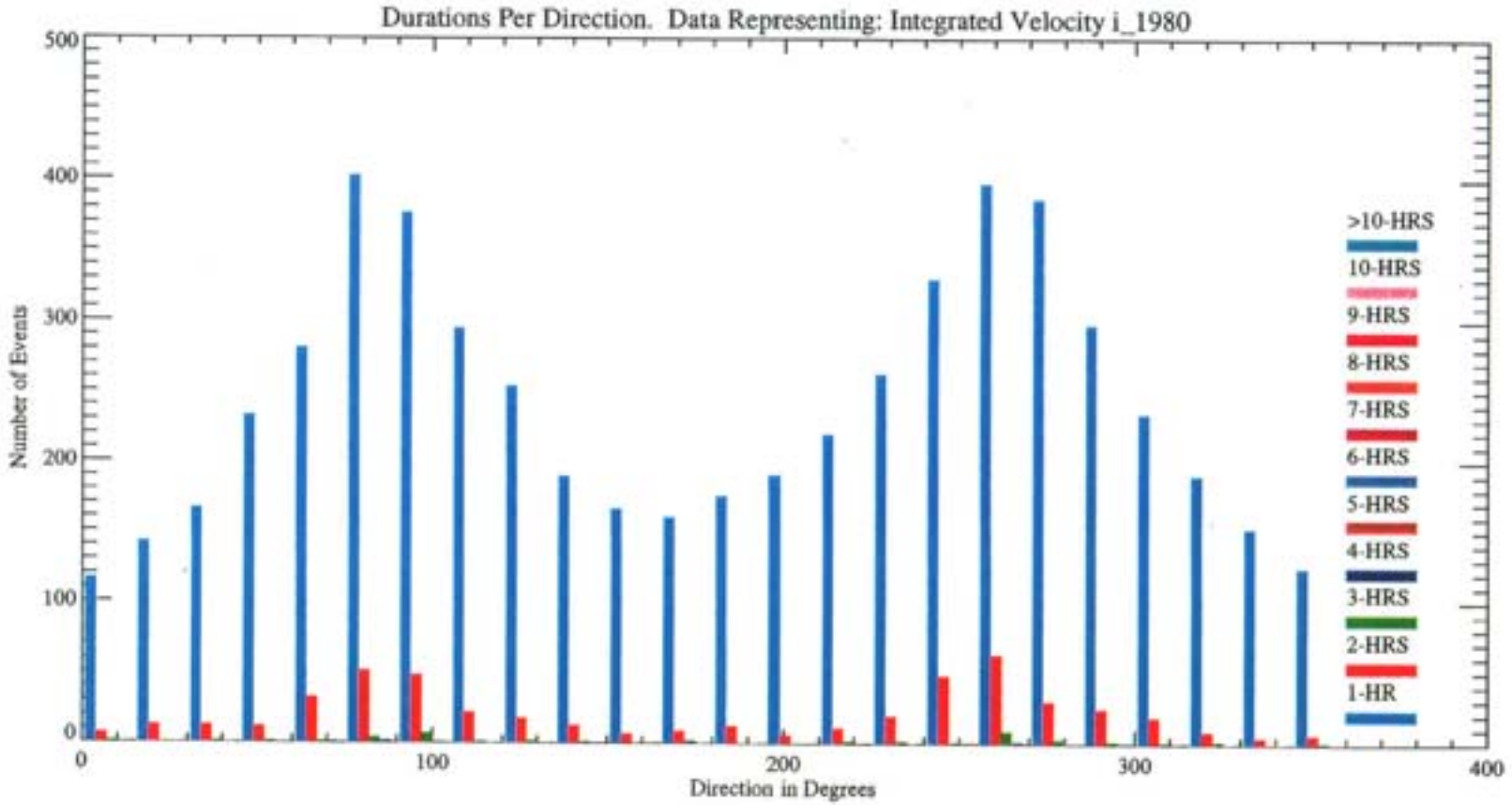
Durations Per Direction. Data Representing: Integrated Velocity i_1980
Number of Events
Direction in Degrees
0
100
200
300
400
500
>10-HRS
10-HRS
9-HRS
8-HRS
7-HRS
6-HRS
5-HRS
4-HRS
3-HRS
2-HRS
1-HR

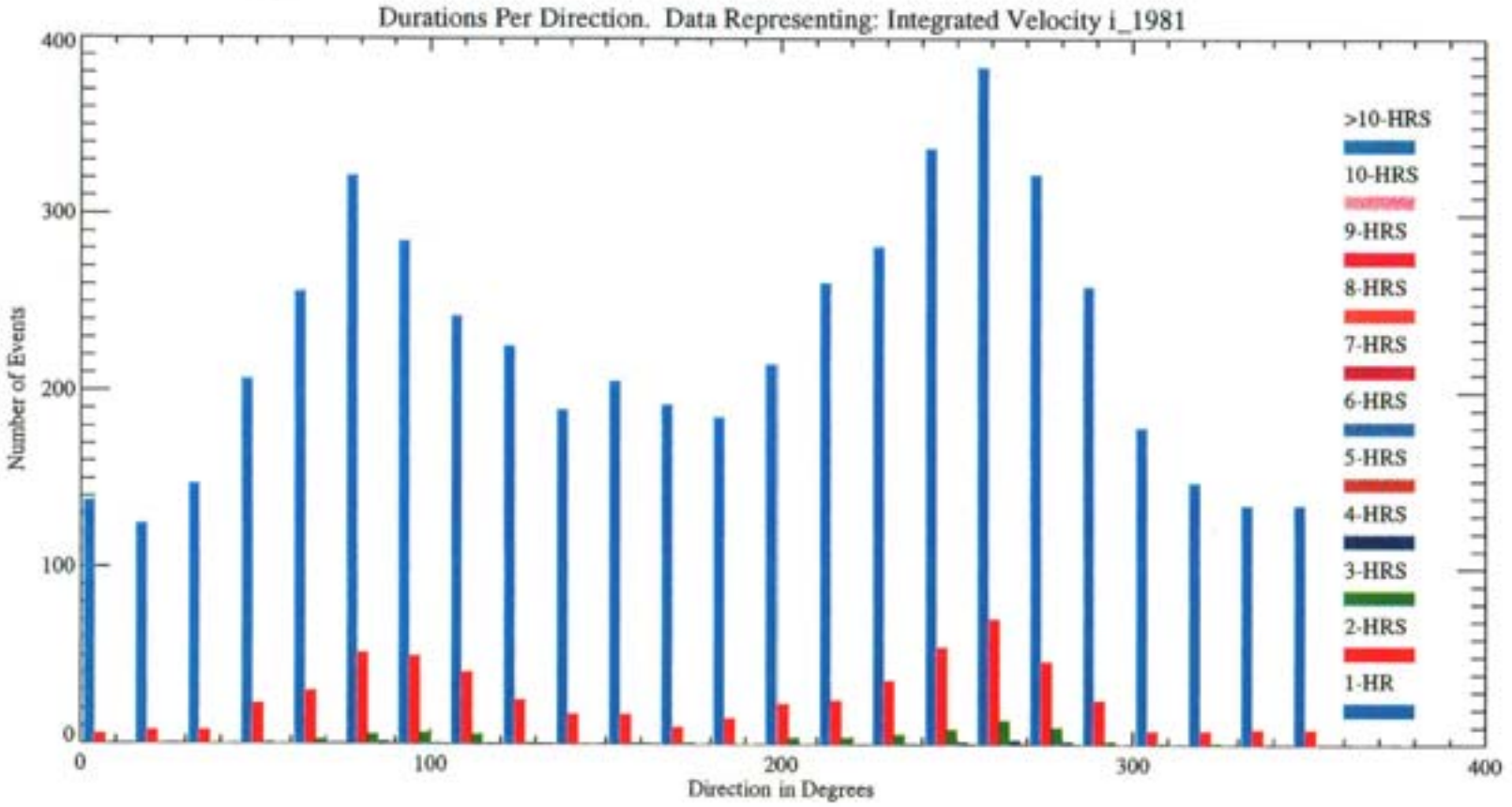
Durations Per Direction. Data Representing: Integrated Velocity i_1981
Number of Events
Direction in Degrees
0
100
200
300
400
>10-HRS
10-HRS
9-HRS
8-HRS
7-HRS
6-HRS
5-HRS
4-HRS
3-HRS
2-HRS
1-HR

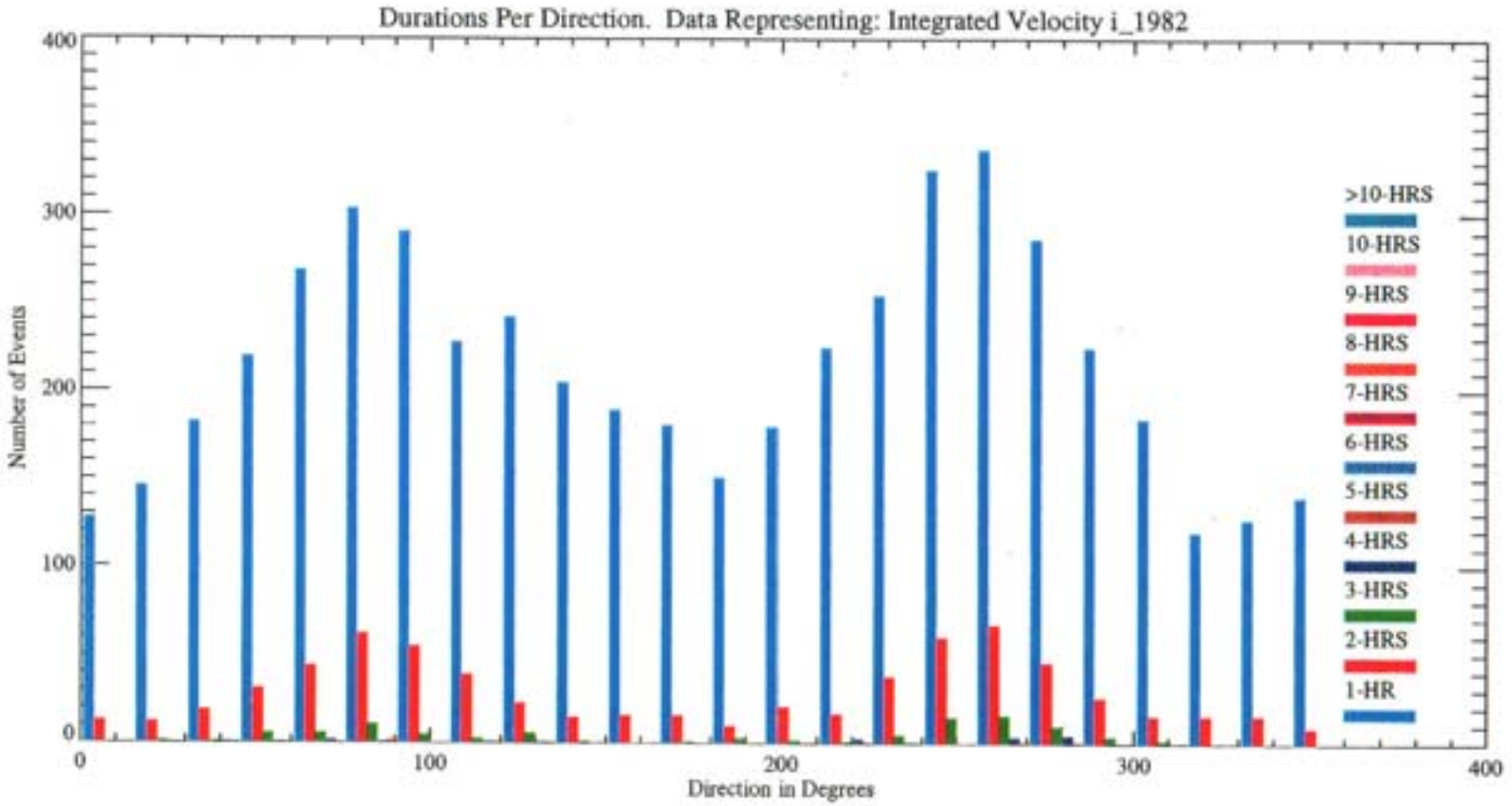
Durations Per Direction. Data Representing: Integrated Velocity i_1982
Number of Events
Direction in Degrees
0
100
200
300
400
>10-HRS
10-HRS
9-HRS
8-HRS
7-HRS
6-HRS
5-HRS
4-HRS
3-HRS
2-HRS
1-HR

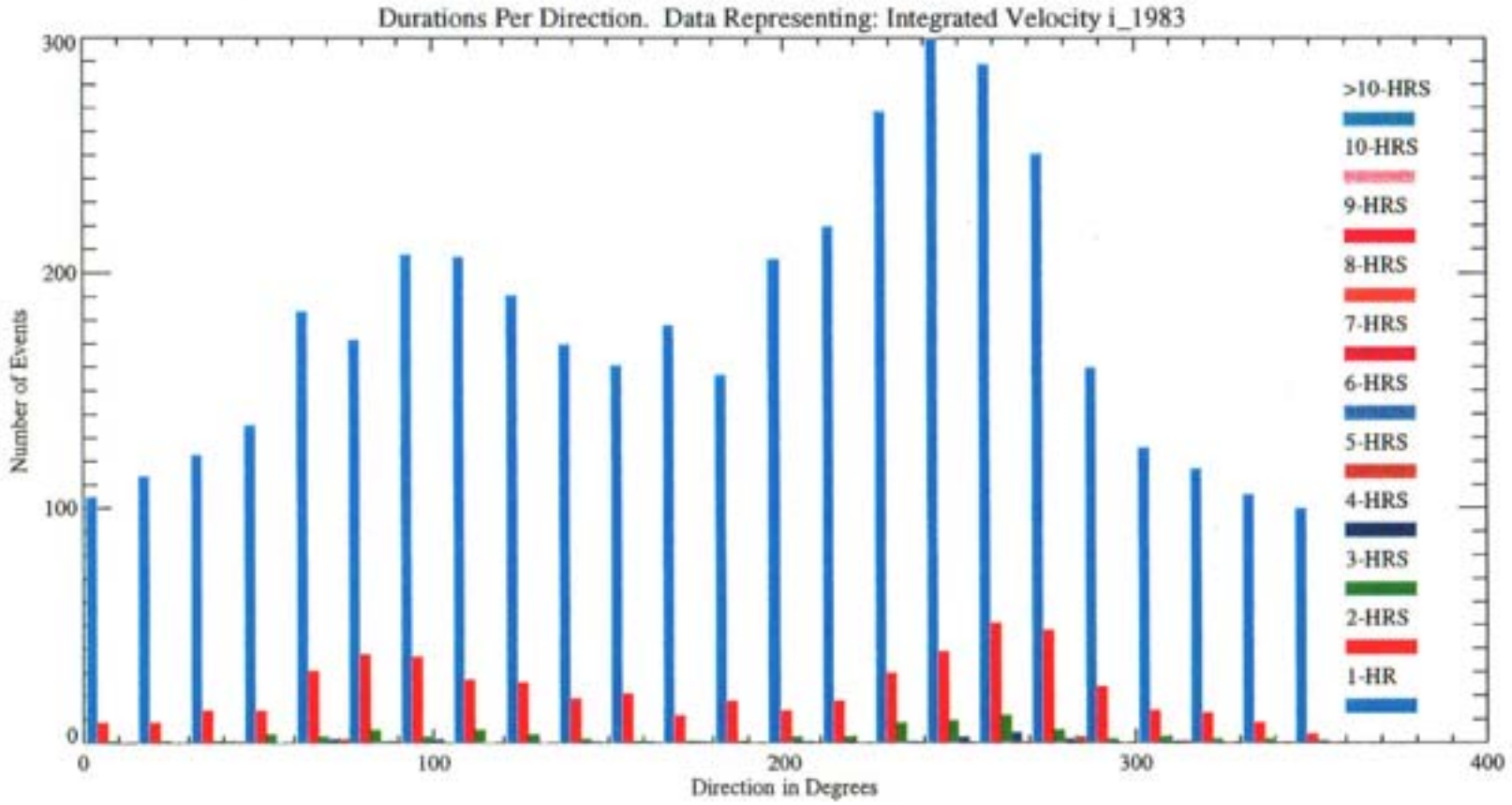
Durations Per Direction. Data Representing: Integrated Velocity i_1983
Number of Events
Direction in Degrees
0
100
200
300
400
>10-HRS
10-HRS
9-HRS
8-HRS
7-HRS
6-HRS
5-HRS
4-HRS
3-HRS
2-HRS
1-HR

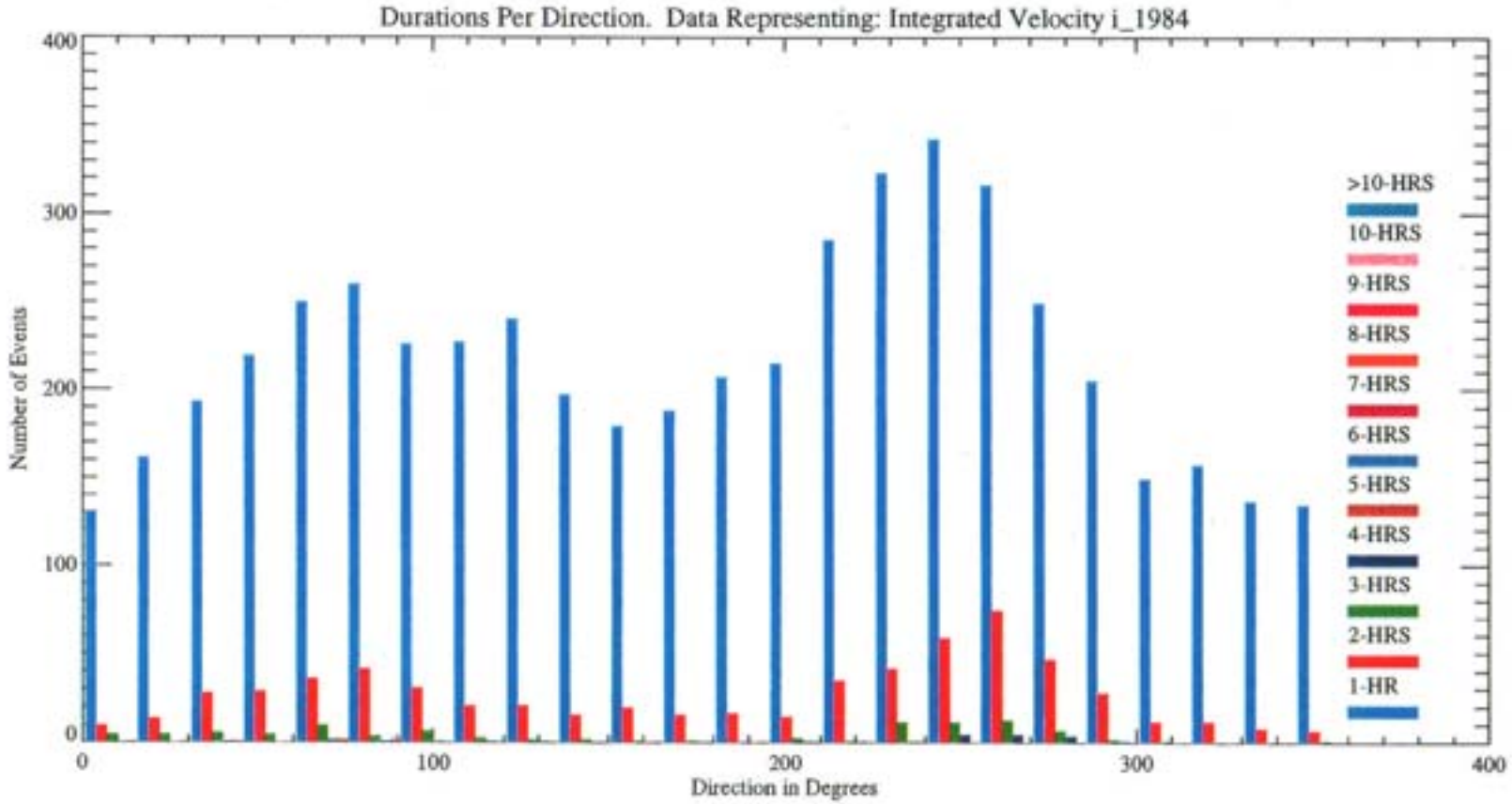
Durations Per Direction. Data Representing: Integrated Velocity i_1984
Number of Events
Direction in Degrees
0
100
200
300
400
>10-HRS
10-HRS
9-HRS
8-HRS
7-HRS
6-HRS
5-HRS
4-HRS
3-HRS
2-HRS
1-HR

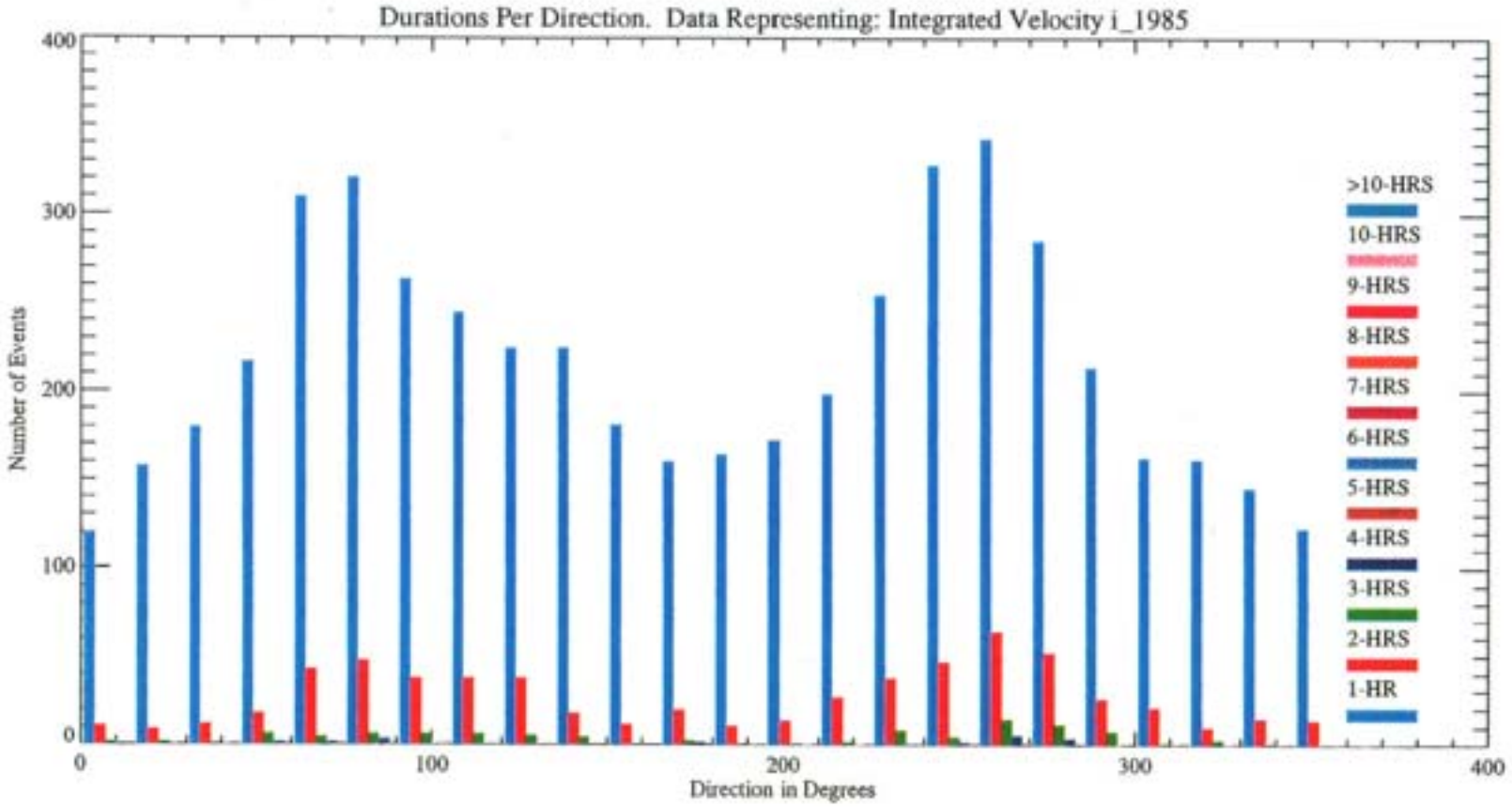
Durations Per Direction. Data Representing: Integrated Velocity i_1985
Number of Events
Direction in Degrees
0
100
200
300
400
>10-HRS
10-HRS
9-HRS
8-HRS
7-HRS
6-HRS
5-HRS
4-HRS
3-HRS
2-HRS
1-HR

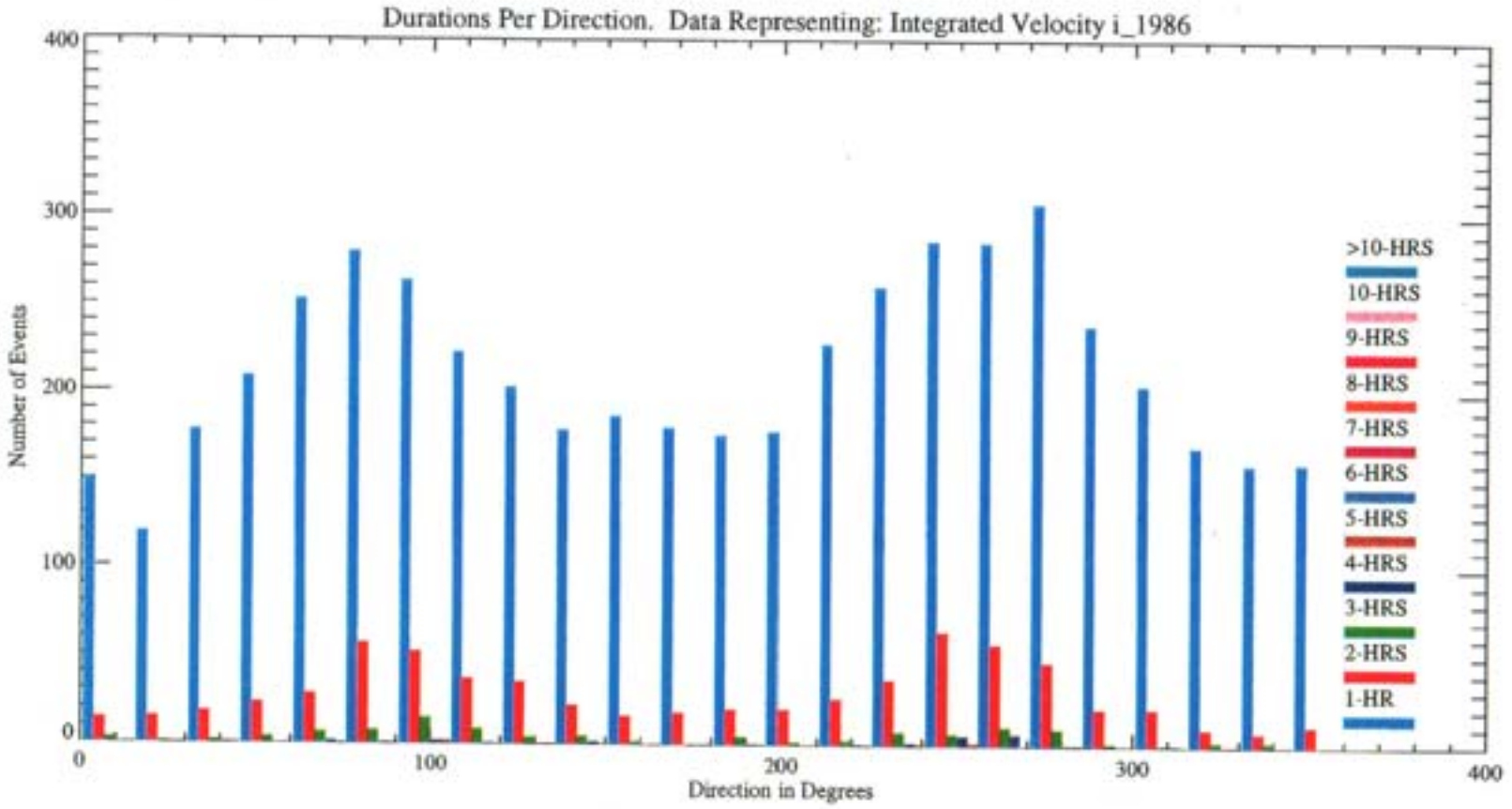
Durations Per Direction. Data Representing: Integrated Velocity i_1986
Number of Events
Direction in Degrees
0
100
200
300
400
>10-HRS
10-HRS
9-HRS
8-HRS
7-HRS
6-HRS
5-HRS
4-HRS
3-HRS
2-HRS
1-HR

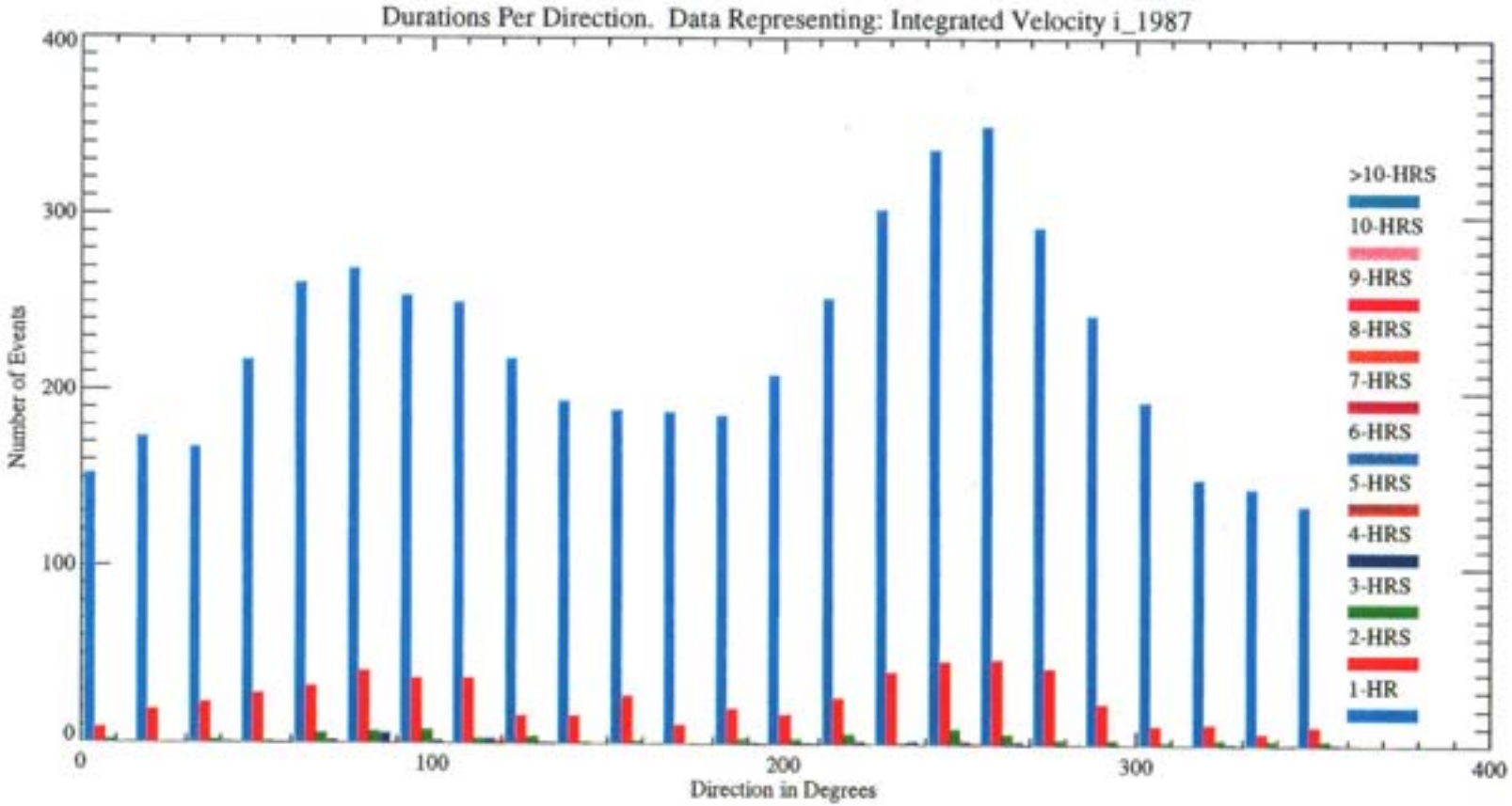
Durations Per Direction. Data Representing: Integrated Velocity i_1987
Number of Events
Direction in Degrees
0
100
200
300
400
>10-HRS
10-HRS
9-HRS
8-HRS
7-HRS
6-HRS
5-HRS
4-HRS
3-HRS
2-HRS
1-HR

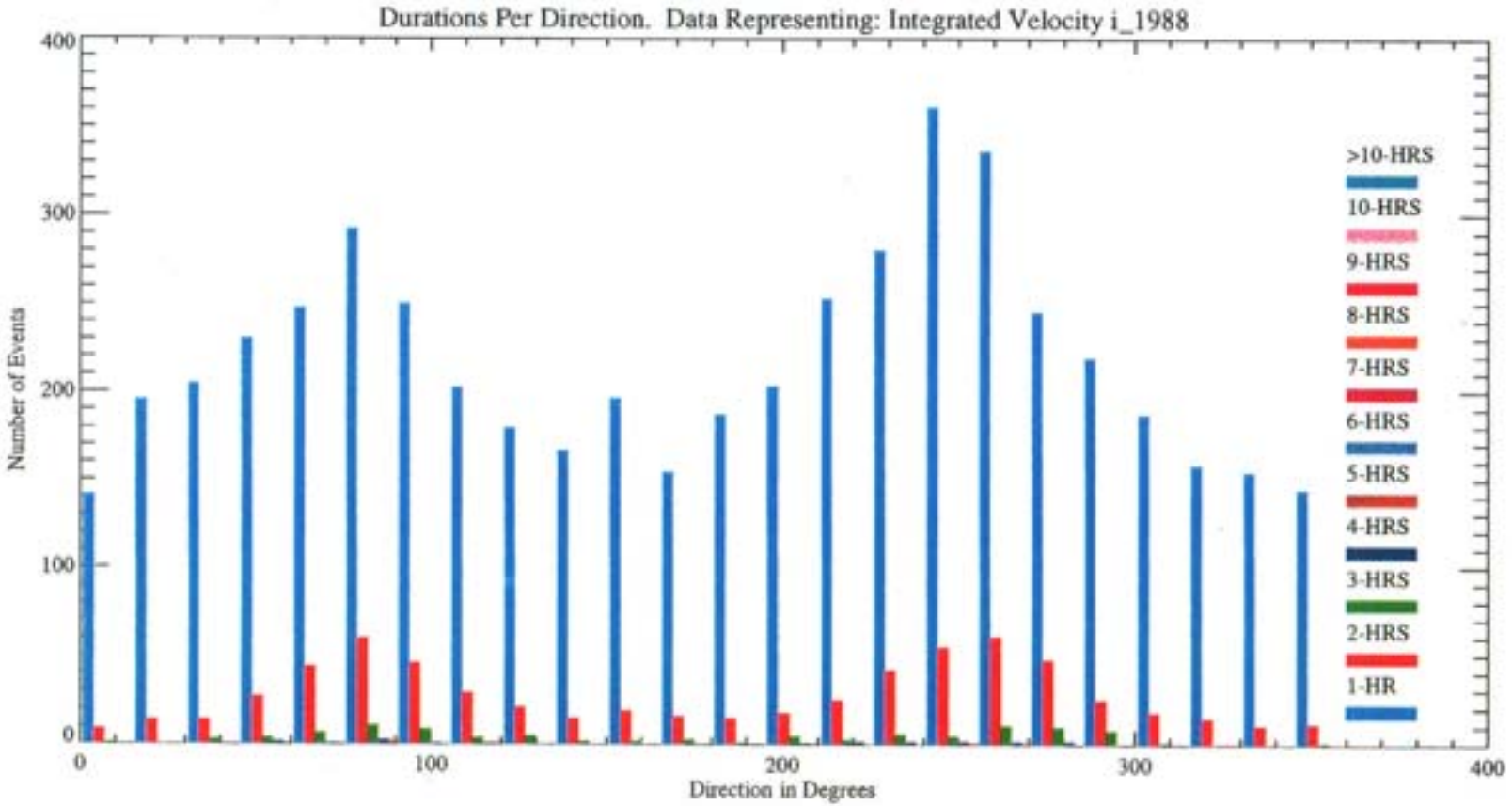
Durations Per Direction. Data Representing: Integrated Velocity i_1988
Number of Events
Direction in Degrees
0
100
200
300
400
>10-HRS
10-HRS
9-HRS
8-HRS
7-HRS
6-HRS
5-HRS
4-HRS
3-HRS
2-HRS
1-HR

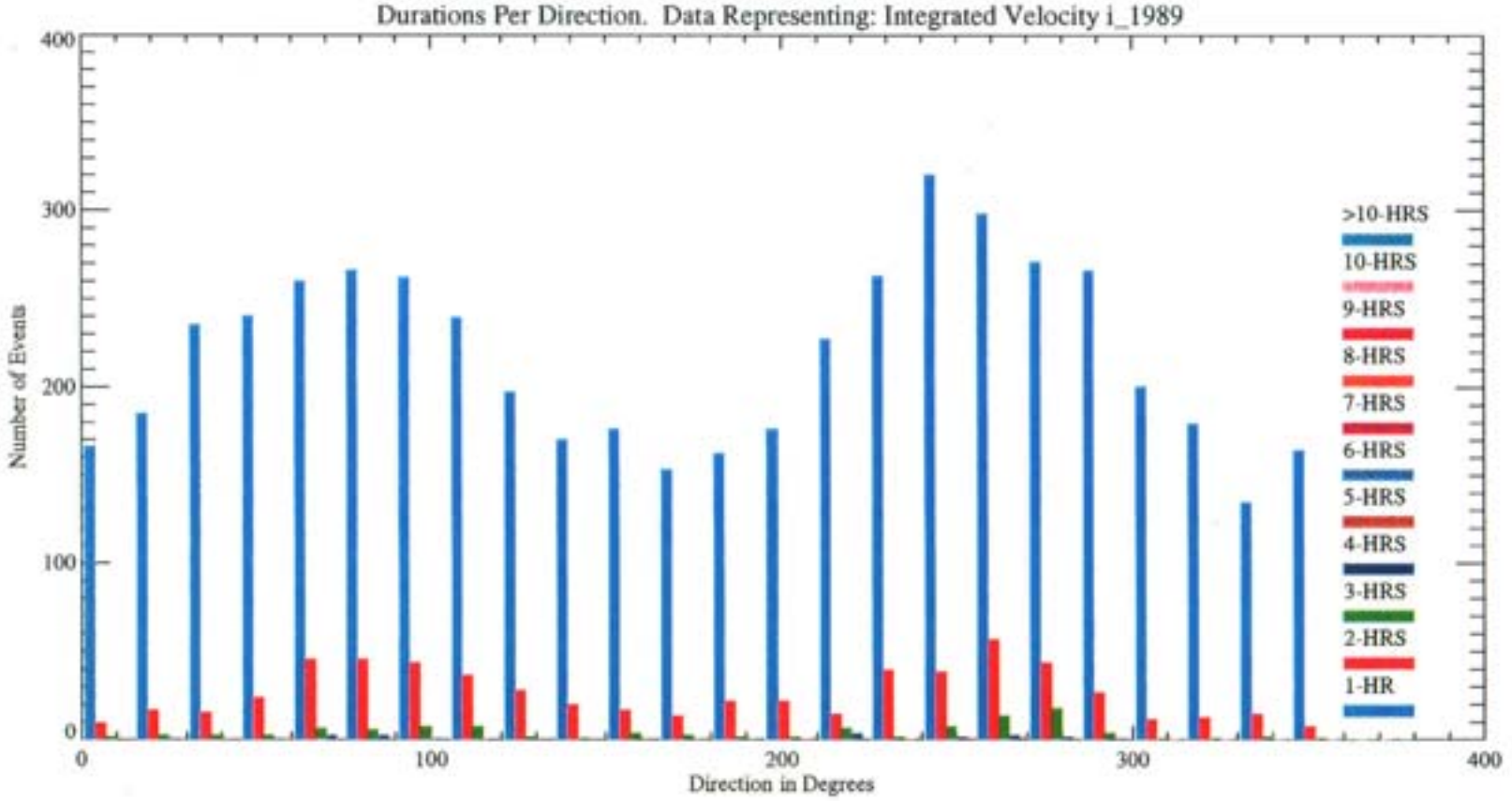
Durations Per Direction. Data Representing: Integrated Velocity i_1989
Number of Events
Direction in Degrees
0
100
200
300
400
>10-HRS
10-HRS
9-HRS
8-HRS
7-HRS
6-HRS
5-HRS
4-HRS
3-HRS
2-HRS
1-HR

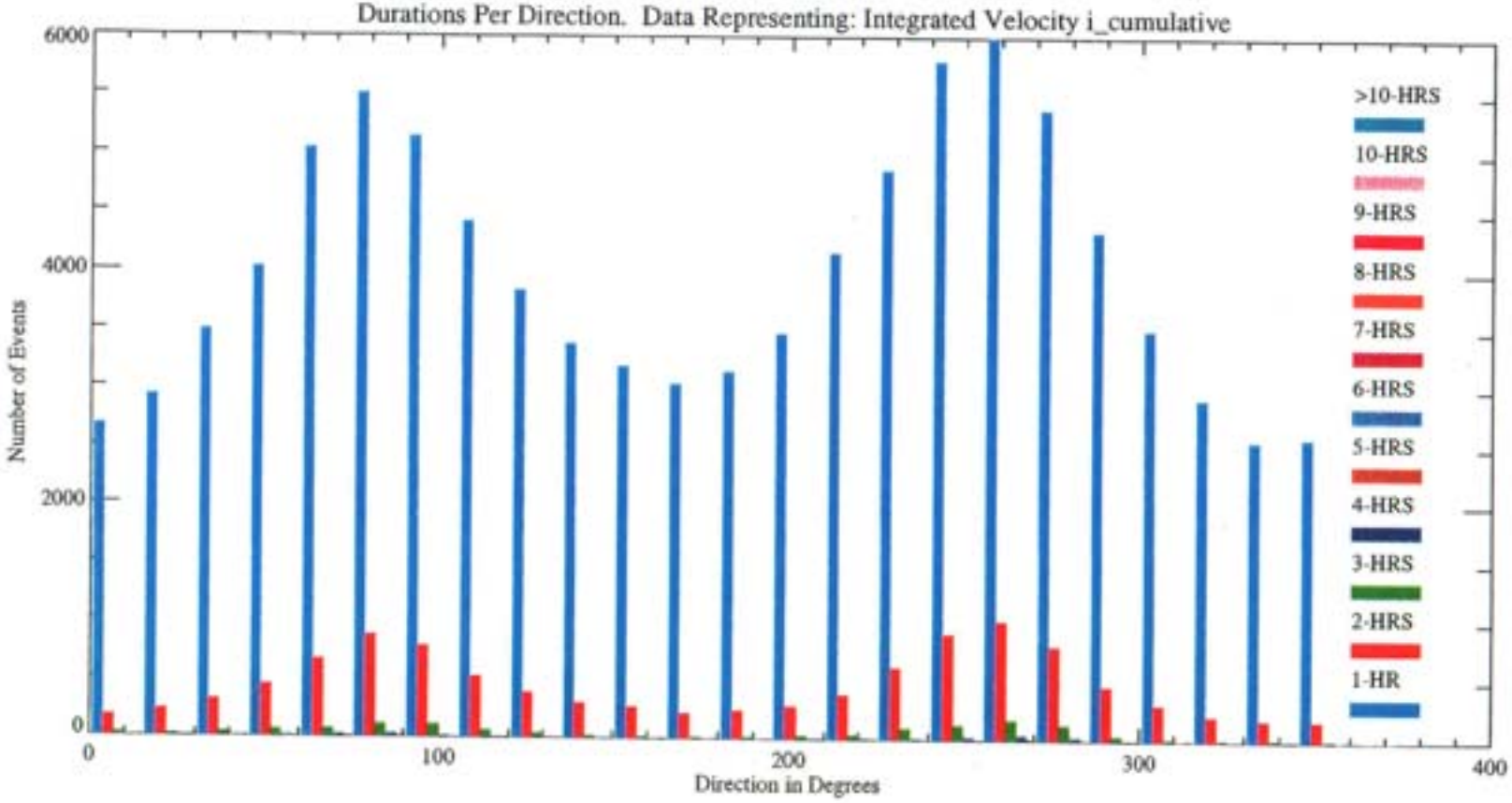
Durations Per Direction. Data Representing: Integrated Velocity i_cumulative
Number of Events
Direction in Degrees
0
2000
4000
6000
0
100
200
300
400
>10-HRS
10-HRS
9-HRS
8-HRS
7-HRS
6-HRS
5-HRS
4-HRS
3-HRS
2-HRS
1-HR

APPENDIX C
The Longest Duration/Direction Plots

The following plots will show the longest durations that have been registered for each one of the years and the seasons. The cumulative data is also represented.

Figure Captions

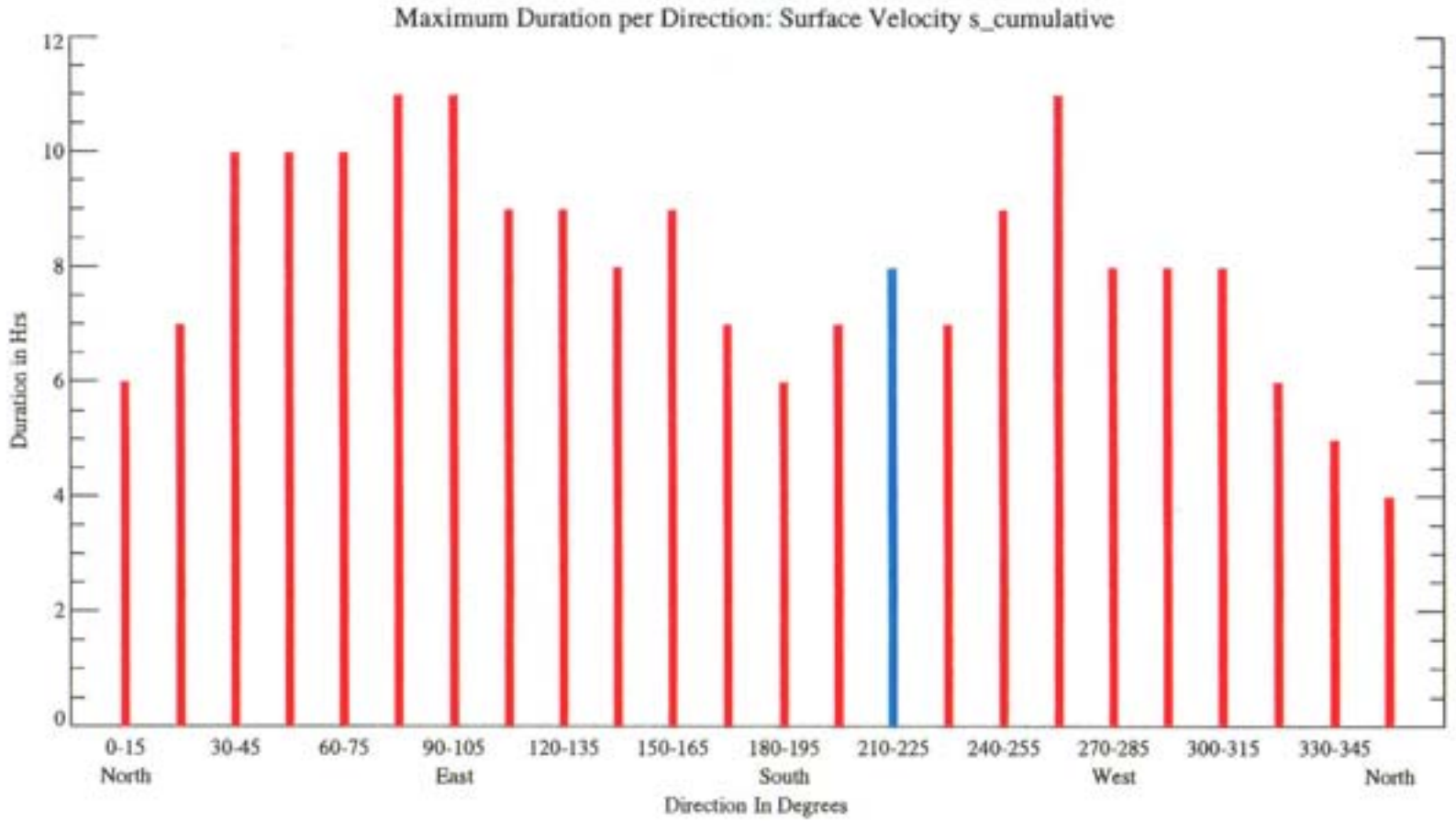
Maximum Duration per Direction: Surface Velocity s_cumulative
Duration in Hrs
0
2
4
6
8
10
12
0-15
North
30-45
60-75
90-105
East
120-135
150-165
180-195
South
210-225
240-255
270-285
West
300-315
330-345
North
Direction In Degrees

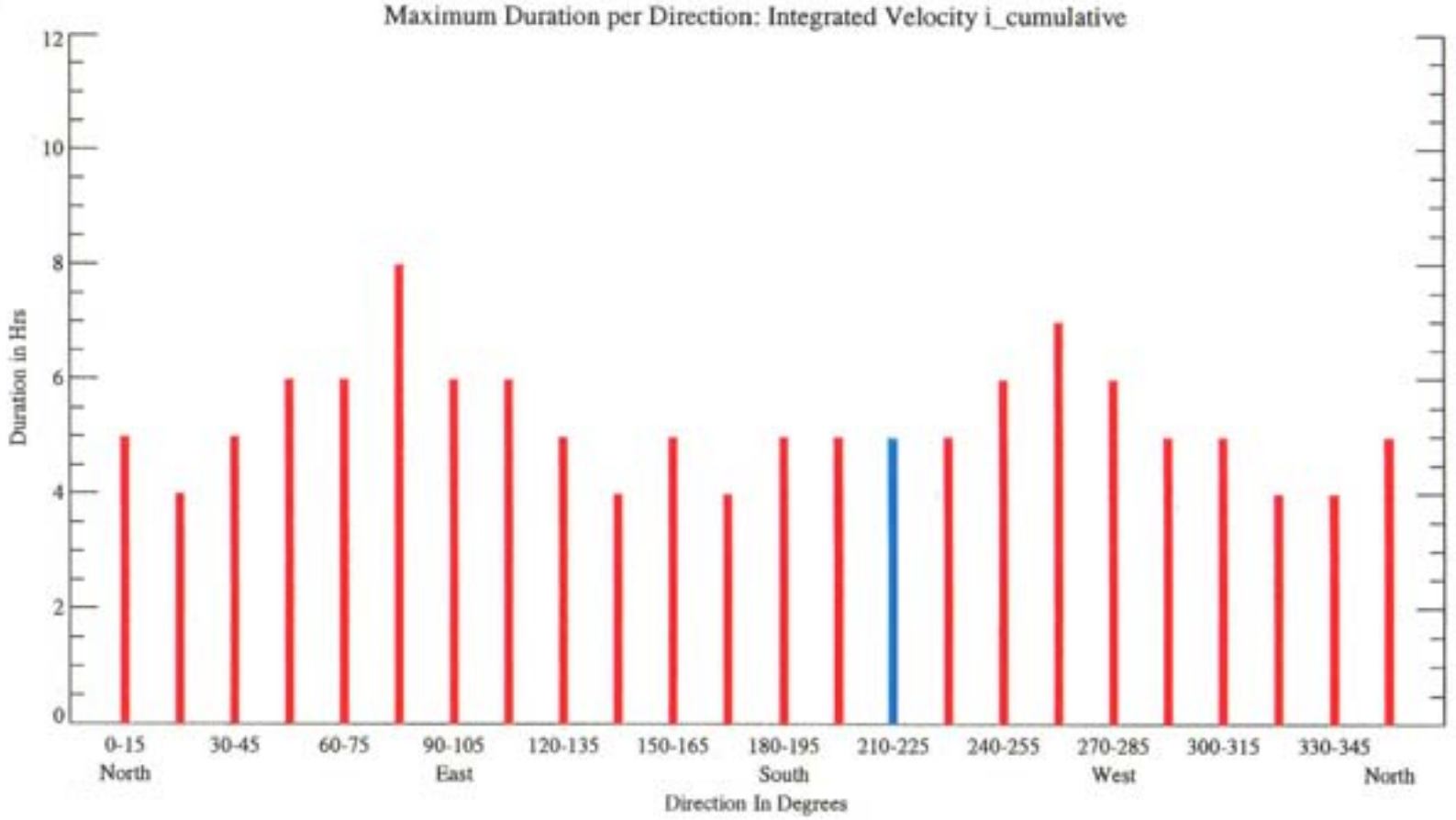
Maximum Duration per Direction: Integrated Velocity i_cumulative
Duration in Hrs
0
2
4
6
8
10
12
0-15
North
30-45
60-75
90-105
East
120-135
150-165
180-195
South
210-225
240-255
270-285
West
300-315
330-345
North
Direction In Degrees

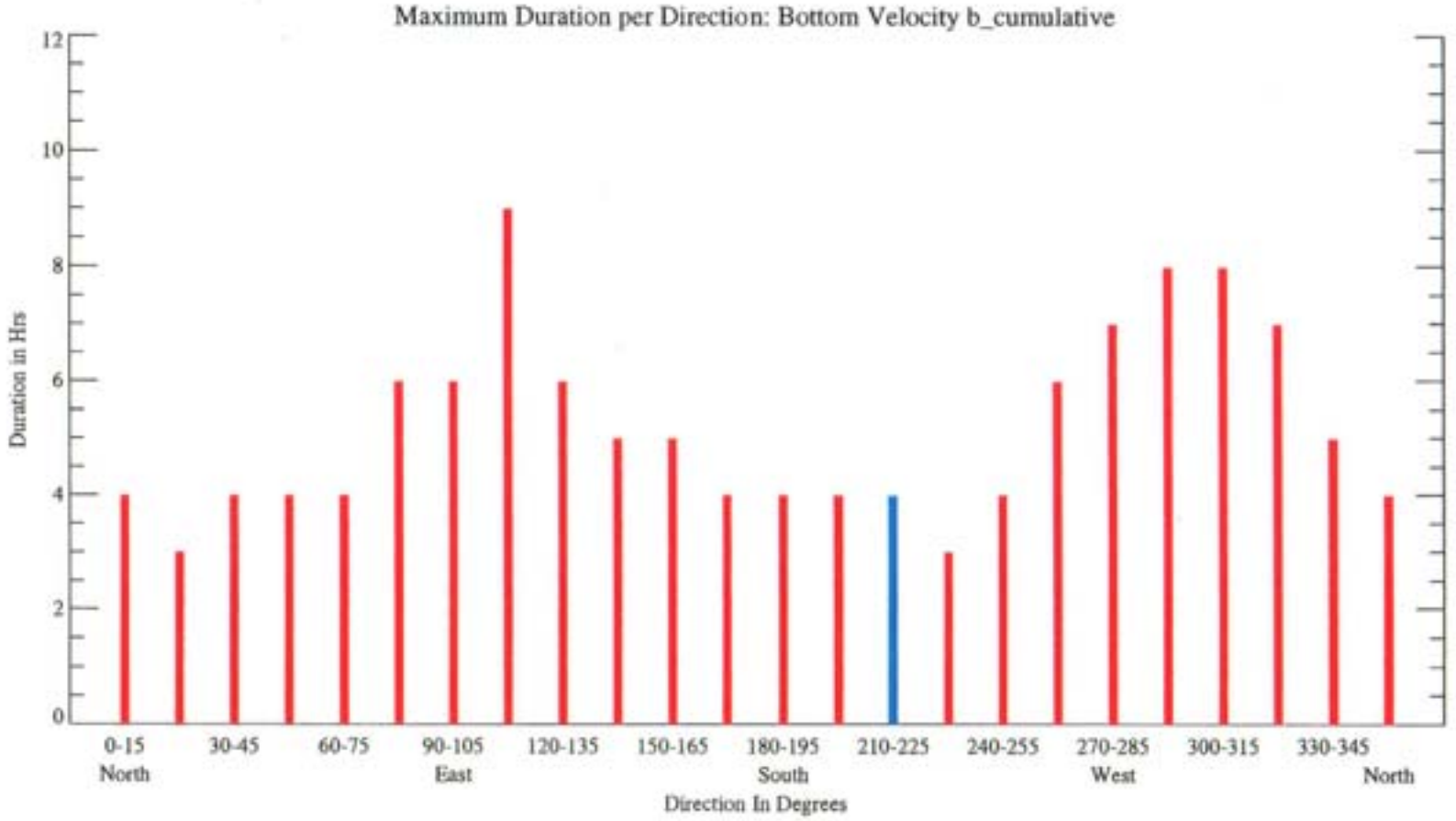
Maximum Duration per Direction: Bottom Velocity b_cumulative
Duration in Hrs
0
2
4
6
8
10
12
0-15
North
30-45
60-75
90-105
East
120-135
150-165
180-195
South
210-225
240-255
270-285
West
300-315
330-345
North
Direction In Degrees

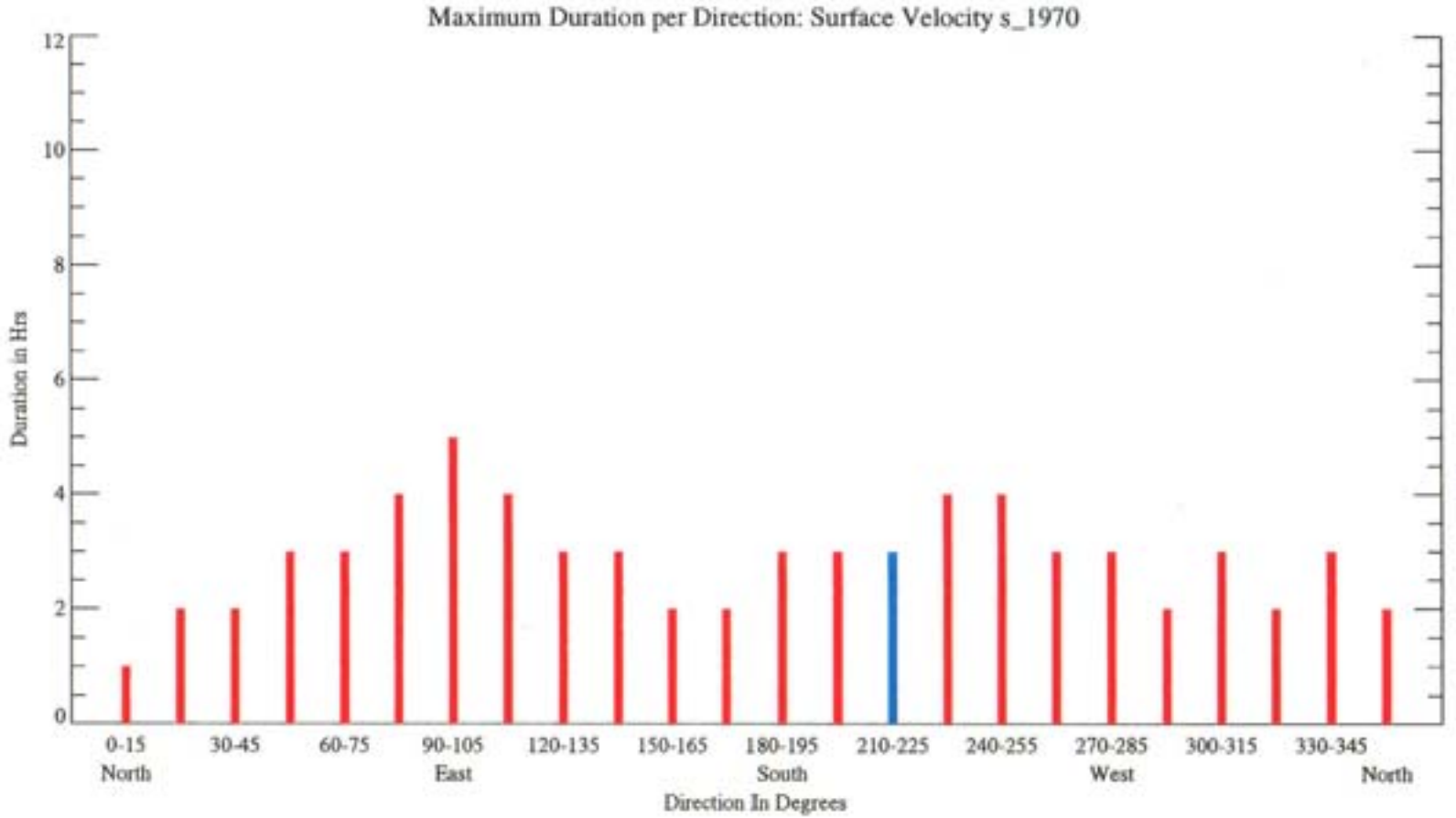
Maximum Duration per Direction: Surface Velocity s_1970
Duration in Hrs
0
2
4
6
8
10
12
0-15
North
30-45
60-75
90-105
East
120-135
150-165
180-195
South
210-225
240-255
270-285
West
300-315
330-345
North
Direction In Degrees

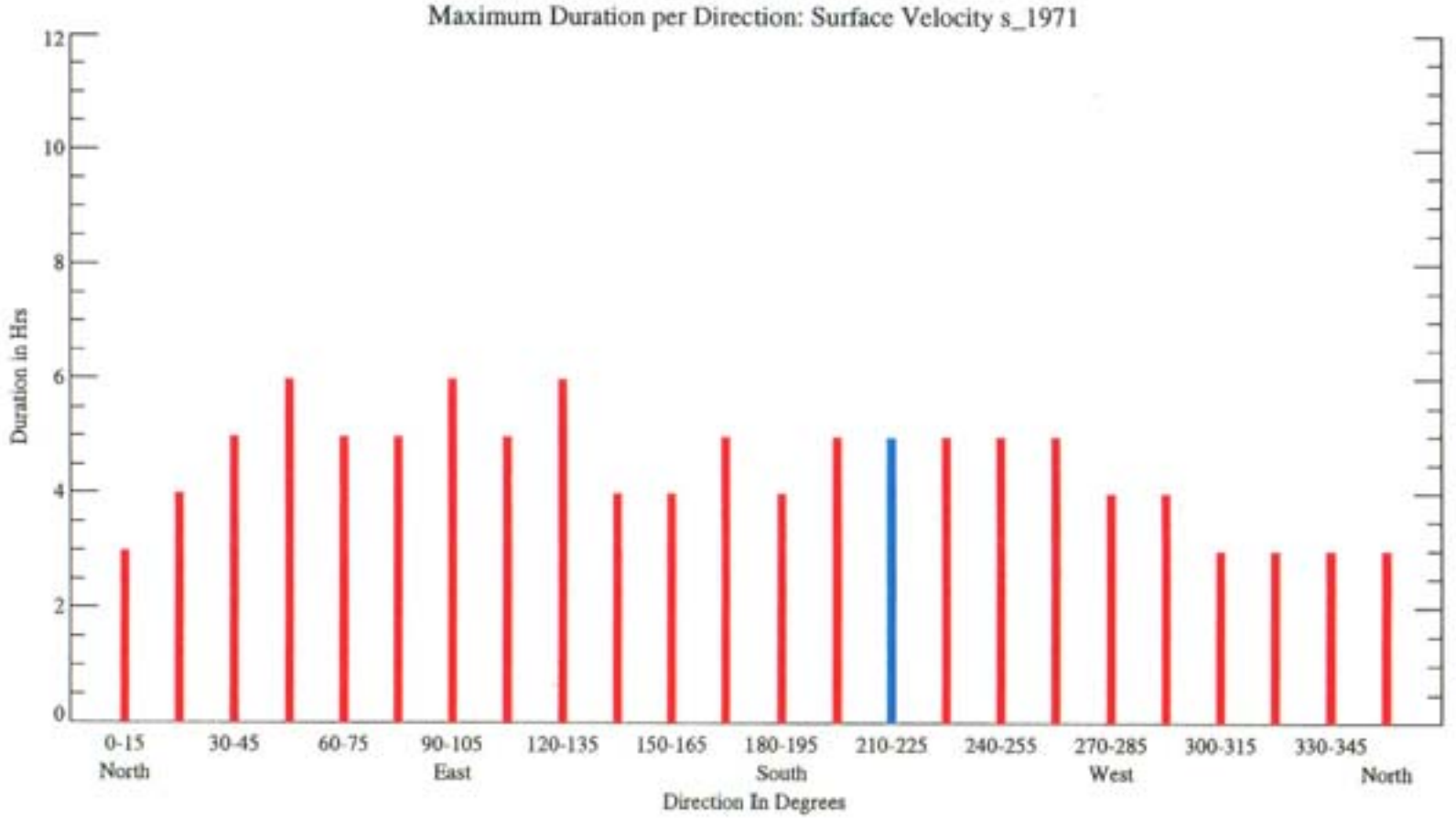
Maximum Duration per Direction: Surface Velocity s_1971
Duration in Hrs
0
2
4
6
8
10
12
0-15
North
30-45
60-75
90-105
East
120-135
150-165
180-195
South
210-225
240-255
270-285
West
300-315
330-345
North
Direction In Degrees

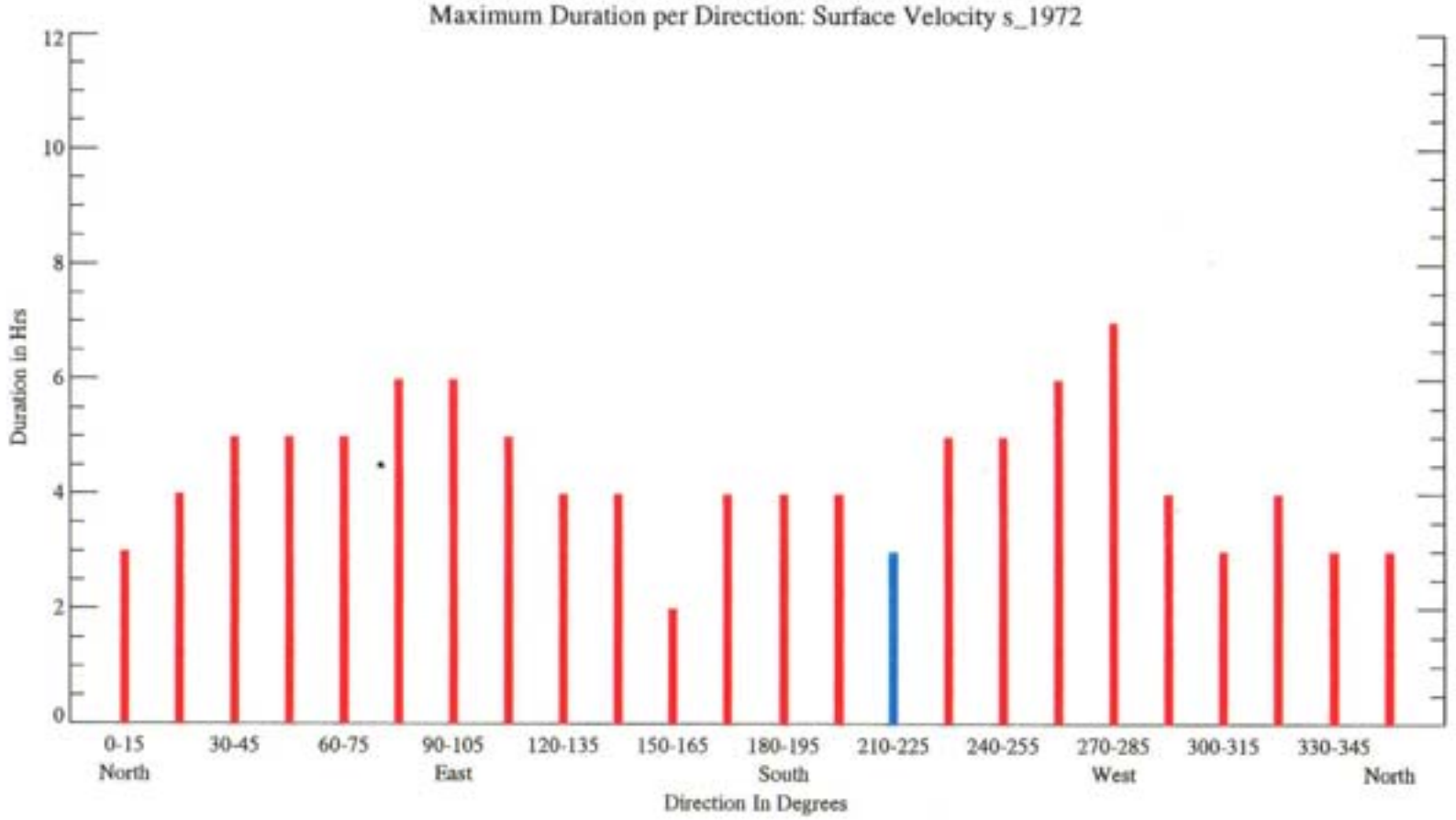
Maximum Duration per Direction: Surface Velocity s_1972
Duration in Hrs
0
2
4
6
8
10
12
0-15
North
30-45
60-75
90-105
East
120-135
150-165
180-195
South
210-225
240-255
270-285
West
300-315
330-345
North
Direction In Degrees

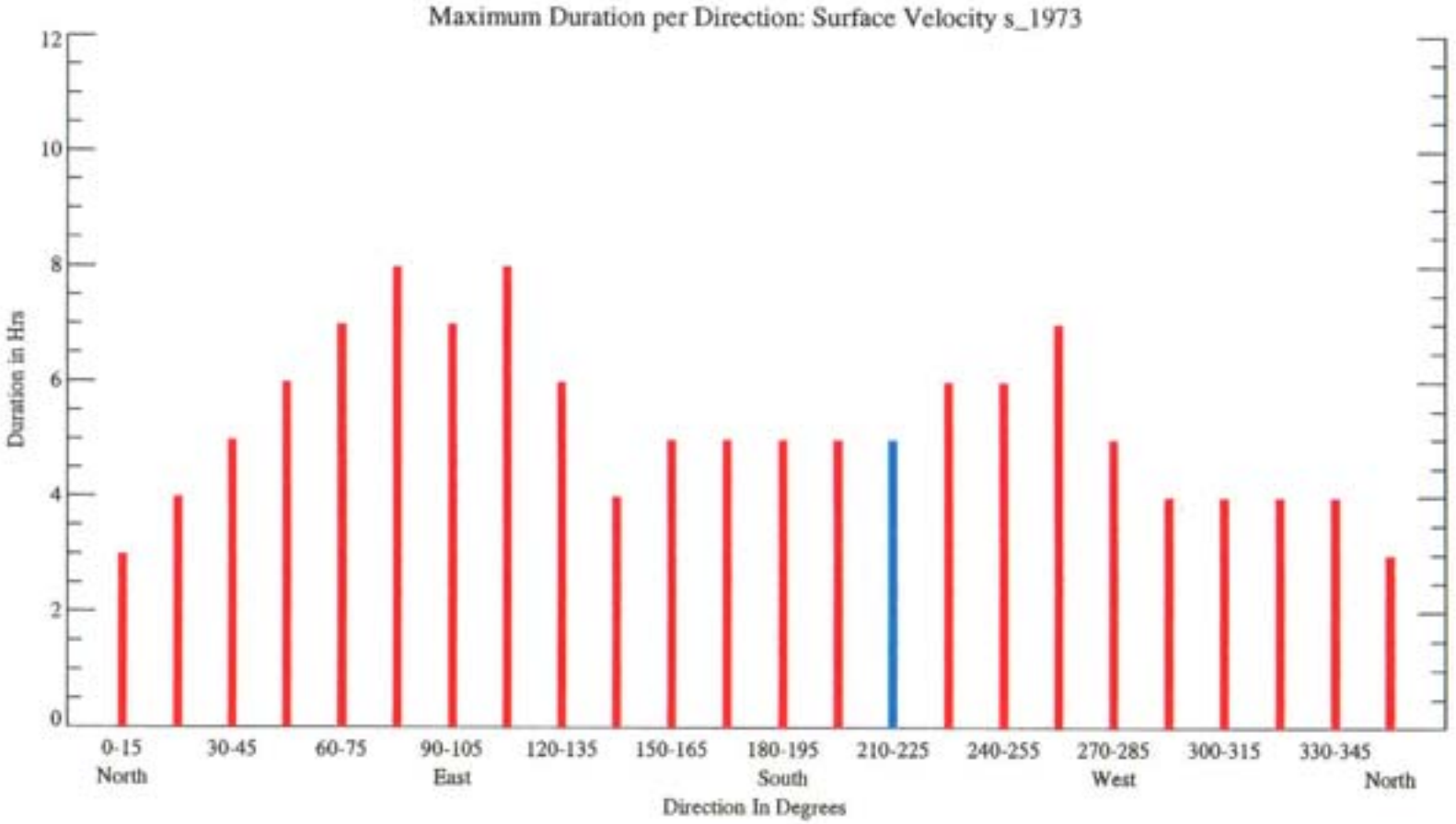
Maximum Duration per Direction: Surface Velocity s_1973
Duration in Hrs
0
2
4
6
8
10
12
0-15
North
30-45
60-75
90-105
East
120-135
150-165
180-195
South
210-225
240-255
270-285
West
300-315
330-345
North
Direction In Degrees

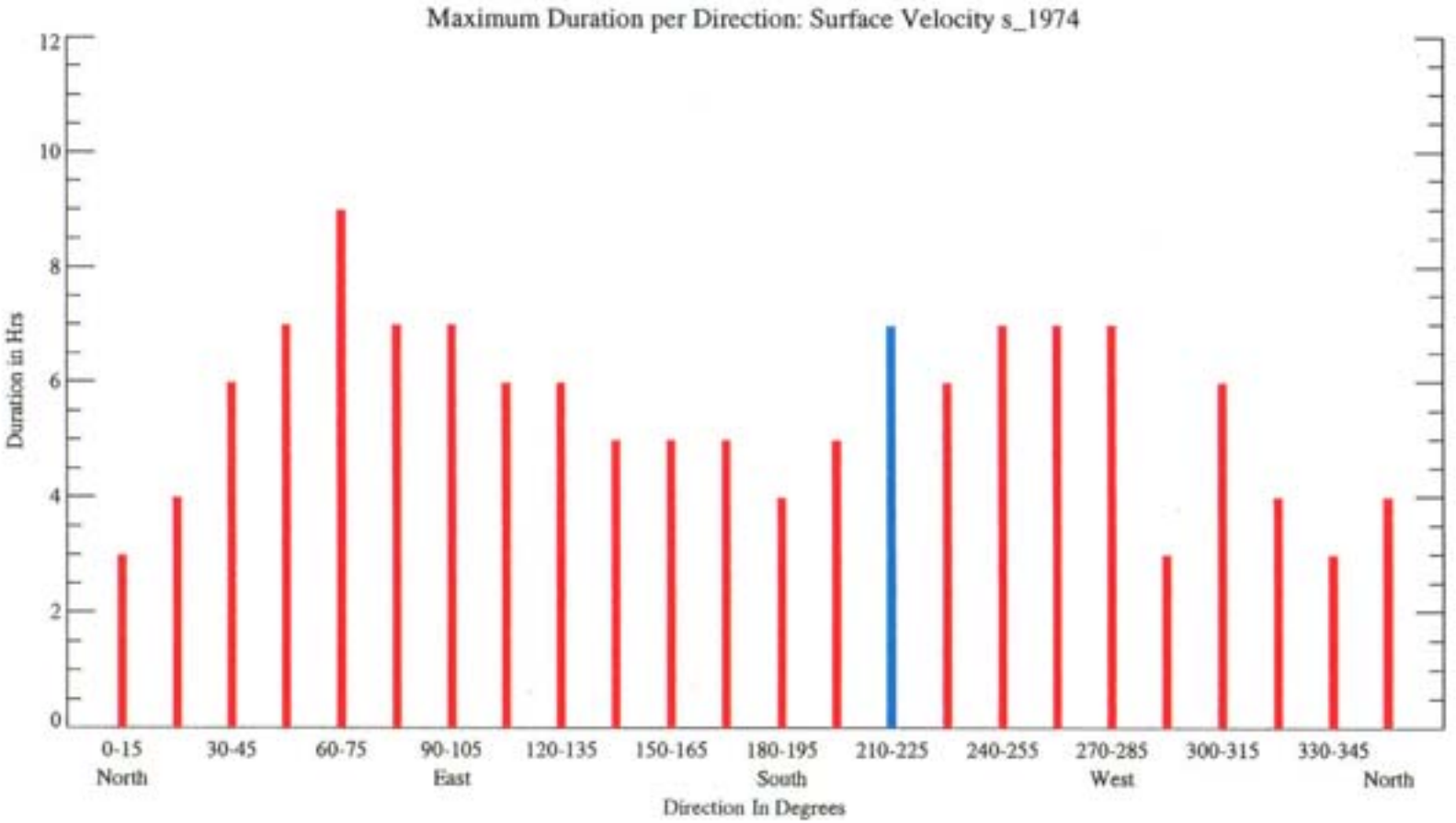
Maximum Duration per Direction: Surface Velocity s_1974
Duration in Hrs
0
2
4
6
8
10
12
0-15
North
30-45
60-75
90-105
East
120-135
150-165
180-195
South
210-225
240-255
270-285
West
300-315
330-345
North
Direction In Degrees

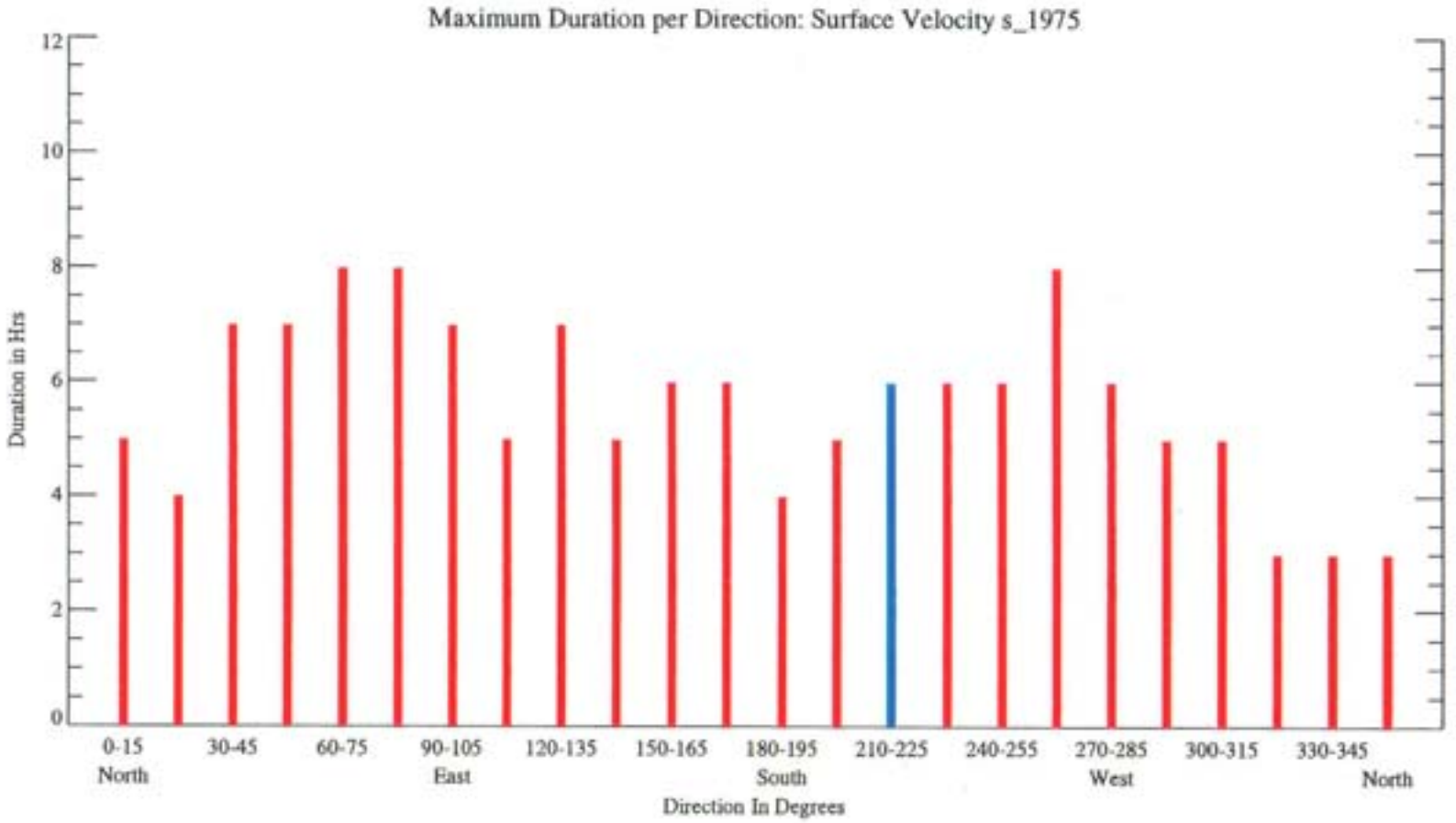
Maximum Duration per Direction: Surface Velocity s_1975
Duration in Hrs
0
2
4
6
8
10
12
0-15
North
30-45
60-75
90-105
East
120-135
150-165
180-195
South
210-225
240-255
270-285
West
300-315
330-345
North
Direction In Degrees

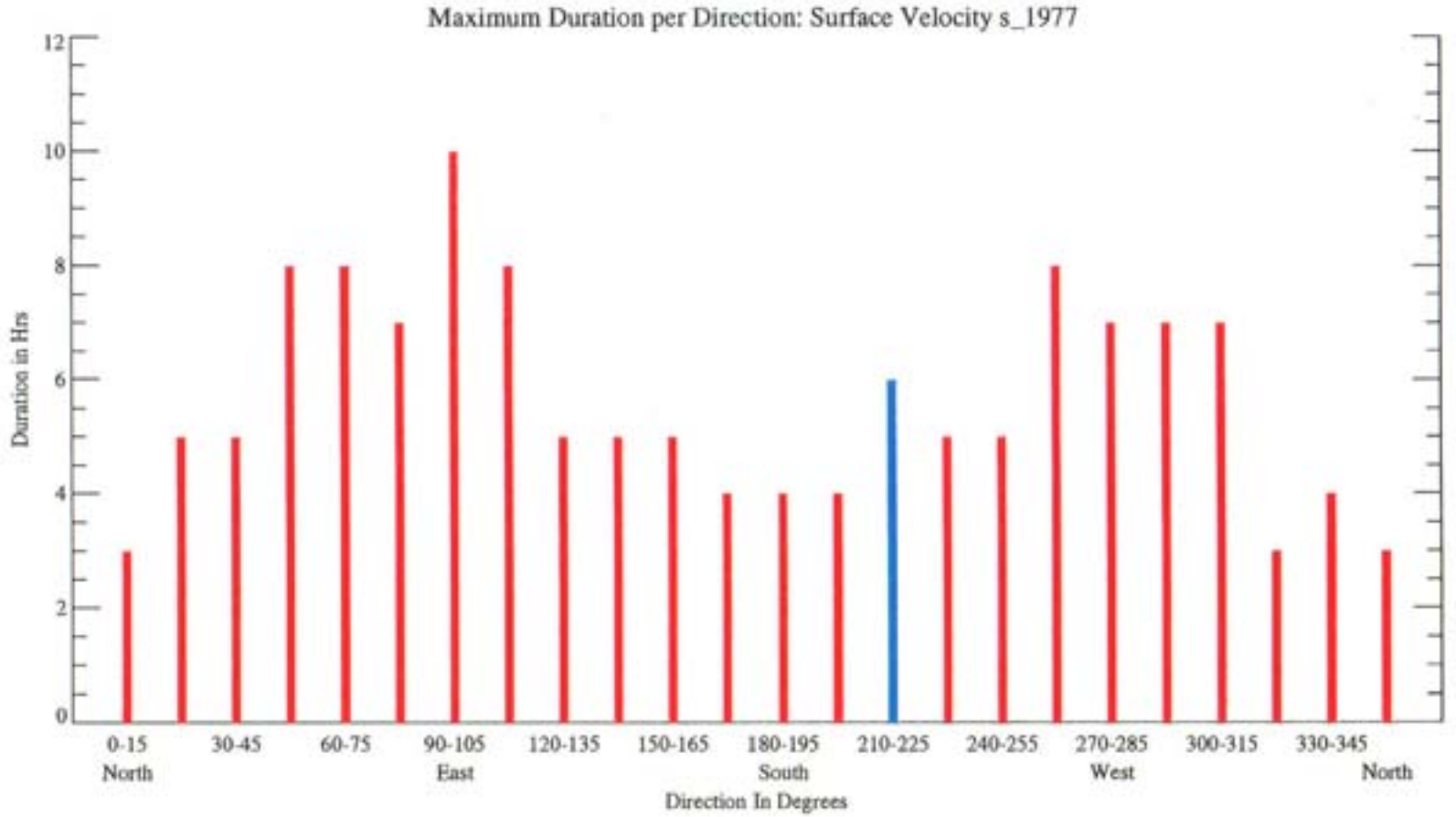
Maximum Duration per Direction: Surface Velocity s_1977
Duration in Hrs
0
2
4
6
8
10
12
0-15
North
30-45
60-75
90-105
East
120-135
150-165
180-195
South
210-225
240-255
270-285
West
300-315
330-345
North
Direction In Degrees

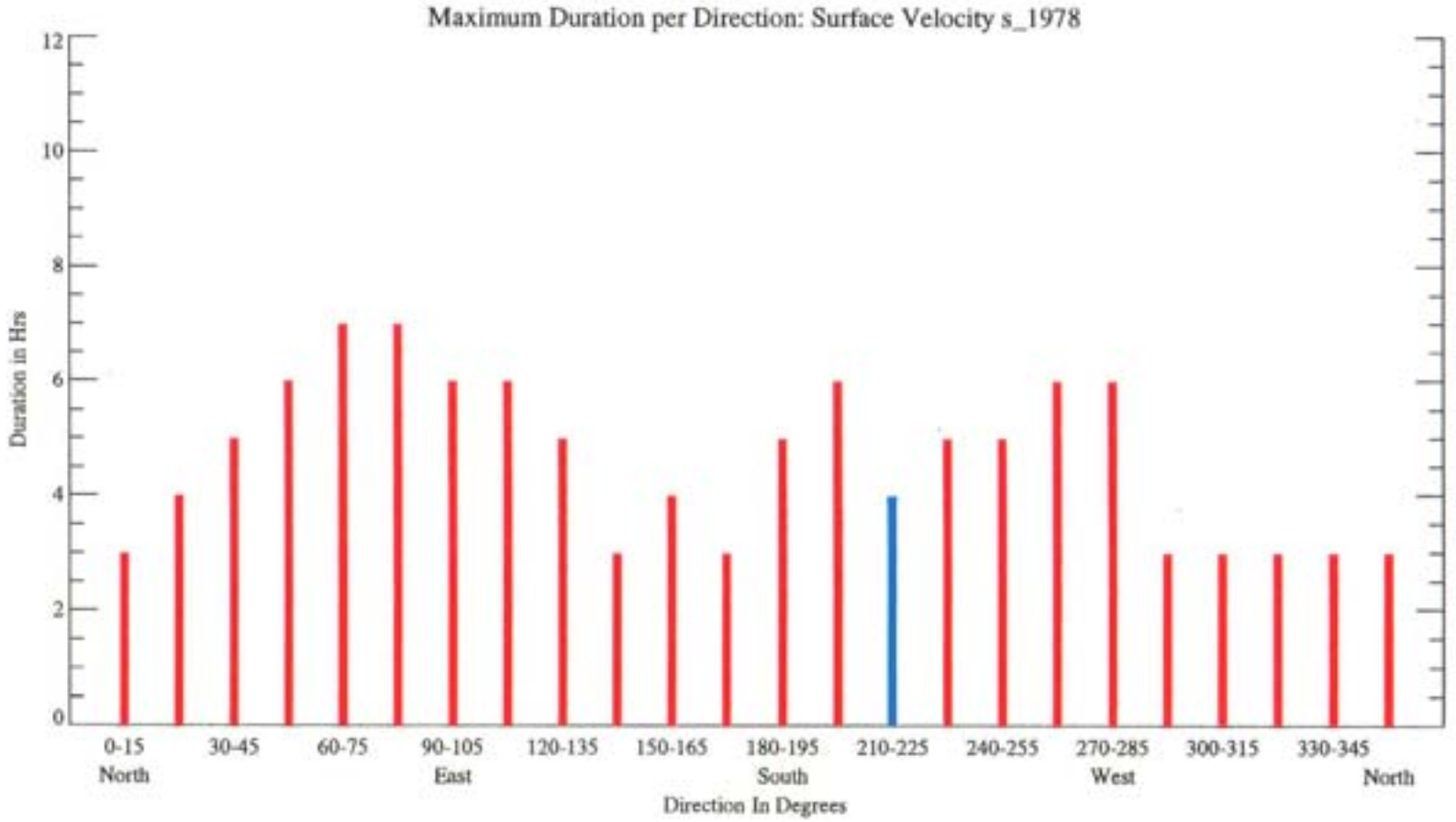
Maximum Duration per Direction: Surface Velocity s_1978
Duration in Hrs
0
2
4
6
8
10
12
0-15
North
30-45
60-75
90-105
East
120-135
150-165
180-195
South
210-225
240-255
270-285
West
300-315
330-345
North
Direction In Degrees

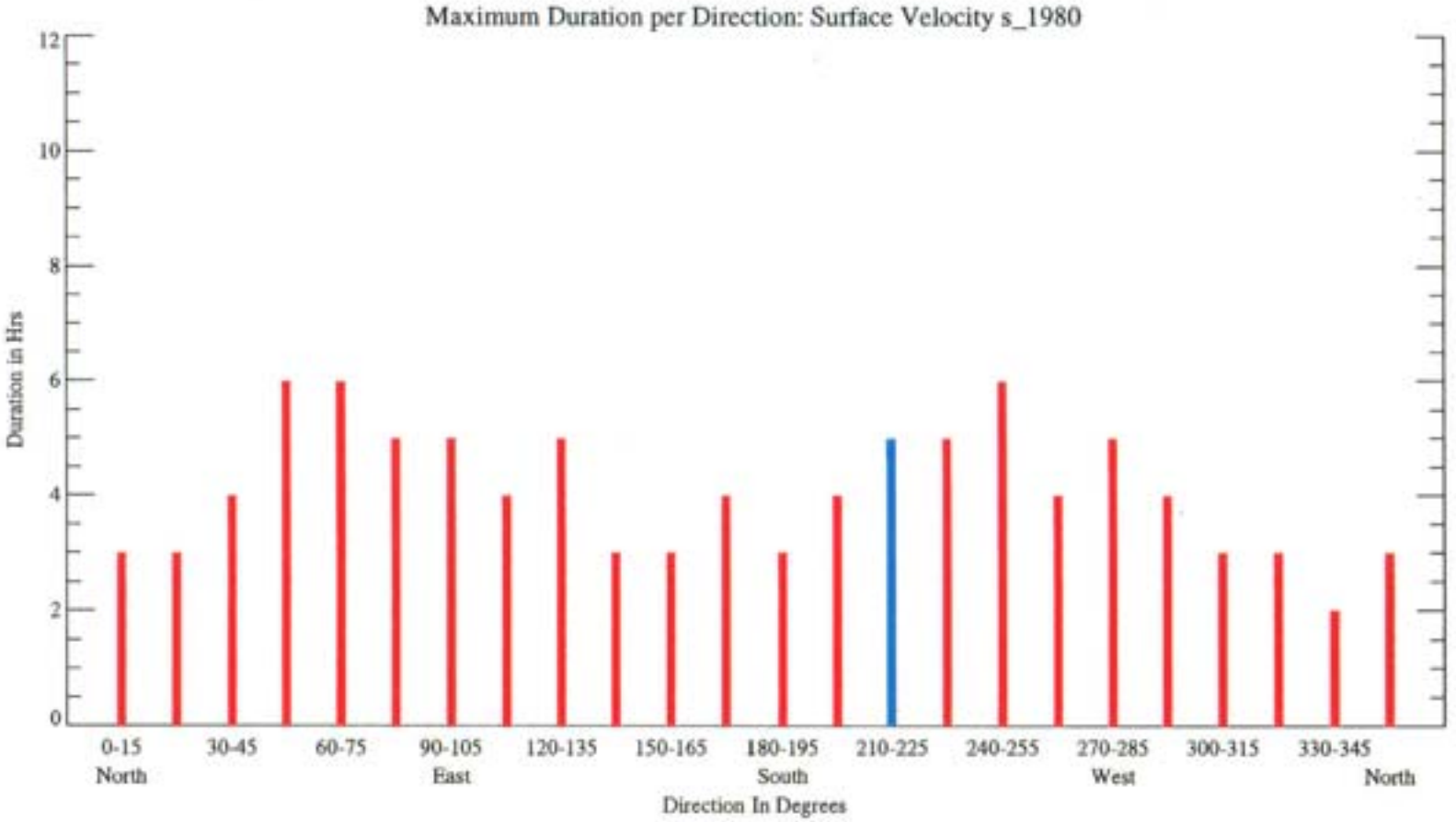
Maximum Duration per Direction: Surface Velocity s_1980
Duration in Hrs
0
2
4
6
8
10
12
0-15
North
30-45
60-75
90-105
East
120-135
150-165
180-195
South
210-225
240-255
270-285
West
300-315
330-345
North
Direction In Degrees

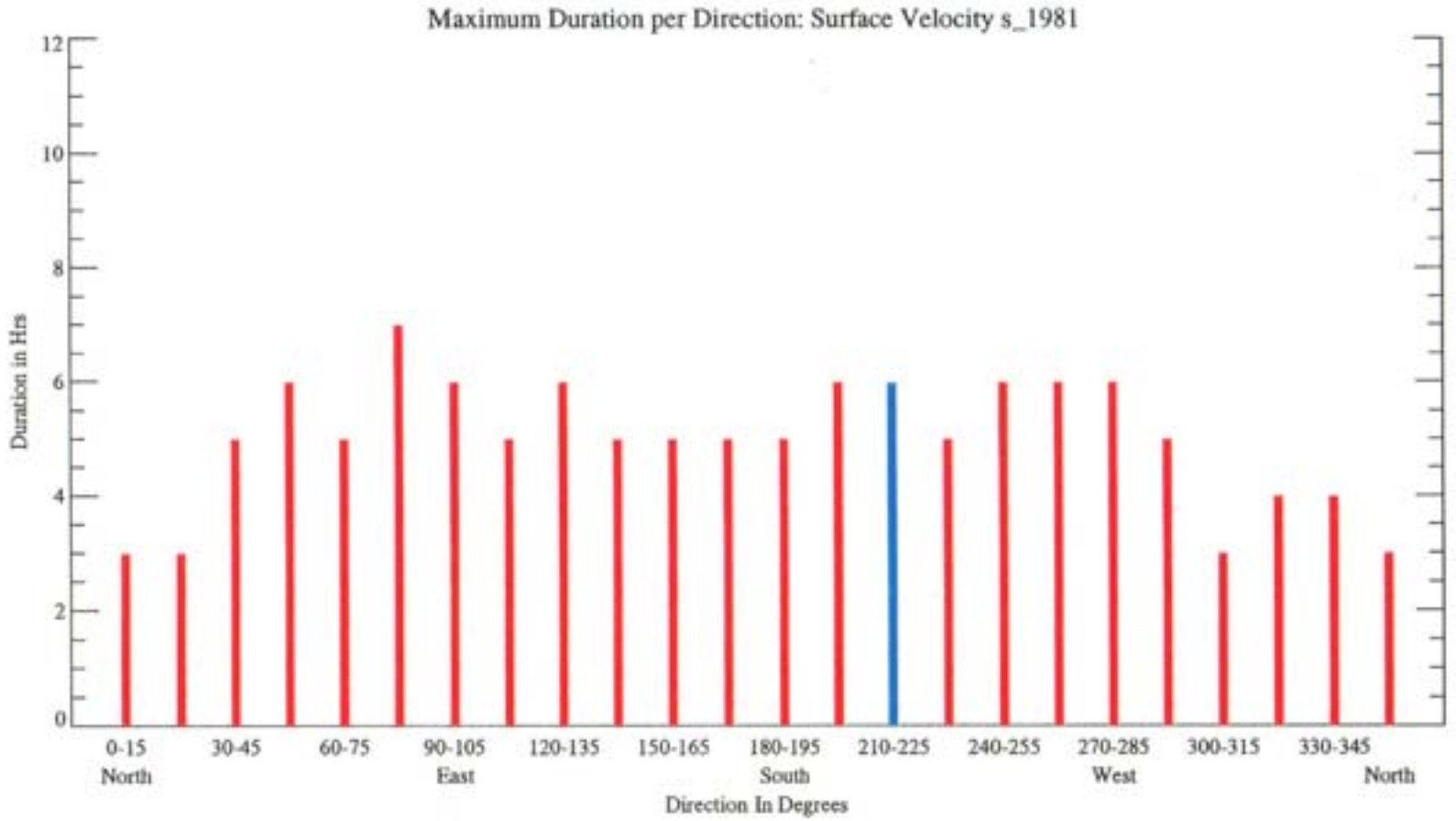
Maximum Duration per Direction: Surface Velocity s_1981
Duration in Hrs
0
2
4
6
8
10
12
0-15
North
30-45
60-75
90-105
East
120-135
150-165
180-195
South
210-225
240-255
270-285
West
300-315
330-345
North
Direction In Degrees

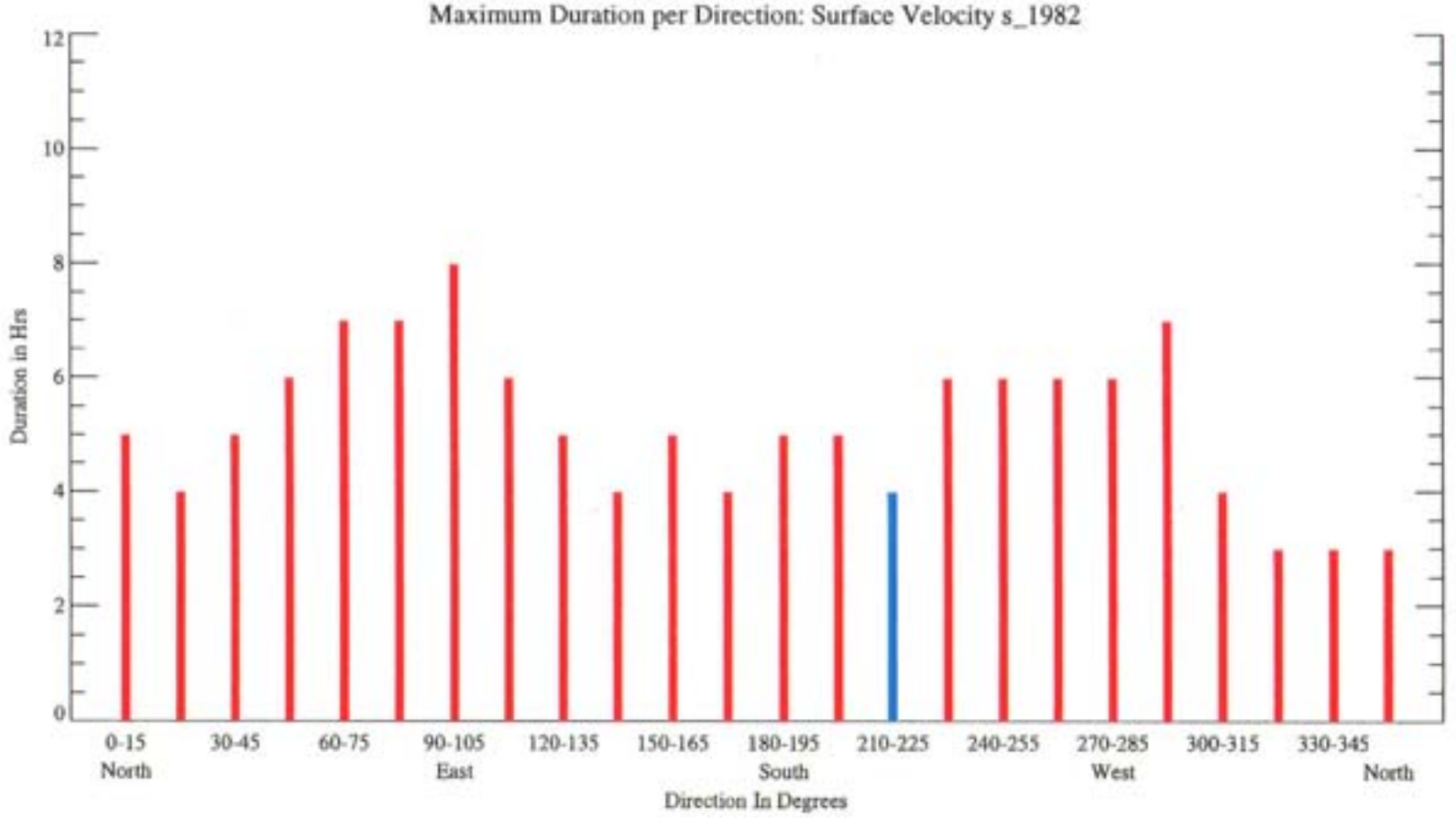
Maximum Duration per Direction: Surface Velocity s_1982
Duration in Hrs
0
2
4
6
8
10
12
0-15
North
30-45
60-75
90-105
East
120-135
150-165
180-195
South
210-225
240-255
270-285
West
300-315
330-345
North
Direction In Degrees

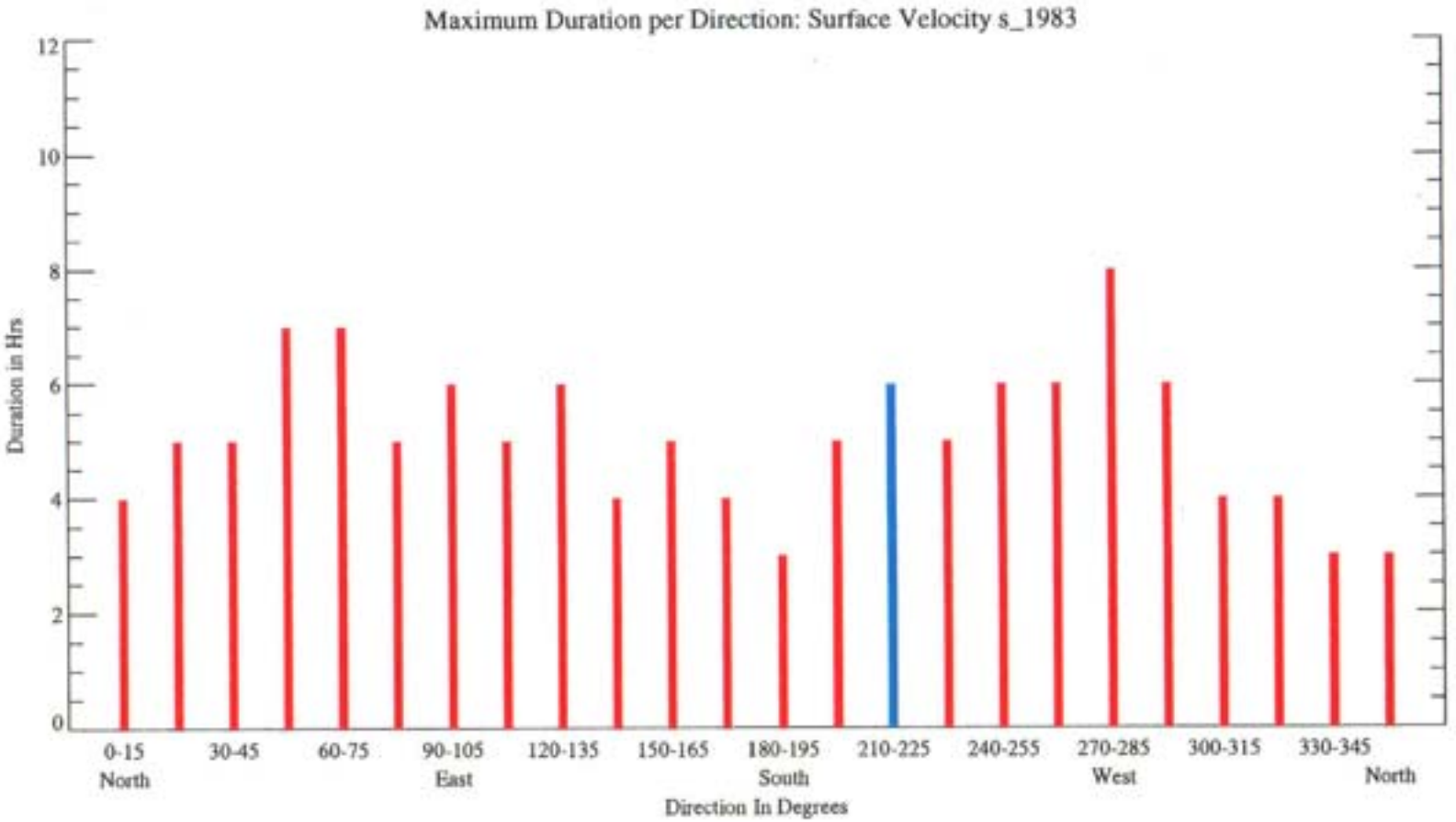
Maximum Duration per Direction: Surface Velocity s_1983
Duration in Hrs
0
2
4
6
8
10
12
0-15
North
30-45
60-75
90-105
East
120-135
150-165
180-195
South
210-225
240-255
270-285
West
300-315
330-345
North
Direction In Degrees

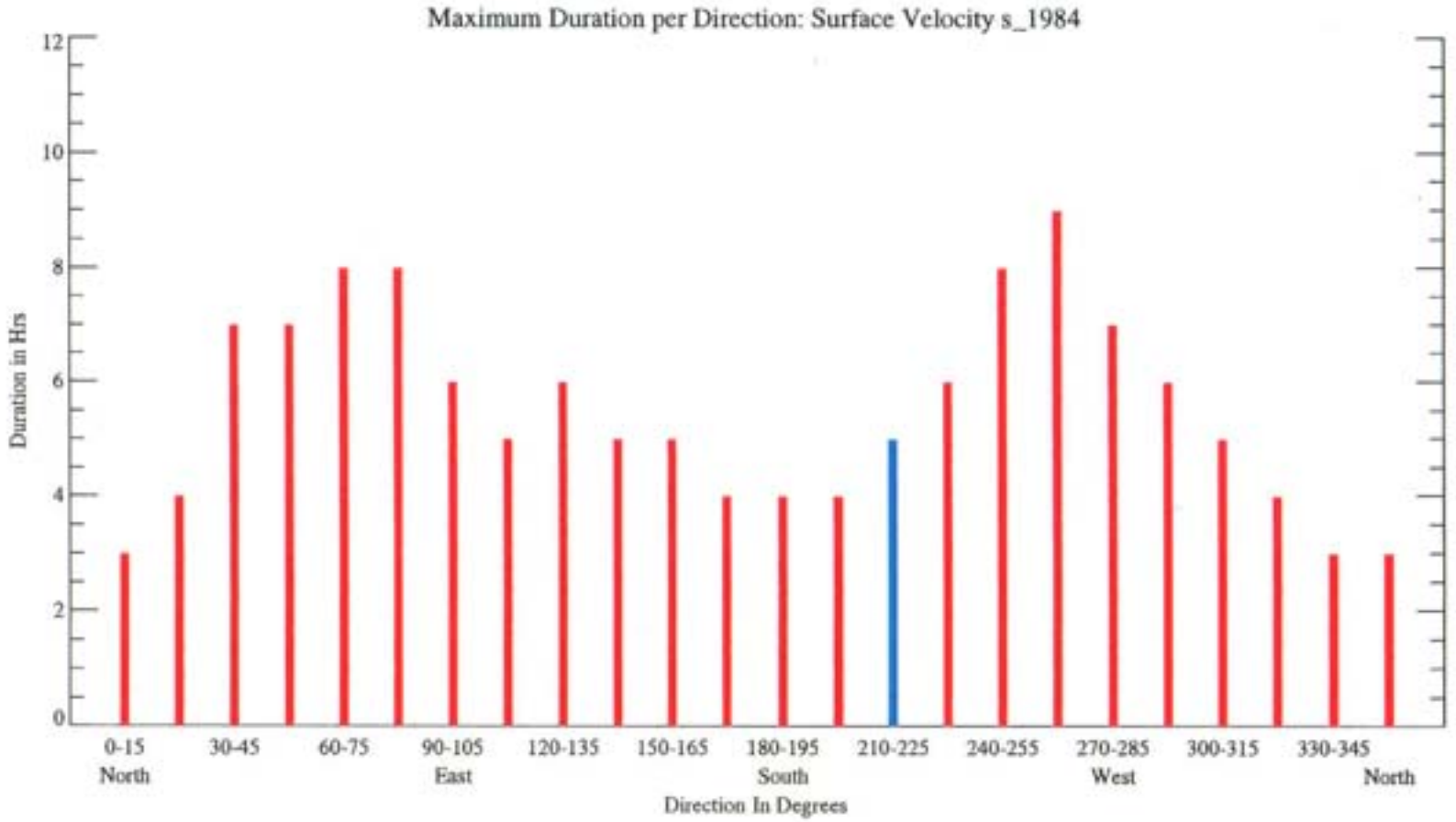
Maximum Duration per Direction: Surface Velocity s_1984
Duration in Hrs
0
2
4
6
8
10
12
0-15
North
30-45
60-75
90-105
East
120-135
150-165
180-195
South
210-225
240-255
270-285
West
300-315
330-345
North
Direction In Degrees

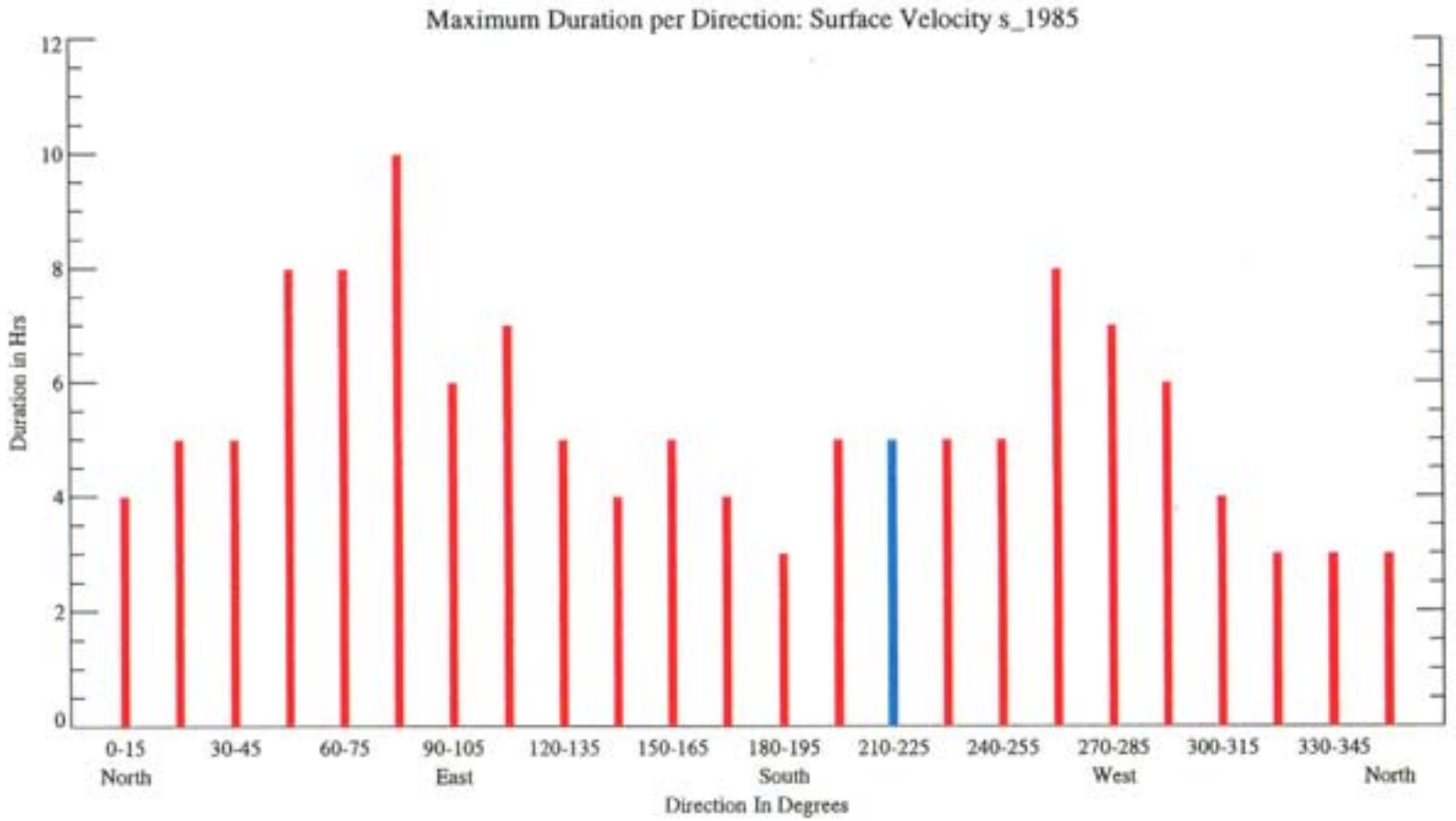
Maximum Duration per Direction: Surface Velocity s_1985
Duration in Hrs
0
2
4
6
8
10
12
0-15
North
30-45
60-75
90-105
East
120-135
150-165
180-195
South
210-225
240-255
270-285
West
300-315
330-345
North
Direction In Degrees

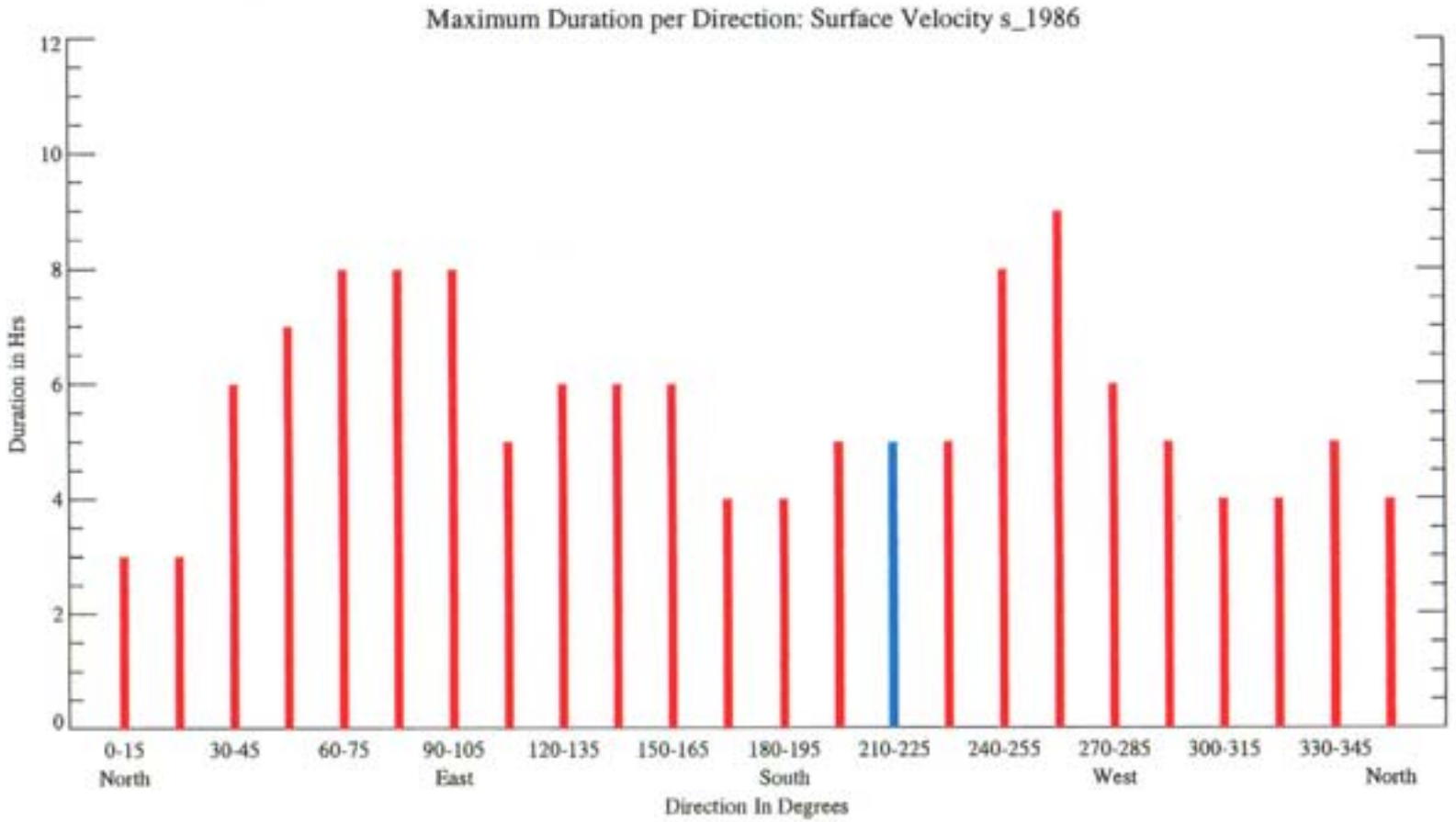
Maximum Duration per Direction: Surface Velocity s_1986
Duration in Hrs
0
2
4
6
8
10
12
0-15
North
30-45
60-75
90-105
East
120-135
150-165
180-195
South
210-225
240-255
270-285
West
300-315
330-345
North
Direction In Degrees

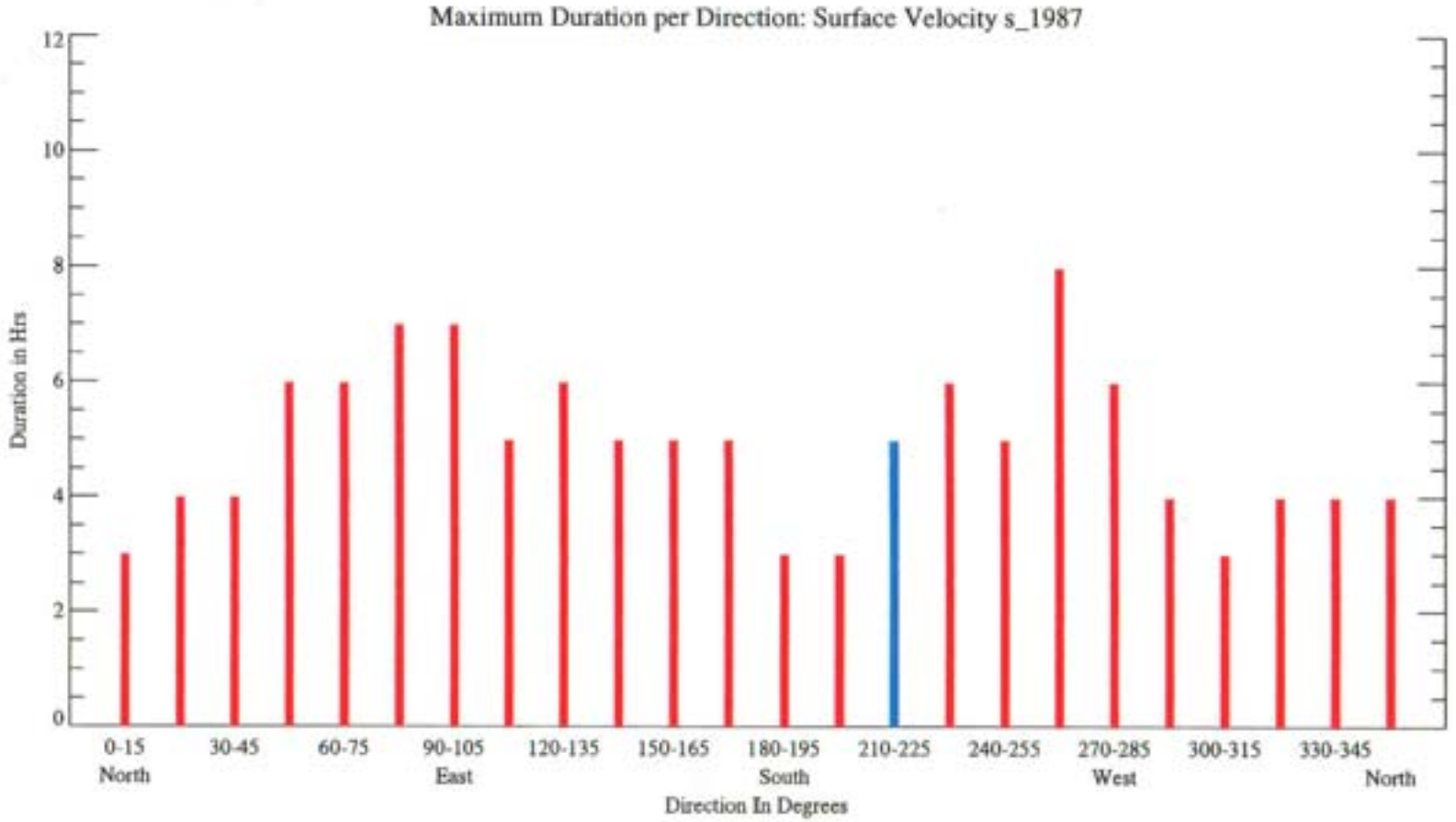
Maximum Duration per Direction: Surface Velocity s_1987
Duration in Hrs
0
2
4
6
8
10
12
0-15
North
30-45
60-75
90-105
East
120-135
150-165
180-195
South
210-225
240-255
270-285
West
300-315
330-345
North
Direction In Degrees

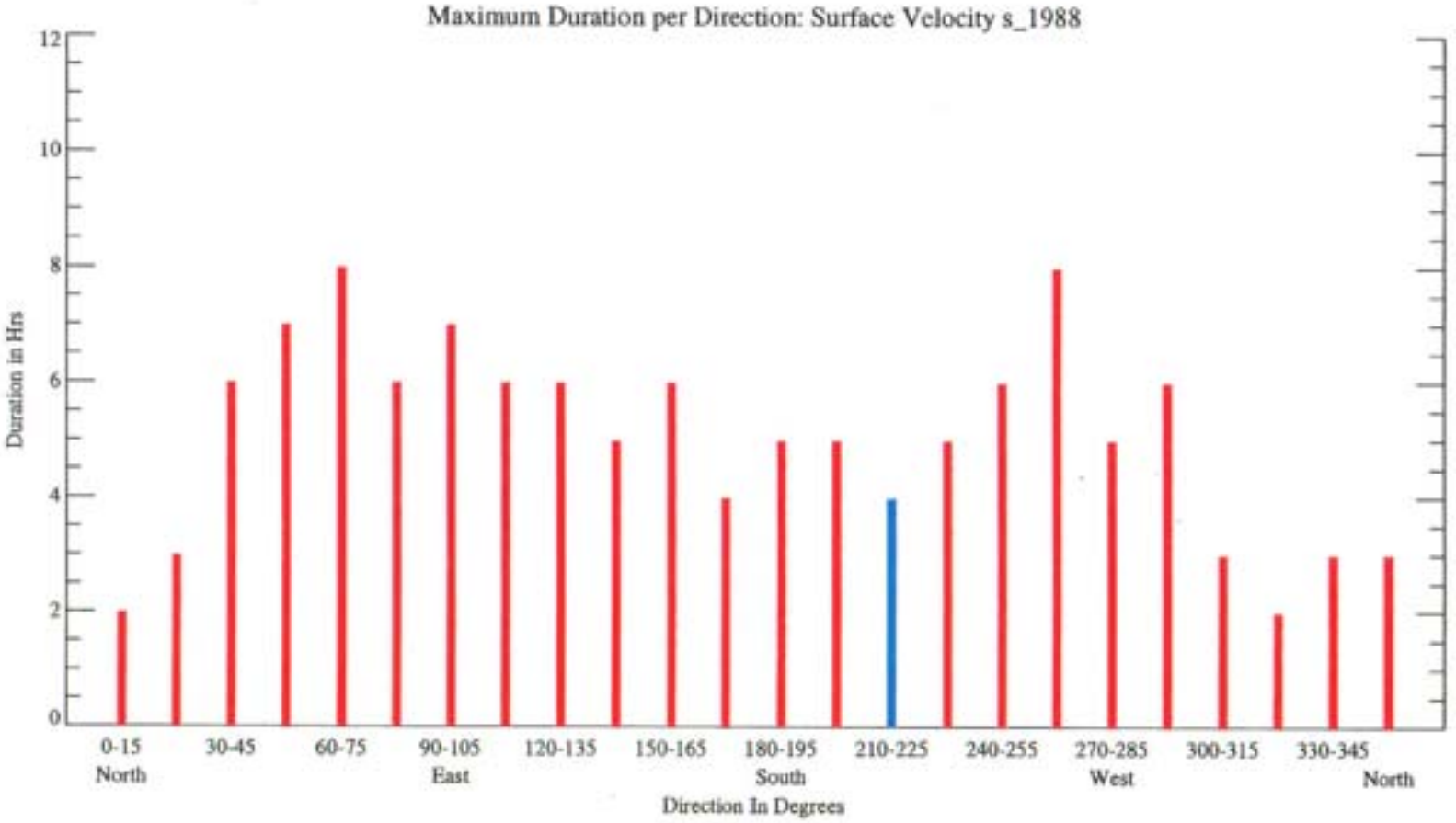
Maximum Duration per Direction: Surface Velocity s_1988
Duration in Hrs
0
2
4
6
8
10
12
0-15
North
30-45
60-75
90-105
East
120-135
150-165
180-195
South
210-225
240-255
270-285
West
300-315
330-345
North
Direction In Degrees

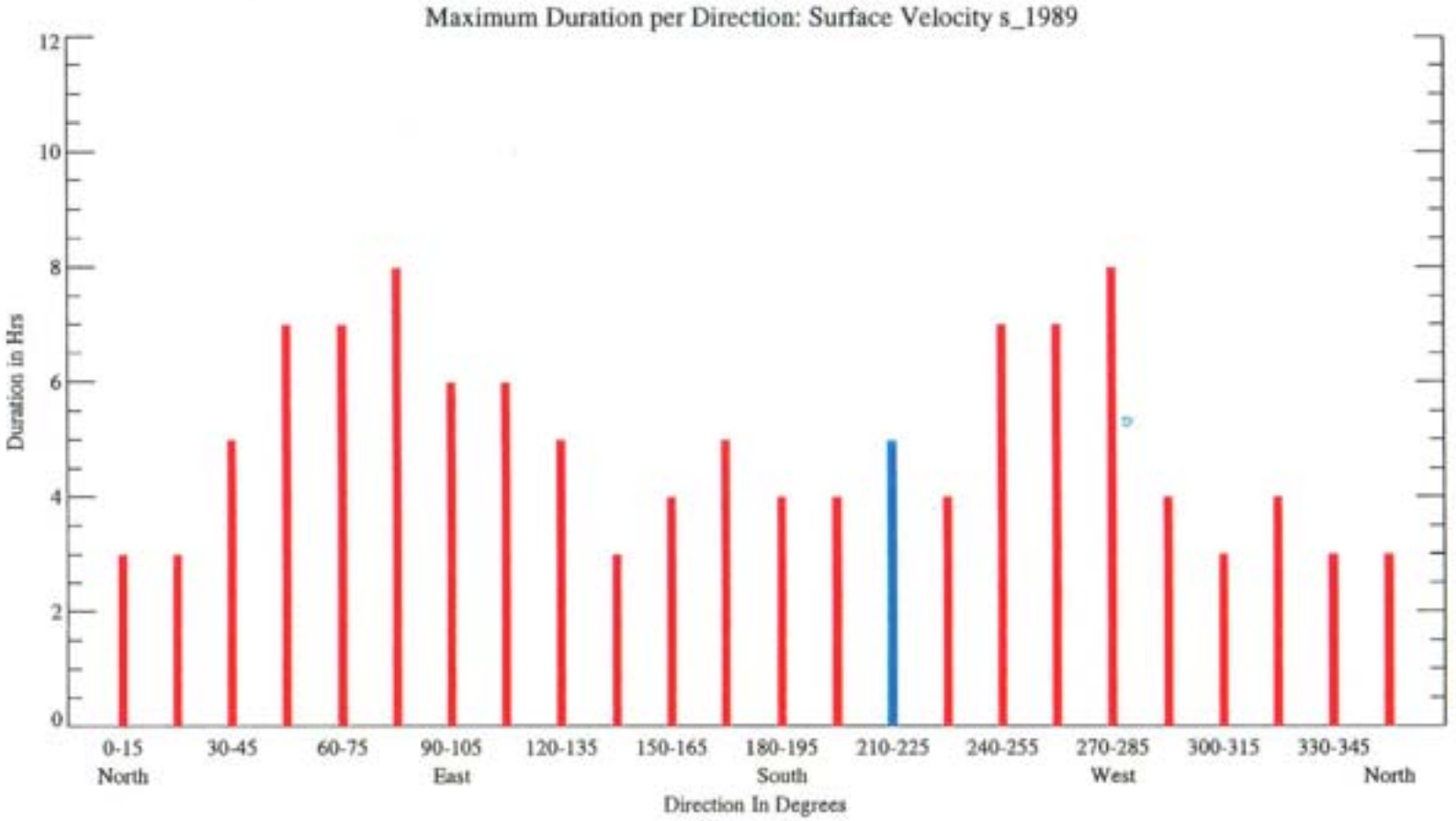
Maximum Duration per Direction: Surface Velocity s_1989
Duration in Hrs
0
2
4
6
8
10
12
0-15
North
30-45
60-75
90-105
East
120-135
150-165
180-195
South
210-225
240-255
270-285
West
300-315
330-345
North
Direction In Degrees

APPENDIX D
The Velocity Magnitude Plots

The following plots will show the magnitudes as a function of direction maximum, minimum, and average magnitudes velocities.

Figure Captions

D.1 Bottom Velocity: Magnitude per Direction for the Year 1971
D.2 Bottom Velocity: Magnitude per Direction for the Year 1972
D.3 Bottom Velocity: Magnitude per Direction for the Year 1973
D.4 Bottom Velocity: Magnitude per Direction for the Year 1974
D.5 Bottom Velocity: Magnitude per Direction for the Year 1975
D.6 Bottom Velocity: Magnitude per Direction for the Year 1977
D.7 Bottom Velocity: Magnitude per Direction for the Year 1978
D.8 Surface Velocity: Magnitude per Direction for the Year 1980

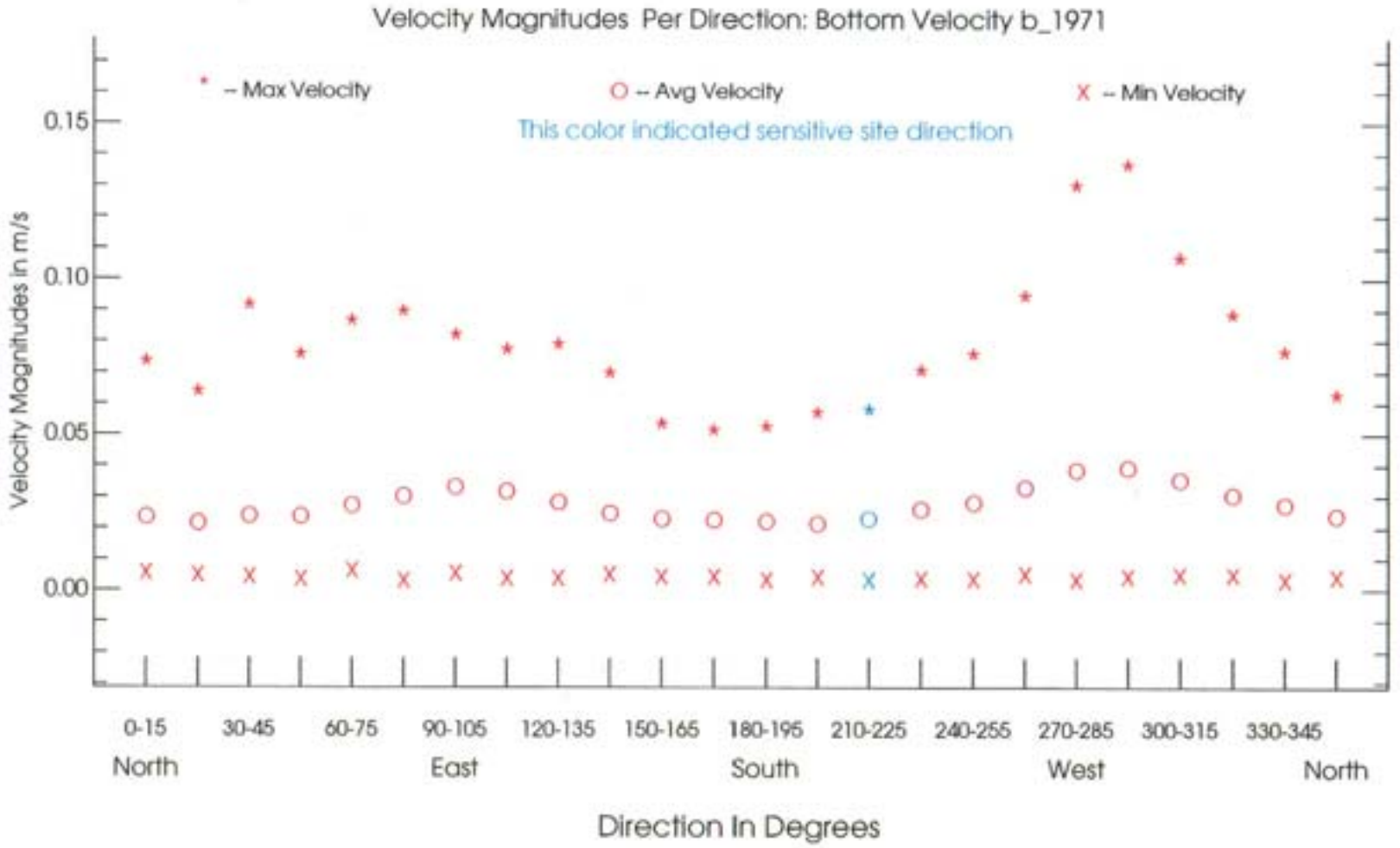
Velocity Magnitudes Per Direction: Bottom Velocity b_1971
* -- Max Velocity
O -- Avg Velocity
X -- Min Velocity
This color indicated sensitive site direction
Velocity Magnitudes in m/s
0.15
0.10
0.05
0.00
0-15
North
30-45
60-75
90-105
East
120-135
150-165
180-195
South
210-225
240-255
270-285
West
300-315
330-345
North
Direction In Degrees

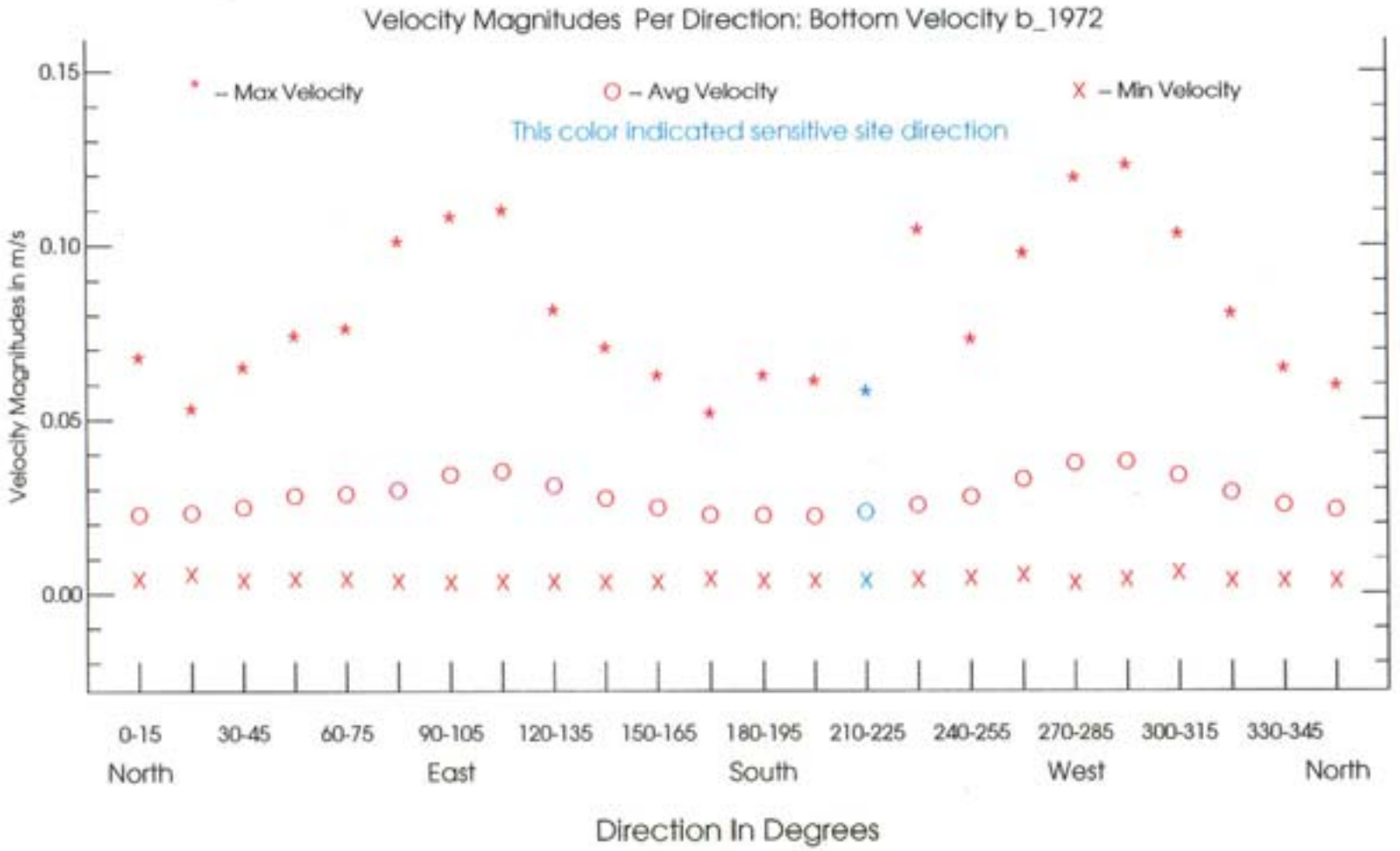
Velocity Magnitudes Per Direction: Bottom Velocity b_1972
* – Max Velocity
O – Avg Velocity
X – Min Velocity
This color indicated sensitive site direction
Velocity Magnitudes in m/s
0.15
0.10
0.05
0.00
0-15
30-45
60-75
90-105
120-135
150-165
180-195
210-225
240-255
270-285
300-315
330-345
North
East
South
West
North
Direction In Degrees

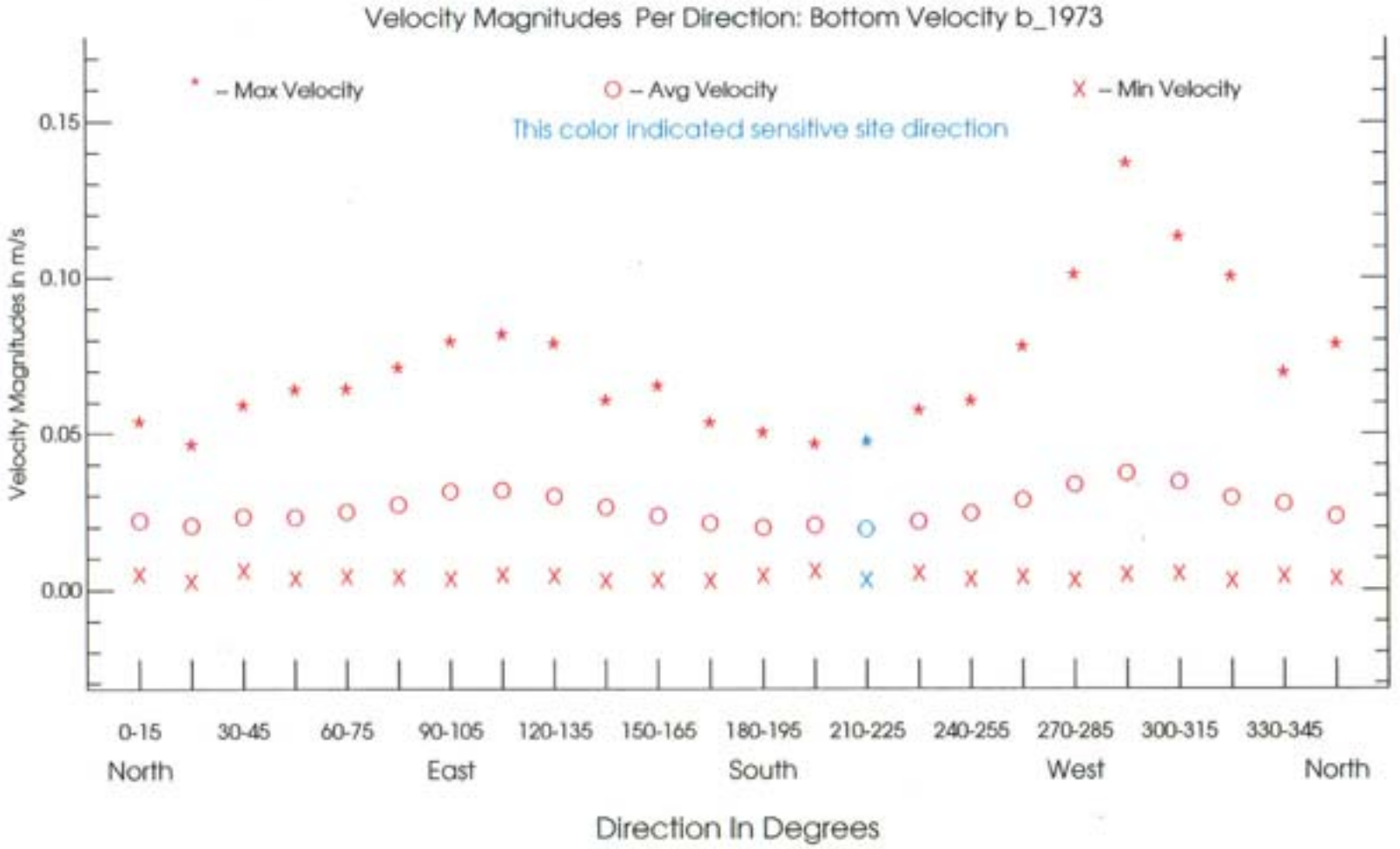
Velocity Magnitudes Per Direction: Bottom Velocity b_1973
* – Max Velocity
O – Avg Velocity
X – Min Velocity
This color indicated sensitive site direction
Velocity Magnitudes in m/s
0.15
0.10
0.05
0.00
0-15
30-45
60-75
90-105
120-135
150-165
180-195
210-225
240-255
270-285
300-315
330-345
North
East
South
West
North
Direction In Degrees

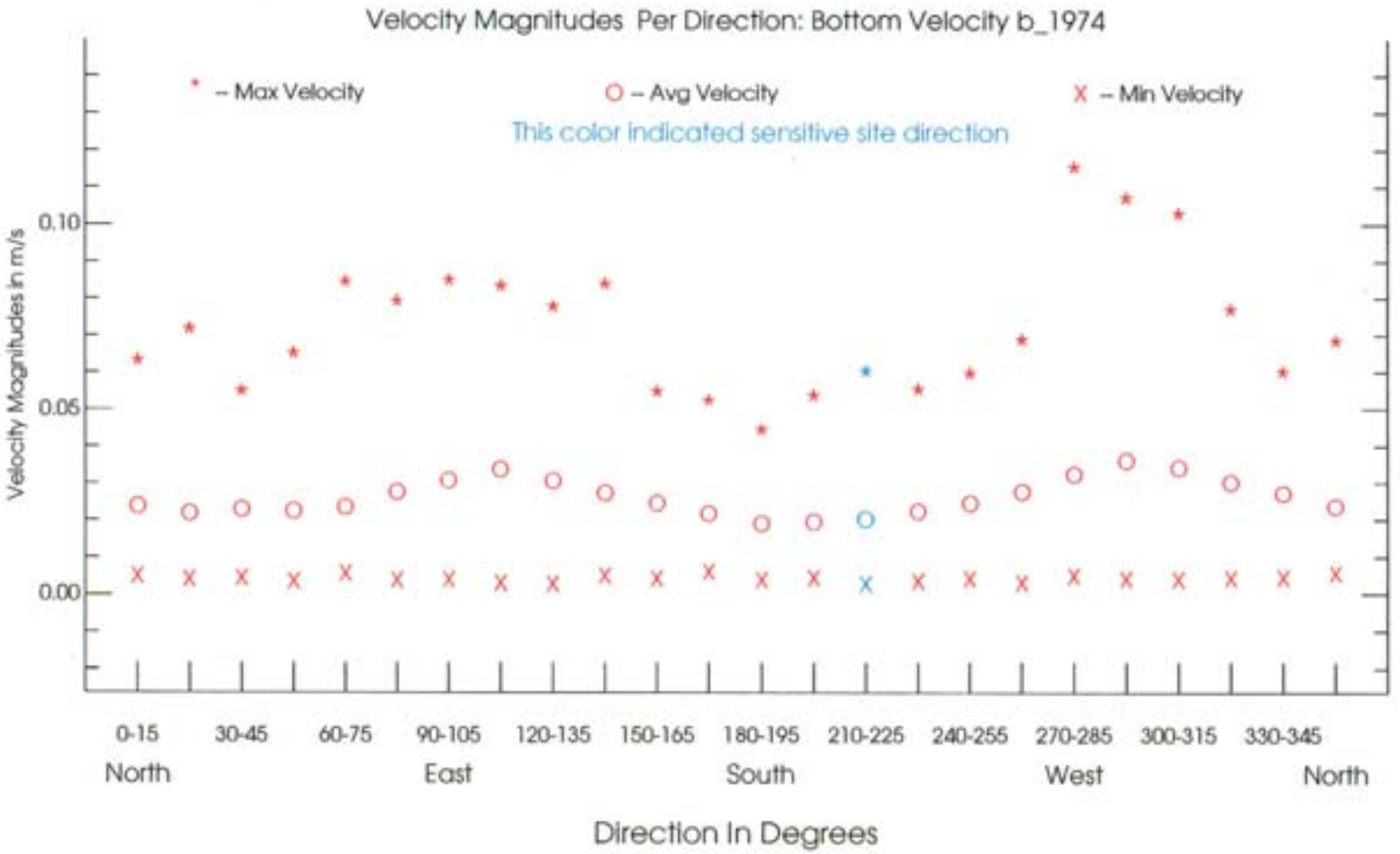
Velocity Magnitudes Per Direction: Bottom Velocity b_1974
* – Max Velocity
O – Avg Velocity
X – Min Velocity
This color indicated sensitive site direction
Velocity Magnitudes in m/s
0.10
0.05
0.00
0-15
30-45
60-75
90-105
120-135
150-165
180-195
210-225
240-255
270-285
300-315
330-345
North
East
South
West
North
Direction In Degrees

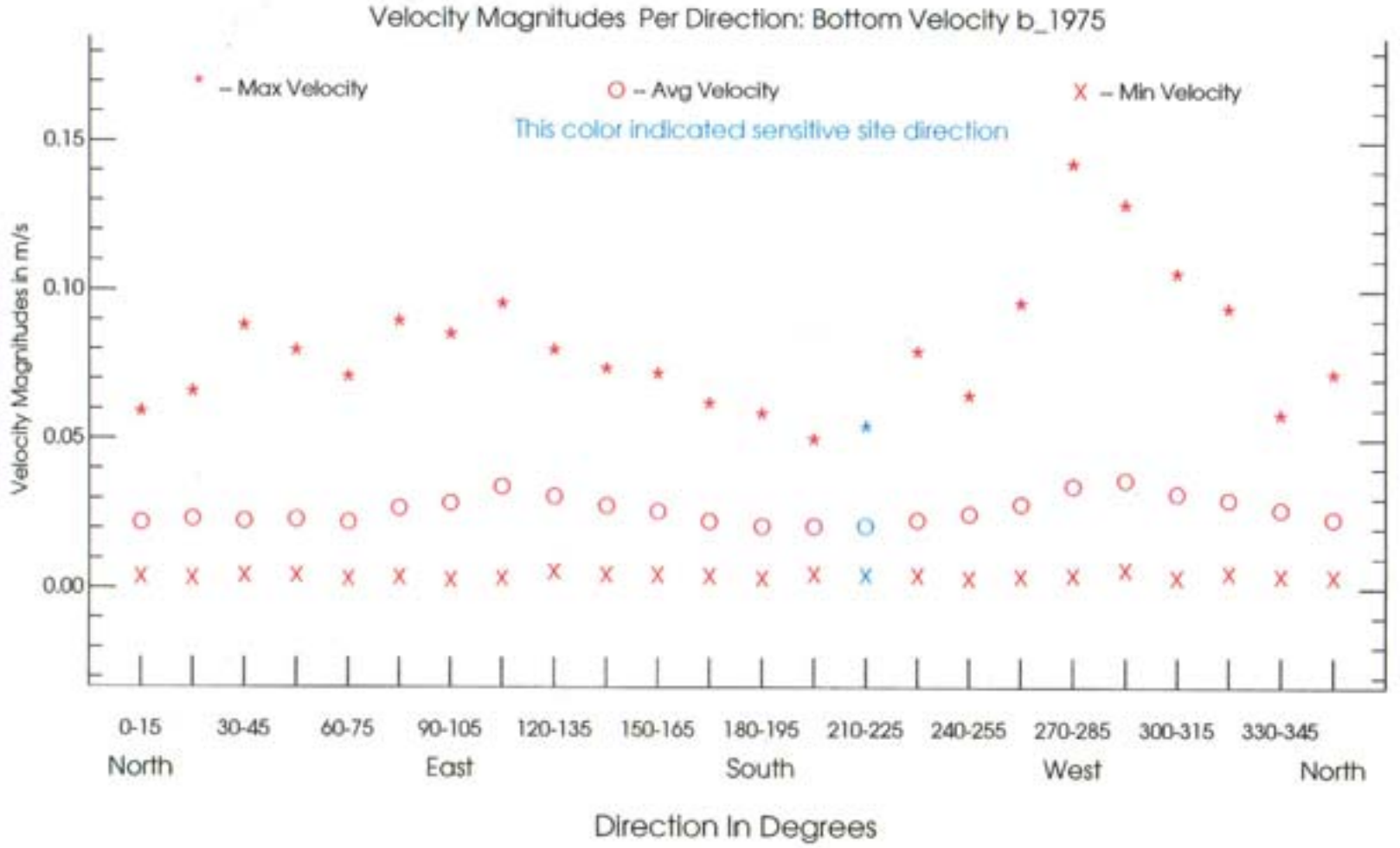
Velocity Magnitudes Per Direction: Bottom Velocity b_1975
* -- Max Velocity
O -- Avg Velocity
X -- Min Velocity
This color indicated sensitive site direction
Velocity Magnitudes in m/s
0.15
0.10
0.05
0.00
0-15
30-45
60-75
90-105
120-135
150-165
180-195
210-225
240-255
270-285
300-315
330-345
North
East
South
West
North
Direction In Degrees

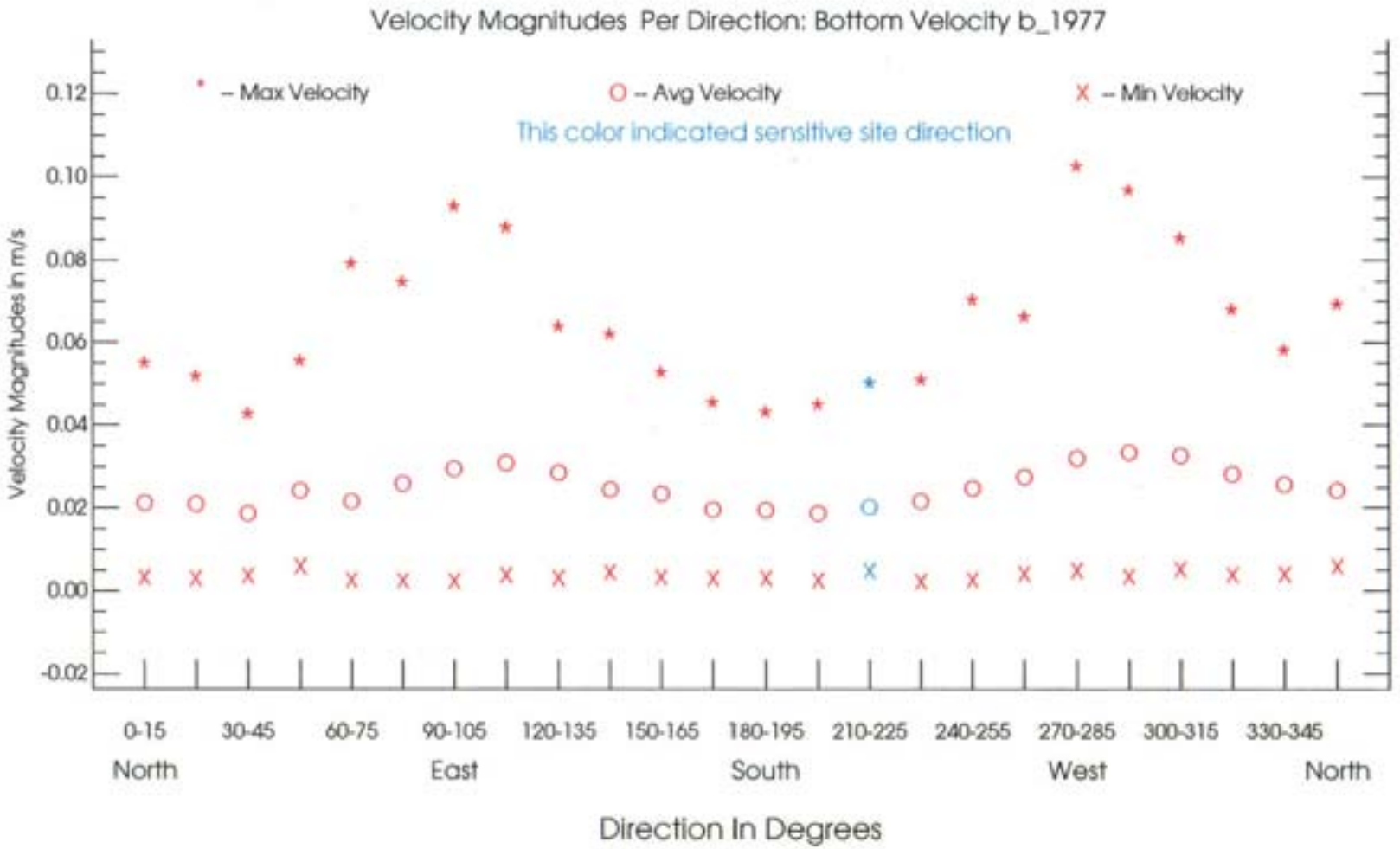
Velocity Magnitudes Per Direction: Bottom Velocity b_1977
* -- Max Velocity
O -- Avg Velocity
X -- Min Velocity
This color indicated sensitive site direction
Velocity Magnitudes in m/s
0.12
0.10
0.08
0.06
0.04
0.02
0.00
-0.02
0-15
30-45
60-75
90-105
120-135
150-165
180-195
210-225
240-255
270-285
300-315
330-345
North
East
South
West
North
Direction In Degrees

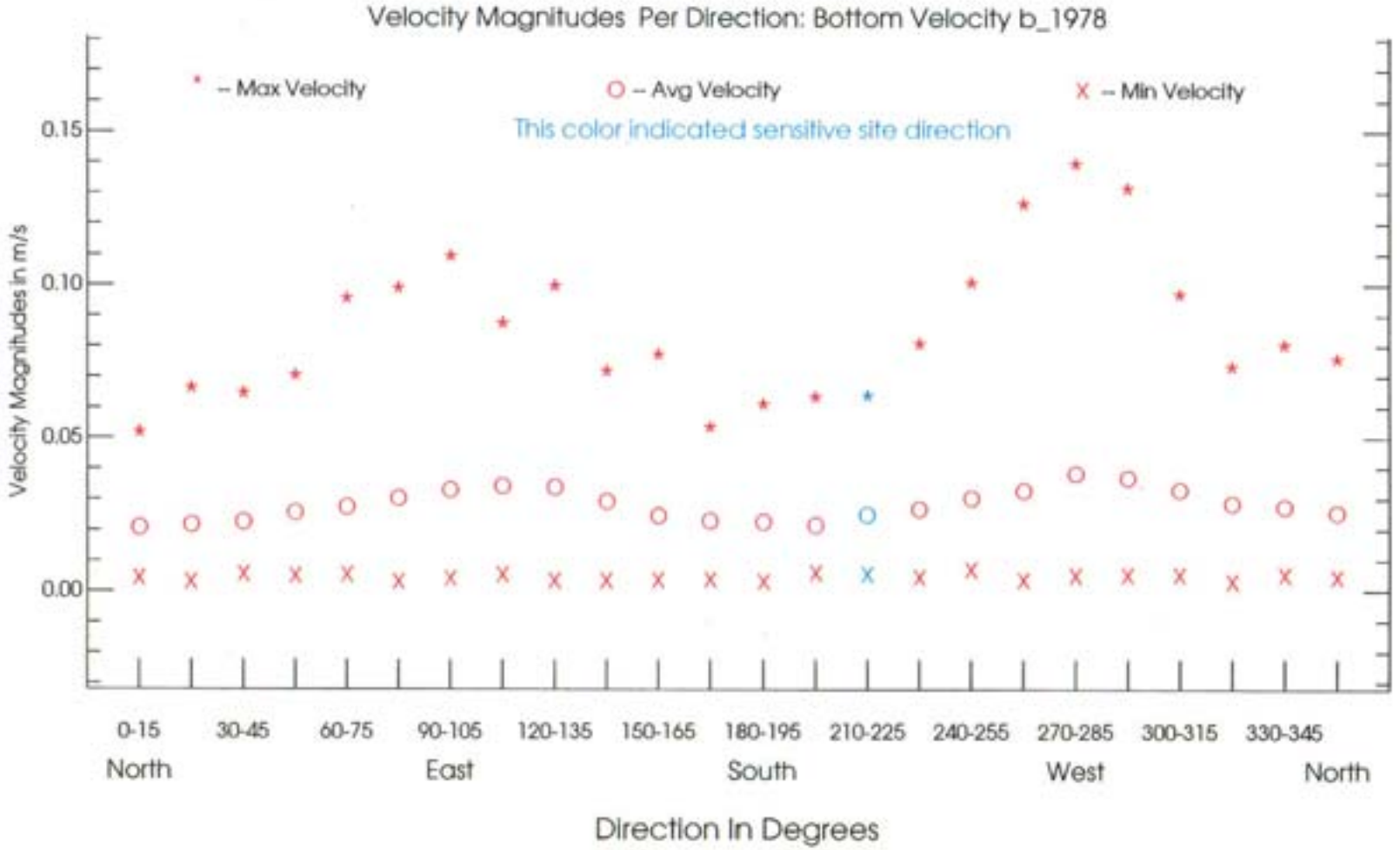
Velocity Magnitudes Per Direction: Bottom Velocity b_1978
* -- Max Velocity
O -- Avg Velocity
X -- Min Velocity
This color indicated sensitive site direction
Velocity Magnitudes in m/s
0.15
0.10
0.05
0.00
0-15
30-45
60-75
90-105
120-135
150-165
180-195
210-225
240-255
270-285
300-315
330-345
North
East
South
West
North
Direction In Degrees

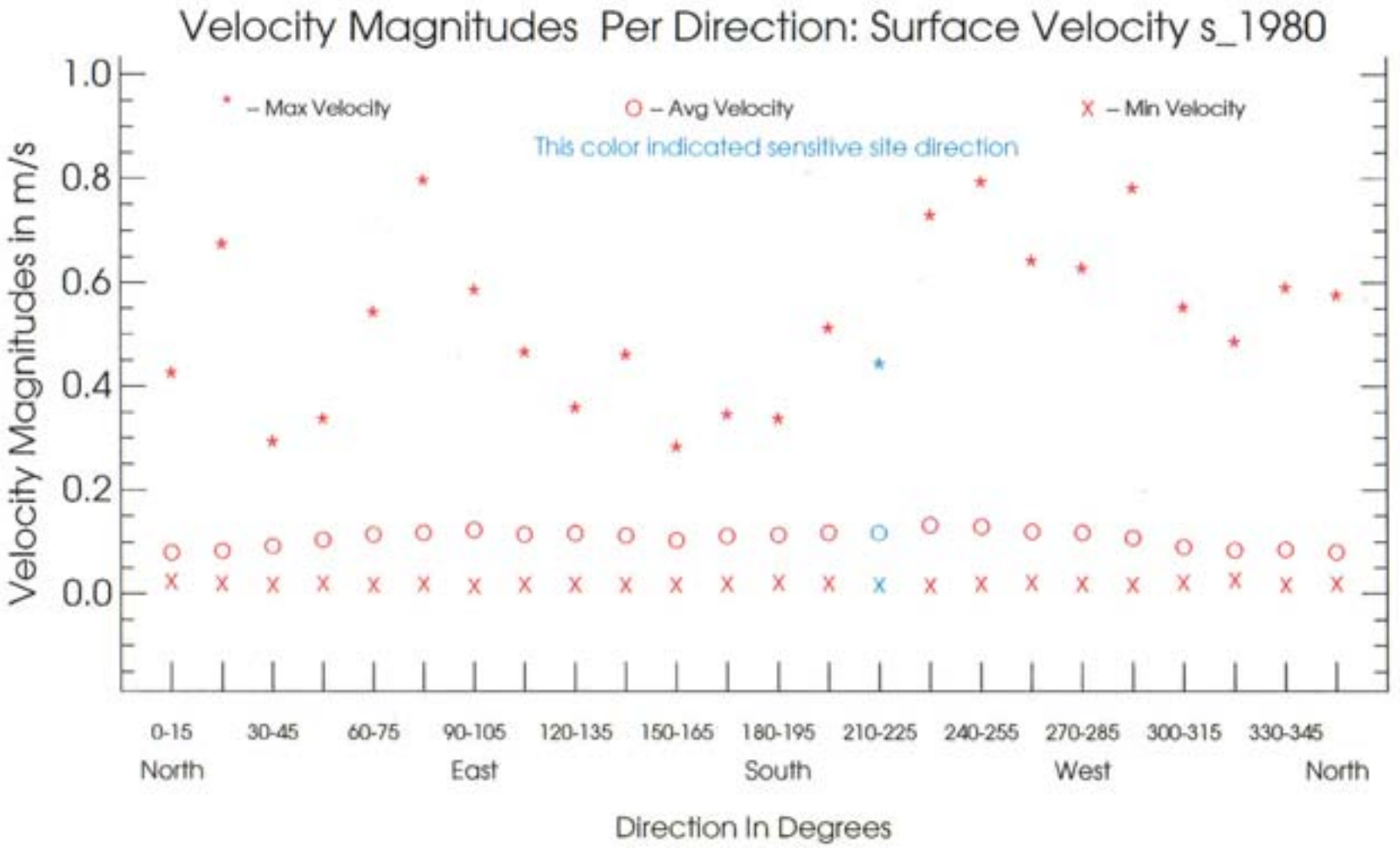
Velocity Magnitudes Per Direction: Surface Velocity s_1980
Velocity Magnitudes in m/s
1.0
0.8
0.6
0.4
0.2
0.0
* – Max Velocity
O – Avg Velocity
X – Min Velocity
This color indicated sensitive site direction
0-15
30-45
60-75
90-105
120-135
150-165
180-195
210-225
240-255
270-285
300-315
330-345
North
East
South
West
North
Direction In Degrees

APPENDIX E
The Distance Traveled Plots

The following plots will show the magnitudes as a function of direction maximum, minimum, and average magnitudes velocities.

Figure Captions

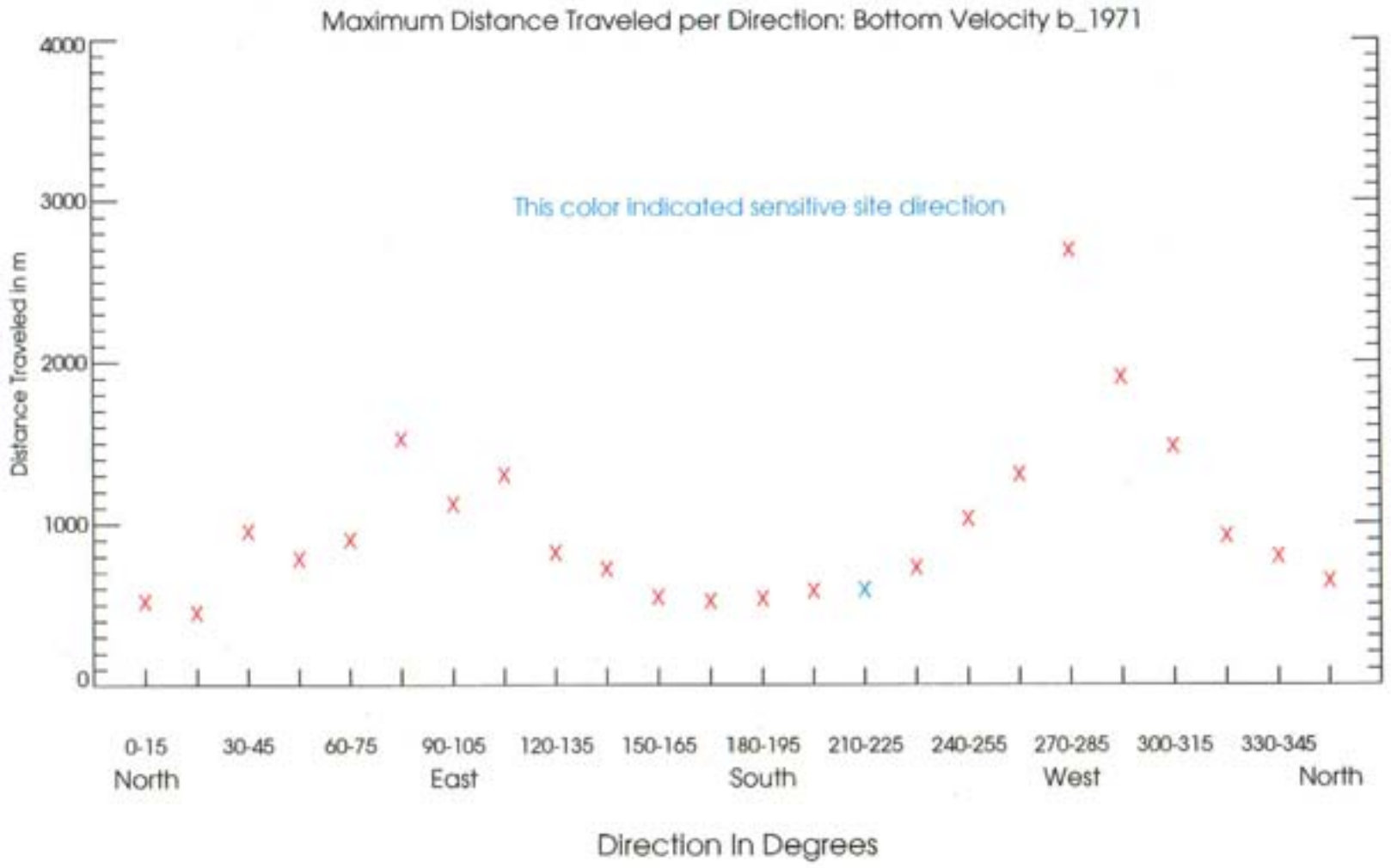
Maximum Distance Traveled per Direction: Bottom Velocity b_1971
This color indicated sensitive site direction
Distance Traveled in m
4000
3000
2000
1000
0
0-15
North
30-45
60-75
90-105
East
120-135
150-165
180-195
South
210-225
240-255
270-285
West
300-315
330-345
North
Direction In Degrees

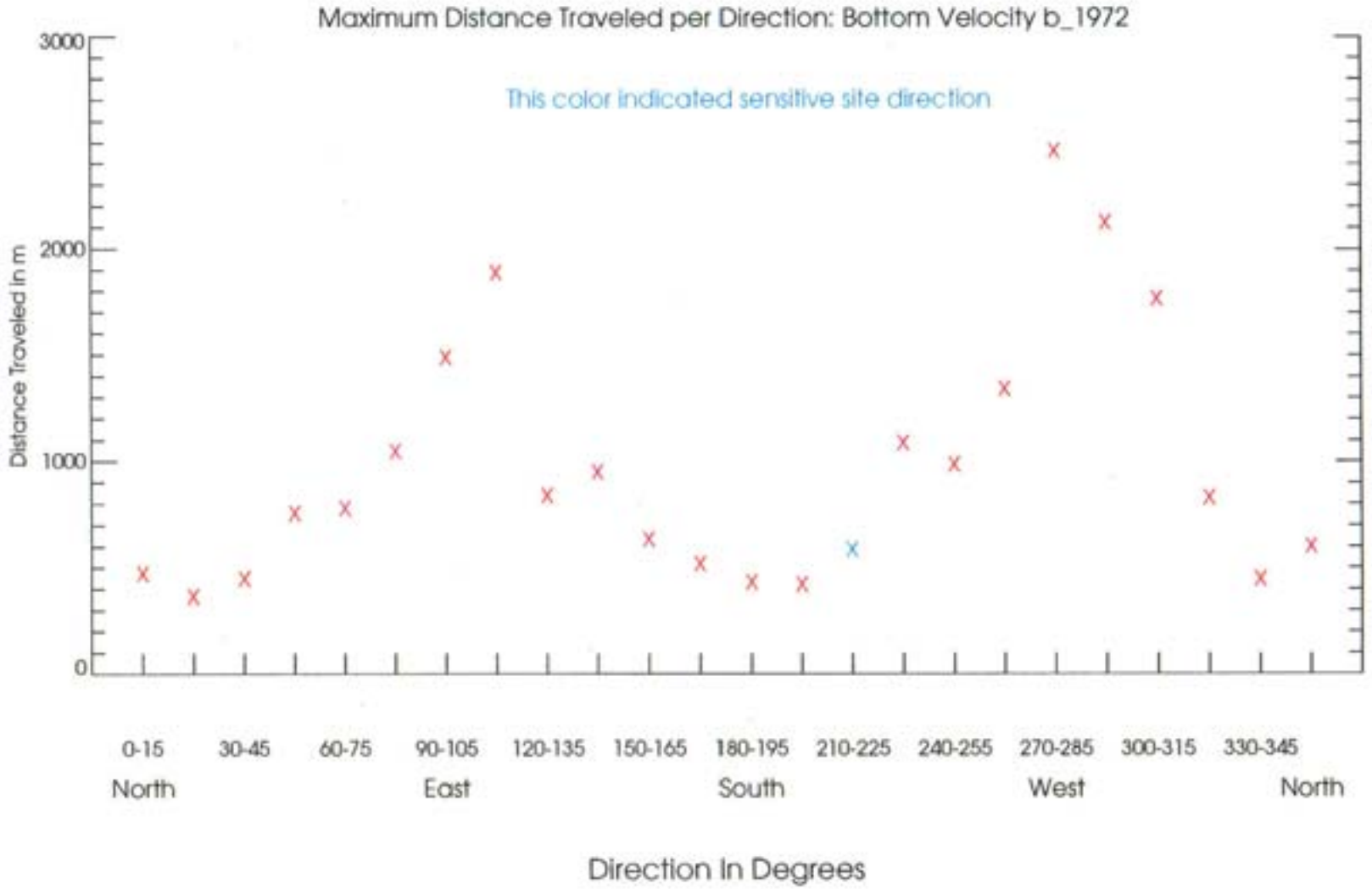
Maximum Distance Traveled per Direction: Bottom Velocity b_1972
This color indicated sensitive site direction
Distance Traveled in m
3000
2000
1000
0
0-15
30-45
60-75
90-105
120-135
150-165
180-195
210-225
240-255
270-285
300-315
330-345
North
East
South
West
North
Direction In Degrees

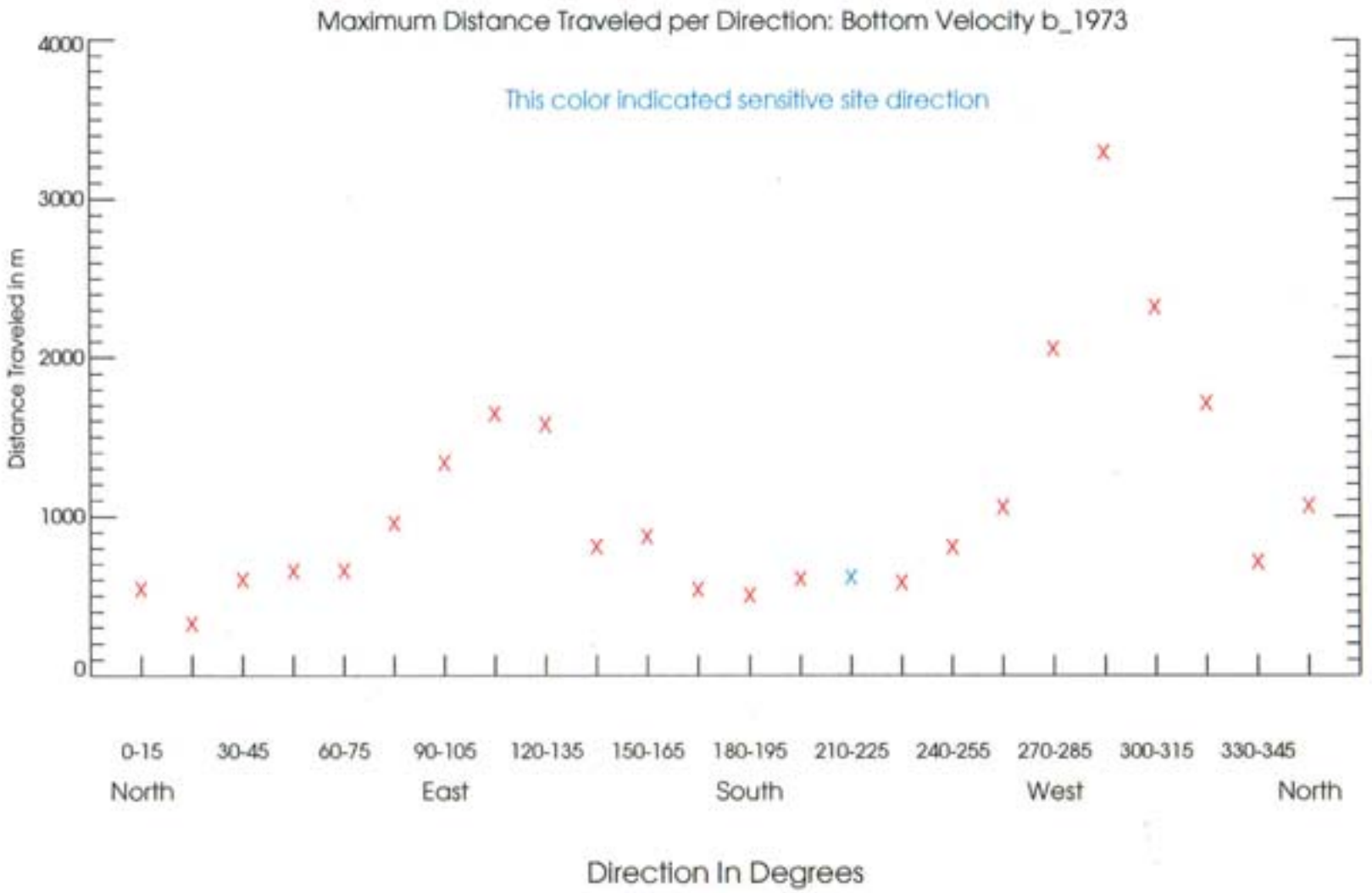
Maximum Distance Traveled per Direction: Bottom Velocity b_1973
This color indicated sensitive site direction
Distance Traveled in m
4000
3000
2000
1000
0
0-15
30-45
60-75
90-105
120-135
150-165
180-195
210-225
240-255
270-285
300-315
330-345
North
East
South
West
North
Direction In Degrees

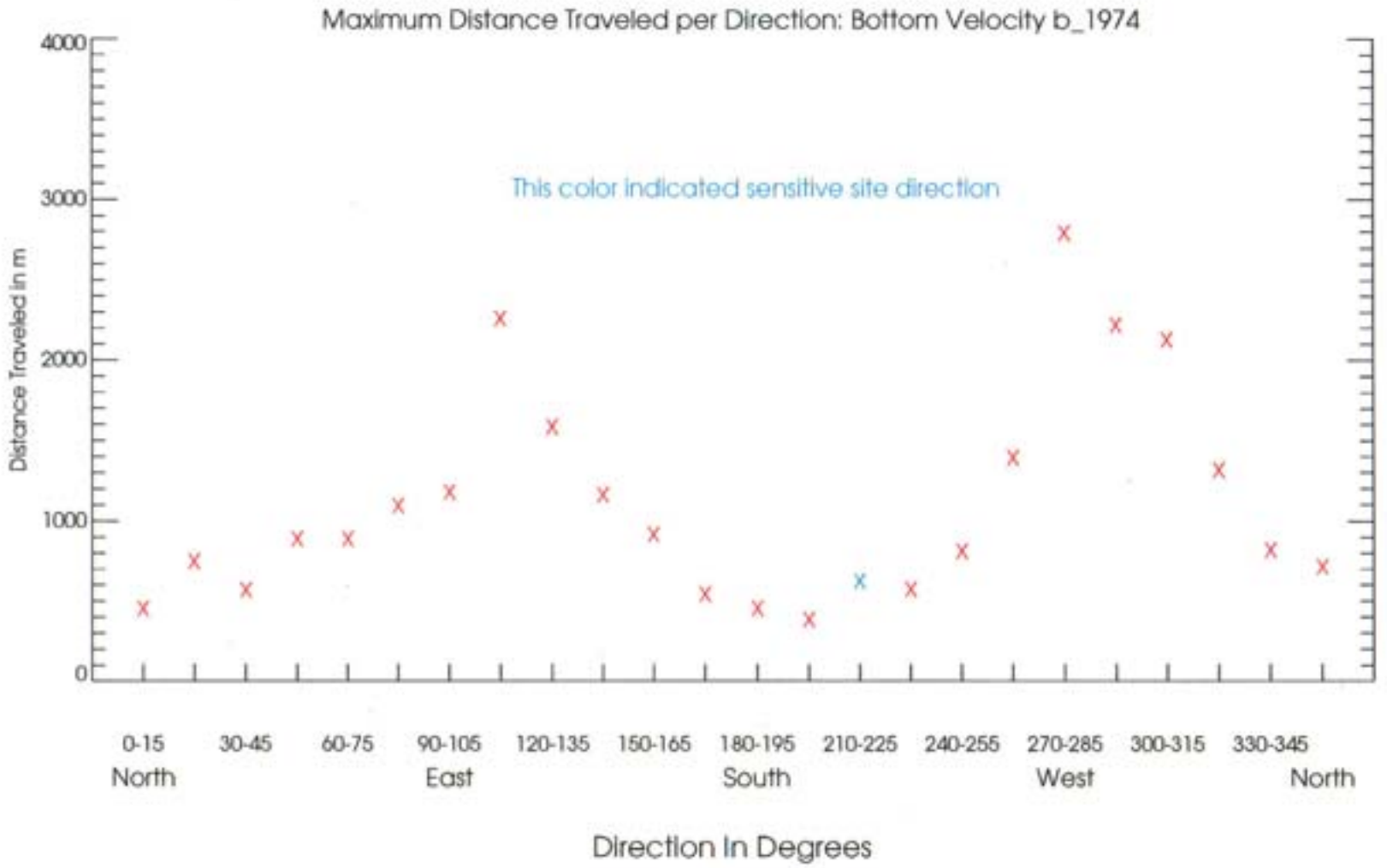
Maximum Distance Traveled per Direction: Bottom Velocity b_1974
This color indicated sensitive site direction
Distance Traveled in m
4000
3000
2000
1000
0
0-15
North
30-45
60-75
90-105
East
120-135
150-165
180-195
South
210-225
240-255
270-285
West
300-315
330-345
North
Direction In Degrees

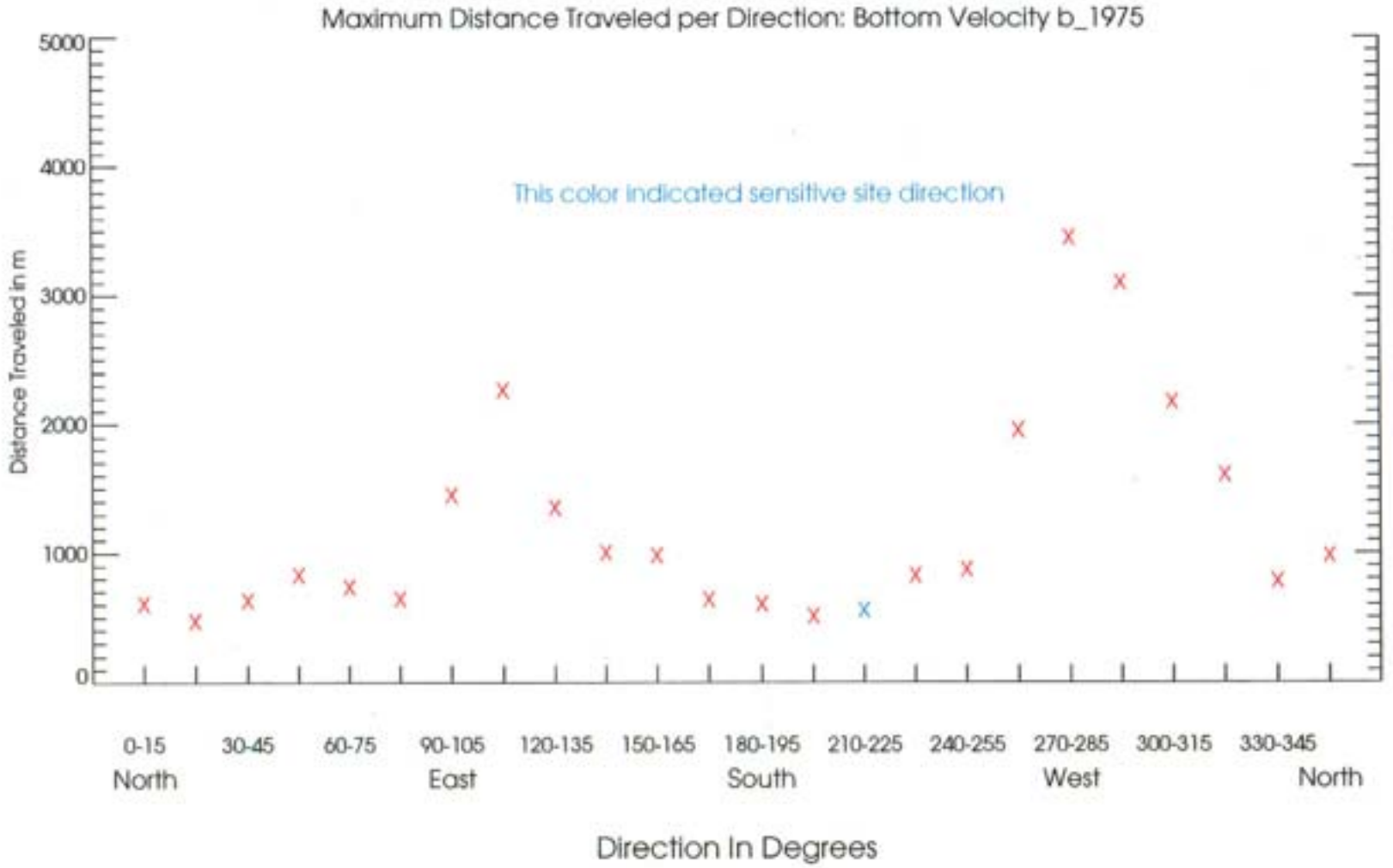
Maximum Distance Traveled per Direction: Bottom Velocity b_1975
This color indicated sensitive site direction
Distance Traveled in m
5000
4000
3000
2000
1000
0
0-15
North
30-45
60-75
90-105
East
120-135
150-165
180-195
South
210-225
240-255
270-285
West
300-315
330-345
North
Direction In Degrees

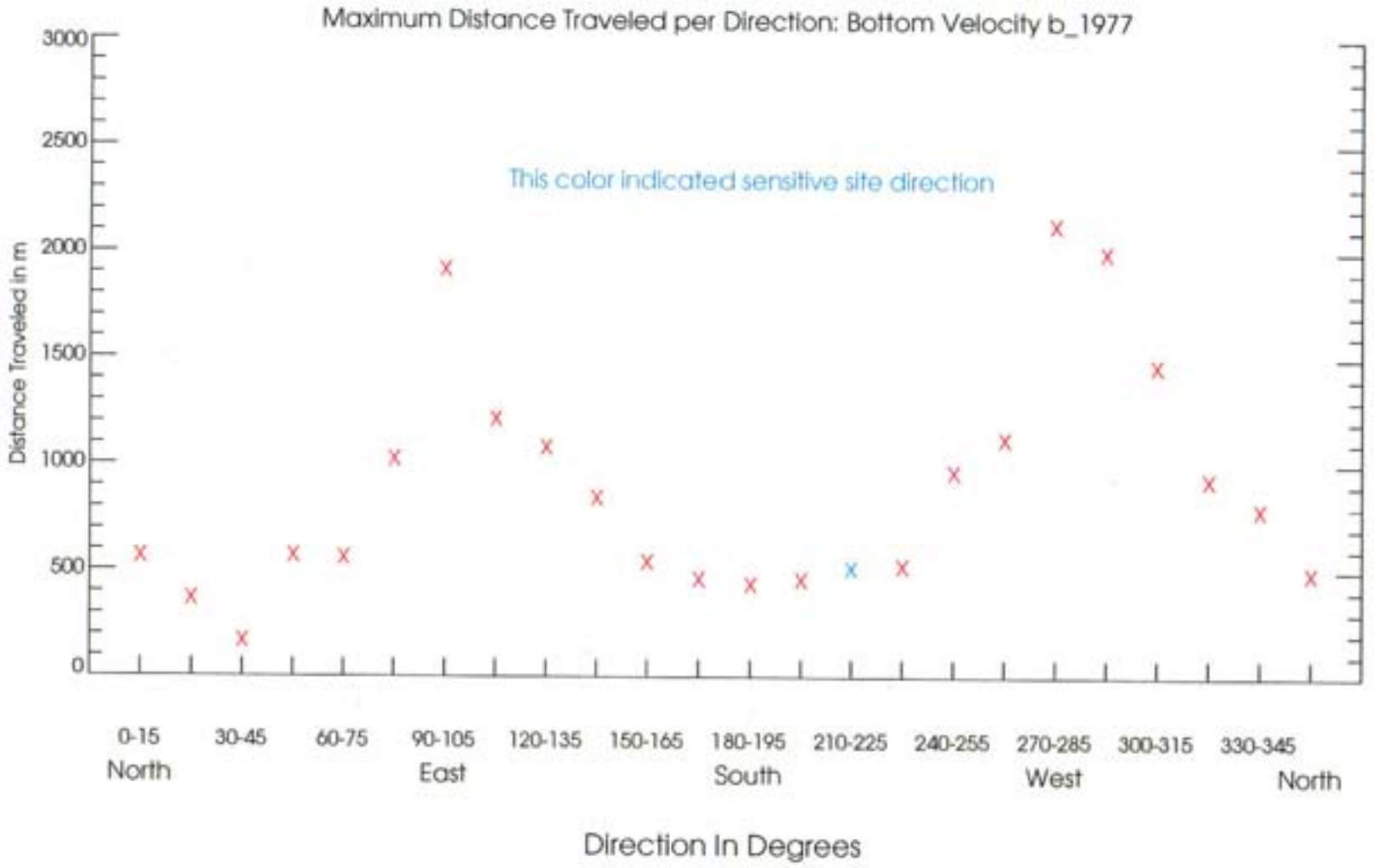
Maximum Distance Traveled per Direction: Bottom Velocity b_1977
This color indicated sensitive site direction
Distance Traveled in m
3000
2500
2000
1500
1000
500
0
0-15
North
30-45
60-75
90-105
East
120-135
150-165
180-195
South
210-225
240-255
270-285
West
300-315
330-345
North
Direction In Degrees

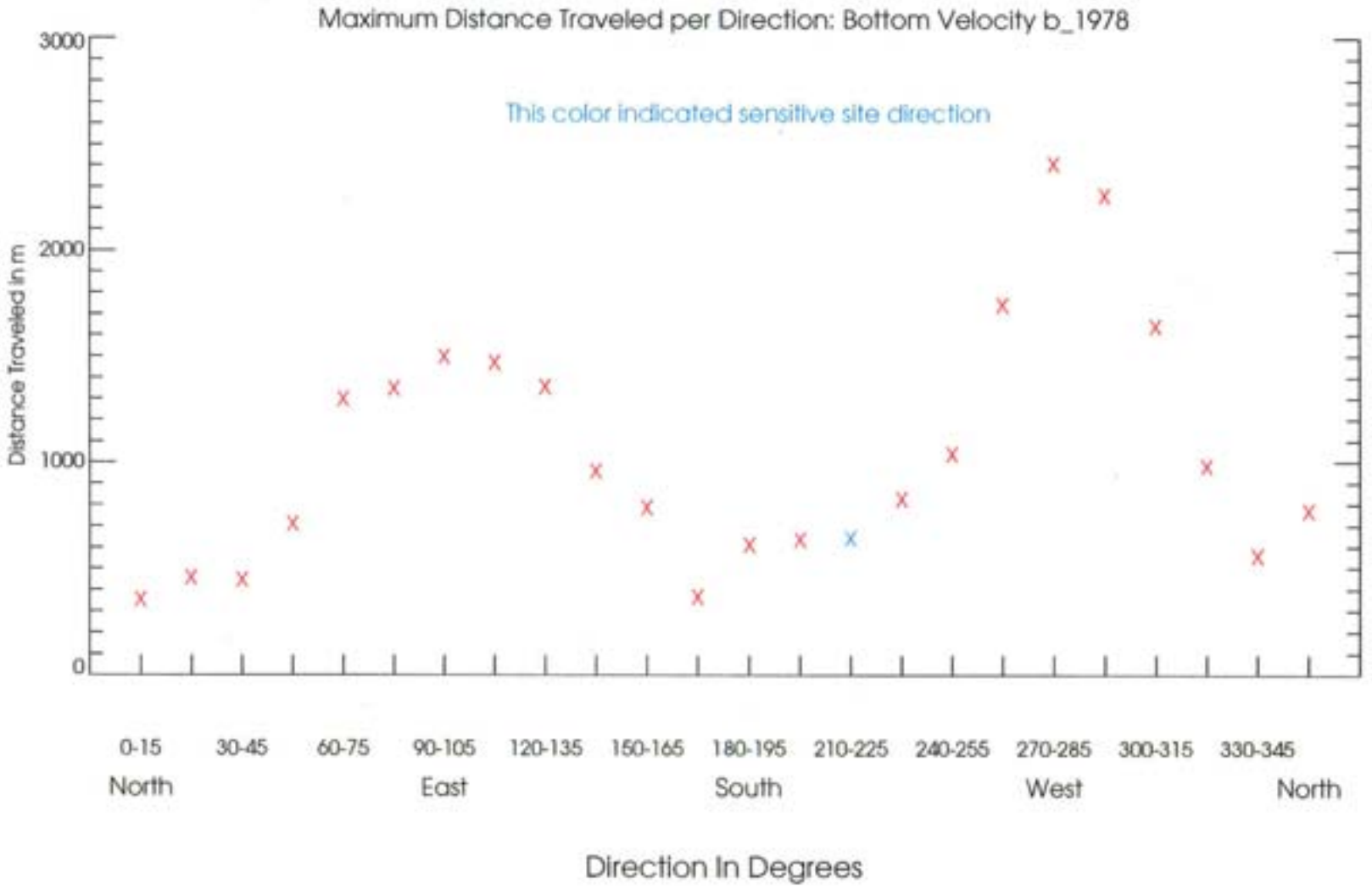
Maximum Distance Traveled per Direction: Bottom Velocity b_1978
This color indicated sensitive site direction
Distance Traveled in m
3000
2000
1000
0
0-15
30-45
60-75
90-105
120-135
150-165
180-195
210-225
240-255
270-285
300-315
330-345
North
East
South
West
North
Direction In Degrees

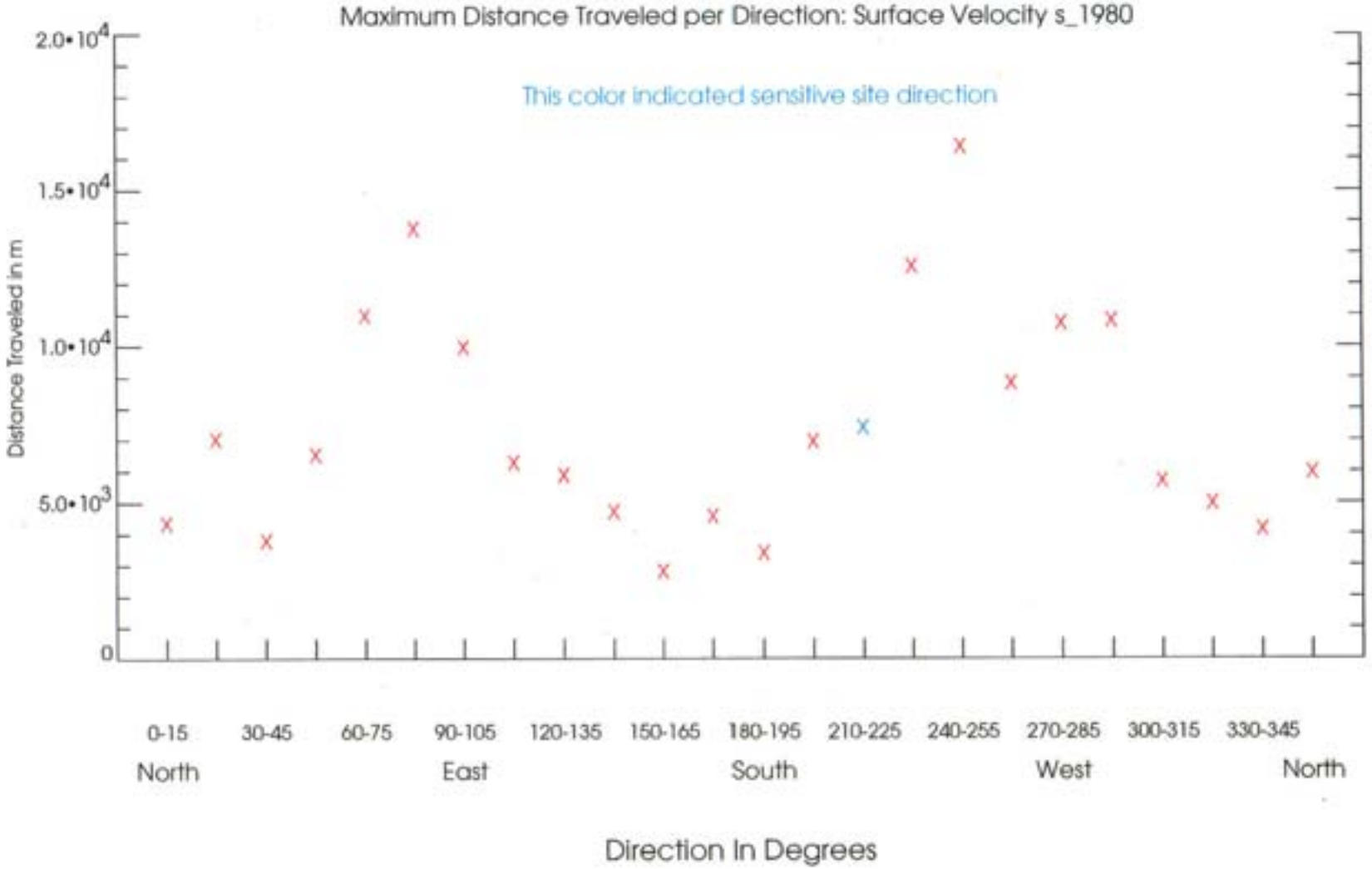
Maximum Distance Traveled per Direction: Surface Velocity s_1980
This color indicated sensitive site direction
Distance Traveled in m
2.0•10^4
1.5•10^4
1.0•10^4
5.0•10^3
0
0-15
30-45
60-75
90-105
120-135
150-165
180-195
210-225
240-255
270-285
300-315
330-345
North
East
South
West
North
Direction In Degrees

Integrated Analysis of the Impact of Unconfined Placement Activities on Near-Shore Sensitive Areas

REPORT No. 3
A Multi-Size, Multi-Source Formulation for Determining Impacts of Sediments on Near-Shore Sensitive Sites

By

Keith W. Bedford
Panagiotis Velissariou
Vasilia Velissariou
Yong Guo

Department of Civil and Environmental Engineering and Geodetic Science
The Ohio State University
Columbus, Ohio

Contract DACW39-95-K-0018
US Army Corps of Engineers
Waterways Experiment Station
Vicksburg, MS

September 8, 1999

Table Of Contents

List of Tables

List of Figures

Introduction

Maintenance and improvement of navigation channels in Lake Erie require extensive and recurring dredging operations. The dredged material is disposed either in confined disposal facilities or, more commonly at offshore disposal sites. The unconfined placement of dredged material, however, raises concerns of potential adverse impacts on sensitive near-shore areas. Such sensitive sites are typically beaches, and municipal or private water intakes.

In an effort to evaluate the relative impact of different sediment sources on sensitive near-shore areas a multi-grain, multi-source sediment transport formulation was used, largely focusing on the impacts of the disposed sediments at the existing disposal site in the Western basin of Lake Erie. In this study four sediment sources were selected to represent the sediment inputs in Lake Erie, namely: a) lake bottom sediments, b) the sediments originating from the disposal site, c) suspended sediment inputs from Maumee River, and d) suspended sediment inputs from the Detroit River. The sediments of each source are represented using three size classes (sand, silt, and clay) but the sediment particle diameters for these classes vary slightly among the sources. This was necessary for two reasons: First, to be able to "track" the different particle sizes originating from different sources; Second, to ensure that the settling velocities, as calculated by the sediment model, will be, if not identical, very close in value.

The above approach allows the identification of the sources of the sediment material transported at the sensitive area and, evaluates the relative intensity of the sediment load transported from each source, to the total load transported. The sediment size

distributions of the suspended and bottom sediments found in Lake Erie will be presented in Chapter 3 of this report.

The calculations were performed using the CH3D circulation model coupled with a sediment model, known as CH3D-SED model (Spasojevic and Holly, 1994). The latest model includes a module for the advection and turbulent diffusion of the suspended sediments, as well as a sediment module that describes the evolution of the lake bottom (as bottom sediments are being transported) and the entrainment of the bottom sediments. Both sediment modules are discussed in detail in Chapter 2 of this report. The initial and boundary conditions required for the model runs are discussed in Chapter 4.

This study covers, a one year ice-free test period, from April 1, 1997 to December 31, 1997. The model results were saved every hour, resulting in "huge" amounts of data that demanded significant disk storage and data reduction and management. The nine-month model run was split in bi-weekly model runs at the end of which the results from the last two time steps were saved in a so-called "hot start" file. This "hot start" file is all that is needed to proceed to the next bi-weekly run.

The model results include: a) the full 3-D velocity field, b) the 2-D vertically averaged velocity field, c) the 3-D temperature field, d) the 3-D sediment concentration field, e) the bottom sediment fraction distributions and, f) the changes of the bottom elevation. From these results, trajectory maps and time traces of the variables have been generated.

Chapter 1
Site Characteristics

1.1 Lake Erie Bathymetry

Lake Erie is the Southern-most and fourth largest of the Great Lakes with a total area of 25667 km^2. The length of the lake is approximately 388 km with a maximum width of 92 km. Its maximum depth is 64 m (observed at the Eastern basin) which makes it the shallowest of all the Great Lakes. Due to its shallowness, it is susceptible to weather effects, especially to wind induced seiches. The lake receives waters from the St. Clair River, Lake St. Clair the Detroit River, the Grand River, the Sandusky River, the Cuyahoga River and the Maumee River.

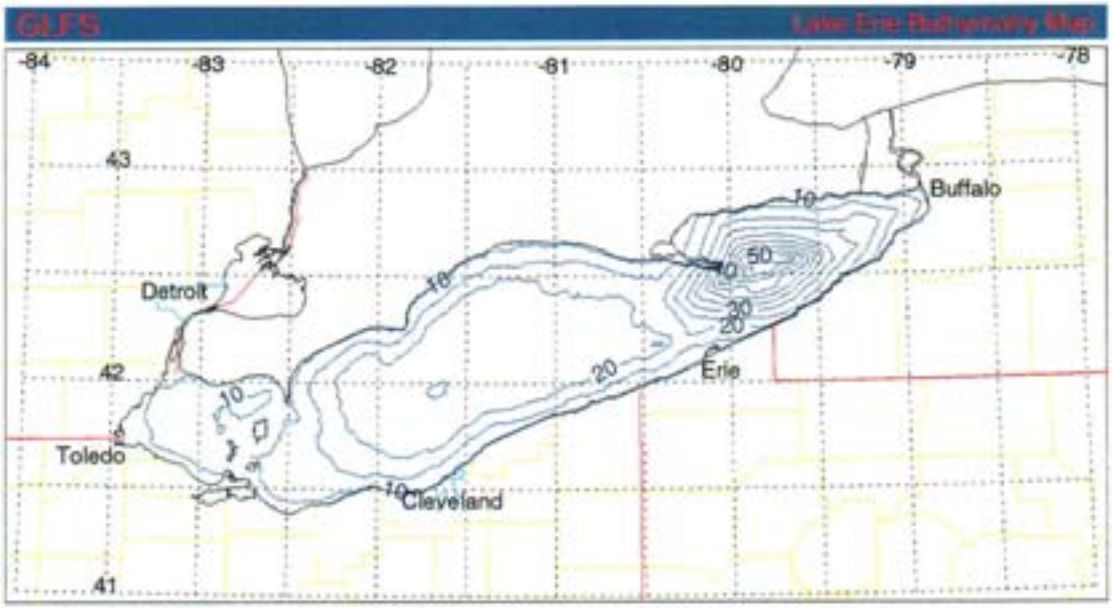

Figure 1.1 Lake Erie bathymetry map.

Erosion of the shorelines and sediment discharge from the streams cause a continuous accumulation of sediments at the lake bottom, considering that the only natural outlet of Lake Erie is the Niagara River.

1.2 Site Characteristics

The Western basin of Lake Erie (Figure 1.2) is bounded at the North by Canada at the East by a transect from Marblehead Point through Kelley's Island to Pelee Point and at the South by the Ohio mainland. Its maximum depth is about 10 m. The main sources of riverine sediment inputs are the Maumee River, accounting for 37% of the total riverine discharge in the lake(Herdendorf et al., 1977), and the Detroit River. The bottom of the Western basin of Lake Erie is composed mostly of mud (semi-fluid silt and clay-sized particles) which covers about 3/5 of the total area, followed by sand at about 1/5, and mixtures of sand and mud for the remaining portion (Verber, 1957).

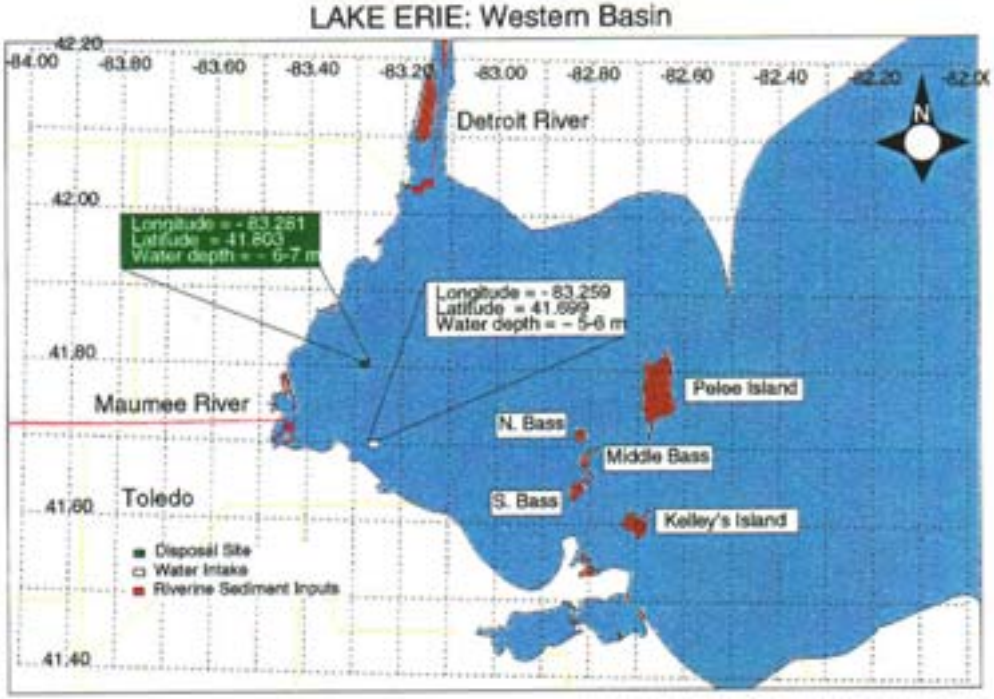

Figure 1.2 Location of the disposal and water intake sites at the western basin of Lake Erie.

The location of interest for the present study is the Toledo, Ohio, water intake area, which is located 12600 m south south-east the disposal site. The disposal site is located at 41°48.6' N, and 83°17.0' W, in water of 6.1 m to 7.0 m depth relative to IGLD Low Water Datum.

Chapter 2
Methods of Study

2.1 Model Selection

The numerical hydrodynamic model used in this study to calculate the free water surface displacements, the three components of the velocity, and the temperature of Lake Erie, is the CH3D (Curvilinear Hydrodynamics in 3 Dimensions) circulation model. The model was developed at the US Army Corps of Engineers Waterways Experiment Station.

In the present study, CH3D has been used in its sigma stretched version. This version also includes a two-equation turbulence closure model, known as the k-ε model, for the parameterization of turbulence (Chapman et al., 1996). The suspended sediment volumetric concentrations, the bed-surface particle size fractions, the bed elevations and the density changes due to the presence of suspended sediment, have been calculated using the CH3D-SED model. CH3D-SED was developed at the Iowa Institute of Hydraulic Research during the period from August 1991 to December 1993. It includes a three-dimensional suspended sediment module and a two-dimensional mobile bed sediment module, which have been properly modified and coupled with CH3D-WES (Spasojevic and Holly, 1994).

2.2 The Hydrodynamic Model

The CH3D hydrodynamic model, is a 3-D, non-linear primitive equation circulation model. The basic assumptions incorporated into the model are: a) the vertical distribution of the fluid pressure can be described by the hydrostatic approximation and b) the

Boussinesq approximation and the eddy viscosity approach can describe the turbulence mixing. The hydrodynamic equations governing the circulation of the lake include the continuity equation, the momentum equations and the conservation equation for the thermal energy. These equations in a Cartesian coordinate system (x, y, z) are:

$$\frac{\partial u}{\partial x}+\frac{\partial v}{\partial y}+\frac{\partial w}{\partial z}=0 \tag{2.1}$$

$$\frac{\partial u}{\partial t}+\frac{\partial u^2}{\partial x}+\frac{\partial uv}{\partial y}+\frac{\partial uw}{\partial z}=f\cdot v-\frac{1}{\rho_0}\frac{\partial p}{\partial x}+\frac{\partial}{\partial x}\left[A_h\frac{\partial u}{\partial x}\right]+\frac{\partial}{\partial y}\left[A_h\frac{\partial u}{\partial y}\right]+\frac{\partial}{\partial z}\left[A_v\frac{\partial u}{\partial z}\right] \tag{2.2}$$

$$\frac{\partial v}{\partial t}+\frac{\partial uv}{\partial x}+\frac{\partial v^2}{\partial y}+\frac{\partial vw}{\partial z}=-f\cdot u-\frac{1}{\rho_0}\frac{\partial p}{\partial y}+\frac{\partial}{\partial x}\left[A_h\frac{\partial v}{\partial x}\right]+\frac{\partial}{\partial y}\left[A_h\frac{\partial v}{\partial y}\right]+\frac{\partial}{\partial z}\left[A_v\frac{\partial v}{\partial z}\right] \tag{2.3}$$

$$\frac{\partial p}{\partial z}=-\rho\cdot z \tag{2.4}$$

and

$$\frac{\partial T}{\partial t}+\frac{\partial uT}{\partial x}+\frac{\partial vT}{\partial y}+\frac{\partial vT}{\partial z}=\frac{\partial}{\partial x}\left[K_h\frac{\partial T}{\partial x}\right]+\frac{\partial}{\partial y}\left[K_h\frac{\partial T}{\partial y}\right]+\frac{\partial}{\partial z}\left[K_v\frac{\partial T}{\partial z}\right] \tag{2.5}$$

Integrating equation (2.4), from z to η which implies a hydrostatic vertical pressure distribution, reveals:

$$\frac{p}{\rho_0}=g(\eta-z)+g\int_z^{\eta}\frac{\rho_{cw}-\rho_0}{\rho_0}dz \tag{2.6}$$

In the above equations (2.1 through 2.6), u, v and w, are the velocity components in the x, y and z directions respectively; and T is the temperature. The free water surface is located at $z = \eta(x, y, z)$ and the bottom is at $z = H(x, y)$ where, η, is the free water surface elevation and H defines the bottom topography. The Coriolis parameter, f, is defined as $2\cdot\Omega\cdot\sin\theta$, where Ω is the rotational speed of the earth and θ is the latitude; p is the pressure; ρ_0 is a reference density; g is the gravitational acceleration; and ρ_{cw} is the in situ density which is a function of temperature, salinity and time. The quantities A_h,

K_h denote the horizontal turbulent eddy viscosity and eddy diffusivity coefficient respectively and, the quantities A_v, K_v denote the vertical turbulent eddy viscosity and eddy diffusivity respectively.

The relationship between density, temperature and salinity is given by (Spasojevic and Holly, 1994):

$$\rho_{cw} = \frac{P}{a + 0.698 \cdot P} \tag{2.7}$$

where ρ_{cw} is the density (g/m^3). The functions P and a, are calculated as follows:

$$P = 5890 + 38 \cdot T - 0.375 \cdot T^2 + 3 \cdot S \tag{2.8}$$

$$a = 1779.5 + 11.25 \cdot T - 0.0745 \cdot T^2 - (3.8 + 0.01 \cdot T) \cdot S \tag{2.9}$$

where T is the temperature in degrees Celsius and S is the salinity in parts per thousand (ppt).

Equations (2.1) through (2.4) have been expressed and they are used in non-dimensional forms. Dimensionless parameters introduced by this process are the Froude number, the Densimetric Froude number, the horizontal and vertical Ekman number and the Rosby number.

2.2.1 The k-ε Turbulence Model

One of the main features in numerical hydrodynamic modeling is the parameterization of turbulence. CH3D uses a two-equation turbulence closure model known as the k-ε model (Rodi, 1980). According to this model the relation between the eddy viscosity, A, and the parameters, k, and ε, is determined by dimensional analysis and it can be written as:

$$A = c\frac{k^2}{\varepsilon} \tag{2.10}$$

where c, is an empirical constant, k, is the turbulence energy per unit mass and ε, is the rate of dissipation of turbulence energy. The distributions of k and ε are determined from transport equations as follows:

$$\frac{\partial k}{\partial t}+u_i\frac{\partial k}{\partial x_i}=\frac{\partial}{\partial x_i}\left[\frac{A}{\sigma_k}\frac{\partial k}{\partial x_i}\right]+P+G-\varepsilon \tag{2.11}$$

and

$$\frac{\partial \varepsilon}{\partial t}+u_i\frac{\partial \varepsilon}{\partial x_i}=\frac{\partial}{\partial x_i}\left[\frac{A}{\sigma_\varepsilon}\frac{\partial \varepsilon}{\partial x_i}\right]+c_1\frac{\varepsilon}{k}(P+c_3G)-c_2\frac{\varepsilon^2}{k} \tag{2.12}$$

where: P and G are the stress and buoyancy production of the kinetic energy. The values of the empirical constants are non tunable as they have been obtained from numerous experimental applications: $c = 0.09$, $\sigma_k = 1$, $\sigma_\varepsilon = 1.3$, $c_1 = 1.41$, $c_2 = 1.92$, and $c_3 = 1.0$ ($G > 0$) or, $c_3 = 0 - 0.2$ ($G < 0$).

2.2.2 The Curvilinear and the Sigma Coordinate Transformations

The numerical solution of the governing 3-D partial differential equations requires discretization of the natural field into a collection of elemental volumes (cells). This discretization must conform to the boundaries of the natural flow field in a way that the boundary conditions can be represented accurately. The use of a curvilinear coordinate system gives a solution to this problem by providing coordinate lines coincident with all boundaries. The transformation of the physical field with the curvilinear coordinates as the independent variables maps the boundary segments in the physical field to vertical or horizontal lines in the transformed field. The transformed field appears to be composed of rectangular blocks and the points neighboring the computation site can be readily identified.

The partial derivatives with respect to Cartesian coordinates are related to partial derivatives with respect to curvilinear coordinates by the chain rule, which are written as

(J. F. Thompson et al., 1985):

$$A_{x_i} = A_{\xi^j}\left(\xi^j\right)_{x_i} \quad (i, j = 1, 2, 3) \tag{2.13}$$

where A, is a scalar-valued function and ξ^j are the contravariant base vectors of the curvilinear coordinate system. In the CH3D model the (x, y) horizontal coordinates are transformed in the (ξ, η) horizontal general (non-orthogonal) curvilinear coordinates and the fluid velocity is transformed such that its components are contravariant. From equation (2.11), for i, j = 1,2 and $A_{x_1} = u$, $A_{x_2} = v$, $x_1 = x$, $x_2 = y$, $A_{\xi^1} = \bar{u}$, $A_{\xi^2} = \bar{v}$, $\left(\xi^1\right)_{x_i} = x_\xi$, $\left(\xi^2\right)_{x_1} = x_\eta$, $\left(\xi^1\right)_{x_2} = y_\xi$, $\left(\xi^2\right)_{x_2} = y_\eta$, we obtain the Cartesian velocities (u, v) in terms of the contravariant components $\bar{u}$, $\bar{v}$ as:

$$u = x_\xi \bar{u} + x_\eta \bar{v} \quad \text{and} \quad v = y_\xi \bar{u} + y_\eta \bar{v} \tag{2.14}$$

In the vertical direction, another type of transformation has been adopted by the developers of the CH3D model. Upon this transformation the vertical coordinate, z, has been transformed to an independent variable sigma (σ) such that:

$$\sigma = \frac{z - \eta}{\eta + H} \tag{2.15}$$

where H, is the water depth from the datum where z = 0, and η, is the free water surface displacement.

The so called "sigma stretching", transforms the physical domain in the vertical plain, into a rectangular computational domain with upper boundary $\sigma = 0$, and lower boundary $\sigma = -1$. Its use simplifies computational disadvantages in the vicinity of bathymetric irregularities introduced by the use of Cartesian coordinates.

2.3 The Sediment Model

Sediment is transported by the water, in suspension, saltation or rolling and sliding on the bed. Distinction and separate study of each different mode is difficult and even impossible. From practical point of view, the sediment transport is divided into two main categories: a) bed load transport, and b) suspended load transport, referring to sediment carried above bottom by the fluid. In the CH3D-SED model, the two modes of transport are formulated separately, but interactions between them have been accounted for. The sediment equations of the model describe the behavior of a non-uniform sediment mixture, which is represented by an appropriate number of sediment size classes.

2.3.1 Bedload Transport and Bed Evolution

Considering the elemental volume ΔV (Figure 2.1) with dimension Δl – at least equal to the maximum average saltation length – and a thickness E_m that coincides with the thickness of the active layer, defined as the upper layer of the bed including the bed surface, and assuming a uniform sediment size distribution within this volume, the conservation of mass equations can be written as (Spasojevic and Holly, 1994):

For each size class separately:

$$\rho_s(1-p)\frac{\partial(\beta E_m)}{\partial t}+\nabla\vec{q}_b+S_e-S_d-S_F=0 \qquad (2.16)$$

For the sum of all size classes:

$$\rho_s(1-p)\frac{\partial(E_m)}{\partial t}+\sum(\nabla\vec{q}_b+S_e-S_d-S_F)=0 \qquad (2.17)$$

with the constraint: $\sum\beta=1$.

In the above equations, p, is the porosity of the bed material and ρ_s is the density of the sediment (both assumed to be constant); β represents the fraction of the mass of one

particular size class over the mass of all sediment particles in the elemental volume; and $\vec{q}_b$ is the bedload mass flux expressed as a two-dimensional vector parallel to the bed surface. The bedload is calculated in CH3D-SED by using an empirical relation proposed by Van Rijn (1984a). For one particular size class the bedload flux is given as:

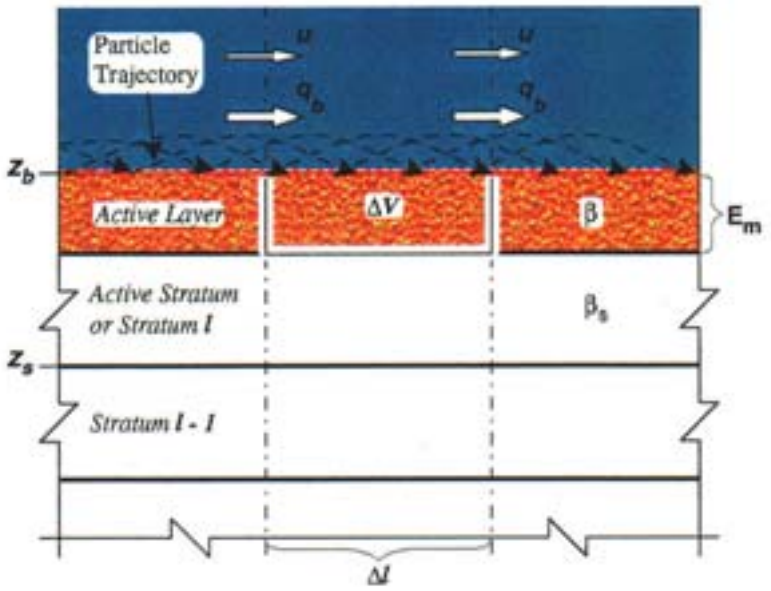

Figure 2.1 Schematic representation of bed-material finite elemental volume and the stratum control volumes (source: Spasojevic and Holly, 1994).

$$(q_b)_s = 0.053 \cdot \rho_s \cdot \sqrt{(s-1)gD_s}\,\frac{D_s}{D_{*s}^{0.3}}\left[\frac{u_*^2 - u_{*c}^2}{u_{*c}^2}\right]^{2.1} \qquad (2.18)$$

where, D_{*s}, is the dimensionless particle diameter; u_*, is the bed shear velocity; and u_{*c}, is the critical shear velocity.

The source term, S_e, represents the entrainment of the bed sediments into the water column and has been modeled as an upward near bed mass diffusion term. The source term, S_d, represents the settling of suspended sediments and has been modeled as a

downward near bed settling velocity flux. The source term, S_F, describes the exchange of sediment particles between the active layer elemental volume and an elemental volume immediately underneath, called the active stratum elemental volume (Spasojevic and Holly, 1994).

With the assumption that the active floor elevation does not change, the mass conservation equations for an elemental active stratum volume can be written as:

For each size class separately:

$$\rho_s(1-p)\frac{\partial}{\partial t}\left[\beta_s(z_b - E_m)\right] + S_F = 0 \tag{2.19}$$

For the sum of all size classes:

$$\rho_s(1-p)\frac{\partial}{\partial t}(z_b - E_m) + S_F = 0 \tag{2.20}$$

with the constraint: $\sum\beta_s = 1$, where, z_b, is the bed elevation and β_s, is the active stratum fraction of the mass of one particle size class over the mass of all sediment particles.

2.3.2 Suspended Load Transport

The advection and turbulent diffusion of each particular size class of the suspended sediment can be expressed in mathematical form as:

$$\frac{D(\rho C)}{Dt} = \frac{\partial}{\partial x}\left[D_h\frac{\partial(\rho C)}{\partial x}\right] + \frac{\partial}{\partial y}\left[D_h\frac{\partial(\rho C)}{\partial y}\right] + \frac{\partial}{\partial z}\left[D_v\frac{\partial(\rho C)}{\partial z}\right] + \frac{\partial}{\partial z}(\rho C w_f) \tag{2.21}$$

where:

$$\frac{D(\rho C)}{Dt} = \frac{\partial(\rho C)}{\partial t} + \frac{\partial(\rho C u)}{\partial x} + \frac{\partial(\rho C v)}{\partial y} + \frac{\partial(\rho C w)}{\partial z} \tag{2.22}$$

In the above equations, C is the ratio of the mass of one particular sediment size class

to the mass of all size classes within an elemental volume ΔV, ρ, is the density of the sediment-water mixture, represented by all size classes. The expression used by CH3D-SED for the density of the mixture is (Zhou and Mc Corquodale, 1992, as cited by Spasojevic and Holly, 1994):

$$\rho = \rho_{cw} + C \cdot \left(1 - \frac{1}{s-1}\right) \tag{2.23}$$

where, ρ_{cw}, is the density of the clear water that is mentioned in section 2.2, and it is a function of the temperature and the salinity; and s, is the dimensionless sediment density.

The last term in equation (2.21) represents the gravitational settling of the suspended sediment particles. The expression used in CH3D-SED for the determination of the fall (settling) velocity varies with the size of the sediment particles. For the Stokes range, that is, for particles less than 100 μm the settling velocity is given as:

$$w_f = \frac{1}{18} \frac{(s-1) g D_s^2}{\nu} \tag{2.24}$$

For particles between 100 μm and 1000 μm (Zanke 1977, as cited by Spasojevic and Holly, 1994) the settling velocity is given as:

$$w_f = 10 \frac{\nu}{D_s} \left[\sqrt{1 + \frac{0.01(s-1) g D_s^3}{\nu^2}} - 1 \right] \tag{2.25}$$

where, D_s, is the particle diameter, and ν, is the kinematic viscosity.

The horizontal mass diffusion coefficients, D_h, are assigned constant values in CHD3D-SED (input), while the vertical diffusion coefficient, D_v, is being related to the vertical turbulent eddy viscosity, A_v, as proposed by Van Rijn, 1984b:

$$D_v = \beta_d \left[1 + \left(\frac{C}{C_0}\right)^{0.8} - 2\left(\frac{C}{C_0}\right)^{0.4} \right] A_v \tag{2.26}$$

where, C_0, represents the maximum concentration near the bottom and has been assigned a value equal to 0.65, and β_d, is a correction factor, constant over the depth.

The equations that describe the sediment processes, similarly with the hydrodynamic equations, have been expressed in non-dimensional form and the Cartesian coordinates have been transformed into horizontal curvilinear coordinates and sigma-stretched vertical coordinates.

2.4 Coupling of the Hydrodynamic and Sediment Models

The hydrodynamic process and the sediment process have not been coupled directly, instead a separate module has been dedicated to the sediment process, that has been further divided into two sub-modules; one for the bedload transport and bed evolution and a second one for the suspended sediment transport. According to the developers of the CH3D-SED model such a way of coupling the two parts of the model is justified by the use of a small time step since it minimizes the error introduced by the temporary uncoupling.

The assumptions for the coupling of the hydrodynamic and the sediment process made by the developers of the CH3D-SED model are: a) the transport of single bed sediment particles and the transport of the suspended sediment have the same time scale as the fluid flow process, b) the global changes in bed level and bed-surface particle size distribution have longer time scales, c) the suspended sediment concentration does not change abruptly and d) the density of the water-sediment mixture does not change within a computational time step.

The two main program moduli communicate fully and continuously. The hydrodynamic part of the CH3D-SED model provides information about the fluid velocities, water depths and temperature changes that are required input for the sediment part. The sediment model in return provides information about the changes of the bed elevation, the bed surface roughness due to the changes of the bed-surface size

distributions and changes of the density that is being corrected to represent the sediment-water mixture (Spasojevic and Holly, 1994).

2.5 Numerical Solution

2.5.1 Computational Grid and Numerical Schemes

The computational solution of the governing equations is obtained using a staggered grid, which implies that the different variables are evaluated either at the full grid points or, at the half grid points. Indeed, the vertical velocities are computed at the full grid points, while horizontal velocities, temperature, density, and concentrations are computed at the half grid points (Figure 2.2).

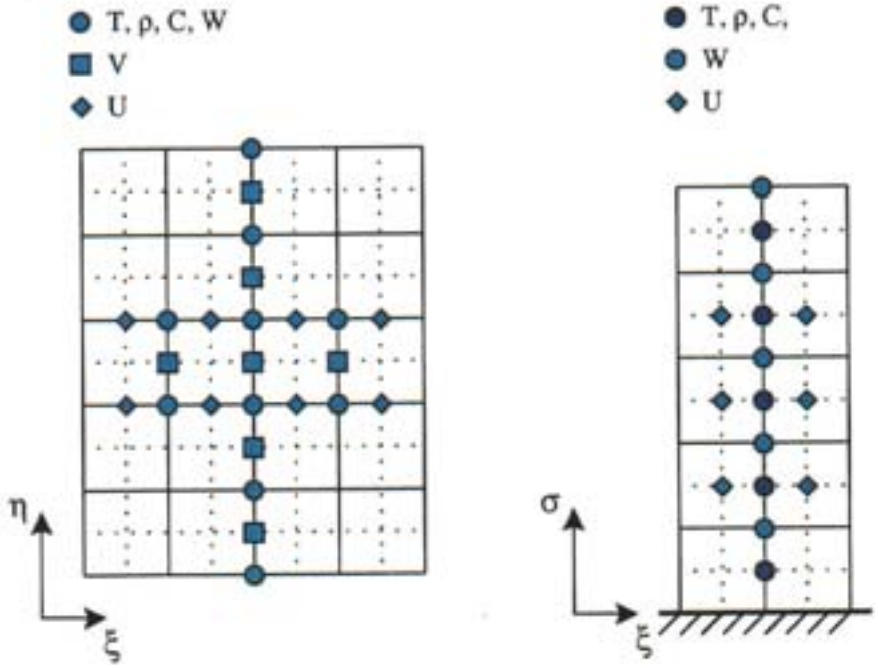

Figure 2.2 Schematic representation of the numerical staggered grid.

Discretization of the partial differential equations leads to a system of linear algebraic equations, which are solved using both an internal and an external solution mode. The external mode solution proceeds by calculating the water surface displacements, and the vertically integrated flow velocities. The internal mode solution proceeds by calculating the vertical component of the velocities, the temperature, the suspended sediment concentrations, and the deviation of the horizontal velocity components from the vertically integrated velocities.

Implicit numerical schemes are used to discretize all the terms of the vertically integrated continuity equation, and the water-surface slope and bottom friction terms in the vertically integrated momentum equations. For the convective terms in the momentum equations, Roaches second upwind difference scheme (Roache, 1972, as cited by Spasojevic and Holly, 1994) is used, while an upwind difference scheme is used to evaluate the bedload flux and the settling velocity terms.

Finally the Quickest method (Leonard, 1979), a spatially and temporally third order scheme is used to discretize the conservation of mass equation for the suspended sediment and the advective terms of the temperature equation.

2.5.2 The Sequence of the Hydrodynamic Computations

In both the hydrodynamic calculations and the sediment calculations, CH3D-SED uses a set of input files for internal model initialization (time step for the calculations, time length of the calculations, type of boundaries, e.t.c), and for the definition of the different physical constants and variables used in the calculations. The steps performed during the hydrodynamic calculations are outlined below:

- Read the values of model initialization parameters from the main model input file. Here is defined the time step used in the model calculations, the number of the time steps, the location of the rivers, the type of the flow rates for the rivers (constant or, variable), e.t.c
- Read the bathymetry data of Lake Erie, and the corresponding values of the (x, y) coordinates. Transform the above data into the curvilinear and sigma

coordinate domain.

- Set the water depths at the faces of each computational cell.
- Create the 2-D and 3-D arrays required for the storage of the values of the variables being calculated.
- Read the wind speed data supplied, and calculate the wind stresses at the water free surface.
- Read the 2-D temperature data supplied at the water free surface
- Calculate the total water depths from the latest water surface elevations.
- Read the river inflow data supplied for the three rivers considered (Maumee, Detroit, and Niagara).
- Calculate the water densities and evaluate the baroclinic terms in the momentum equations.
- Calculate the eddy viscosity and eddy diffusivity coefficients.
- Calculate the vertically integrated flow field from the vertically integrated equations of the fluid motion.
- Calculate the total water depths at the next time level.
- Calculate the 3-D velocity field. The vertical sum of the horizontal components of the 3-D velocity is forced to match the vertically integrated values of the velocity to make sure that the continuity equation is satisfied.
- Calculate the convective and diffusion terms in the momentum equations and use them to compute the vertically averaged flow field and the 3-D velocity field at the next time step.
- Finally, calculate the 3-D temperature field.

The above steps are the ones performed by CH3D-SED for the particular computations required for this project. In other words, other features of the model have been turned off. The model, after completion of the computations, is set up to provide the hourly values for the following variables: a) the 3-D temperature field, b) the 2-D water surface elevation field, c) the 2-D vertically integrated velocity field, and d) the 3-D velocity field.

2.5.3 The Sequence of the Sediment Computations

The computations for the sediments involve the close interaction of the two sediment modules incorporated into CH3D-SED, that is, the bottom mobile bed module which performs the required computations for the bottom sediments, and the suspended sediment module which performs the calculations for the sediments in suspension in the water column. The computational steps are as follows:

- Solve the conservation of mass equation for each assigned sediment particle class of all the active layer sediment size fractions, and the global conservation of mass equation for the bed sediments.
  - All equations are solved together.
  - The concentrations of the suspended sediments are known from the previous iteration.
  - The solution gives the active layer sediment size fractions and the bed surface elevations.
- Solve the conservation of mass equations for a particular sediment size class, of suspended sediment, along the vertical direction above the same bottom grid point.
  - The solution gives the volumetric concentrations for a particular size class of suspended sediment.
- For each suspended sediment size class repeat the previous step.
- Repeat the above steps all over the computational domain.

The model, after completion of the above computations, provides the hourly values for the following variables: a) the 3-D concentration field for each sediment size class, b) the 2-D bed elevation changes, c) the 2-D distribution of the bottom sediment class fractions.

Chapter 3
Data Collection and Analysis

The decision to engage CH3D-SED in this project came out of its ability to model sediments of various grain sizes and its ability to model the sediments originating from different sources. It is note worthy to mention here that, the extensive use of CH3D-SED required by this project, is the first time ever attempted (to the best of our knowledge). The way the model was implemented and the implications and requirements of its application to the present project will extensively discussed in Chapter 4.

The data required for CH3D-SED, that is the data required to establish the boundary and initial conditions for the model, can be categorized as follows: a) meteorological data, b) hydrological data and c) sediment data.

3.1 Meteorological Data

The circulation models require that the boundary conditions and the forcing function at the free water surface are correctly set. The forcing function is the wind speed or, wind stress, at the free surface and it is usually obtained from measured data or from atmospheric models that pass this information to the circulation model. The information is passed either, directly by coupling the two models or, indirectly by obtaining the information after the atmospheric model simulation is completed.

The availability of the extensive databases of the Great Lakes Forecasting System made it a natural choice to use these databases to obtain the meteorological data required by CH3D-SED. The database chosen was the year 1997, and for the ice-free period between April 1 to December 31, 1997.

The meteorological data obtained from GLFS were the wind speeds and the temperature field at the free water surface of Lake Erie. The GLFS gathers these data from the Marine Observation data set (MAROBS), which include data from twenty Canadian and US. weather stations, 5 Coast Guard stations, 3 NOAA-AES buoys, 2 CMAN stations and 12 Airways stations. After GLFS receives the data from MAROBS, it processes them to get the values of the wind speeds and temperatures over the entire Lake Erie numerical grid (209 x 57 grid points in the horizontal direction).

The hourly wind speed data are adjusted to reflect: a) a common anemometer height and b) the over-water conditions. The two components (U, V) of the wind speed for each horizontal grid point of the Lake Erie are obtained by interpolation every hour (Kuan, 1995).

The temperature data coming from MAROBS have a time differential of six hours and they are interpolated by GLFS over the entire Lake Erie grid for every hour. Further manipulation of the wind and the temperature data is not required for use in CH3D-SED. From these data the model internally calculates the wind stresses.

3.2 Hydrological Data

The accurate modeling of Lake Erie requires the inclusion of its tributaries data as well. For this study only the three dominant tributaries were considered, that is, the Detroit River, the Maumee River and of course the Niagara River.

3.2.1 River Flow Rates

The Maumee and Detroit rivers, with a sediment loading of 1.8×10^6 ton/yr and 1.4×10^6 ton/yr (Kemp et al., 1976) respectively, are the most significant tributary sources of sediment input to Lake Erie and do so in the Western Basin. The total sediment input that originates from all the other tributaries does not exceed 0.6×10^6 ton/yr. The proximity of the two rivers to the disposal and water intake sites makes them important

factors in the sediment modeling for the western basin. The Niagara River on the other hand is the only natural outlet for Lake Erie with a total sediment output of 4.5×10^6 ton/yr (Kemp et al., 1976).

CH3D-SED requires the time varying flow rates of the rivers being considered. The daily flow rates of the above rivers were obtained from the U.S.G.S databases. The daily flow rates for Maumee and Niagara rivers were available for the simulation year 1977 and were directly used as model input.

As far as Detroit River is concerned, measured data are sparse and not available for the simulation year. Considering the fact that the flow rates of Detroit river over the years have a very close resemblance and small value variations (G. F. Koltun, 1990), the latest available data from the USGS database (USGS Water Resources of the United States) were used, which are the data from the year 1977. The flow rate data are shown in Figure 3.1 and Figure 3.2. Figure 3.1 displays the data as is, while Figure 3.2 displays the data with the averaging applied for Detroit River. Both the figures are included for comparison reasons.

3.3 Sediment Data

The sediment modeling requires the inclusion of all the major sediment sources. The sediment sources in Lake Erie are the bottom sediments, the riverine sediment inputs, the disposal site unconfined sediments and of course the sediments originating from the shore erosion. Despite the fact that shore erosion is extremely important in sediment forecasting, and a very significant sediment source, it wasn't considered in this study simply because the purpose is to determine the relative intensity of the impacts of the other four sources on the water intake site.

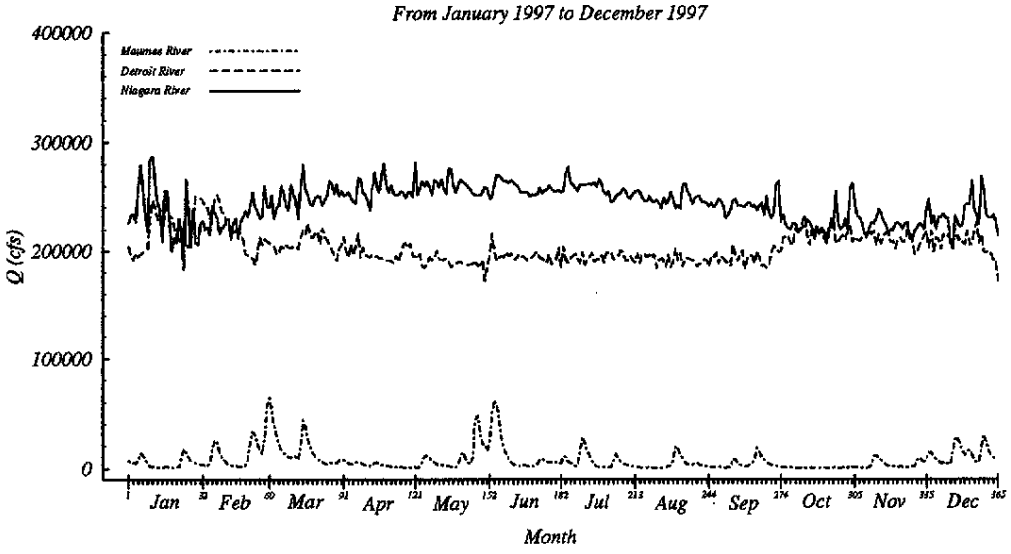

Figure 3.1 Daily flow-rates for the Maumee, Detroit and Niagara Rivers for the simulation year 1997.

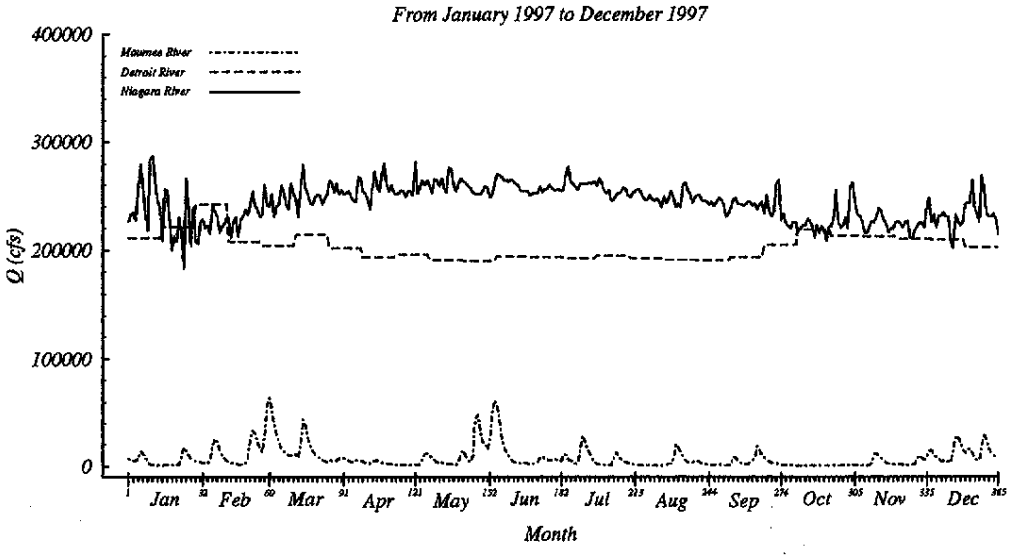

Figure 3.2 Daily flow-rates for the Maumee, Detroit and Niagara Rivers with smoothing applied on the Detroit River data (simulation year 1997).

3.3.1 Lake Bottom Characteristics and Sediment Analysis

Qualitative information about the bottom sediments and their grain size distribution for Lake Erie was obtained by Thomas et al. (1976). The authors used both sediment sampling and acousting profiling to examine 275 sampling locations all over the lake. Their results, presented in Figure 3.3, show a distribution of the bottom sediments based upon four basic types which are identified as follows: a) sand and/or gravel (S), b) post-glacial mud (M), c) soft gray mud with some sand (M) and d) glacial sediments (GL).

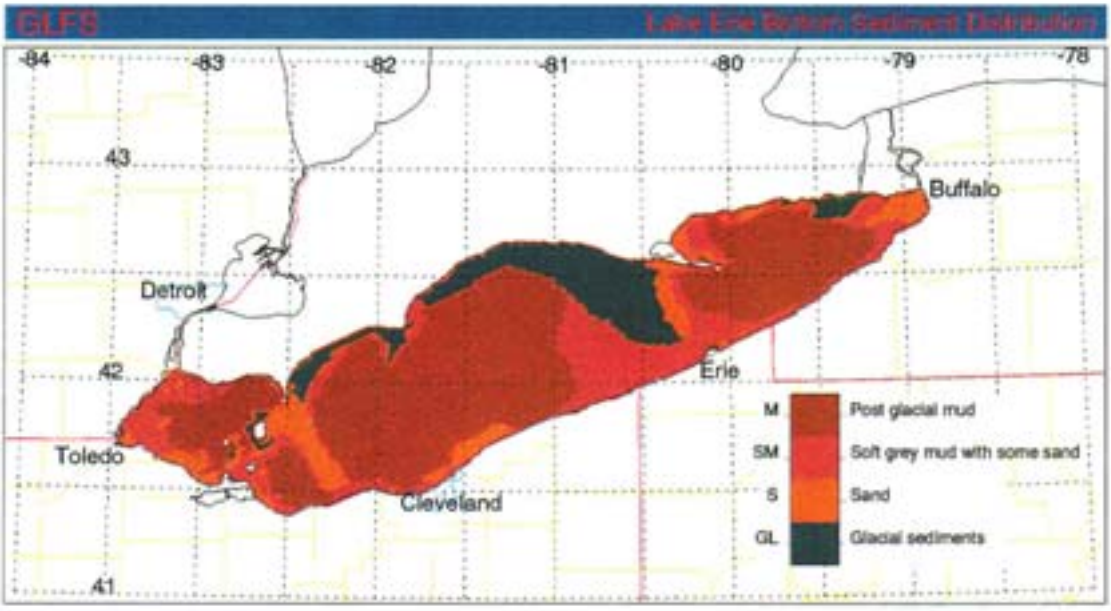

Figure 3.3 Distribution of the bottom sediment types for Lake Erie.

Following the qualitative distribution of the bottom sediments described above, each grid point at the bottom of the lake, depending upon its location, is assigned one of these types. The next step in this analysis is to identify the above types with fractions representing the sediment grain sizes present.

Quantitative information about the bottom sediments of Lake Erie has been obtained from the technical report prepared by Herdendorf et al., 1978. Grab sediment samples

were taken at 2594 positions from the lake bottom. About 1670 of these samples were analyzed mechanically for grain size by the sieve method to estimate the percent of silt and clay. The results were reported as the percentages of sand, silt and clay contents of the samples.

To classify the sediments into different size classes the Wentworth sediment grade scale is used. According to this scale a sediment particle with diameter between 0.62 – 2.00 mm is classified as sand, with a diameter between 0.004 to 0.62 mm is classified as silt, and with a diameter less than 0.004 mm is classified as clay.

To estimate the percent of sand, silt and clay contained in each one of the four sediment types we first identified the samples taken within the region of each sediment type. Then we calculated the average percent of each size class for each sediment type using the following formula:

$$F_{ji} = \frac{1}{N_i} \sum_{k=1}^{N_i} f_{jk} \tag{3.1}$$

where F_{ji} is the average percent of each size class for each sediment type; i, is each sediment type (M, S, GL, SM); N_i is the number of samples corresponding to each sediment type; f_{jk} is the percent of each size class for each sample N_i; and j, is each size class (sand, silt, clay). The results of this analysis are shown in Table 3.1.

Table 3.1 Definition of the sediment fractions for the sediment types in Lake Erie.

Sediment Type	*No. of Samples N*	*Sand*	*Silt*	*Clay*
M	759	0.0 %	70.0 %	30.0 %
SM	137	70.0 %	20.0 %	10.0 %
S	361	97.0 %	2.0 %	1.0 %
GL	410	55.0 %	35.0 %	10.0 %

3.3.2 Disposal Site Sediment Analysis

A field data collection project (ARMS) was contacted the summer of 1996 (Fan and Bedford, 1998) at the disposal site. During the experiment, suspended sediments grab samples were taken at two positions (at about 1.0 m above the bottom, labeled Top, and at 10 to 15 cm above the bottom, labeled Bottom). Analysis of the grab samples (Fan and Bedford, 1998) gave the results shown in the following table.

Table 3.2 Total suspended solid analysis for the sediments at the disposal site.

Sample Date	*Sample No.*	*Filter Disk Mass (g)*	*Filter Disk SS Mass (g)*	*Sample Volume (mL)*	*TSS (mg/L)*	*Mean TSS (mg/L)*	*STD (mg/L)*
8/2 Bottom	1-1	0.1974	0.2007	208	15.87		
	1-2	0.1963	0.1997	188	18.09	16.58	1.31
	1-3	0.1983	0.2010	171	15.79		
8/2 Top	2-1	0.2037	0.2040	203	1.48		
	2-2	0.2020	0.2023	211	1.42	1.45	0.04
	2-3	0.1935	0.1936	205	(0.49)*	(1.13)*	(1.12)*
8/14 Bottom	3-1	0.2004	0.2046	211	19.91		
	3-2	0.1985	0.2034	220	22.27	21.89	1.82
	3-3	0.1967	0.2022	234	23.50		
8/22 Bottom	4-1	0.1915	0.2025	213	51.64		
	4-2	0.1918	0.2036	224	52.68	52.90	1.39
	4-3	0.2000	0.2124	228	54.39		
8/22 Top	5-1	0.1919	0.1924	220	2.27		
	5-2	0.1912	0.1917	238	2.10	2.06	0.24
	5-3	0.1976	0.1980	222	1.80		
9/11 Bottom	6-1	0.1927	0.2028	232	45.53		
	6-2	0.1861	0.1984	236	52.12	49.15	3.71
	6-3	0.1974	0.1910	224	51.79		
9/11 Top	7-1	0.1831	0.1855	230	10.43		
	7-2	0.1931	0.1957	229	11.35	10.25	1.20
	7-3	0.1993	0.2014	234	8.97		

* Numbers in parentheses represent outliers or statistics including outliers.

From the mean TSS reported in Table 3.2 calculations included first, the average between the bottom and the top locations for each day and second, the average suspended sediment concentration over the four day interval. The average sediment concentration for the disposal site obtained by this procedure was about 22 mg/L.

The area of the lake bottom that is occupied by the disposal site is about 6.31 km^2. The area, however, surrounding one grid point on the 2x2 km resolution grid is only 4 km^2. Conservation of mass makes it necessary to adjust the average suspended sediment concentration. The adjustment was made using the following formula:

$$(ASSC)_2 = \frac{A_1 \cdot (ASSC)_1}{A_2} \tag{3.2}$$

where, A_1 is the bottom area of the disposal site, A_2 is the effective bottom area corresponding to the grid point, $(ASSC)_1$ is the average suspended sediment concentration corresponding to A_1 and $(ASSC)_2$ is the average suspended sediment concentration corresponding to A_2. The adjusted average suspended sediment concentration for the disposal site was calculated to be 35 mg/L.

Grain size distributions for the bottom sediments at the disposal site have been reported by the Toledo Harbor Planning Group in 1998. The analysis of the samples distributions was performed using the CRL method 485. The method allows distinction between particles passing the #200 sieve which can be identified as silt and clay and retains sand and gravel. The average of four samples showed a 96.2 % of silts and clays and a 3.8 % of sands and gravel.

Analysis of grab samples from the disposal site was also performed by the Automatic Particle Size Analyzer (HIAC Model-320), at the Coastal Engineering Laboratory at O.S.U, and the d_{50} was determined for each sample. Table 3.3 shows the results of the analysis (Fan and Bedford, 1998).

The d_{50} value of the sediment sample gives the particle diameter at which 50 % by weight is finer or coarser. From Table 3.3, the value for is d_{50} 0.04164 mm, which is within the limits of the silts.

Table 3.3 Values of d_{50} for the sediments at the disposal site.

Sample Date	*Sample Number.*	*d_{50} (μ) Each Sub-sample*	*Mean d_{50} (μ) Each Sample*	*STD (μ)*
8/2 Bottom	1-1	51.29	45.55	8.12
	1-2	39.81		
8/2 Top	2-1	39.11	36.11	4.24
	2-2	33.11		
8/14 Bottom	3-1	43.35		
	3-2	41.69	42.90	1.06
		43.65		
8/22 Bottom	4-1	45.60		
	4-2	43.15	43.97	1.41
	4-3	43.15		
8/22 Top	5-1	43.65		
	5-2	41.69	41.12	2.86
	5-3	38.02		
9/11 Bottom	6-1	45.37		
	6-2	42.66	42.16	3.48
	6-3	38.46		
9/11 Top	7-1	43.15	39.73	4.84
	7-2	36.31		

Sediment particles with diameter greater than d_{50} can be identified as 46.2 % by weight to be silts and 3.8 % by weight to be sands and gravel. Sediment particles with diameters less than d_{50} have been assumed to be well graded with an equal contribution from the silt and clay size classes.

3.3.3 Sediment Analysis for the Maumee and Detroit Rivers

Detailed suspended sediment concentration data for both Maumee and Detroit rivers are sparse to non-existent and the main source of sediment data for the Maumee river

used in this report is the annual USGS Water-Data Report of Ohio for the water year October 1991 to September 1992 (US Geological Survey, 1993).

The suspended sediment concentration C (mg/L) is reported on a daily basis, along with the mean values of the flow rate Q (ft^3/s) for Maumee River. The regression between the values of the concentration and the flow rate (Figure 3.4) shows a linear trend with a coefficient of determination of $R^2 = 0.75$, which is described by the following equation:

$$C = 0.015 \cdot Q + 12.116 \tag{3.3}$$

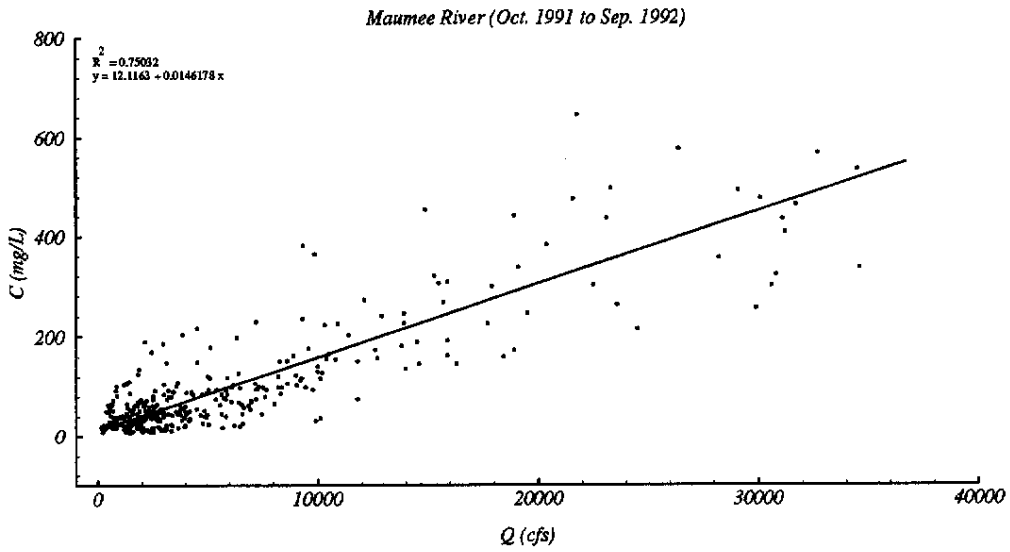

Figure 3.4 Linear regression between the daily flow-rates and the daily concentrations of the suspended sediment at Maumee River (water year 1992, US Geological Survey, 1993).

Since the relationship between C, and Q, is defined, it is apparent that the concentration of the suspended sediments for Maumee river can be estimated for the simulation year 1997, by use of the recorded daily flow rates along with equation (3.2).

The results are shown in Figure 3.5.

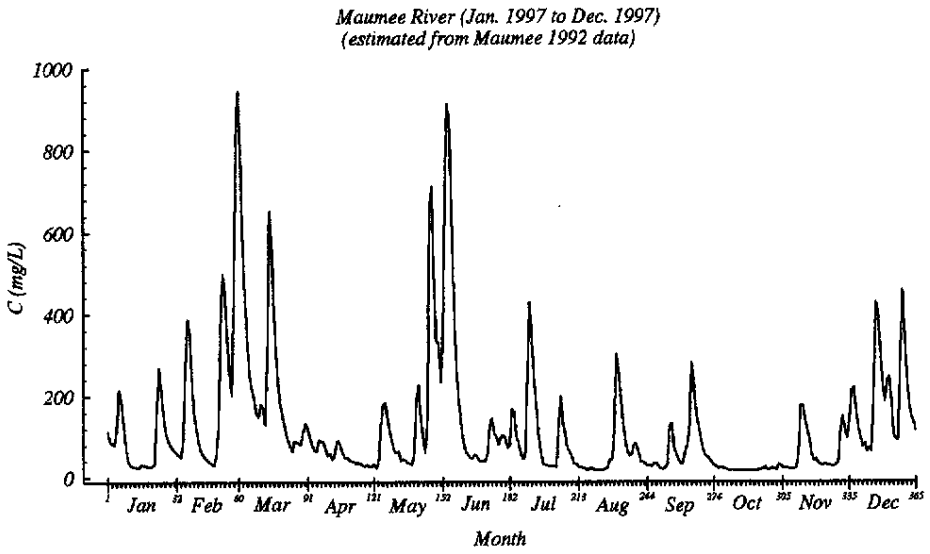

Figure 3.5 Time trace of the estimated daily concentrations of the suspended sediment at Maumee River (simulation year 1997).

As far as Detroit River is concerned, detailed sediment concentration data are not available. However, Kemp et al. (1976), have reported the sediment loading of fine grained material from the various sediment sources in Lake Erie, and the results of their work are summarized in Figure 3.6. The data used to create this sediment-loading map span a 35-year period and, therefore, it was assumed that the relative loading from the various sources can be applied to the simulation year 1997 too.

Defining the riverine sediment loading as:

$$SL \approx 0.9 \cdot C \cdot Q \tag{3.4}$$

where, SL (ton/yr) is the sediment loading, C (mg/L) is the average daily concentration, Q (ft^3/s) is the average daily flow rate, and 0.9 is the units conversion factor, the total

sediment loading for the whole year is simply given by:

$$TSL \approx 0.9\sum_{i=1}^{N} C_i \cdot Q_i \tag{3.5}$$

where TSL (tons/yr) is the total sediment loading and N is the number of the days in a year.

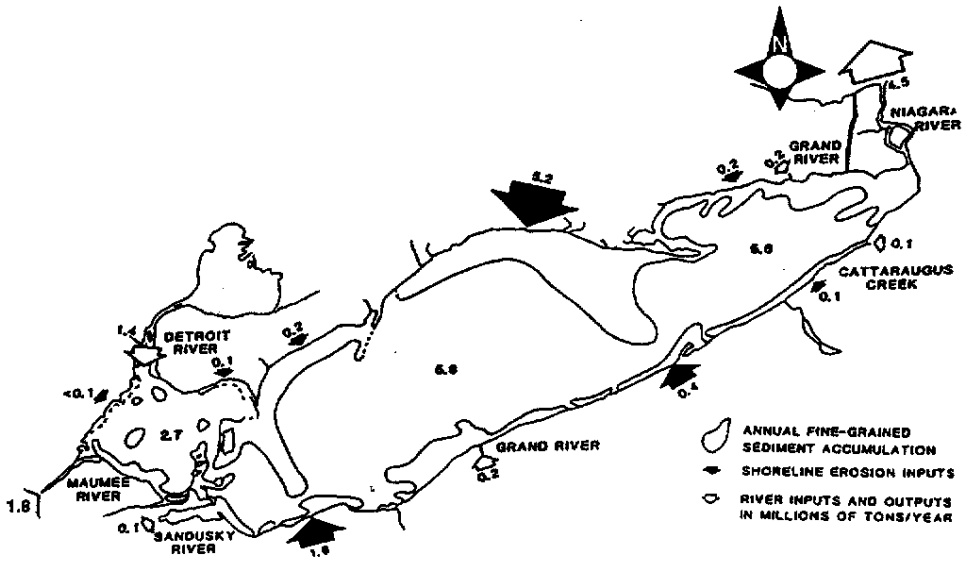

Figure 3.6 Location of major sources and sinks of fine-grained sediment material in Lake Erie (Kemp et al., 1976).

Using the data from Figure 3.6, an average coefficient, $\bar{f}$, which represents the relative sediment loading between the Detroit and Maumee Rivers can be defined as follows:

$$\bar{f} = \frac{(TSL)_D}{(TSL)_M} = \frac{\sum_{i=1}^{N} C_{D_i} \cdot Q_{D_i}}{\sum_{i=1}^{N} C_{M_i} \cdot Q_{M_i}} = \frac{1.4 \cdot 10^6}{1.8 \cdot 10^6} \approx 0.77 \tag{3.6}$$

where the subscripts "D" and "M" denote the Detroit and Maumee Rivers respectively.

Assuming now that $\bar{f}$ is constant throughout the year, the daily averaged concentration of the suspended sediments at Detroit River can be estimated using equation (3.6) and the results are shown in Figure 3.7.

$$C_D = \bar{f} \cdot C_M \cdot \frac{Q_M}{Q_D} \tag{3.7}$$

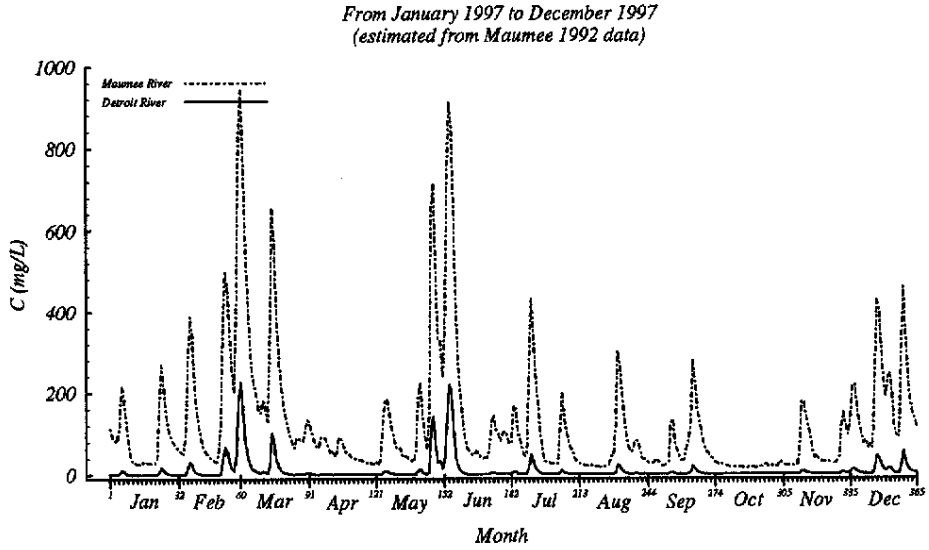

Figure 3.7 Estimated concentrations of the suspended sediments for Maumee and Detroit Rivers (simulation year 1997).

In addition to suspended-sediment loads, the particle-size distribution of the suspended sediment for the two rivers needed to be estimated. Available data for the Detroit River describe a suspended sediment mixture with 87 to 100 percent particles classified as silt and clay (US Geological Survey, 1975b). An average of 6 percent by weight for the sand size class was used in the present study for the Detroit River. An average of 7.5 percent by weight for the sand size class has been estimated for the Maumee River (Toledo Harbor Planning Group in 1993). Finally, a 30 to 70 percent contribution from the clay and silt size classes respectively has been assumed for both the Detroit and the Maumee Rivers.

Chapter 4
Model Implementation

4.1 Numerical Grid

Lake Erie is 388 km long and 92 km wide with a southwest to northeast alignment. In order to establish the "x" coordinate axis along the longitudinal axis of the lake the flow domain is rotated by 27.33° clockwise. The resolution of the numerical grid used in CH3D-SED is 2x2 km which yields 209, "I", grid points in the "x" direction and 57, "J", grid points in the "y" direction (normal to the "x" direction).

The grid domain extends outside the flow domain, that is, spans some land area around the lake. All the land grid points are assigned with a water depth equal to zero, so they can be identified during the model calculations. CH3D-SED in order to accommodate irregular horizontal domains uses a curvilinear coordinate system in the horizontal direction, and internally establishes the flow domain from the grid domain using the grid points with water depth other than zero.

In the vertical direction CH3D-SED uses the σ-coordinate system in order to accommodate for the depth variation throughout the lake. In this project fourteen grid points in the vertical direction were used, resulting in thirteen irregularly spaced vertical slices in the (x, y, z)-coordinate system. The free water surface is identified at $\sigma = 0$, while the lake bottom is identified at $\sigma = -1$. The σ-spacings are closer together near the free water surface and further apart near the bottom. A maximum physical vertical spacing of ~ 6 m is found in the eastern basin of Lake Erie, and a minimum vertical spacing of ~ 0.0375 m is found in the western basin of Lake Erie (Kuan, 1995).

With respect to the numerical grid described above, the location of the various sites considered in this project are shown in the following table:

Table 4.1 Location of the different sources in the numerical grid of the Lake Erie.

Location	*I*	*J*	*Latitude*	*Longitude*
Maumee River	4	46	41.7182	-83.4379
Detroit River	22	56	42.0320	-83.1721
	23	56	42.0406	-83.1508
Niagara River	199	16	42.8484	-78.8945
Disposal Site	12	47	41.8033	-83.2805
Water Intake Site	10	41	41.6992	-83.2589

4.2 Boundary Conditions

A detailed description of the type of boundary conditions the CH3D-SED model uses, for both its hydrodynamic and sediment part, can be found in the Mobile Bed Hydrodynamics Report (Spasojevic and Holly, 1994). However, in this part of the report the specifics of how the riverine and the free water-surface meteorological boundary conditions were implemented in this project will be discussed. These boundary conditions can be divided into three sections: a) meteorological boundary conditions, b) hydrodynamic boundary conditions, and c) sediment boundary imposed at the river boundaries and at the bottom of the lake.

4.2.1 Meteorological Boundary Conditions

The meteorological boundary conditions imposed at the free water surface of the lake are the 2-D wind and temperature fields. CH3D-SED for its hydrodynamic calculations requires the definition of the wind shear stress tensor at the free water surface of the lake. The two components of the wind stress tensor are calculated from the free water-surface wind speed as follows:

$$\left(\tau_\xi\right)_s = C_D \cdot \rho_a \cdot W_\xi^2 \qquad \text{and} \qquad \left(\tau_\eta\right)_s = C_D \cdot \rho_a \cdot W_\eta^2 \tag{4.1}$$

where $(\tau_\xi)_s$ and $(\tau_\eta)_s$ are the wind shear stresses in the ξ and η directions at the free surface respectively, W_ξ and W_η are the wind speed components, ρ_a is the density of the air and C_D is the drag coefficient.

Having defined the wind shear stresses, the boundary conditions for the flow velocities at the free surface are then defined as:

$$A_v \frac{\partial \overline{u}}{\partial z} = \frac{\left(\tau_\xi\right)_s}{\rho_a} \qquad \text{and} \qquad A_v \frac{\partial \overline{v}}{\partial z} = \frac{\left(\tau_\eta\right)_s}{\rho_a} \tag{4.2}$$

The wind velocities, required for the above calculations, were obtained from GLFS, as explained in Chapter 3, and a typical 2-D wind field is shown in Figure 4.1.

CH3D-SED has been slightly modified to accept space and time varying temperature at the free water-surface for each time step. These data are readily available from GLFS for the whole simulation period. Since the temperature data are available in six-hour intervals, CH3D-SED internally interpolates for the temperature values for each time step. A typical 2-D temperature field is shown in Figure 4.2.

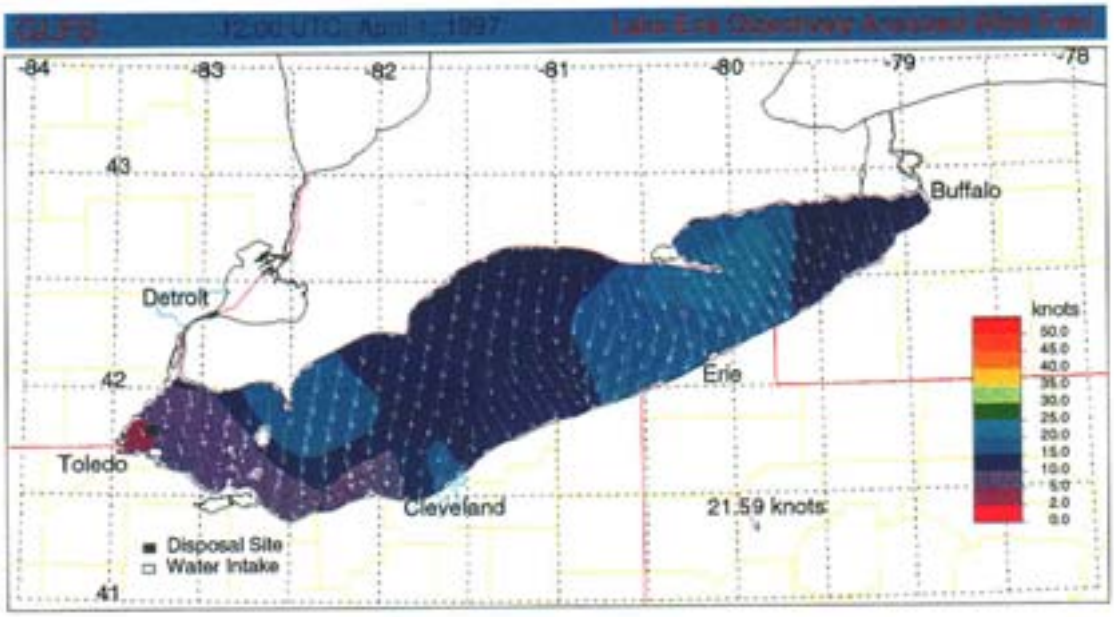

Figure 4.1 Wind field at the free water-surface as obtained from GLFS.

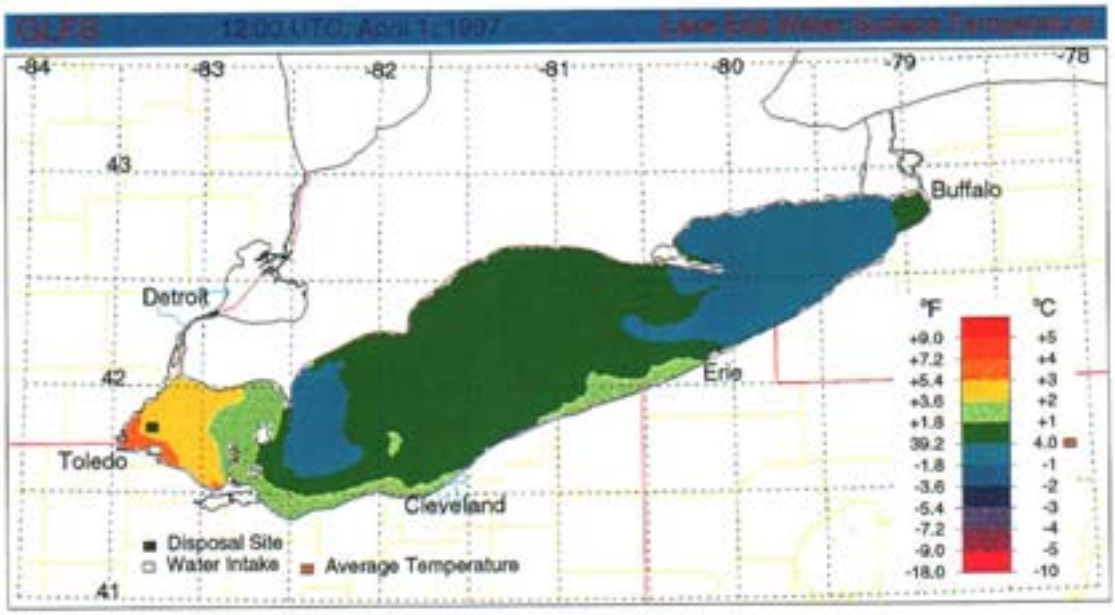

Figure 4.2 Temperature field at the free water-surface as obtained from GLFS.

4.2.2 Hydrodynamic Boundary Conditions

The riverine boundary conditions require the definition of the flow-rates, imposed at the river boundaries. As mentioned earlier, only the three major tributaries were considered in the present simulation, two of which, the Maumee and Detroit Rivers, are inflow boundaries and the Niagara River is the only outflow boundary in the lake. The boundary conditions for the inflow and the outflow boundaries are simply the daily averaged flow rates, Q, the values of which were determined by the methods described in Chapter 3.

CH3D-SED is using the assigned flow-rates to calculate the velocity profiles at the boundaries (fourteen vertical grid points), which define the boundary conditions for the velocity field at these locations. In the case of the Detroit River, the total daily flow-rate was evenly divided between the two grid points that the river occupies.

4.2.3 Sediment Boundary Conditions

The simulation of the sediment distribution in Lake Erie required the definition of twelve sediment size classes (Table 4.2). These twelve sediment classes were equally divided among the four sediment sources and the grain sizes (particle diameters) were selected to represent the typical sediment particle sizes found in Lake Erie. As shown in Table 4.2, each source was assigned three size classes.

The selected "sand diameters" range between 150 and 147 μ and they can be identified as fine sand. The "silt diameters" range between 50 and 47 μ, putting them in the coarse silt range, while the "clay diameters" range between 4 and 3 μ, putting them in the coarse clay range.

For each source, CH3D-SED requires the definition of the percentage of each sediment class as a fraction of all sediment classes at the source. These fractions were determined by the methods described in Chapter 3 and they are shown in Table 4.2.

While the flow-rates for the hydrodynamic part of the simulation were specified at all three tributaries, in the case of the sediment boundary conditions, the Niagara River was treated as an open boundary. Therefore, the daily average concentrations for the suspended sediment were only specified for Maumee and Detroit Rivers.

Table 4.2 Definition of the twelve sediment size classes and their fractions for the four sediment sources in Lake Erie.

Location	*Size Class*	*Grain Diameter (μ)*	*Grain Size Fractions (%)*
Lake Bottom (Source #1)	1	150	Refer to Table 3.1
	2	50	
	3	4	
Disposal Site (Source #2)	4	149	3.8
	5	49	72.2
	6	3.7	24.0
Maumee River (Source #3)	7	148	7.5
	8	48	65.0
	9	3.3	27.5
Detroit River (Source #4)	10	147	6.0
	11	47	65.0
	12	3	29.0

The daily concentration C (mg/L) of each sediment class was found by multiplying the fraction for that class with the average daily concentrations at each tributary. The concentration profiles at the tributaries (fourteen vertical grid points) were assumed constant for each sediment class.

4.3 Initial Conditions

The initial conditions for the 3-D velocity and the suspended sediment concentration fields are rather simple. Both the flow velocities and the concentrations were initialized to be zero everywhere in the lake. The concentration profile of the suspended sediment at the disposal site was initialized with a constant value of 35 mg/L (all sediment classes). For each sediment class, the constant concentration profile was determined by

multiplying the total concentration of 35 mg/L with the fraction of that class.

The bottom sediments in Lake Erie were assigned three sediment classes throughout the lake, but for each grid point, a different class fraction distribution was assigned according with the methods described in Chapter 3. For the grid point corresponding to the disposal site the class fractions used are the same as the ones used for the suspended sediment.

4.4 Model Runs and Time Considerations

The computer used for the model simulation is a Silicon Graphics Origin 2000 system located at the OSU Super Computer Center (http://oscinfo.osc.edu/hardware/). This computer is a shared memory multiprocessor system, consisting of twenty-four 250 MHz IP27 processors and 3 GB of main memory. Each processor has a MIPS R10000 CPU and a MIPS R10010 floating point unit. The "sequential" version of the CH3D-SED model used for the present simulation was running on just one processor, and therefore, could not take full advantage of the capabilities of the computer. Undergoing research at the GLFS lab, in coordination with the Army Corps of Engineers, aims in the development of a "full parallel" version of CH3D-SED, so that CPU and real time requirements can be minimized.

4.4.1 Model Runs

The initialization of the model itself, according to the initial and boundary conditions for the flow field discussed earlier, requires that the model runs for some period of time ("model spin up") before the beginning of the actual model simulation. The "spin up" period used for this simulation was one week prior to April 1, 1997.

The large memory and storage requirements, and CPU time, made it necessary to break the whole simulation period into eighteen "14-day" periods and one "10-day" period, thus dividing the whole model simulation into nineteen individual model runs. The "interface" between individual runs was the so called "hot start file" created after

each run, which is simply a file containing all the variable values from the previous two time steps all over the numerical grid.

The use of a 10 min time step is a) within the limits of the stability and convergence criteria of the numerical schemes set by the CH3D-SED model and b) within the requirements of the hydrodynamic and the sediment model coupling. The CPU time required for the completion of one time step was ~ 45 s, and most of the computational time was spent for the sediment part of the calculations.

4.4.2 Time Considerations

The use of the CH3D-SED in such an extend, as one might expect, requires a considerable amount of time to be spent at the different stages of the simulation. The time required for the actual execution of a 14-day run, was ~ 26 hours, and the average elapsed time from job submission to job execution was ~ 14 to 20 hours. Therefore, the total time spent for a 14-day run, on average, was ~ 40 to 46 hours, bringing the time required to complete the 9-month simulation to about 760 hours (~ 32 days).

The next stage of the simulation was to compress the model output files, after each model run was completed, and fetch the files to the GLFS computer facilities for further analysis and processing. Usually, the time required for this step was ~ 5-6 hours. The extraction of the hourly data from the model output files and storage in individual files was necessary for faster analysis and graphical representation of the model results. The required time for this stage was about 5 hours per model run.

The graphical representation of the model results includes, in addition to other plots, the creation of 2-D contour maps for the various flow variables, such as vertically averaged flow velocities, suspended sediment concentrations, total mass of suspended sediments, e.t.c. The time required for the creation of one set of contour plots was 1.3 hours per model run per variable. The full set of the contour maps for one variable consists of 6576 plots, for the 9-month simulation period, the creation of which required about 25 hours.

Chapter 5
Results and Summary Conclusions

The model results, as explained in Chapter 4, were stored for every 1-hour time interval and for each output variable in individual files. The total number of these individual files, per variable, for the 9-month simulation period is 6574. The model results were then plotted out in two different graphics formats, Encapsulated Postscript (EPS) and Graphics Interchange Format (GIF89a), producing 13148 plots per variable. These plots are 2-D contour maps either of the vertically averaged variables or, of the values of the flow variable at specified vertical levels above the lake bottom.

The production of the plots in these two graphics formats was essential for two reasons: a) to import these plots in other documents like this report (EPS), and b) to view the plots on the fly or, even produce animations, within a Web Browser. Here only a selected set of these plots is included (Appendix A), while the full set is contained in the CD accompanying this report.

The other set of plots produced, are the summary plots (Appendix B) which are simply time trace plots of different flow variables for the 9-month simulation period. While the contour maps represent the global (all over the lake) behavior of the flow variables at each 1-hour time interval, the time trace plots are localized, and they represent the behavior of the flow variables over time at a specific location in the lake.

In Appendix A of this report are presented the contour maps of the water-surface wind speed and temperature, and the contour maps of the total suspended mass of the "global sediments" originating from the lake bottom and the disposal site. The term "global sediments" is used inclusively here and describes all the sediment classes

assigned to the sediment source (sand, silt and clay). The units used in the total suspended mass contour maps are metric tons per unit depth (tons/m). The total suspended mass has been calculated using the following equation:

$$TSSM = 10^{-6} \cdot \frac{\overline{C} \cdot V_{eff}}{d} = 10^{-6} \cdot \frac{\overline{C} \cdot A_{eff} \cdot d}{d} = 10^{-6} \cdot \overline{C} \cdot A_{eff} \qquad (5.1)$$

where TSSM, is the total suspended mass of the sediments (tons/m), $\overline{C}$, is the vertically averaged concentration (mg/L), V_{eff}, is the effective volume (m^3) where the total suspended mass is calculated, A_{eff}, is the corresponding effective area (m^2), and d, is the water depth (m). The effective area, A_{eff}, is defined as the area of the horizontal square extending half a grid point from the grid point where $\overline{C}$ is calculated, that is, the area occupied between the half grid points: (I-1/2, J-1/2), (I+1/2, J-1/2), (I+1/2, J+1/2) and (I-1/2, J+1/2). For the grid resolution used for this simulation it is: $A_{eff} = 4\ km^2$ (constant).

The physical meaning of the units used for the TSSM, can be interpreted as follows: if a volume of water-sediment mixture is taken equal to 4 km^2 x 2 m, containing 100 tons/m of TSSM and let the water evaporate, then the total mass of the suspended solids will be equal to 200 tons. Therefore, these units for the TSSM serve a dual purpose here: a) to give a "feeling" of the horizontal distribution of the vertically averaged concentration all over the lake, and b) to give a "feeling" of the amount of the suspended sediments in the lake.

In Appendix B of this report are presented the time trace plots of the TSSM at the water intake site and at the disposal site as well. Here are given the time trace plots of the individual sediment classes, as well as the time trace plots of the "global sediments" originating from the different sources.

Another set of plots presented in Appendix B contains the time traces of the "relative intensity" of the "global sediments" originating from the different sources, at the sensitive and the disposal site respectively. The term "relative intensity" is defined

simply as the ratio of the "global sediments" from one source to the "global sediments" from all the sources and is dimensionless (expressed as %).

In all the time trace plots all the hourly data are used (6574 data points) but, the units of the time axis are in year days, so one can see what the behavior of the plotted variable is on a daily basis. January 1, 1997 is year day 1, April 1, 1997 is year day 91 and so on.

The conclusions of the model results as they can be seen from the plots in Appendices A and B are summarized in the following list:

- Relative impact of the different sediment sources at the water intake site.
  - The average relative intensity for the simulation period of the TSSM originating from the disposal site is approximately 0.5 %.
  - Seasonal peaks of the relative intensity of TSSM originating from the disposal site do not exceed the 3.5 % mark.
  - The average relative intensity for the simulation period of the TSSM originating from the lake bottom is approximately 90 %.
  - The average relative intensity for the simulation period of the TSSM originating from the Detroit River is approximately 2 %.
  - The average relative intensity for the simulation period of the TSSM originating from the Maumee River is approximately 7.5 %.
  - From early June to late September the riverine contributions are significantly increased. Observed peaks of the relative intensity reach the 46 % mark for the Maumee River, and the 7.5 % mark for the Detroit River.
  - The contribution of the sediments originating from the disposal site is fairly constant throughout the simulation period, but occasional peaks are observed during storm events. In any case these peaks do not exceed the 3.5 % mark
  - Sand size sediments at the water intake site originate only from lake bottom sediments and not from the rivers or the disposal site.
  - Sand is carried from the lake bottom sediments to the water intake site only during strong storms.
  - Silt size sediments are transported to the water intake site from the lake bottom and disposal site during strong storms. Riverine silt size sediments are not transported to the water intake site.
  - Clay size sediments found at the water intake site originate from all the

assigned sources with major contribution coming from the lake bottom sediments. The riverine contributions are not trivial while, the contribution from the disposal site is low.

- Overall the impact at the water intake site of the sediments originating from the disposal site is fairly small (during storm events) to insignificant.
- This indicates that for other years and severe storm occurrences, the disposal site contribution to the suspended sediment at the water intake is negligible.

- Composition of the suspended sediments at the water intake site.
  - The sediments found at the water intake site are mainly fine size sediments (silt and clay).
  - The majority of the fine sediments at the water intake site are clay size sediments.
  - The majority of the water intake site silt and clay size sediments are transported from the disposal site during the October to December storm period.
  - The majority of the water intake site silt and clay size sediments are transported from the riverine sources during the May to end of July period and again during December.

- Disposal site.
  - Suspended sand and silt size classes found at the disposal site originate from the lake bottom sediments and the sediments at the disposal site. These size classes are entrained only during significant storm events.
  - Disposal site sand and silt size sediments do not result from the riverine sources.
  - Disposal site clay size sediments originate from disposal, lake bottom and riverine sources. Transport occurs continuously during storm and non-storm events.

References

1 R. S. Chapman, R. Chapman and Associate, B. H. Johnson, S. Rao Vemulakonda, 1996. *User's Guide for the Sigma Stretched Version of CH3D-WES, A Three-Dimensional Numerical Hydrodynamic, Salinity and Temperature Model*. Technical Report HL-96-21, November 1996.

2 S. C. Fan and K. W. Bedford, 1998. *Data Analysis of the 1996 ARMS Field Experiments in Western Basin of Lake Erie.* Report no. 1, US Army Corps of Engineers, Contract DACW39-95-K-0018, January 1998.

3 The Great Lakes Forecasting System (GLFS) Database. Internal Database Constructed Yearly from the Great Lakes Nowcasts. Web Address: http://superior.eng.ohio-state.edu/.

4 C. E. Herdendorf and J. E. Zapotosky, 1977. *Effects of Tributary Loading to Western Lake Erie during Spring Runoff Events*. Clear Technical Report, no. 65, International Joint Commission and US EPA, 1977.

5 C. E. Herdendorf, D. B. Gruet, M. A. Slagle and P. B. Herdendorf, 1978. *Descriptions of Sediment Samples and Cores from the Michigan and Ohio Waters of Lake Erie*. Clear Technical Report, no. 85, January 1978.

6 A. L. W. Kemp, R. L. Thomas, C. I. Dell and J. M. Jaquet, 1976. *Cultural Impact on the Geochemistry of Sediments in Lake Erie*. J. Fish. Res. Board Can., 33:440-462, 1976.

7 G. F. Koltun, 1990. *A Statistical Approach to Characterizing Bottom Shear Stress Entrainment and Related Hydrologic and Climatic Phenomena in the Detroit River, Trenton Channel*. MS Thesis, The Ohio State University, Department of Civil Engineering, 1990.

8 C. Kuan, 1995. *Quantitative Skill Assessment of the Princeton Coastal Ocean Circulation Model for Lake Erie*. Ph.D. Dissertation, The Ohio State University, Department of Civil and Environmental Engineering and Geodetic Science, 1995.

9 B. P. Leonard, 1979. *A Stable and Accurate Convective Modeling Procedure Based on Quadratic Upstream Interpolation*. Computer Methods in Applied Mechanics, Vol. 19, pp. 59-98, 1979.

10 W. Rodi, 1980. *Turbulence Models and their Application in Hydraulics*. Monograph, International Association for Hydraulic Research, Delft, The Netherlands, 1980.

11 M. Spasojevic, F. M. Holly Jr., 1994. *Three-Dimensional Numerical Simulation of Mobile-Bed Hydrodynamics*. Contract Report HL-94-2, US Army Corps of Engineers, Waterways Experiment Station, August 1994.

12 R. L. Thomas, J. M. Jaquet, A. L. W. Kemp and C. F. M. Lewis, 1976. *Surficial Sediments of Lake Erie*. J. Fish. Res. Board Can., 33:385-403, 1976.

13 J. F. Thompson, Z. U. A. Warsi, C. W. Mastin, 1985. *Numerical Grid Generation, Foundations and Applications*. Elsevier Science Publishing Co., Inc., New York, 1985.

14 Toledo Harbor Planning Group, 1993. *Long-Term Dredged Material Management Plan within the Context of Maumee River Watershed. Sediment Management Strategy*. Executive Committee Phase 3 Report with Environmental Assessment, December 1993.

15 US Geological Survey, 1975b. *Water Resources Data for Michigan-1974, Part 2*. Water Quality Records: US Dept. Int., Geol. Survey-Water Resources Div., 165 p., 1975.

16 US Geological Survey, 1993. *U.S. Geological Survey Water-Data Report, OH-92-2*. Water Resources Data, Ohio Water Year 1992, Volume 2, St. Lawrence River Basin and Statewide Project Data, Ohio 1993.

17 USGS Water Resources of the United States, 1998. *Database accessible via the World Wide Web*. Web Address: http://www.usgs.gov.

18 L. C. van Rijn, 1984a. *Sediment Transport, Part I: Bed Load Transport*. Journal of Hydraulic Engineering, ASCE, Vol. 110, No 10, pp. 1431-1456, 1984.

19 L. C. van Rijn, 1984b. *Sediment Transport, Part II: Suspended Load Transport*. Journal of Hydraulic Engineering, ASCE, Vol. 110, No 11, pp. 1613-1641, 1984.

20 J. L. Verber, 1957. *Bottom Deposits of Western Lake Erie: Ohio Div*. Shore Erosion Tech. Rept. 4, pp. 4, 1957.

Appendix A

Selected Contour Plots of Various Flow Variables. Simulation Year 1997.

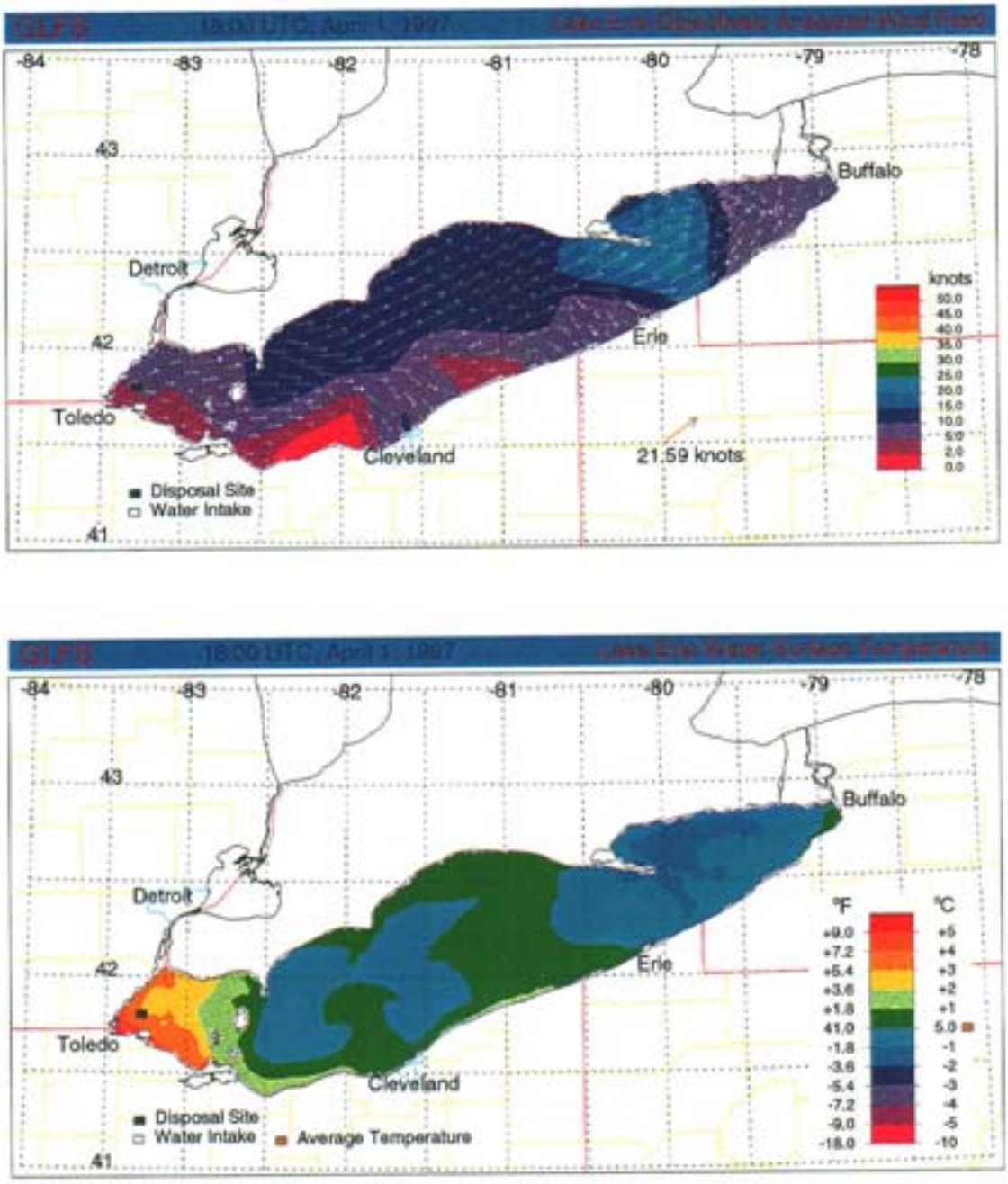

Figure A.1 Water-surface wind speed and temperature distributions for April 1, 1997.

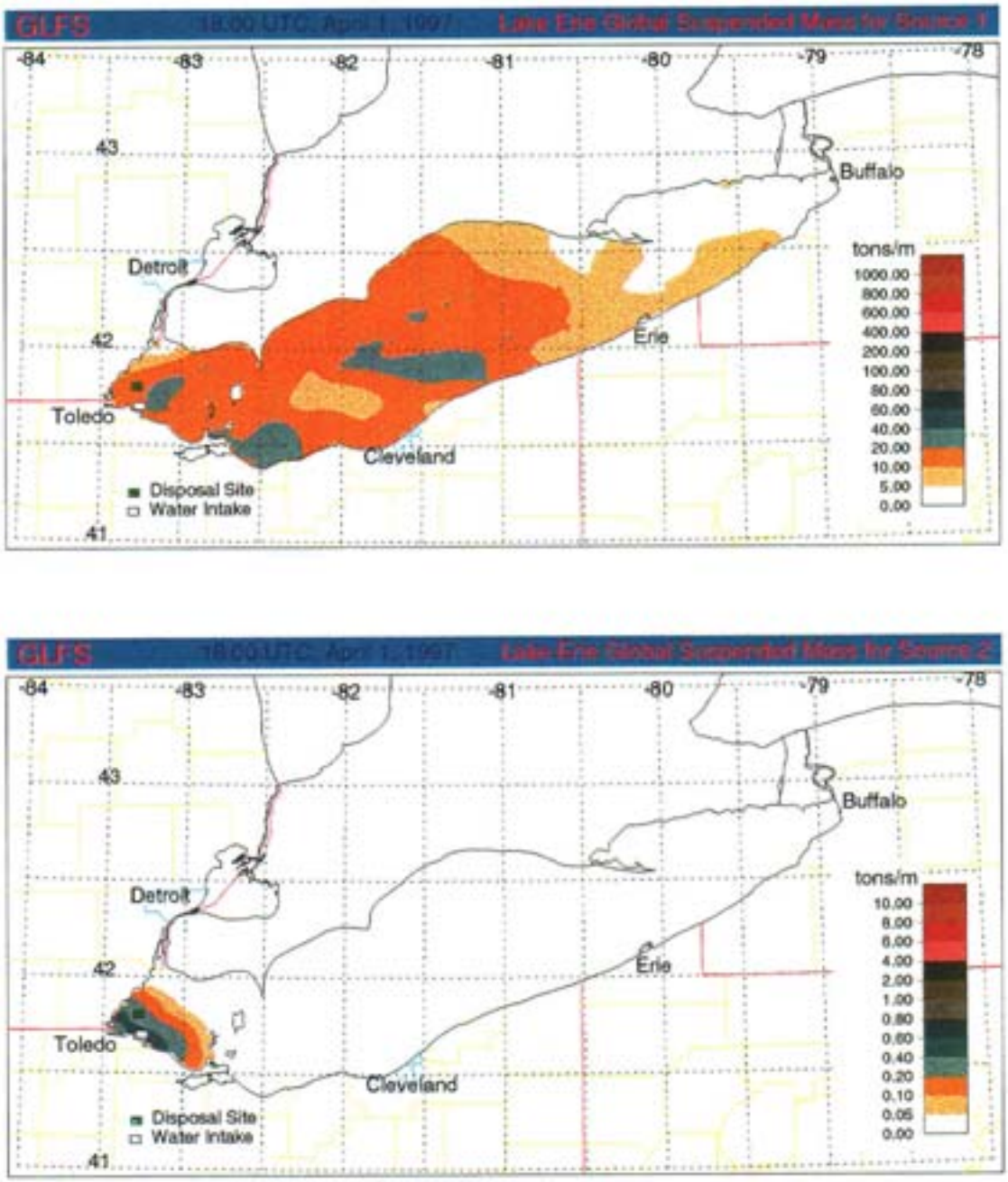

Figure A.2 Horizontal distributions of the global suspended mass of the sediments originating from source 1 (lake bottom) and source 2 (disposal site) for April 1, 1997.

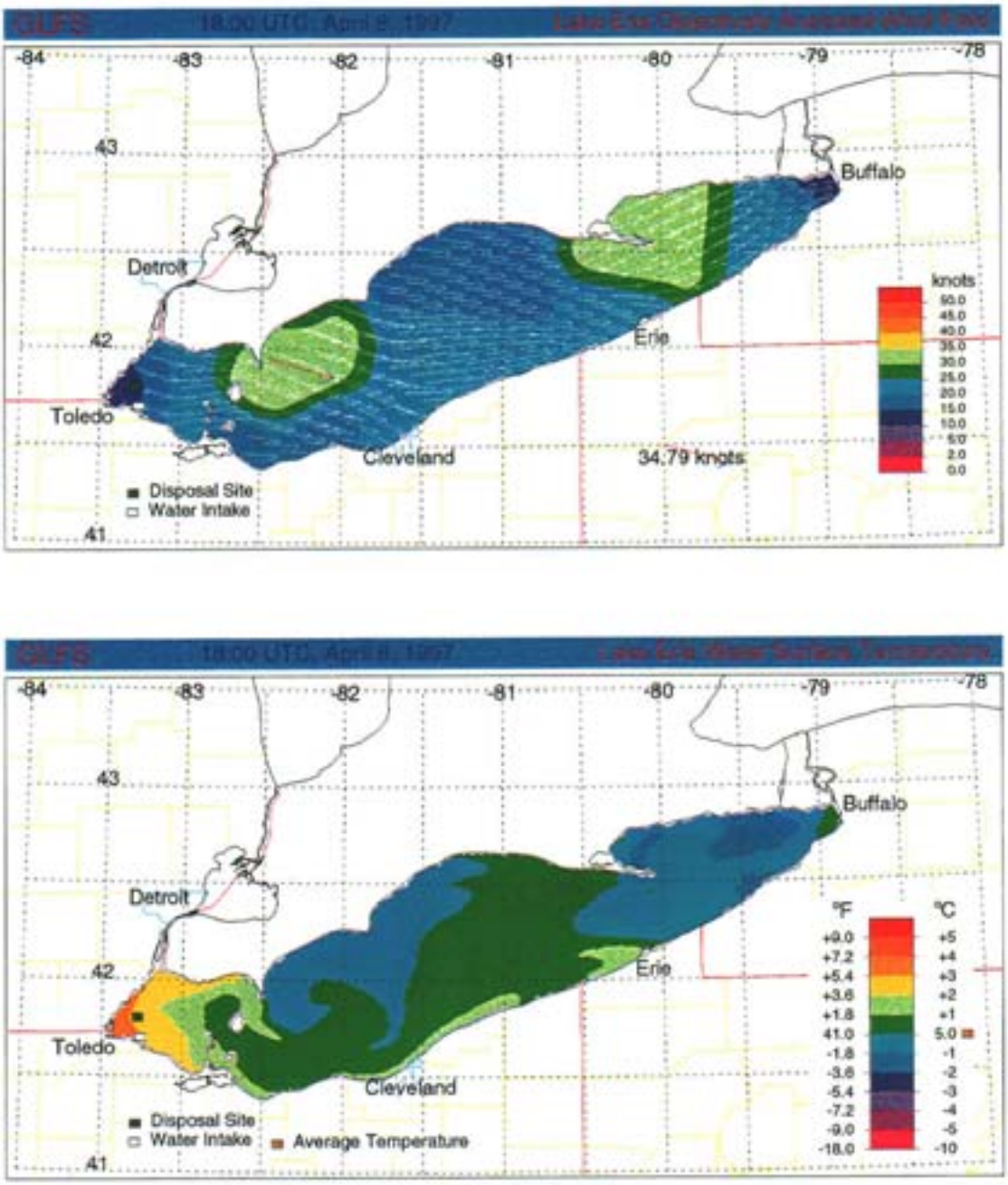

Figure A.3 Water-surface wind speed and temperature distributions for April 8, 1997.

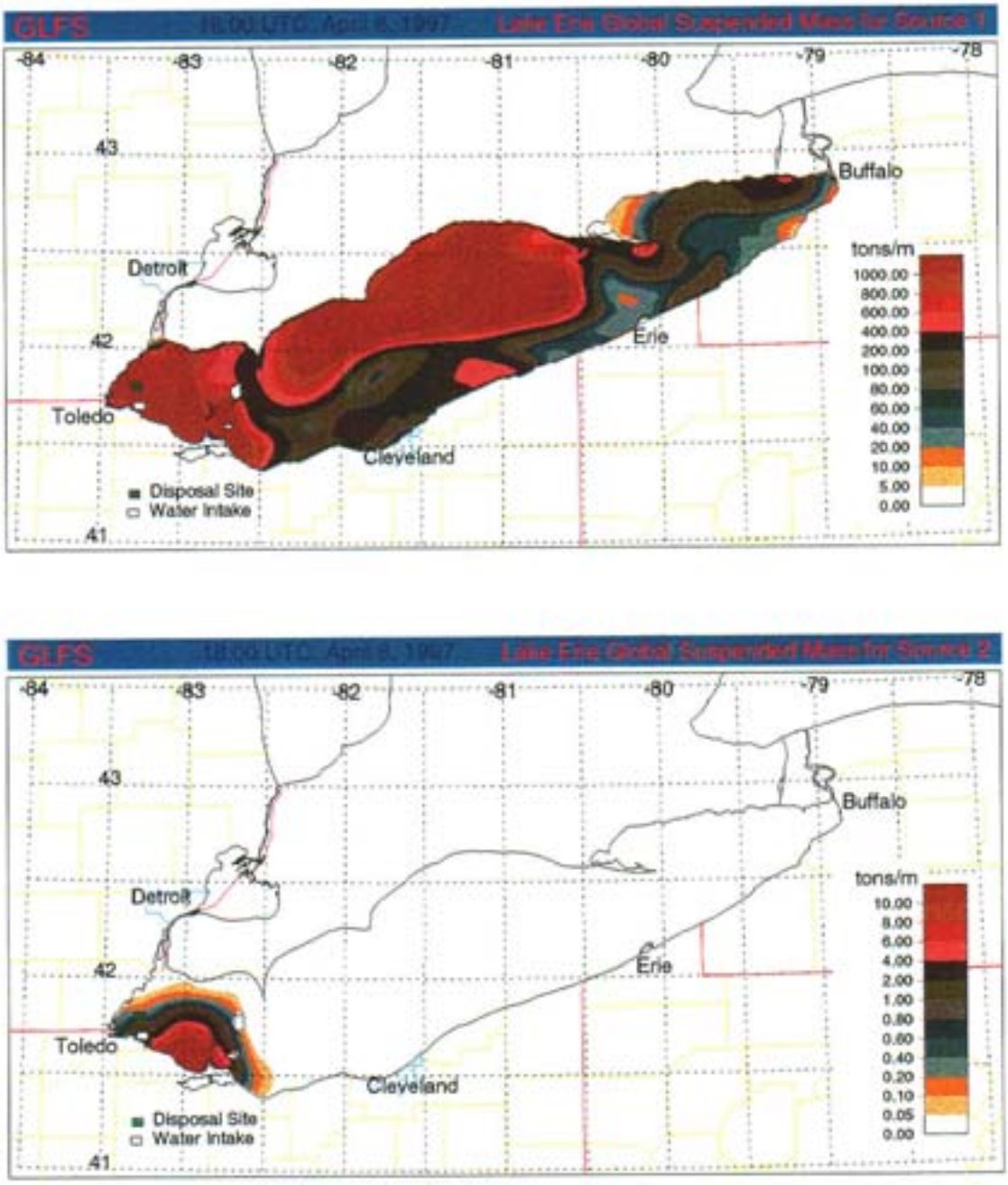

Figure A.4 Horizontal distributions of the global suspended mass of the sediments originating from source 1 (lake bottom) and source 2 (disposal site) for April 8, 1997.

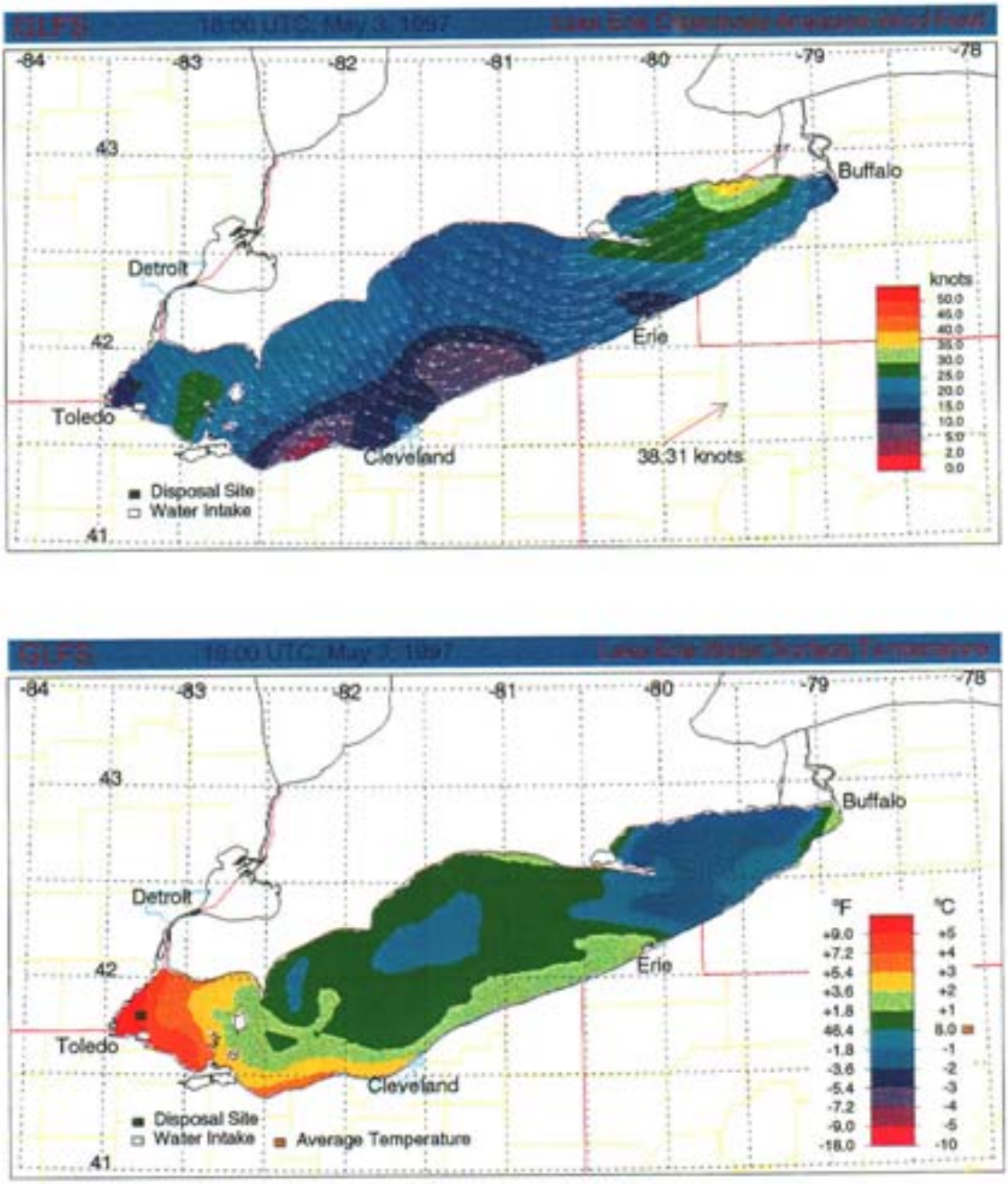

Figure A.5 Water-surface wind speed and temperature distributions for May 3, 1997.

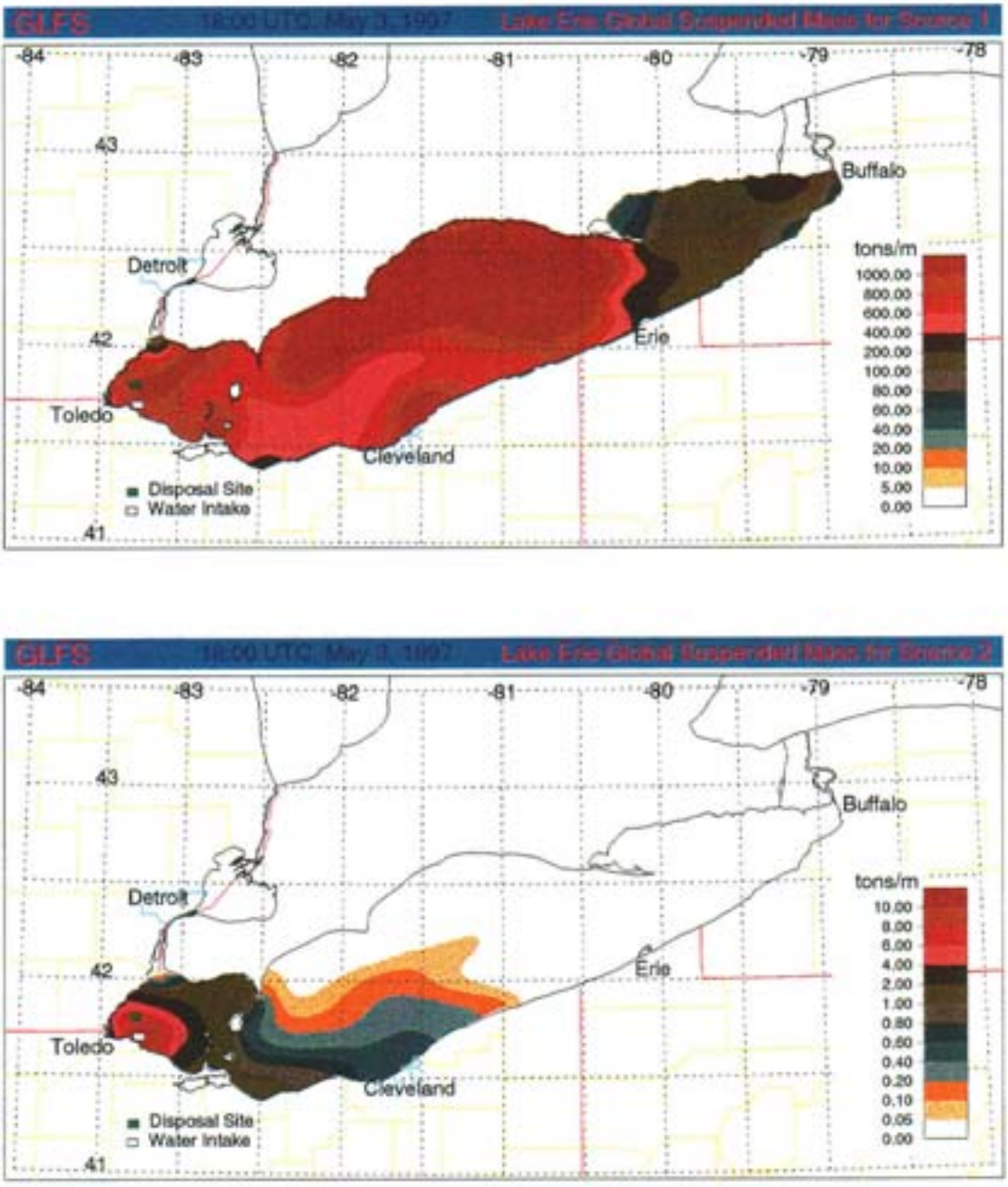

Figure A.6 Horizontal distributions of the global suspended mass of the sediments originating from source 1 (lake bottom) and source 2 (disposal site) for May 3, 1997.

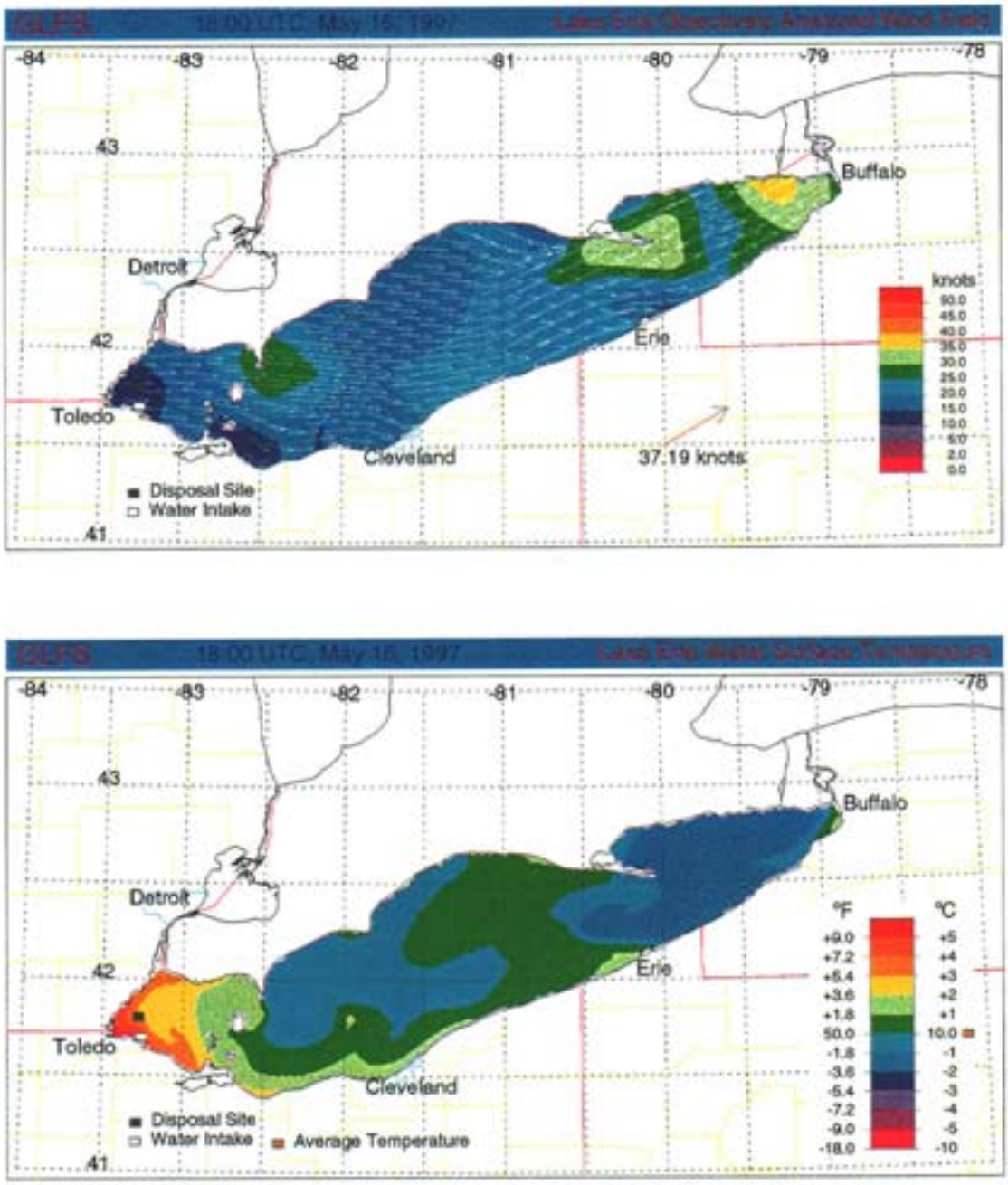

Figure A.7 Water-surface wind speed and temperature distributions for May 16, 1997.

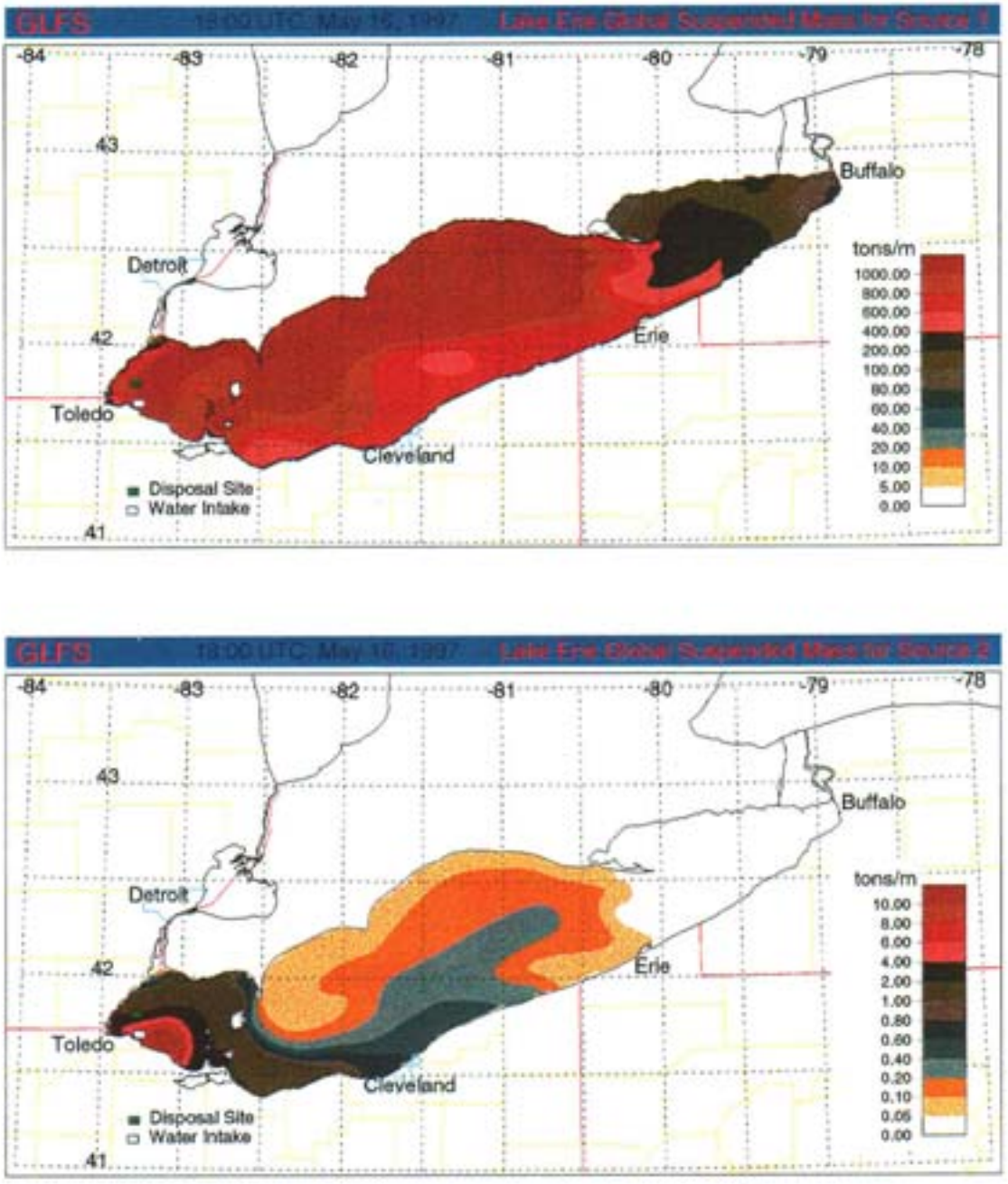

Figure A.8 Horizontal distributions of the global suspended mass of the sediments originating from source 1 (lake bottom) and source 2 (disposal site) for May 16, 1997.

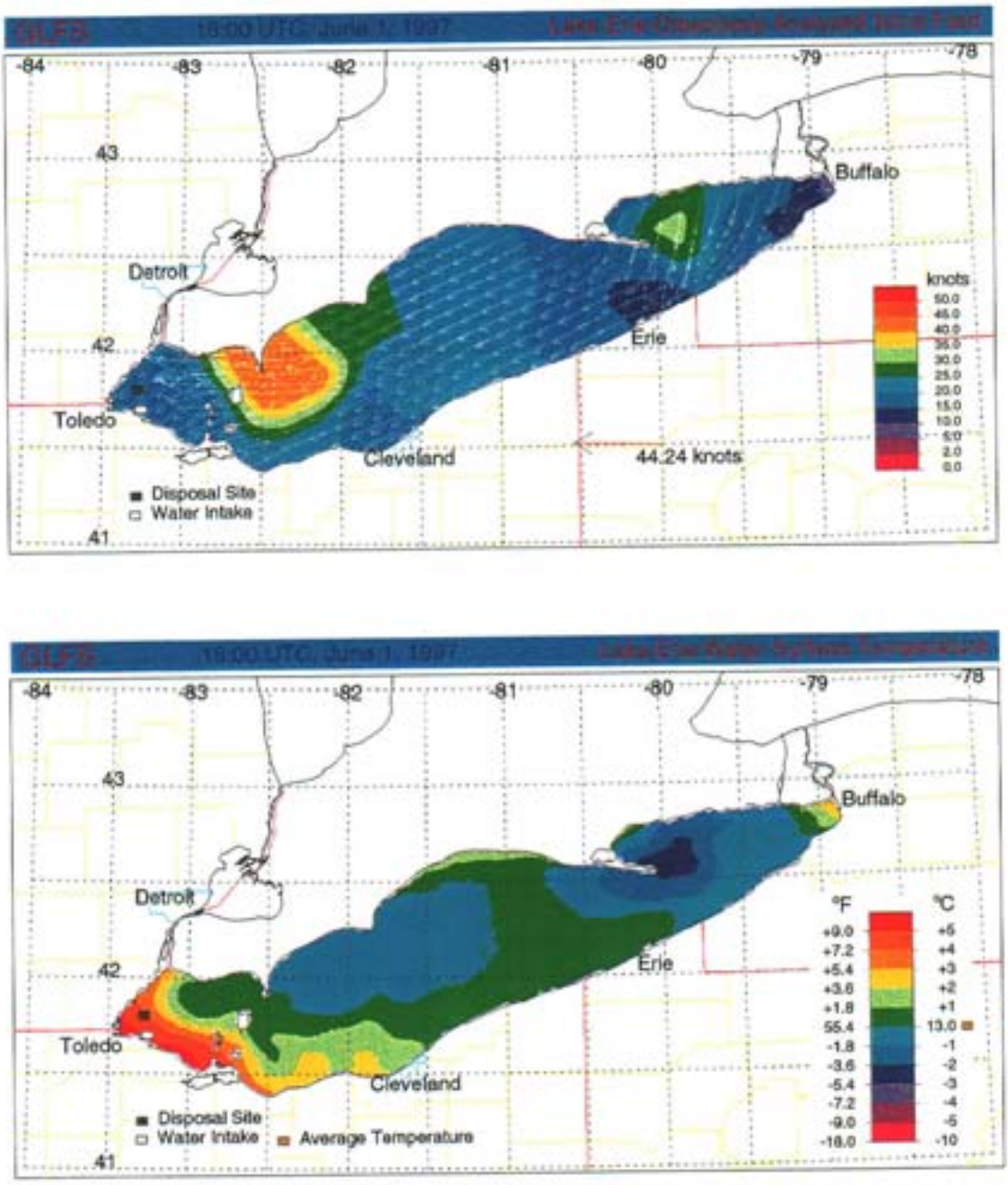

Figure A.9 Water-surface wind speed and temperature distributions for June 1, 1997.

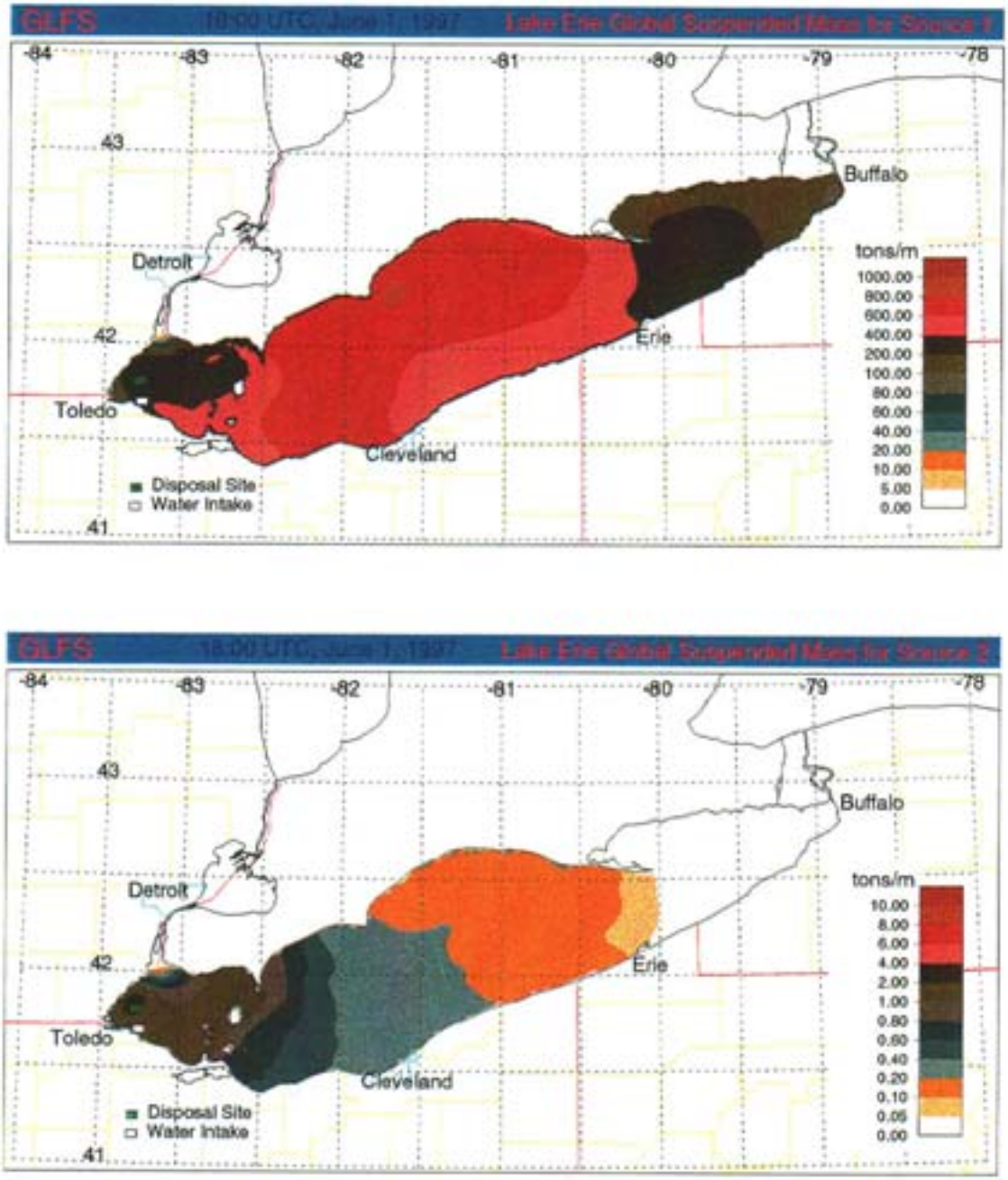

Figure A.10 Horizontal distributions of the global suspended mass of the sediments originating from source 1 (lake bottom) and source 2 (disposal site) for June 1, 1997.

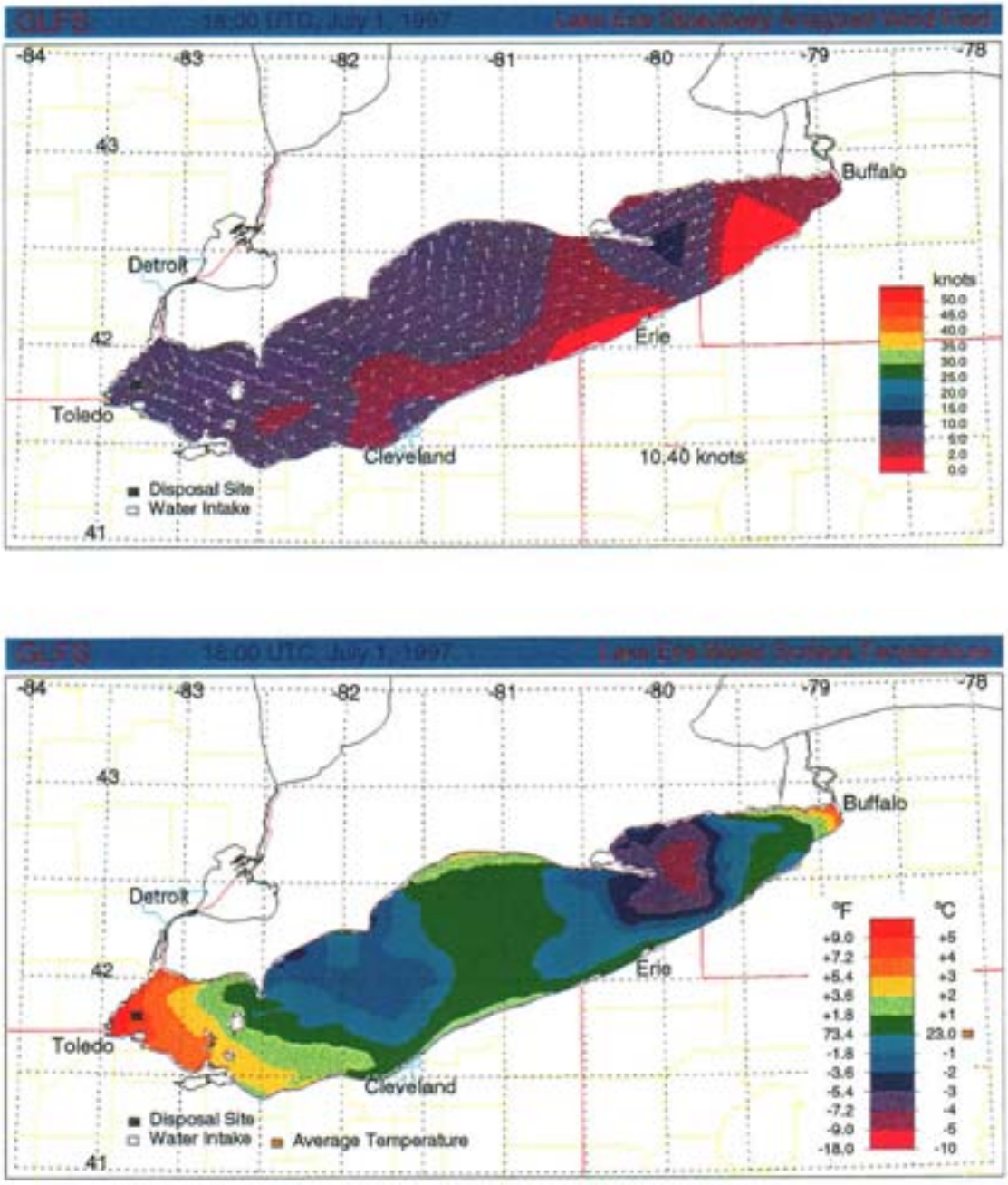

Figure A.11 Water-surface wind speed and temperature distributions for July 1, 1997.

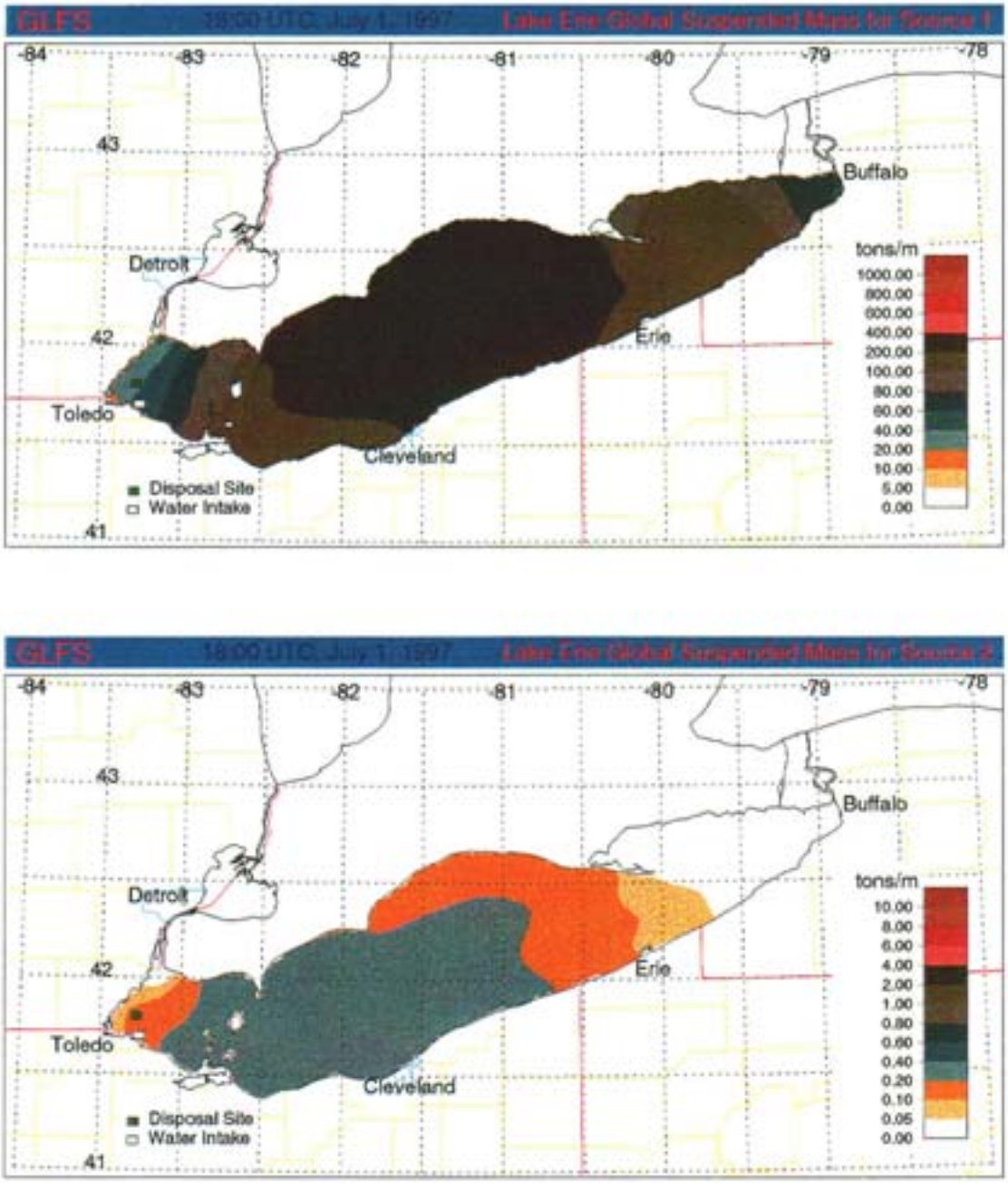

Figure A.12 Horizontal distributions of the global suspended mass of the sediments originating from source 1 (lake bottom) and source 2 (disposal site) for July 1, 1997.

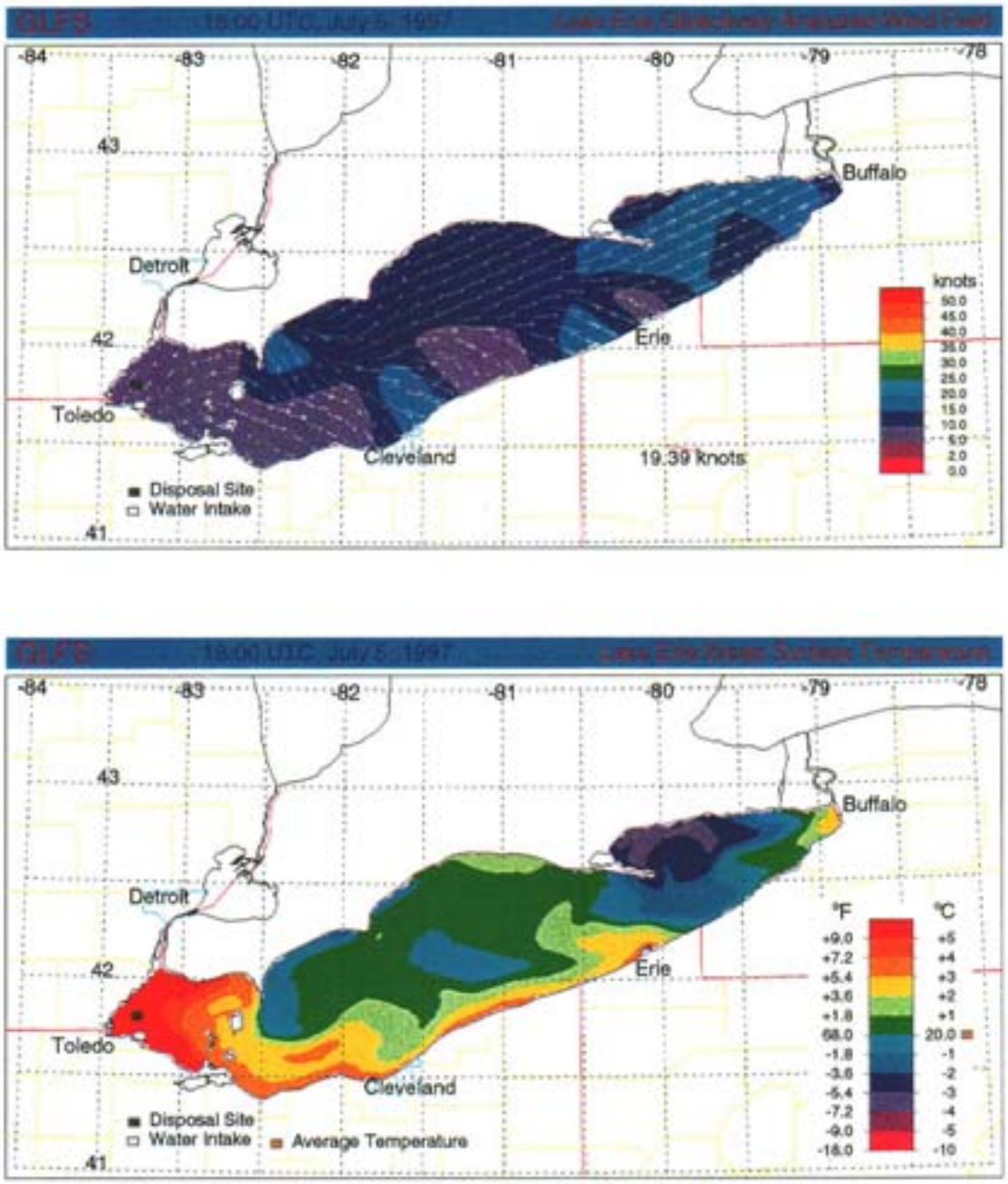

Figure A.13 Water-surface wind speed and temperature distributions for July 5, 1997.

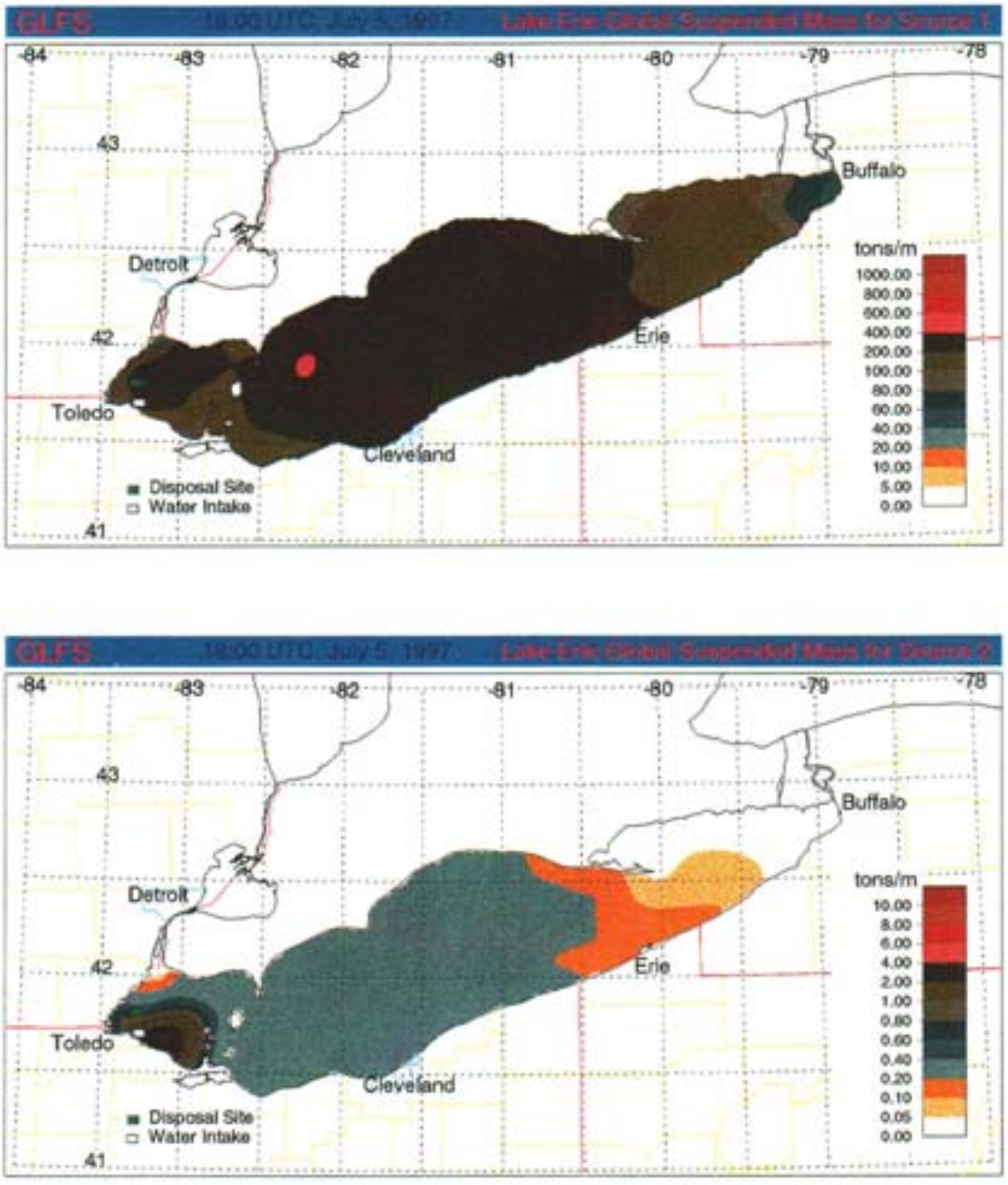

Figure A.14 Horizontal distributions of the global suspended mass of the sediments originating from source 1 (lake bottom) and source 2 (disposal site) for July 5, 1997.

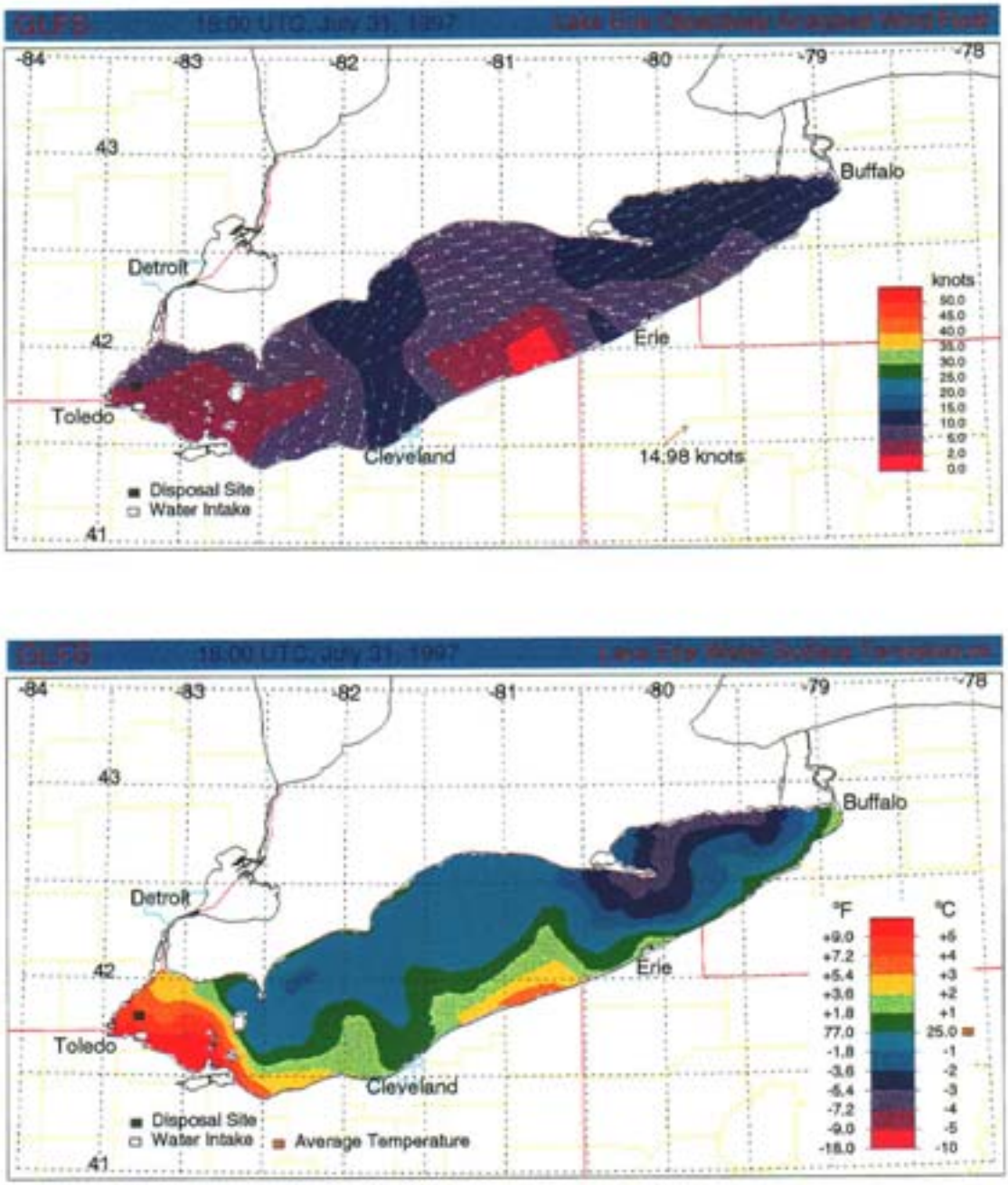

Figure A.15 Water-surface wind speed and temperature distributions for July 31, 1997.

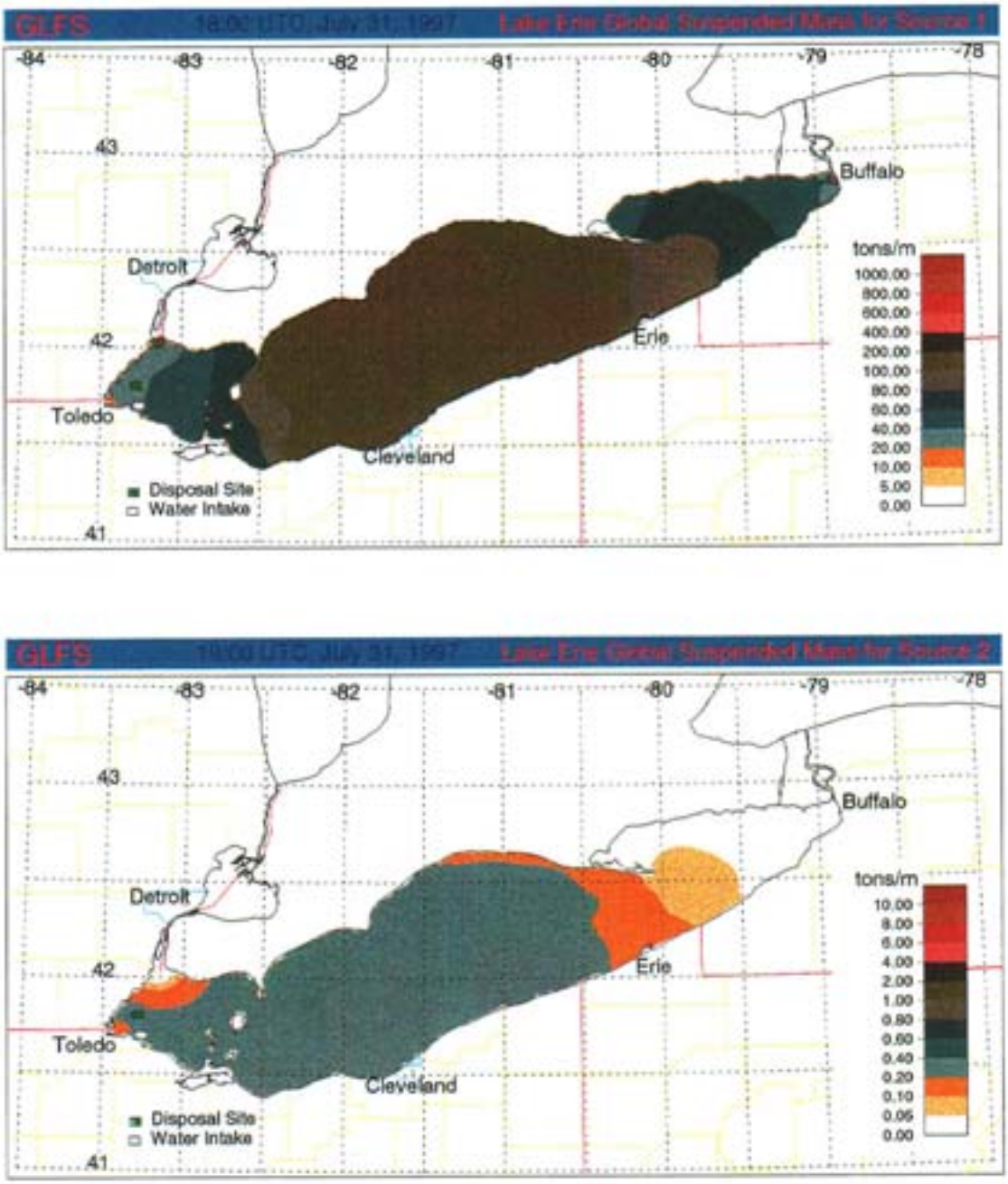

Figure A.16 Horizontal distributions of the global suspended mass of the sediments originating from source 1 (lake bottom) and source 2 (disposal site) for July 31, 1997.

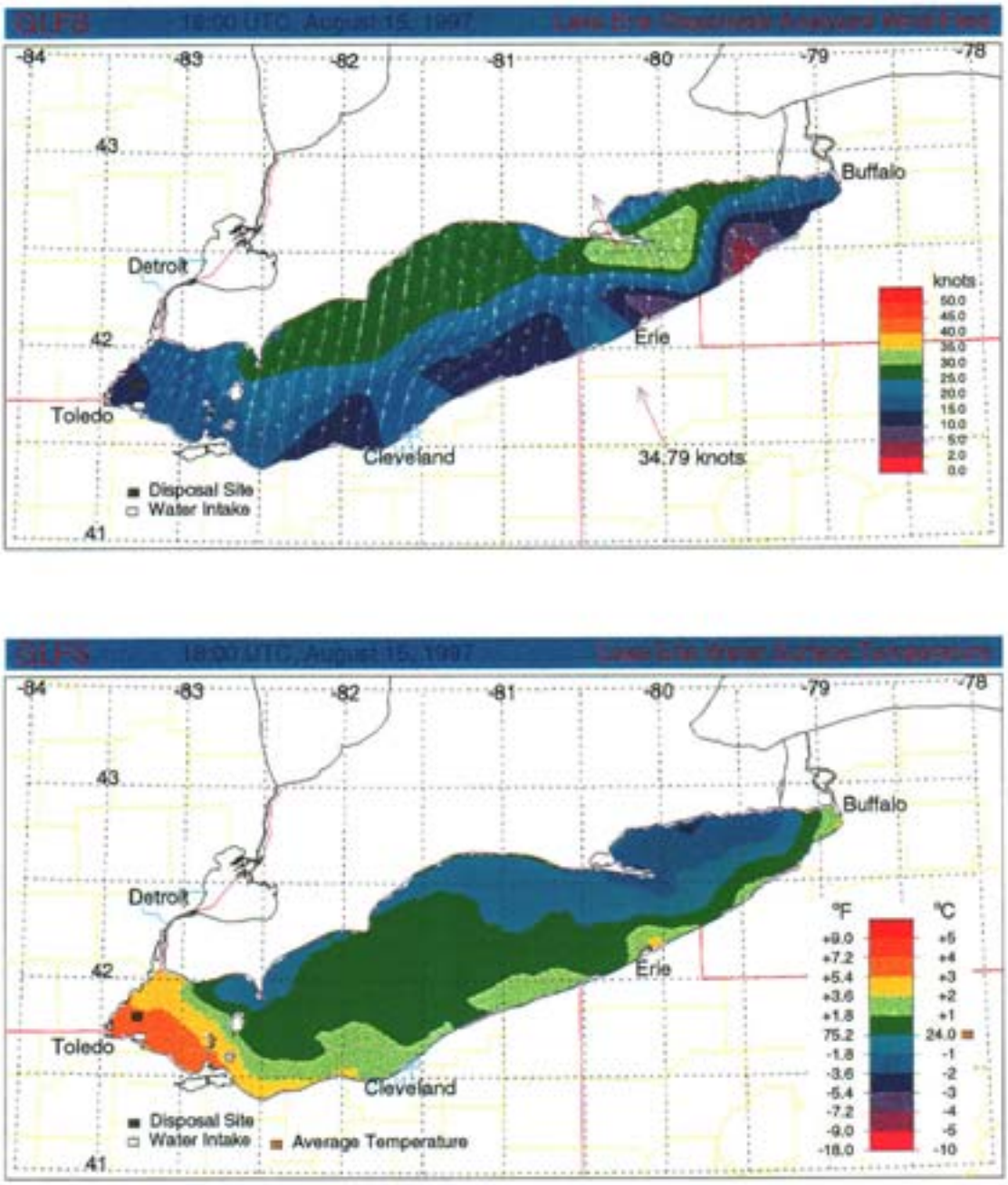

Figure A.17 Water-surface wind speed and temperature distributions for August 15, 1997.

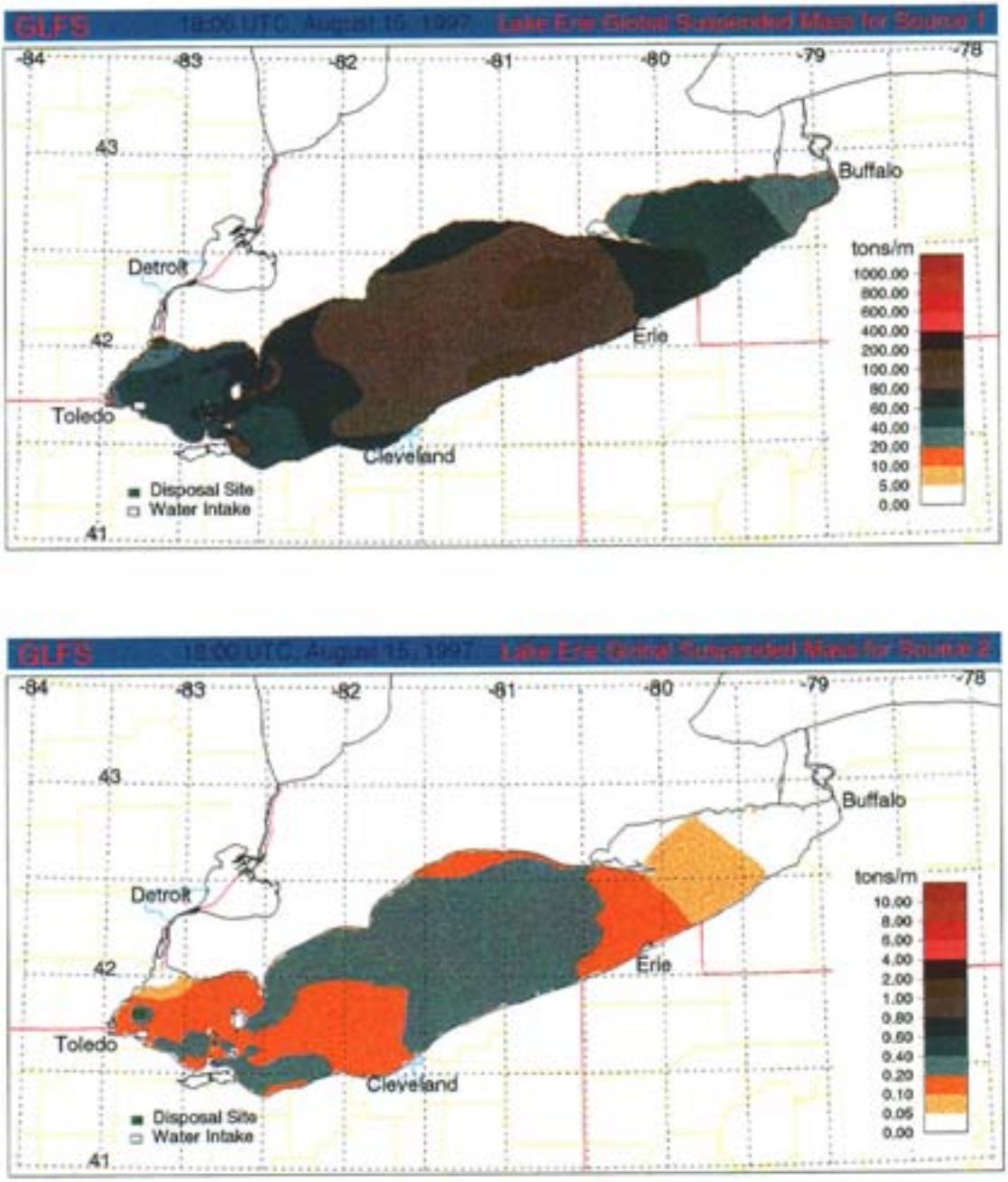

Figure A.18 Horizontal distributions of the global suspended mass of the sediments originating from source 1 (lake bottom) and source 2 (disposal site) for August 15, 1997.

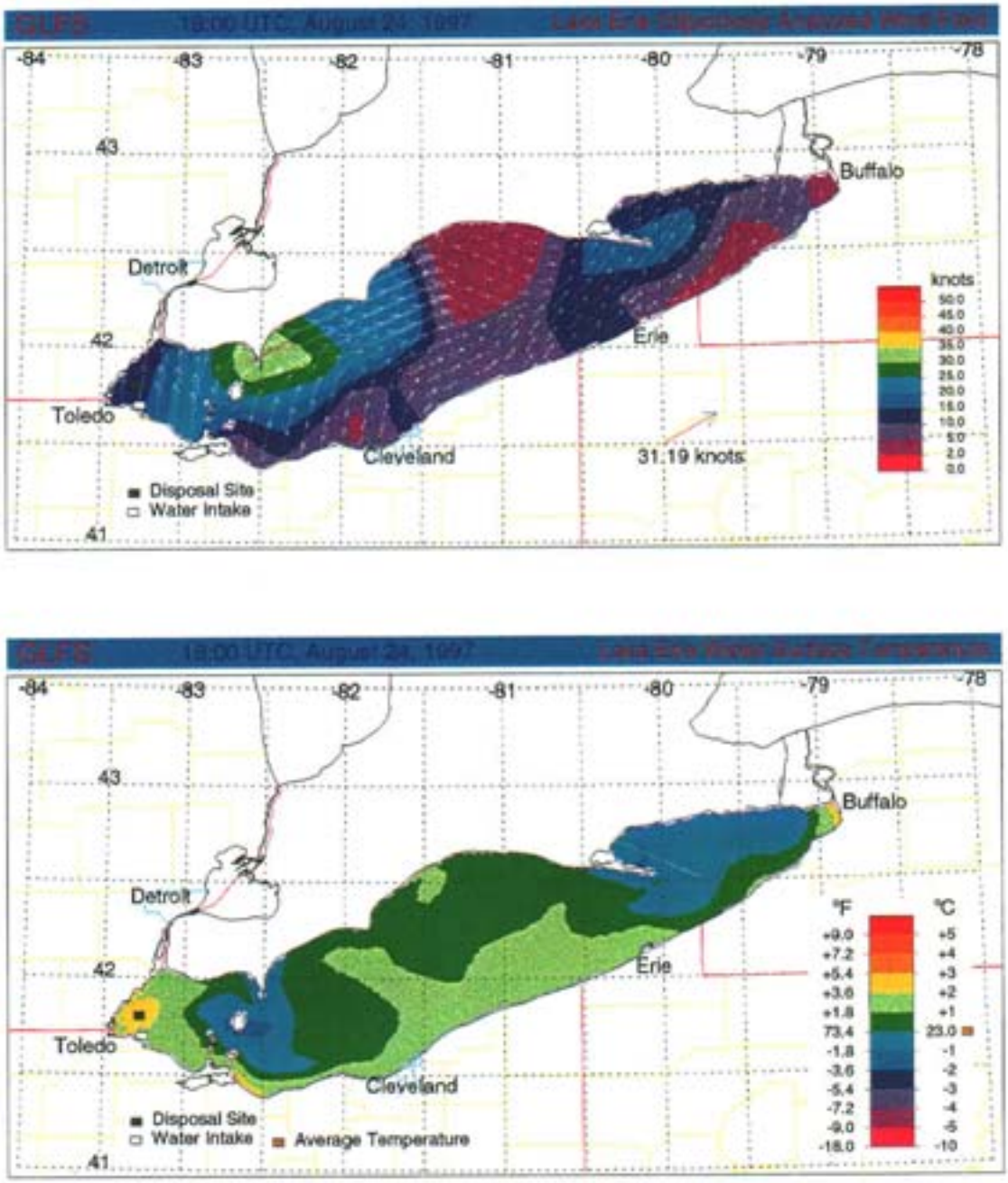

Figure A.19 Water-surface wind speed and temperature distributions for August 24, 1997.

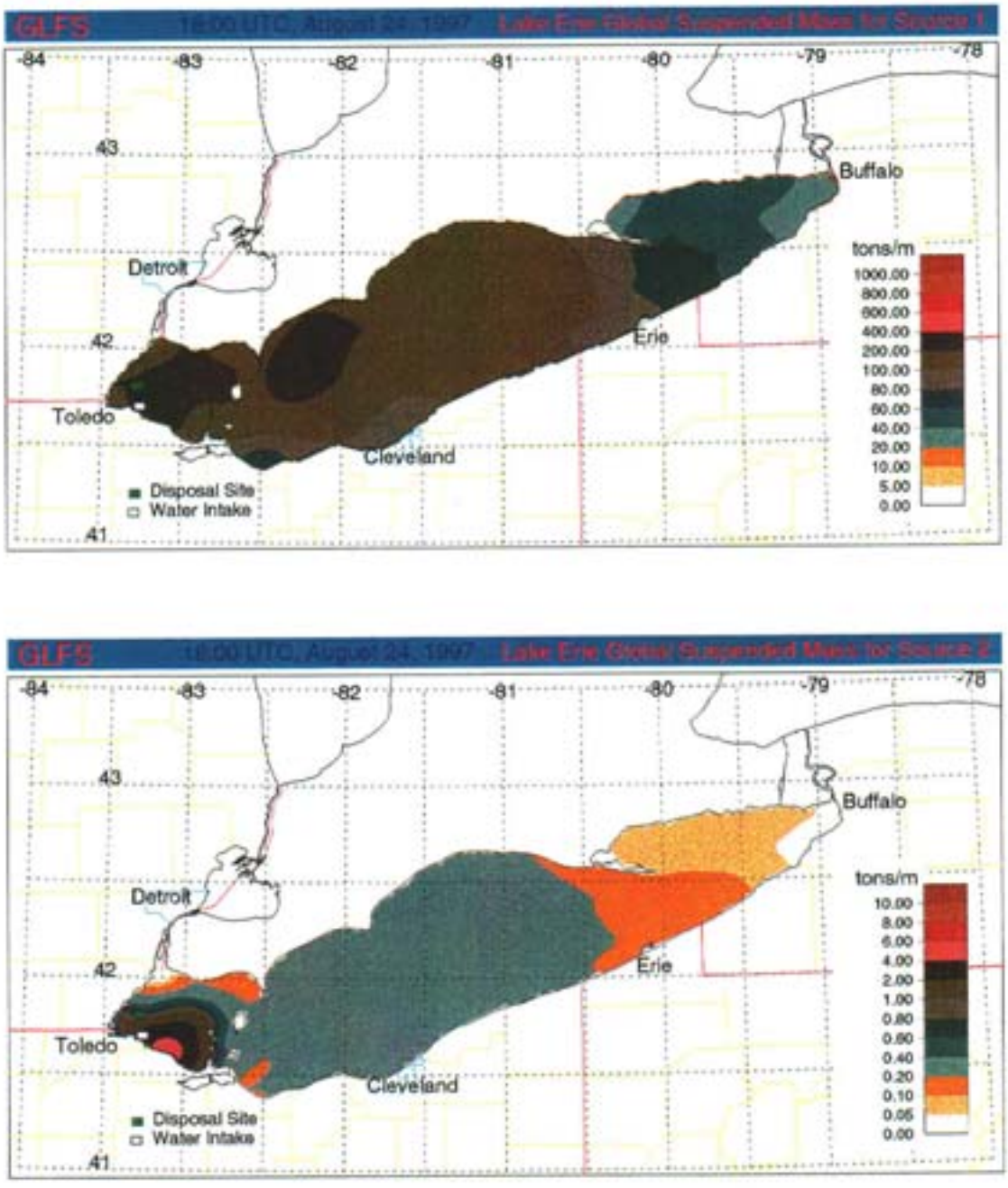

Figure A.20 Horizontal distributions of the global suspended mass of the sediments originating from source 1 (lake bottom) and source 2 (disposal site) for August 24, 1997.

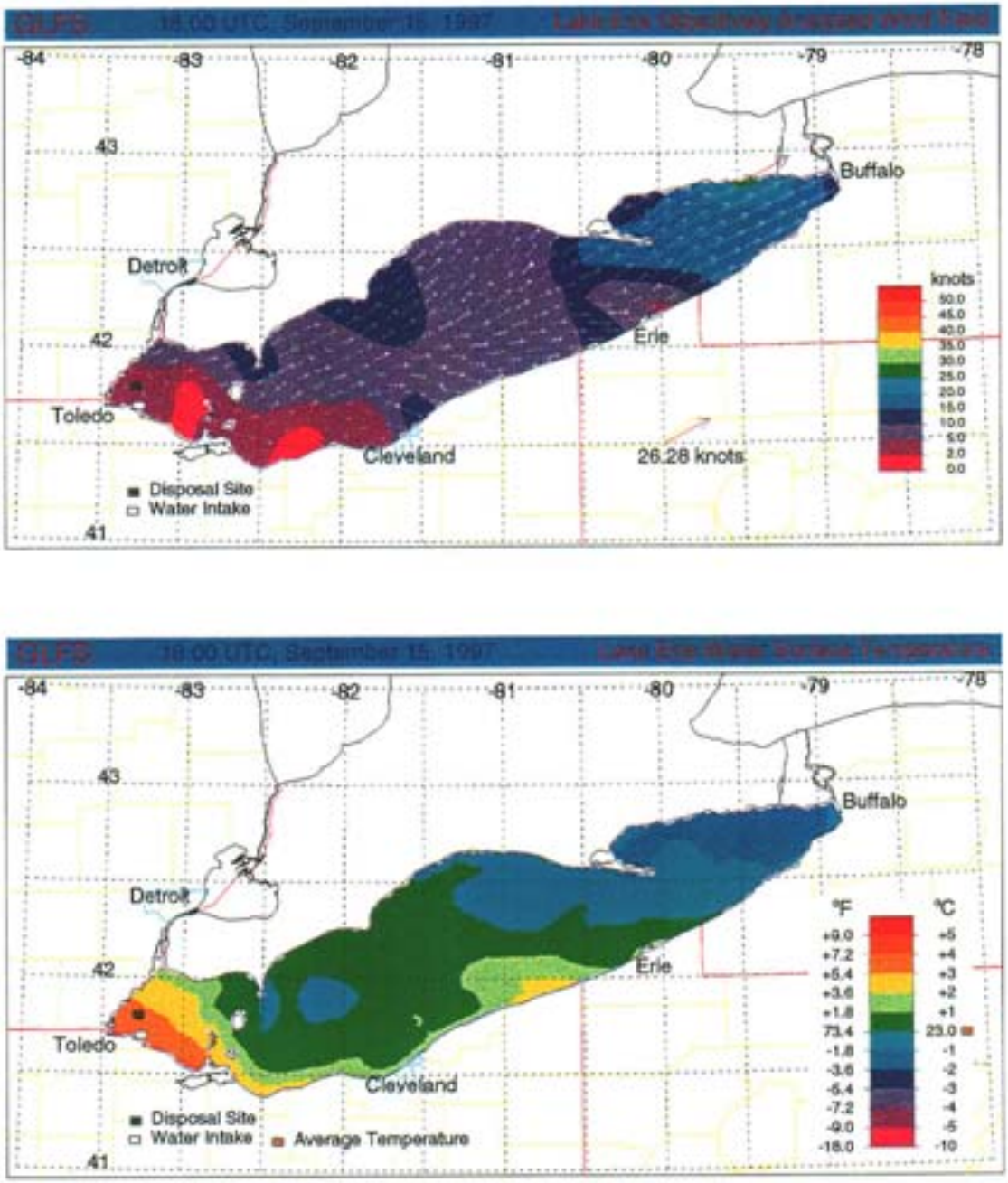

Figure A.21 Water-surface wind speed and temperature distributions for September 15, 1997.

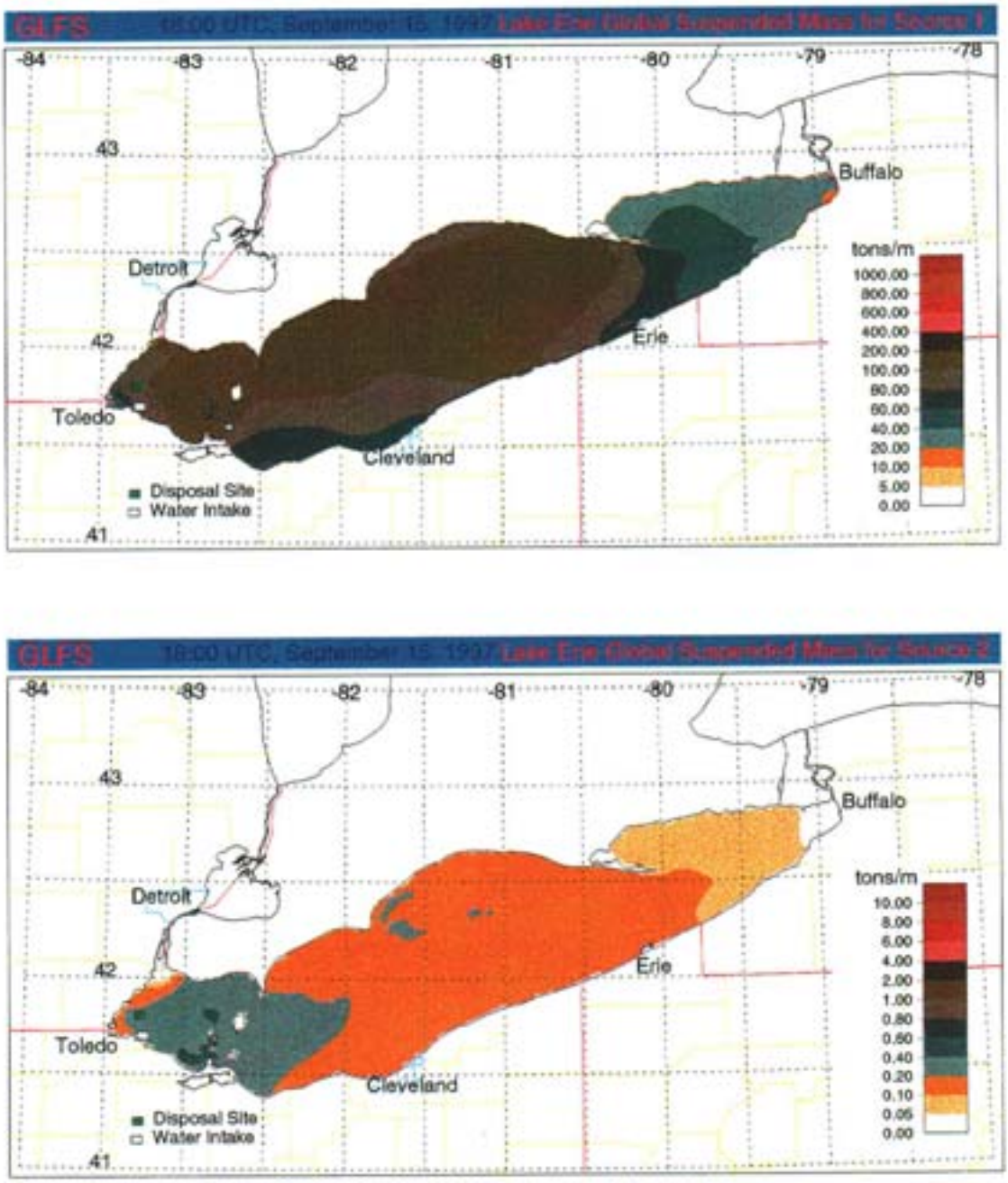

Figure A.22 Horizontal distributions of the global suspended mass of the sediments originating from source 1 (lake bottom) and source 2 (disposal site) for September 15, 1997.

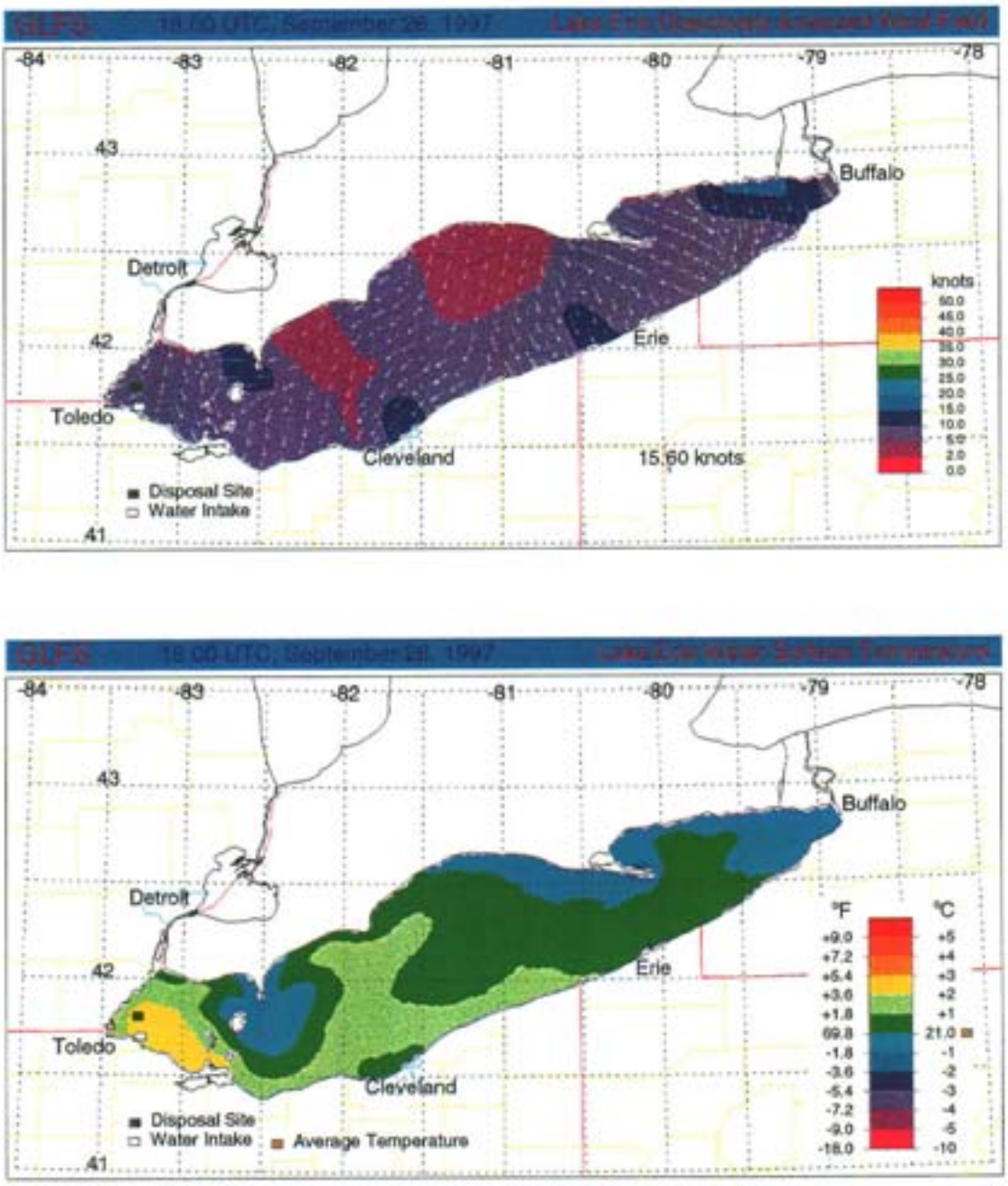

Figure A.23 Water-surface wind speed and temperature distributions for September 26, 1997.

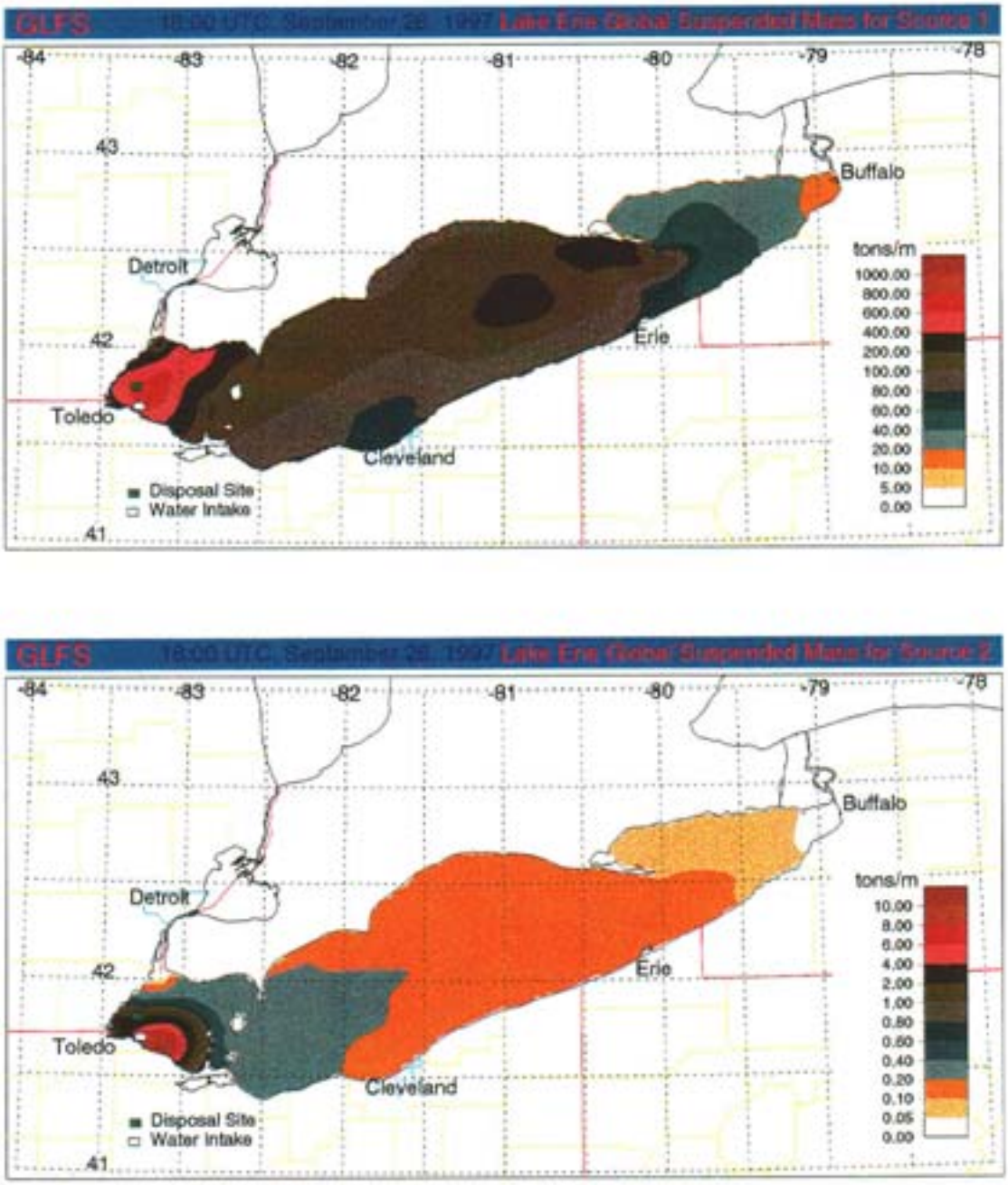

Figure A.24 Horizontal distributions of the global suspended mass of the sediments originating from source 1 (lake bottom) and source 2 (disposal site) for September 26, 1997.

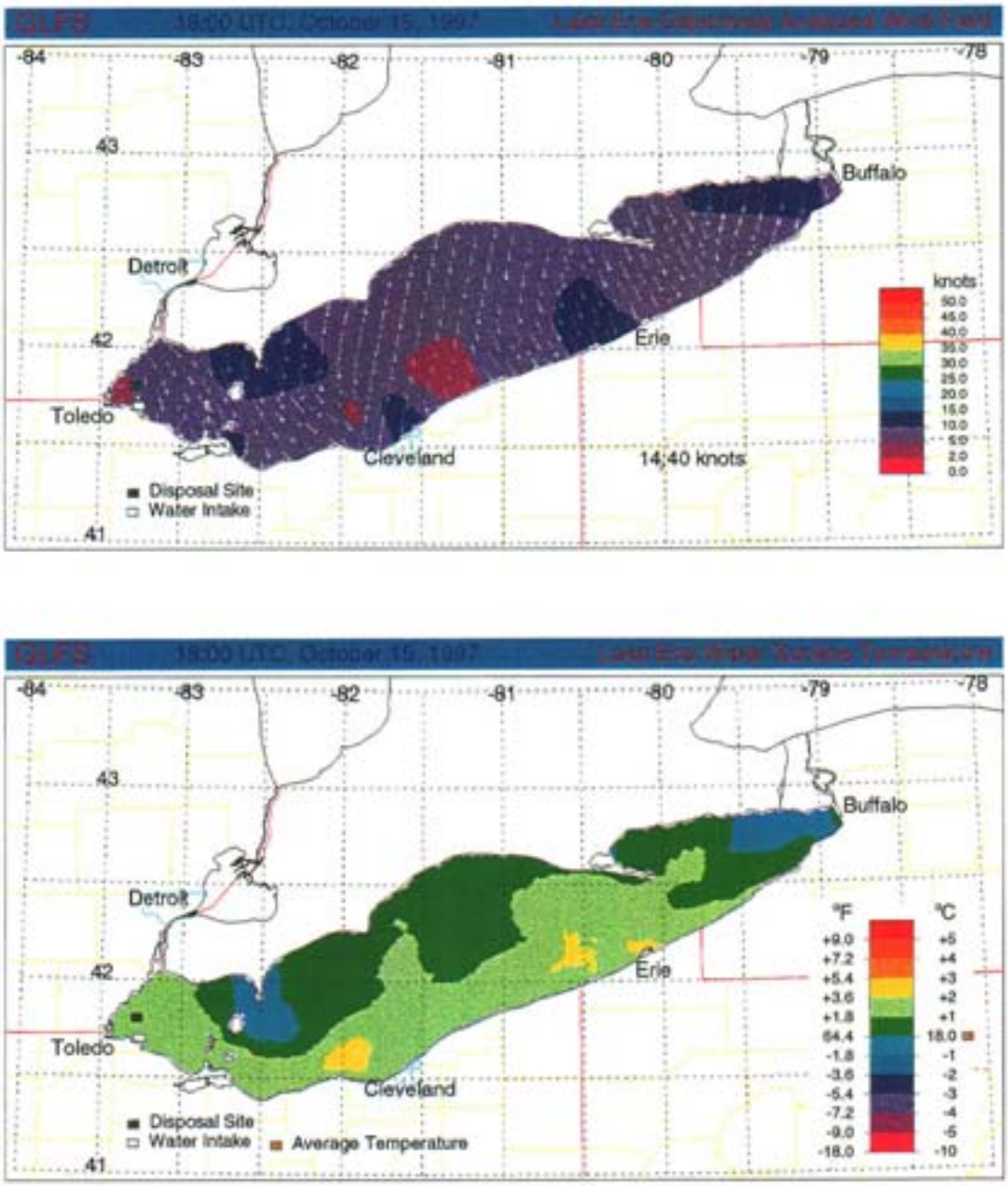

Figure A.25 Water-surface wind speed and temperature distributions for October 15, 1997.

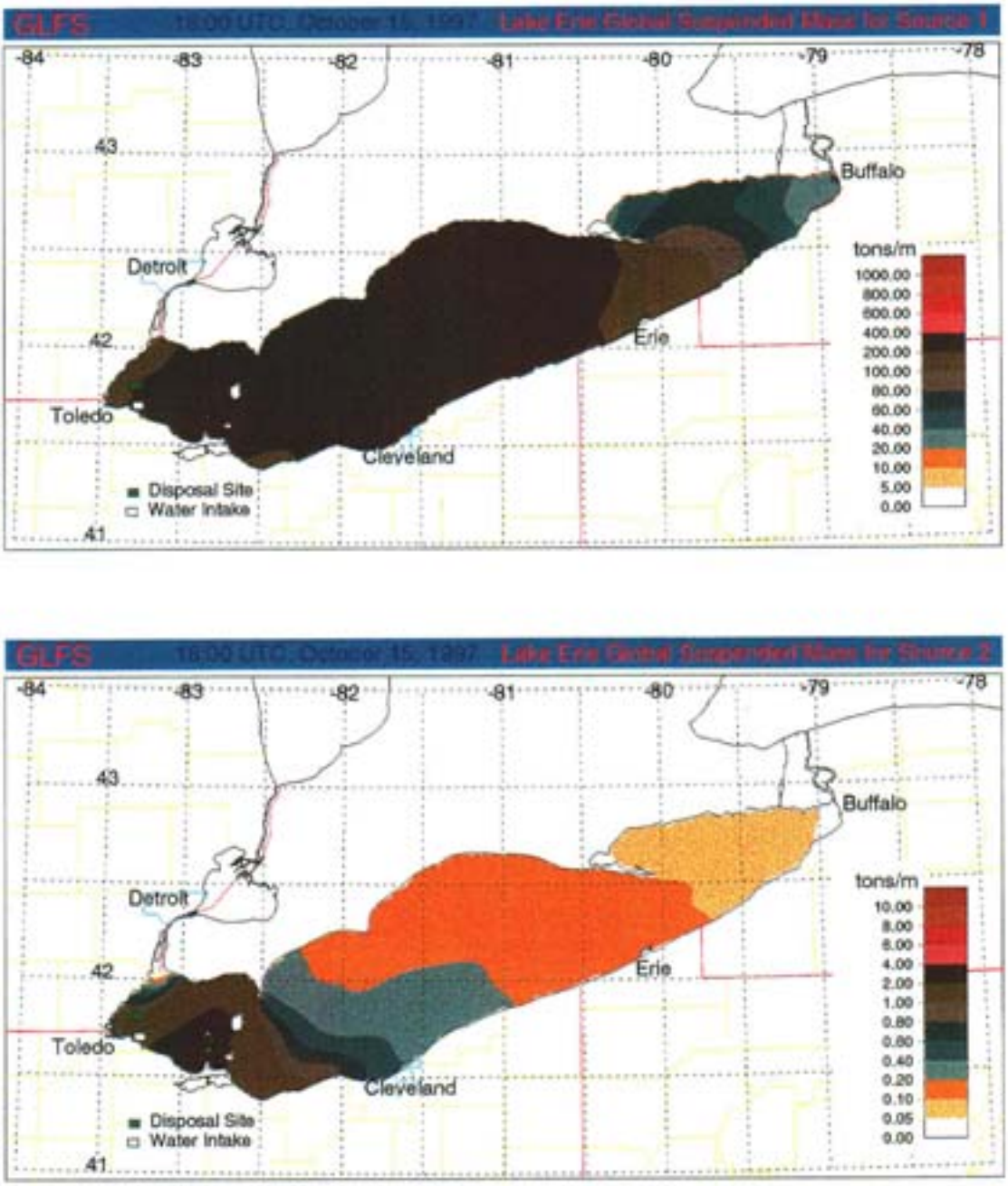

Figure A.26 Horizontal distributions of the global suspended mass of the sediments originating from source 1 (lake bottom) and source 2 (disposal site) for October 15, 1997.

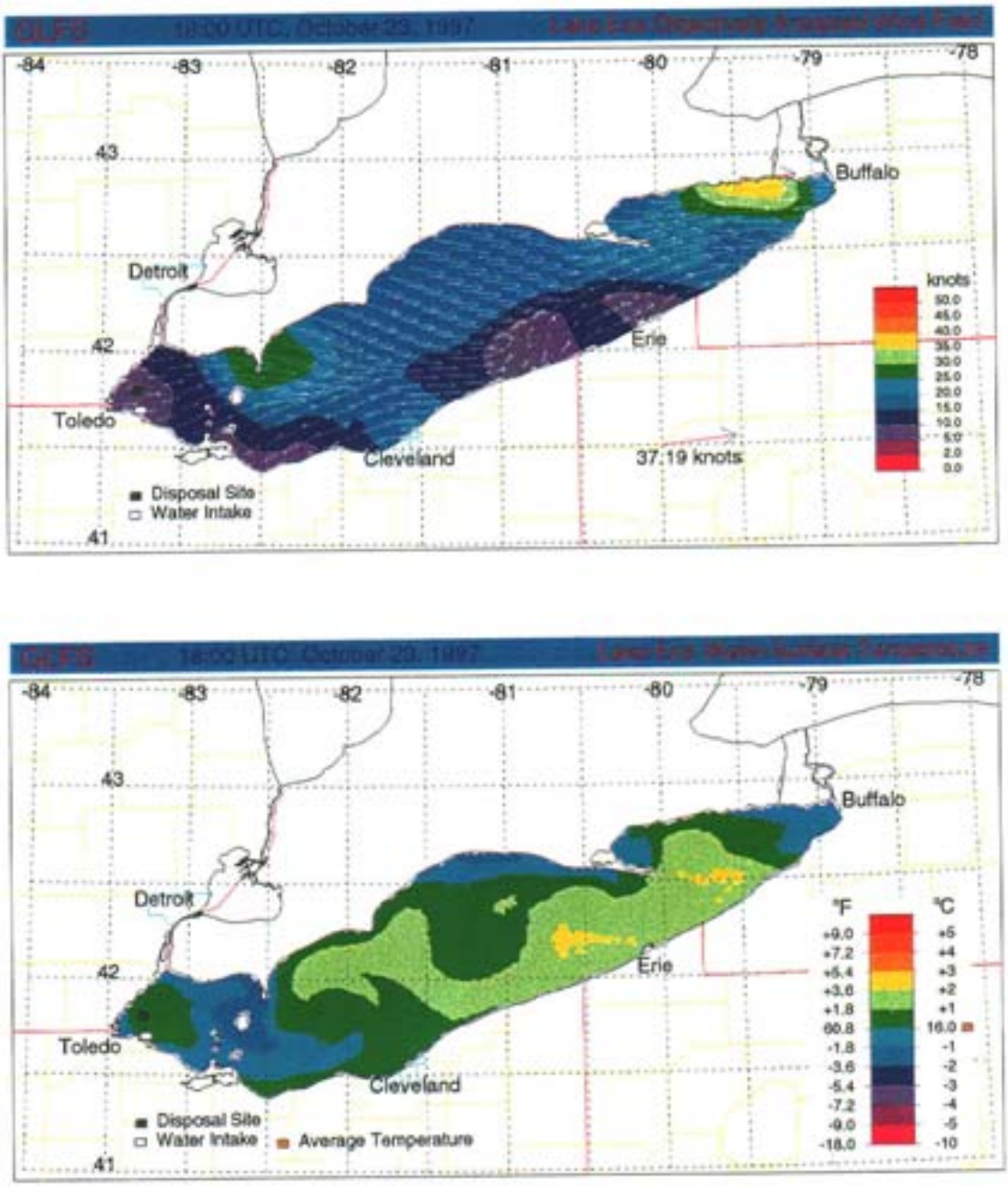

Figure A.27 Water-surface wind speed and temperature distributions for October 23, 1997.

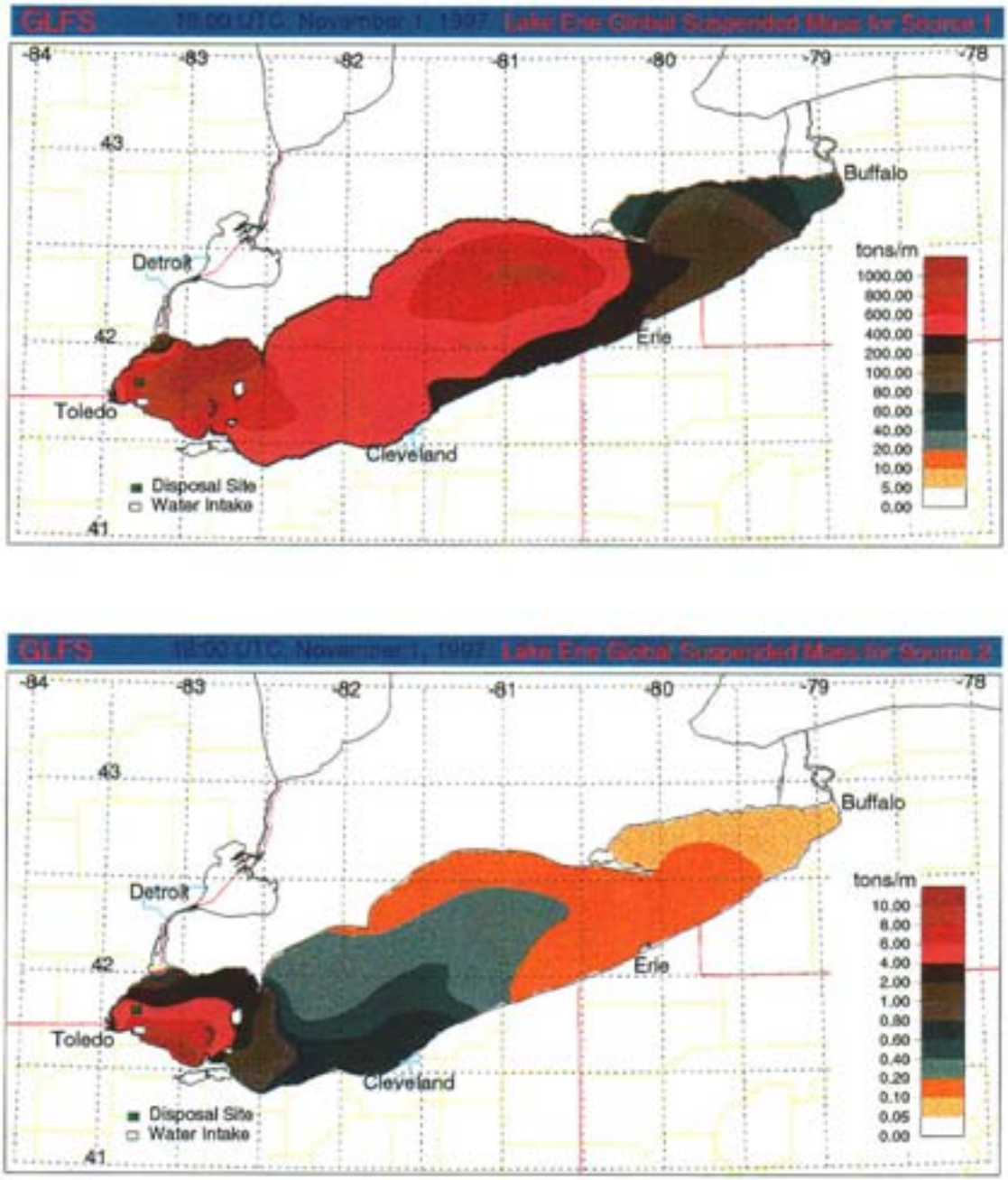

Figure A.30 Horizontal distributions of the global suspended mass of the sediments originating from source 1 (lake bottom) and source 2 (disposal site) for November 1, 1997.

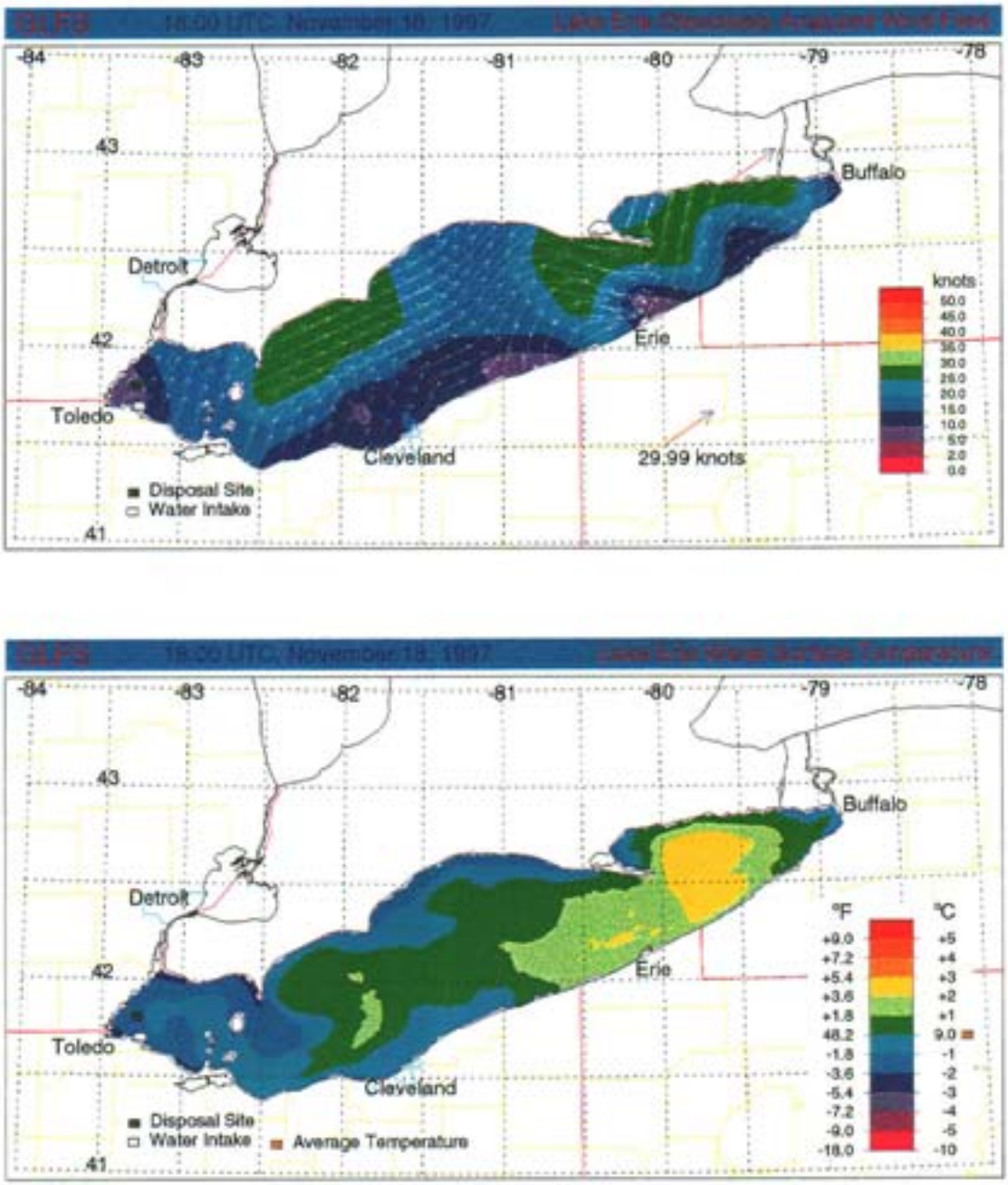

Figure A.31 Water-surface wind speed and temperature distributions for November 18, 1997.

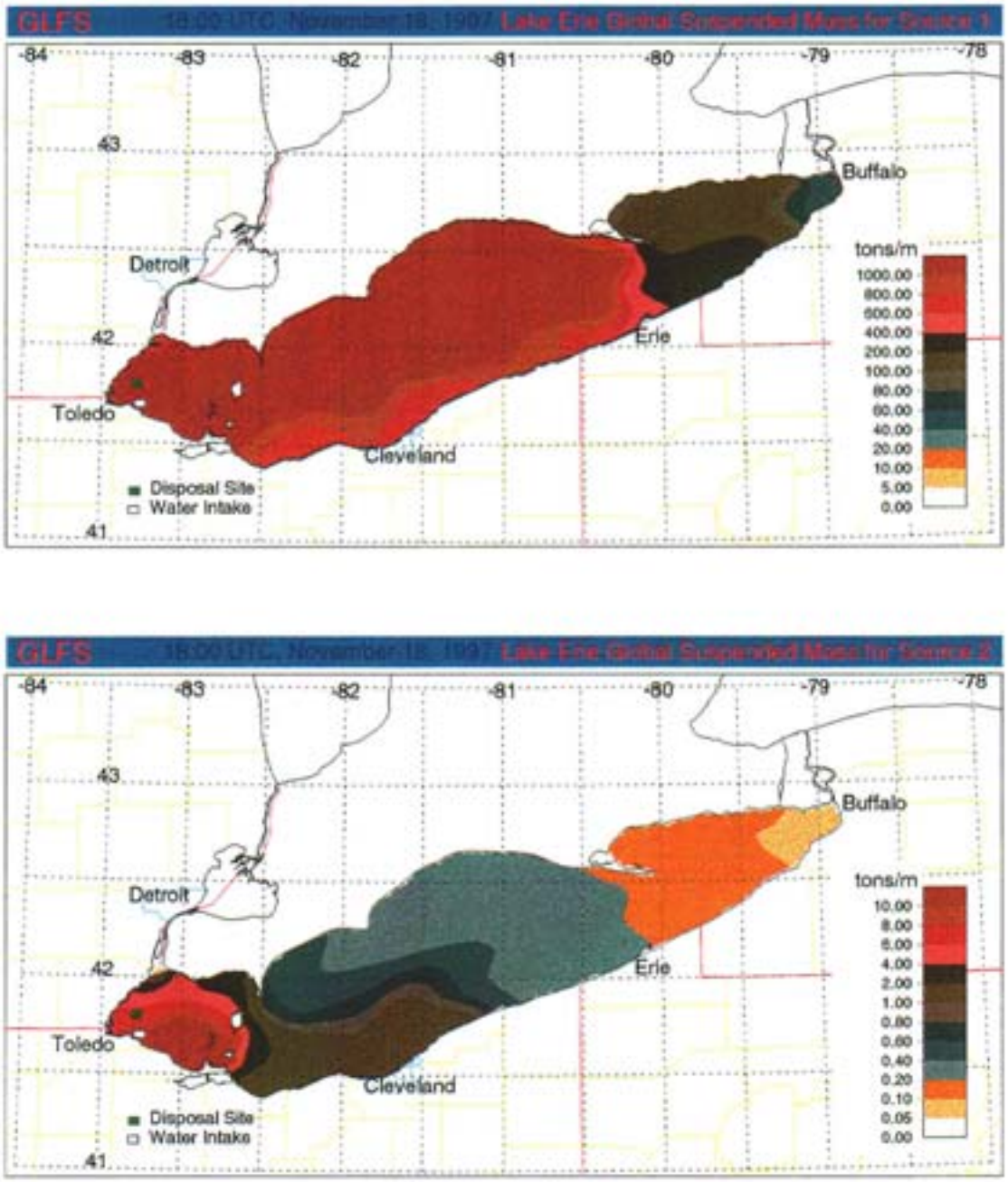

Figure A.32 Horizontal distributions of the global suspended mass of the sediments originating from source 1 (lake bottom) and source 2 (disposal site) for November 18, 1997.

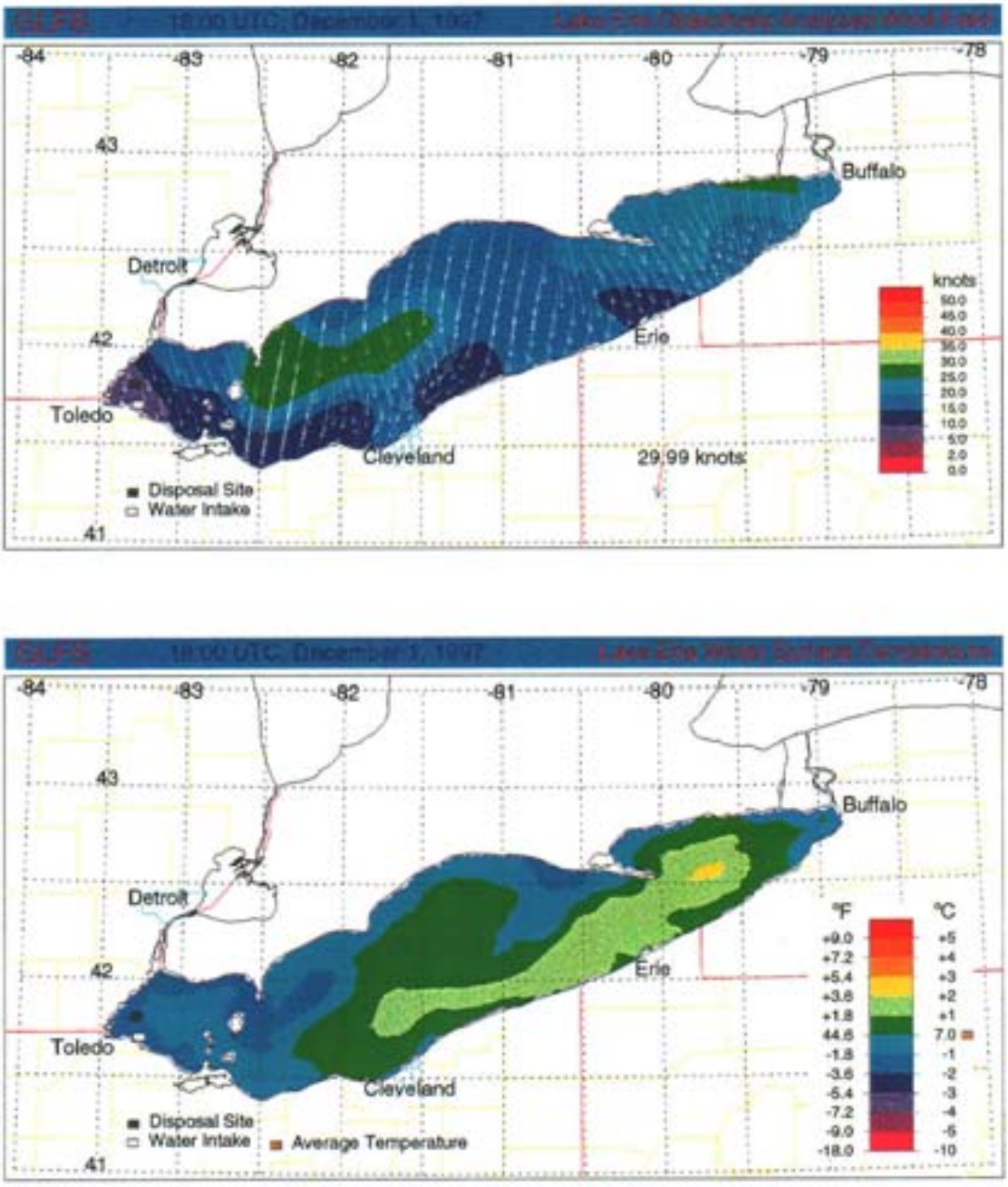

Figure A.33 Water-surface wind speed and temperature distributions for December 1, 1997.

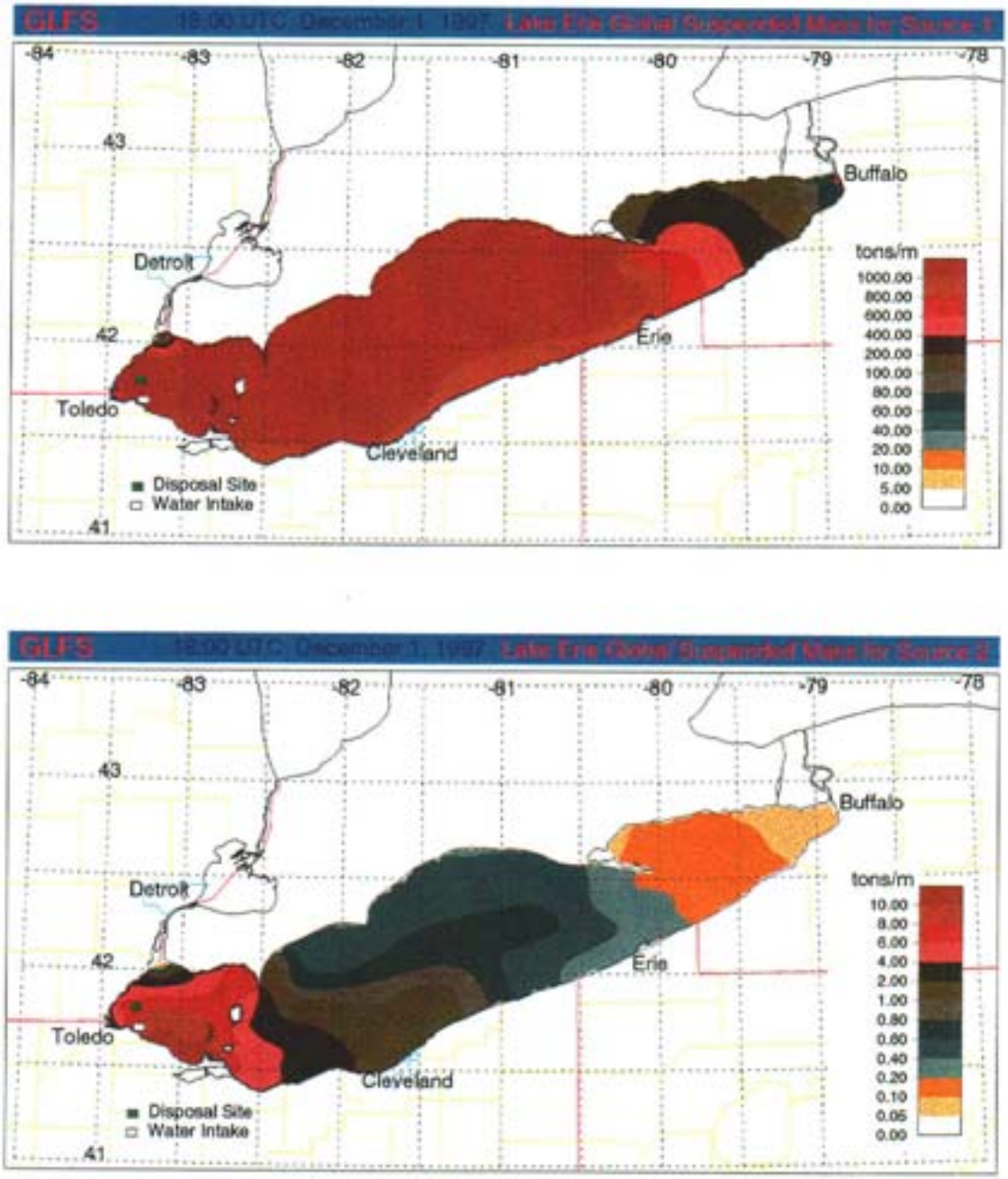

Figure A.34 Horizontal distributions of the global suspended mass of the sediments originating from source 1 (lake bottom) and source 2 (disposal site) for December 1, 1997.

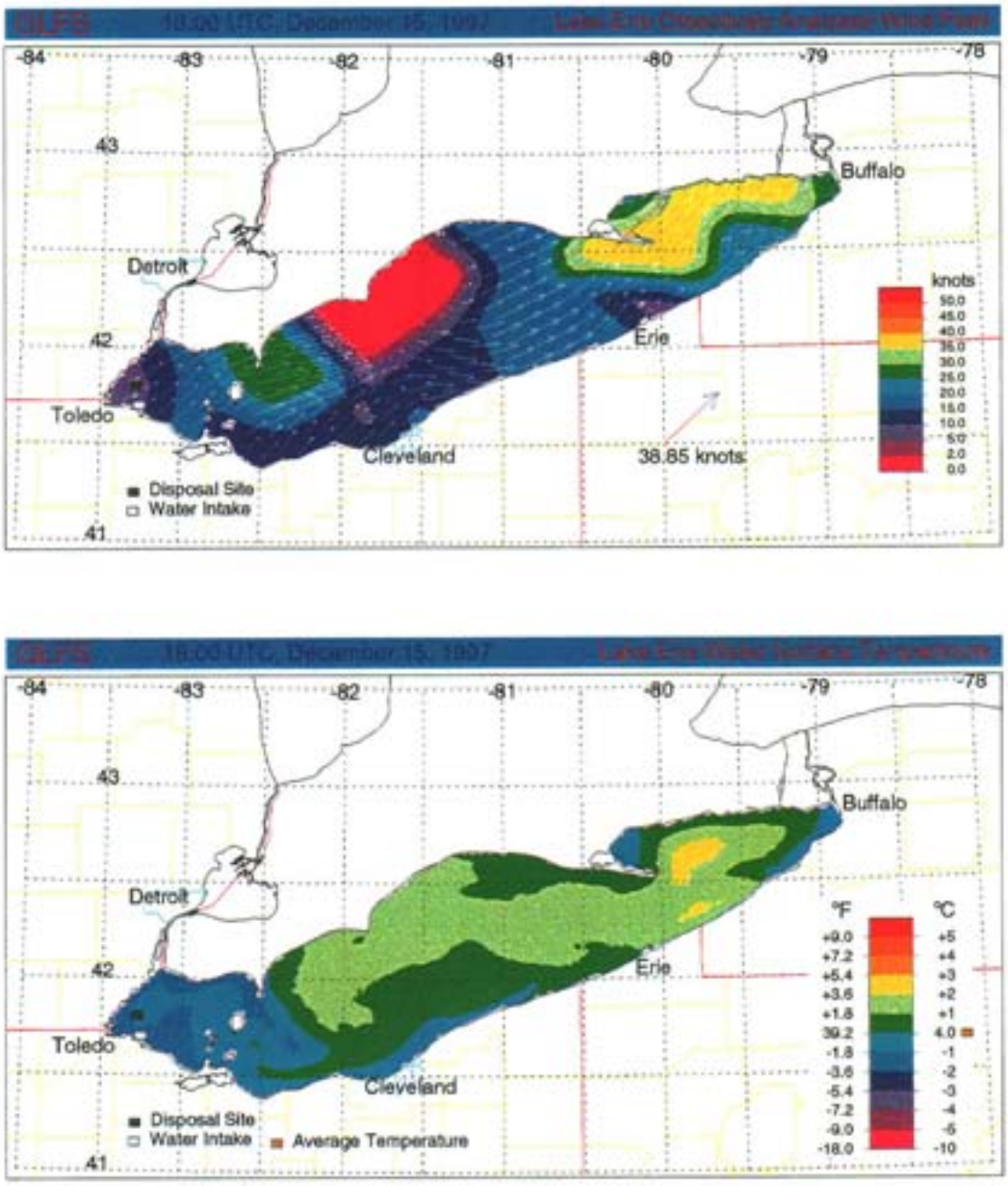

Figure A.35 Water-surface wind speed and temperature distributions for December 15, 1997.

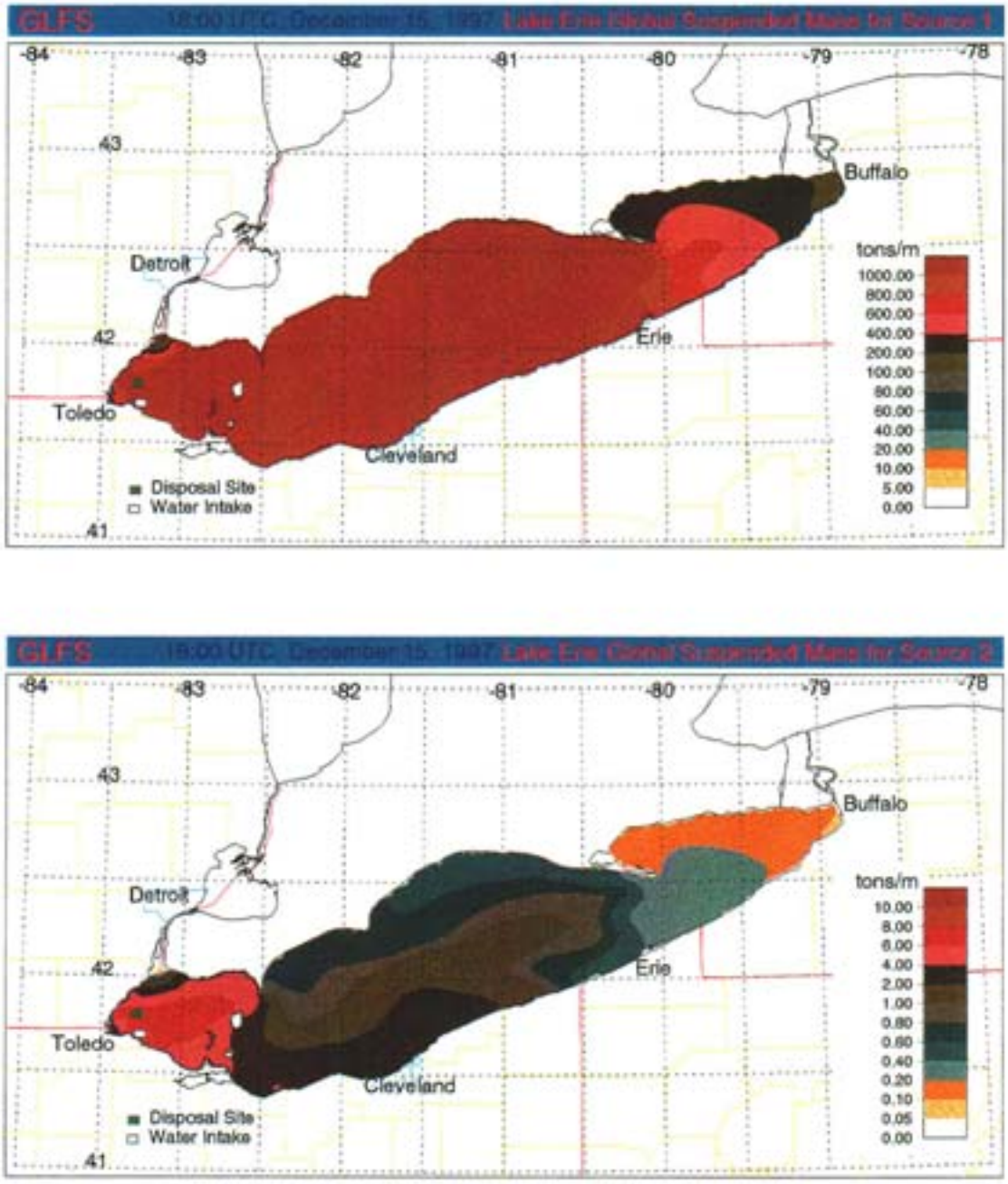

Figure A.36 Horizontal distributions of the global suspended mass of the sediments originating from source 1 (lake bottom) and source 2 (disposal site) for December 15, 1997.

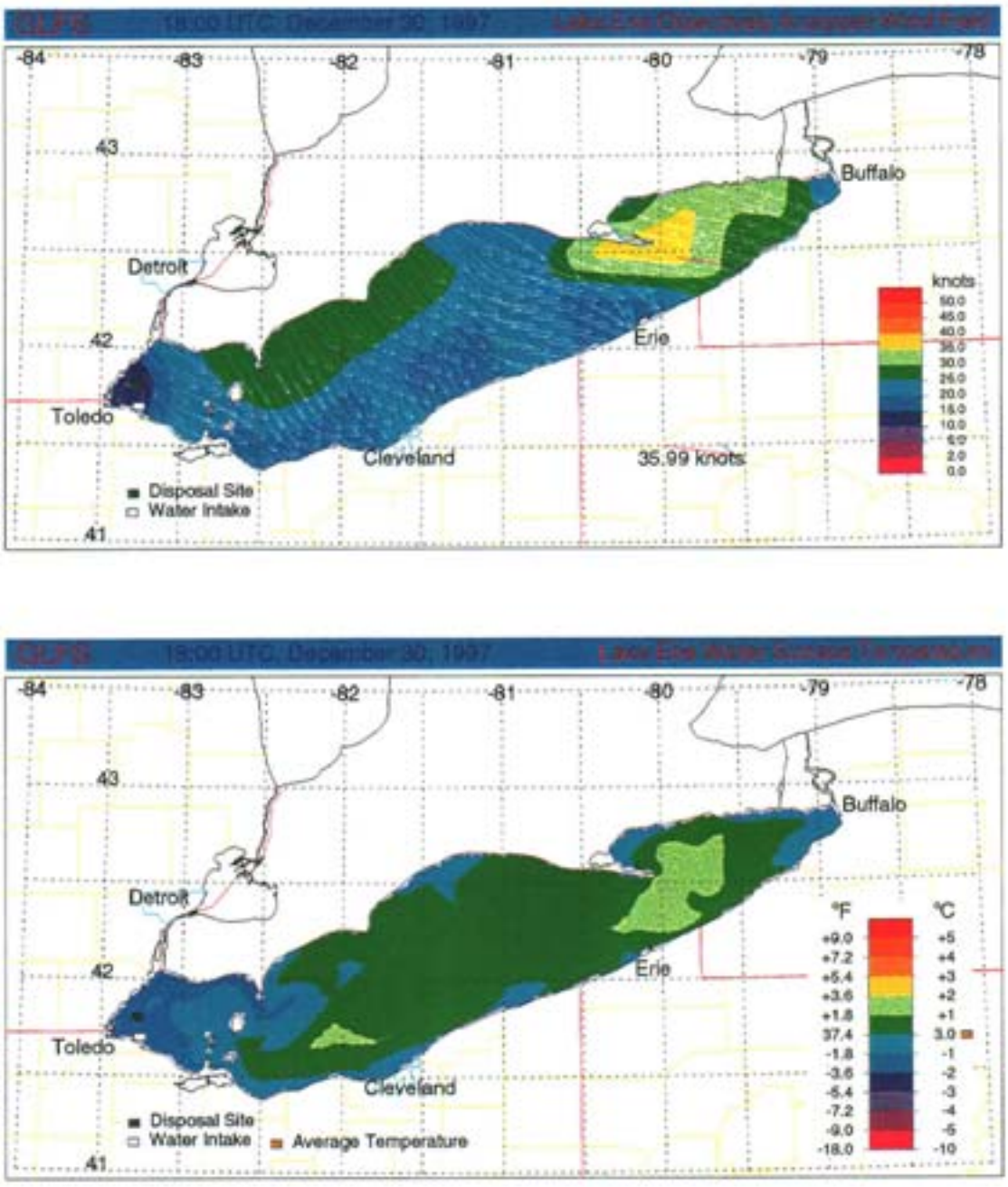

Figure A.37 Water-surface wind speed and temperature distributions for December 30, 1997.

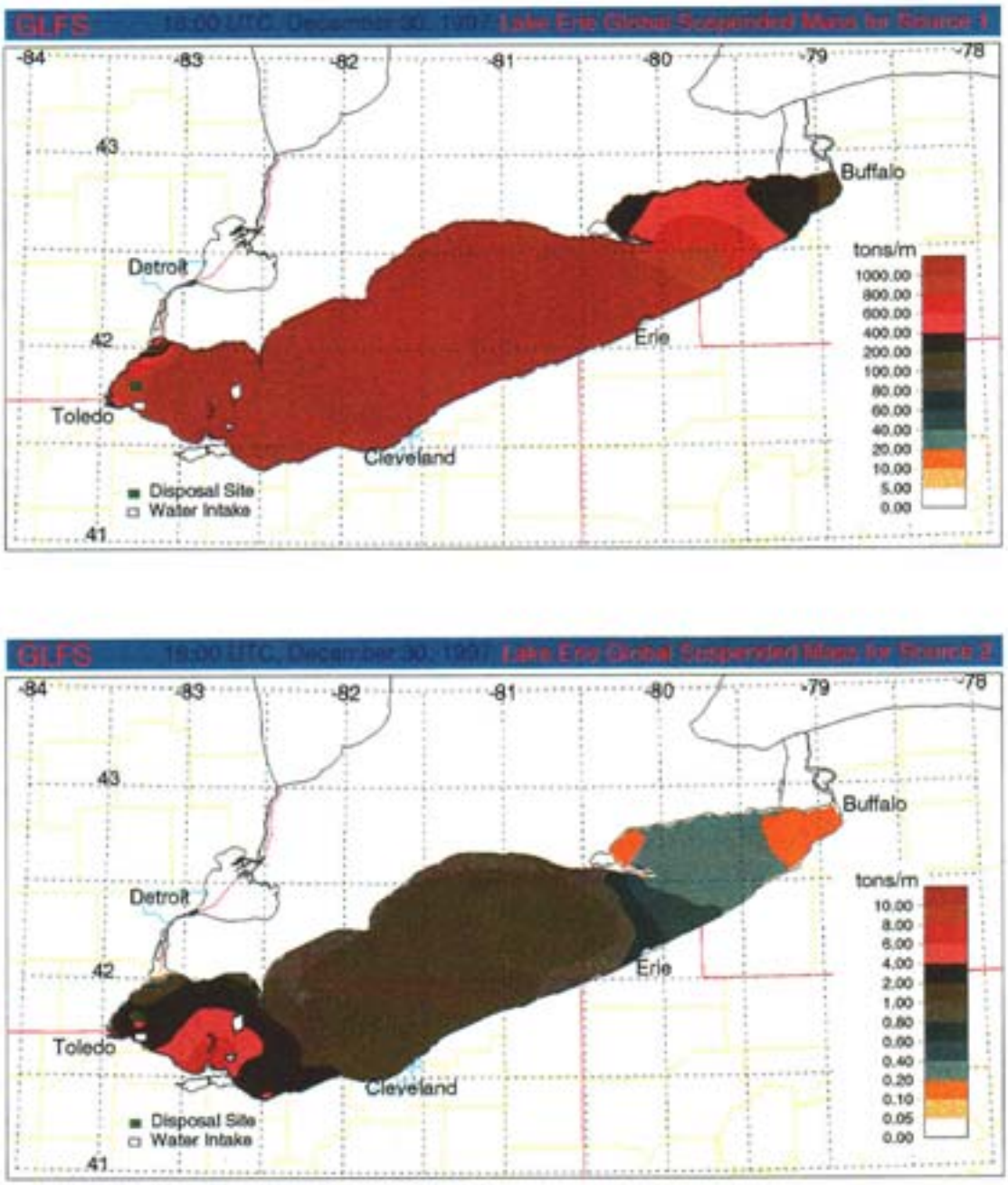

Figure A.38 Horizontal distributions of the global suspended mass of the sediments originating from source 1 (lake bottom) and source 2 (disposal site) for December 30, 1997.

Appendix B

Summary Plots of the Total Suspended Mass of the Sediments Originating from the Different Sources.

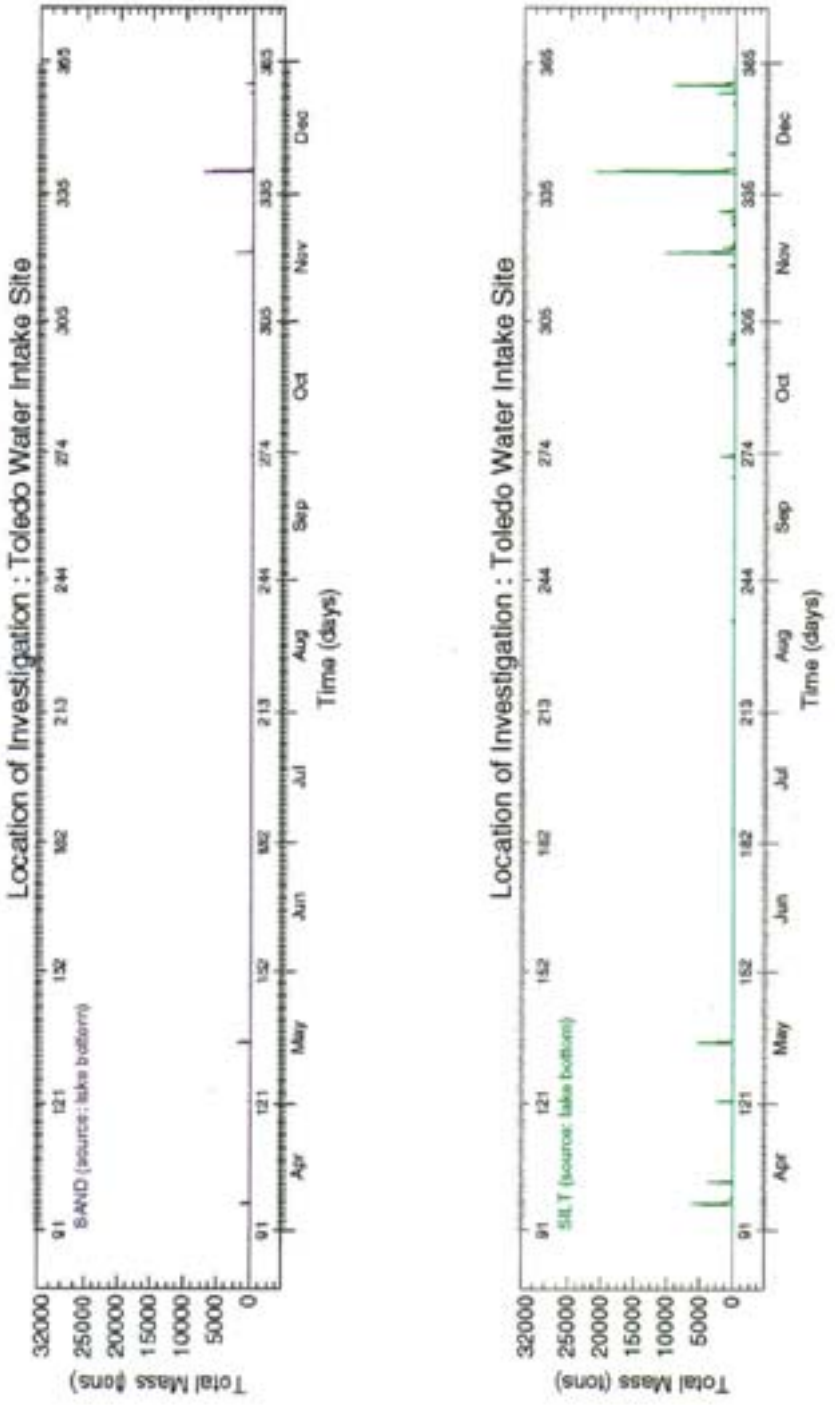

Figure B.1 Time traces of the total suspended mass at the water intake site of the sand and silt sediment classes originating from the lake bottom.

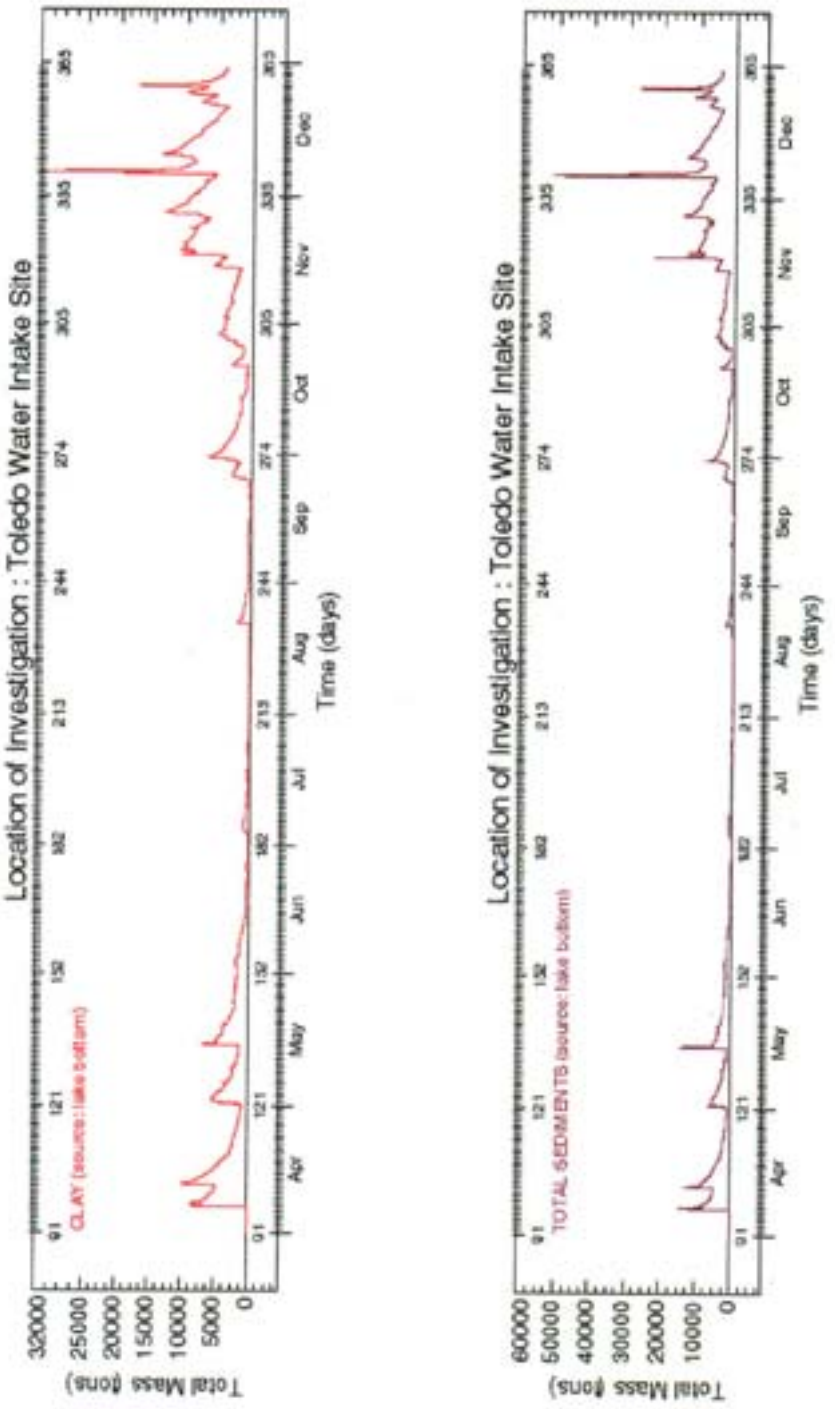

Figure B.2 Time traces of the total suspended mass at the water intake site of the clay sediment class and the global sediments originating from the lake bottom.

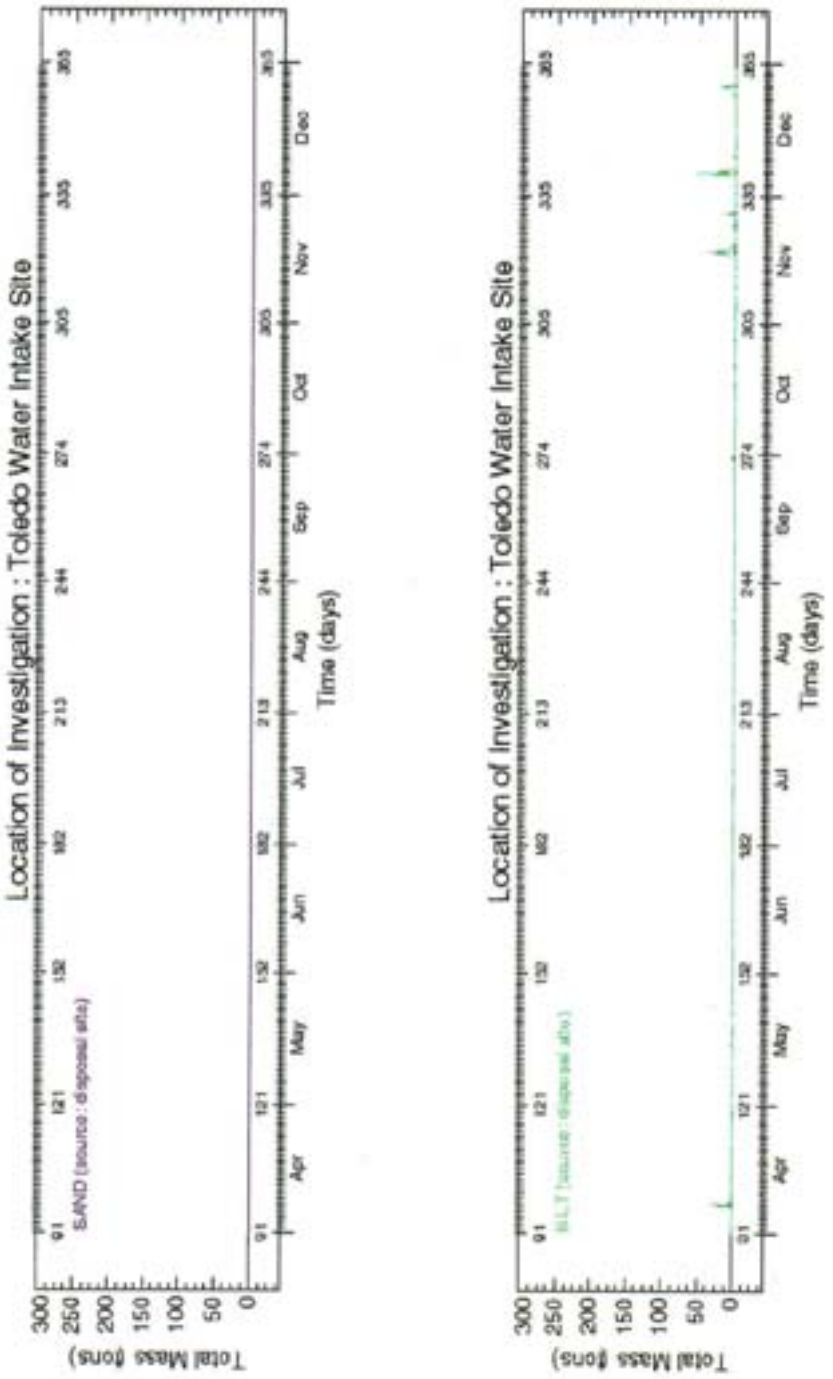

Figure B.3 Time traces of the total suspended mass at the water intake site of the sand and silt sediment classes originating from the disposal site.

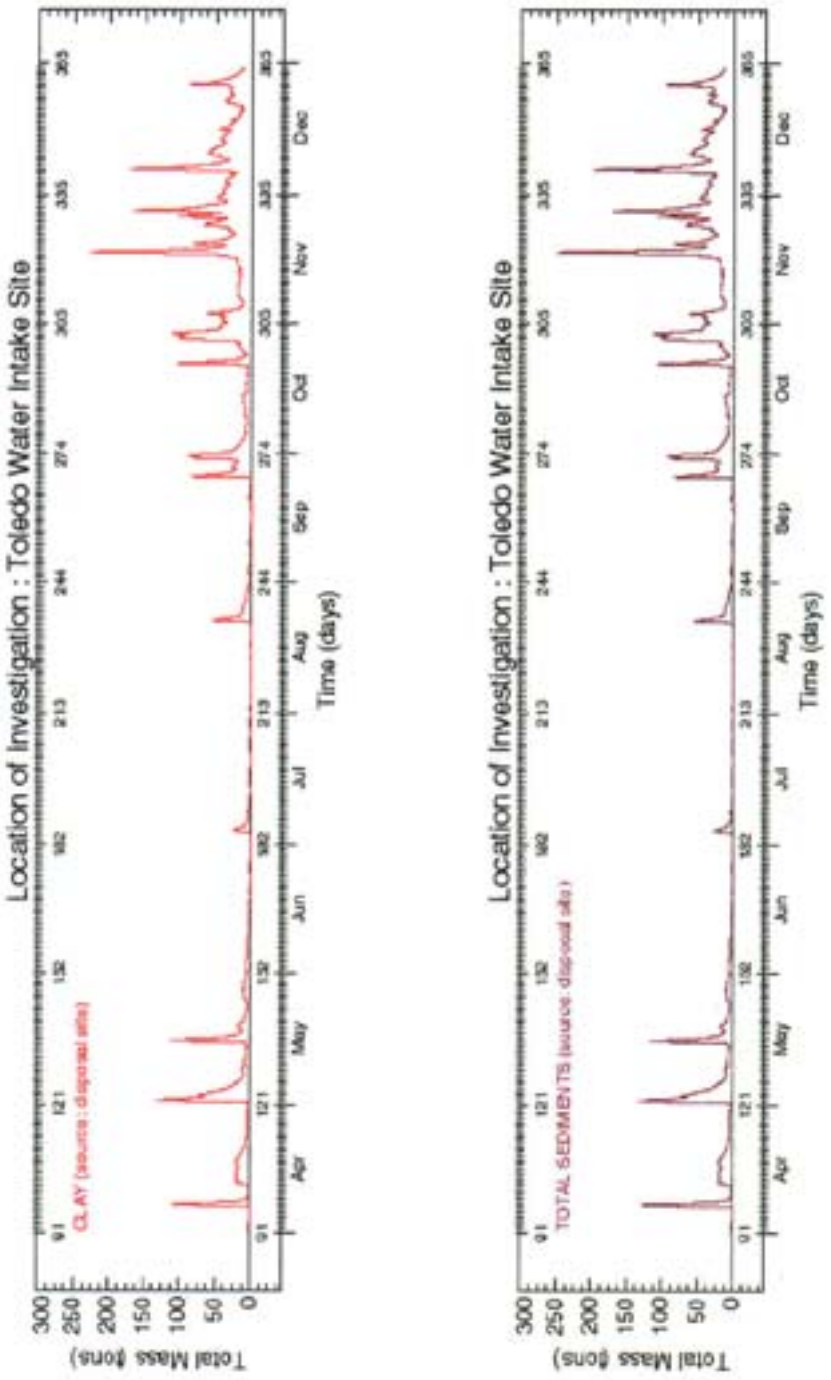

Figure B.4 Time traces of the total suspended mass at the water intake site of the clay sediment class and the global sediments originating from the disposal site.

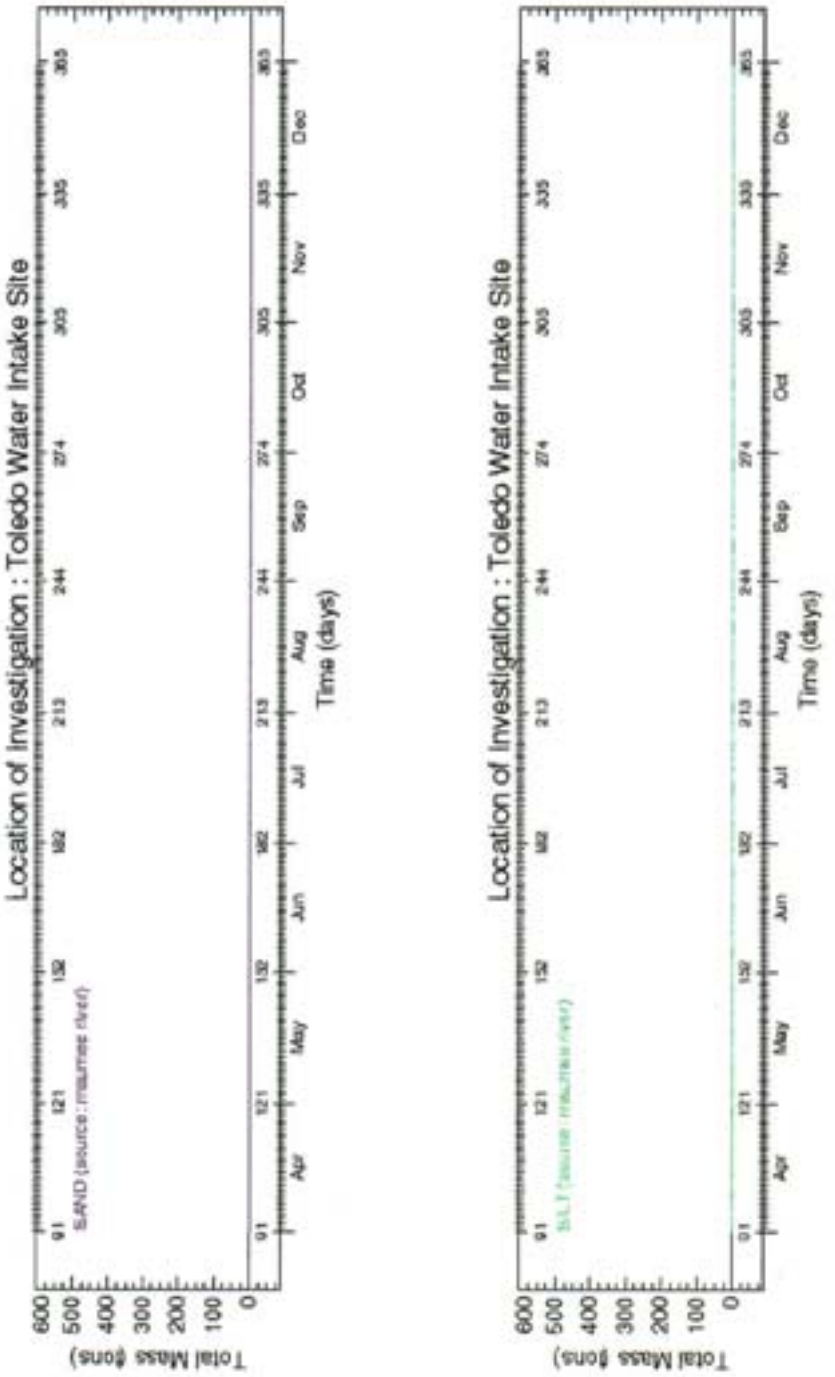

Figure B.5 Time traces of the total suspended mass at the water intake site of the sand and silt sediment classes originating from the Maumee River.

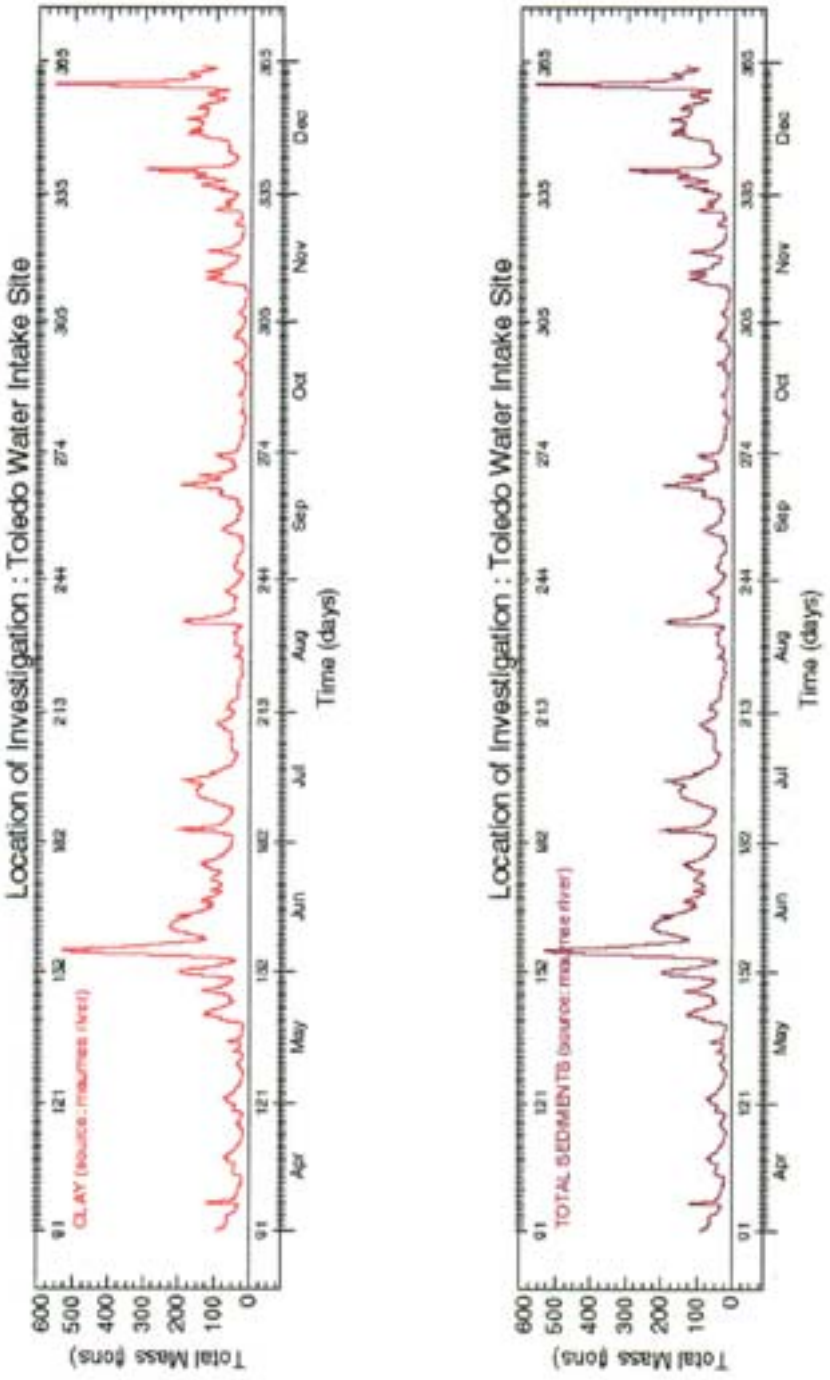

Figure B.6 Time traces of the total suspended mass at the water intake site of the clay sediment class and the global sediments originating from the Maumee River.

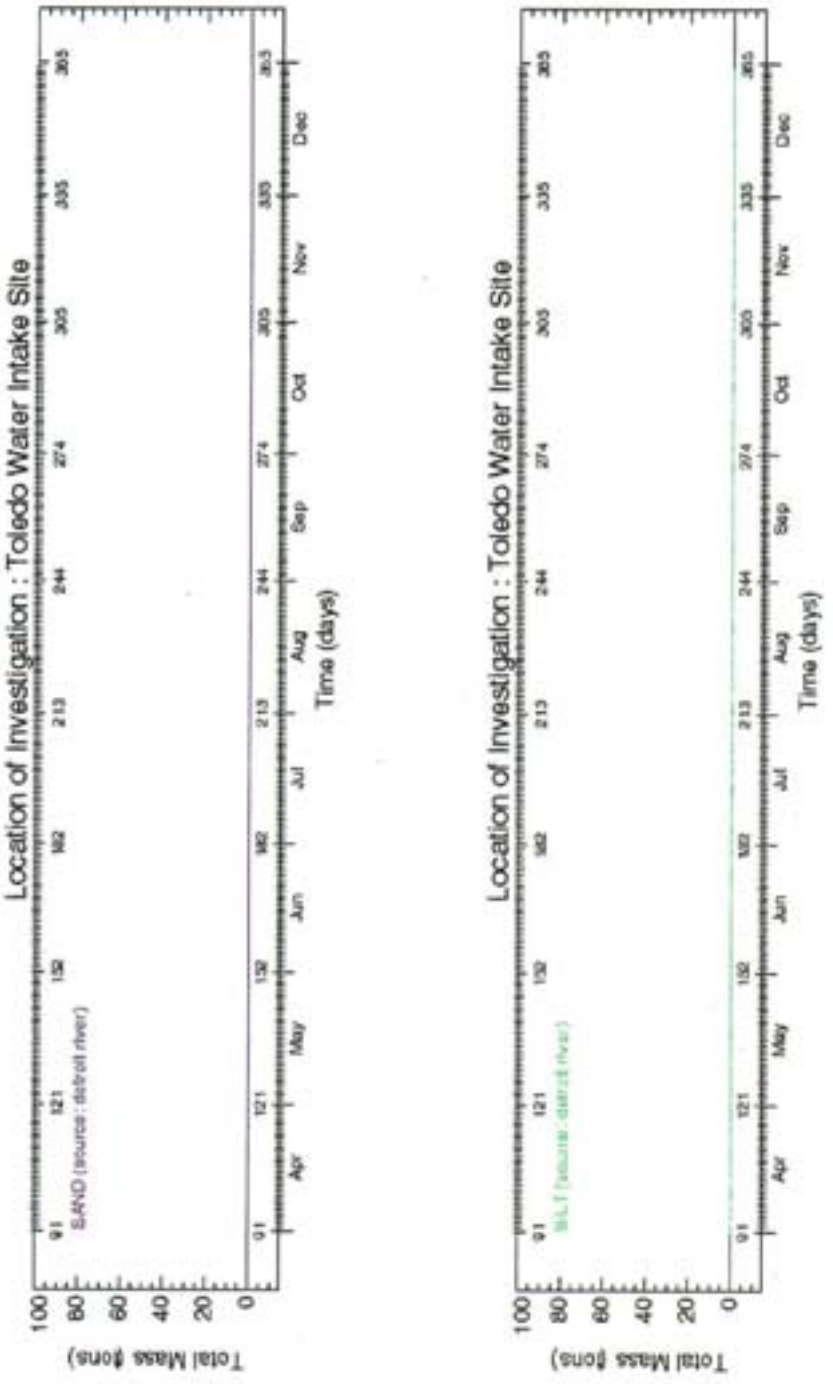

Figure B.7 Time traces of the total suspended mass at the water intake site of the sand and silt sediment classes originating from the Detroit River.

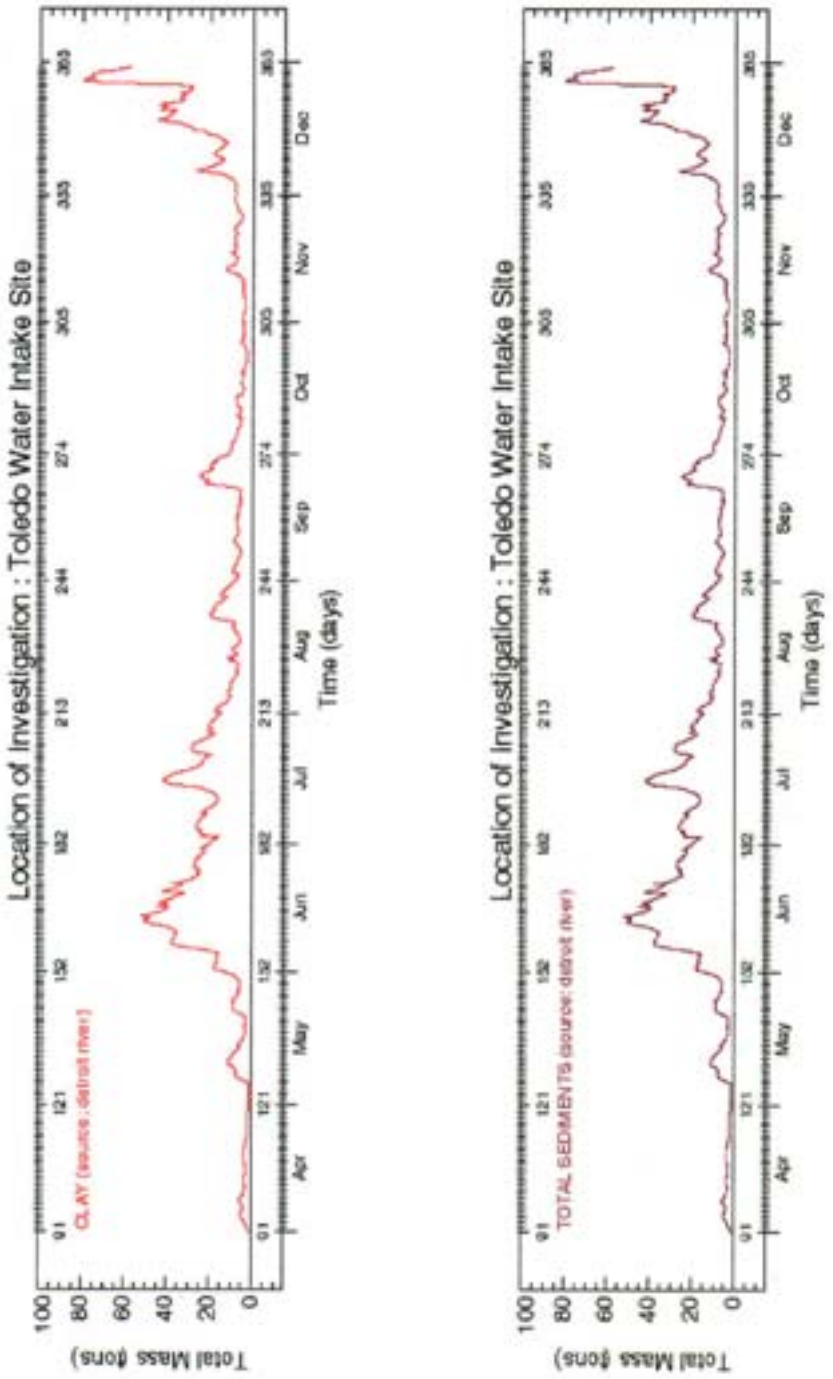

Figure B.8 Time traces of the total suspended mass at the water intake site of the clay sediment class and the global sediments originating from the Detroit River.

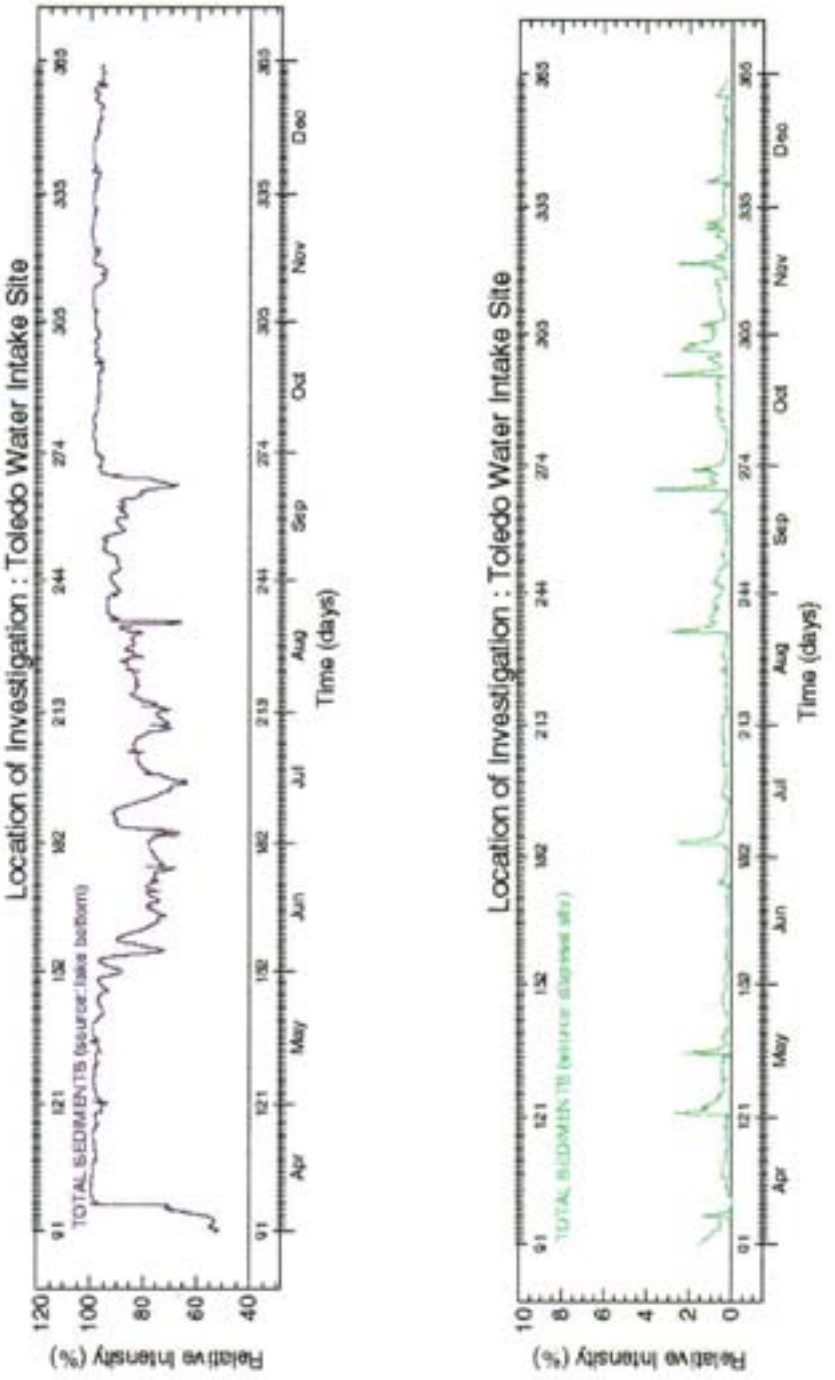

Figure B.9 Relative intensity, percent of the total suspended sediment mass from all sources, at the water intake site of the global sediments originating from source 1 (lake bottom) and source 2 (disposal site).

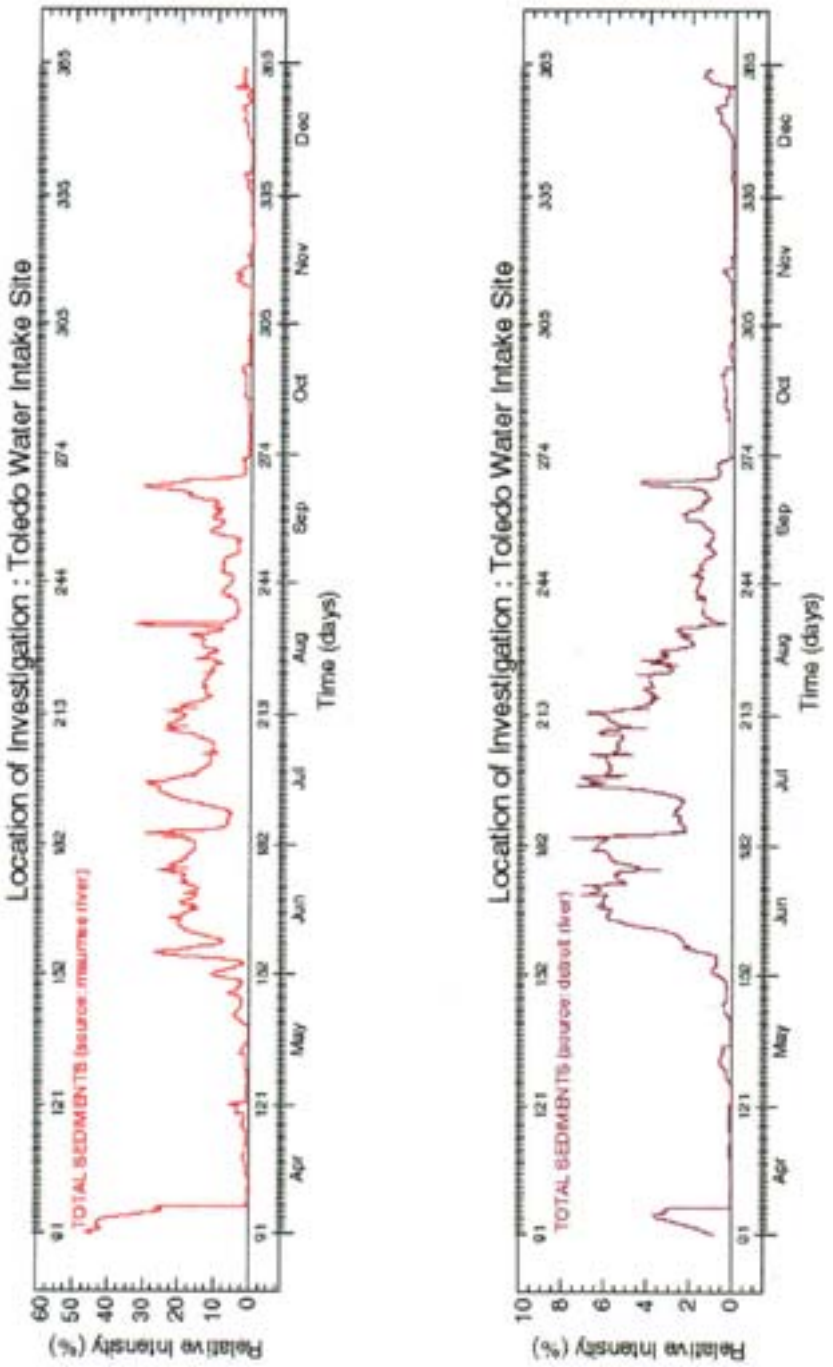

Figure B.10 Relative intensity, percent of the total suspended sediment mass from all sources, at the water intake site of the global sediments originating from source 3 (Maumee River) and source 4 (Detroit River).

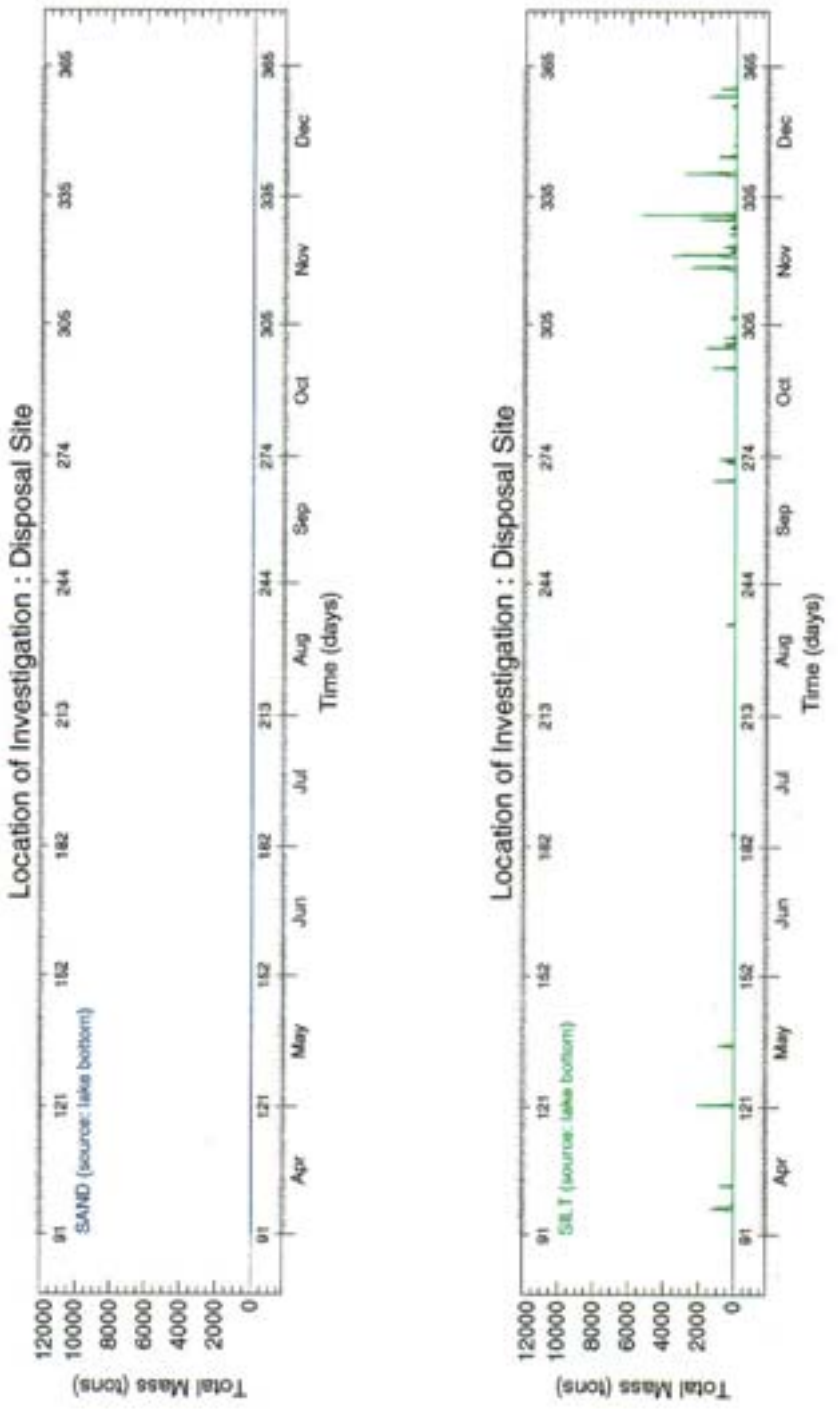

Figure B.11 Time traces of the total suspended mass at the disposal site of the sand and silt sediment classes originating from the lake bottom.

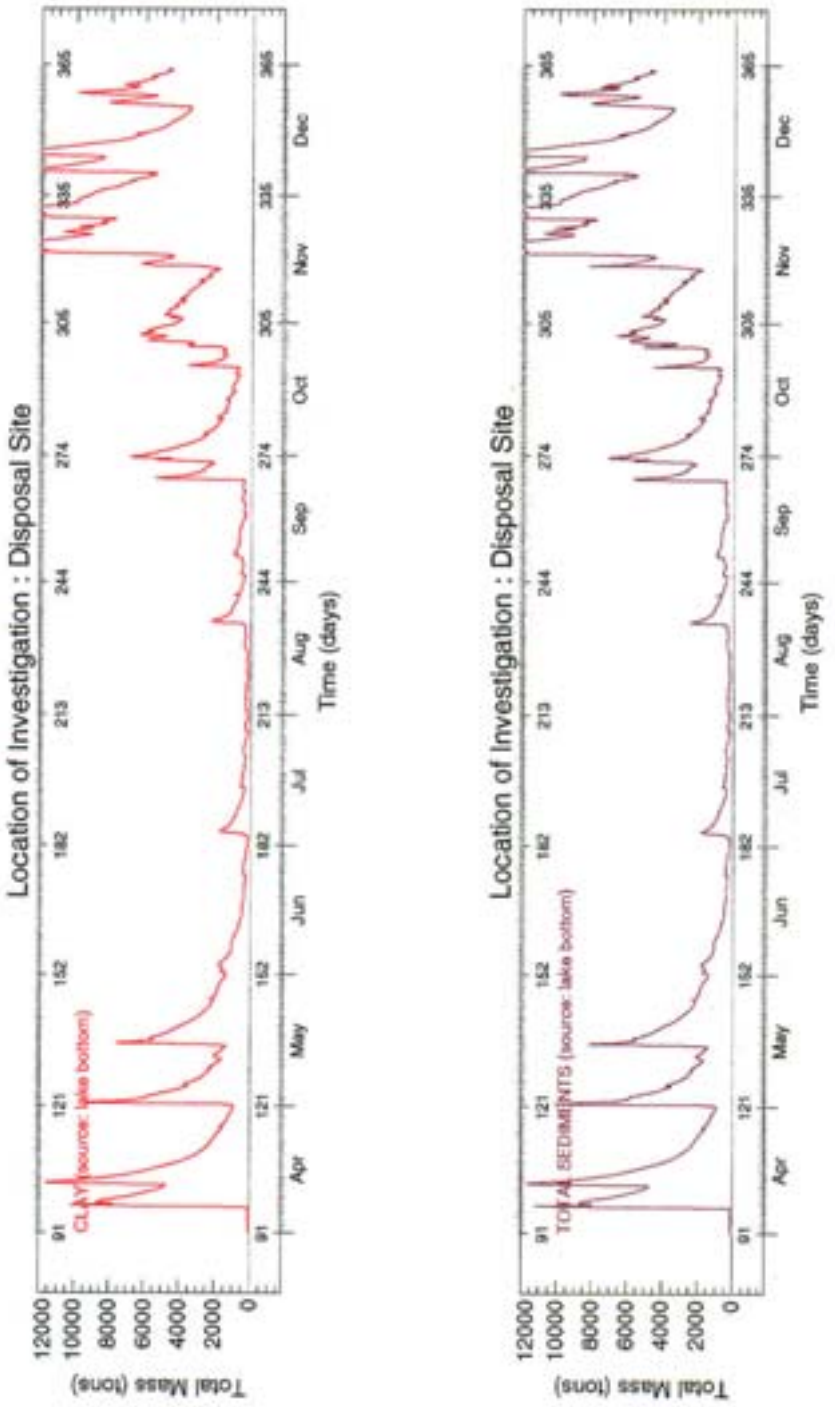

Figure B.12 Time traces of the total suspended mass at the disposal site of the clay sediment class and the global sediments originating from the lake bottom.

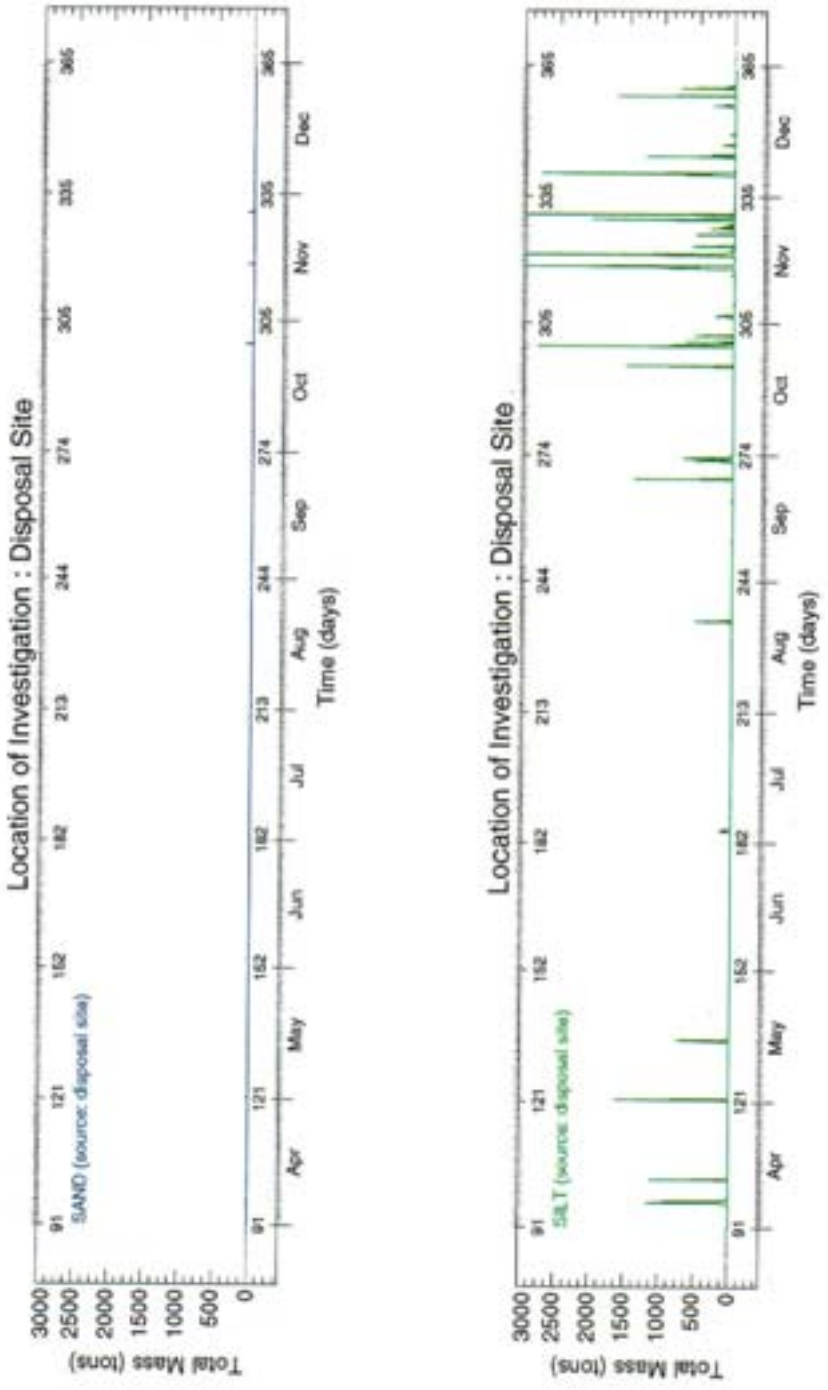

Figure B.13 Time traces of the total suspended mass at the disposal site of the sand and silt sediment classes originating from the disposal site.

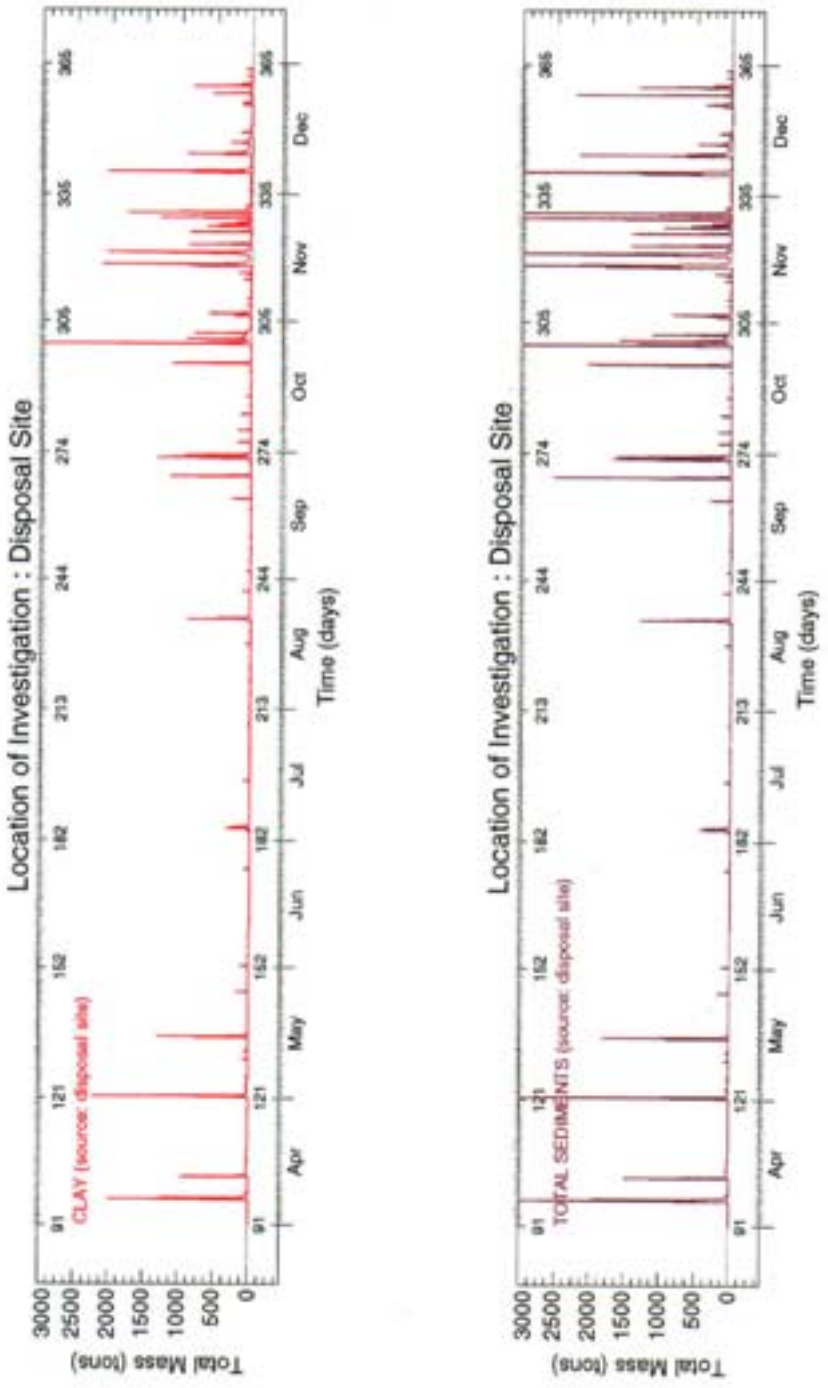

Figure B.14 Time traces of the total suspended mass at the disposal site of the clay sediment class and the global sediments originating from the disposal site.

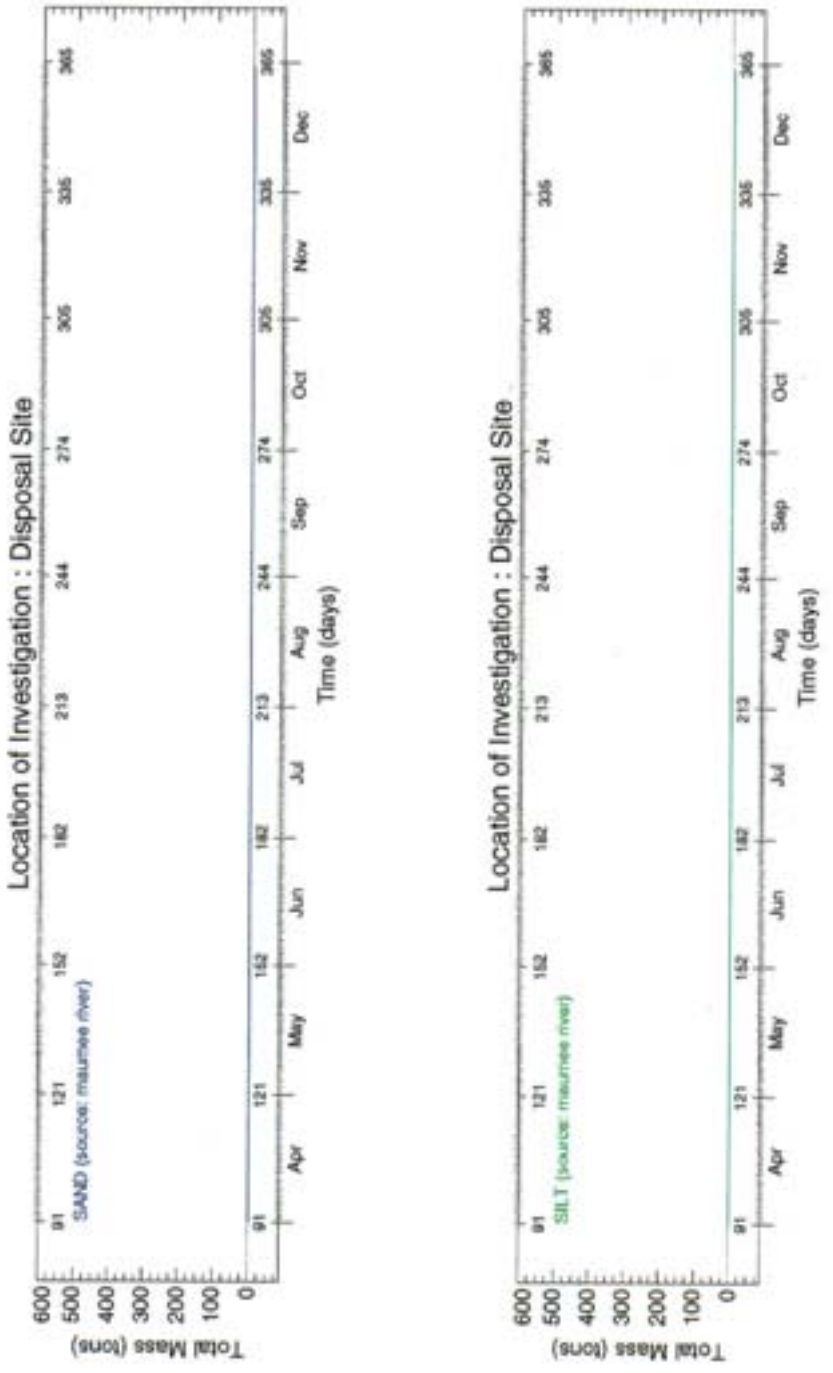

Figure B.15 Time traces of the total suspended mass at the disposal site of the sand and silt sediment classes originating from the Maumee River.

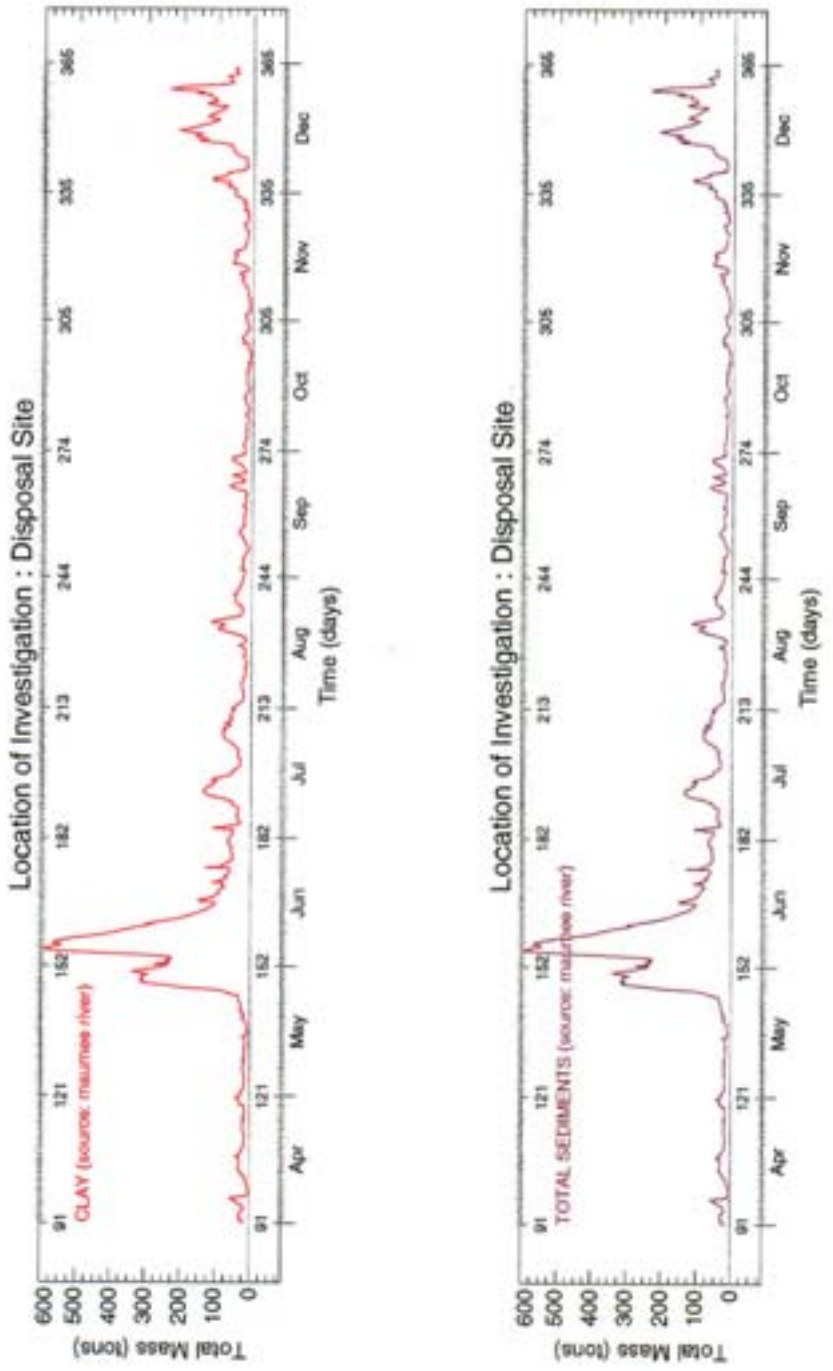

Figure B.16 Time traces of the total suspended mass at the disposal site of the clay sediment class and the global sediments originating from the Maumee River.

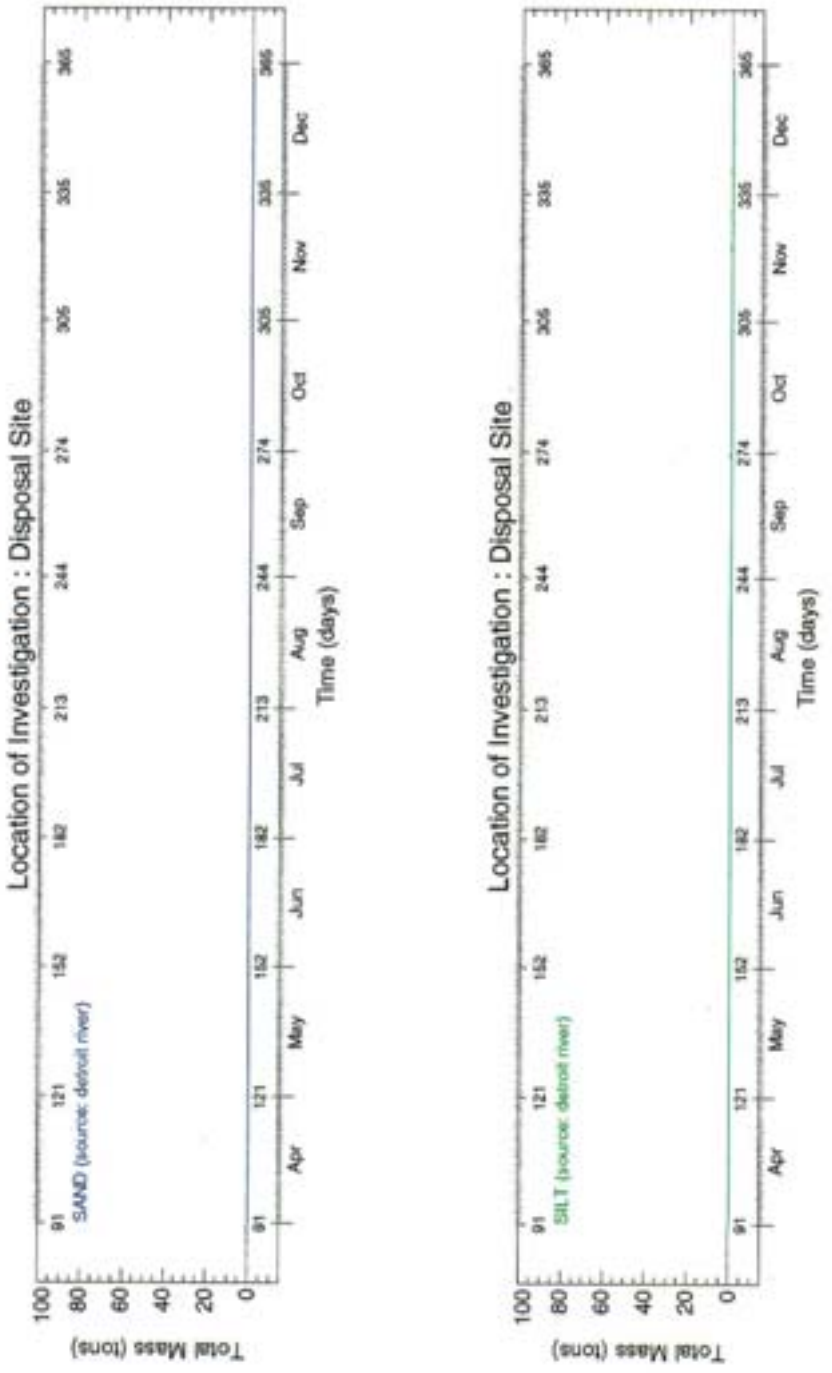

Figure B.17 Time traces of the total suspended mass at the disposal site of the sand and silt sediment classes originating from the Detroit River.

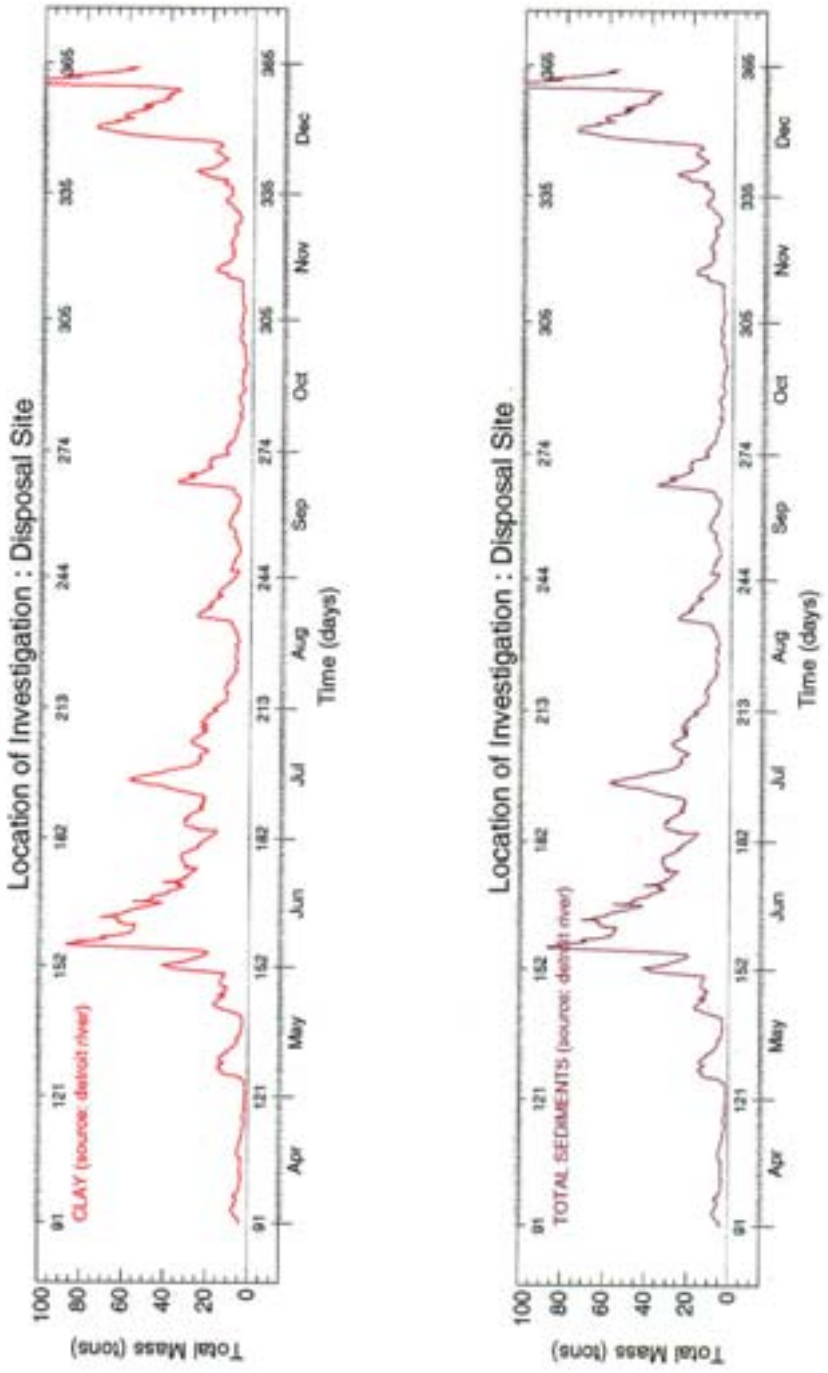

Figure B.18 Time traces of the total suspended mass at the disposal site of the clay sediment class and the global sediments originating from the Detroit River.

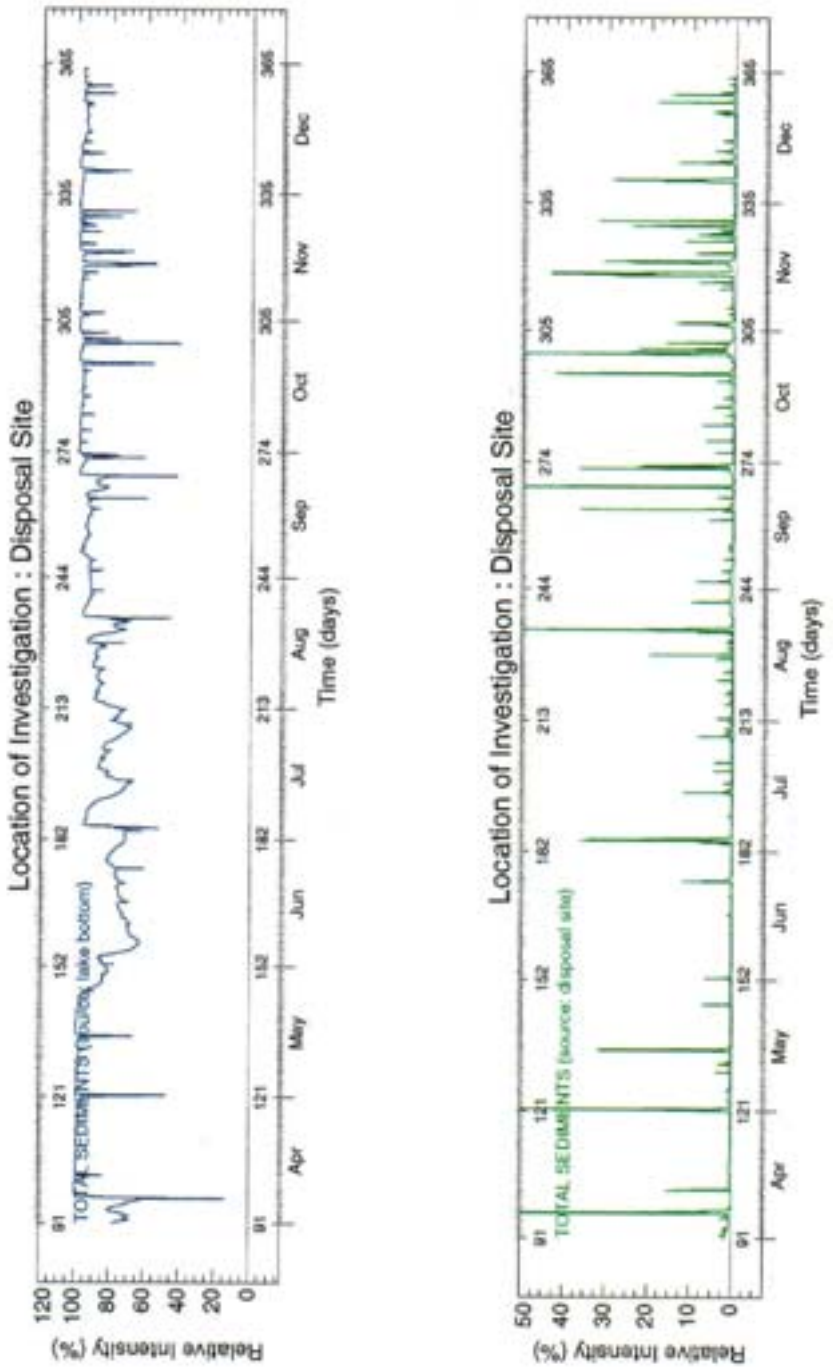

Figure B.19 Relative intensity, percent of the total suspended sediment mass from all sources, at the disposal site of the global sediments originating from source 1 (lake bottom) and source 2 (disposal site).

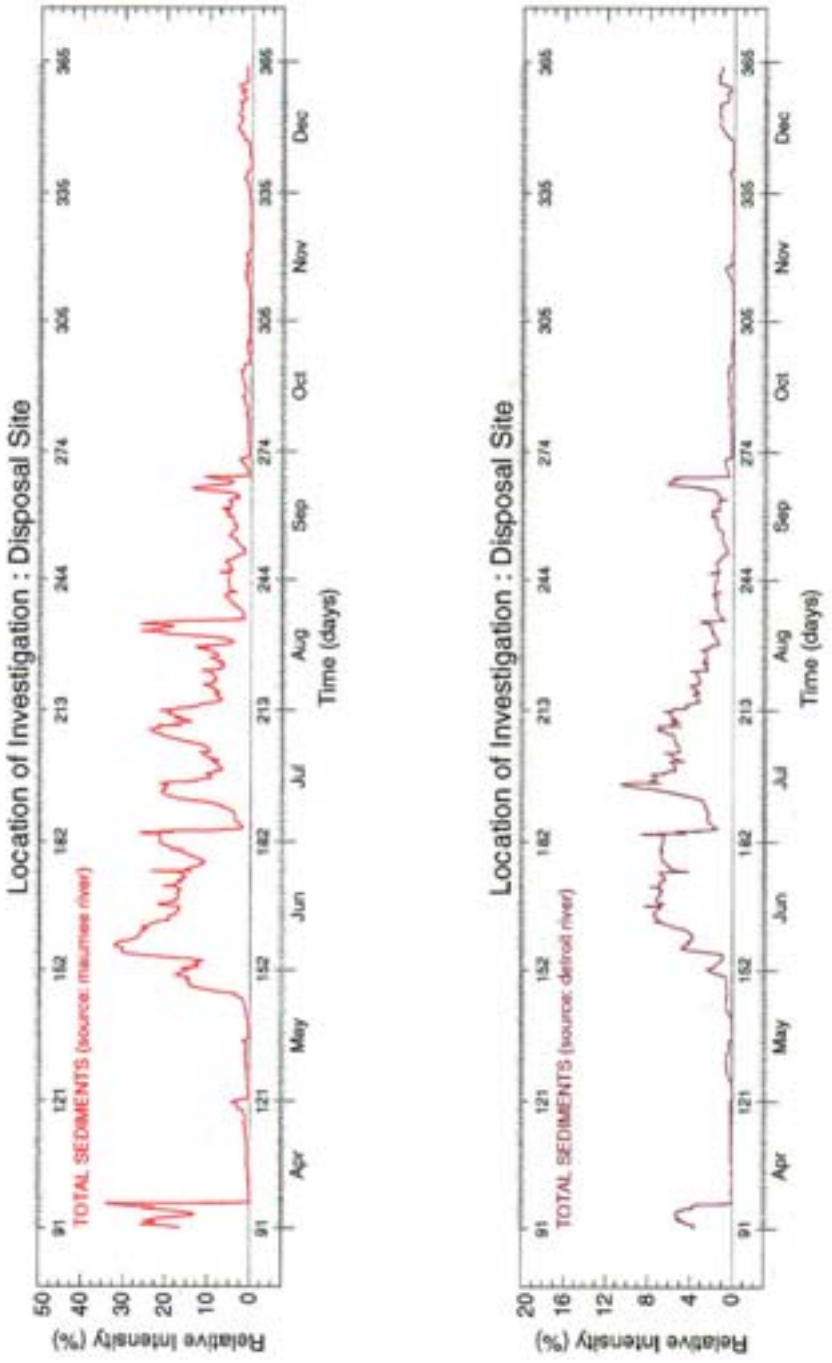

Figure B.20 Relative intensity, percent of the total suspended sediment mass from all sources, at the disposal site of the global sediments originating from source 3 (Maumee River) and source 4 (Detroit River).